Program Final Report

on

FIRST MAJOR IMPROVEMENTS TO THE TWO-CURVE DUCTILE FRACTURE MODEL – PART I MAIN BODY

Emc^2 project number 03-G78-01

to

U.S. Department of Transportation
Research and Special Programs Administration
Washington DC 20590
Agreement No. DTRS56-03-T-0007

and

Pipeline Research Council International, Inc.
Arlington, VA 22209
PRCI PROJECT # PR-276-04505

by

D. Rudland, D.-J. Shim, H. Xu, D. Rider,
P. Mincer, D Shoemaker and G. Wilkowski

Engineering Mechanics Corporation of Columbus
3518 Riverside Drive, Suite 202
Columbus, OH 43221

May 2007

TABLE OF CONTENTS

LIST OF FIGURES

LIST OF TABLES

EXECUTIVE SUMMARY

The most commonly used fracture analyses procedure for the prediction of minimum arrest toughness and fracture speed for axially running cracks in line pipe materials for natural gas transmission pipeline applications is the Battelle Two-Curve approach. This analysis procedure incorporates the gas-decompression behavior with the fracture toughness of the pipe material to predict the minimum Charpy energy required for crack arrest. For this model, the effect of backfill on the propagating crack fracture speeds is lumped into one empirically based "backfill coefficient," which does not distinguish different soil types or strengths. This backfill coefficient was developed from a series of full-scale experiments conducted in the 1970s. Some modifications to this backfill coefficient have been proposed for frozen soil as a function of moisture content, and for water backfill for offshore applications, but no attempt has been made to quantify the effects of soil type, total density or strength on the fracture speeds of propagating cracks in line pipe steels. Some work by other researchers has attempted to model the soil, both theoretically and numerically, but has not taken into account all of the soil characteristics that will affect the crack-driving force; inertial effects, compressive strength behavior under the pipe, and shear strength behavior above the flap formation.

This report presents a joint program between the U.S. Department of Transportation and the Pipeline Research Council International aimed at gathering a better understanding of soil behavior and its affect on the fracture speed of running axial flaws in buried line pipe materials. The results from this program are combined with other full-scale experimental data in developing a modification to the treatment of backfill in the Battelle Two-Curve approach for calculating minimum arrest toughness. This first major improvement to the Battelle Two-Curve approach is incorporated into a computer code called PIPE-DFRAC.

In this program, a series of small-diameter (6-inch) burst experiments (Mojave experiments) with well-controlled soil conditions were conducted to investigate the effects of soil properties on the fracture speeds. In addition a larger program, conducted by the Japan Gas Association (JGA experiments), was conducted that investigated the effects of backfill depth, backfill moisture content, and pipe diameter on the crack arrest behavior of larger diameter (24-inch to 30-inch) X80 line pipe. These results were combined with the Mojave experimental results to gain a better understand of the effects of backfill on the fracture speeds in line pipe steels.

The Mojave experiments were conducted in two series, one each year of the program. In the first series of experiments, the controlled backfill covered one end of the pipe, while the other end of the pipe was unbackfilled for comparison purposes. In the second series of experiments one half of each end of the pipe was backfilled with controlled conditions, with the remaining pipe unbackfilled. The soils used in these experiments consisted of clay, sandy-silt and fine grain sand in order to bound the soils used at the full-scale experimental test sites around the world. Even though there were experimental difficulties during these experiments, the results showed a trend in the fracture speeds with both moisture content and strength.

The strength of the soil was characterized for each soil by a series of standard soil experiments. The soils chosen for the Mojave experiments span the range of soils in the national and international full-scale test sites. In addition to the soils used in the Mojave experiments, the soils

from the Japan Gas Association (JGA, FORCE), Advantica (Spadeadam) and CSM (Sardinian) test sites were also characterized. Each soil was first characterized by sieve analyses and visual characteristics and given a soil classification identification. After determination of optimum moisture content, the soils were characterized for strength by an applicable test, i.e., unconfined compression or triaxial compression for cohesive soils and direct shear or triaxial compression for non-cohesive soils. The results suggested that non-cohesive soils showed no significant shear strength unless a large confining pressure is present. For typical buried pipe, this confining pressure for the soil above the pipe is minimal; therefore, strength will not play a significant role in pipe buried in sand. However, cohesive soils show much high strength for lower confining pressures due to cohesive bond between the soil particles. Soil strength should play a role in the fracture behavior for these soils.

Through a data/information exchange agreement, the recent full-scale experimental results generated by the JGA were used to compliment this effort. The JGA conducted four large-diameter, full-scale crack arrest experiments on X80 line pipe materials. In these experiments, the soil used was sand, the backfill depth was controlled and the moisture content was measured before the experiments. The experiments were conducted on 30-inch diameter and 24-inch diameter pipes with a variety of toughness levels. The results from these highly instrumented experiments suggested that the backfill depth was linearly related to the change in fracture velocities, but the soil strength had little effect. In addition, the difference in the behavior due to the pipe diameter (30-inch versus 24-inch) was found to be insignificant. Finally, the minimum arrest toughness was also related to the depth of the backfill. From these results, a correction to the fracture velocity for backfill depth was developed in this project.

In addition to the full-scale test results, advanced instrumentation for the measurement of crack-tip-opening angle on full-scale experiments was developed. In this effort, two devices were investigated. The first was an electronic device called the Hall Effect device, which uses a sensor that is calibrated to a magnetic field. Once calibrated, this device can track six degrees of freedom between the sensor and the magnet. When mounted on a pipe such that the magnet and sensor span the crack path, the output will give the crack-opening displacement and crack-opening angle as a function of time. The second device is more mechanical and is called the WireCTOA device. In this device, a high strength wire spans the crack path and is attached to a calibrated aluminum sliding rod that is pulled out of a non-metallic block as the crack opens. This movement opens an electronic circuit and marks the time for that particular crack opening displacement. The crack-tip-opening angle is inferred from the fracture speed data and the WireCTOA signals. Since such instrumentation has to tolerate a violent testing environment, extensive development occurred in this program, as well as trials from each device in both the Mojave and JGA experiments. Even though much work is still needed in development of these devices, the WireCTOA device measured a CTOA value of 5 degrees on a pipe joint in a JGA full-scale test with a Charpy energy of 71J. From past small-scale experiments, this result seems reasonable for material with this Charpy energy.

Combining the full-scale results from the JGA and Mojave efforts allowed the development of a modified backfill coefficient for use in the Battelle Two-Curve approach. This modification takes the backfill depth and level of soil cohesiveness into account for better predictions of arrest toughness. However, the data is still limited; therefore, the effect of cohesiveness is only

handled qualitatively. Data from the past experiments used in the original derivation of the backfill coefficient were revisited, however, the details about the soil conditions, i.e., soil type, moisture content, compaction level, were vague and therefore of limited use. In addition, past smaller diameter pipe test results were revisited and the results suggested that the form of the fracture velocity equation, i.e., power of 1/6, may not be a constant value and may be related to the pipe diameter. Again, the data on the soil backfill conditions were vague or missing in many cases; therefore, the actual relationship with pipe diameter could not be verified. In addition, advanced dynamic numerical crack growth analyses were conducted to verify the fracture speeds in unbackfilled conditions, which were severely mispredicted by the Battelle Two-curve approach. The results suggested that the Battelle Two-Curve analysis may not be predicting the correct fracture speed for the smaller diameter pipe and the problem may be in the exponent of the fracture velocity curve. Further analyses are required to verify this conclusion.

The modifications to the backfill coefficient developed in this program were incorporated into a user-friendly Windows-based computer code (PIPE-DFRAC) that utilizes the Battelle Two-Curve approach. Modeled after an older code written for TransCanada PipeLines, PIPE-DFRAC contains not only the trends developed in this program, but corrections for non-linear Charpy effects and recently published statistical correction for toughness as a function of grade level. This user-friendly code is available to all participants of this program.

Finally, there are several aspects of future work that are recommended.

- First of all, the soil characterization can be further refined. The soil strength tests conducted in this effort were standard experiments, but do not capture the true behavior of the soil surrounding the pipeline. Other advanced soil testing techniques are more costly, but possibly more representative for these conditions.
- Second, the effect of diameter needs further investigation. The results suggest that the form of the velocity equation in the Battelle Two-Curve approach should be a function of the pipe diameter, but the results were not sufficient to develop such trends. Additional experiments and numerical analyses are needed to define these trends.
- Third, refinement is needed for each of the CTOA instrumentation developed in this effort. Electrical shielding and calibrations refinement is needed for the Hall Effect device, while torque and epoxy issues need to be addressed for the WireCTOA device.
- Finally, it is recommended that research is continued in developing a numerical model that takes into account the fluid-pipe interaction for decompression calculations, the soil-pipe interaction, and CTOA methodology for crack extension. Once this model is fully developed, sensitivity analyses can be conducted and an easier to use model can be developed. The development of this type of numerical model was proposed to the DOT in 2005 and can be revisited if this work is warranted.

1 INTRODUCTION

The most commonly used fracture analyses procedure used for the prediction of minimum arrest toughness and fracture speed for axially running cracks in natural gas transmission line pipe materials is the Battelle Two-Curve approach. This analysis procedure incorporates the gas-decompression behavior with the fracture toughness of the pipe material to predict the minimum Charpy energy required for crack arrest. For this model, the effect of backfill on the propagating crack fracture speeds is lumped into one empirically based "backfill coefficient," which does not distinguish different soil types or strengths. Some modifications to this backfill coefficient have been proposed for frozen soil as a function of moisture content, and for water backfill for offshore applications, but no attempt has been made to quantify the effects of soil type, total density or strength on the fracture speeds of propagating cracks in line pipe steels.

This report details the results generated from a program sponsored by the US Department of Transportation and the Pipeline Research Council International aimed at making the first improvement to the treatment of soils in the Battelle Two-Curve approach. A series of small-diameter (6-inch) pipe burst tests were conducted with different well-controlled soil backfill conditions. These experiments were conducted at the Emc^2 high-energy pipe experimental facility in Mojave California and thus termed, "Mojave Experiments." Different soil types ranging from cohesive clays to fine grain sands were used as backfill in the burst tests The moisture content and compaction level was well controlled and varied between the experiments. In addition soil strength experiments were carried out to determine the changes in strength with moisture and compaction levels.

Through an information exchange agreement, the results from a series of large-diameter burst tests conducted by the Japanese Gas Association were combined with the results generated in this program to develop trends relating the depth and cohesiveness of soil to the fracture velocities. These trends are incorporated into a Windows-based computer code called PIPE-DFRAC for the calculation of minimum arrest toughness.

Also in this program, unique instrumentation was developed for the measurement of the crack-tip-opening-angle (CTOA) in a full-scale burst test. The CTOA has been shown to be a very useful fracture parameter in predicting stable crack propagation for large amounts of crack growth in engineering materials. The development of this instrumentation focused on an electronic device, termed the Hall Effect Sensor, and a mechanical devices, termed the WireCTOA. The details of the development of each of these devices and their application to both the Mojave and JGA experiments are presented in this report.

This report is divided into three main parts and associated appendices. Part I of the report details the overall conclusions of this report and the development of trends relating backfill and the axial crack fracture speeds. Part II of this report details the experimental results from the Mojave experiments, while Part III of this report details the experimental results from the JGA experiments. Within Part I, Section 2 describes the information exchange agreement between the USDOT, the PRCI, and the JGA. Section 3 describes the background to the Battelle Two-Curve approach, the effects of soils on fracture and the use of the crack-tip-opening angle as a fracture parameter for linepipe steels. Section 4 details the soil characterization efforts conducted in this effort and includes the details of the soil strength experiments conducted.

Sections 5 and 6 summarize the experimental results from the Mojave and JGA testing programs respectively. Section 7 describes the effort to dynamically measure the CTOA during a full-scale experiment. Section 8 describes the modification to the backfill coefficient based on the results from this program and presents some unique results from a dynamic crack growth numerical analysis conducted on unbackfilled small-diameter pipe. Section 9 of this report shows a summary of the PIPE-DFRAC computer code developed in this program that incorporates the Battelle Two-Curve analyses, the most recent non-linear corrections to Charpy and DWTT energies, and the backfill results developed in this program. Section 10 described the future work needed to refine the trends developed in this program and develop a non-empirically based analysis methodology. Finally, Section 11 gives a summary of this report.

2 INFORMATION EXCHANGE AGREEMENT BETWEEN JGA AND DOT/PRCI

As part of an effort to enhance international collaborative efforts in the development of line pipe axial crack arrest experiments and analysis for natural gas transmission applications, an information exchange agreement between the Emc^2 program sponsored by the U.S. DOT, PRCI and the JGA full-scale crack arrest experimental program was initiated. This information exchange was developed so that the experiments and analyses conducted within the programs were shared between the agreement participants, and that the results from these experiments can be used jointly to further the understanding of axial crack arrest in line pipe materials. A summary of the information exchange agreement between the JGA and the Emc^2-PRCI-DOT programs is given in Appendix A.

3 BACKGROUND

3.1 Review of Battelle Two-Curve Approach

The Battelle Two-Curve (BTC) approach is a semi-empirical analysis method for determining the minimum arrest toughness for line pipe steels under normal operating conditions. The approach combines a gas-decompression analysis and a fracture analysis with an iterative process for calculating the minimum arrest toughness.

3.1.1 Review of the development of the original Maxey/Kiefner equations

Embedded in the BTC approach are a series of equations developed by Bill Maxey and John Kiefner [1, 2]. As part of the ductile fracture arrest analysis, it was assumed that there is an effective critical crack length at the onset the crack propagation event. The associated critical axial crack length during the unstable crack propagation is based on a modified Dugdale plastic-zone correction solution. The development of these equations is given in the following subsections.

3.1.1.1 Development of axial through-wall-crack equations

The propagating critical through-wall-crack length relationship used in the ductile crack arrest analysis comes from the Maxey/Kiefner axial through-wall-cracked pipe fracture mechanics analysis. This relationship was originally developed from the Dugdale plasticity correction for an infinite-width flat plate [3]; the crack-driving force (and toughness) was given using a plane stress intensity factor as shown below.

$$\pi K_c^2/(8c\sigma_f^2) = \ln\{\sec[\pi\sigma/(2\sigma_f)]\} \quad (1)$$

Where,

$2c$ = Total axial through-wall crack length, inch*
σ_f = Flow stress, ksi
σ = Hoop stress at failure, ksi and
K_c = Critical plane-stress stress-intensity factor, ksi-in$^{0.5}$.

There is a higher crack-driving force in the axially cracked pipe case than the flat-plate case due to the pipe bulging outward from the pressure. For the axial crack in the pipe, a Folias bulging factor (M_T) modification accounts for this, and is included in Equation 2.

$$\pi K_c^2/(8c\sigma_f^2) = \ln\{\sec[\pi M_T \sigma_h/(2\sigma_f)]\} \quad (2)$$

Where,

σ_h = Hoop stress at failure, and
M_T = Folias bulging factor for a through-wall axial crack.

The original Folias bulging-factor relationship [4] was derived from elastic shell theory, and is the ratio of the stress intensity factors for the same size crack in an infinitely long cylinder and an infinite flat plate, see Equation 3. The details of this bulging factor have been fully discussed elsewhere [5].

$$M_T = K_{shell}/K_{plate} \quad (3)$$

An important aspect is that the bulging factor was only derived using elastic analyses. The application of the bulging factor to elastic-plastic and fully plastic (limit-load) conditions have been assumed to be valid from reasonable comparisons to experimental results. Now that elastic-plastic fracture mechanics can be conducted numerically with relative ease, the bulging factors could be assessed through the elastic to fully plastic conditions by comparing the solution for an axial crack in the pipe to a crack in a plate. For the finite element analyses, it would be necessary to determine what length of pipe and width of plate specimen is necessary to simulate an infinite conditions.

3.1.1.2 The contributions by Maxey/Kiefner

There were two practical difficulties in using Equation 2. The first is that there is no standardized laboratory test procedure for measuring K_c, so a correlation with a mill test is needed. The second was to define the flow stress of the material. The significant contributions of the Maxey/Kiefner work [6] were in defining these two parameters in a practical manner so that the pipeline industry could apply Equation 2.

The first significant contribution of the Maxey/Kiefner work was to empirically correlate K_c and Charpy V-notch upper-shelf impact energy for ductile fracture. This work was done prior to the existence of any procedures for determining the change in material fracture resistance with crack growth, i.e., the J-R curve. Consequently, the initial crack length and the Charpy toughness

* English units are shown since that was what was used in the original derivation

value were used to determine the failure pressure. This empirical relationship is given in Equation 4.

$$12C_v/A_C = K_c^2/E = G_c \quad (4)$$

where,

C_v = Charpy V-notch impact energy, ft-lb
A_C = Net-section area of the Charpy specimen, i.e., 0.124 in^2
E = Elastic modulus, psi
K_c = Plane-stress critical stress intensity factor, $psi\text{-}in^{0.5}$
G_c = Plane-stress strain energy release rate, $in\text{-}lb/in^2$

The full-scale ductile fracture ***initiation*** data used to establish this relationship is given in Figure 1. The data used in this case were those where the failure stress was toughness dependant.

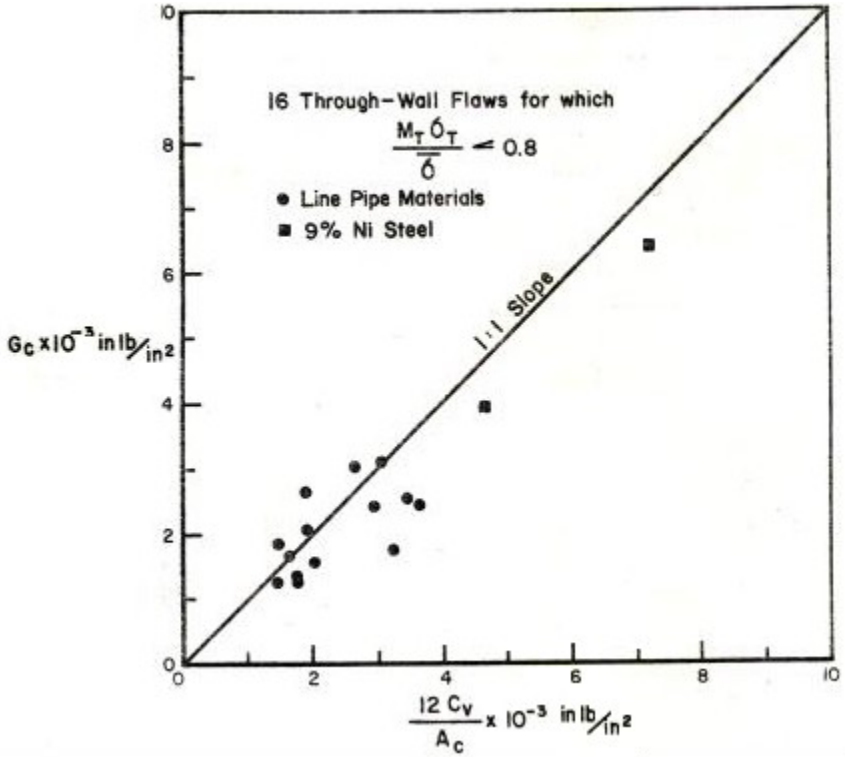

Figure 1 Maxey's correlation of G_c from full-scale fracture *initiation* tests to Charpy upper-shelf energy

The value of 12 in Equation 4 converts feet to inches when English units are used. Combining Equation 4 with Equation 2 gives

$$12\pi C_v E/(8c\sigma_f^2 A_c) = \ln\{\sec[\pi M_T \sigma_h/(2\sigma_f)]\} \quad (5)$$

Since the time of the Maxey/Kiefner work in 1972, the J-R curve methodology has been developed and standardized [7]. K can be converted to J in small-scale yielding and when combined with Equation 2 this gives

$$\pi JE/(8c\sigma_f^2) = \ln\{\sec[\pi M_T \sigma_h/(2\sigma_f)]\} \quad (6)$$

With a J-R curve for the material, one can then make crack growth and maximum load predictions that are more fundamentally based. A key assumption is that the elastic bulging factor is still applicable in the elastic-plastic range.

The second major contribution from the Maxey/Kiefner work was the definition of flow stress. The use of flow stress was actually first suggested by Hahn [8]. The flow stress concept is a simple way to account for material strain-hardening by assuming the material is elastic-perfectly plastic. The empirical aspect is to define at what level between the yield and ultimate strength the flow stress corresponds to. In the work by Maxey/Kiefner, it was assumed that for flaws in the base metal, the flow stress should be equal to the yield strength plus 10 ksi (68.95 MPa). This was somewhat of an arbitrary selection for line pipe steels of late 1960 vintage or earlier, i.e., X65 or lower-grade steels. There were two experimental X100 steels that had yield-to-ultimate strength ratios close to 0.8, i.e., there was a significant amount of strain hardening in this early experimental high-strength steel. Modern X100 line pipes made by a thermal mechanical controlled process have much higher yield-to-ultimate ratios (>0.90). It is more typical that the flow stress is taken as the average of yield and ultimate strength in other fracture mechanics applications [9], which gives similar flow stress values for lower-grade line pipe steels as the yield plus 10-ksi definition. In this effort, the flow stress was estimated as the average of the actual yield and ultimate strengths.

3.1.2 Axial crack stability analyses

Once an axial crack starts to propagate, the continued crack propagation depends on the decompression behavior of the internal fluid compared with the crack velocity. For instance, brittle fractures may propagate at 1,000 to 1,500 meters per second. In a natural gas pipeline, the initial acoustic velocity of the gas is about 350 meters per second. Since the brittle fracture speed is faster than the decompression wave, the crack would continue to propagate at the initial pressure level. Brittle fractures of up to 17.7 km (11 miles) in length in gas pipelines have been reported in the 1950's. Water, on the other hand, can rapidly decompress, and hence, except for very brittle materials, will decompress faster than the cracks can propagate and arrest the initially unstable crack. This is the reason why hydrostatic proof testing is recommended over pneumatic proof testing.

Brittle fracture arrest criteria are provided in terms of Charpy energy and the DWTT specimen shear area percent [10]. Soon after the gas pipeline industry solved the brittle fracture arrest problem, they encountered the propagating ductile fracture problem [11,12]. Ductile fractures propagate much slower than brittle fractures, so the decompression behavior of the internal fluid is very significant in predicting ductile fracture arrest.

3.1.3 Decompression behavior and limitation of current models

The decompression behavior of the pressurized fluid depends highly on whether the fluid is an ideal gas (i.e., methane, air, etc.), a subcooled fluid undergoing two-phase decompression (i.e., liquid carbon dioxide at 25 C or subcooled water in a nuclear power plant reactor piping at 260 to 310 C), or a single-phase gas that undergoes two-phase decompression (i.e., rich natural gas with heavy hydrocarbons). These decompression behaviors are schematically illustrated in

Figure 2 as taken from Reference 13. (Note: this figure could also be shown in a temperature-entropy diagram as well since the decompression behavior is a constant entropy process.) Figure 2 shows the decompressed pressure, P_d, as a function of the instantaneous pressure-wave acoustic velocity to initial acoustic velocity (v/v_a). Methane will behave as an ideal gas in these conditions, and the initial acoustic velocity is about 405 meters per second, whereas rich natural gas may decompress into the two-phase region. The two-phase decompression behavior of the gas will increase the pressure at a given wave velocity relative to pure methane decompression behavior, and hence increase the required toughness for ductile fracture arrest. The wave velocity is the instantaneous acoustic velocity (as the gas decompresses it cools down and the acoustic velocity decreases) minus the velocity of the gas flowing toward the rupture. There is a decompressed pressure with an instantaneous acoustic/wave velocity that may correspond to a speed that a ductile fracture can propagate.

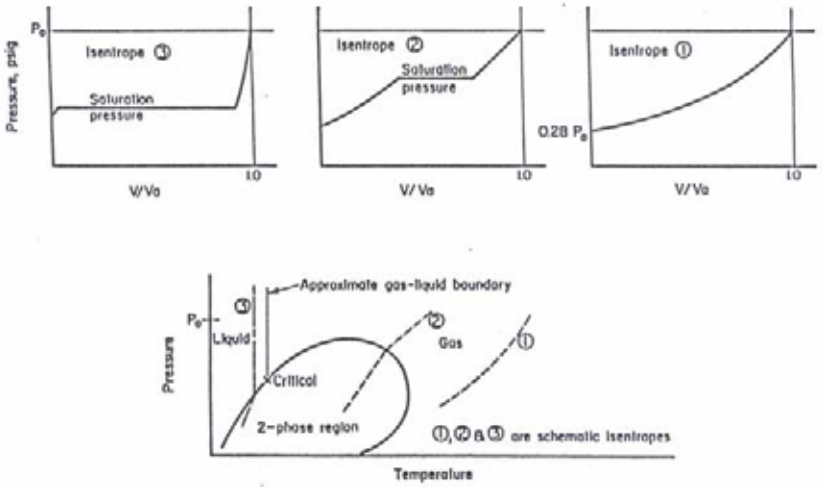

Figure 2 Schematic of decompression behavior for ductile fracture arrest considerations

3.1.3.1 Ideal gas

Theoretical derivations exist to define the decompression behavior based on the ideal gas laws [14]. The assumptions are that the expansion is isentropic, a sudden full pipe cross-sectional opening occurs, and the fluid mixture is and remains homogeneous. A relationship between the wave velocity and the local pressure is given in Equation 7.

$$P_d = P_i\left[\frac{2}{\gamma+1}+\left(\frac{\gamma-1}{\gamma+1}\right)\frac{V}{V_a}\right]^{\frac{2\gamma}{\gamma-1}} \tag{7}$$

Where,

P_d = Decompressed pressure level,
P_i = Initial line pressure,
V = Pressure wave velocity,
V_a = Acoustic velocity of gas at initial pressure and temperature, and
γ = Initial specific heat of gas.

Note that the relationship above is only valid after the crack has propagated some distance from the origin. Close to the origin, the pressure decays more slowly due to the fact that a full-bore opening does not develop immediately. At first, only a slit is present, and decompression is delayed. This delay causes higher fracture speeds near the origin and increases the required toughness for quick arrest.

3.1.3.2 Rich gas

Rich natural gas is defined as natural gas containing hydrocarbons heavier than methane in such quantities that may be extracted commercially, or that may require removal to render the residue gas suitable for fuel use or pipeline transit. These hydrocarbons cause a two-phase decompression that acts differently than ideal gases and requires a more complex procedure for estimating the decompression behavior. The most commonly used gas decompression prediction tool for rich gases is GASDECOM [15]. This decompression program, which is a public domain code, is based on a detailed equation-of-state [16] that has modified empirical constants known to give accurate estimates on isentropic decompression behavior and has been verified with full-scale experiments. *Note that inaccurate decompression predictions can be made with GASDECOM if gas compositions vastly different from than those used in calibrating/verifying the code are used.* The GASDECOM code works reasonably well for typical gas compositions that are 85-percent pure methane or leaner (higher methane content) and pressures below 2,200 psig. The richer the gas, the more problems higher-pressure gas cases will have at lower initial gas temperatures, i.e., initial temperature below 0C could have problems for these cases.

GASDECOM uses a homogeneous-equilibrium model, which implies that there is no slip velocity between vapor and liquid phases. The fluid is treated as if it is homogeneous and the average density of the mixture is used in the calculations. The calculations assume the flow is one dimensional, which is reasonable within the pressurized pipe ahead of the crack tip in the uncracked pipe, but not true behind the crack tip in the "flap" region.

3.1.4 Backfill

In addition to accounting for the decompressed pressure, there is another difference between brittle and ductile fracture. This difference is the effect of the surrounding medium. The driving force for a ductile fracture has not only the hoop stress component at the crack tip (using the decompressed pressure), but also a component from the pressure on the pipe "flaps" behind the crack tip which tend to tear the pipe apart, see Figure 3. Because pipe flap displacement drives the ductile crack, the surrounding medium or backfill will provide some resistance to the dynamic-crack-driving force.

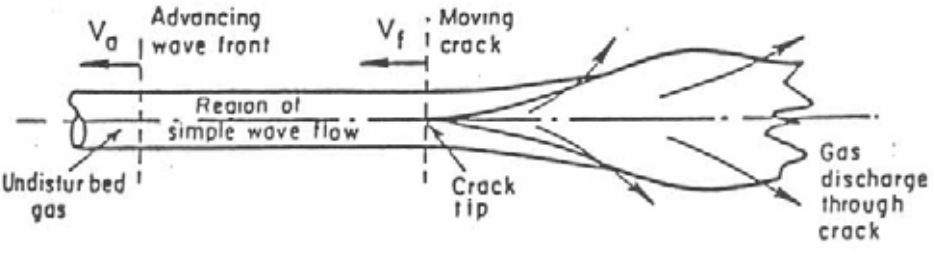

Figure 3 Flap formation in unstable axial crack propagation

This backfill resistance has been determined empirically from numerous experiments. In Reference 2, Maxey conducted a series of pipe fracture experiments with pure methane with both soil backfill and no backfill. As shown in Figure 4, the fracture velocity in the backfilled cases decreases significantly as compared to experiments with no backfill. In addition, Maxey also showed that even the smallest amount of backfill (~3 inches), could cause a large decrease in the crack-driving force and minimum arrest toughness, i.e., the decrease in driving force was the same for 30 inches and 3 inches of backfill cover. Typically, all unfrozen soil types are lumped together into one backfill coefficient since this was an investigation of first-order effects during the early experimental days.

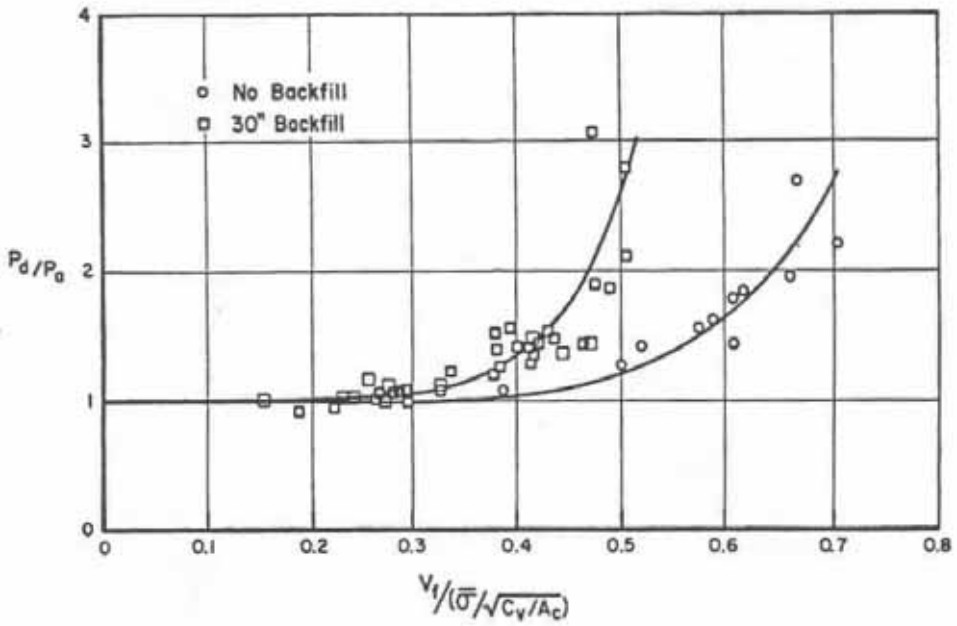

Figure 4 Ductile fracture velocity for backfill and no backfill

The moisture content of the soil can have a large impact on the calculated minimum arrest toughness. As described in Reference 17, the backfill constants change as a function of moisture content in the frozen soil. Figure 5 shows that for moisture content of 10 percent, the backfill constant can decrease by 30 percent as compared to the unfrozen backfill constant. This can decrease the calculated minimum arrest toughness by approximately 20 percent.

For offshore pipeline cases, the backfill condition is water. A few full-scale pipe tests have been conducted for the A.G.A. [18]. It was found that for dynamic fracture, water actually gave greater restraint than soil and the effective backfill coefficient was 33 for water compared to 39[†] for soil. Additionally, for offshore pipelines there is an external overpressure wave in the water that occurs from the gas pressure on the water once the fracture event starts. Accounting for this effect is somewhat complicated, but the overpressure wave reduces the crack-driving force and

[†] In English units

could cause arrest earlier than if only the water backfill coefficient is used. Ignoring this effect would be conservative.

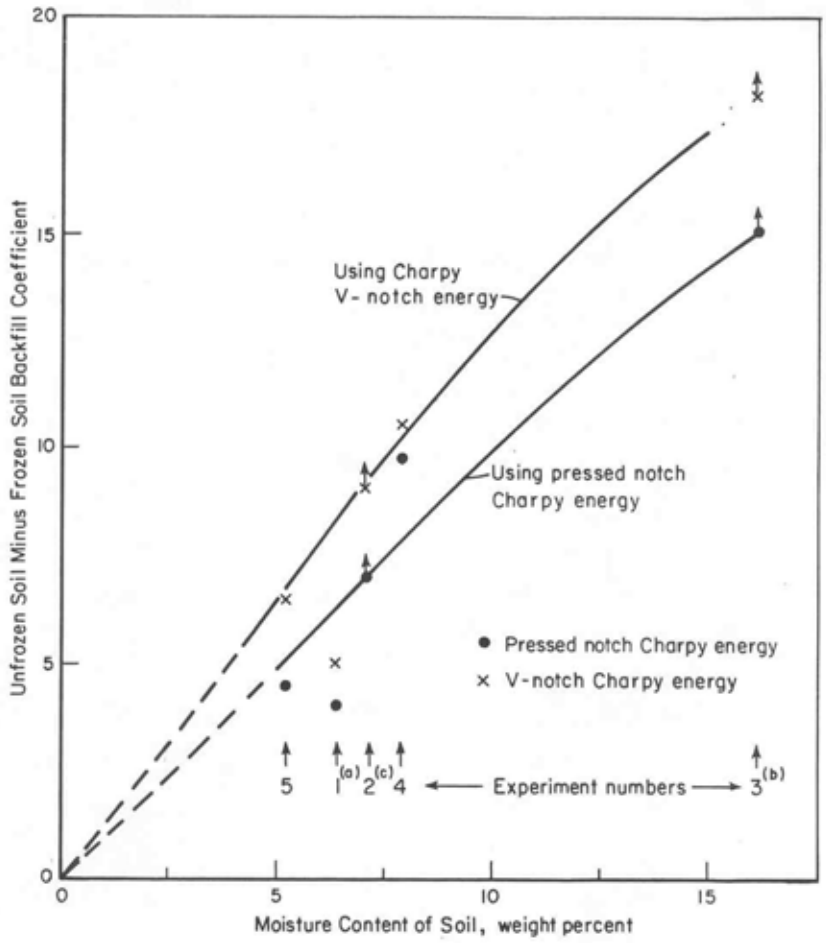

Figure 5 Change in backfill coefficient as a function of moisture content for frozen backfill (unfrozen soil backfill was 39 for this case, English units)

3.1.5 Fracture speed

There are two older analytical models that exist for making fracture-speed calculations. The Maxey model in Reference 1 is more empirical, whereas the analysis in Reference19 is more theoretical, but in reality still has an empirically adjusted parameter. Both models were developed from work sponsored at Battelle by the American Gas Association. Because it has been validated by more experiments and lends itself more easily to two-phase flow decompression analyses, the Maxey analysis has been commonly used in the oil and gas industry.

The Maxey ductile fracture model determines a relationship between the fracture speed, V_f, and the decompressed pressure or hoop stress, where

$$V_f = \left[\frac{C_B \sigma_f}{\sqrt{CVP}}\right]\left[\frac{\sigma_d}{\sigma_a} - 1\right]^{1/6} \tag{8}$$

V_f = fracture speed, m/s
C_B = backfill constant backfill constant (2.76 for no backfill, 2.00 for soil backfilled and 1.71 for water backfilled pipe)[‡]
σ_f = flow stress (SMYS + 10 ksi [68.9MPa]), MPa
CVP = Charpy V-notch upper-shelf energy for a 2/3-thickness specimen, J
σ_d = decompressed hoop stress ($P_d R_m/t$), MPa
σ_a = arrest stress, MPa
P_d = decompressed pressure, MPa
R_m = mean pipe radius, mm
t = pipe or tube thickness, mm

and

$$\sigma_a = \left[\frac{2\sigma_f}{3.333\pi}\right]\arccos\left\{\exp\left[-\frac{(18.75CVPE\pi)}{24\sigma_f{}^2(R_m t)^{0.5}}\right]\right\} \quad (9)$$

with
E = elastic modulus, MPa.

Note: in Equation 8, P_d/P_a could be used in place of σ_d/σ_a, where P_a is the arrest pressure. Also, Equation 9 is essentially Equation 5 with $M_T = 3.33$. The M_T value of 3.33 corresponds to the Maxey assumption that there is a critical crack length during unstable crack propagation of a certain unique value, i.e., for arrest the crack length (2c) was equal to $6(R_m t)^{0.5}$.

3.1.6 Explanation of the Battelle Two-Curve approach

To determine whether a crack will propagate, the relationship between the decompressed pressure or hoop stress versus the fracture speed is then compared with the decompressed pressure versus the fluid wave velocity relationship. The variation of gas decompression velocity and fracture velocity with pressure determines the potential for sustained propagation or arrest. Comparing the trends given by Equations 8 and 9, arrest can be calculated. Figure 6 shows a schematic representation of the fracture and decompression curves. As the measured toughness (Charpy in this case) is increased, the fracture curve moves above and below the decompression curve. If the toughness curve is below the decompression curve, no further decompression can take place, and the fracture would continue to propagate. If the toughness curve falls above the decompression curve, the decompression velocity is higher than the fracture velocity for all pressures. In this case, the arrest will occur. Through an interactive process, the tangency point between these curves can be found that represents the point where the decompression velocity and the fracture speed are equal for a given pressure. This point defines the boundary between arrest and propagation and marks the minimum toughness value needed for arrest. There are several software codes such as GasFrac[§] (TransCanada proprietary code) and DynaFrac (PRCI code) that perform these calculations and iteratively find the intersection point.

[‡] Using stress in ksi and 2/3 Charpy toughness in ft-lbs, the backfill constants are 53.7 for no backfill, 39 for soil backfill and 33.2 for water backfill
[§] GasFrac was used as the basis for PIPE-DFRAC, see Section 9.

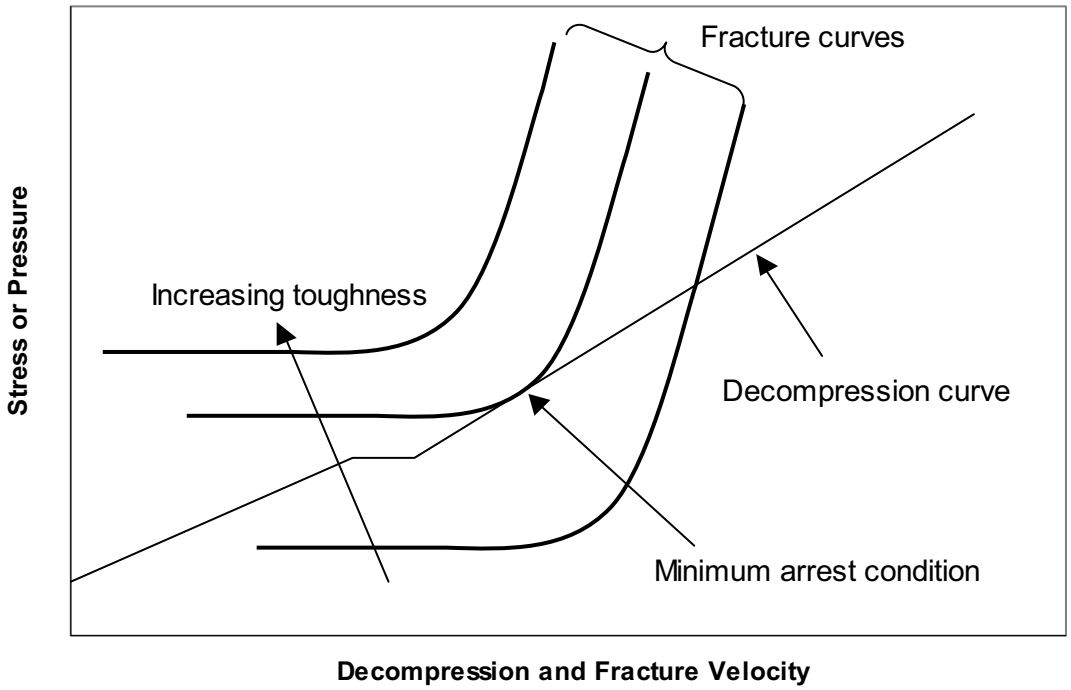

Figure 6 Interaction between decompression and fracture velocity shown schematically

3.2 Review of Backfill Resistance

As discussed in the previous section, the effects of backfill have been accounted for in the BTC analysis by an empirical correction factor that is based on a series of full-scale crack propagation experiments. This correction factor is for all types of unfrozen backfill and does not distinguish between soil types or soil properties. Because of the empiricism of this approach, the actual behavior of the soil is not modeled. However, other researchers have investigated the actual soil-pipe interaction.

In the 1970's while the empirical backfill coefficients were being developed, researchers at Ohio State University and Battelle [19] developed a more theoretical model for the equation of motion for a cracked pipe. In this model, the soil was considered to only have an inertial restraint behind the crack tip and was modeled using a Winkler foundation (beam-on-elastic foundation) model ahead of the crack tip. Typically, the Winkler foundation is a model that represents the stiffness and the dampening effects of the soil surrounding a pipe or other object. The stiffness of the soil is represented with springs and the spring constant is determined from the shear modulus of the soil. In reality, this modulus depends on many parameters including the soil type and moisture content, confining pressure, etc. The inertial component of the model was simplistic and assumed that the ejection of a "plug" of soil is caused by the gas expulsion pressure and resisted by the density of the soil. Soil strength did not play a role.

On a similar note, AISI conducted a series of experiments in attempts to aid in the design of mechanical crack arrestors [20]. In these experiments, they attached a matrix of lead weights on

the pipe surface. As the crack passed between these lead weights, the weight of the lead restricted the flap formation and arrested the crack. These experiments illustrated the influence of the inertial aspect of the backfill on the propagation of cracks in line pipe.

From work done by Wilkowski [17] on ductile fracture in frozen soils, the experiments on 6-inch diameter and 12-inch diameter pipe tests showed that the change in the backfill coefficient was directly related to the moisture content of the frozen soil. The moisture content of the frozen soil in turn is related to the strength of the frozen soil. Hence these series of experiments showed that strength of the soil can also have an effect on the backfill coefficient.

Recently, researchers in Italy [21] have developed a numerical model for including the effects of soil constraint during crack propagation in large-diameter gas pipelines. In this effort, they modeled the soil using a one-dimensional representation with an explicit-type of analysis that combines the soil, the pipe and a simplistic equation-of-state for the gas decompression. The soil elements were lumped masses connected by spring elements, and the spring constant was developed from a compressive constitutive model developed solely for that effort. This constitutive model takes into account the plastic behavior of the soils. The procedure models the compressive behavior below and to the sides of the pipe as well as the soil ejection from the top of the pipe. However, no interaction between the soil elements is modeled, i.e., the soil does not have strength. In addition, the soil properties were taken directly from the literature and are not related to the actual soil characteristics. Finally, this model is complex with many adjustable parameters and needs to be calibrated using full-scale pipe test data before it can make reasonable predictions.

From this past research there are three main effects the soil contributes to the crack propagation resistance:

- Inertial behavior: The soil weight on the pipe and the reaction force it exerts as the crack flaps and the escaping pressure dynamically moves the soil. If the weight is sufficiently high, the crack will not propagate, which suggests that very deeply buried pipe may always arrest a ductile fracture.
- Compressive behavior around the pipe: As the pipe displaces during the fracture event, the compressive constitutive behavior of the soil restricts this motion both behind and in front of the running crack tip. The soils shear modulus and the compressive plastic behavior will be important.
- Soil strength: For the soil that is not directly above the crack opening being ejected by the expulsion of gas, the moving crack flaps will compress this soil, causing a shear failure at the top surface. Therefore, the soil shear strength will be important.

A comprehensive model of the soil-pipe interaction will have to take into account all three aspects of the soil influence. Currently, a model like this is not available.

3.3 CTOA Background

3.3.1 Using CTOA for steady-state propagation

The crack-tip-opening-angle (CTOA) criterion has been used for many years in the aerospace community for predicting the onset of crack propagation [22]. The premise of the criterion is that when the applied load causes the CTOA in a structure to surpass the critical value of the CTOA, crack extension occurs. It has been argued that this value of the critical CTOA is a

material property and is independent of the geometry of the specimen used to generate it. It has also been shown [22] that the CTOA is independent of crack growth during stable crack propagation, see Figure 7.

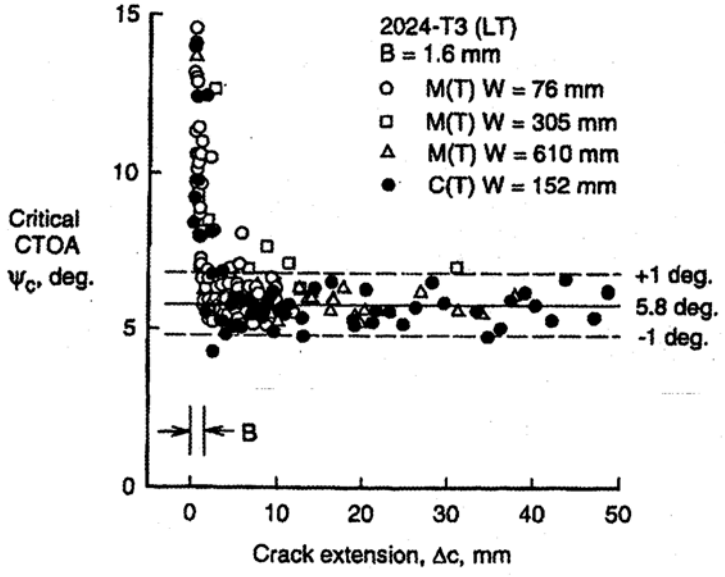

Figure 7 Experimental results [22] showing CTOA reaching steady-state

Several researchers have proposed that the CTOA is an appropriate parameter for characterizing the crack propagation resistance of high-toughness line pipe steels [23, 24, 25]. Work by CSM, SNAM, SwRI and PRCI led to the development of the Two-Specimen CTOA test procedure [26]. In Reference 26, an approach was developed that allowed the calculation of the critical CTOA using the dynamic fracture results from two specimens with different notch depths. These specimens are three-point bend specimens similar to the drop-weight tear test (DWTT) specimen but with a straight notch machined in the place of the standard pressed notch. It is argued that the critical CTOA is directly related to the amount of energy required to drive the fracture propagation process.

$$(CTOA)_c = (180/\pi)C_1 S_c/\sigma_{df} \qquad (10)$$

Where,

C_1	=	Constant (2,571 for CTOA in degrees),
S_c	=	$[(E/A)_{shallow}-(E/A)_{deep}]/28$ (J/mm^3),
$(E/A)_{shallow}$	=	Energy/area for a shallow-notched (a = 10 mm; a/w = 0.13) specimen,
$(E/A)_{deep}$	=	Energy/area for a deep-notched (a = 38 mm; a/w = 0.5) specimen,
σ_{df}	=	Dynamic flow strength = 1.3(quasi-static flow strength)[**],
a	=	Crack depth, and
w	=	Specimen width.

[**] Flow strength is defined here as the average of the yield and ultimate strengths.

This method has been shown to work reasonably well with lower-toughness pipes but the results are questionable for high-toughness materials [27]. The original work in Reference 26 was verified for Charpy energies up to about 200 J and grades in the range of X60-X80. The method assumes that the initiation energy of the two specimens is comparable. However, current research [27] by the initial CTOA developers [26] shows that this is not true for medium- to high-toughness line pipe steels. In addition, the definition described in Equation 10 is dependent on the dynamic flow stress of the material. The authors of Equation 10 [26] used a value 30 percent higher than the quasi-static flow stress, where much lower values have been found while looking at dynamic load-displacement data from instrumented DWTT specimens[28] .

In References 29, 30, and 31, a series of dynamic 50.8 mm (2-inch) diameter axial crack experiments were conducted, where the CTOA was measured using a high-speed framing camera (10,000 frames/sec). The results of these tests suggested a large decrease in the measured CTOA with an increase in crack velocity, see Figure 8. In addition, research by the Emc^2 staff [32] describes a series of dynamic fracture toughness experiments performed on a pendulum drop-weight tear test machine where the CTOA was measured using a high-speed video camera. The results from these experiments suggested that the CTOA is a function of fracture speed. As shown in Figure 9, there is a region during a typical pressed-notch drop-weight tear test (PN-DWTT) where the CTOA is constant. During this time, the crack speed is also constant. However, as the crack speed slows the CTOA increases.

If the constant measured CTOA values are plotted against crack velocity for a variety of specimens, the variability of the measured CTOA with fracture speed becomes apparent, see Figure 10. This figure shows that the chevron-notched DWTT specimen (CN-DWTT) has about the same CTOA and crack speed as the standard PN-DWTT, while both the static-precracked DWTT (SPC-DWTT) and the CTOAS (short-flaw-depth specimen from [26]) specimens have a much smaller CTOA and much higher fracture speeds. The results from a deeply back-slotted (back slot was 50 percent of uncracked ligament) specimen[††], whose fracture speed was approximately 85 m/s (280 ft/sec), showed only a 5-degree measured CTOA compared to the 7 to 10-degree CTOA for the other specimens.

[††] The back-slotted specimen is under development and is intended to remove the tail end of the load-displacement response in order to better isolate the steady-state propagation energy. The high crack velocity was an unexpected outcome for the deeply back-slotted specimens.

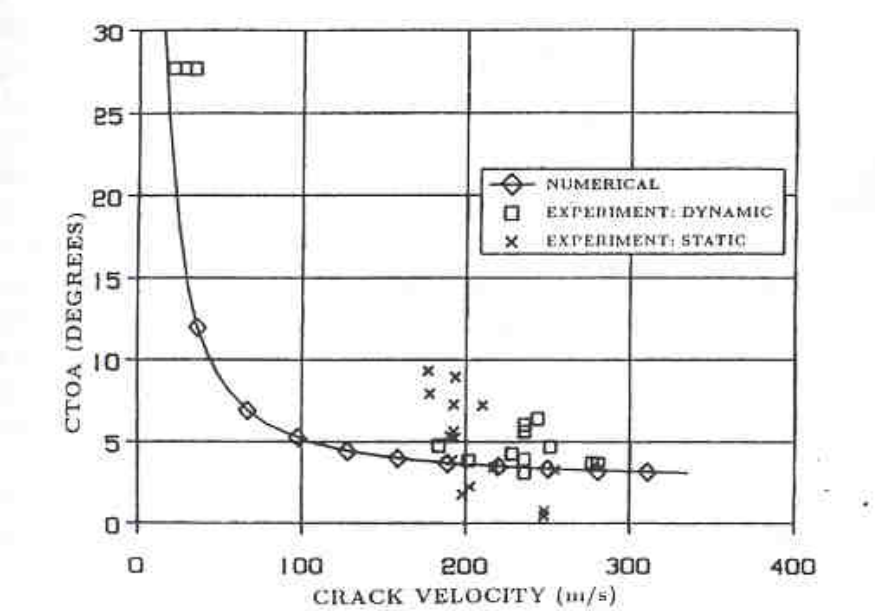

Figure 8 Comparison of ring model analysis scheme and experimental results from Reference 30

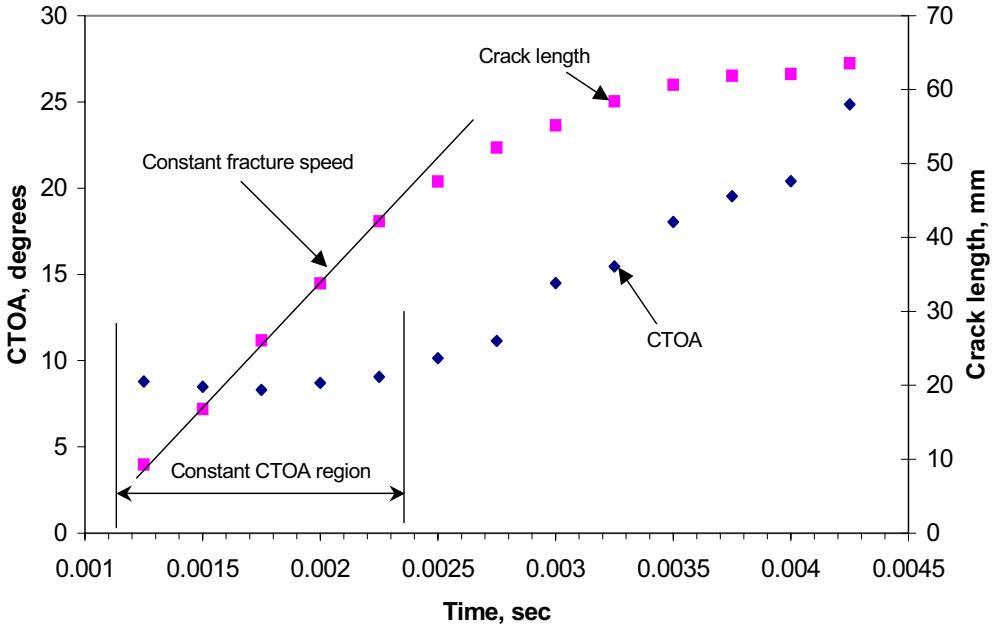

Figure 9 CTOA and crack length as a function of time from a PN-DWTT specimen

The implication of the results shown is that the measured CTOA value obtained from DWTT-type specimens may not be a consistent material parameter. It may be dependent on crack speed. Therefore, if a measured value of CTOA is to be used in predicting full-scale line pipe fracture behavior, a specimen with very high crack speeds must be developed, or a procedure for relating the laboratory specimens to the full-scale behavior must be developed. Until the dependence of the measured CTOA on fracture speed is fully defined and understood, the applicability of using this parameter in defining steady-state fracture toughness in line pipe steel remains unclear.

An additional aspect that is generally being agreed to by researchers is that there appears to be a greater scatter in the measured CTOA values than in energy values from Charpy or DWTT testing. As can be seen in Figure 11, the scatter is rather large, and for the same propagation energy, the CTOA values can vary by a factor of two. This is greater variability than the BTC correction factors of 1.4 to 1.7 on Charpy energy for higher-toughness materials.

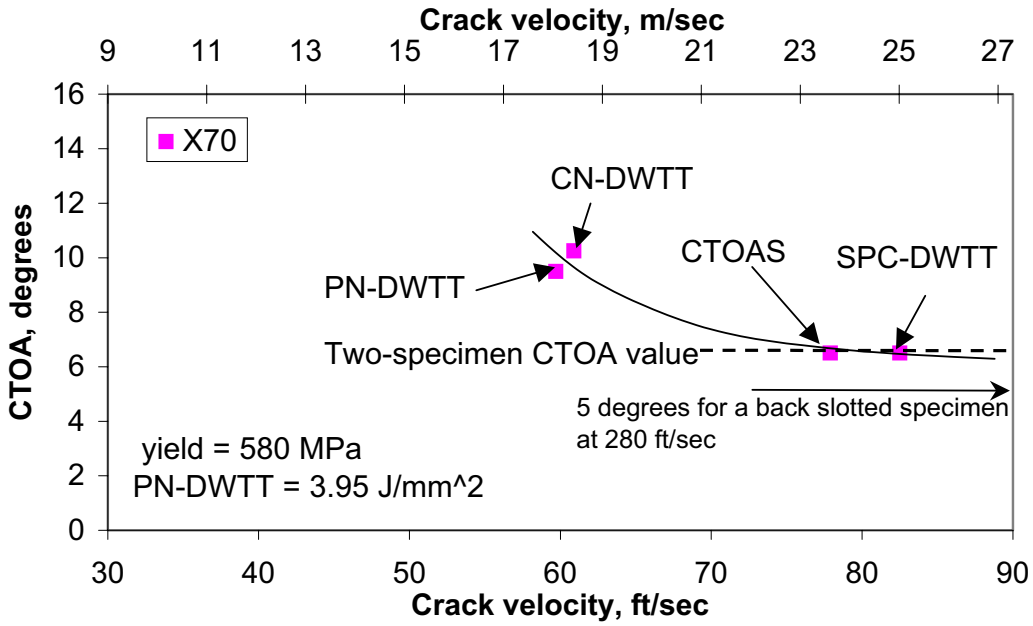

Figure 10 Measured CTOA versus fracture speed for different DWTT specimen conditions after approximately one-wall thickness of crack growth

Therefore, the CTOA appears to be a viable measure of the true crack propagation resistance in line pipe steels; however, currently there is not a reliable technique to make an accurate measurement in the laboratory that reflect full-scale behavior. There are several techniques that are currently being used, both visual and calculation methods, but the scatter and the crack-speed dependence in the data adds a great deal of uncertainty to these methods. In addition, there have been no measurements of CTOA from full-scale experiments to verify these laboratory measurements. Until a reliable method for measuring the CTOA in full-scale experiments is developed and verified, or a laboratory experiment is developed that accurately simulates the behavior in the full-scale test, i.e., loading, loading rate, etc., it is difficult to use the CTOA as a reliable fracture parameter for predicting axial crack arrest in line pipe steels.

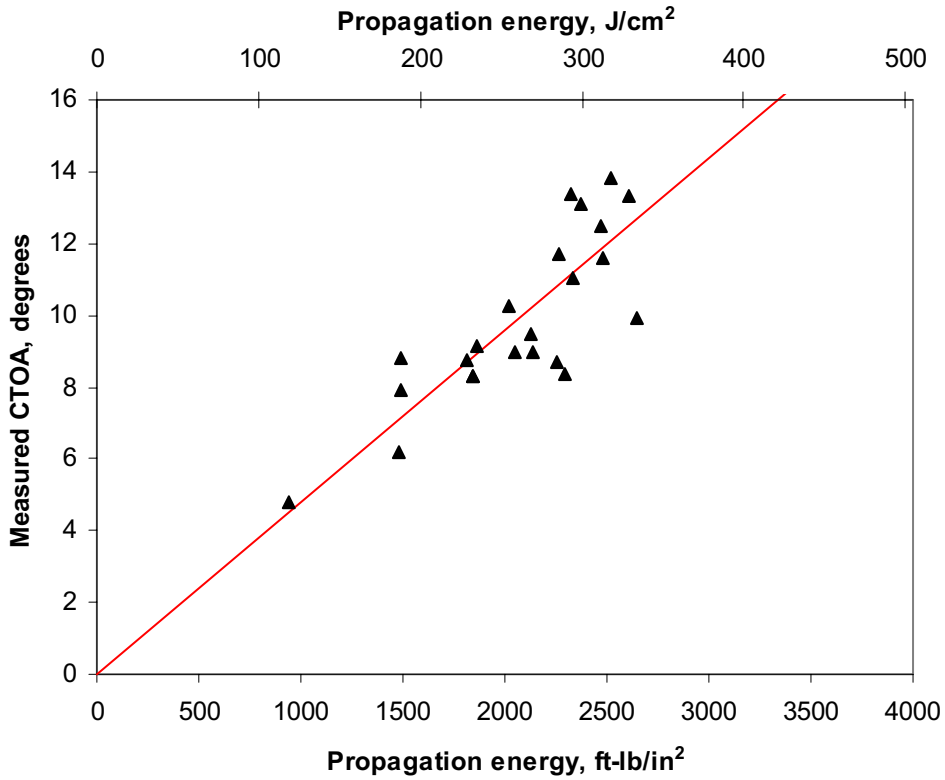

Figure 11 CTOA versus propagation energy for linepipe steels ranging from X52 to X100

4 SOIL CHARACTERIZATION

The selection of the soil used in this effort is very important to the outcome of the project. It is known that the soil types at the full-scale test sites around the world vary greatly and could lead to scatter in the minimum arrest toughness values from those experiments. Therefore, in developing a backfill coefficient that is a function of soil properties, a wide range of soils need to be used. It is known that the soil at the Advantica (Spadeadam) test site in the UK and the original Battelle Athens test site contained clay that at times was very wet, while the test site at CSM (Sardinian) in Italy and the Emc^2 test site contain sand. Therefore, it was desired to use these types of soils in the experiments. It was felt that using a clay and sand with a variety of moisture and compaction levels would reasonably bound the soil behaviors. In addition to characterizing the soils used in this effort, soils from the JGA, Spadeadam and Sardinian test sites were characterized for comparison purposes.

4.1 Soil Classifications

The Unified Soil Classification System from the American Society for Testing and Materials (ASTM) D 2487 standard classifies soils into three major categories, coarse grain, fine grain, and organic. The classification levels for the grain soils are based on their sieve number and are shown in Table 1. This classification system was used in this program to label the soils chosen. ASTM D421 and D422 are used for the particle size analyses of these soils.

4.2 Summary of Soil Experiments

Understanding the stresses exerted on the soil from a buried pipe that is experiencing axial crack propagation is difficult. The soil behavior in compression must play a role since the jet force expelled from the crack opening pushes the pipe down compressing the under burden soil and absorbing some of the energy. Shear strength of the soil is important since as the flaps behind the running crack push on the soil and the weight of the soil reacts against this force causing the soil to fail in shear. In addition, the soil weight and its inertial component will play a part in constraining the crack flaps during crack propagation. Therefore, not one soil property, but probably all three play a significant role in producing the measured fracture speeds in axial crack propagation in line pipe steels.

Basic concepts indicate a soil can derive strength from two sources; friction between particles and cohesion between particles [33].

- Cohesionless soils, such as gravel, sand, and silt, derive strength from friction between particles.
- Cohesive soils, composed mainly of clay, derive strength from the attraction, or bond, between particles.
- Mixtures of cohesionless and cohesive soils derive strength from both friction between particles and cohesion.

The frictional resistance between soil particles is dependent on the overburden pressure above the particles and the angle of internal friction between the particles. The total available shear strength (frictional resistance) is equal to the normal force times the tangent of ϕ (tangent of ϕ is equal to the coefficient of friction between the soil particles). The equation for frictional resistance is commonly written as shown in Equation 11.

$$\tau = \sigma \tan \phi \tag{11}$$

A pile of "dry" sand will have friction angle between particles of about 30 degrees [33]. The coefficient of friction between individual particles depends on both their hardness and the surface roughness. However, the measured friction angle of a soil sample will also depend on the interlocking of particles that may be caused by the density of the sample.

The concept of cohesive strength is dependent on quantities such as the ionic bond between soil grains. Dry granular soils are unstable at slopes steeper than their friction angle between particles. However, clay can be cut vertically and still remain stable. Clay particles maintain their shape due to attractive forces (cohesion) between adjacent clay particles. The magnitude of the cohesion is dependent on the distance between individual clay particles. The greater the separation between the particles, the lower the attractive force is between the particles and the smaller the cohesion. The separation between adjacent clay particles is maintained by water molecules. As water is squeezed out due to external applied loads, separation decreases and cohesion increases. A unique relationship exists between the shear strength and water content of clay.

Table 1 Unified Soil Classification System (ASTM D2487)

Major Divisions			Group Symbol	Typical Names
Coarse-Grained Soils More than 50% retained on the 0.075 mm (No. 200) sieve	**Gravels** 50% or more of coarse fraction retained on the 4.75 mm (No. 4) sieve	Clean Gravels	GW	Well-graded gravels and gravel-sand mixtures, little or no fines
			GP	Poorly graded gravels and gravel-sand mixtures, little or no fines
		Gravels with Fines	GM	Silty gravels, gravel-sand-silt mixtures
			GC	Clayey gravels, gravel-sand-clay mixtures
	Sands 50% or more of coarse fraction passes the 4.75 (No. 4) sieve	Clean Sands	SW	Well-graded sands and gravelly sands, little or no fines
			SP	Poorly graded sands and gravelly sands, little or no fines
		Sands with Fines	SM	Silty sands, sand-silt mixtures
			SC	Clayey sands, sand-clay mixtures
Fine-Grained Soils More than 50% passes the 0.075 mm (No. 200) sieve	**Silts and Clays** Liquid Limit 50% or less		ML	Inorganic silts, very fine sands, rock four, silty or clayey fine sands
			CL	Inorganic clays of low to medium plasticity, gravelly/sandy/silty/lean clays
			OL	Organic silts and organic silty clays of low plasticity
	Silts and Clays Liquid Limit greater than 50%		MH	Inorganic silts, micaceous or diatomaceous fine sands or silts, elastic silts
			CH	Inorganic clays or high plasticity, fat clays
			OH	Organic clays of medium to high plasticity
Highly Organic Soils			PT	Peat, muck, and other highly organic soils

Prefix: G = Gravel, S = Sand, M = Silt, C = Clay, O = Organic
Suffix: W = Well Graded, P = Poorly Graded, M = Silty, L = Clay, LL < 50%, H = Clay, LL > 50%

The time required for water to dissipate from between soil particles varies generally with the size of the particles. The shear strength of granular soil increases immediately as the load increases. The strength of a pure cohesive soil increases very slowly after load is applied since consolidation is required for strength gain. For practical purposes most cohesive clay soils

contain some non-cohesive silt or sand. Hence under an increased load some increase in soil strength can be expected. The shear strength of any soil is typically described as shown in Equation 12,

$$\tau_f = c + \sigma \tan\phi \tag{12}$$

where; c = cohesion
ϕ = angle of internal friction
σ = normal stress on the failure plane
τ_f = shear strength
This equation is commonly called the Mohr-Coulomb Failure Criterion.

The majority of strength tests are conducted on cohesive soils, as obtaining undisturbed samples of non-cohesive soils is difficult. Strength tests on cohesive soils are conducted on high quality undisturbed samples obtained from thin wall tubes. The most common soil strength tests are as follows:

- The Direct Shear Test is a relatively simple test used to measure the shear strength of coarse grain soils. This experiment is considered a "drained" experiment since excess porous pressure is allowed to be relieved by the use of porous stones in the test arrangement. This test is not recommended for silts and clays as test sample drainage cannot be controlled during the test. Retained pore water can falsely increase the strength of a supposedly drained sample. In this experiment, a normal force is added to the specimen and the specimen is then sheared to failure. The failure does not occur on the weakest plane, but on the plane along the split of the shear box. The ASTM standard for this experiment is ASTM D3080.
- The Unconfined Compression Test is the simplest and quickest laboratory method used to measure the shear strength of a cohesive soil. In this experiment, an unconsolidated, undrained specimen is prepared in a cylindrical shape. With no external confinement, compressive loads are added until a shear failure occurs. Test results, especially with increasing depth, are conservative and misleading due to the release of overburden stress when the sample is removed from below ground and tested. The ASTM standard for this experiment is ASTM D2166.
- The Triaxial Compression Test is a strength test where the sample is subjected to confining pressures similar to those which existed in the ground before sampling. In general, triaxial tests may be done on soil samples which have either been consolidated in the lab to the effective overburden pressure before testing or left unconsolidated and tested at total overburden pressure. The consolidated triaxial compression test duplicates as accurately as possible the sample's conditions in the ground and gives an accurate indication of in situ shear strength. This experiment is probably the best for measuring the shear strength of soils, but can be expensive. The ASTM standard for this experiment is ASTM D2850 for unconsolidated soil and ASTM D4767 for consolidated soil.

In reality, none of these tests measure the true dynamic strength of the soil as needed for modeling a running axial crack in a buried pipeline. In that case, the moving flaps behind the crack tip displace the mass of the soil, which leads to both inertial and strength effect, i.e., the pipe must move the weight of the soil as well as fail the soil in shear in order to displace it from

the ditch. In addition, the behavior is highly dynamic, and it stands to reason that the strength properties of a cohesive soil are strain-rate sensitive. It was not within the scope of this program to develop the actual soil properties needed in developing a numerical model, but rather to begin to understand the effects of soil properties on the fracture behavior. Therefore, for this effort, standard soil characterization is all that is required in order to begin to understand these effects. It is suggested that more detailed soil characterization be carried out in order to develop soil properties needed for detailed numerical modeling, see Section 10.

4.3 Mojave Soils

For the small-diameter Mojave fracture experiments, the objective was to run identical experiments with different soils at different moisture and compaction levels in order to identify how these parameters affect the fracture speeds. Therefore, a wide variety of soils was required. The soils used were characterized for type and strength. Soils Engineering, Inc, a subcontractor to Emc^2, conducted the experiments for soil characterization. The details of their experiments on each of the Mojave soil types can be found in Appendix B.

4.3.1 Soil characterization

It was known from the start of the program, that both sand and clay were required to bound the behavior experienced by the full-scale test facilities throughout the world. Since the Emc^2 Mojave test site has sand as its native soil, this was the first soil that was selected. Sieve analysis of this soil suggests that more than 50% of the grains passed a No.4 sieve, giving it a rating as fine-grain sand. Further inspection found no fines and characterized the sand as yellowish-brown in color with a non-cohesive behavior. The classification symbol for this soil is SW.

For the second soil, a clay was desired. Extensive searching in the area of the Mojave, California Emc^2 test site revealed few suppliers of clay. Boydston Construction in Ridgecrest California found a supply of calcium bentonite clay from Matcon Corporation. Matcon characterized the soil as a medium swelling California bentonite clay containing a mixture of clay materials. Though it has many uses, the main application of this material is an additive to natural soils to reduce permeability and provide an effective water barrier. Sieve analysis of this soil suggested that 78% passed a No. 200 sieve, giving it a rating of a fine grain soil. Further inspection characterized the soil has a highly plastic, greenish-gray clay. The classification symbol for this soil is CH.

The third soil was taken about 3-to-4 feet below the sandy surface in Mojave. This soil contained a large amount of calcium, which significantly increased the cohesiveness and bonding of the soil. Sieve analysis suggested that 64% of the soil passed a No. 200 sieve, while 99% passed the No. 4 sieve, giving it a rating of sand. Further inspection found 36% silt present giving it a characterization of Sandy Silt that is medium grade, cohesive, and non-plastic. The classification symbol for this soil is SC.

4.3.2 Optimum moisture

The Proctor curve, per ASTM D1557-00 Method A, for the native sand soil at the Mojave test site is shown in Figure 12. The straight line shown on this figure, and in all Proctor curve figures in this section, represents the theoretical saturation line with zero air voids. The data shown in this figure indicate that the maximum dry density of the sand is 1.76 g/cm^3 (110 lb/ft^3), with an

optimum moisture content of 11.4%. Note that the moisture in the sand in the as-tested condition was 1.3%**.** It is also interesting to note that the Proctor curve is relatively flat with increasing moisture content. This is typical of sand. As water is added to sand, the water fills the gaps between the sand particles and increases the overall density, but the dry density remains relatively constant.

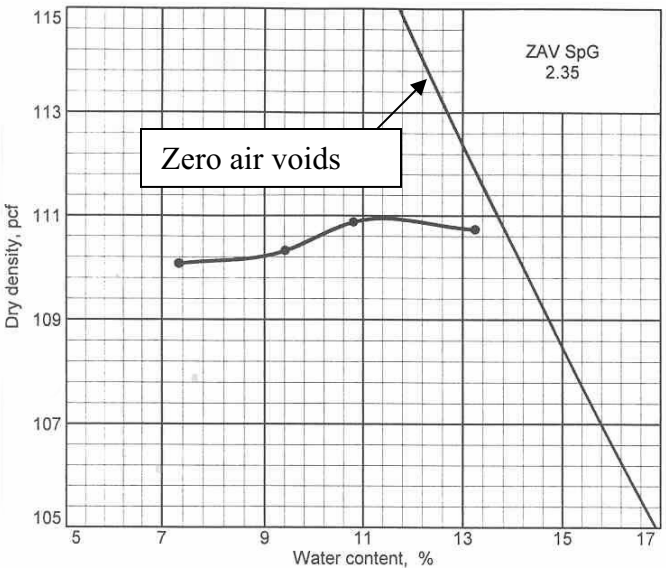

Figure 12 Proctor curve for native Mojave sand

The Proctor curve for the clay shipped to the Mojave site is shown in Figure 13. In this case, the maximum dry density is 1.56 g/cm^3 (97.7 lb/ft^3) with an optimum moisture content of 25.5%. Comparing these figures illustrates the difference between clay and sand as far as water absorption is concerned. For the clay, the dry density increases significantly as the water content increases, which is typical of cohesive clay.

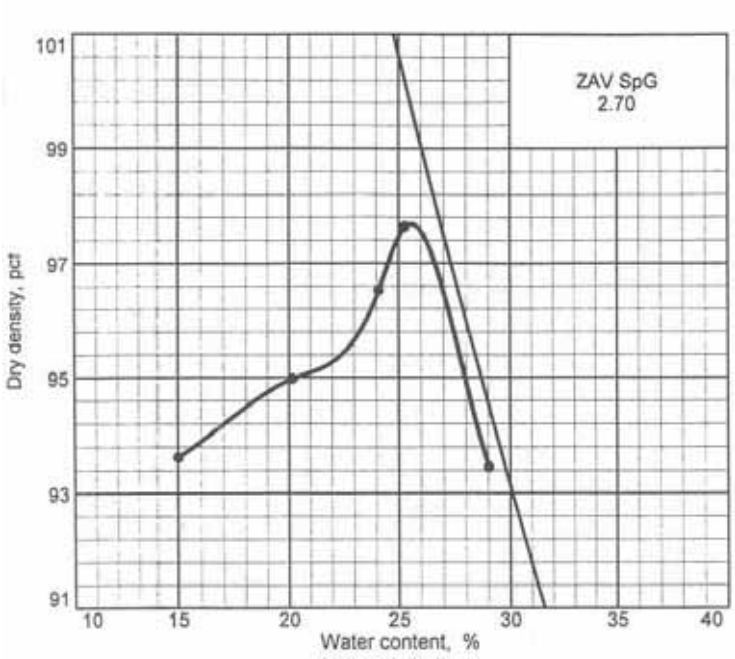

Figure 13 Proctor curve for bentonite clay

Finally, the Proctor curve for the sandy-silt soil found about 3 feet below the top sand at the Mojave site is shown in Figure 14. This soil has a much higher dry density of 2.02 g/cm^3 (126.3 lb/ft^3), with an optimum moisture of 9.8%. This material has about the same optimum moisture content as the sand, but is much more cohesive, making this an excellent choice for the third soil to be used.

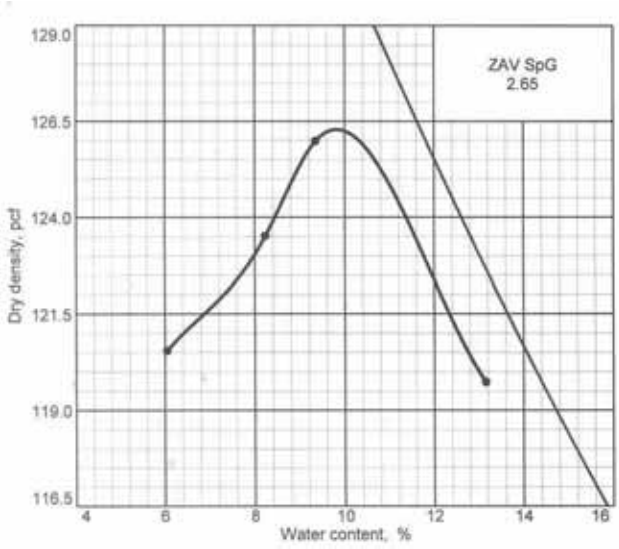

Figure 14 Proctor curve for sandy silt at Mojave test site

It should be noted that each of the Proctor curves represents the soils in the fully compacted condition (100%). If the moisture content is the same, but the compaction is less, the dry density available will also be less. Since it is next to impossible to get 100% compaction uniformly in

the field, it is assumed that 90% compacted represents the maximum field compaction and the soil has properties as defined by the Proctor curve.

4.3.3 Soil strength

Typically soil strength properties are measured to aid in foundation design and are not designed to give the properties needed for this type of analysis. Therefore, in this effort, standard strength properties for the soils were generated and it was determined whether any trends with strength were apparent. In the future it may be necessary to design an in-situ experiment that correctly captures the strength behavior needed for modeling this effect, as well as examine any dynamic effects on the soil strength and stiffness.

In this effort, the standard soil strength experiments conducted included the direct shear test and the unconfined compression test as described earlier. The results of the direct shear tests on the Mojave sand are shown in Figure 15. In this figure, tests were conducted at 4%, 11% and 18% moisture. The light, heavy, and dashed lines are the best-fit presentation of the data for the 4%, 11% and 18% moisture, respectively. For both the dry (4%) and the saturated (18%) cases, the cohesion (intercept of best-fit line) is shown to be zero. However, at optimum moisture (11%), the sand showed slight cohesion with a slightly lower angle of internal friction. This behavior is typical of sand and is attributed to the cohesion between the water molecules and not cohesion of the sand.

For the sandy silt, the results of the direct shear tests are shown in Figure 16. These tests were performed at 2% below optimum moisture and in a saturated condition. In these cases, both the angle of internal friction and the cohesion seem to be a function of the moisture content. Since this sandy silt contained 26% clay, it was considered cohesive, and an unconfined compression test was conducted.

This unconfined compression test was performed at 2% below optimum moisture, which was 10% in this case. Since one of the direct shear tests was also conducted at 8% moisture, these results can be directly compared, as illustrated in Figure 17. In the unconfined compression test, the sample failed at 506 kPa (73.4 psi), giving a shear strength of 253 kPa (36.7 psi), which is much lower than is predicted from the direct shear test. For the lower two direct shear tests, the failure surface is very close to that of the unconfined compression. For the higher normal stress, the direct shear testing apparatus forces the sample to fail on the plane between the two halves of the test fixture (horizontal) and not on the critical shear plane (~45 deg).

For the clay material, no direct shear test was completed since conducting drained direct shear tests on clays can be expensive due to time it takes for the dissipation of the excess pore water pressure during the experiments. Therefore, only an unconfined compression experiment was completed. In this experiment, the sample failed at 620 kPa (89.9 psi) giving a shear strength of 310 kPa (45 psi).

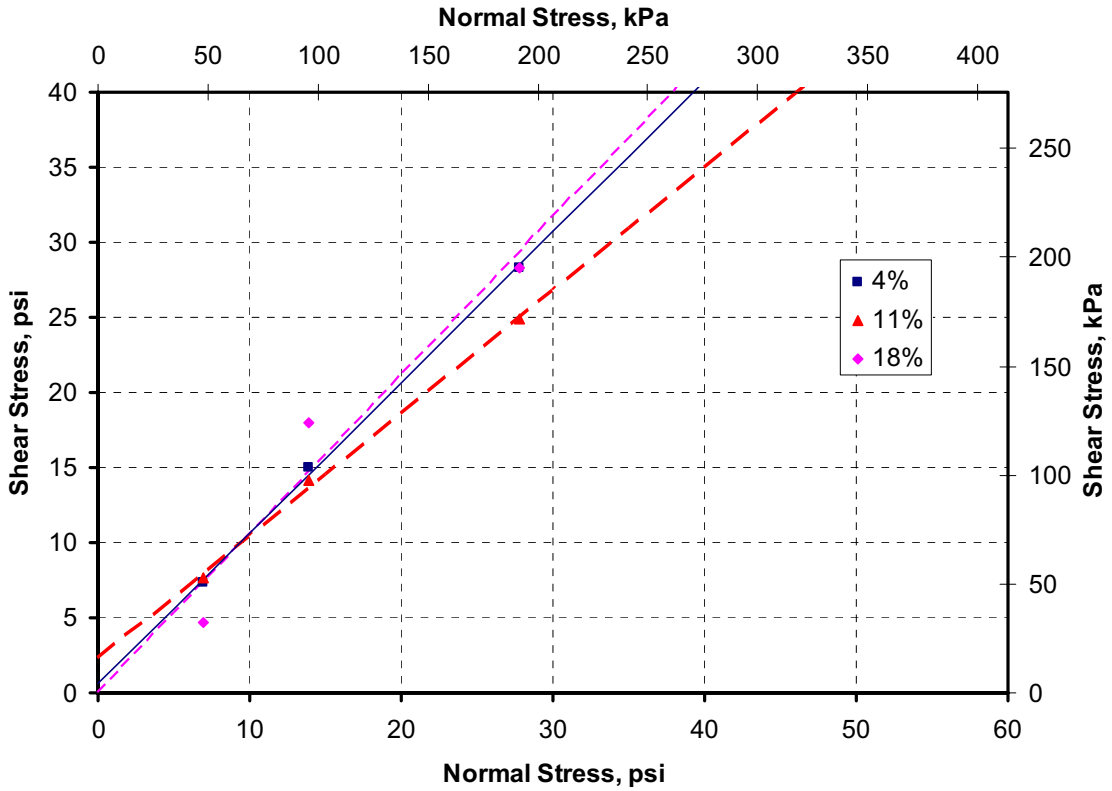

Figure 15 Direct shear test results for Mojave sand

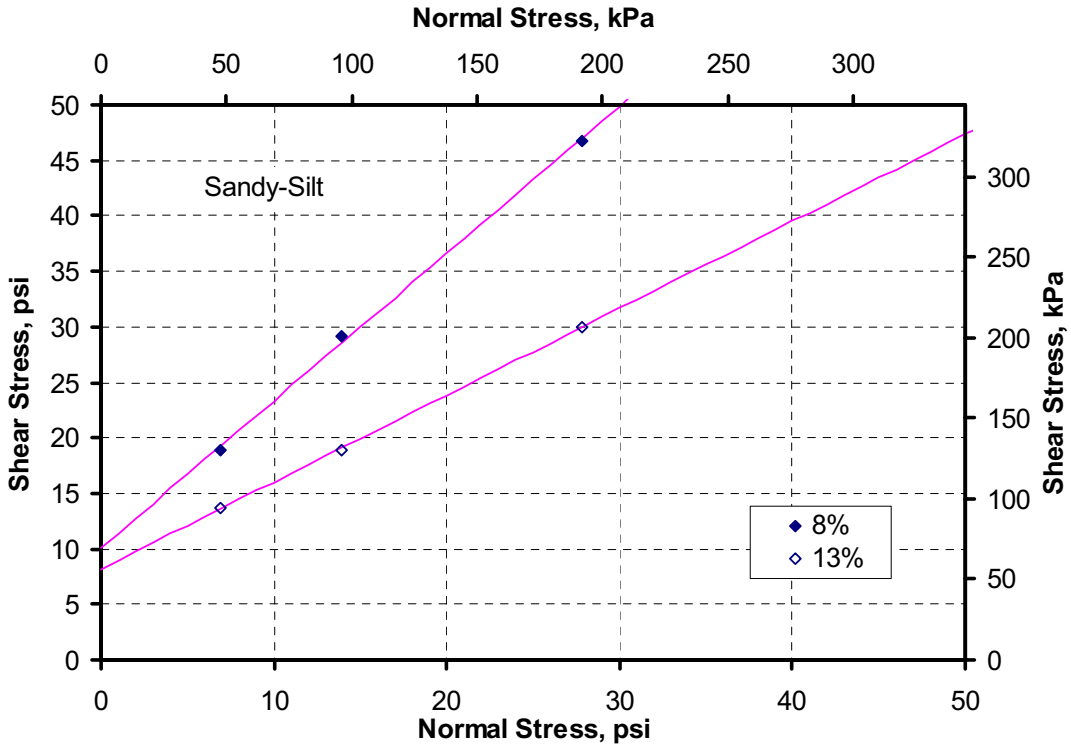

Figure 16 Direct shear test results for Mojave sandy silt

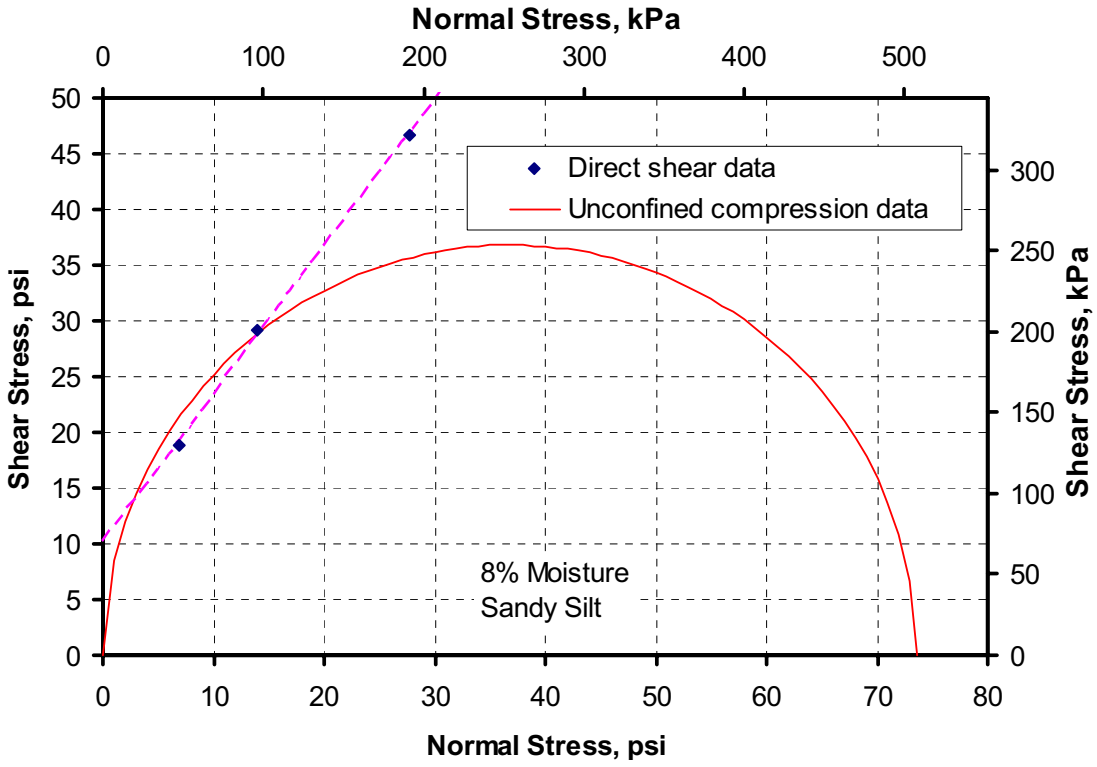

Figure 17 Comparison of direct shear and unconfined compression test results for sandy silt

4.4 JGA Soils

The typical soil at the FORCE test site in Denmark is clay mixed with sand. However, since it is typical for the Japanese to backfill their line pipe with sand, FORCE technology trucked sand to the test site that was typical of the sand the Japanese use in the field. The sand was characterized after each experiment from samples taken directly from the test pit before the experiment. An independent contractor to the JGA conducted the experiments. The JGA soil tested in this effort was NOT the native soil at the FORCE test site, but the sand trucked in especially for the JGA experiments. The details of the soil experiments can be found in Appendix C.

4.4.1 Soil characterization

The soil used in the JGA experiments was similar for all experiments conducted in that series. It was characterized as medium grain sand with some gravel and clay mix with a yellowish brown color. It was designated as non-cohesive. The optimum moisture from the Proxler test was 9.8% on average.

4.4.2 Soil strength

For the medium grain sands used in the JGA experiments, direct shear tests and triaxial compression tests were completed. As expected these tests gave about the same results as is shown in Appendix C. In contrast to what was done for the Mojave sand, the JGA also tested the soil in both the full-consolidated and unconsolidated states. They investigated levels of compaction from 90% to 100%. Their results indicate that the strength behavior of the sand is directly related to the amount of compaction present. An example of the JGA sand at 12% moisture is shown in Figure 18.

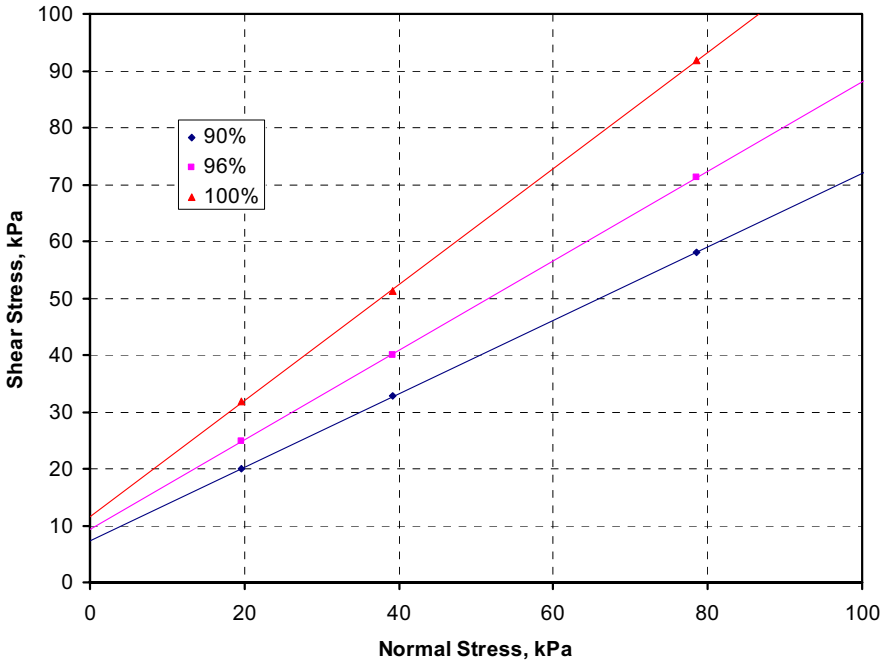

Figure 18 Direct shear results for JGA sand at 12% moisture

Comparing the sands strengths at the fully compacted condition, the effect of moisture content can be estimated, as shown in Figure 19. These results are similar to what was shown by the Mojave sand results. As the moisture content is increased, the apparent cohesion of the sand increases until the water content gets too high, at which time the cohesion begins to decrease. This is typical of sand and, as mentioned before, illustrates the cohesion between the water particles and not actual cohesion of the sand particles.

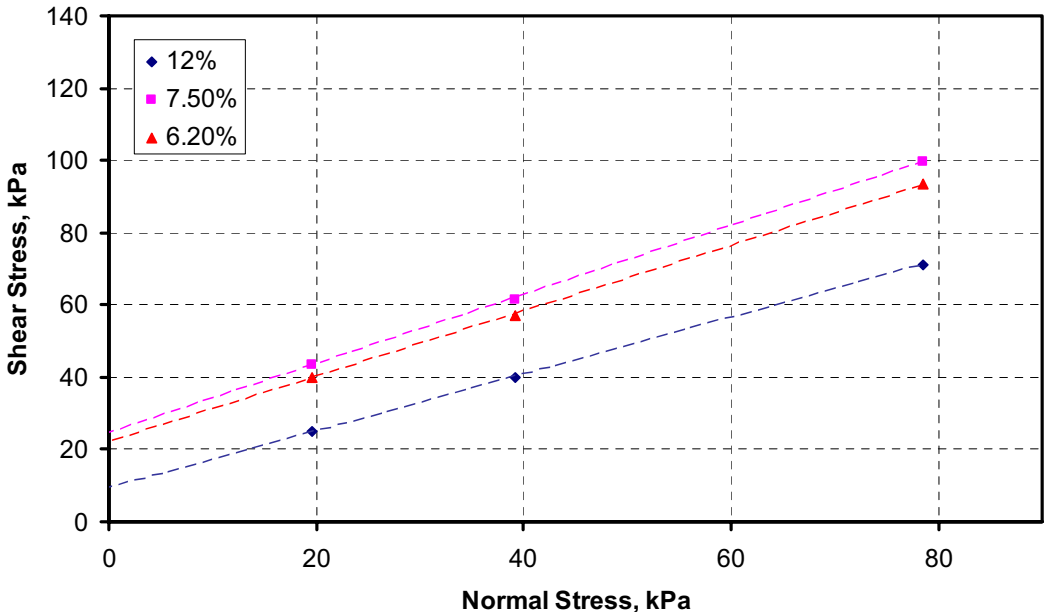

Figure 19 Direct shear results for full-compacted sand from JGA experiments

4.5 Soils from Other Test Sites

As part of this effort, the other major full-scale pipe burst test sites around the world were contacted and asked if they would be willing to participate in generating soil strength properties similar to those generated in this effort. Both Advantica (UK) and Centro Sviluppo Materiali (CSM, Italy) agreed to participate. The soils at the Spadeadam (Advantica) test site are clay-like with high cohesion, while the soils at the Sardinian (CSM) test site are mainly sand. Both locations agreed to pull soils directly from the test sites and perform soil characterization and strength tests as a function of moisture content. The purpose of this task was to investigate the difference in the standard strength and characterization of these soils and not to use this data to judge any past or future full-scale experiments. The detailed soil characterization results from the Sardinian (CSM) test site are given in Appendix D. The detailed soil characterization results from the Spadeadam (Advantica) test site are given in Appendix E.

4.5.1 Soil characterization

The soil at the Sardinian test site was characterized as clay with pebbles with an optimum moisture content of 7.45%, while at the Spadeadam test site the soil was characterized as red/brown clay/silt with fine to coarse grain sand, gravel and sandstone with an optimum moisture content of 12%. Using the classification system from Table 1, the soil from the Sardinian site would be characterized as a sand with fines (SC), while the soil from the Spadeadam site would be characterized as a fine grain soil (clay – CL).

4.5.2 Soil strength

Since the soil at Spadeadam is classified as a fine-grain cohesive soil, and the Sardinian soil was classified as a coarse grain, non-cohesive soil, there are different techniques for the measurement of shear strength, as explained in Section 4.2 of this report. Therefore, for the sands and gravels, both the direct shear and the triaxial compression test were used to measure the shear strength. For the clay, a triaxial and unconfined compression tests were conducted to measure the shear strength.

For the Sardinian soil, the details of these experiments are given in Appendix D, and the results are shown in Figure 20. It should be noted that since the Sardinian soils were non-cohesive soils, the effects of moisture content on the strength behavior is minimal; therefore, these experiments were only conducted in the saturated condition. In this figure, the direct shear results were generated per ASTM D3080 and the compression test was conducted per ASTM D4767 as described in Section 4.2. The compression experiments were conducted at three consolidation levels that provide a failure envelope that is captured well by the direct shear experiments. It should be noted that the triaxial compression test is more accurate at predicting shear stress than the simpler direct shear experiments.

For the Spadeadam soil, the details of these experiments are given in Appendix E, and the results are given in Figure 21. In this case, the Spadeadam soil is cohesive, and the direct shear test is not applicable, so the unconfined compression and triaxial experiments were conducted. It should be noted that the soils tested in the UK were done so by the applicable British standard and not the ASTM standards listed earlier. These standards are typically the same, with small differences in the wording and reporting. In addition, the experiments were conducted at a

variety of moisture contents to determine the effect of moisture content on the cohesive soils. The results from these experiments suggest that the strength of this soil decreases with increasing moisture content. In fact, in going from 50% to 110% of the optimum moisture content, the strength of the soil dropped by 30%. In addition to the unconfined compression experiment, the triaxial compression experiments with a backpressure of 25kPa, showed the same trends as the unconfined compression experiments but with a 30% increase in strength.

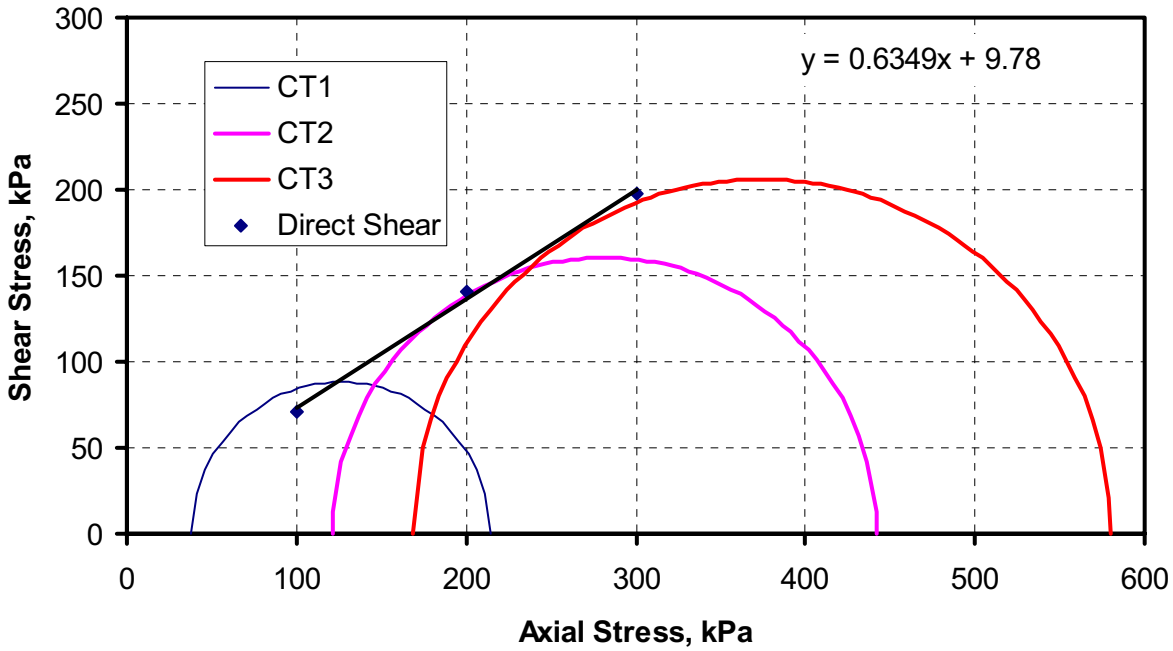

Figure 20 Direct shear and triaxial compression results for the Sardinian soils

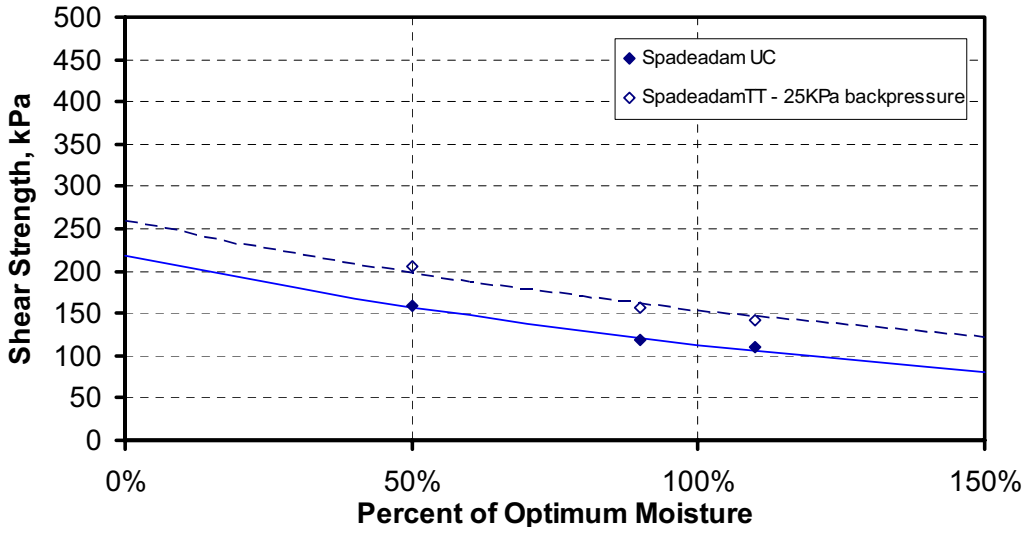

Figure 21 Shear strength results from Spadeadam soil

4.6 Comparisons of Soils

In this section of the report, the soil characteristics and soil strength properties from the various test sites are compared. The sieve analyses are presented first in order to demonstrate the difference in grain size and composition for the soil, followed by a comparison of the shear strength for the similar soils.

4.6.1 Soil characterization

For each of the soils used in the Mojave testing, as well as at the JGA, Spadeadam and Sardinian test sites, a sieve analysis was completed. The results of these analyses are shown in Figure 22. As explained in Section 4.2, soils are classified by the amount of soil that passes through each sieve classification. For instance, for a soil to be considered a coarse-grain soil, 50% of the soil must be retained in a No. 200 (0.075mm) sieve. If more than 50% passes, the soil is considered a fine-grained soil. For the soils shown in Figure 22, only the Spadeadam soil and the Mojave clay are considered fine-grain soils. In addition, if 50% or more of the soil is retained in a No. 4 (4.75 mm) sieve, the soil is considered gravel. In this case, there is no soil considered pure gravel; however, the Sardinian soil is very close with 52% passing through the No. 4 sieve.

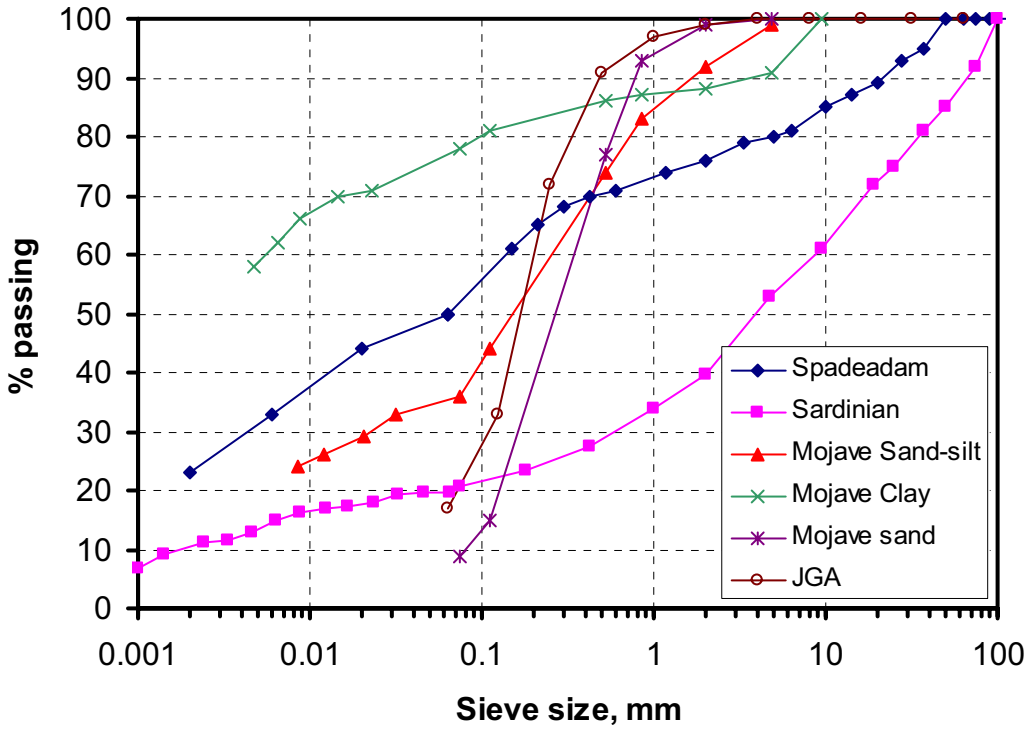

Figure 22 Sieve analysis for all soils tested

The sieve analysis can be broken down into categories by characterizing the soils as sand, silt, clay or gravel. This comparison is shown in Figure 23. This figure illustrates the large amount of gravel present in the Sardinian soil as well as the large percentage of sand in the Mojave and JGA soils. Interestingly, even though the Spadeadam soil has equal amounts of clay, silt, sand and gravel, it has less clay than that used in Mojave. From these analyses, it is expected that the Mojave clay, sandy-silt and the Spadeadam soil would be the most cohesive, due to their fine grain characteristics and amount of clay and silt in the soil.

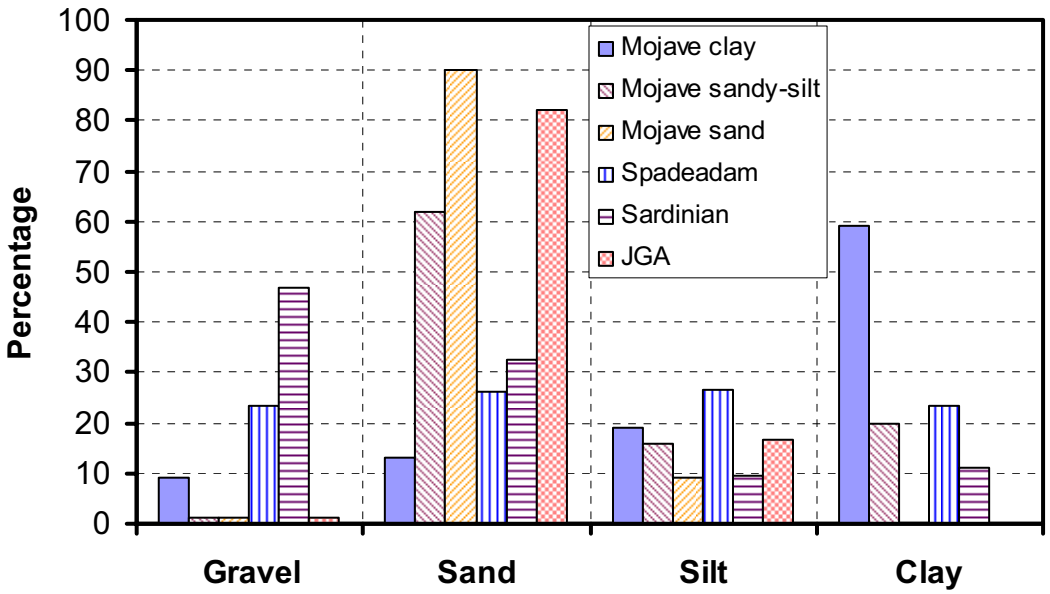

Figure 23 Percentage of constituents for soils tested in this program

Finally, the dry density and optimum moisture content for each of the soils tested are given in Table 2. Curiously, the dry densities at optimum moisture are very similar between the soils, even though the optimum moistures are very different. In addition, the optimum moisture of the non-cohesive sands at Mojave is very similar to that of the very cohesive soils at the Spadeadam site, indicating that the overall densities of these soils are similar. Since the densities are similar, it is expected that the effects of the inertial component of the soil resisting the crack propagation would be similar for these soils. However, due to their difference in cohesiveness, it is expected that the more cohesive soil, with its higher strength, would provide more resistance to crack propagation.

Table 2 Comparison of dry density and optimum moisture for soils tested

Soil	Dry Density g/cm^3	Optimum moisture %
Mojave – sand	1.76	11.4
Mojave – silt	2.02	9.8
Mojave – Clay	1.55	25.5
JGA	1.91	9.8
Sardinian	2.18	7.4
Spadeadam	1.92	12

4.6.2 Soil strength comparison

Due to the difference in the cohesive nature of the soils tested, a comparison of the soil strength properties will only be made for similar soils, i.e., the non-cohesive soil strength will not be directly compared to the cohesive soil strength.

As a direct comparison, the strength results from the direct shear tests for the soils at the JGA, Mojave, and Sardinian test sites are shown in Figure 24. In this figure, the closed symbols represent the Mojave sands at the specified moisture content, while the open symbols represent

the JGA and Sardinian soils at the specified moisture content. As expected, the intercept or cohesion increases with moisture content until a specified maximum, then decreases. Overall, the slopes of the lines for the Mojave and JGA soils in Figure 24 are not all that different, as would be expected with well-graded sand, but it is clear that the Mojave sand has a slightly lower slope than the JGA sand which is directly related to the grain size. In addition, the slope of the data for the Sardinian soil is much lower than either the JGA or Mojave soils. Again, this difference is due to the grain size of the Sardinian soil. As illustrated in Figure 23, the Sardinian soil has a large percentage of gravel, making it a much larger grain soil than either the Mojave or JGA sand. Another important point is that without applied normal stress, the shear stresses of these soils are very low. Even at the optimum moisture, the cohesion is only about 24 kPa (3.5 psi). This low value suggests that the available soil resistance for axial crack propagation from a strength perspective is very low for sands, which indicates that inertial component of the soil resistance must be prevalent.

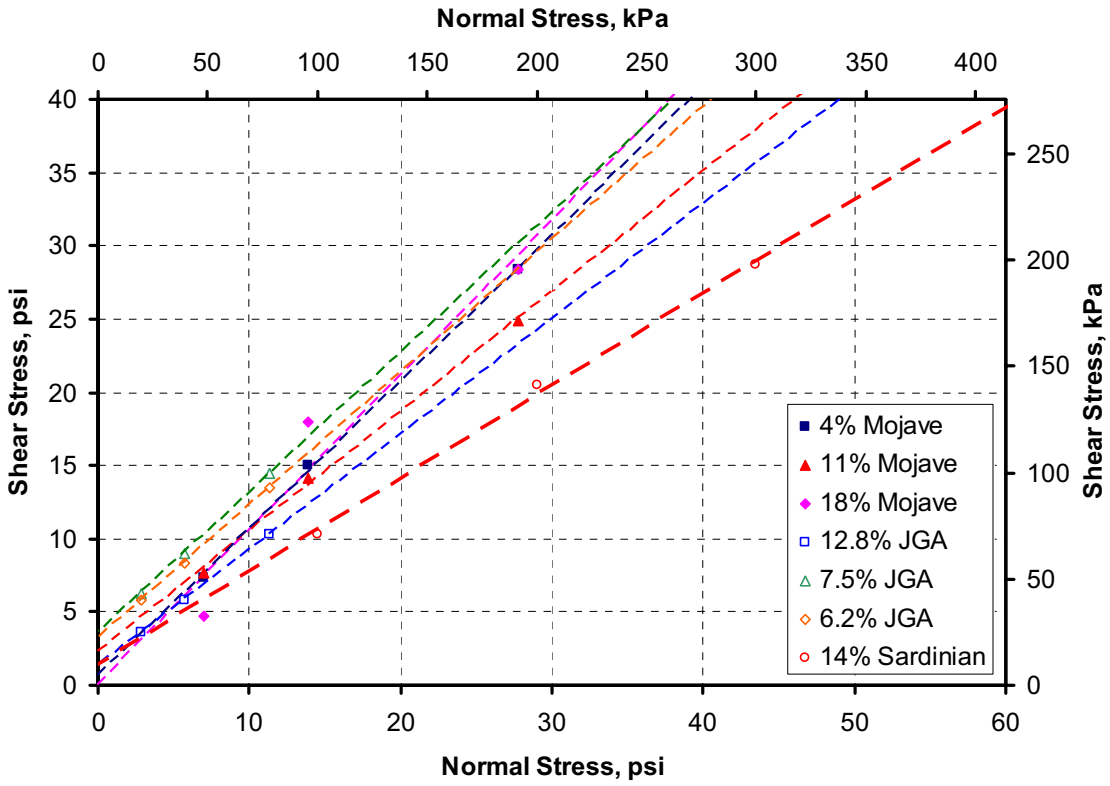

Figure 24 Comparison of Mojave, JGA, and Sardinian sand strength results

This behavior is further documented when the slope and intercept of the strength curves (Equation 12) are plotted as a function of moisture content for the sands tested, see Figure 25. The intercept, or cohesion, of the strength curves follow a log-normal type relationship indicating no cohesion for moisture contents less than 3% and greater than 17%. Also, the friction angle (slope) does not seem to be highly influenced by the moisture content with only a 5 degree difference in measured friction angle.

Even though the Mojave and JGA soils appear to follow a similar trend, the results from the Sardinian experiments seem to fall slightly outside of these trends. As illustrated in Figure 25, the intercept is slightly higher and the friction angle is slightly lower than the trends illustrated in the figure. In fact, the friction angle for the Sardinian soil falls below the average minus 3 times the standard deviations of the Mojave and JGA data. As mentioned before, this difference is mainly due to the grain size differences between the soils.

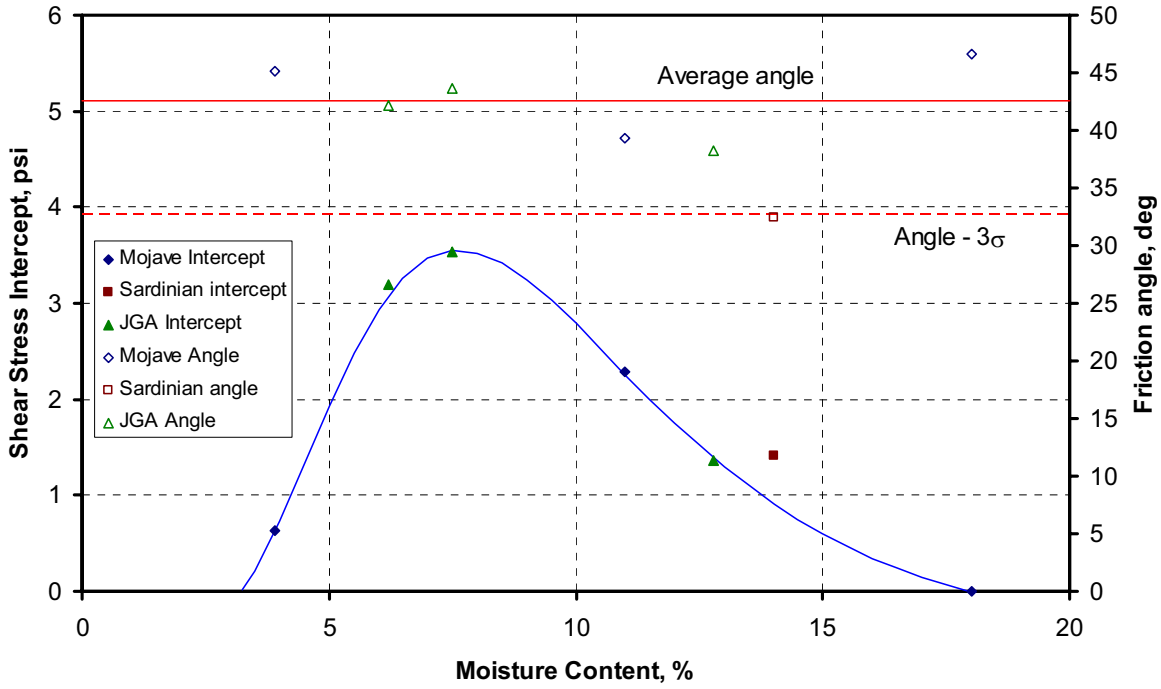

Figure 25 Comparison of cohesion and friction angle for the sands tested in this effort

A comparison of the shear strength for the cohesive soils is given in Figure 26. In this figure, the data from the Spadeadam test site was measured as a function of moisture content with both the unconfined compression and consolidated, undrained triaxial compression experiments. For the triaxial experiments, a 25kPa backpressure was used to simulate the soil at a certain depth. The unconfined compression experiments conducted on the Mojave clay and sandy-silt both showed a much higher shear strength than the Spadeadam soil. It is suspected that the shear strength of the soil may add to the resistance for axial crack propagation. In comparing the strengths of the cohesive soils to that of the non-cohesive soils, it is clear that the cohesive soils have 3 to 10 times more strengths than the non-cohesive soils. As mentioned earlier, it is suspected that for the non-cohesive soils, the majority of the soil resistance to crack propagation comes from the inertial component of the soil. The cohesive soils will have a combination of inertial and strength.

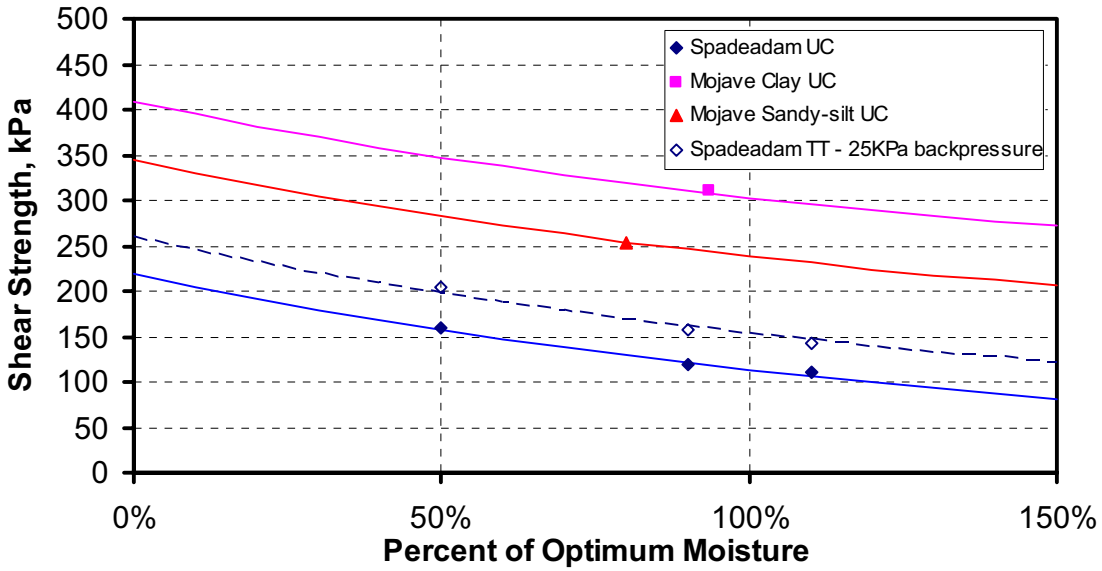

Figure 26 Shear strength comparison for cohesive soils

In summary, a couple of points about the soil experiments need to be made:

- These experiments were not meant to model the load-carrying behavior of the soil that exists during a full-scale crack propagation experiments. These standard experiments were meant only to give a relative feel for the strength and characterization of these soils. More detailed soil experiments are needed before the properties needed for numerical simulation of the soil behavior during the crack propagation process can be obtained.
- The comparisons of soil properties between the test sites were not meant to bias one test site over the other, but to simply compare and contrast the soil used at those sites.
- Soil inertial and strength properties were investigated in this effort, but it is recognized that the soil compressive linear and non-linear stiffness, i.e., the soil behavior under the pipe, will add to the resistance of the soil. Even though this property was not investigated in this effort, it will be important to the overall contribution of the soil to the crack propagation process.

5 SUMMARY OF MOJAVE EXPERIMENT

The purpose of the Mojave experiments was to determine how well-controlled soil backfill conditions affect the fracture speed of running axial cracks in line pipe materials. In order to begin to answer that question, a series of small diameter bursts tests were planned. These small-scale experiments are miniature versions of the full-scale pipe crack arrest experiments used to determine minimum arrest toughness in line-pipe steels. The idea was to conduct these experiments in low toughness pipe material that would be chosen so that steady-state axial crack propagation could be easily obtained[‡‡]. Small-diameter pipe was chosen so that a number of these experiments could be conducted within a reasonable budget. As discussed in the previous section of this report, three different soils were chosen that encompass the range of soils used in the full-scale test sites across the world. In this section of the report, a summary of those experiments is presented. Part II of this report gives the details for this experimental effort.

[‡‡] An explosive cutter was used to introduce a through-wall crack into the pipe. The length of this cutter was greater than the critical crack length at these conditions.

The pipe experiments for this study were conducted at the Emc^2 operational high-energy full-scale pipe-burst test site. It is remotely located in the Mojave Desert for safety reasons. Emc^2 has conducted about 12 full-scale large-diameter tests over the last four years for proprietary applications to new material designs. Some of this work was performed on composite-wrapped pipe, and some on newer higher-grade line pipe steels [34].

5.1 Pipe Material

The material chosen for use in this program was 1020 DOM (drawn over mandrel) mechanical tubing. This tubing has a nominal outer diameter of 152.4 mm (6-inch) with a wall thickness of 3.2 mm (0.125 inch)[§§]. Each pipe had a nominal length of 8.8 m (29 feet). This material was chosen over line pipe steel since current pipe mills do not produce line pipe steels with the sufficiently low upper-shelf toughness that is required for crack propagation in these experiments. This DOM tubing material was successfully used in a number of past small-scale ductile fracture pipe tests [35]. This tubing is heavily cold-worked so the yield strength is high and the Charpy energy is low[***]. One-foot rings from each of the 23 pipes were sent for material property characterization. Tensile properties were extracted from one pipe length in both the longitudinal and transverse direction to verify the mill test report. The material has strength comparable to X70 line pipe.

5.2 Test Matrix

The original plan for the Mojave experiments was to perform six small-diameter crack propagation experiments each year of the program (12 total). Each of these crack propagation experiments was to be conducted with different soil types under different moisture/compaction conditions. Each experiment would use one soil type on one half of the pipe and no soil on the other side of the pipe. This way a relative change in the fracture speeds could be determined. The original plan for the first-year Mojave experiments was to perform four experiments on a clay soil (cohesive) and two experiments with the native Mojave sand soil (non-cohesive). The second year of experiments was to include four experiments on the third soil type (some combination of cohesive and non-cohesive) and the remaining two experiments on the native sand. However, as is typical with large experimental programs, experimental difficulties, and unexpected results caused the test plan to be modified as the program progressed. The test plan used is explained next.

For the first series of tests, the testing setup used is shown in Figure 27. In this series of experiments, one half of the pipe was covered with the test soil, while the second half was unbackfilled. The unbackfilled data were used as a reference that was common to all tests. In each of these cases, the backfill covered the pipe for 20 diameters in length and to a depth of three diameters. The backfill depth of three diameters was chosen in order to provide sufficient inertial effect, and to aid in mixing and preparing the soil. Data from Reference 13 suggest that backfill depths of 76 mm (3 inches) to four diameters did not affect the fracture speed within the scatter of the data.

[§§] The effect of pipe diameter on the experimental results is discussed in Section 8.3.

[***] The measured full-size equivalent Charpy energy ranged from 39 to 50J with an average transition temperature of 110-120F.

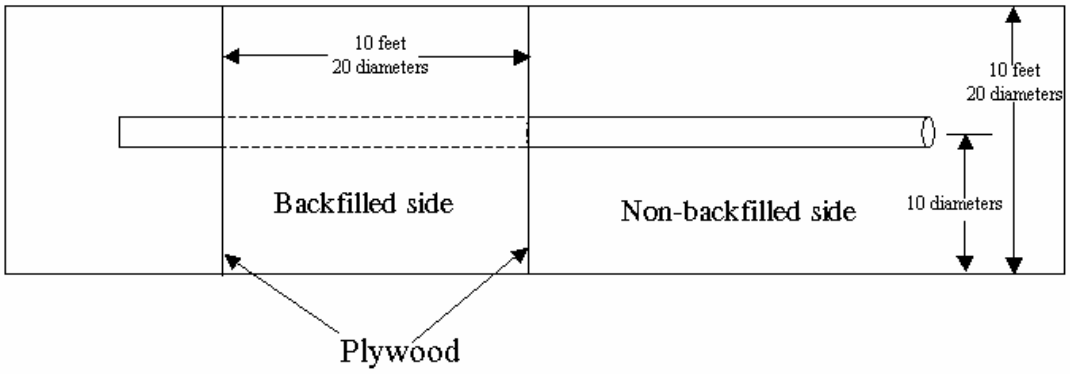

a.) Top view

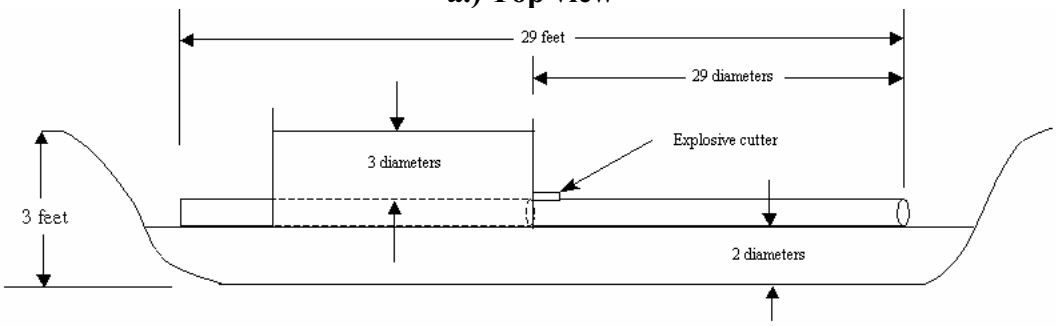

b.) Side view

Figure 27 Schematic of test pit

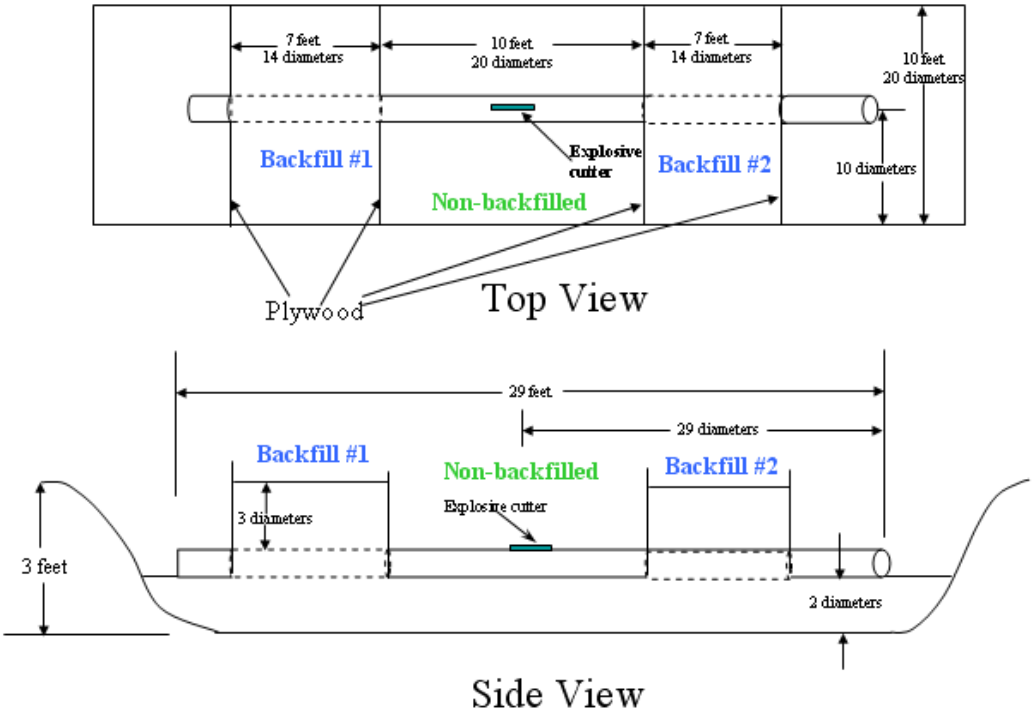

Figure 28 Schematic of test layout for Year 2 tests

In order to reduce the cost per experiment and to obtain more data per experiment, the testing arrangement was modified for the second series of Mojave experiments, see Figure 28. In this series of experiments, two different backfills were used on either side of the pipe, separated by an unbackfilled section that was 20 diameters long. In each of these experiments the backfill covered the pipe for a length of 14 diameters and a depth of three diameters.

In each of the experiments, the soils were prepared as explained in Part II of this report. The final soil conditions for each of the experiments are given in Table 3.

Table 3 Soils used in each Mojave experiment

Test Number	Description
1-1	Dry sand (2% moisture, 86% compact)
1-2	Clay (39% moisture, 72% compacted)
1-3	Clay (15% moisture, 90% compacted)
1-4	Clay (25% moisture, 90% compacted)
1-5	Dry sand (2% moisture, 86% compact)
2-1a	Dry sand (2% moisture, 86% compact)
2-1b	Wet sand (10.5% moisture, 98% compact)
2-2a	Clay (26% moisture, 90% compact)
2-2b	Clay(19% moisture, 92% compact)
2-3a	Sandy Silt (9% moisture, 90% compact)
2-3a	Sandy Silt (12.5% moisture, 94% compact)

5.3 Summary of Results

For these experiments, instrumentation was used to directly measure the fracture speeds, the pipe pressure and the pipe temperature. Details on the instrumentation include:

- Approximately 50 timing wires for measurement of fracture speeds. These wires were spaced about 152 mm (6-inch) apart along the length of the pipe.
- Pressure transducers attached to the endcap and on the fill line were used to measure the static pressure before the tests. Dynamic measurement of gas decompression was not taken since it was not of significance in these experiments.
- Several thermocouples were used both on the pipe surface and in the gas to record the test temperature before the burst.

Additional advanced instrumentation was applied to the second series of experiments to dynamically measure the forces between the soil and pipe during the burst experiment, as well as the dynamic crack-tip-opening angle as the crack propagated. The advanced CTOA instrumentation results will be presented in Section 7 of this report.

The details for each experiment are given in Part II of this report. An example of the timing wire data from the first series of experiments is shown in Figure 29. In this figure, the solid diamond symbols are the timing wire data in the unbackfilled section of the pipe, while the open symbols are the timing wire data in the soil. The solid line represents an idealized representation of the decompression wave as it hits the endcaps and reflects back to the fracture. In reality, after the decompression wave hits the endcap, the decompression wave speed will not remain constant

and will increase as it travels toward the large opening. However, this simplistic representation gives a feel for the location of the decompression wave relative to the crack tip.

The fracture speeds from these experiments were calculated from a linear regression of the data in the steady-state fracture speed region. For the unbackfilled section, this region extended from about two diameters to twenty diameters from the origin. For the backfilled side of the pipe, the steady-state region spanned from about two diameters to about six-to-seven diameters from the origin[†††].

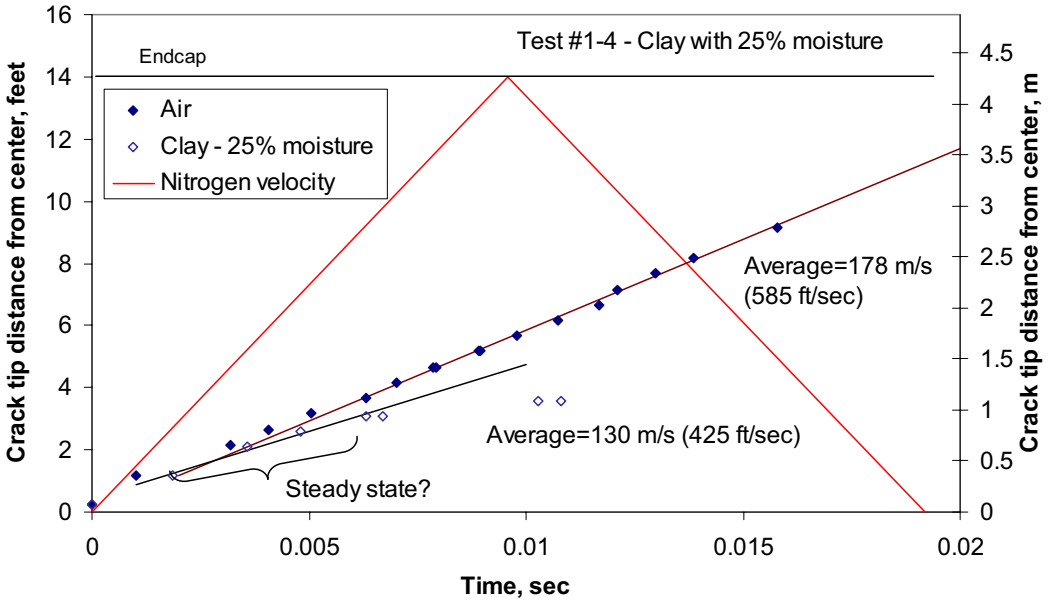

Figure 29 Timing wire results from Experiment 1-4

An example of the timing wire data from the second series of experiments is shown in Figure 30. In this figure, the diamond symbols represent the timing wire data from the side of the pipe with the 12.5% moist sandy silt, while the solid square symbols represent the timing wire data for the side of the pipe with 9% moist sandy silt. The decompression wave is shown in a similar fashion as before.

The fracture speeds from these experiments were again calculated from the data that was present during steady-state fracture, i.e. constant fracture speeds. For each case, in the unbackfilled portion, the steady-state region spanned from two diameters from the origin until the backfilled region (approximately 10 diameters from the origin). In the soil, a slight change in fracture speed occurred as the crack entered the soil region, remained steady-state for about six diameters and then began to arrest from the reflected wave.

[†††] Note that in this figure, only the data during steady-state fracture were used in calculation of the fracture speed. For the backfilled data, the data at 0.01 sec were not used. For both cases shown the correlation coefficient (r^2) is greater than 95%.

A summary of the fracture speed results from the Mojave experiments is shown in Table 4. As shown in this table, there were some experimental difficulties that occurred during each series of experiments.

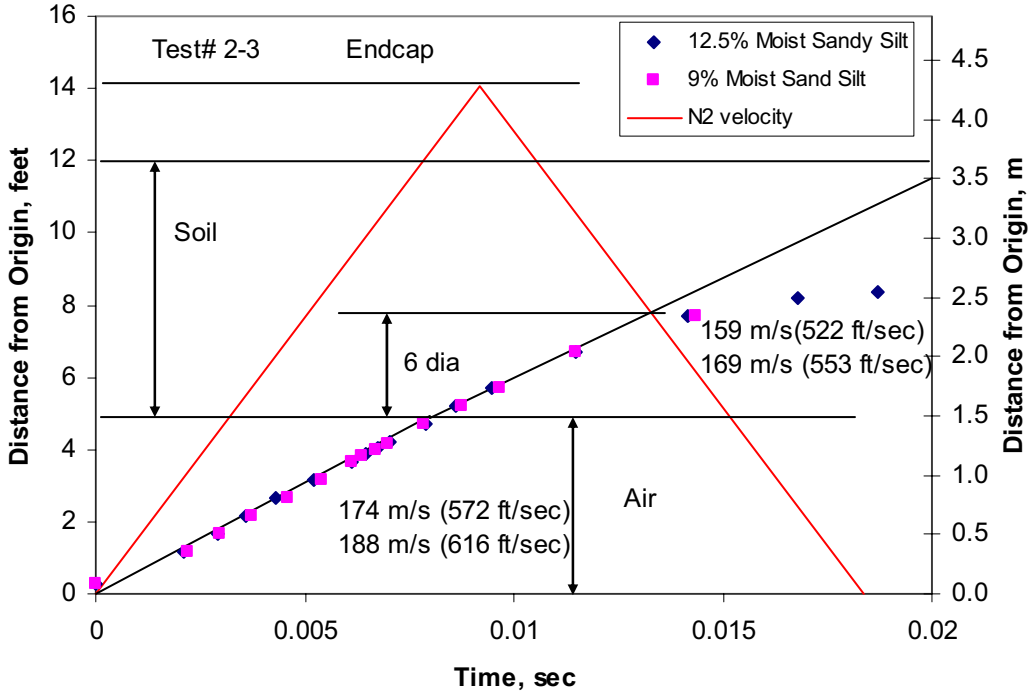

Figure 30 Timing wire results from Experiment 2-3

Table 4 Fracture speed results[‡‡‡] from Mojave experiments

Test Number	Pressure MPa (psi)	Unbackfilled V_f m/s (ft/sec)	Backfilled V_f m/s (ft/sec)	Note
1-1	19.0 (2750)	N/A	N/A	Failure at endplug
1-2	14.8 (2150)	N/A	N/A	No steady-state fracture
1-3	8.6 (1250)	N/A	N/A	Endplug failure
1-4	20.3 (2950)	178.3 (585)	129.5 (425)	
1-5	20.3 (2950)	197.2 (647)	183.8 (603)	
2-1a	27.6 (4000)	NA	NA	Valve failure
2-1b	27.6 (4000)	NA	NA	Valve failure
2-2a	24.8 (3600)	NA	NA	Base metal ring off
2-2b	24.8 (3600)	NA	NA	Base metal ring off
2-3a	24.8 (3600)	187.8 (616)	168.6 (553)	
2-3a	24.8 (3600)	174.3 (572)	159.1 (522)	

[‡‡‡] In all cases, the correlation coefficients for the calculated fracture speeds were greater than 95%.

During the first series of experiments, re-useable end plugs were used to retain the pressure boundary during the experiments. Endplugs of a different design had been used successfully in past experiments [17, 35, 36], but these newer endplugs failed several times during the first series of experiments. (The older endplugs could not be found anywhere to purchase for this project.) The endplugs were replaced with welded endcaps for the second set of tests. Precautions were taken to assure that the welding process did not significantly degrade the strength of the pipe material.

During the second-year experiments, an unexpected valve failure caused an overpressurization of one of the experiments. In this experiment, the pressure relief valve stuck in the closed position, and before word could get to the nitrogen pumper truck operator, the pressure in the pipe rose above 27.6 MPa (4,000psi) and the pipe failed.

Finally, in the second series of experiments, an unexpected ring off occurred in the unbackfilled region of one of the experiments. This test results raises an important point about conducting these types of experiments. In this particular test, the soil underneath the pipe in the unbackfilled region close to the origin area was very loosely compacted sand. It is suspected that due to the minimal support under the pipe, a large bending moment was placed on the pipe from the downward jet force that occurs as the crack propagates. This large bending moment, coupled with the tearing action from the large flap movements behind the crack, can cause the maximum principal stress to shift from circumferential to some combination of circumferential and axial causing the pipe to tear around the circumference.

Ring-offs in small-diameters pipe tests are not uncommon and have occurred near the origin in some past 2-inch and 4-inch pipe tests by British Gas [37], University of Washington [38], and Battelle [39]. All of these tests had the pipes fully supported on the bottom. Also in some 6-inch diameter nuclear pipe test with axial cracks, the pipe was supported by jacks close to the origin, and the cracks rang off before reaching the support [40]. Hence the stiffness of the soil ***under*** the pipe is important in determining how longitudinal stresses can develop ahead of the crack.

5.4 Summary of Soil Pressure Results

In an attempt to measure the forces between the soil and the pipe, several transducers were placed on the pipe surface. The details of these transducers are given in Part II of this report. Due to some experimental difficulties and the extent of the crack growth in each experiment, no data was obtained from the soil pressure transducers. However, some interesting data was developed from the soil pressure film. In Experiment 2-3, there were four types of film placed on the pipe; medium (9.6 MPa – 49MPa [1,400 -7,100 psi]), low (2.4 MPa – 9.6 MPa [350-1400 psi]), superlow (0.5MPa – 2.4 MPa [70-350 psi]) and ultra low (0.2MPa – 0.5 MPa [28-85 psi]). For this experiment, a photograph of the film after the experiment is shown in Figure 31. The data from this figure indicates that the superlow and ultra low films were saturated. In addition, the medium film shows almost no change in color. Therefore, the results indicate that the soil pressure falls between 2.4 MPa (350 psi) and 9.6 MPa (1,400 psi).

Figure 31 Soil pressure film data from Experiment 2-3

6 SUMMARY OF JGA EXPERIMENT

The Japanese Gas Association (JGA) conducted a series of full-scale burst experiments on X80 line pipe material. This extensive testing program data was shared with the PRCI/DOT program through an information exchange agreement; see Section 2 of this report. The JGA conducted four full-scale crack-arrest experiments at the FORCE technology test site in Denmark as part of a Japanese government initiative to further the understanding of ductile crack arrest in line pipe materials. These experiments were conducted over a two-year period. The details of these experiments are given in Part III of this report.

6.1 Test Matrix

The JGA experimental burst-test program consisted of four[§§§] major full-scale experiments on X80 line pipe materials. For the tests conducted, the test conditions can be found in Table 5, while the average gas composition can be found in

Experiment Date	Diameter, mm	Nominal Wall thickness, mm	Pressure, MPa	Hoop Stress, %SMYS	Temp, C	Backfill	
						Type	Depth, m
Nov 2004	762	17.5	18.5	73	6.1	Sand/Air	1.5
June 2005	762	17.5	16.2	64	19.2	Air/Air	N/A
Oct 2005	762	17.5	18.5	73	13.7	Sand/Sand	1.0/0.5
June 2006	610	14	18.2	72	20	Sand/air	1.5

Table 6.

[§§§] Other smaller scale verification experiments were conducted but not reported here.

Table 5 Test conditions for four JGA experiments

Experiment Date	Diameter, mm	Nominal Wall thickness, mm	Pressure, MPa	Hoop Stress, %SMYS	Temp, C	Backfill	
						Type	Depth, m
Nov 2004	762	17.5	18.5	73	6.1	Sand/Air	1.5
June 2005	762	17.5	16.2	64	19.2	Air/Air	N/A
Oct 2005	762	17.5	18.5	73	13.7	Sand/Sand	1.0/0.5
June 2006	610	14	18.2	72	20	Sand/air	1.5

Table 6 Average gas composition for four JGA experiments

Gas	Composition, mole%
methane	89.24
ethane	5.93
propane	2.39
i-butane	0.39
n-butane	0.54
i-pentane	0.12
n-pentane	0.08
hexane	0.07
nitrogen	0.35
carbon dioxide	0.90
Total	100.00

The typical instrumentation used on each experiment included:

- 100 timing wires for the measure of fracture speed,
- 30 pressure transducers for the measurement of dynamic decompression behavior,
- Various thermocouples for measurement of pipe and gas temperature before the experiment,
- A variety of other instrumentation such as accelerometers, soil pressure gages, soil pressure film, and
- Advanced instrumentation for the measure of dynamic CTOA. This instrumentation was only used on the last experiment.

6.2 Summary of Results

From the data given in Part III of this report, the average fracture speed per joint can be calculated for each experiment. In this case, a linear regression of the fracture speeds in the regions that were considered steady-state fracture was performed. The average fracture speeds are plotted at the center of the joint location with respect to the origin as shown in Figure 32. Even though the test pressure was lower in the June test as compared to the other experiments, the fracture speeds were higher than the cases with soil backfill, illustrating the effects of soil on the fracture speeds. Interestingly, the fracture speeds do not appear very different between the 1.6 m and the 1.0 m of sand overburden. However, the fracture speeds for the 0.5 m overburden

seems slightly higher than both the 1.0 m and 1.6 m of sand overburden. In addition, the difference in the diameter does not seem to have a large affect on the fracture speeds; however, with only one smaller diameter test result, the effect of diameter is not conclusive.

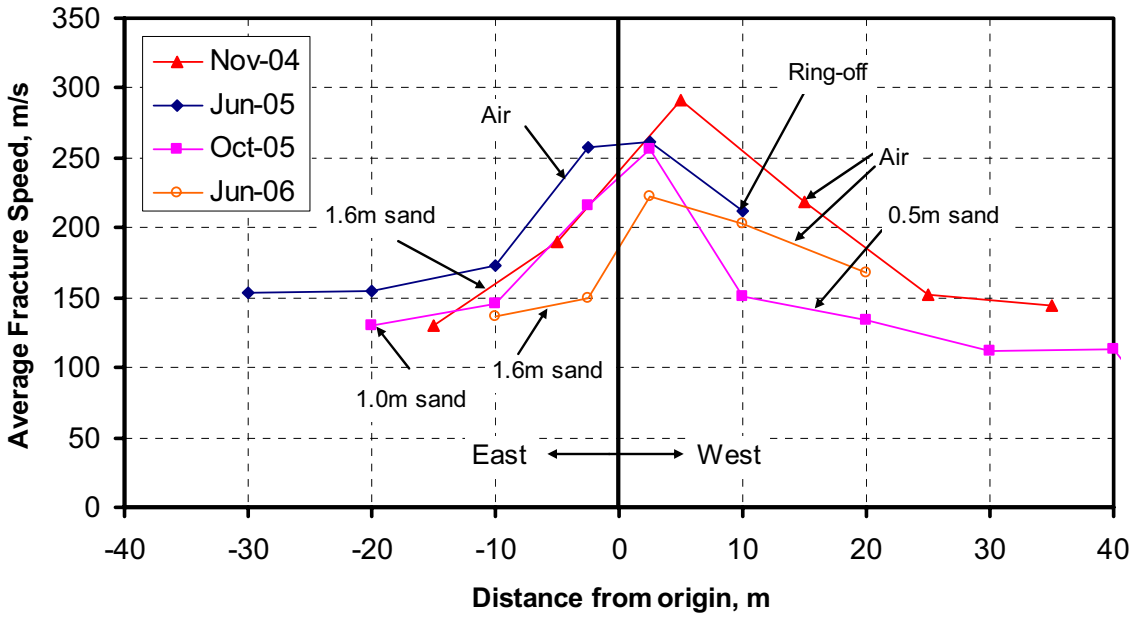

Figure 32 Average fracture speed per joint for JGA experiments

Fracture speed predictions made for each experiment using the BTC approach with the original soil backfill coefficient can be compared to the actual measured fracture speeds to illustrate the effects of the soil on the fracture speeds. This comparison is shown in Figure 33. In this figure, the y-axis is the slope of the fracture speed curve, i.e., the slope of the predicted versus measured fracture speeds, as a function of the backfill depth. This figure illustrates an increase in fracture speed slope as the depth of backfill increases. This figure also suggests that when using the original soil backfill coefficient, the calculated fracture speeds (with the original backfill coefficient) will under predict the actual fracture speeds until the backfill depth is between 2 and 2.5 times the diameter of the pipe.

In addition, the effect of backfill depth on the minimum arrest toughness can be illustrated by plotting the ratio of the measured and predicted arrest toughness, as shown in Figure 34. In this figure, the depth of the backfill was normalized by the pipe diameter. In addition, the data points represent the average or best predicted value, while the error bands represent the range of Charpy energy between the last propagate and arrest joints. A trend has formed which illustrates that there is significant relationship between the backfill depth and the minimum arrest Charpy energy. These data also suggest that for this soil, with its moisture, compaction, and strength properties, a depth of 1.5*Diameter is needed for reliable predictions of the minimum Charpy energy at arrest.

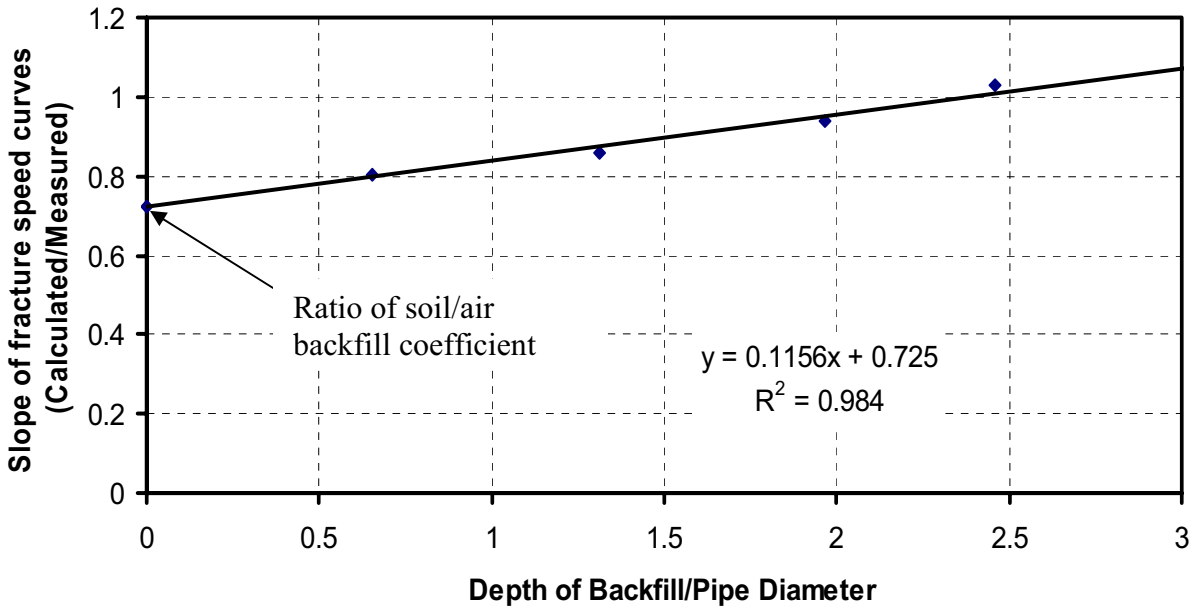

Figure 33 Relationship between the fracture speed and the depth of backfill from the JGA experiments

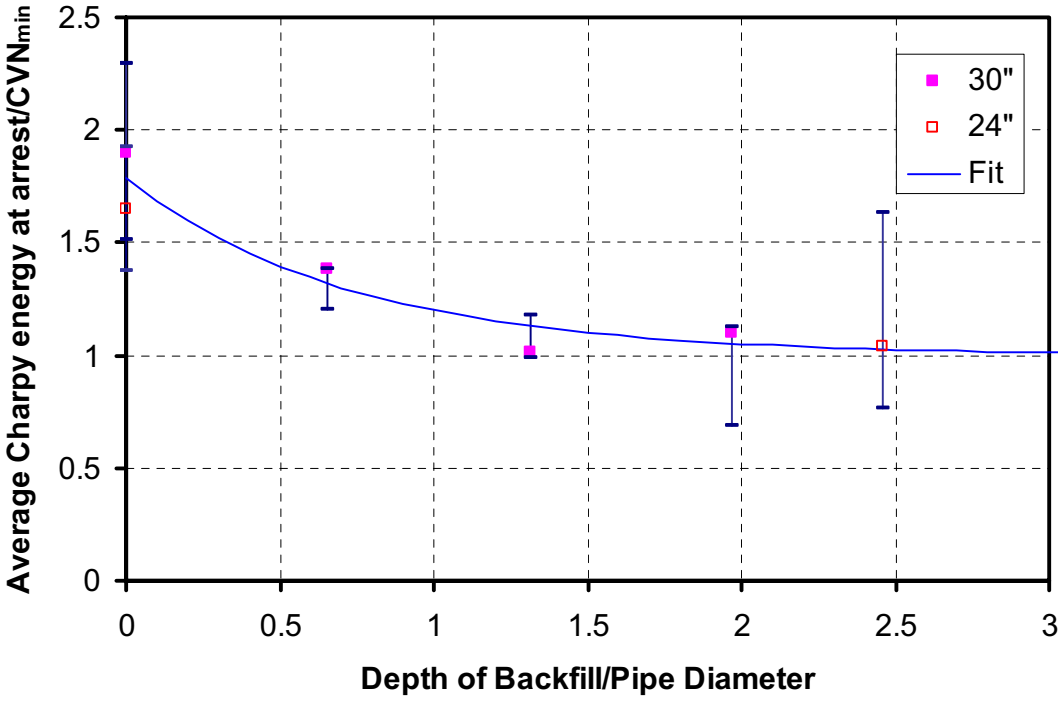

Figure 34 Relationship between minimum arrest toughness and depth of backfill from the JGA experiments

6.3 Summary of Soil Pressure Results

At the request of Emc^2, FORCE technology installed eight FlexiForce A201 force transducers to the surface of the pipe in the October 2005 JGA experiment to measure the force between the sand and the pipe during the burst. These gages have an active cell that is 9.5 mm (0.375 inch) in diameter and were glued directly to the pipe. The gages were located in the first test joint on both sides of the pipe. Circumferentially, they were placed on the south side of the pipe and at locations:

1. 50 mm from top dead center,
2. 22.5 degrees from top dead center,
3. 45 degrees from top dead center, and
4. 90 degrees from top dead center.

The amplifiers for these gages were built by Emc^2 and calibrated statically in the laboratory. A sample of the calibration curves is shown in Figure 35. During calibration it was noticed that the output of the gage was sensitive to the actual gage used and the exactness of the loading. For instance, the output changed slope if the load was applied to the gage with an offset of 1.5 mm. However, since the goal of these gages was to output an order of magnitude load between the soil and pipe, it was decided that an average calibration would suffice. It should be noted that in no cases did the gage output a positive voltage for any loading arrangement. In addition, in all cases, the gages returned to their initial output voltage after the load was removed from the sensor.

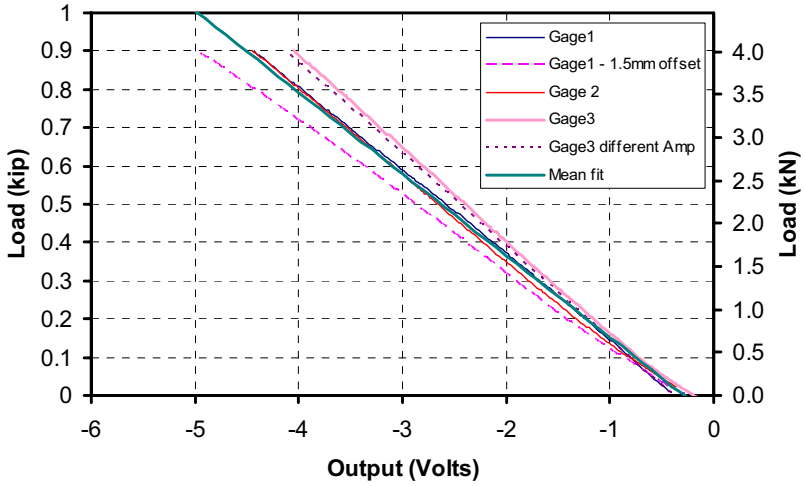

Figure 35 Calibration for the soil pressure gages

The output of the gages from the October 2005 experiment is shown in Figure 36. The trends for the data on the east side of the pipe were similar and are not shown here. The trends shown in Figure 36 were highly unexpected. In this figure, the y-axis is the output of the gage, while the x-axis is the crack-tip distance from the gage location. As the crack approached the gages, the signal from the gages was relatively quiet. About 0.5 m before the crack reached the sensor location, the output began to change. In fact, the initial movement is negative, but then the response from the gages is both positive and negative, which was never observed in the laboratory.

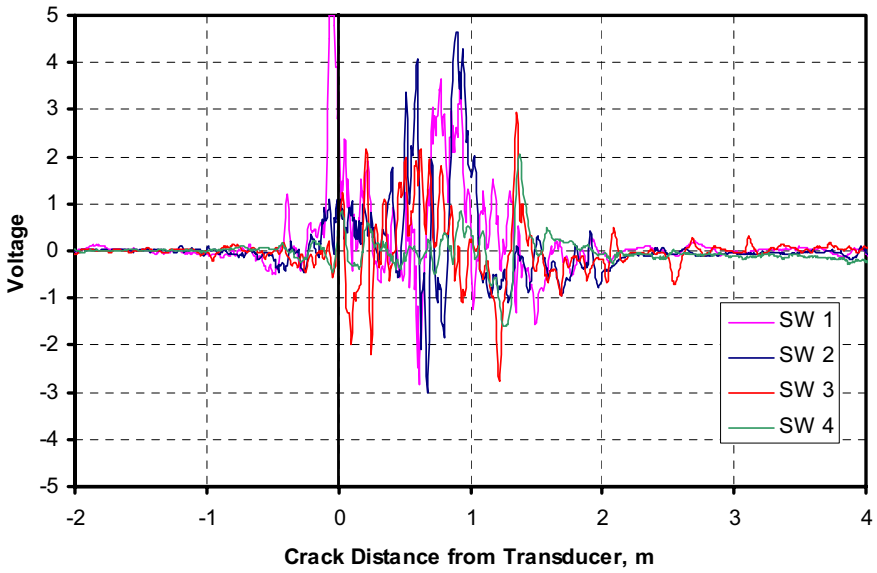

Figure 36 Soil pressure transducer output from the west side of the October 2005 experiment

After checking and rechecking the amplifier and gages, impact experiments on these gages were conducted. In this case, the gage was placed between two flat platens and struck with a hammer. An oscilloscope was attached to the gage and without excitation or amplification of the signal, the gage output a sinusoidal type signal, see Figure 37. This result implies that the gage is producing an EMF signal as a dynamic load is applied. Emc^2 staff has had several conversations with the manufacturer of the gages and they were unaware of any EMF signal issues from their gages. According to the manufacturer brochures, the gages have a response time of 5 microseconds and can respond to large impact loads. However, they have admitted that the gages are piezoelectric elements, which by nature generate EMF signals. Further investigation of these gages is required before they can be used in this application.

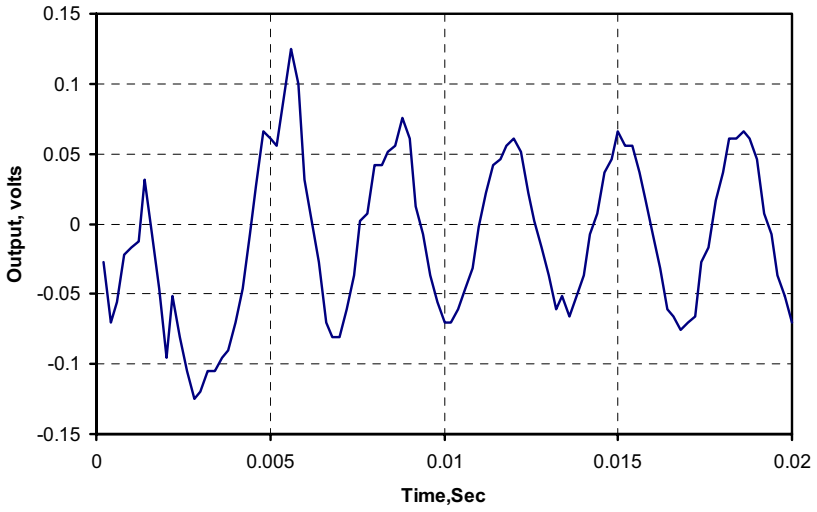

Figure 37 Output of soil gage with no amplification or excitation when impacted with hammer

In addition to the soil pressure gages, pressure sensitive film was placed on the July 2005 preliminary and the October 2005 full-scale experiment. For the July 2005 experiment, the procedure for attaching the film to the pipe was not sufficient and much of it was destroyed in the experiment. For what did survive the experiment, the film looked saturated.

For the October 2005 experiment, the film was secured to the pipe in different ways. First, most of the films consisted of two sheets of material, i.e., a donor and a receiver. The only exception to this was the higher capacity film (1,400-7,100 psi), which was only one sheet of film. For the 350-1,400 psi sheet, the film was secured to the pipe two different ways, i.e., with the donor side to the pipe in one case and the receiver side to the pipe in another case. In all other cases, the receiver side was placed to the pipe. Emc^2 supplied FORCE technology with the procedure for gluing the film to the pipe surface. The results from the October 2005 experiment are shown in Figure 38. From this figure, the film with only one sheet and the film where the donor was placed to the pipe did not withstand the force of the burst and were destroyed as the pipe pushed through the sand. For the case where the receiver was placed on the pipe, some useful data was obtained. As shown in Figure 38, the ultra low film (28-85 psi) seems fully saturated, while the low film (350-1,400 psi) appears to have no color at all on top of the pipe, but appears saturated at 90 degrees. Therefore, the forces at the top of the pipe appear to fall between 70-350 psi. Since the color seems more white than red for this film, it suggests that the stress on the pipe falls closer to the 70 psi than the 350 psi. Looking at the saturated ultra low film, the soil stress must be greater than 85 psi. Using engineering judgment, it can be assumed that the soil stress on the pipe falls in the range of 100-150 psi. These results are very similar to the results generated in the small-diameter burst tests described in the last section of this report.

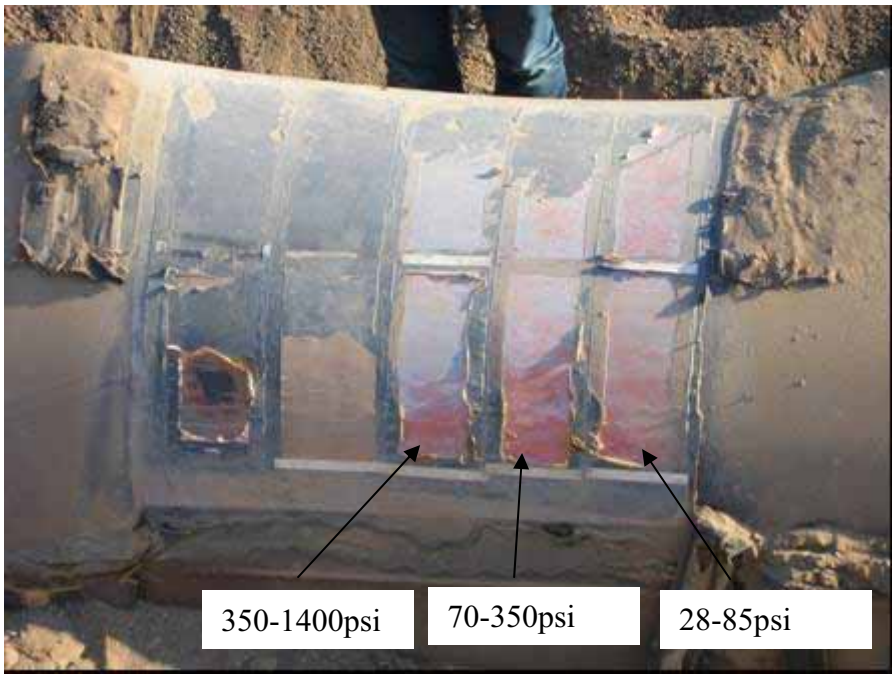

Figure 38 Photograph of soil sensitive film on west side of pipe used in October 2005 experiment

7 MEASUREMENT OF CTOA IN FULL-SCALE TESTS

As discussed in Section 3 of this report, the crack-tip-opening angle (CTOA) has been shown to be a useful fracture parameter for describing crack propagation and arrest in line pipe steels. Several laboratories around the world have developed testing procedures for measuring CTOA in small-scale specimens under both quasi-static and dynamic loads [41,42]. Note that the dynamic rates used in these experiments can be up to an order of magnitude slower than the actual loading rates seen in full-scale experiments. Currently, there are no data for physical CTOA measurements in full-scale pipe experiments to verify that laboratory experiments reproduce the full-scale behavior. As explained earlier, there is some limited data showing that the critical CTOA for crack propagation depends on the fracture speed. Therefore, it was the purpose of this effort to develop instrumentation and make the first direct measurement of the dynamic CTOA on a full-scale burst experiment.

7.1 Development of Hall Effect Device

The development of the Hall Effect device for measurement of CTOA was conducted in stages as the testing in this program progressed. This section of the report describes the development of this device.

7.1.1 Sensor, magnet and amplifier

The sensor used in this device is a continuous-time, ratiometric, linear Hall Effect sensor. The manufacturer of this sensor is Allegro and the part number for the sensor is A1301. The technical specifications for this sensor can be found in Appendix F. The sensors are optimized to accurately provide a voltage output that is proportional to an applied magnetic field. These devices have a quiescent output voltage that is 50% of the supply voltage.

The magnets used for the Hall Effect device were rare earth neodymium iron boron magnets. These magnets are supplied by Amazing Magnets and come in a variety of sizes and grades. For use in the first and second generation devices, the magnets used were model number R250B, which are ¼"dia x ¼" long magnets with a N45 grade. For the third generation Hall Effect device, the magnet used was model number R1000B, which is ¼"dia x 1.0" long with a grade of N40.

The amplifier for this device was developed at Emc^2 and was designed to run off a constant voltage power supply. The details of the Hall Effect amplifier and wiring are given in Appendix G The schematics shown in Appendix G contain the amplifier elements for the second and third-generation Hall Effect device. Since the first-generation device only used one sensor, the amplification unit only used one leg of the amplifier schematic shown in Appendix G.

7.1.2 First-generation Hall Effect device

The objective of the first-generation Hall Effect device was to prove that the device can be used on a pipe during a burst test and that a signal would be collected. The first generation device used only once Hall Effect sensor and a small (Grade N45) magnet. The device was mounted in a simple wooden fixture and glued to the pipe surface using a 5-minute epoxy. The device on a Mojave experiment during the first series of experiments is shown in Figure 39. Results from high-speed video footage of the experiments indicated that the 5-minute epoxy was not sufficient to secure the device to the pipe as the plasticity developed from the running crack. The data did

suggest that the signal increased as the bond between the pipe and fixture failed. Therefore, the results of this generation device was that the sensor was capable of measuring the required displacement, but additional work was needed to secure the device to the pipe.

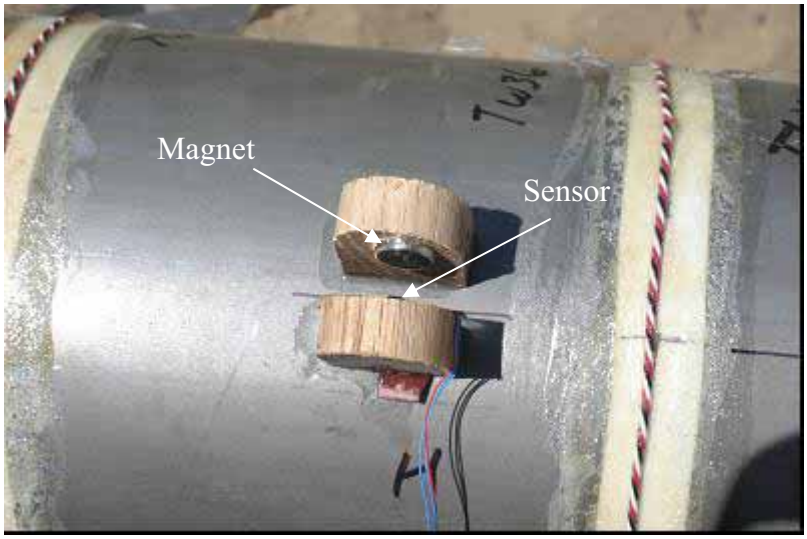

Figure 39 First generation Hall effect device installed on pipe

7.1.3 Second-generation Hall Effect device

The second-generation Hall Effect device was developed between the first and second series of Mojave experiments. Several changes were made to the device to improve its functionality:

- In attempts to capture the three-dimensional movement between the sensor and magnet, an array of Hall Effect sensors was employed. Five sensors were used in an array in order to capture the translational and rotation degrees of freedom.
- To increase the strength of the supports, fiberglass was used in place of wood. The fiberglass would increase the strength of the support and also provide the necessary insulation between the device and the pipe surface.
- To increase the bond strength between the fixture and the pipe, a specially manufactured high-ductility epoxy was used. This epoxy can tolerate 6% strain and has sufficiently high strength. It is a two-part epoxy that required clean, rough surfaces for good bonding, and completely set up in 2 hours with an adequate amount of working time. The surfaces of the pipe were roughened by a Dremel grinding wheel to get a better bonding surface.
- Finally, a larger magnet was employed in attempts to increase the initial distance between the sensor array and the magnet. This space was necessary to allow the crack to travel between the magnet and sensor, which in turn allowed the fixtures to be located further from the crack-tip plastic fields that caused the disbonding in the earlier experiments.

A photograph of the second-generation Hall Effect device is shown in Figure 40. The results from this generation device, as described in Part II of this report, indicated that most of the displacement due to the crack was in the circumferential (opening) direction, with some minimal movement in the other directions. The output was also linear with fracture speed.

Therefore, this data suggests that if the output of this device is linear with displacement, then the opening of the crack (CTOA) is constant with crack location.

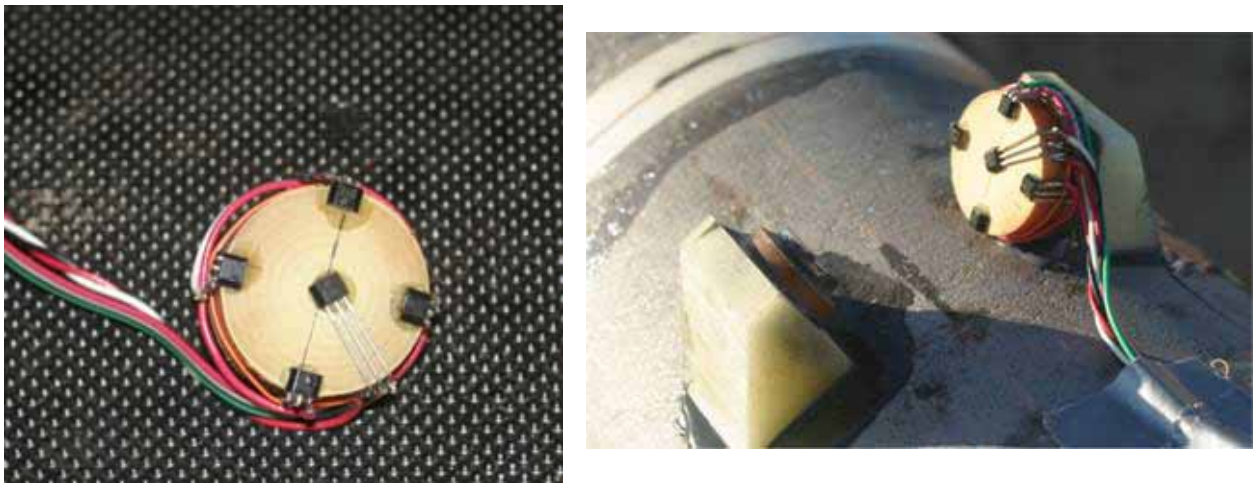

Figure 40 Second-generation Hall Effect device mounted on pipe

However, there were still some issues with this generation device that needed attention:

- In this device, the magnet was placed close to the wall of the pipe in order to make it less likely to the sheared off during the experiment. However, the location of the magnet relative to the steel pipe affected the magnetic field, and thus the reading from the sensor.
- The fixturing was designed to be perpendicular to the pipe surface and since the magnet and the sensors were not initially parallel (due to the pipe curvature), the top and bottom sensors gave different initial readings which made the calibration difficult.

7.1.4 Third-generation Hall Effect device

The third-generation Hall Effect device was developed for use on the final JGA full-scale experiments. Several enhancements were made in the development:

- New support fixtures were developed. These support fixtures were designed from aluminum and allowed the device and sensor to begin parallel at the start of the experiment. The fixture also supplied sufficient space between the magnet and pipe so that the pipe metal did not affect the magnetic field. A schematic of the support fixture is shown in Figure 41. These support fixtures also increased the initial distance between the sensor and magnet to allow a larger clearance for the crack to travel through.
- A larger magnet was required to support the larger initial distance between the magnet and sensor.
- A detailed calibration scheme was developed. Using five sensors to track the movement between the sensor and the magnet required laboratory calibration. The third-generation device was fully calibrated before use in the JGA experiment.

A photograph of the third-generation Hall Effect device on the June 2006 JGA experiment is shown in Figure 42.

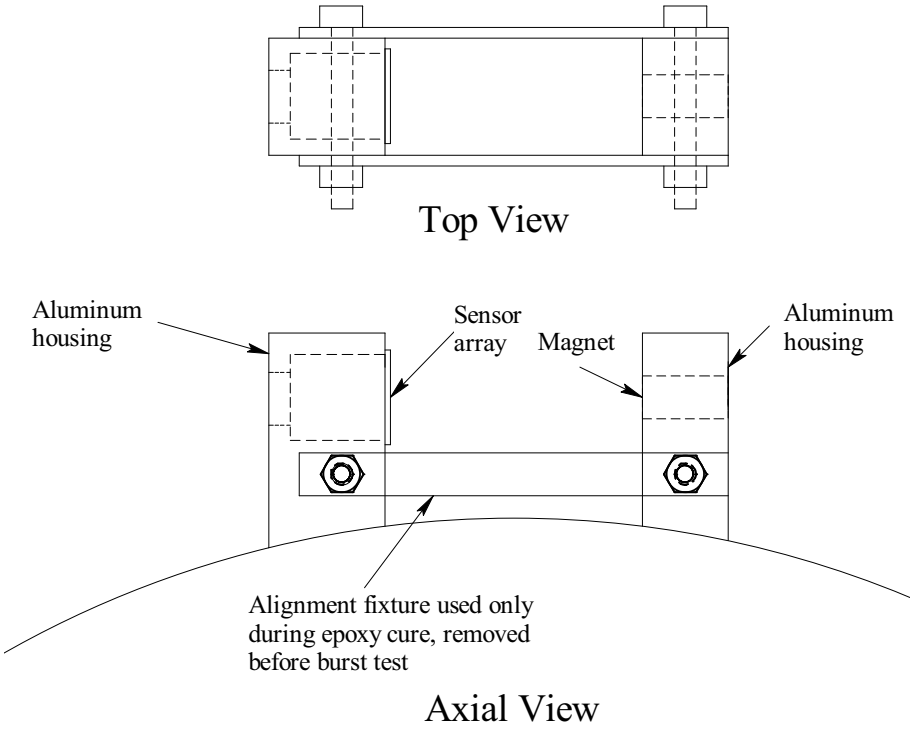

Figure 41 Hall Effect device layout

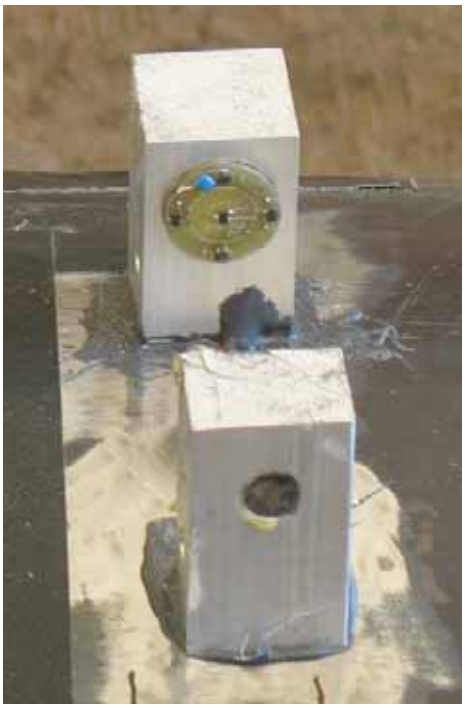

Figure 42 Photograph of third generation Hall Effect sensor on JGA experiment

7.2 Development of WireCTOA Device

The Hall Effect device described in the last section of this report is a purely electronic device for the measurement of displacement (and hence CTOA). In this section of the report, a mechanical device for measurement of the CTOA called the WireCTOA device is described. The initial concept for this device was to have a series of timing wires with a predetermined amount of slack allowing the wires to break at different crack-opening displacements than a typical tight timing wire. The difficulty with this concept was that the timing wires used were copper wires and had a large elongation to failure. The elongation to failure in various commercially available copper and aluminum wires was much larger than desired; a notching procedure is required for low strain failure. Although ways to notch the wires in a manner that gave consistent results were investigated, it was determined that this was not a reasonable approach to take for this device since it was difficult to reproduce the behavior consistently. Instead of relying on breaking of a wire that spans the opened crack, it was decided to have a stronger wire that opens an electrical contact, which would be more precise and repeatable.

The development of the WireCTOA device evolved to the final design shown in Figure 43. Figure 44 shows a photograph of the WireCTOA devices on the Mojave test pipes, as well as the Hall Effect device and timing wires.

There are four key subassemblies in the WireCTOA device.

- The high-strength small-diameter wire that spans across the crack and pulls the sliding bar across the contacting brass-tipped set screws. This is standard music wire of a specific diameter.
- A sliding bar with a socket-head screw to secure the end of the music wire.
- An anchor block that has a clearance hole for a sliding aluminum bar and electrical conducting brass-tipped set screws. This block is made from an electrical non-conducting high-strength composite material.
- Another anchor block with set screws that pretensions the wire and secures it with set screws. This block is made from aluminum.

Key aspects that required analysis and testing of each of these subassemblies are briefly described below.

Music Wire – This wire has to be strong enough to span the crack and not deflect or deform from the pressure loads of the exhausting gas coming from the crack opening of about 25 mm (1 inch). Analyses were conducted to determine the deflection of the wire and what the pullout forces would be from the pressure loading. Larger-diameter wire gives a greater strength, but the large diameter also increases the loads on the wire from the pressure. An optimal diameter was determined.

Sliding Bar – There are two key aspects to the sliding bar subassembly design. One aspect is how the music wire is attached to the sliding bar. The second is how the brass-tipped conducting screws are tightened. (1) The music wire has a very high strength (~2 GPa [300 ksi]), therefore, with the diameter needed, it cannot be bent to a tight radius. The wire is attached to the aluminum sliding bar with the use of a steel socket head screw that crimps the wire into the aluminum bar. The aluminum is much softer than the music wire, and deforms as the socket

head screw is tightened. The depth of the socket-head screw hole below the music wire clearance hole is a critical parameter. It was experimentally determined that if this depth was too great, the music wire would break at loads less than expected due to the excessive bending of the wire. Once the proper depth of the socket-head screw hole was determined, tests were performed to determine the proper torque on the socket-head screw. (2) The second aspect of this subassembly was how the surface finish affected the torque requirements on the brass-tipped set screws. These set screws hold the rod in place to resist the force exerted on the wire from the decompressing gas. Experiments were conducted to determine the pull-out force of the rod from the block with different brass-tipped set-screw torques, surface finishes, and with and without graphite lubrication. It was experimentally determined that there was less scatter in the results when unlubricated aluminum rods were used with a 100 grit final surface polishing. The pullout force was directly related to the brass-tipped set-screw torque. This force needs to be above the force from the pressure pull-out loads.

Sliding Bar Anchor Block – This anchor block needed to be made from an electrical non-conducting material. A cross-plied-mat composite material with a strength of 345 MPa (50 ksi) was chosen. This material had to be non-conducting since the brass-tipped setscrews carried the electrical signal of interest. Key aspects of this subassembly were selecting the proper composite orientation to maximize the strength, and determining the brass set screw maximum torques that could be applied before cracking the composite block. It was experimentally determined that the composite block failed when the set screw torque was above 35 in-lb, which is much higher than the 10-in-lb of torque that is required to resist the pressure loading. With the factor of 3.5 on the torque limit, the composite material holding the set screw in place should not creep from the time it was tightened to the time of the test.

Pre-tension Anchor Block – This block is made out of aluminum and has two steel set screws that are used to secure the music wire. These two screws are redundant, and potentially one of them could be eliminated. The torque required to secure the music wire is a critical parameter, and was determined experimentally. As in the sliding rod case, the depth of the set-screw hole relative to the clearance hole for the music wire is a critical dimension. Experiments were conducted with composite material, steel, aluminum, and brass to determine the best way to secure the music wire. Aluminum had the correct strength and ductility to deform and hold the wire in place without damaging the wire.

A final aspect was how to best attach the two anchor blocks to the test pipe. An adhesive that was too brittle (i.e., super glue or off-the-shelf 5-minute epoxy) would allow the device to debond from the pipe due to the deformation of the pipe walls, as documented in one of the high-speed videos from the first series of Mojave tests. Spot welding brass screws to the pipe with a stud-gun did not provide sufficient strength for this WireCTOA device. For the final design, a specially manufactured high-ductility epoxy was used to secure the blocks to the pipe. This epoxy could tolerate 6% strain and still have sufficiently high strength. This was a two-part epoxy that required clean, rough surfaces for good bonding, and completely set up in 2 hours with an adequate amount of working time. The surfaces of the pipe were roughened by a Dremil grinding wheel to get a better bonding surface.

The deformation of the pipe walls is also one of the factors that determine the minimum distance that the anchor blocks can be located from the crack plane. The reduction in thickness back from the crack plane from past pipes tested in the first set of Mojave experiments was measured. This distance was relatively small due to the low toughness of the material and smaller thickness of the pipe in our Mojave tests. This distance could be a more significant consideration in large-diameter pipe tests with thicker and tougher material.

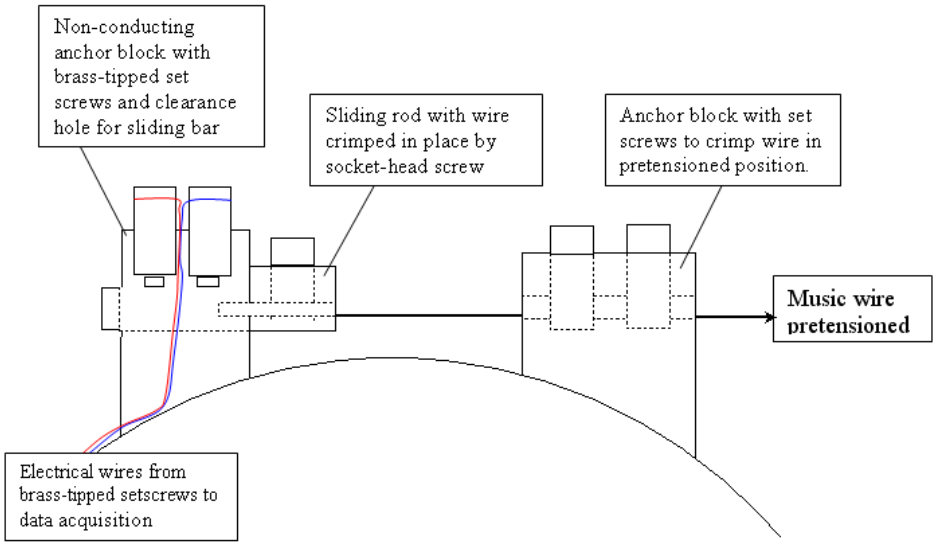

Figure 43 CTOA Wire device assembly on 6" pipe tests (drawn to scale)

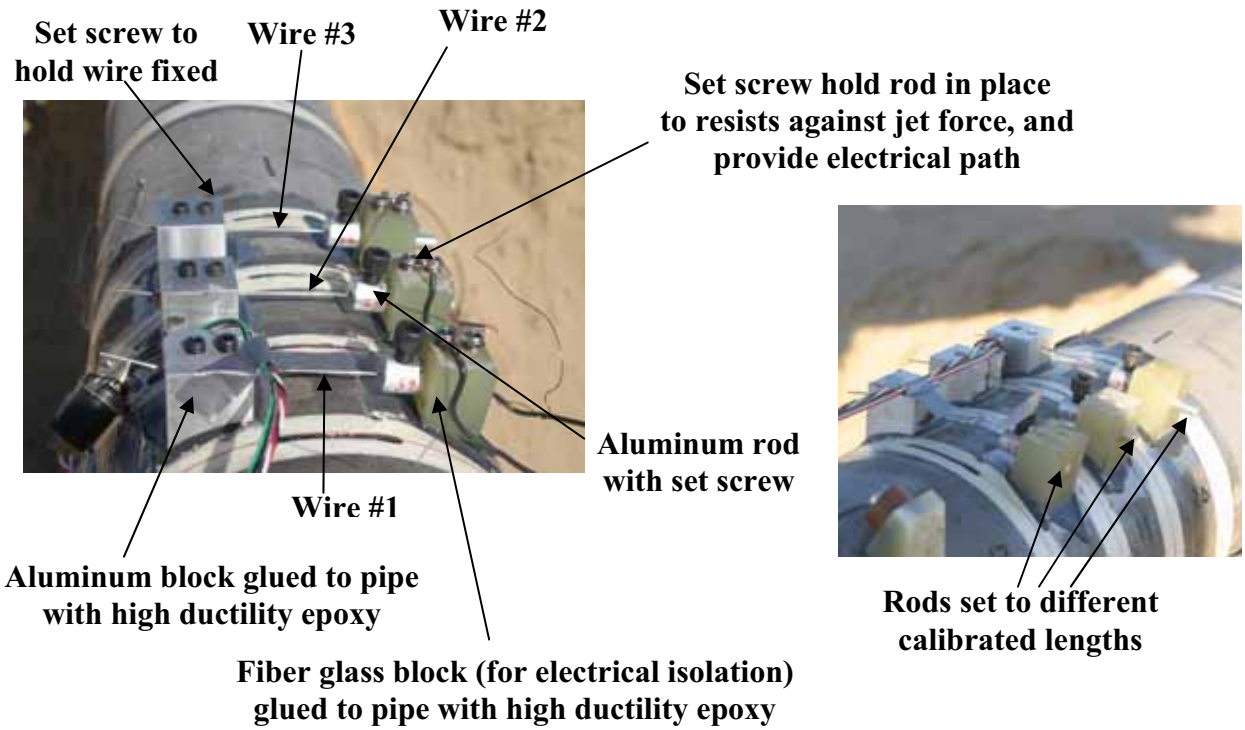

Figure 44 Photo of three WireCTOA devices and timing wires on Mojave test pipe

The testing of the WireCTOA was not successful in the Mojave experiments. In many cases, the cracks did not travel far enough to reach the WireCTOA device. However, in the few cases where the crack passed through the device, the tension used for the set screws that held the aluminum rod in place was too severe and either the high strength piano wire failed or the epoxy failed. For application on the JGA experiment, this torque value was decreased.

7.3 Lessons Learned from Mojave Experiments

As explained in Part II of this report, both the Hall Effect and WireCTOA devices were applied to select Mojave experiments. The experience with these devices obtained during the Mojave experiment allowed significant refinements to be made to both devices. The major lessons learned from using these devices on the Mojave experiment include:

- The Hall Effect sensor can be used to track the crack-opening displacement at a unique location as the crack passes the sensor. It appears that the change in the output signal from the device is linear with the change in crack tip location, which suggests constant CTOA.
- A high ductility epoxy is needed to secure the support fixtures to the pipe. The ductility is needed since the high plastic strains on the crack flanks can debond the fixtures from the pipe if low ductility epoxy is used.
- The pipe surface can affect the magnetic field and thus the output from the Hall Effect device.
- The success of the WireCTOA device is heavily dependent on the torque chosen to secure the aluminum rod. If the torque is too high, the force will fail the epoxy before the rod is pulled out.

These lessons were used in the guiding the final development of the devices used in the JGA experiment.

7.4 Application to JGA Experiment

Both the Hall Effect and WireCTOA devices were placed on a pipe joint in the June 2006 JGA experiments. Originally, the devices were planned to be used in both the unbackfilled side and backfilled sides of the experiment, however, scheduling conflicts did not allow Emc^2 to travel to Denmark until after backfilling had already begun. Therefore, the devices were only placed on the unbackfilled side of the experiment. A photograph of the devices on the JGA pipe is shown in Figure 45.

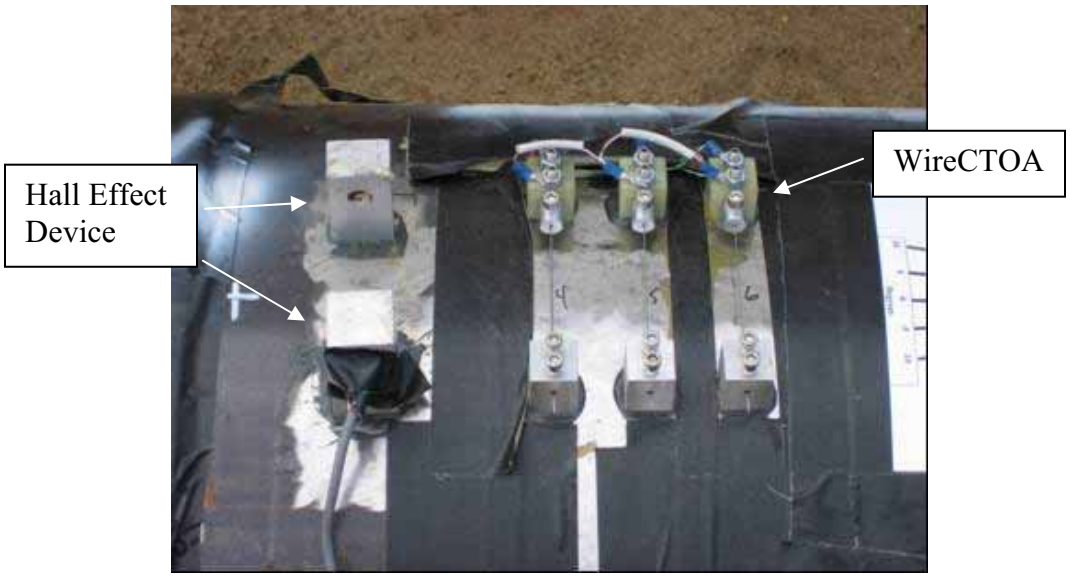

Figure 45 Photograph of extra instrumentation on June 2006 experiment

7.4.1 Case 4 test conditions

As explained in Part III of this report, the June 2006 experiment was conducted on June 20, 2006 at FORCE Technology. The pipe test was conducted with an average temperature of 20C and at a pressure of 18.31 MPa. The east side of the pipe was backfilled with 1.5m of sand, while the west side was unbackfilled. The layout for this test is shown in Figure 46.

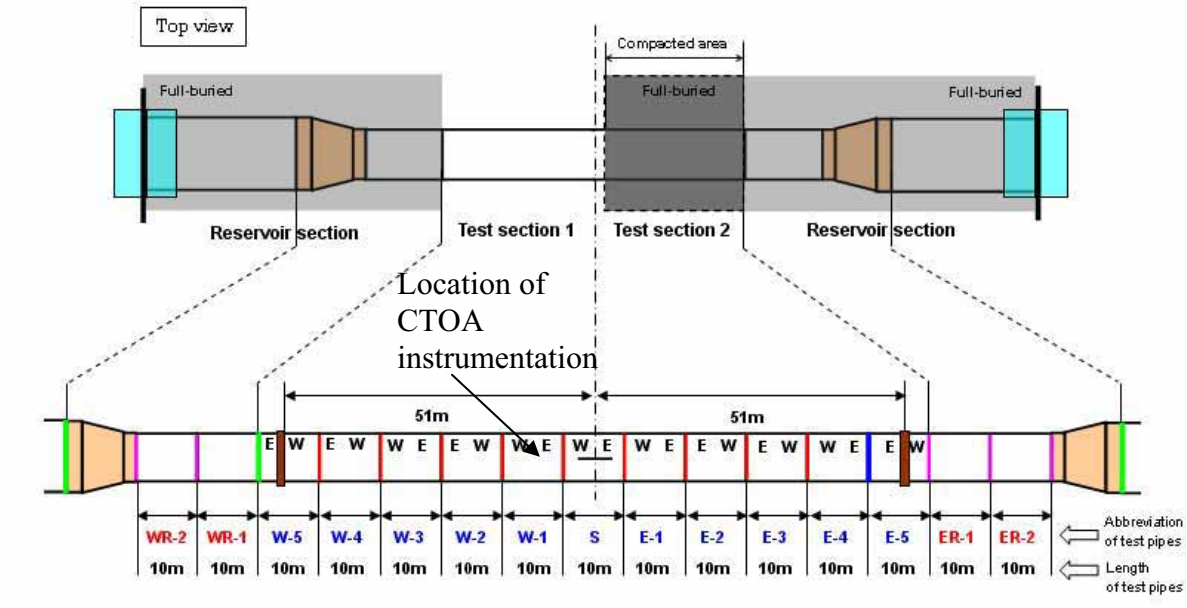

Figure 46 Layout for June 2006 experiment

The test section consisted of eleven 10 m long sections. Each pipe joint had an outer diameter of 610 mm and a nominal wall thickness of 14 mm. The extra CTOA instrumentation was placed

on the pipe section in Joint W1, which had an average Charpy energy of 71J. In helping with the location of the crack tip, additional timing wires were added around the WireCTOA device. A layout of the devices on the pipe relative to FORCE's Timing Wire #11 is given in Figure 47.

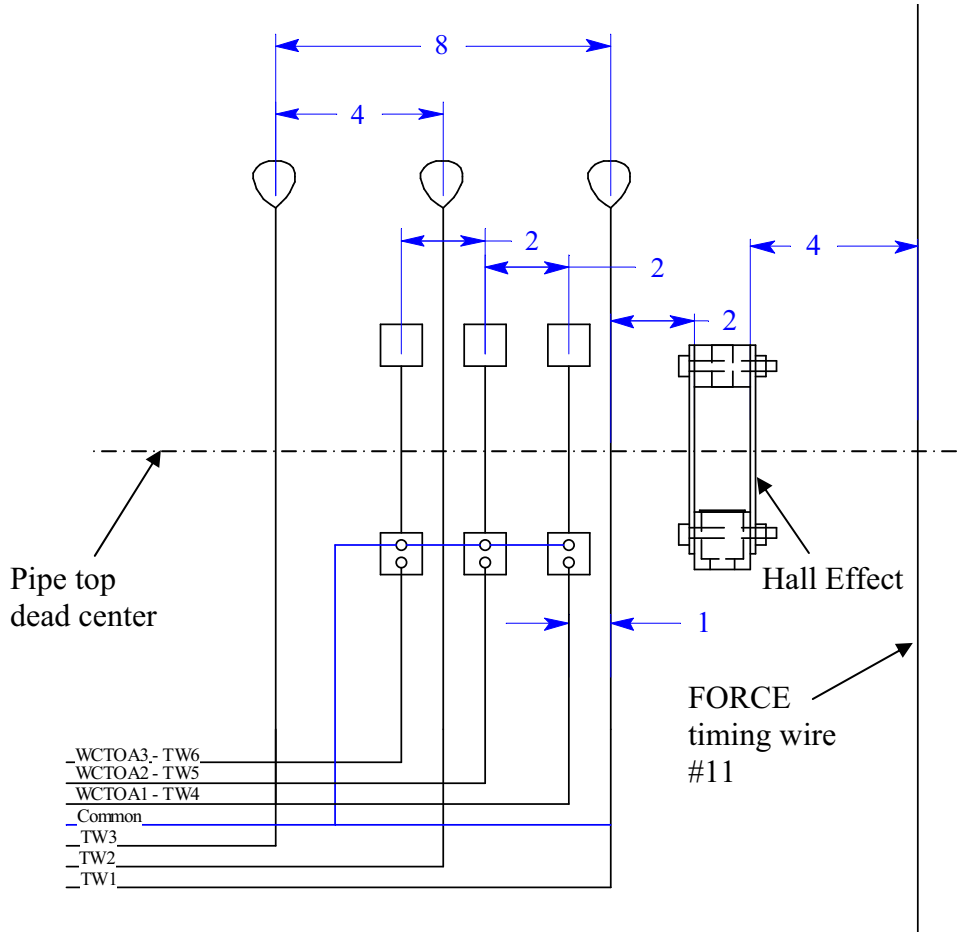

Figure 47 CTOA instrumentation layout (dimension in inches)

7.4.2 Hall Effect device

7.4.2.1 Calibration

The Hall Effect device was calibrated in the laboratory prior to its use in the JGA experiment. The device was calibrated for both translational and rotational movement between the sensor and magnet. The translational calibration curves are shown in Figure 48, while the rotational calibration curves are shown in Figure 49. In both of these figures, the data points represent output from the individual sensors. The location labels indicates the sensor location on the face of the device. The translational values indicate that all sensors respond in a similar fashion when the translation is inline with the axis of the sensor. The rotational calibration shows not much sensitivity when the rotation occurs around the center of the sensor. It is believed that this calibration is sufficient since the translation that occurs in a burst test between the magnet and sensor will dominate over the other degrees of freedom.

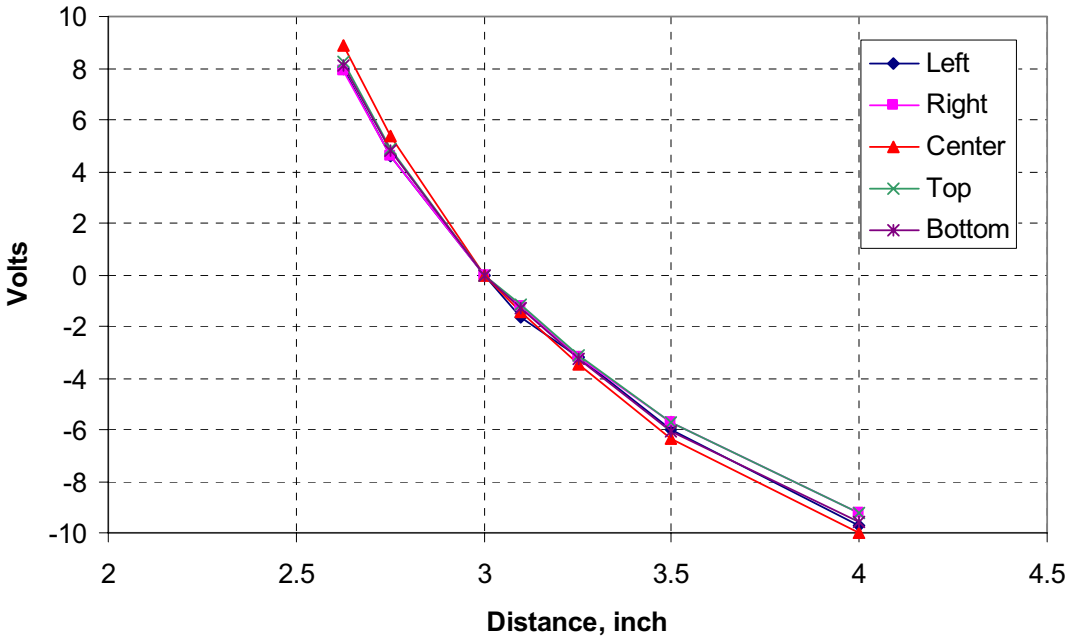

Figure 48 Hall Effect translational calibrations

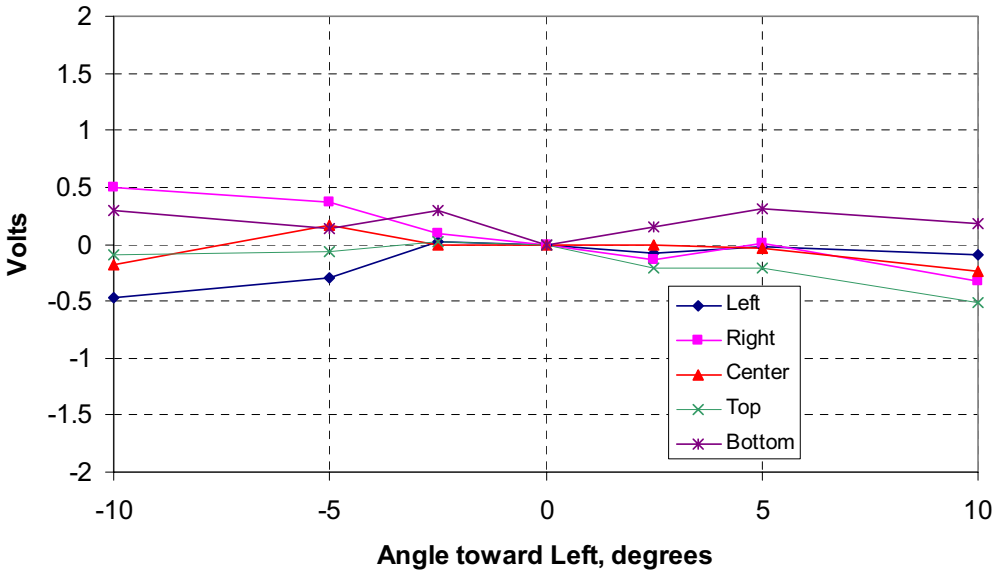

Figure 49 Hall Effect rotational calibrations

7.4.2.2 Results

The results from the Hall Effect device are shown in Figure 50. In this figure, the time equal to zero corresponds to the time when the explosive cutter was ignited. As shown in this figure, the device behaved well prior to the start of the test, and continues to behave well until 0.0094 seconds after the event began. At this time, all of the devices began cycling between 5 and -5 volts (saturation limits of the amplifier). From the fracture speed results, the crack passed the Hall Effect sensors at a time of 0.047 seconds. At this point in the voltage response, a large change from -5 to 5V occurs, but the time period in which this change occurs is too fast to be due

to a response from the Hall Effect device. As described in detail in Part III of this report, it is suspected that an electromagnetic pulse from the creation of the opening during the test affected the Hall Effect sensors. Since a change in magnetic field can affect the sensors, and since the device saturated at about the same time the camera is affected, the most logical conclusion is that a magnetic pulse occurred. This problem did not occur in the Mojave burst tests with the Hall Effect device.

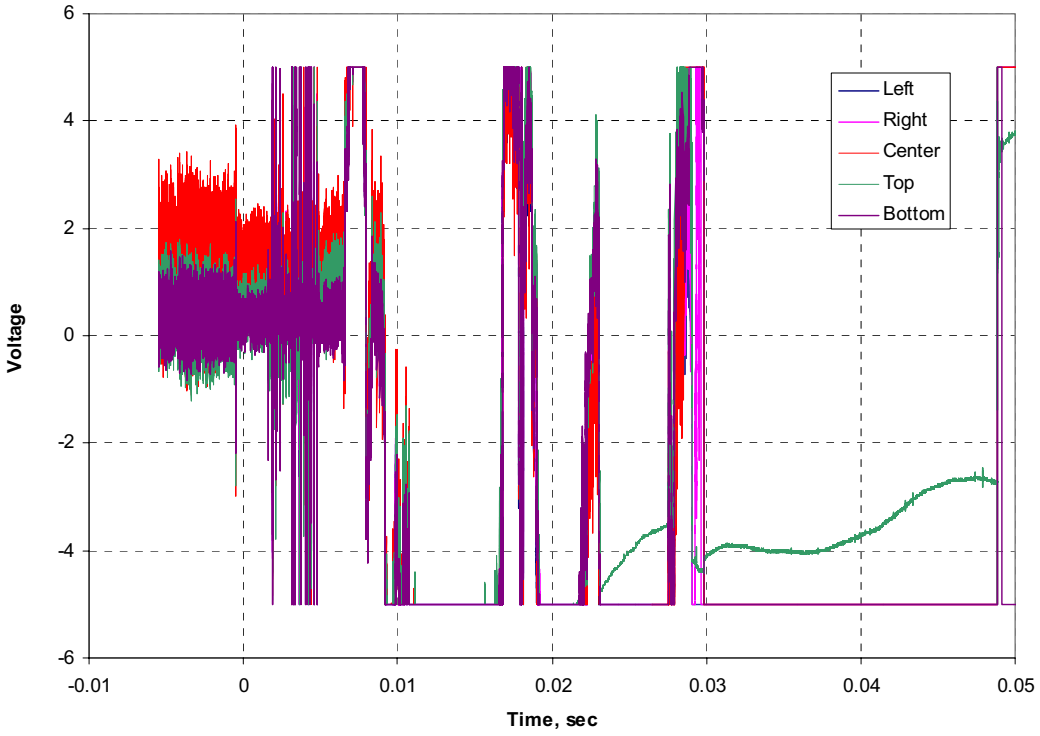

Figure 50 Experimental results from the Hall Effect device

7.4.3 WireCTOA device

The raw data from the WireCTOA device is shown in Figure 51. This figure illustrates that the device produced clean signals as the crack passed the tight timing wires and the WireCTOA device. The reduced WireCTOA data is shown in Figure 52. This figure shows the time for break versus the physical distance from the origin for the WireCTOA (solid triangle), Emc^2 tight timing wire (solid square), and the FORCE tight timing wire (solid diamond) data. The solid line in this figure represents the fit to the FORCE timing wire data for the datapoints shown. The data from the Emc^2 timing wires fall very close to the fit from the FORCE data. However, there is one datapoint (10.9 m from origin) that failed later than the other wires. Realistically, these timing wires may fail before the crack tip reaches the wires due to the plasticity ahead of the crack, but physically cannot fail late. Therefore it stands to reason that the actual crack tip may be slightly behind that measured from the FORCE timing wire data. If the trend from the FORCE data is offset to capture the last Emc^2 timing wire failure, this line (heavy dashed) represents the bound of the actual crack tip location. The final line shown (heavy center line) is a straight fit through the Emc^2 timing wire data. This fit may capture the slight variations in crack tip location that may occur between the FORCE timing wire data.

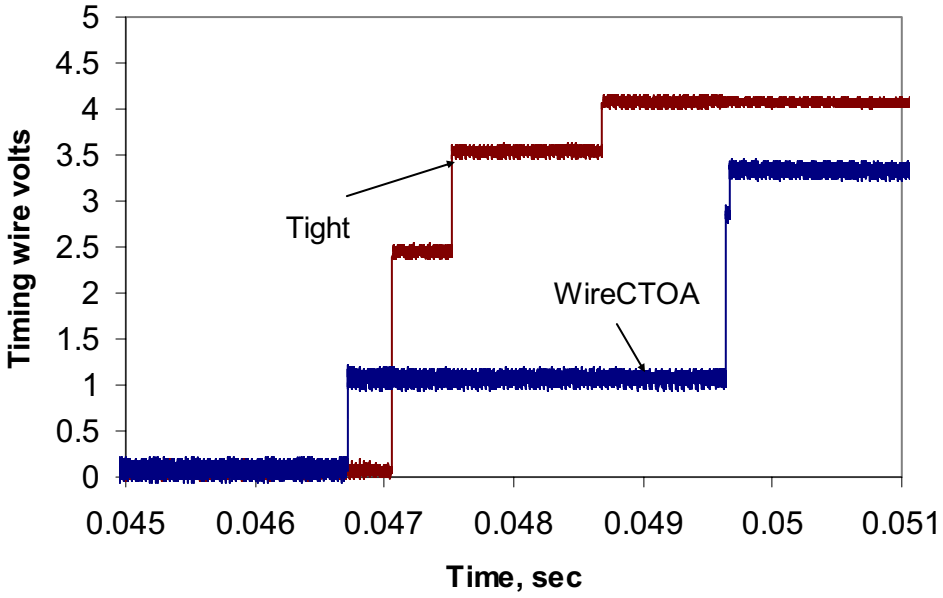

Figure 51 Raw data from the WireCTOA device and Emc^2 timing wires

The solid triangles in Figure 52 represent the WireCTOA results from this experiment. It should be noted that the three WireCTOA devices were designed with three different length aluminum rods, to assure that all of the devices did not pull out (fail) at the same time. In this experiment, the WireCTOA devices at 10.74 m (WCTOA1) had a rod length of 24.8 mm (0.975 inch), at 10.79 m (WCTOA2) had a rod length of 31.4 mm (1.235 inch), and at 10.84 m (WCTOA3) had a rod length of 37.97 mm (1.495 inch). From the data, it is clear that the WCTOA2 failed early, i.e., the crack tip was about 0.3 m (11.8 inches) behind the device when it failed. The other two devices failed at about the same time. It is suspected that WCTOA1 disbonded from the pipe, but the electric connection was not lost, since the crack was well beyond the device when it failed. Only the WCTOA3 device acted properly. From this device an estimate of the CTOA can be made. A CTOA calculation schematic is given in Figure 53. Using the three estimations of the crack-tip location, the CTOA can be estimated as 3.6 deg, 5.1 deg or 6.3 deg. It is suspected that the heavy dashed line is the most accurate representation of the actual crack tip location; therefore the estimate of the CTOA from this experiment is 5.1 deg. Interestingly, the average CTOA from the three devices is 5 deg.

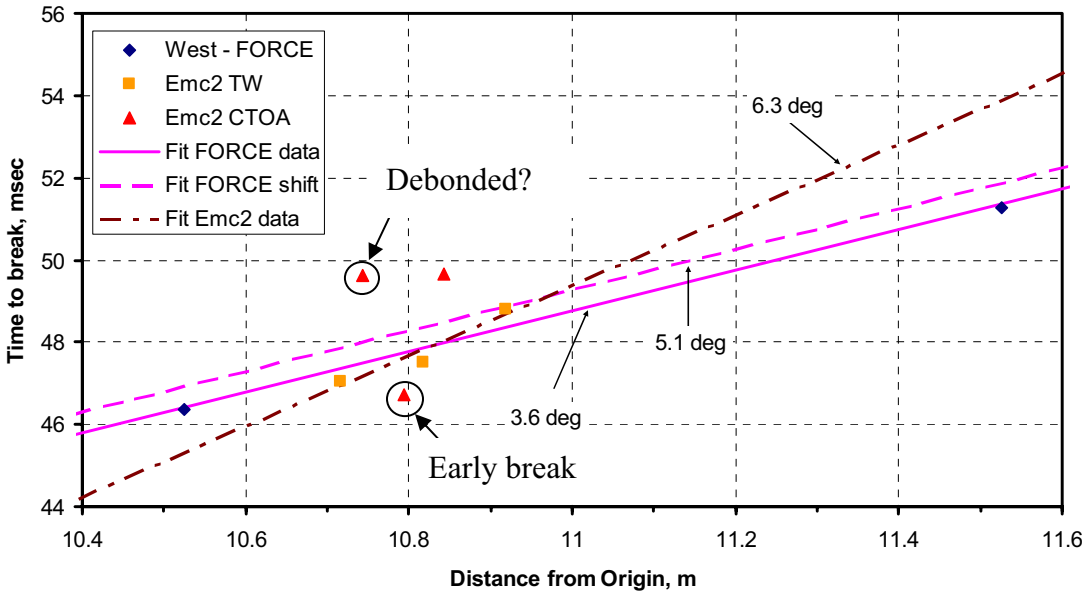

Figure 52 Reduced data from WireCTOA device

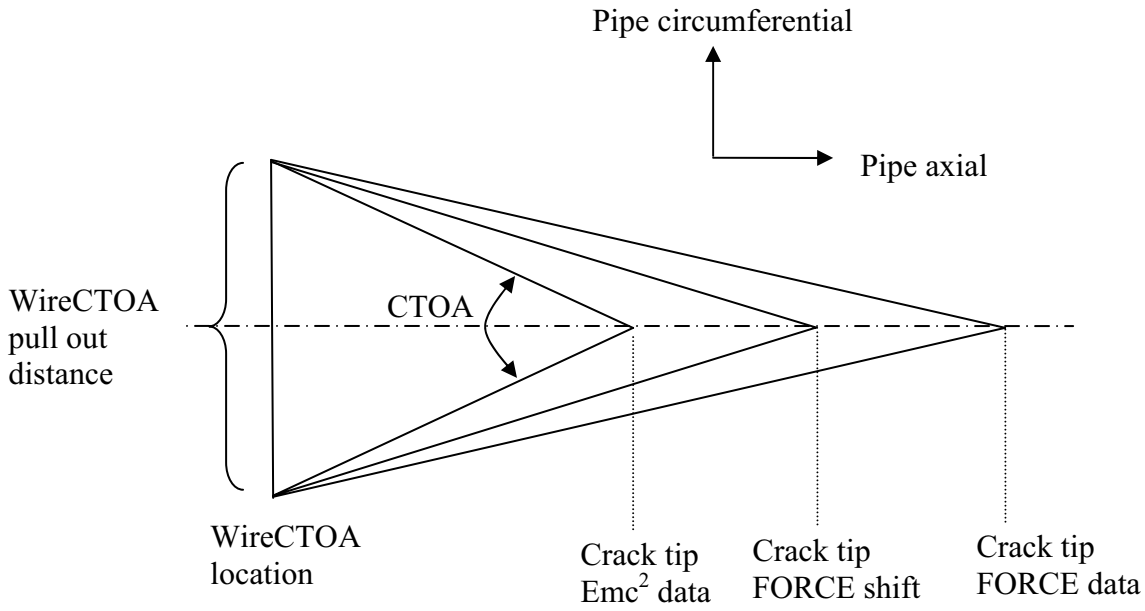

Figure 53 WireCTOA calculation schematic

7.4.4 Verification of CTOA

Direct verification of the CTOA measurement made during the June 2006 burst test is not possible due to the failure of the high-speed camera (see Part III for details); however, other test data on similar materials can be used to justify the value measured in this effort. It is important

to point out that this is the first direct measurement of a CTOA value from a full-scale high energy burst test. Some visual measurement of running cracks have been recorded in the literature, but no direct measurement of CTOA has been made on any full-scale, high-energy burst test on line pipe materials.

There have been some measurements of CTOA from small-scale, DWTT experiments that can be used to get an understanding of the magnitude and scatter in these measurements. In Reference 43, highly instrumented DWTT experiments were conducted. In these experiments, high-speed video was used to record the CTOA during steady-state fracture in these specimens. In one particular case, the material DWTT energy was about the same as that in Pipe W1 from the June 2006 experiment, i.e., the PN-DWTT energy for Pipe 42 from Reference 43 was 3.95 J/mm^2, while for the W1 pipe, the PN-DWTT energy was 4.08 J/mm^2. The results from the instrumented DWTT experiments are shown in Figure 54.

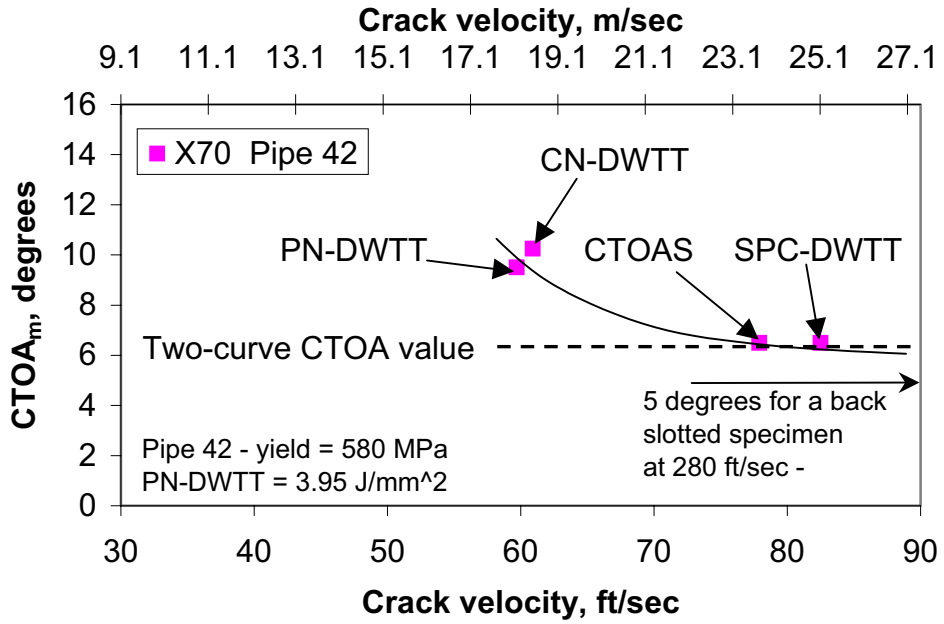

Figure 54 CTOA versus crack speed for lower toughness X70 line pipe steel

In Figure 54, several different specimen results are shown. PN-DWTT, CN-DWTT, CTOAS, and SPC-DWTT represent pressed-notch DWTT specimen, Chevron-notched DWTT specimen, shallow-notched specimen from the CSM Two-Specimen CTOA approach, and static-precracked DWTT specimen, respectively. Each of these specimens has a different amount of crack initiation energy due to the notch configuration, but has the same overall specimen size. The difference in crack initiation energy changes the DWTT hammer speed and thus the fracture speed. As shown in this figure, the measured CTOA (CTOA$_m$) decreases with increasing fracture speed. From this data, it appears that the decrease in CTOA levels off at higher fracture speeds. This fact is supported by the deeply backslotted data shown in Figure 54. For this specimen, a PN-DWTT specimen was backslotted so that the ligament of the specimen is placed more in tension than bending, which is closer to the behavior in a pipe. By adding this backslot, the crack speed increased about 450%. The measured CTOA was 5 degrees, which is only 1 degree smaller than the CTOA at a much lower fracture speed. From that limited amount of

data, it can be inferred that CTOA is a function of the loading rate/fracture speed, but value is relatively constant at fracture speeds that occur in typical full-scale tests.

Since the DWTT energies between the JGA test pipe W1 and the Pipe 42 material shown in Figure 54 are similar, it seems that the CTOA values would be comparable. However, a couple of points need to be considered.

- The pipes are different grades, i.e., W1 is an X80, while Pipe 42 is an X70. This may affect the CTOA results.
- The measurement made from Pipe 42 was at a recorded fracture speed of 85m/s (280ft/sec), while the average fracture speed through Pipe W1 was 202 m/s (663 ft/sec). As noted earlier, this speed difference may not make a significant difference in the CTOA measurement.
- There can be significant scatter in CTOA measurements.

The magnitude of the scatter in CTOA measurements can be estimated from data presented in Reference 28. In that paper, the J-R curve was calculated from the instrumented DWTT results from pipes with grades ranging from X52 to X100. The slope of the J-R curve, which is directly proportional to the true steady-state fracture energy in the specimen, is plotted against the measured CTOA as shown in Figure 55. In this figure, the red dashed lines represent the magnitude of the scatter in these measurements. From this figure, the scatter in a CTOA of 5 degrees is about ±1 degree. Therefore, the CTOA results from Joint W1 fall within the typical CTOA scatter for the measurement made from Pipe 42. Due to the differences listed above, this is not definitive verification of the CTOA measurement taken during the full-scale experiment, but it is qualitative evidence that this value is reasonable.

In addition to measurement of CTOA in small-scale specimens, there have been some pipe test visual measurements made of CTOA. One such set of experiments is from Reference 29. In this work, very small diameter (2-inch) pipe tests were conducted. The pipe strength was comparable to an X70. These tests were conducted and an experimental split-ring model to predict CTOA was developed in Reference 30. The comparison of the experimental results and the numerical predictions is shown in Figure 56. The experimental results suggest the CTOA measured was approximately 5 ±2 degrees. The authors of Reference 30 then used this model to predict the CTOA in a series of Japanese pipe experiments. Some of these experiments were on 48-inch diameter X70 with rich natural gas. They compared the calculated CTOA with the Charpy energy as shown in Figure 57. Using a best-fit line, the calculated CTOA at a Charpy energy of 71J is 5.25 degrees, which is also within the scatter described above.

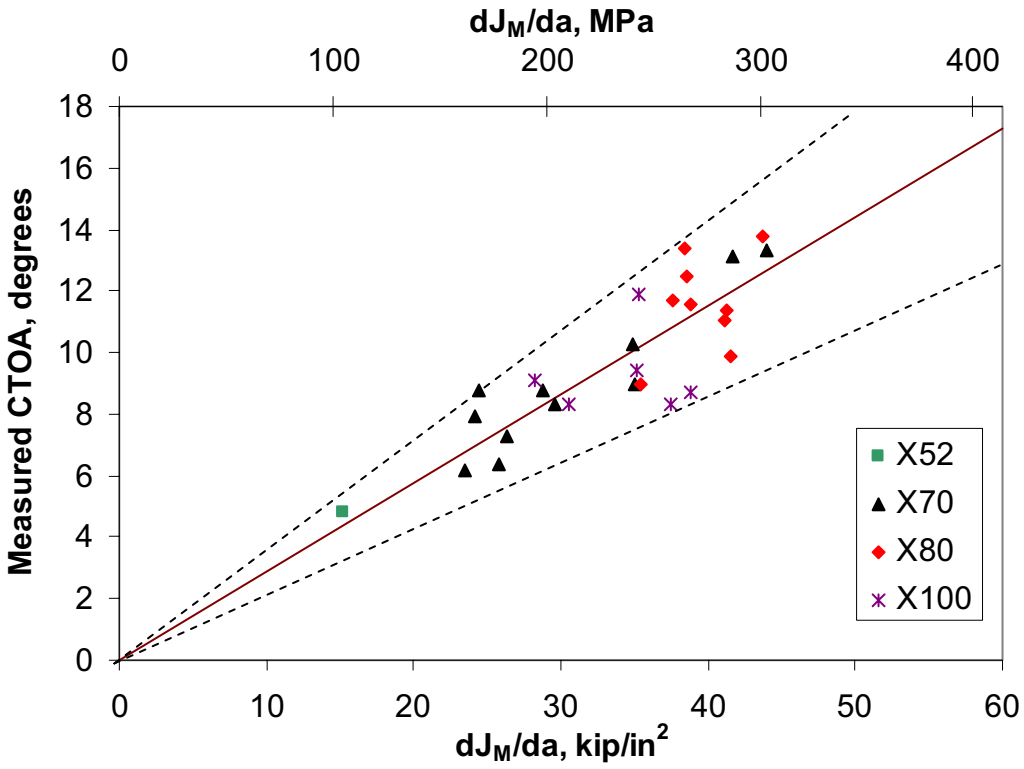

Figure 55 Measured CTOA versus dJ_M/da for a variety of linepipe steels

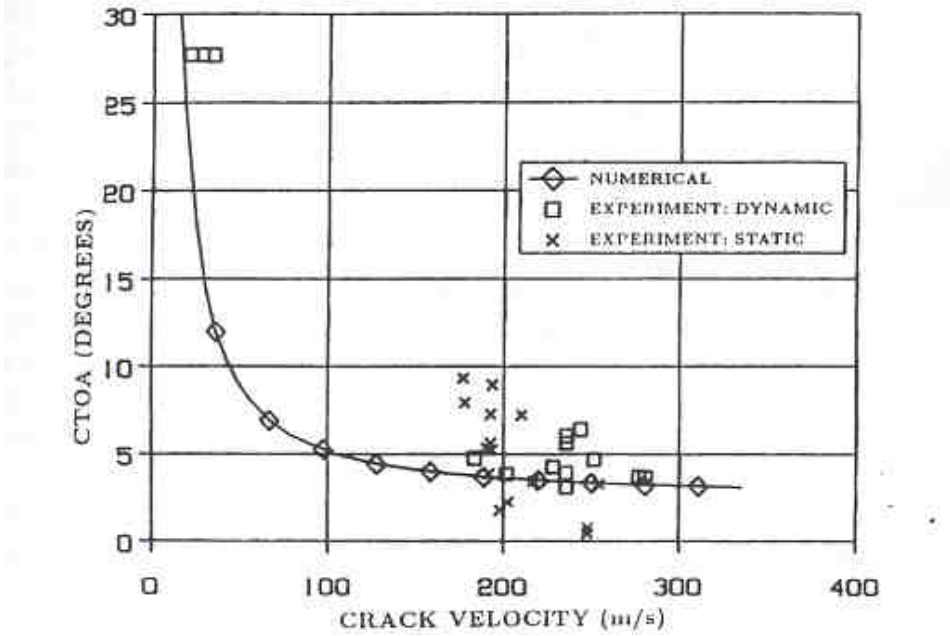

Figure 56 Comparison of ring model analysis scheme and experimental results from Reference 29. Figure used with permission from Journal of Pressure Vessel Technology.

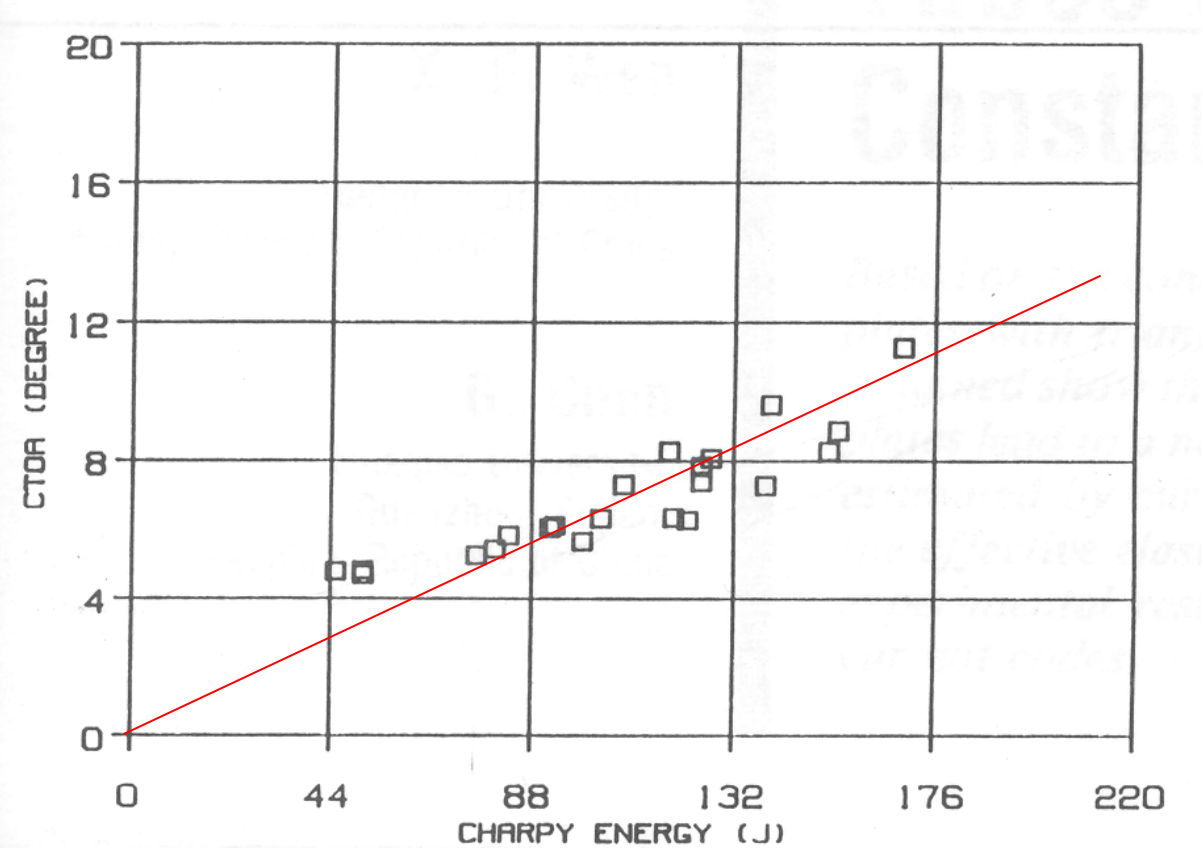

Figure 57 Calculated CTOA versus Charpy energy for pipe test materials from Reference 30. Figure used with permission from Journal of Pressure Vessel Technology.

These examples do not definitively verify the measurement of CTOA made on this pipe test; however, they do give circumstantial evidence that the measurement of CTOA is reasonable.

8 MODIFICATION OF BACKFILL COEFFICIENT

In this section of the report, the results from this program are used to make a modification to the backfill coefficient in order to make better predictions of fracture speed and minimum arrest toughness. The results and conclusions from both the Mojave and JGA testing are used in making this assessment. In addition, the original full-scale data that was used by Maxey [44] in developing the original backfill coefficient was revisited and categorized by soil type.

8.1 Effects of Soil Depth

The results from the JGA effort suggest that that depth of the soil is important to both the fracture speeds and the predictions of minimum arrest toughness. This effect can be further investigated by plotting the data from both the JGA and Mojave experiments on the same scales. For instance, if the sand Mojave experiment is shown with the JGA sand experiments, a similar trend is seen, see Figure 58. As shown in this figure, a trend is clearly forming that shows an increase in Charpy energy needed for arrest as the backfill depth increases. The trends with and without the Mojave experiment are very similar.

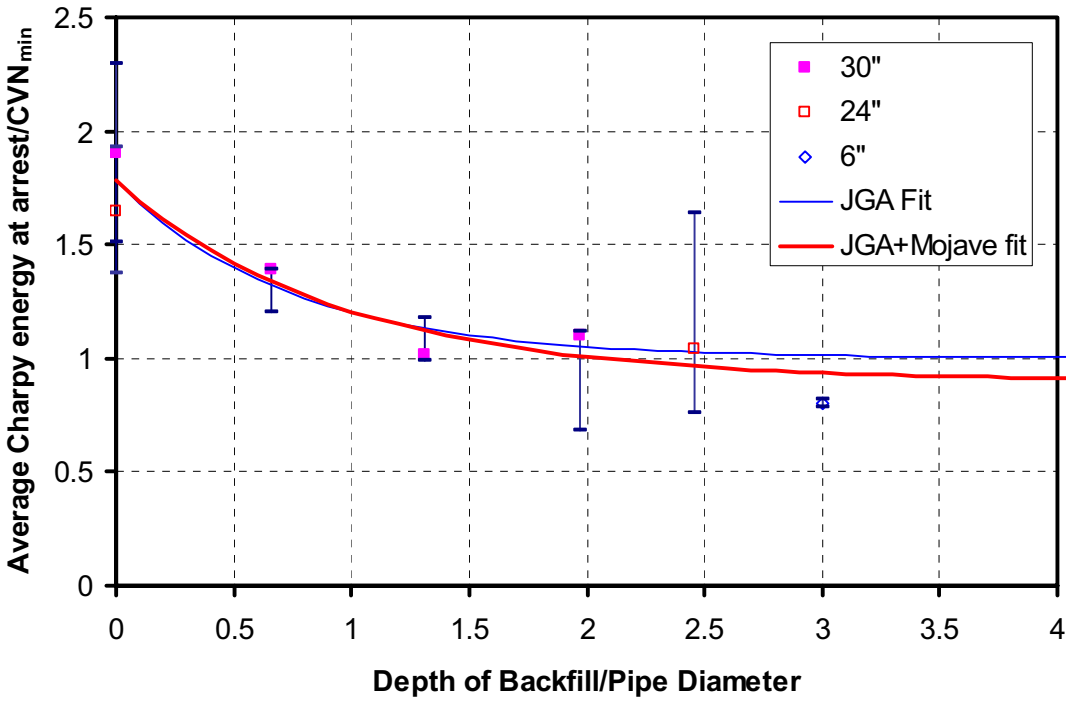

Figure 58 Effects of backfill depth on sand experiments

The same effect can be seen if the fracture speeds are considered, see Figure 59. As with the previous figure, the Mojave and JGA sand results are presented together in this figure. The linear trend in the figure is the same as is presented in Part III of this report. As explained in Part III of this report, the y-axis is the ratio of the fracture speeds from the predictions using the original soil backfill and the measurements made during the experiment. This figure illustrates that the Mojave sand experiment falls in line with the JGA experiments when the effects of soil on the fracture speed are considered. In this figure, the linear fit represents the correction to the original backfill coefficient as a function of backfill depth and can be represented as

$$K = 0.156 * \frac{\text{Backfill depth}}{\text{Diameter}} + 0.725 \tag{13}$$

This factor can then be used directly with the fracture velocity equation as shown below:

$$V_f = \left[\frac{C_B \sigma_f}{K\sqrt{CVP}}\right]\left[\frac{\sigma_d}{\sigma_a} - 1\right]^{1/6} \tag{14}$$

where C_B is the original backfill coefficient for soil and the other variables are described earlier.

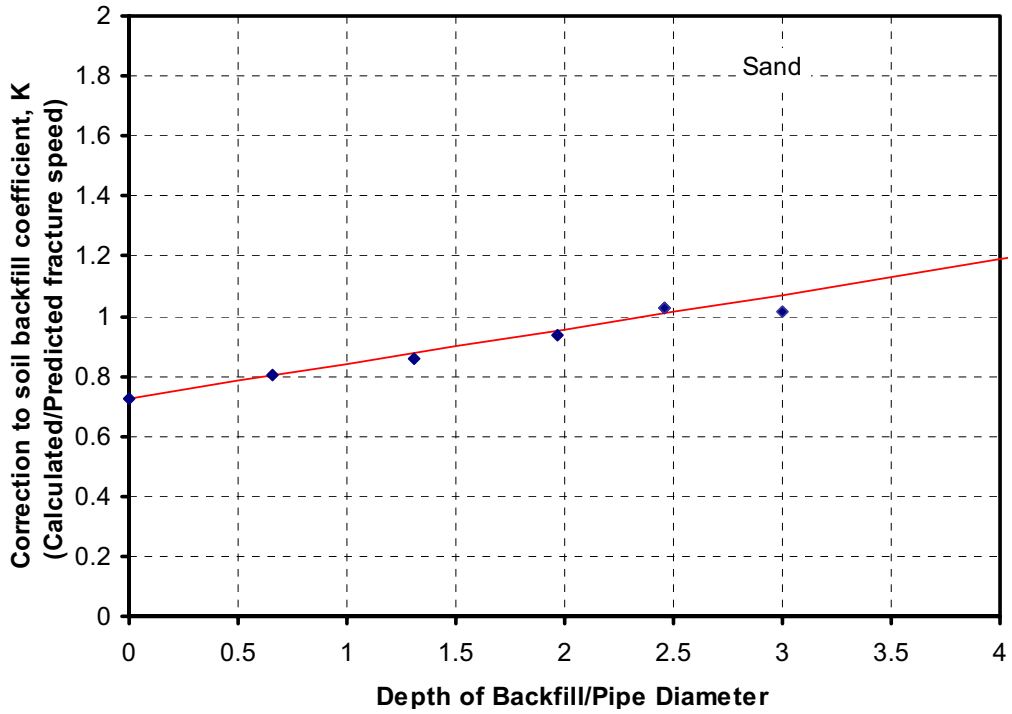

Figure 59 Effects of backfill depth on fracture speed for sand experiments

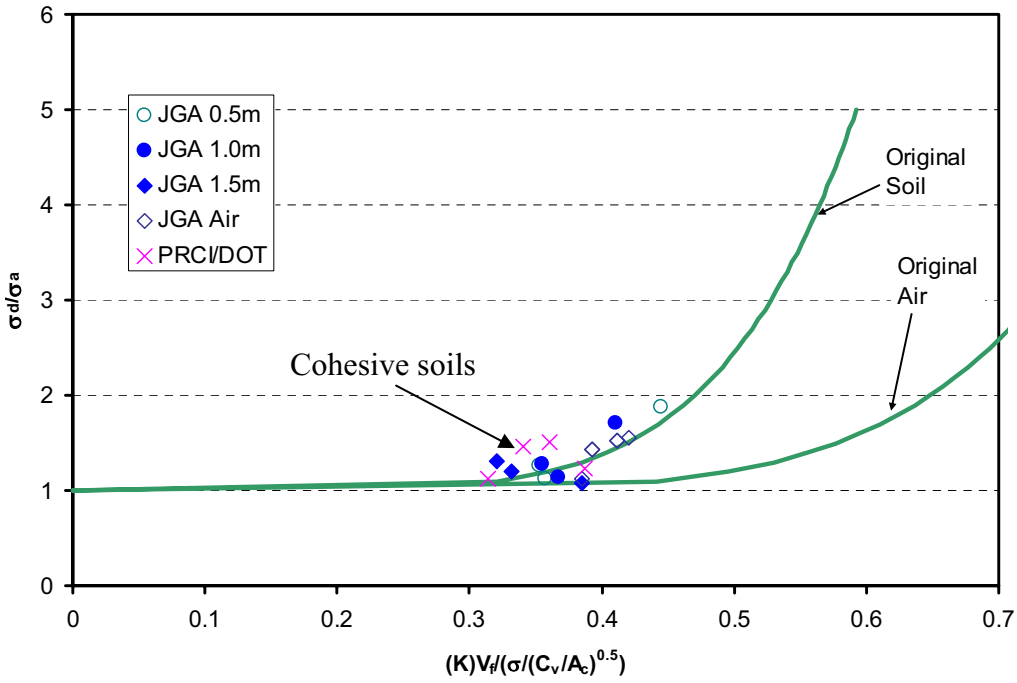

Figure 60 Decompressed pressure versus fracture velocity for the Mojave and JGA experiments

Figure 60 illustrates the same fracture velocity values plotted against the ratio of the decompressed pressure at the crack tip and the arrest stress. This plot is basically a representation of Equation 14. The solid lines on this figure represent the fracture velocity

equation with the original soil and air backfill coefficients. This data suggests that with the backfill depth correction, the original soil backfill coefficient does an excellent job at predicting the decompressed pressure at the crack tip. In addition to the JGA and Mojave sand experiments, the Mojave experiments with cohesive soils are also shown in this figure. These data appear fall slightly higher than the non-cohesive soils, but not very far from the non-cohesive scatter.

8.2 Effects of Soil Strength

As noted earlier, fine grain sands do not have significant shear strength with limited confining pressure, and the strength that they do have is derived from the friction between the grains. In order to increase the apparent shear strength of sand, the normal force acting on the sand has to be increased accordingly. For a pipe buried in sand, the only normal force acting on the sand above the pipe is the weight of the sand itself. Therefore, for the most part, the effects of the sand on the fracture velocities of axial running cracks in buried pipe are driven by inertial effects and not strength effects. However, for more cohesive soils, the shear strength increases and is more a function of the consolidation of the soil and less dependent on the normal force applied. Therefore, it can be expected that strength will play a role in the fracture velocities.

The effects of soil strength can be first investigated by determining the effects of the moisture content on the fracture velocities. Since the moisture was shown to directly impact the strength of the cohesive soils, it is appropriate to look at this factor first. The comparison of the moisture content versus the fracture velocity is shown in Figure 61 for the Mojave and JGA experiments. In this figure, the y-axis is a normalized fracture velocity since the materials used in the pipe tests had different flow stresses and Charpy energies. In addition, the fracture velocities have been corrected for backfill depth using the relationship described earlier (Equation 13). The trend shown in this figure is the same as described in Part II of this report and is a fit to the Mojave data. The JGA data seems to fall in line with the Mojave data in this instance. The results from this figure suggest that the fracture velocities are influenced by the moisture content, but the effect is not large. In fact there appears to be only a 25% change in the normalized fracture velocity with a very large change in the moisture content. This trend suggests that moisture does not play a large role in the effects of backfill on the fracture speeds.

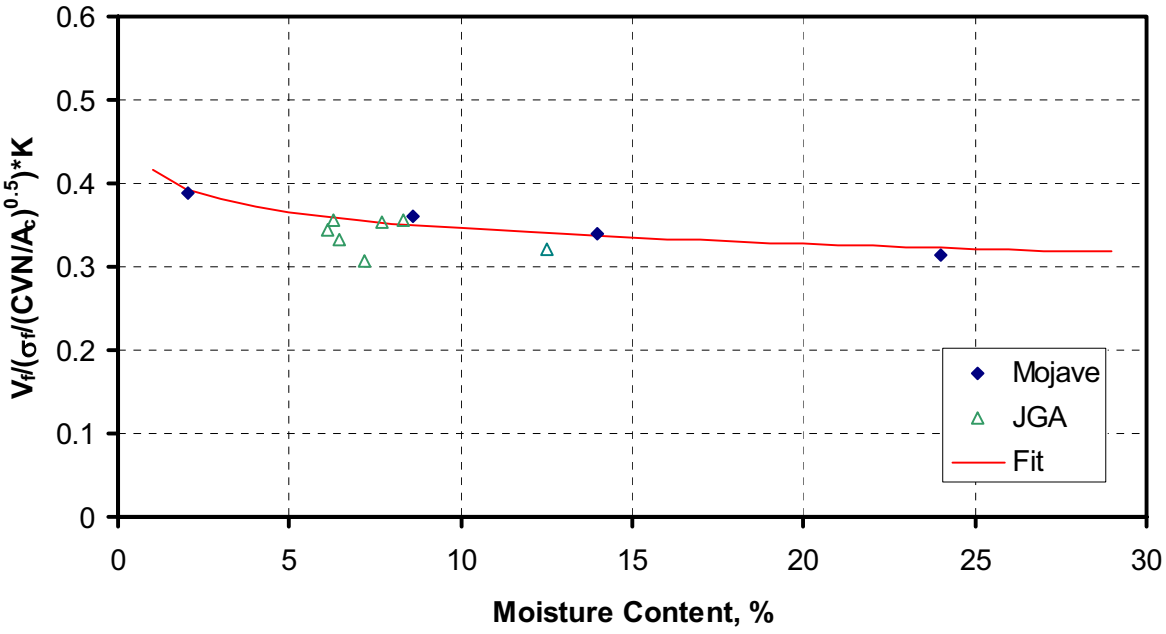

Figure 61 Comparison of fracture velocity and moisture content

As described in Section 4 of this report, standard shear strength experiments were carried out on the soils used in this investigation. These experiments included direct shear tests for the non-cohesive soils and unconfined compression experiments for the cohesive soils, and therefore, the x-axis in Figure 62 represents the strength from those experiments at the soil conditions of the pipe experiment. As explained earlier, these soil experiments do not model the behavior in the pipe experiments and are only meant to give a relative understanding of the strengths of these soils. The trends shown in this figure represent two possible fits through the Mojave data only. As expected the sand experiments from the JGA fall very close together and show very little shear strength. Surprisingly, the Mojave experiments with clay and sandy-silt also show little influence of soil strength on the fracture velocities. The non-linear trend suggests that for soil shear strengths greater than 40 psi, the fracture velocities begin to decrease. However, there is only limited data to substantiate this claim.

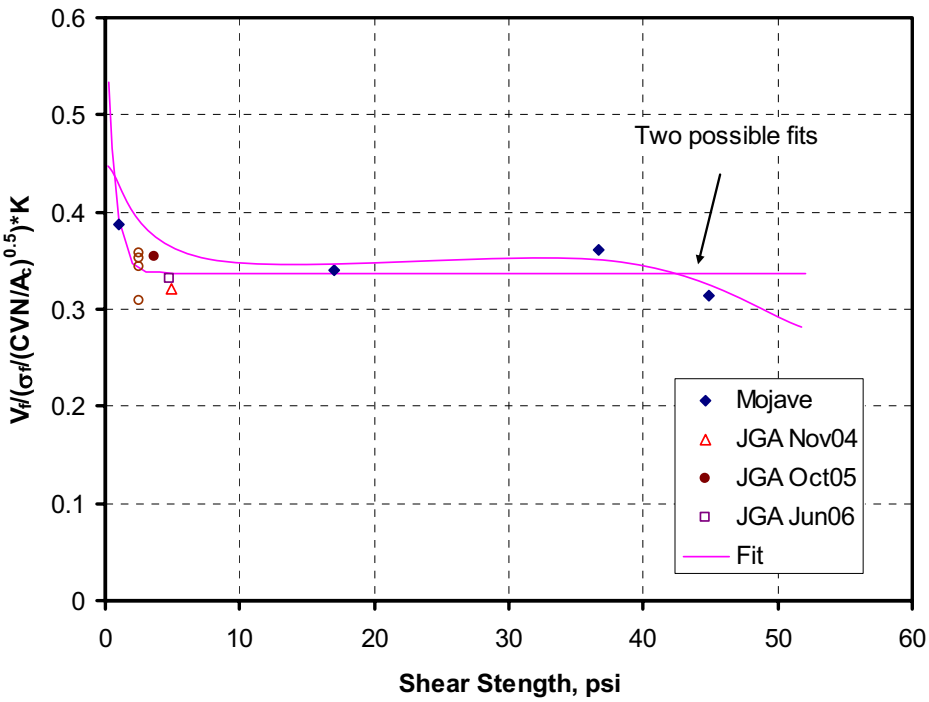

Figure 62 Effects of soil shear strength of the fracture velocity

The data can be plotted in terms of decompressed stress as shown in Figure 63. This figure is very similar to Figure 60, expect for the addition of the original data used by Maxey [44] in generating the backfill coefficient. For the data in Figure 63:

- Only experiments with Charpy energies less than 100J were considered[****]. This restriction was placed in order to eliminate any error caused by the non-linear behavior of the Charpy energy with respect to the true propagation resistance [23, 24, 28]. Due to this restriction, the recent experiments conducted by CSM and Advantica on higher grade materials can not be used in this comparison.
- From the data in Reference 44, only the data from the Athens test site was considered. The native soil at the Athens test site is clay. The soil from these experiments was never characterized or classified.
- For some of the Athens experiments, some type of sand was used as backfill, but it is unknown what type of sand was used. The sands used were never characterized or classified.
- Conversations with Bill Maxey and Herb Wilburn (former Columbus Gas Employee that worked on the Athens experiments) about the preparation of the soil led to inconclusive results. It appears that some compaction was performed, but the actual level of compaction in those experiments is unknown. In addition, the actual moisture content level of the Athens soil is unknown.
- There is no strength data available for the Athens soils.
- Typically, the backfill depth for the Athens tests was 30 inches, and it was assumed if the backfill depth was not mentioned, it was assumed to be 30 inches.

[****] For the JGA experiments, pipe material with a Charpy energy less than 100J was always used as the first test joint.

- These unknowns add great uncertainty to the results presented below.

The results from Figure 63 suggest that many of the available results from the Athens experiments fall above the original soil line when accounting for the backfill depth. This trend suggests that soil strength is playing a role in the fracture behavior. This seems in contradiction to the results given earlier, but it is possible that the soil experiments conducted do not correctly capture the strength behavior of these soils.

From Figure 63, the JGA and Mojave sand experiments, the JGA air experiments and the Maxey air experiments all fall on the original soil line after accounting for backfill depth. This suggests that for non-cohesive sands, this correction is sufficient. Most of the Maxey clay experiments, some of the Maxey sand experiments, and the Mojave cohesive soil experiments are well represented by the line labeled "Medium." In addition, there are a few Maxey experiments that are better represented by the line labeled "Heavy." Therefore, for the available data, it appears that the strength of the soils can be characterized by either Light, Medium or Heavy cohesiveness. The difficulty comes in attempting to relate these categories to particular soil conditions. At this point, the full-scale experimental data on medium and high cohesive soil backfills are not sufficient to clearly define the categories. The soil data from the older Athens experiments was not characterized for this type of analyses. In addition, the uncertainties in the in-situ soil conditions for these experiments may aid in misrepresenting the trends with soil strength. Therefore, until further full-scale applicable experimental data with cohesive soils are available, these trends will have to be used to represent the effects of soil strength on the fracture velocity.

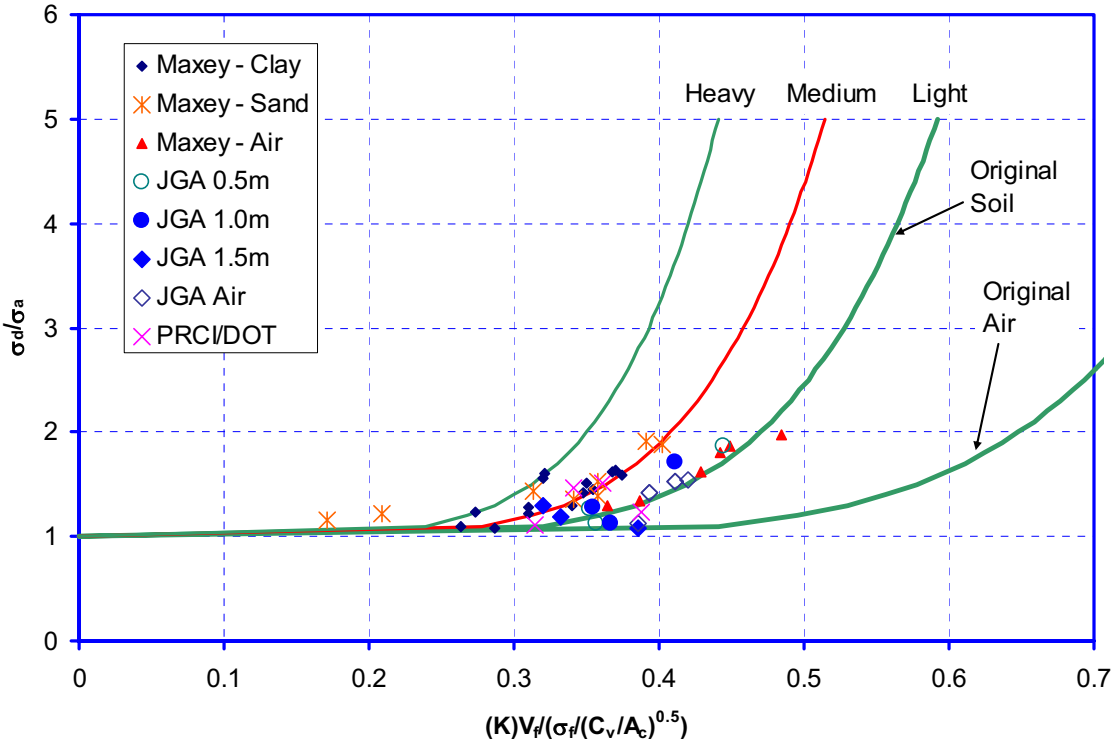

Figure 63 Decompressed pressure versus fracture velocity for the Mojave, JGA, and Maxey experiments

8.3 Effects of Diameter

8.3.1 Soil backfilled

As discussed in Part II of this report, the data suggests that there might be a diameter effect in the calculation of fracture speed for the backfill experiments. From the data developed by the JGA, the difference between the experimental results for a 30-inch diameter and 24-inch diameter pipe seem small, however, the 6-inch pipe tests seems to follow a trend somewhat different than the larger diameter pipes. Figure 64 shows the results from the soil backfill experiments conducted in this program, as well as similar smaller diameter pipe test conducted in other efforts[††††]. Included in this figure are the original fracture speed curve with the original soil backfill coefficient and the best fit curve for this data. Interestingly, the data follows the original trend for normalized fracture speeds up to 0.5, but deviates significantly for fracture speeds greater that this value. This data is not corrected for backfill depth since the actual depth of all of the experiments is unknown.

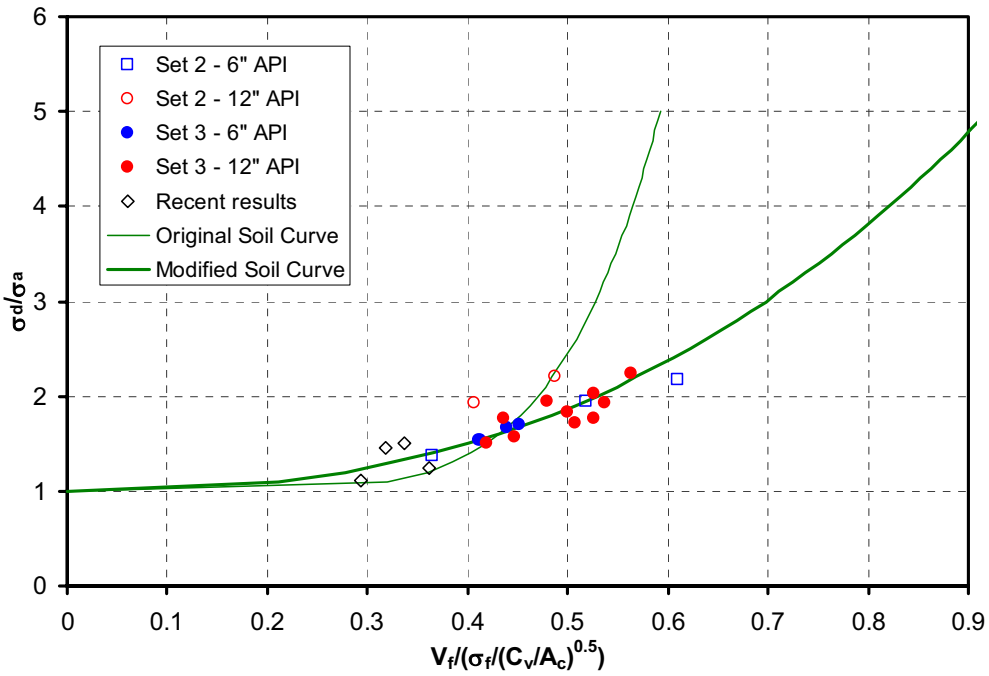

Figure 64 Fracture velocity as a function of decompressed stress for small-diameter pipes with soil (sand) backfill

Even though there appears to be an effect of diameter on the fracture speeds, the limited data on the soil type, moisture content, and backfill depth leads to a large amount of uncertainty in the trend curves given above.

8.3.2 No backfill

In addition to the difference seen with the soil backfilled cases, there was some discrepancy with the unbackfilled small-diameter experiments as well. As described in Part II of this report, the

[††††] Part II of this report details the specifics of these additional small-diameter experiments.

small-diameter data generated in this effort, was combined with other published small-diameter data to assess the accuracy of the predictions of fracture velocity, as shown in Figure 65. In this figure, the X-axis is the measured fracture speed and the Y-axis is the predicted fracture speed using the Battelle Two-curve approach with the original soil backfill coefficient. The details from the data sets labeled Set 1, Set 2, and Set 3 are given in Part II of this report. This data shows that even though there is considerable scatter, the soil experiments are well predicted using the Battelle Two-curve approach with the original soil[‡‡‡‡] backfill. However, the unbackfilled (labeled air backfill in the figure) data suggests there is large discrepancy in the predictions of fracture speed. After a detailed check of the Battelle Two-curve approach for this size pipe, no error could be found in the calculation. In order to investigate this difference in predicted and measured fracture speeds, an advanced numerical model was developed in attempts to predict the fracture speed. The results from these analyses are given in the next section.

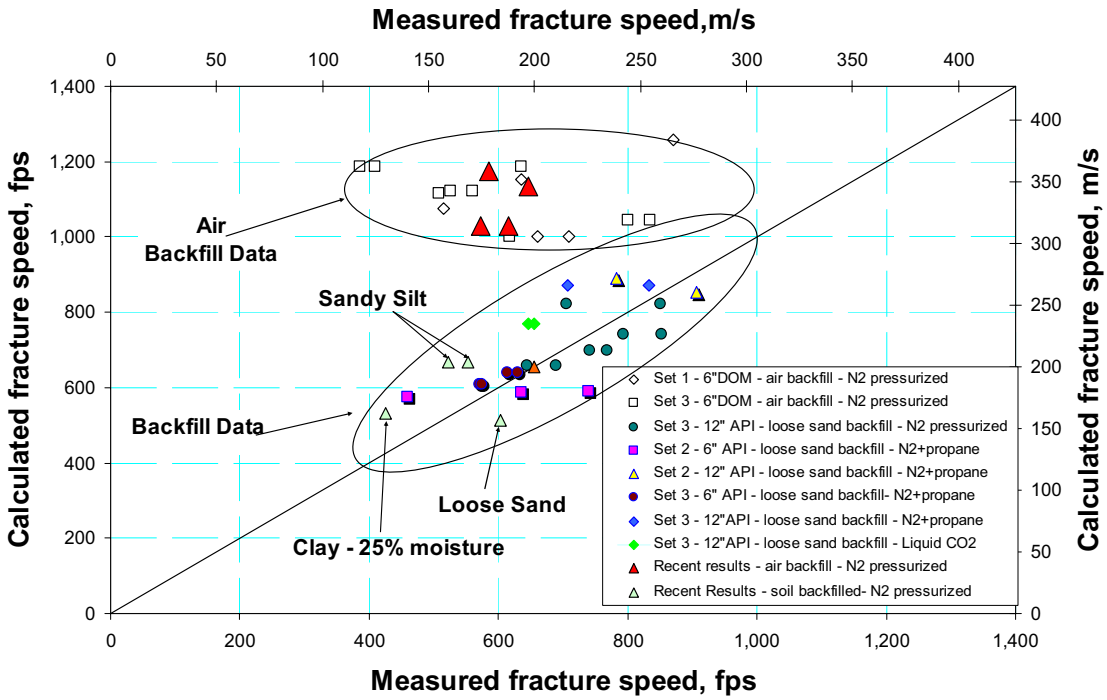

Figure 65 Comparison of experimental and calculated fracture speeds from current and past small-diameter pipe fracture experiments

8.3.3 Small-diameter unbackfilled numerical analyses

These analyses were developed and conducted in this effort to gain insight into the differences in predicted versus measured fracture speeds in the small-diameter pipe experiments conducted in this effort. The results suggest that fundamental basis of the Battelle Two-curve may be diameter sensitive since this large difference was observed without the influence of soil backfill. The details of the analyses development as well as the results generated are given in Appendix H. This section of the report only briefly describes the results and their implications.

[‡‡‡‡] Note that this scatter may be significantly reduced per the results in Figure 64.

In this effort, a dynamic ductile crack growth model was developed to simulate an axially running crack in a pipe with no (air) backfill. The model was developed using the finite element (FE) program ABAQUS/Explicit [45]. A 2-D pressure decay model was used to simulate the gas decompression behind the moving crack tip. The initial models were used to simulate one of the Mojave 6-inch pipe test (Test 1-5) with no backfill. The details of Test 1-5 can be found in Section 5 of this part of the report, or in Part II of this report.

Two different methods for the simulation of crack growth were attempted; cohesive elements and contact surfaces. In the development of this portion of the model, there were many considerations that went into defining the crack growth criteria. First of all, it is recognized that any advanced crack propagation model should be driven by the crack-tip opening angle (CTOA), since this has been shown to be reasonably valid parameter for predicting steady-state crack growth [21, 26, 27, 28] in line pipe steels. However, the commercial finite element code, ABAQUS, does not contain a failure mechanism based on the CTOA. Therefore for this effort, some approximations had to be made. Secondly, any material properties that may be needed for the calibration of such a model may not be available, so adjustments to the cracking parameters will be needed in order to match the fracture speeds in the experiments.

The first method employed was the cohesive element which is embedded in ABAQUS. A bilinear type of traction-separation curve is used to define the constitutive behavior of the cohesive elements. To define the bilinear curve, two of the three parameters, i.e. Γ, σ_{max}, and $\delta_{critical}$, are required. Here, Γ is the area under the traction-separation curve which is actually the effective cohesive energy density, or the work of separation per unit area of cohesive surface, σ_{max} is the maximum traction which corresponds to damage initiation point, and $\delta_{critical}$ is the critical separation between the two surfaces when the cohesive element are deleted from the FE model. Typically, these parameters can be developed through experiments. However, in this case, the Γ was set equal to the fracture toughness of the material and the σ_{max} value was varied until the predicted fracture speed matched that of the experiment.

The second method used contact surfaces to simulate the crack plane. An initial crack is simulated by setting the stress on the crack-face contact surface to zero. The other portion of the surface on the crack plane is kept closed by a proper surface stress, which is larger than the stress caused by the internal pressure and external forces. In this model, the critical CTOA can be used directly; the contact surfaces can be made to release when the instantaneous CTOA surpasses this critical value. A great effort was used for adjusting the contact properties since the distance between the surfaces in contact should be kept as close as possible to zero for CTOA calculations, which means a high stiffness for the contact elements. However, a high stiffness in ABAQUS/Explicit produces a small time increment and unacceptable computer time.

The details of the finite element model used in this effort are given in Figure 66. Since the current effort was aimed to simulate the air backfilled side of Test 1-5, the FE model was generated for a pipe with no backfill on both sides. For this model, due to symmetry conditions, a quarter model was employed as shown in Figure 66. The cutter crack was modeled as an initial crack. Also, only a portion of the pipe (five times the diameter in length) was modeled in the axial direction since the experimental results suggested that the crack reached steady-state after it

grew approximately two times the diameter of the pipe. This was also done to reduce the computational time required for the explicit analysis.

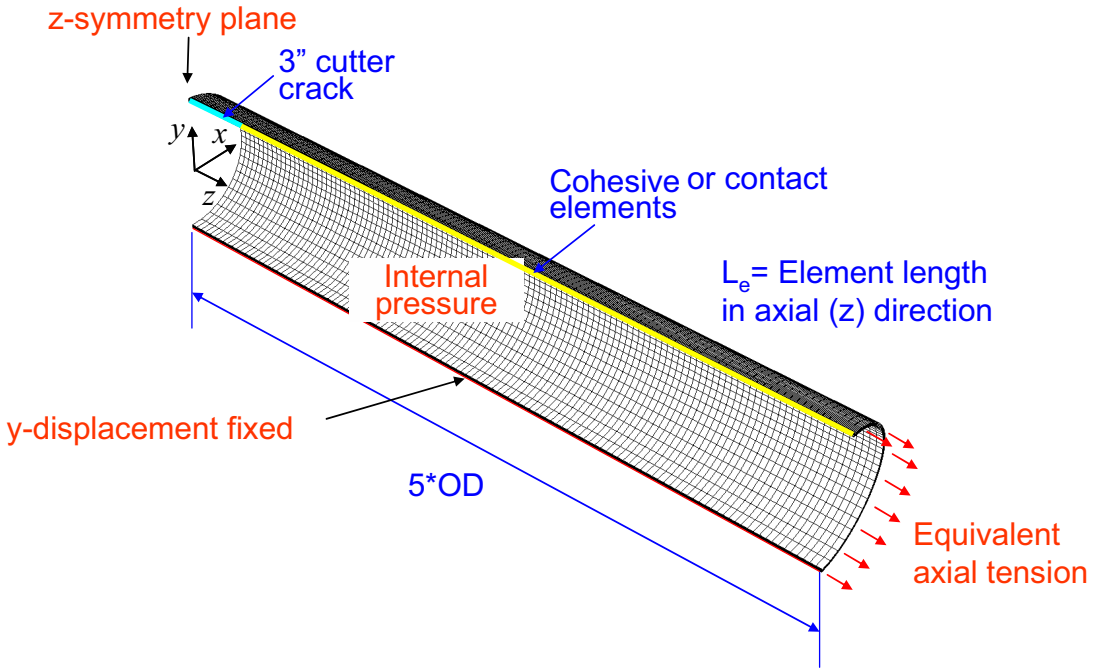

Figure 66 Finite element model used for the present work

8.3.3.1 Results using contact surfaces

The difficulties in defining the contact properties, including the closure pressure ahead of the crack tip significantly degraded the usefulness of this method. In fact, for the cases considered in this effort, steady-state fracture velocities could not be obtained with the model. It was decided that further work is needed before this model could be used in predicting steady-state crack growth.

8.3.3.2 Results using cohesion element

Since the cohesive element had several parameters that could be modified, predictions of steady-state fracture speeds were obtained. The numerical results for predicting Experiment 1-5 are shown in Figure 67. In this figure, the solid lines represent the predictions with the FE model and cohesive elements. The L_e term is the size of the element at the crack tip. The dashed lines are linear extrapolations of the numerical results, and the data points are the measured values for Experiment 1-5. From this data, the calculated fracture speeds are 200 m/s (L_e = 6.35 mm) and 198.8 m/s (L_e = 3.175mm) as compared to the measured fracture speed of 197.2 m/s. This is excellent agreement, but is expected since the properties of the cohesive element were adjusted to get this agreement.

From the model, the instantaneous CTOA can be extracted, as illustrated in Figure 68. As the fracture speed becomes constant, the CTOA also becomes constant. However, as expected, the CTOA is highly mesh size dependent. Since the smaller mesh size captured the fracture speeds

more accurately, it can be assumed that the CTOA taken at this element size will also be more accurate.

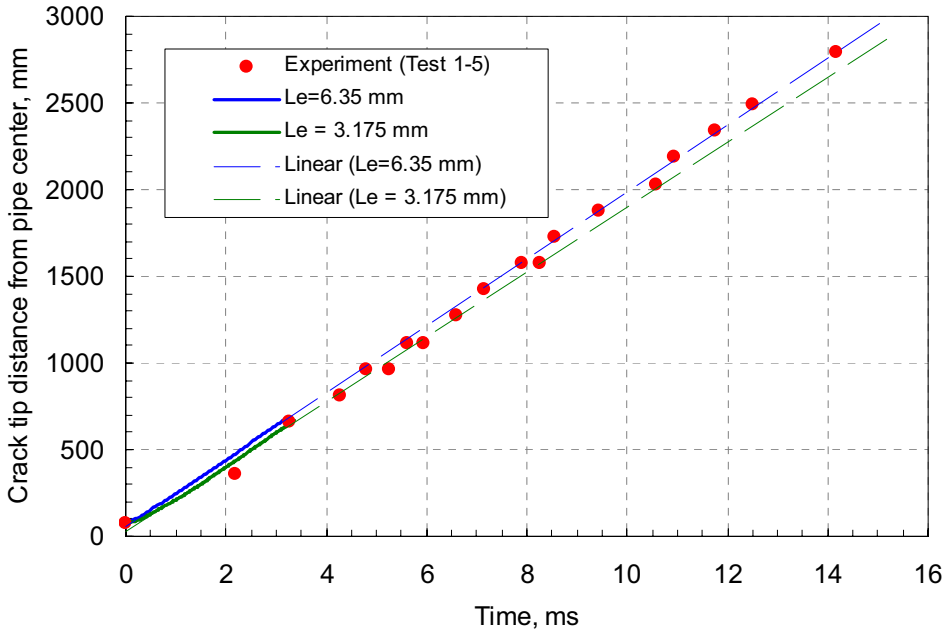

Figure 67 Comparison of predictions to experiment for crack tip position

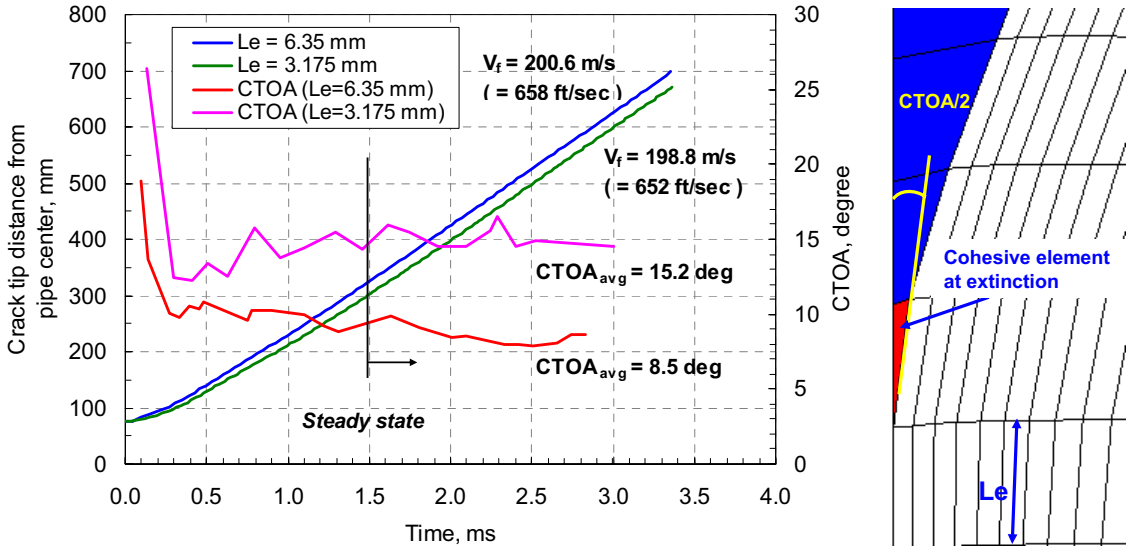

Figure 68 Fracture speed and CTOA calculated from FE analyses

To validate the CTOA value calculated from the FE model, a Drop Weight Tear Test (DWTT) specimen was tested using this pipe material. Since the pipe wall thickness was thin, a laminated DWTT specimen was designed, built and tested. The details of this testing are found in Appendix H. The CTOA was measured with a high speed digital camera and was found to be 7.8 degrees, which is reasonable close to the calculated value of 8.5 degrees. Therefore, since the calculated CTOA was in reasonable agreement with the experimentally measured value, the

model is reasonably predicting the experiment results. Therefore, the very high fracture speeds predicted by the Battelle Two-Curve analyses (Figure 65) must be in error.

As mentioned in Section 8.3.1, the results from the small diameter pipe experiments suggest that the exponent on the Battelle Two-Curve fracture velocity equation may not be appropriate. As described in Part II of this report, the experimental data available suggests this exponent should be 1/2.65 instead of 1/6. Figure 69 shows a comparison of predictions using the Battelle Two-curve analysis for Experiment 1-5 with the 1/2.65 (modified) and 1/6 (original) exponent. As expected, the original analysis predicted a fracture speed of 281 ft/sec. However, the modified curve predicted a fracture speed of 198 m/s. Even though the figure looks as if an arrest would occur, the fracture curve actually crosses the decompression curve, with an intersection at 198 m/s. This is remarkably close to the experimental value of 197.2 m/s. Clearly further work is needed to better define the true fracture trend for smaller diameter pipes.

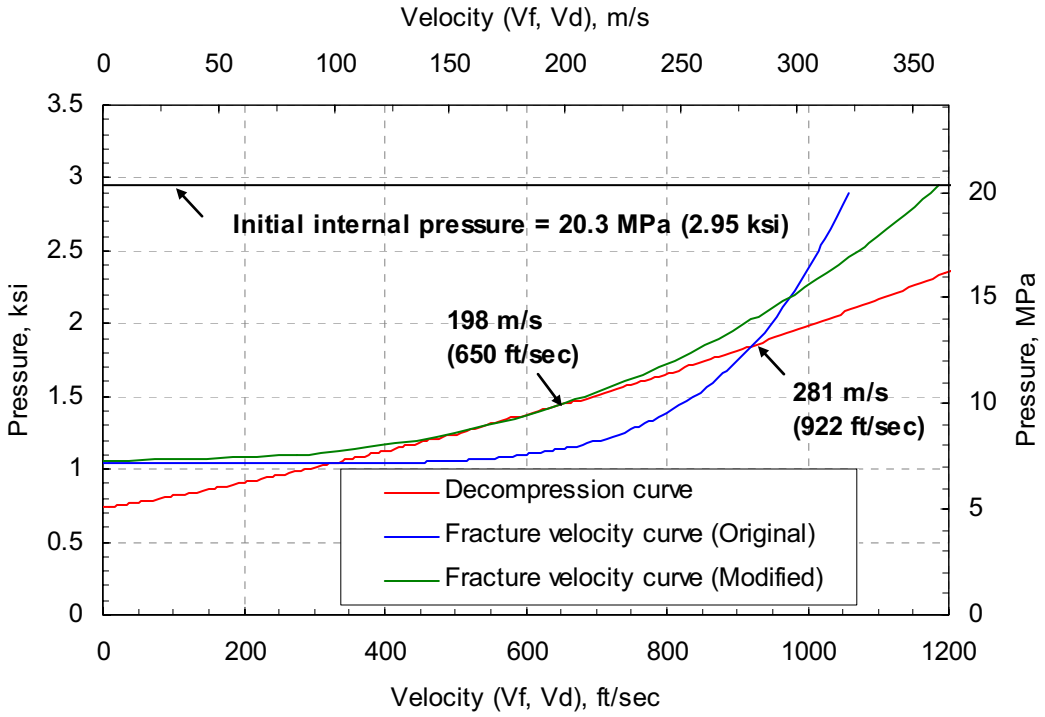

Figure 69 Fracture speed predictions for Test 1-5 using the original and the modified Battelle Two-Curve method

9 DEVELOPMENT OF PIPE-DFRAC

As part of this effort, a computer code was written to make prediction of minimum arrest toughness and fracture velocities for axial cracks running in line pipe material. The basis of this new code is the Battelle Two-Curve analysis as described earlier in this report. The computer code developed in this effort was modified from a code written for TransCanada Pipeline called GASFRAC. This version of the code was updated with new iteration techniques, an advance user friendly GUI interface, updated correction factors for non-linear toughness effects, and includes the results generated in this program. The computer code comes with a detailed online

help file, which acts as the computer code's users manual. This section of the report gives a brief overview of the features of this new computer code.

9.1 Running PIPE-DFRAC

The PIPE-DFRAC program is available to the U.S. DOT, PRCI and JGA as a deliverable from this effort. The installation program for use of this code is supplied on the CD that accompanies this report. Typical installation procedures are followed and PIPE-DFRAC is installed on the computer's harddrive. PIPE-DFRAC is run by simply selecting the icon from the Windows start menu. Figure 70, Figure 71, and Figure 72 show examples of the opening, input and output screens. Some of the new features of the PIPE-DFRAC code are given, but the user should consult the online help for more information.

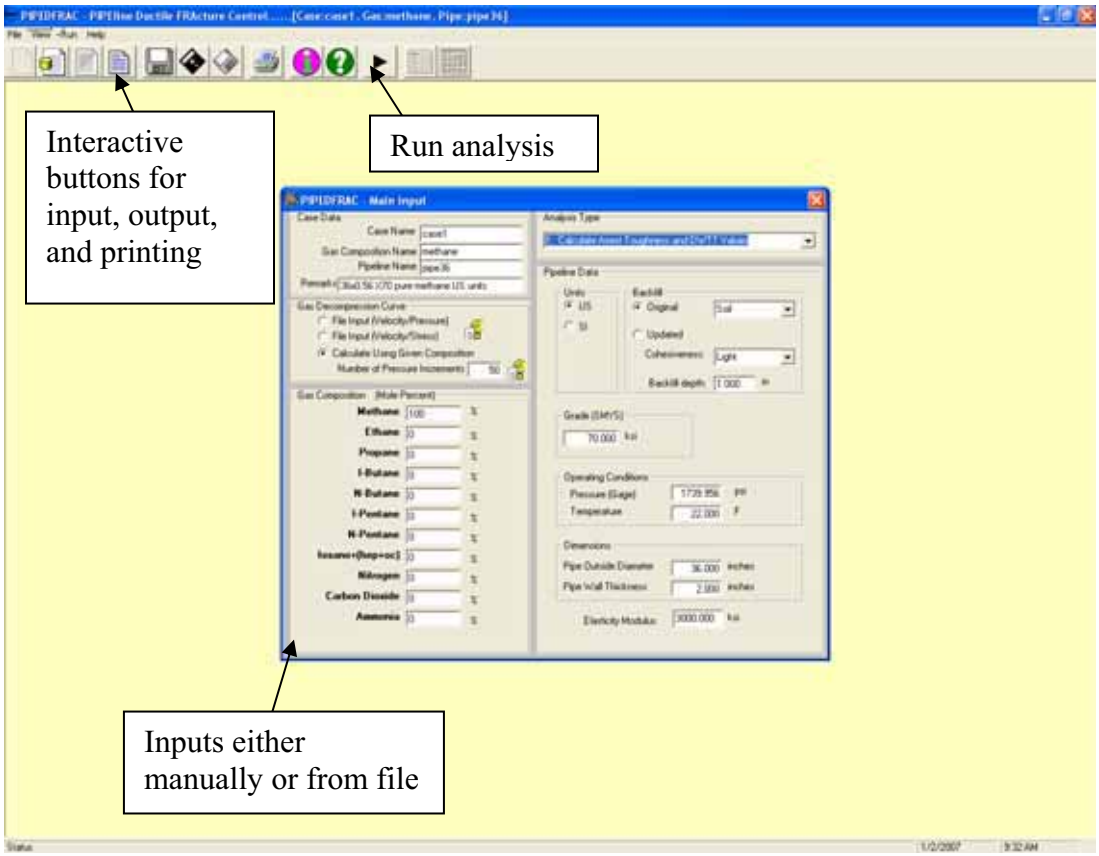

Figure 70 PIPE-DFRAC input screen

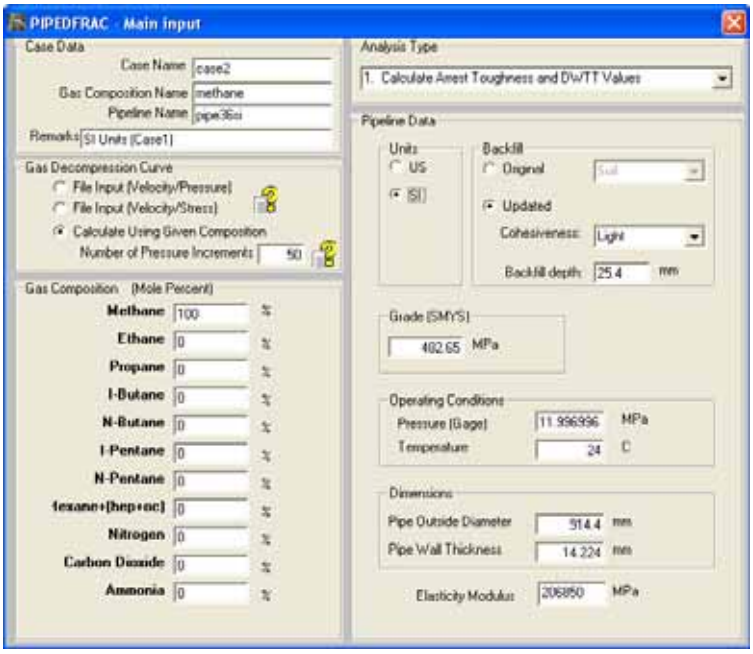

Figure 71 PIPE-DFRAC typical input

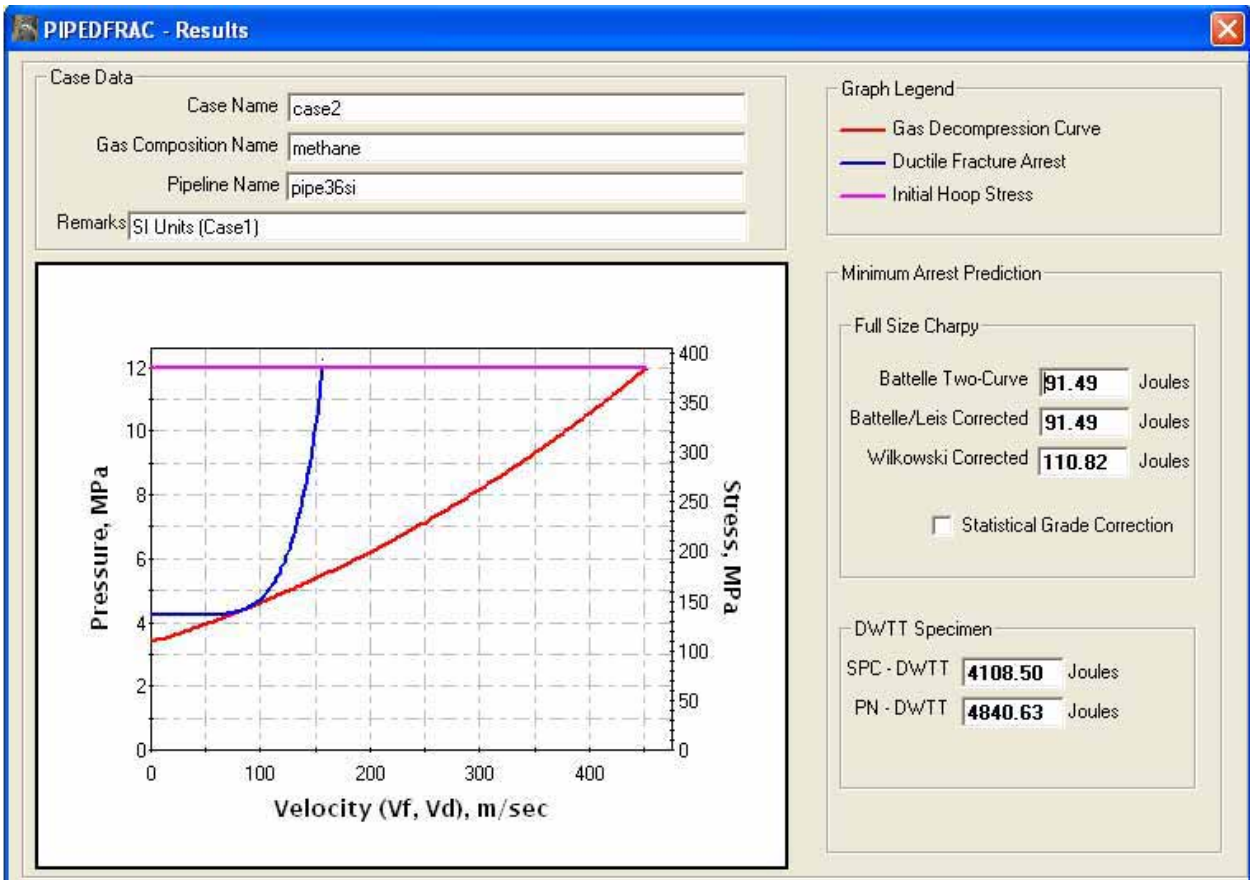

Figure 72 Typical PIPE-DFRAC output

9.2 User Friendly Highlights

As part of the development of this computer code, the user-friendliness of the GASFRAC code was increased in PIPE-DFRAC by the addition of the following items:

- The interface was modified to include a drop down menu structure and interactive buttons for input, output and printing.
- Running an analyses and switching between input and output was made easy by use of quick switch buttons.
- A new interpolation routine was developed for locating the tangent point between the fracture and decompression curves for more accurate minimum arrest toughness determination.
- The limit of 50 decompression data points was removed to improve the minimum arrest toughness prediction.
- Both pressure and stress are plotted with velocity on the more aesthetically pleasing output plot, and headers were added to the comma delimited output.
- An interactive help file has been created to help the user with the difficult input options.

9.3 Non-linear Effects on Toughness

One of the main issues in the line pipe fracture arrest community is the effect of non-linear toughness on the Charpy energy at crack arrest. For high toughness (>100J) line pipe steels, the Charpy energy does not represent the true propagation resistance of the material, and forms a non-linear relationship with the actual propagation resistance. The details and history behind this problem is too detailed to describe here, but much research has been conducted looking at how to modify the results from the BTC approach to account for this effect. A detailed paper by Emc^2 staff [46] describes this issue and presents many of the most recently used correction factors. In addition, these corrections were compared to the full-scale pipe test database and using statistical analysis procedures, additional correction factors were developed. These correction factors are implemented into the PIPE-DFRAC code. As shown in Figure 72, the option of using these statistical corrections is available to the user.

9.4 Backfill Effects

The backfill effects developed and demonstrated in this report are incorporated into the PIPE-DFRAC computer code. As shown in Figure 71, the option for choosing the updated backfill coefficients or using the original coefficients exists. The equations embedded in the code include both backfill depth and soil cohesiveness.

9.5 Diameter Effects

The effects of pipe diameter demonstrated as part of this effort have not been currently incorporated into the PIPE-DFRAC code. The data presented in this report suggests that the form of the velocity equation, i.e., the exponent on the velocity equation, may need to be modified for smaller-diameter pipe experiments. As discussed in the next section, additional experiments are needed before the effect of diameter can be fully defined. Therefore, until this data can be developed, and the trends more thoroughly defined, the trends shown in this report have not been included in the PIPE-DFRAC code.

10 FUTURE WORK

The research conducted in this effort was the first attempt at characterizing and understanding the true influence of the soil backfill on the propagation and arrest behavior of running axial cracks in line pipe materials. Through this research, progress was made on the development of trends relating the backfill depth to the fracture speeds as well as a first look at the effects of soil strength on fracture speeds. In addition, the measurement of dynamic CTOA on the JGA June 2006 experiment demonstrated that is it possible to make these very complex measurements. However, there are many aspects of this work that need additional research in order to refine the conclusions and trends given in this report. This section of the report defines areas where additional research is needed.

10.1 Soil Characterization

In this effort, standardized soil experiments were used to classify the strength of the soils used to backfill line pipe. Although these standard soil strength experiments give an adequate measure of the absolute strength of the soil, the complex loadings that occur put unknown loads on the soil which may affects how the soil reacts. Realistically, understanding the compressive behavior and elastic stiffness of soils are as important as understanding the soil shear strength and density influences on the crack driving force. There are some advanced soil experiments which employ a bladder placed into the soil with pressure and displacements recorded during the soil failure. These types of tests may give a more realistic feel for the strength of the soil.

10.2 Diameter Effect

The results from many of the past small-diameter experiments suggest that the trends used by Maxey may not accurately predict the behavior. In fact, the exponent in the fracture velocity equation (Equation 14) may be a function of the pipe diameter. The advanced numerical analyses conducted for unbackfilled pipe tests confirmed that this exponent may be in error for smaller diameter pipes. The JGA results suggest there is no significant difference in behavior for pipe sizes between 24 and 30 inches in diameter. In order to clarify this issue, a more complete set of small diameter pipe tests is required. In this series of experiments, pipe diameters ranging from 6-inch to 18-inch diameter are needed to fully capture the diameter effect. In addition, the experiments must be completed with detailed backfilling procedures with fully characterized soils to guarantee that the effects of the backfill do not influence the fracture speed results. With these results, figures such as Figure 64 can be generated and trends can be developed as a function of diameter.

10.3 CTOA Measurement

In this program, the first attempt was made to make a physical measurement of the CTOA in a full-scale burst test. As with the development of any advanced testing instrumentation, there are many bugs and nuances that have to be worked out of the design. Below is a listing of the additional development that is needed for the CTOA instrumentation.

Hall Effect

- An electrical shield is needed so that if EMF pulses occur, they do no interfere with the magnetic field of the device.
- The influence of the pipe metallic surface on the magnetic field has to be addressed. In the June 2006 experiment, the Hall Effect fixturing was placed far enough away from the

pipe to eliminate this influence. However, if the device is to be used in buried pipe, the device will have to be brought closer to the pipe to prevent the device from being sheared off during the burst event.

- A more robust calibration is required. The calibration developed in this program was very insensitive to rotational differences between the magnet and the sensor. Since the movement of the flaps will cause both rotational and translational movement between the sensor and magnet, this calibration will have to be improved.

WireCTOA

- The main issue with the WireCTOA device is the selection of the torque values for securing the aluminum slide rod to the fiberglass support block. In the Mojave experiments, the torque value chosen was too high, and the rods did not slide out before other failures occurred. In the JGA experiment, some of the device worked properly, while some of it either debonded or failed early. This portion of the design of this device needs further development.
- Another issue is the time dependent behavior of the epoxy bond. In all of the Mojave experiments, the pipe and WireCTOA fixture surfaces were roughed with a Dremel tool in order to increase the bond strength. In the JGA experiments, the underside of the fixture surfaces were actually gouged with a Dremel tool in order to increase this bond even more. In the JGA experiment, the WireCTOA devices were applied to the pipe about three weeks before the actual experiment. In that time, in some cases, the bond failed between the epoxy and pipe wall. In laboratory experiments, the same behavior was observed after one week with the piano wire fully tensioned. This result suggests that the pipe surface preparation procedures may be insufficient. Additional work is needed to improve the reliability of the bond between the pipe and fixtures.

10.4 Advanced Fracture Modeling

The first two items in this section are highly experimental and could be very costly in the long run. Another option for handling these effects is to develop a comprehensive numerical model that takes into account all of the factors driving the propagation and arrest of the axial running cracks. In this effort, an initial model was developed for unbackfilled small-diameter pipes. Simplifications were used in the treatment of gas decompression and crack extension. This model did not address issues such as soil interaction or attempt to predict actual decompression behavior. Up to this point, it has been very difficult to perform such analyses due to computational time issues and numerical issues with the interaction between the decompression and the structural event. However recently, a computational tool has been made available for modeling this very dynamic fracture event. The ABAQUS finite element structural analysis code has been paired with the FLUENT[§§§§] computational fluid mechanics code in order to handle these fluid-structural problems. In addition, over the last few years, great progress has been made in computational efficiency, making very complex numerical models less CPU time consuming. These changes allow for the detailed finite element modeling of the ductile fracture problem that was not practical in the past. In particular, the FLUENT code can calculate the 3D two-phase sonic flow of decompressing rich gas (using the RSK equation of state), and iterate with the ABAQUS program to give the proper gas pressure on the inside of the pipe even in the

[§§§§] It was beyond the scope of this current program to incorporate FLUENT into the numerical model developed.

cracked section during the transient conditions at the start of the test. Past efforts at CSM in Italy, and those presented in this report have had to use empirical relationships for the gas pressure in the cracked-pipe section during steady-state conditions even for an ideal gas, and are not applicable to today's richer natural gases of interest. An effort like this will have to encompass the gas dynamics/decompression aspects (now handled by the FLUENT/ABAQUS fluid structure interaction programs), the fracture analysis by CTOA, and the pipe soil interactions in ABAQUS.

The properties of different soils relative the backfill behavior were explored in this program, but without a dynamic FE model, the true effects of the soil, i.e., elastic stiffness, strength, or density (inertial resistance) of the soil, can not be truly evaluated for use in the current empirical models. Varying these parameters in full-scale testing is not practical or economical (especially for off-shore or arctic applications). Additionally, it is known that in the limit for very low toughness materials, the CTOA becomes small, and the pipe behaves as if it is not backfilled. Hence, the backfill contribution to the crack-driving force should also depend on the deformation capability of the pipe material.

Therefore in order to fully understand and characterize the behavior of axially running cracks in buried linepipe, an advanced numerical model is needed. This model can capture the complex interactions between the soil and the pipe, between the gas and the pipe and can be used to drive the crack by the CTOA methodology. Using this model, sensitivity analyses can be conducted and easier to use, arrest models can be developed. The development of this type of numerical model was proposed to the DOT in 2005 and can be revisited if this work is warranted.

11 SUMMARY

This report details the results generated from a program sponsored by the U.S. Department of Transportation and the Pipeline Research Council International with an information exchange agreement with the Japanese Gas Association aimed at making the first improvement to the treatment of soils in the BTC approach. Small and large scale fracture propagation experiments with well-controlled backfill conditions were conducted and the results were used to better characterize the effects of soil on the fracture velocity. A modification to the backfill coefficient was suggested and incorporated into the Battelle Two-Curve approach for the calculation of minimum arrest toughness. Several important accomplishments and findings were generated in this effort:

- A series of small diameter (6-inch) pipe crack propagation experiments were completed over a two-year period to investigate the effects of backfill on the fracture speeds. The pipe tests were conducted in partial buried conditions with soils ranging in cohesiveness, moisture content and compaction level. The results from these experiments suggested that the moisture level and possible the strength of the soil affect the fracture speeds.
- Each of the soils used in this effort were tested in the laboratory and characterized for optimum moisture, grain size, soil type and strength. The results suggested that the sands have limited shear strength in the absence of normal forces as compared to the silts and clays. It was recognized that these simple soil tests do not represent the loads seen by the soils during the experiment, but were conducted to give a general feel of the relative strength differences between the soils.
- A series of larger diameter (24 and 30-inch) crack arrest experiments were conducted by the JGA. Sand backfill was used in all cases, but the depth of the backfill was varied for

these experiments. The results from this effort suggest that the depth of the backfill is directly related to the change in fracture velocity.

- Comparing the experimental results with the strength levels generated from the soil experiments suggest that the effect of soil strength is minimal when the depth of the backfill is compensated for in the analysis. This fact may only hold true for smaller diameter pipe experiments,
- Analyzing the Mojave results with other small diameter buried pipe experiments suggested that the trends originally developed between the decompressed stress level and the fracture velocity may not be applicable to 6-inch pipe tests. Incomplete data on the soil type, backfill depth and moisture conditions for the older small diameter pipe experiments make it difficult to draw definite conclusions about the effect of diameter.
- For the larger diameter pipes, the results generated in this program were combined with the original data used to develop the original backfill coefficient. The original laboratory books were investigated to determine if information about the backfill was available. Even though some data was available, details about the soil type, moisture and strength were not available. When this data was plotted against the trends developed in this program, the results suggested that the strength of the some of the soils used at that time must have been higher than those used in this program. Therefore, it was decided to categorize the soils by cohesiveness and adjust the backfill coefficient accordingly.
- Using the results from this program and a program originally written for TransCanada, the windows-based computer code PIPE-DFRAC was developed. This code incorporates the BTC methodology for predicting fracture speeds and minimum arrest toughness. It also includes a user-friendly GUI interface and recent advances in statistical corrections for non-linear toughness effects.
- Unique instrumentation was developed for the measurement of the CTOA in a full-scale burst test. The development of this instrumentation focused on an electronic device, termed the Hall Effect sensor, and a mechanical devices, termed the WireCTOA. These devices were placed on both the Mojave and the final JGA experiment. Results from the Mojave experiments indicated that both devices were capable of making this measurement, but failed to generate numbers due to design issues. In the final design iteration in this program, the WireCTOA device on the JGA experiment measured a CTOA of 5 degrees on a section of pipe with a Charpy energy of 71J. Even though direct verification of the value is not possible, other results seem to confirm that this is a reasonable value for the pipe with this Charpy energy.
- The discrepancies noted in the fracture speed predictions for small-diameter unbackfilled experiments were investigated using advanced numerical techniques. Dynamic crack propagation analyses were conducted to make predictions of CTOA and fracture speed for one of the unbackfilled pipe experiments conducted in this effort. The results accurately predicted both the fracture speed measured in the experiment and the CTOA measured from an instrumented DWTT specimen. Since these predictions match the experiments reasonable well, the discrepancy appeared to be attributed to the exponent used in the fracture velocity equation. Using the modified exponent developed in this effort, the predictions of fracture velocity for this one test were excellent. Further analysis refinement and validation are required before this conclusion about the fracture velocity equation can be verified.

- Many options for further research were suggested and included further refinement of soil strength properties, investigation into the effect of diameter, further development of the CTOA instrumentation, and the further development of an advanced numerical model to correctly simulate the buried pipe behavior. This type of model can be used with sensitivity analyses to correctly model the behavior of an axially running crack in buried line pipe.

12 REFERENCES

1 Maxey, W., Keifner, J. F., and Eiber, R. J., "Ductile Fracture Arrest in Gas Pipelines," A.G.A. Catalogue number L32176, May 1976.

2 Kiefner, J.F., Maxey, W.A., Eiber, R.J., and Duffy, A.R., "Failure Stress Levels of Flaws in Pressurized Cylinders," *Progress in Flaw Growth and Fracture toughness Testing, ASTM STP 536*, American Society for Testing and Materials, 1973, pp. 461-481

3 Dugdale, D.B., "Yielding of Steel Sheets Containing Slits," Journal of Mech. and Physics, Vol. 18. pp. 100, 1960.

4 Folias, E.S., "The Stresses in a Cylindrical Shell containing an Axial Crack," ARL 64-174, Aerospace Research Labs, Oct. 1694.

5 Wilkowski, G., Rudland, D., and Wang, Y-Y., "Review and Assessment of Axial Crack fracture Mechanics Solutions," Final Report to Tokyo Gas, March 2001

6 Kiefner, J. F., and others, "Failure Stress Levels of Flaws in Pressurized Cylinders," Progress in Flaw Growth and Fracture Toughness Testing, ASTM STP 536, American Society for Testing and Materials, pp 461-481, 1973.

7 ASTM E1820-06e1, "Standard Test Method for Measurement of Fracture Toughness," American Society of Testing and Materials International, Volume 03.01, 2007

8 Hahn, G. T., Serrate, M., and Rosenfield, A. R., "Criteria for Crack Extension in Cylindrical Pressure Vessels," International Journal of Fracture Mechanics, Vol. 5, No. 3, September 1969, pp. 187-210.

9 G. M. Wilkowski, and P. M. Scott, "A Statistical Based Circumferentially Cracked Pipe Fracture Mechanics Analysis for Design on Code Implementation," Nuclear Engineering and Design, Vol. III, 1989, pp. 173-187.

10 Maxey, W. A., and others, "Brittle Fracture Arrest in Gas Pipelines:' A.G.A. Report L5 1433, April 1983.

11 Smith, R. B., and Eiber, R. J., "Field Failure Survey and Investigations," 4th Symposium on LinePipe Research, Pipeline Research Committee of American Gas Association, November 1969.

12 Eiber, R. J., "Field Failure Investigations" Paper G, 5th Symposium on Line Pipe Research, Pipeline Research Committee of American Gas Association, November 1974.

13 Maxey, W. A. "Fracture Propagation" in 5th Symposium on Line Pipe Research, American Gas Association Catalogue No. L30174, Nov. 1974.

14 Rudinger, George, *Wave Diagrams for Nonsteady Flow in Ducts*, D. Van Nostrand Company, Inc. New York (1995).

15 Eiber, R.J., Bubenik, T.A., and Maxey W.A., "Fracture Control Technology for Natural Gas Pipelines," NG-18 Report No. 208 to Line Pipe Research Supervisory committee of the Pipeline Research Committee of the American Gas Association, Project PR-3-9113, December 1993.

16 Hopke, S.E., and Lin C.J., "Application of the BWRS Equation to Natural Gas Systems," Paper presented at the 75th National AIChE Meeting, Denver (March 1974).
17 Wilkowski, G.M., and Eiber R.J., "The Evaluation of Ductile Fracture Propagation Behavior in Frozen Soil," Battelle final report to Northwest Alaskan Pipeline Corporation, September 1980.
18 Maxey, W. A., "Experimental Evaluation of Fracture Propagation in an Underwater Gas Pipeline," NG-18 Report 153, February 1985.
19 Popelar, C., Rosenfield, A.R., and Kanninen, M.F., "Steady-state Crack Propagation in Pressurized Pipelines with Backfill," ASME Joint Pressure Vessel and Piping Division and Petroleum Division Conference, Mexico City, September 19-23, 1976.
20 A.K. Shoemaker, R.F. McCartney, and K.D. Ives, "Mechanical Crack-Arrestor Concepts for Line-Pipe Applications," Materials Engineering in the Artic, ASM edited by M.B. Ives, May 1977.
21 Salvini, P., Bernardo, G., Demofonti, G., and Mannucci, G., "Numerical model of the backfill constraint effect during fracture propagation on buried large diameter gas pipelines," Pipeline Technology, volume 1, R. Denys (editor), 2000.
22 Dawicke DS, Piascik RS, and Newman JJ, "Prediction of Stable Tearing and Fracture of a 2000-Series Aluminum Alloy Plate Using a CTOA Criterion," ASTM STP 1296, 1997, pp. 90-104.
23 Wilkowski, G.M., Maxey, W.A., and Eiber, R.J., "Use of DWTT energy for Predicting Ductile Fracture Behavior in Controlled rolled Steel Line Pipes," Canadian Metallurgical Quarterly, Vol. 19, 1980 pp 59-77.
24 Rothwell, A.B., "Fracture Propagation Control for Gas Pipelines – Past, Present and Future," Pipeline Technology, Volume 1, Proceedings of the 3rd International Pipeline Technology Conference, Ed. R. Denys. Pp. 387-405, May 2000.
25 Kanninen, M.F., Grant, T.S., Demofonti, G., and Venzi, S., "The Development and Validation of a Theoretical Ductile Fracture Model," Eighth Symposium on Line Pipe Research, Paper 12, Pipeline Research Committee of AGA, Arlington, VA, Catalog No. L51680, 1993.
26 Demofonti G, et al, "Step by Step Procedure for the Two Specimen CTOA Test," Pipeline Technology, ed. R. Denys, vol. II, Elsevier Science, 1995, pp. 503-512.
27 Demonfonti, G., and Mannucci, G., "Mill Test Techniques for Predicting Crack Arrestibility in High Toughness Steels," On-going Project for Pipeline Research Committee, American Gas Association, (PR-182-9903).
28 D.L. Rudland, Wang, Y.Y., Wilkowski, G.M., and Horsley, D., "Characterizing Dynamic Fracture Toughness of Linepipe Steels Using the Pressed-Notch Drop Weight Tear Test Specimen," *Engineering Fracture Mechanics* 71 (2004) 2533-2549
29 Emery, A.F., Kobayashi, A.S., Love, W.J, Place, B.W., Lee, C.H., and Chao, Y.H., "An Experimental and Analytical Investigation of Axial Crack Propagation in Long Pipes," Engineering Fracture Mechanics, Vol 23, No.1 Jan 1986, pp 215-226.
30 Emery, A.F., Chao, Y.H., Kobayashi, A.S., and Love, W.J., "Numerical Modeling of Full-scale Pipe Rupture Tests," ASME Journal of Pressure Vessel Technology, 1992, 114, pp 265-270.
31 Kokaly, MT, Lee, J and Kobayashi, AS, "Dynamic Ductile Fracture of 7075-T6 - An Experimental Analysis," Int. J. Solids and Structures, 2001: 38: 1935-1942

32 Rudland, D.L, Feng, Z., Wang, Y-Y.,Wilkowski, G., Horsley, D, and Glover, A, "Experimental Investigation of CTOA In Linepipe Steels." Engineering Fracture Mechanics, 70(3-4) 2003, pp 567-577.
33 Das, Braja M., "Principles of Geotechnical Engineering," Fifth Edition, Copyright 2002, Wadworth Group.
34 C. W. Peterson, K. T. Colbett, D. Fairchild, S. Papka, and M. L. Macia, "Improving Long-Distance Gas Transmission Economics: X120 Development Overview", Proceedings of 4th International Conference on Pipeline Technology, Vol. 1, May 9-13 2004, Ostend, Belgium, Scientific Surveys, Inc., pp.3-29.
35 Wilkowski, G. M., and Eiber, R. J., "CAGSL Model Crack Arrestor Program," Report to Northern Engineering Services Company, Ltd., July 1977.
36 Wilkowski, G., Scott, P., and Maxey, W., "Design and Optimization of Mechanical Crack Arrestors for Pipelines," NG-18 Report 134, July 1983.
37 Poynton, W.A., and Christian, J.R., "An Experimental Study of Shear Fracture Propagation using Small Scale Models," Symposium of Crack Propagation in Pipelines, Paper 5, British Gas Corporation, Newcastle upon Tyne, England, March 26&27, 1974.
38 Kobayashi, A.S., Emery, A,F., Love, W.J., and Chao, Y. –H., "Subsize Experiments and Numerical Modeling of Axial Rupture of Gas Transmission Lines," Journal of Pressure Vessel Technology, Vol. 110, May 1988, pp. 155-160.
39 Wilkowski, G., Rudland, D., and Rothwell, B, "How to Optimize the Design of Mechanical Crack Arrestors," IPC2006-10357, Proceedings of IPC 2006, 2006 International Pipeline Conference, September 25-29, 2006, Calgary, Alberta, Canada.
40 Tang, H.T., Duffey, R.B, Singh, A., and Bausch, P., "Experimental Investigation of High Energy Pipe Leak and Rupture Phenomena," Proceedings of the 1985 Pressure Vessel and Piping Conference, ASME, PVP-Vol 98-8, June 23-26 1985, pp. 125-134.
41 Andrews, R. M., Hashemi, S. H., Howard, I. C., Yates, J.R., and Edwards, A., "A Study of Ductile Failure Processes in High Strength Linepipe using Damage Mechanics Methods", In Proceedings of the 4th International Conference on Pipeline Technology, Ostend, Belgium, Vol.1, pp. 441-455, 2004.
42 Darcis, P., Kohn, G., Bussiba, A., McColskey,J.D., McCowan, C.N., Fields, R., Smith, R., and Merritt, J., "Crack Tip Opening Angle: Measurement And Modeling Of Fracture Resistance In Low And High Strength Pipeline Steels," IPC2006-10172, Proceedings of IPC 2006, 2006 International Pipeline Conference, September 25-29, 2006, Calgary, Alberta, Canada.
43 D.L. Rudland, G.M. Wilkowski, Z. Feng, Y.-Y. Wang, D. Horsley, A. Glover, "Experimental Investigation of CTOA in Linepipe Steels," *Engineering Fracture Mechanics*, 70, (3-4), (2003), pp. 567-577.
44 Maxey, W.A., Kiefner, J.F., Eiber, R.J., and Duffy, A.R., "Experimental Investigation of Ductile Fractures in Piping," IGU/C 34-73, GNICE 73, 12th World Gas Conference, 1973
45 *ABAQUS Version* 6.5, ABAQUS Inc., Providence, USA (2005).
46 Wilkowski, G., Rudland, D., Xu, H, and Sanderson, N., "Effects of Grade on Ductile Fracture Arrest for Gas Pipelines," IPC2006-10350, Proceedings of IPC 2006, 2006 International Pipeline Conference, September 25-29, 2006, Calgary, Alberta, Canada.

Appendix A – Information Exchange Agreement Letter

Technology for Energy Pipelines

Pipeline Research Council International, Inc.
1401 Wilson Blvd • Suite 1101 • Arlington, VA 22209
703/387-0190 • 703/387-0192 Fax • www.prci.com

Lee M. Stewart
Chairman

George W. Tenley, Jr.
President
gtenley@prci.org

(1) DOT
(2) File

December 9, 2004

Dr. Naoto Hagiwara
Manager, Gas Pipeline Fracture Control Project
Tokyo Gas Co, Ltd.
Pipeline Engineering Research Laboratory
1-7-7 Suehiro-cho, Tsurumi-ku
Yokohama, 230-0045, JAPAN

LETTER AGREEMENT

Between the Japanese Gas Association (JGA) and Pipeline Research Council International, Inc. (PRCI), Regarding Information Sharing on a JGA Project "*Gas Pipeline Fracture Control*" and a PRCI Project "*First Major Improvements to the Two-Curve Fracture Arrest Model*"

Dear Dr. Hagiwara:

This Letter Agreement sets forth the terms of agreement between the Japanese Gas Association (JGA) and Pipeline Research Council International (PRCI) to exchange detailed technical information from the JGA project titled "*Gas Pipeline Fracture Control*" and the PRCI/DOT project titled "*First Major Improvements to the Two-Curve Fracture Arrest Model*" (PRCI Reference PRCI-276-04505; DOT DTRS56-03-T-0007). Although this Agreement is between PRCI and JGA, the PRCI project is co-funded by the U.S. Department of Transportation (USDOT). Hence, as part of this Agreement, JGA agrees to allow PRCI to release the JGA information to the USDOT and the contractor involved in both projects, Engineering Mechanics Corporation of Columbus ("Emc^2"), under terms described below.

A major consideration in this agreement is the proprietary nature of the data. PRCI will maintain confidentiality of the JGA data and strictly limit its dissemination to PRCI members and Emc^2. In like manner, JGA will ensure the confidentiality of the PRCI data if JGA releases it to private companies that are members of this project or to METI. However, the USDOT is required to make certain information publicly available. We have determined that the USDOT is satisfied with the detailed information being released to Emc^2, so that only a summary of the JGA information would be given directly to the USDOT and made publicly available. A similar procedure is being used for the PRCI data being given to the USDOT that limits to summaries the data that USDOT may make available to the public. It is understood by the parties to this agreement that the JGA data are the property of the Ministry of Economy, Trade and Industry. Accordingly, USDOT and PRCI need the permission of JGA prior to utilization of the data and similarly, JGA needs the permission of PRCI prior to the utilization of the PRCI data.

The direct exchange of the detailed information under this Agreement will involve a determination of what is really of interest by the technical representatives of JGA, PRCI, and USDOT. This information could involve digital photos, movies, spreadsheets of test data (e.g., burst tests and material property tests), reports, and computer codes developed in these programs. Representatives of PRCI, DOT, and JGA would also be allowed to attend or witness any full-scale tests conducted by either party.

The PRCI technical representative for this project is Mr. Brian Rothwell. For your information, Dr. Gopala Vinjamuri is the USDOT technical representative, and Mr. Warren Osterberg is the USDOT contract administrator. Please provide us with the name of the JGA Technical Representative, in addition to the JGA Contract Administrator, who will provide his or her name and signature below.

This Agreement will be effective upon the signature of the authorized JGA Contract Administrator, provided below. Please have the Contract Administrator sign two originals, and return one to me.

Warmest personal regards,

George W. Tenley, Jr.
President, PRCI

12/9/04
Date

JGA Contract Administrator

12/19/04
Date

Appendix B – Mojave Soil Experiment Details

Mojave Sand

Grain Size Distribution Report

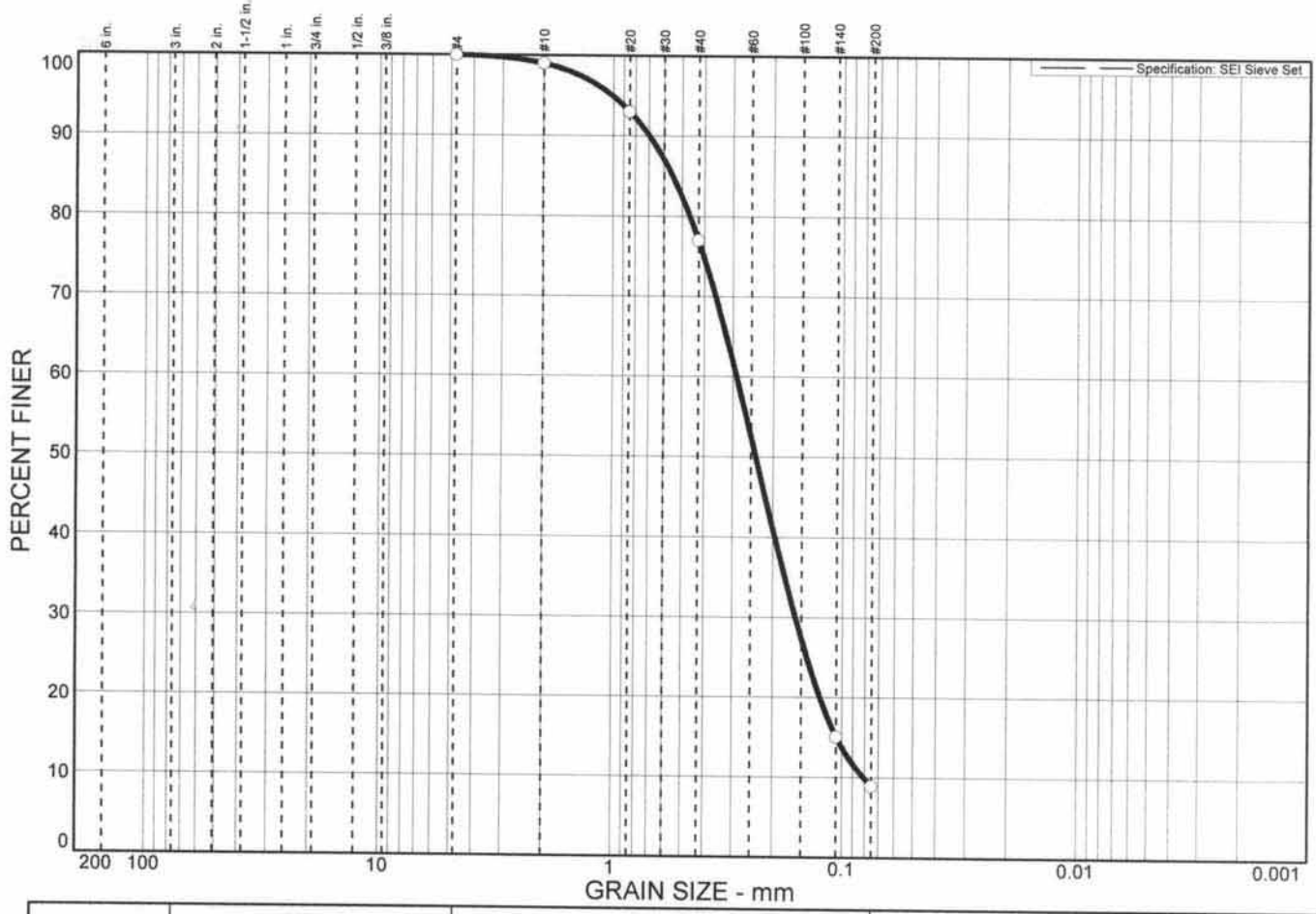

	% + 3"	% GRAVEL		% SAND			% FINES	
		CRS.	FINE	CRS.	MEDIUM	FINE	SILT	CLAY
○	0	0	0	1	22	68	9	

SOIL DATA

SYMBOL	SOURCE	SAMPLE NO.	DEPTH (ft.)	DESCRIPTION	USCS
○		5595	Random	WELL-GRADED SAND (trace of fines)	SW-SM
				yellowish brown, fine grade, non-cohesive	
				SAND EQUIVALENT VALUE = 26	

Grain Size Distribution Report

SOILS ENGINEERING, INC.

Client: Engineering Mechanics Corp. of Columbus

Project: Geotechnical Engineering & Testing Services
Axial Crack in Gas Pipeline Research Project

Project No.: 10884 **Figure** A-2

GRAIN SIZE DISTRIBUTION TEST DATA

Client: Engineering Mechanics Corp. of Columbus
Project: Geotechnical Engineering & Testing Services
Axial Crack in Gas Pipeline Research Project
Project Number: 10884

Sample Data

Source:
Sample No.: 5595
Elev. or Depth: Random **Sample Length(in./cm.):**
Location: Ridgecrest - Boydston Construction
Description: WELL-GRADED SAND (trace of fines)
yellowish brown, fine grade, non-cohesive
USCS: SW-SM

Mechanical Analysis Data

	Initial	After wash
Dry sample and tare=	1325.70	1252.80
Tare =	397.00	397.00
Dry sample weight =	928.70	855.80

Minus #200 from wash= 7.8 %
Tare for cumulative weight retained= 397.00

Sieve	Cumul. Wt. retained	Percent finer	Specification Limits, percent	Deviation, percent
# 4	398.80	100	0 to 0	+ 100
# 10	408.50	99	0 to 0	+ 99
# 20	464.40	93	0 to 0	+ 93
# 40	614.70	77	0 to 0	+ 77
# 140	1189.00	15	0 to 0	+ 15
# 200	1242.70	8.9	0 to 0	+ 9

Fractional Components

Gravel/Sand based on #4
Sand/Fines based on #200
% + 3" = **% GRAVEL =**
% SAND = 91 **(% coarse =** 1 **% medium =** 22 **% fine =** 68)
% FINES = 9

D_{85}= 0.55 D_{60}= 0.29 D_{50}= 0.24
D_{30}= 0.16 D_{15}= 0.11 D_{10}= 0.08
C_c= 1.0829 C_u= 3.5716

Maximum Density - Optimum Moisture Test Report

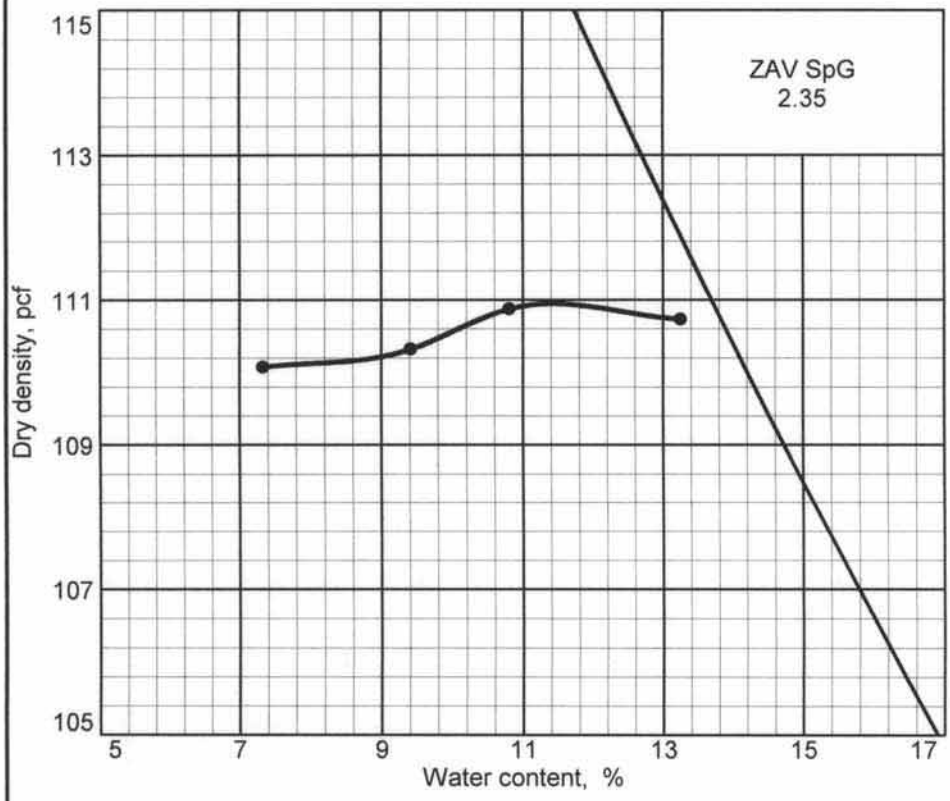

Curve No.
02

Test Specification:
ASTM D 1557-00 Method A Modified

Hammer Wt.: 10 lb.
Hammer Drop: 18 in.
Number of Layers: five
Blows per Layer: 25
Mold Size: .03333 cu.ft.

Test Performed on Material Passing No.4 **Sieve**

Soil Data

NM N/A **Sp.G.**
LL N/A **PI** N/A
%>No.4 0 **%<#200** 8.9
USCS SW-SM **AASHTO** N/A

TESTING DATA

	1	2	3	4	5	6
WM + WS	3827.6	3898.9	3937.4	3866.4		
WM	2041.5	2041.5	2041.5	2041.5		
WW + T #1	358.20	359.90	354.50	349.40		
WD + T #1	347.50	344.50	336.60	336.70		
TARE #1	201.50	202.00	201.50	201.80		
WW + T #2						
WD + T #2						
TARE #2						
MOISTURE	7.3	10.8	13.2	9.4		
DRY DENSITY	110.1	110.9	110.7	110.3		

TEST RESULTS

Maximum dry density = 110.9 pcf

Optimum moisture = 11.4 %

Material Description

WELL-GRADED SAND (trace of fines)
yellowish brown, fine grade, non-cohesive

Project No. 10884 **Client:** Engineering Mechanics Corp. of Columbus
Project: Geotechnical Engineering & Testing Services
Axial Crack in Gas Pipeline Research Project
• **Location:** Ridgecrest - Boydston Construction

Remarks:
Tested By: BF
Test Date: 08/17/04
Sample # 5595

Maximum Density - Optimum Moisture Test Report

SOILS ENGINEERING, INC.

Figure C-2

MOISTURE DENSITY TEST DATA

Client: Engineering Mechanics Corp. of Columbus
Project: Geotechnical Engineering & Testing Services
Axial Crack in Gas Pipeline Research Project
Project Number: 10884

Specimen Data

Source:
Sample No.: 5595
Elev. or Depth: Random **Sample Length(in./cm.):**
Location: Ridgecrest - Boydston Construction
Description: WELL-GRADED SAND (trace of fines)
yellowish brown, fine grade, non-cohesive
USCS Classification: SW-SM **AASHTO Classification:** N/A
Natural Moisture: N/A **Liquid Limit:** N/A **Plasticity Index:** N/A
Testing Remarks: Tested By: BF
Test Date: 08/17/04
Sample # 5595
Percent retained on No.4 sieve: 0
Percent passing No. 200 sieve: 8.9 **Specific gravity:**

Test Data And Results For Curve 02

Type of test: ASTM D 1557-00 Method A Modified
Mold Dia.: 4.00 in. **Hammer Wt.:** 10 lb. **Drop:** 18 in.
Layers: five **Blows per Layer:** 25

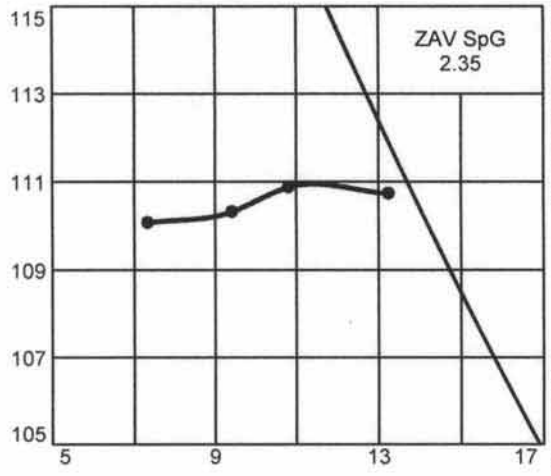

POINT NO.	1	2	3	4
WM + WS	3827.6	3898.9	3937.4	3866.4
WM	2041.5	2041.5	2041.5	2041.5
WW+T	358.20	359.90	354.50	349.40
WD+T	347.50	344.50	336.60	336.70
TARE	201.50	202.00	201.50	201.80
MOIST	7.3	10.8	13.2	9.4
MOISTURE	7.3	10.8	13.2	9.4
DRY DEN	110.1	110.9	110.7	110.3

Max dry den= 110.9 pcf **Opt moisture=** 11.4 %

Oversize Correction Not Applied

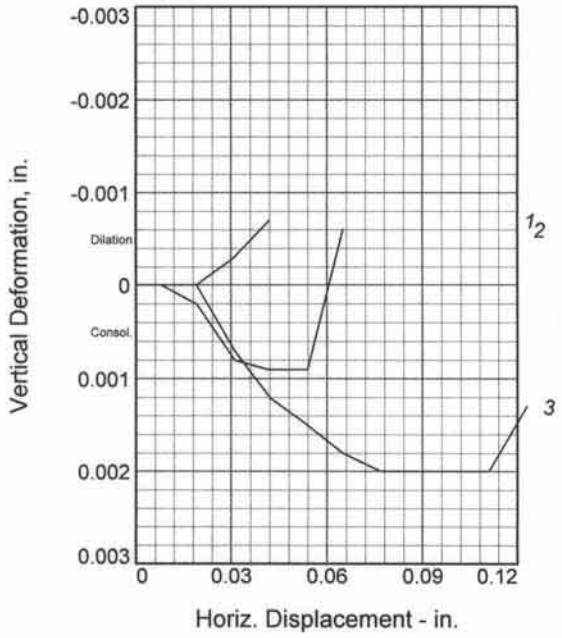

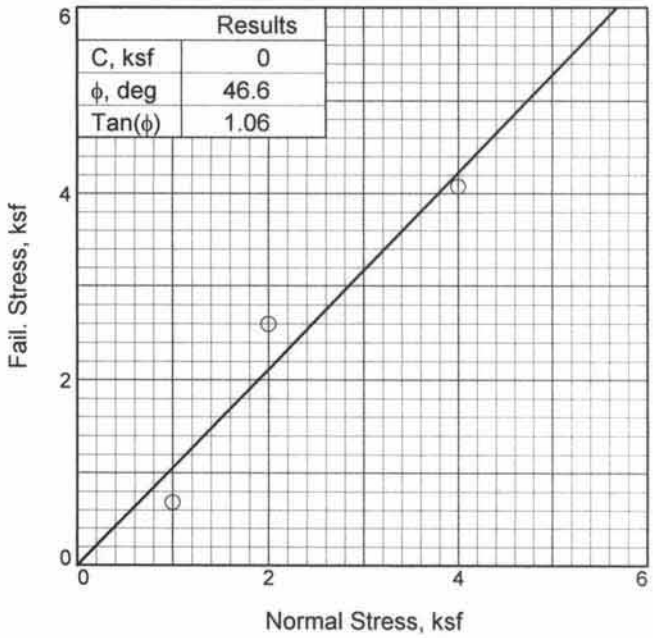

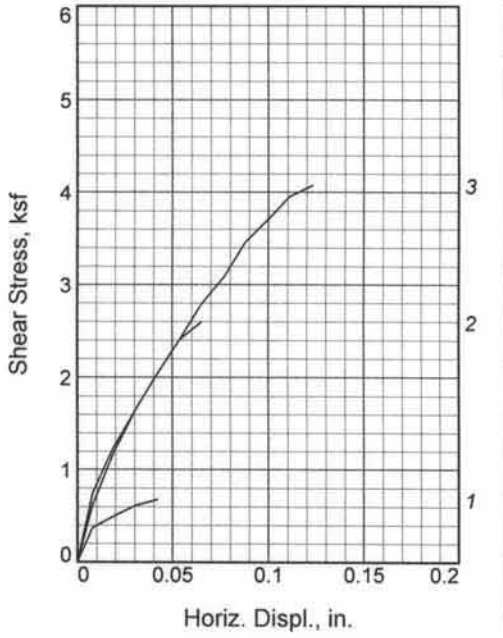

Sample No.		1	2	3
Initial	Water Content, %	19.4	16.2	17.0
	Dry Density, pcf	104.5	112.5	105.5
	Saturation, %	88.2	91.2	79.1
	Void Ratio	0.5834	0.4708	0.5679
	Diameter, in.	2.38	2.38	2.38
	Height, in.	1.00	1.00	1.00
At Test	Water Content, %	19.4	16.2	17.0
	Dry Density, pcf	104.5	112.5	105.5
	Saturation, %	88.2	91.2	79.1
	Void Ratio	0.5834	0.4708	0.5679
	Diameter, in.	2.38	2.38	2.38
	Height, in.	1.00	1.00	1.00
Normal Stress, ksf		1.00	2.00	4.00
Fail. Stress, ksf		0.68	2.59	4.08
Displacement, in.		0.04	0.07	0.12
Ult. Stress, ksf				
Displacement, in.				
Strain at peak, %		1.8	2.7	5.2

Sample Type: Remolded @ moisture 10.8%
Description: WELL-GRADED SAND (trace of fines)
LL= N/A **PL=** **PI=** N/A
Assumed Specific Gravity= 2.65
Remarks: Test Date: 08/22/04

Client: Engineering Mechanics Corp. of Columbus

Project: Geotechnical Engineering & Testing Services
Axial Crack in Gas Pipeline Research Project
Location: Ridgecrest - Boydston Construction
Sample Number: 5595 **Depth:** Random
Proj. No.: 10884 **Date:** 08/11/04

DIRECT SHEAR TEST REPORT

SOILS ENGINEERING, INC.

Figure E-1

Tested By: AL **Checked By:** JW

DIRECT SHEAR TEST

9/27/2004

Date: 08/11/04
Client: Engineering Mechanics Corp. of Columbus
Project: Geotechnical Engineering & Testing Services
Axial Crack in Gas Pipeline Research Project
Location: Ridgecrest - Boydston Construction
Depth: Random **Sample Number:** 5595
Description: WELL-GRADED SAND (trace of fines)
yellowish brown, fine grade, non-cohesive
SAND EQUIVALENT VALUE = 26
Remarks: Test Date: 08/22/04
Type of Sample: Remolded @ moisture 10.8%
Assumed Specific Gravity=2.65 **LL=**N/A **PL=** **PI=**N/A

Parameters for Specimen No. 1

Specimen Parameter	Initial	Consolidated	Final
Moisture content: Moist soil+tare, gms.			175.500
Moisture content: Dry soil+tare, gms.			151.900
Moisture content: Tare, gms.			30.400
Moisture, %	19.4	19.4	19.4
Moist specimen weight, gms.	145.1		
Diameter, in.	2.38	2.38	
Area, in.²	4.43	4.43	
Height, in.	1.00	1.00	
Net decrease in height, in.		0.00	
Wet Density, pcf	124.8	124.8	
Dry density, pcf	104.5	104.5	
Void ratio	0.5834	0.5834	
Saturation, %	88.2	88.2	

Test Readings for Specimen No. 1

Primary load ring constant = 1.9 lbs. per input unit
Secondary load ring constant = 1.9 lbs. per input unit
Crossover reading for secondary load ring = 1.9 input units
Normal stress = 1 ksf
Strain at peak, % = 1.8
Fail. Stress = 0.68 ksf **at reading no.** 4

No.	Horizontal Def. Dial in.	Load Dial	Load lbs.	Shear Stress ksf	Vertical Def. Dial in.
0	0.0000	0.00	0.0	0.00	0.0353
1	0.0080	6.00	11.4	0.37	0.0353
2	0.0190	8.00	15.2	0.49	0.0353
3	0.0310	10.00	19.0	0.62	0.0356
4	0.0420	11.00	20.9	0.68	0.0360

SOILS ENGINEERING, INC.

Parameters for Specimen No. 2

Specimen Parameter	Initial	Consolidated	Final
Moisture content: Moist soil+tare, gms.			184.800
Moisture content: Dry soil+tare, gms.			163.600
Moisture content: Tare, gms.			32.800
Moisture, %	16.2	16.2	16.2
Moist specimen weight, gms.	152.0		
Diameter, in.	2.38	2.38	
Area, in.^{2}	4.43	4.43	
Height, in.	1.00	1.00	
Net decrease in height, in.		0.00	
Wet Density, pcf	130.7	130.7	
Dry density, pcf	112.5	112.5	
Void ratio	0.4708	0.4708	
Saturation, %	91.2	91.2	

Test Readings for Specimen No. 2

Primary load ring constant = 1.9 lbs. per input unit
Secondary load ring constant = 1.9 lbs. per input unit
Crossover reading for secondary load ring = 1.9 input units
Normal stress = 2 ksf
Strain at peak, % = 2.7
Fail. Stress = 2.59 ksf **at reading no.** 6

No.	Horizontal Def. Dial in.	Load Dial	Load lbs.	Shear Stress ksf	Vertical Def. Dial in.
0	0.0000	0.00	0.0	0.00	0.0344
1	0.0080	10.00	19.0	0.62	0.0344
2	0.0190	19.00	36.1	1.17	0.0342
3	0.0310	27.00	51.3	1.67	0.0336
4	0.0420	33.00	62.7	2.04	0.0335
5	0.0540	39.00	74.1	2.41	0.0335
6	0.0650	42.00	79.8	2.59	0.0350

SOILS ENGINEERING, INC.

Parameters for Specimen No. 3

Specimen Parameter	Initial	Consolidated	Final
Moisture content: Moist soil+tare, gms.			177.700
Moisture content: Dry soil+tare, gms.			156.900
Moisture content: Tare, gms.			34.200
Moisture, %	17.0	17.0	17.0
Moist specimen weight, gms.	143.5		
Diameter, in.	2.38	2.38	
Area, in.²	4.43	4.43	
Height, in.	1.00	1.00	
Net decrease in height, in.		0.00	
Wet Density, pcf	123.4	123.4	
Dry density, pcf	105.5	105.5	
Void ratio	0.5679	0.5679	
Saturation, %	79.1	79.1	

Test Readings for Specimen No. 3

Primary load ring constant = 1.9 lbs. per input unit
Secondary load ring constant = 1.9 lbs. per input unit
Crossover reading for secondary load ring = 1.9 input units
Normal stress = 4 ksf
Strain at peak, % = 5.2
Fail. Stress = 4.08 ksf **at reading no.** 11

No.	Horizontal Def. Dial in.	Load Dial	Load lbs.	Shear Stress ksf	Vertical Def. Dial in.
0	0.0000	0.00	0.0	0.00	0.0370
1	0.0080	12.00	22.8	0.74	0.0370
2	0.0190	20.00	38.0	1.24	0.0370
3	0.0310	27.00	51.3	1.67	0.0363
4	0.0420	33.00	62.7	2.04	0.0358
5	0.0540	39.00	74.1	2.41	0.0355
6	0.0650	45.00	85.5	2.78	0.0352
7	0.0770	50.00	95.0	3.09	0.0350
8	0.0880	56.00	106.4	3.46	0.0350
9	0.1000	60.00	114.0	3.71	0.0350
10	0.1110	64.00	121.6	3.95	0.0350
11	0.1230	66.00	125.4	4.08	0.0357

SOILS ENGINEERING, INC.

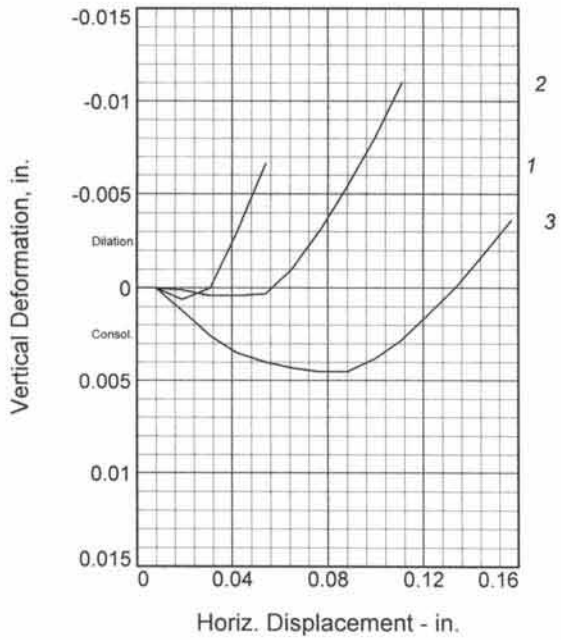

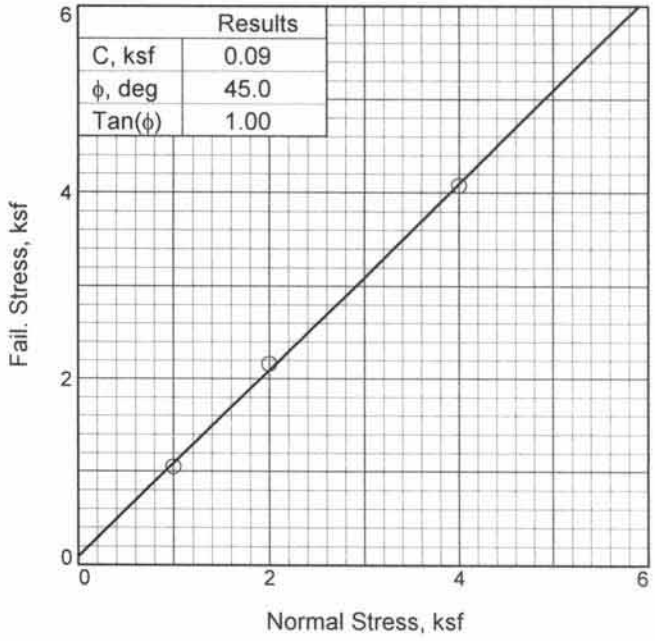

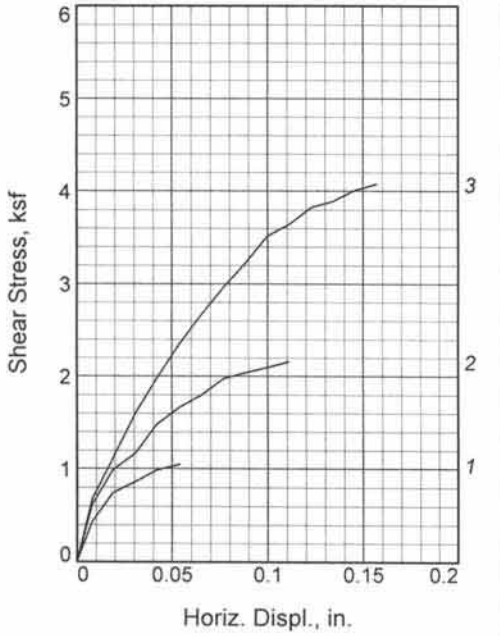

Sample No.		1	2	3
Initial	Water Content, %	3.9	3.9	3.9
	Dry Density, pcf	99.1	98.4	97.3
	Saturation, %	15.5	15.3	14.7
	Void Ratio	0.6700	0.6817	0.7010
	Diameter, in.	2.38	2.38	2.38
	Height, in.	1.00	1.00	1.00
At Test	Water Content, %	3.9	3.9	3.9
	Dry Density, pcf	99.1	98.4	97.3
	Saturation, %	15.5	15.3	14.7
	Void Ratio	0.6700	0.6817	0.7010
	Diameter, in.	2.38	2.38	2.38
	Height, in.	1.00	1.00	1.00
Normal Stress, ksf		1.00	2.00	4.00
Fail. Stress, ksf		1.05	2.16	4.08
Displacement, in.		0.05	0.11	0.16
Ult. Stress, ksf				
Displacement, in.				
Strain at peak, %		2.3	4.7	6.6

Sample Type: Remolded / Unsaturated
Description: CLAYEY SAND; dark yellowish brown, fine grade, cohesive / Shear # 1 3.9% mc
LL= N/A **PL=** **PI=** N/A
Assumed Specific Gravity= 2.65
Remarks: Test Date: 11/10/05
Sample was remolded @ 3.9% moisture into a 2.5" x 6" tube. Then the sample was extracted into a 1" x 2.375" ring.
Figure C-1

Client: ENGINEERING MECHANICS CORP. OF COLUMBUS
Project: GAS PIPELINE CRACK ARREST RESEARCH
Location: Native Surface
Sample Number: 11545 **Depth:** Random
Proj. No.: 11418 **Date:**

DIRECT SHEAR TEST REPORT

SOILS ENGINEERING, INC.

Tested By: PS **Checked By:** JW

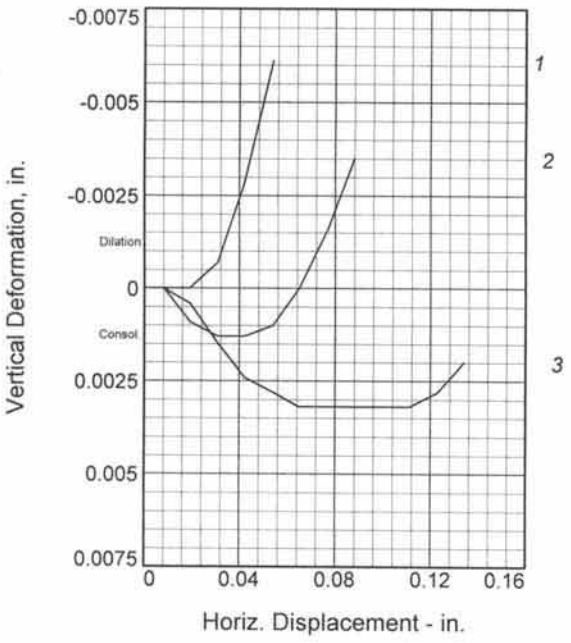

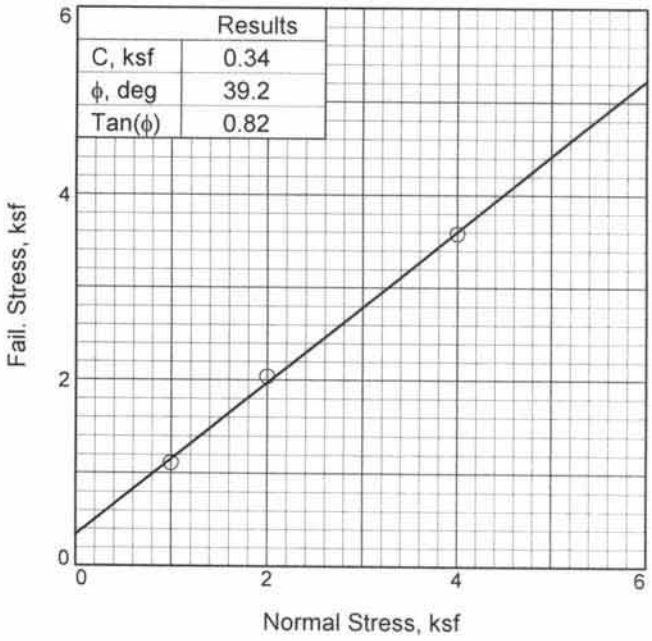

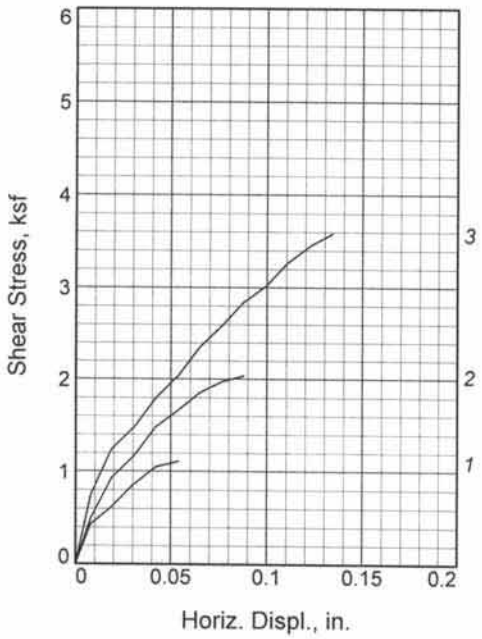

Sample No.		1	2	3
Initial	Water Content, %	11.2	11.1	11.1
	Dry Density, pcf	102.1	99.8	97.7
	Saturation, %	47.8	44.8	42.4
	Void Ratio	0.6207	0.6585	0.6935
	Diameter, in.	2.38	2.38	2.38
	Height, in.	1.00	1.00	1.00
At Test	Water Content, %	11.2	11.1	11.1
	Dry Density, pcf	102.1	99.8	97.7
	Saturation, %	47.8	44.8	42.4
	Void Ratio	0.6207	0.6585	0.6935
	Diameter, in.	2.38	2.38	2.38
	Height, in.	1.00	1.00	1.00
Normal Stress, ksf		1.00	2.00	4.00
Fail. Stress, ksf		1.11	2.04	3.58
Displacement, in.		0.05	0.09	0.13
Ult. Stress, ksf				
Displacement, in.				
Strain at peak, %		2.3	3.7	5.6

Sample Type: Remolded / Unsaturated
Description: CLAYEY SAND; dark yellowish brown, fine grade, cohesive / Shear # 2 11.1% mc
LL= N/A **PL=** **PI=** N/A
Assumed Specific Gravity= 2.65
Remarks: Test Date: 11/10/05
Sample was remolded @ 11.1% moisture into a 2.5" x 6" tube. Then the sample was extracted into a 1" x 2.375" ring.

Figure C-2

Client: ENGINEERING MECHANICS CORP. OF COLUMBUS

Project: GAS PIPELINE CRACK ARREST RESEARCH

Location: Native Surface

Sample Number: 11545 **Depth:** Random

Proj. No.: 11418 **Date:**

DIRECT SHEAR TEST REPORT

SOILS ENGINEERING, INC.

Tested By: PS **Checked By:** JW

Mojave Sandy-Silt

Grain Size Distribution Report

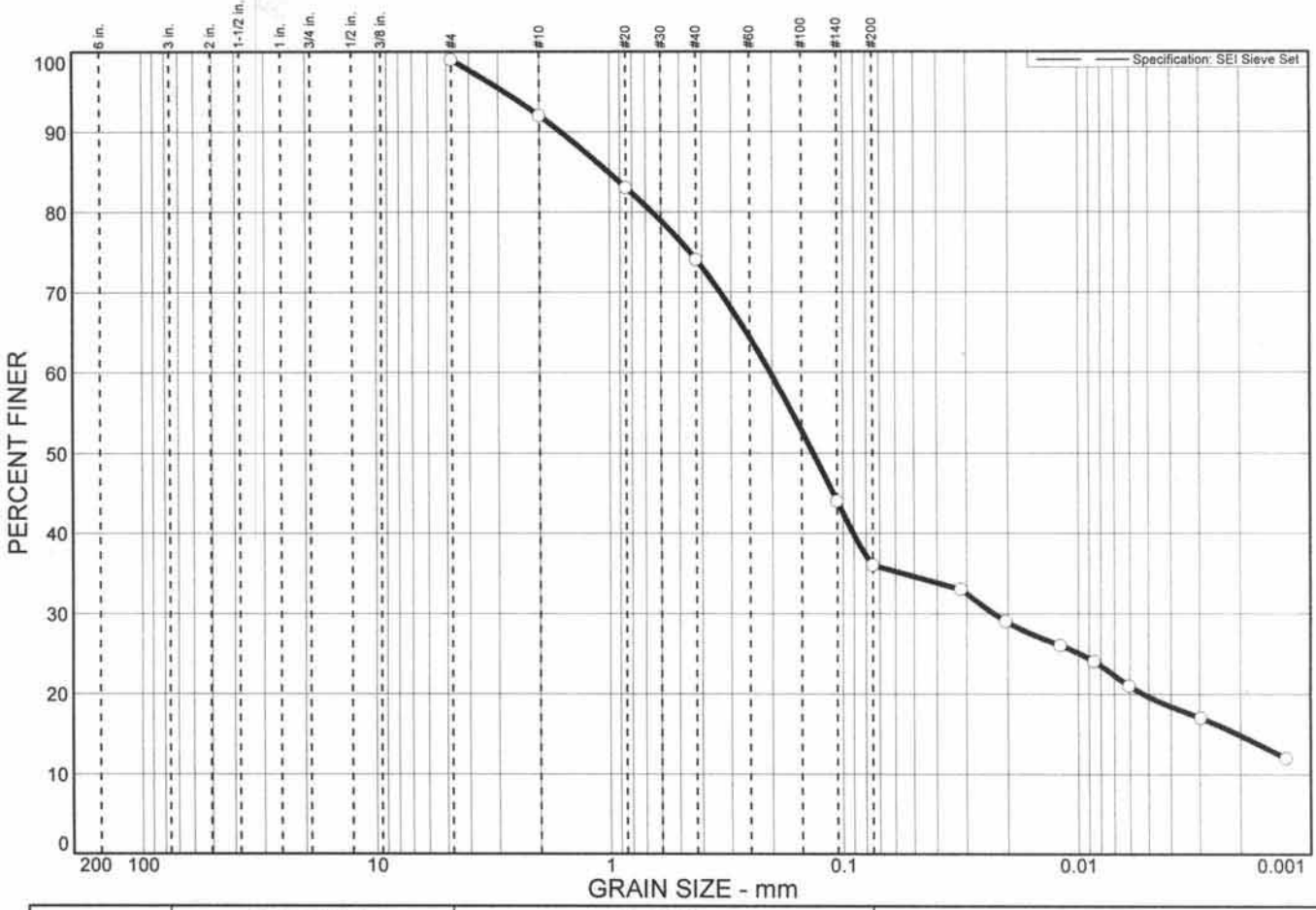

	% + 3"	% GRAVEL		% SAND			% FINES	
		CRS.	FINE	CRS.	MEDIUM	FINE	SILT	CLAY
○				7	18	38	16	20

SOIL DATA

SYMBOL	SOURCE	SAMPLE NO.	DEPTH (ft.)	DESCRIPTION	USCS
○		5613	3-4'	CLAYEY SAND	SC
				light yellowish brown, medium Grade, Cohesive, non-plastic	
				Location - Bottom of Clay Test Pit	

Grain Size Distribution Report

SOILS ENGINEERING, INC.

Client: Engineering Mechanics Corp. of Columbus

Project: Geotechnical Engineering & Testing Services
Axial Crack in Gas Pipeline Research Project

Project No.: 10884 **Figure** A-3

GRAIN SIZE DISTRIBUTION TEST DATA

Client: Engineering Mechanics Corp. of Columbus
Project: Geotechnical Engineering & Testing Services
Axial Crack in Gas Pipeline Research Project
Project Number: 10884

Sample Data

Source:
Sample No.: 5613
Elev. or Depth: 3-4' **Sample Length(in./cm.):**
Location: Bottom or Clay Test Pit
Description: CLAYEY SAND
light yellowish brown, medium Grade, Cohesive, non-plastic *Location - Bottom of Clay Test Pit*
USCS: SC

Mechanical Analysis Data

	Initial	After wash
Dry sample and tare=	805.00	593.80
Tare =	125.40	125.40
Dry sample weight =	679.60	468.40

Minus #200 from wash= 31 %
Tare for cumulative weight retained= 125.40

Sieve	Cumul. Wt. retained	Percent finer	Specification Limits, percent	Deviation, percent
# 4	130.60	99	0 to 0	+ 99
# 10	176.80	92	0 to 0	+ 92
# 20	239.60	83	0 to 0	+ 83
# 40	303.40	74	0 to 0	+ 74
# 140	507.20	44	0 to 0	+ 44
# 200	558.10	36	0 to 0	+ 36

Hydrometer Analysis Data

Separation sieve is #10
Percent -#10 based upon complete sample= 92
Weight of hydrometer sample: 69.9
Calculated biased weight= 75.98
Table of composite correction values:

Temp, deg C:	24.0	25.0	27.0	26.0
Comp. corr:	-2.0	-2.0	-1.0	-2.0

Meniscus correction only=
Specific gravity of solids= 2.65
Specific gravity correction factor= 1.000
Hydrometer type: 152H
Effective depth L= 16.294964 - 0.164 x Rm

Elapsed time, min	Temp, deg C	Actual reading	Corrected reading	K	Rm	Eff. depth	Diameter mm	Percent finer
0.10	24.0	32.0	30.0	0.0130	32.0	11.0	0.1366	39
2.00	24.0	27.0	25.0	0.0130	27.0	11.9	0.0317	33
5.00	24.0	24.0	22.0	0.0130	24.0	12.4	0.0204	29
15.00	24.0	22.0	20.0	0.0130	22.0	12.7	0.0120	26
30.00	24.0	20.0	18.0	0.0130	20.0	13.0	0.0086	24

Elapsed time, min	Temp, deg C	Actual reading	Corrected reading	K	Rm	Eff. depth	Diameter mm	Percent finer
60.00	25.0	18.0	16.0	0.0128	18.0	13.3	0.0061	21
250.00	27.0	14.0	13.0	0.0126	14.0	14.0	0.0030	17
1440.00	26.0	11.0	9.0	0.0127	11.0	14.5	0.0013	12

Fractional Components

Gravel/Sand based on #4
Sand/Fines based on #200
% + 3" = **% GRAVEL =**
% SAND = 63 **(% coarse =** 7 **% medium =** 18 **% fine =** 38**)**
% SILT = 16 **% CLAY =** 20

D_{85}= 1.01 D_{60}= 0.20 D_{50}= 0.13
D_{30}= 0.02 D_{15}= 0.00

Maximum Density - Optimum Moisture Test Report

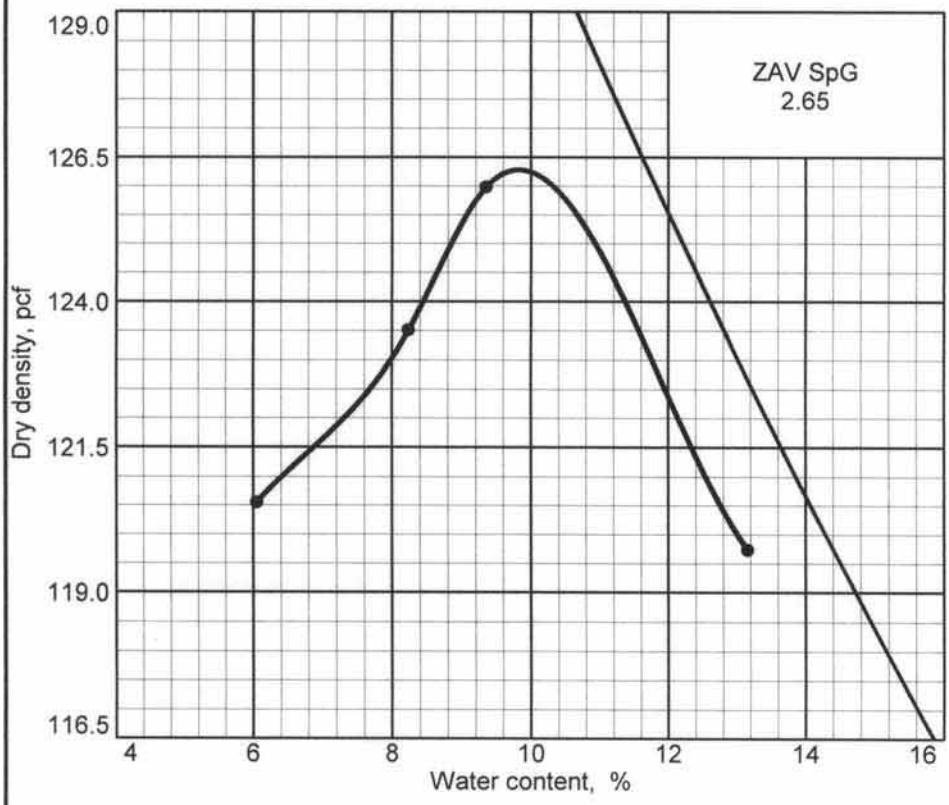

Curve No.
03

Test Specification:
ASTM D 1557-00 Method A Modified

Hammer Wt.: 10 lb.
Hammer Drop: 18 in.
Number of Layers: five
Blows per Layer: 25
Mold Size: .03333 cu.ft.

Test Performed on Material Passing No.4 **Sieve**

Soil Data

NM	N/A	**Sp.G.**	2.65
LL	N/A	**PI**	N/A
%>No.4	1	**%<#200**	36
USCS	SC	**AASHTO**	N/A

TESTING DATA

	1	2	3	4	5	6
WM + WS	3993.0	4339.1	4089.8	3920.7		
WM	1972.0	2256.4	2041.5	1988.0		
WW + T #1	363.50	358.20	389.50	369.80		
WD + T #1	351.20	344.80	367.70	360.20		
TARE #1	201.80	201.50	202.00	201.50		
WW + T #2						
WD + T #2						
TARE #2						
MOISTURE	8.2	9.4	13.2	6.0		
DRY DENSITY	123.5	126.0	119.7	120.5		

TEST RESULTS

Maximum dry density = 126.3 pcf

Optimum moisture = 9.8 %

Material Description

CLAYEY SAND
light yellowish brown, medium Grade, Cohesive, non-plastic

Project No. 10884 **Client:** Engineering Mechanics Corp. of Columbus
Project: Geotechnical Engineering & Testing Services
Axial Crack in Gas Pipeline Research Project
• **Location:** Bottom or Clay Test Pit

Remarks:
Tested By: PS
Test Date: 08/24/04
Sample Number: 5613

Maximum Density - Optimum Moisture Test Report

SOILS ENGINEERING, INC.

Figure C-3

MOISTURE DENSITY TEST DATA

Client: Engineering Mechanics Corp. of Columbus
Project: Geotechnical Engineering & Testing Services
Axial Crack in Gas Pipeline Research Project
Project Number: 10884

Specimen Data

Source:
Sample No.: 5613
Elev. or Depth: 3-4' **Sample Length(in./cm.):**
Location: Bottom or Clay Test Pit
Description: CLAYEY SAND
light yellowish brown, medium Grade, Cohesive, non-plastic
USCS Classification: SC **AASHTO Classification:** N/A
Natural Moisture: N/A **Liquid Limit:** N/A **Plasticity Index:** N/A
Testing Remarks: Tested By: PS
Test Date: 08/24/04
Sample Number: 5613
Percent retained on No.4 sieve: 1
Percent passing No. 200 sieve: 36 **Specific gravity:** 2.65

Test Data And Results For Curve 03

Type of test: ASTM D 1557-00 Method A Modified
Mold Dia.: 4.00 in. **Hammer Wt.:** 10 lb. **Drop:** 18 in.
Layers: five **Blows per Layer:** 25

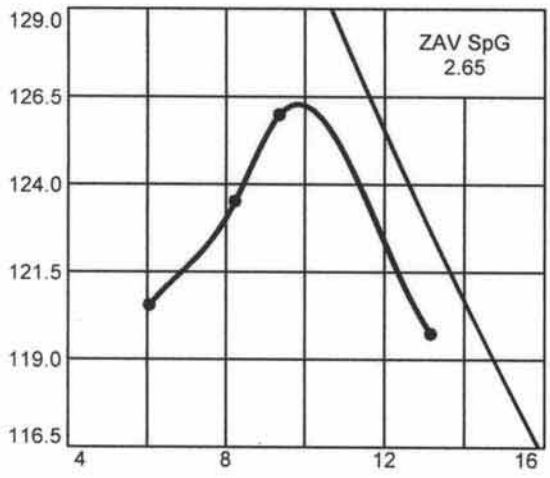

POINT NO.	1	2	3	4
WM + WS	3993.0	4339.1	4089.8	3920.7
WM	1972.0	2256.4	2041.5	1988.0
WW+T	363.50	358.20	389.50	369.80
WD+T	351.20	344.80	367.70	360.20
TARE	201.80	201.50	202.00	201.50
MOIST	8.2	9.4	13.2	6.0
MOISTURE	8.2	9.4	13.2	6.0
DRY DEN	123.5	126.0	119.7	120.5

Max dry den= 126.3 pcf **Opt moisture=** 9.8 %

Oversize Correction Not Applied

CONSOLIDATION TEST REPORT

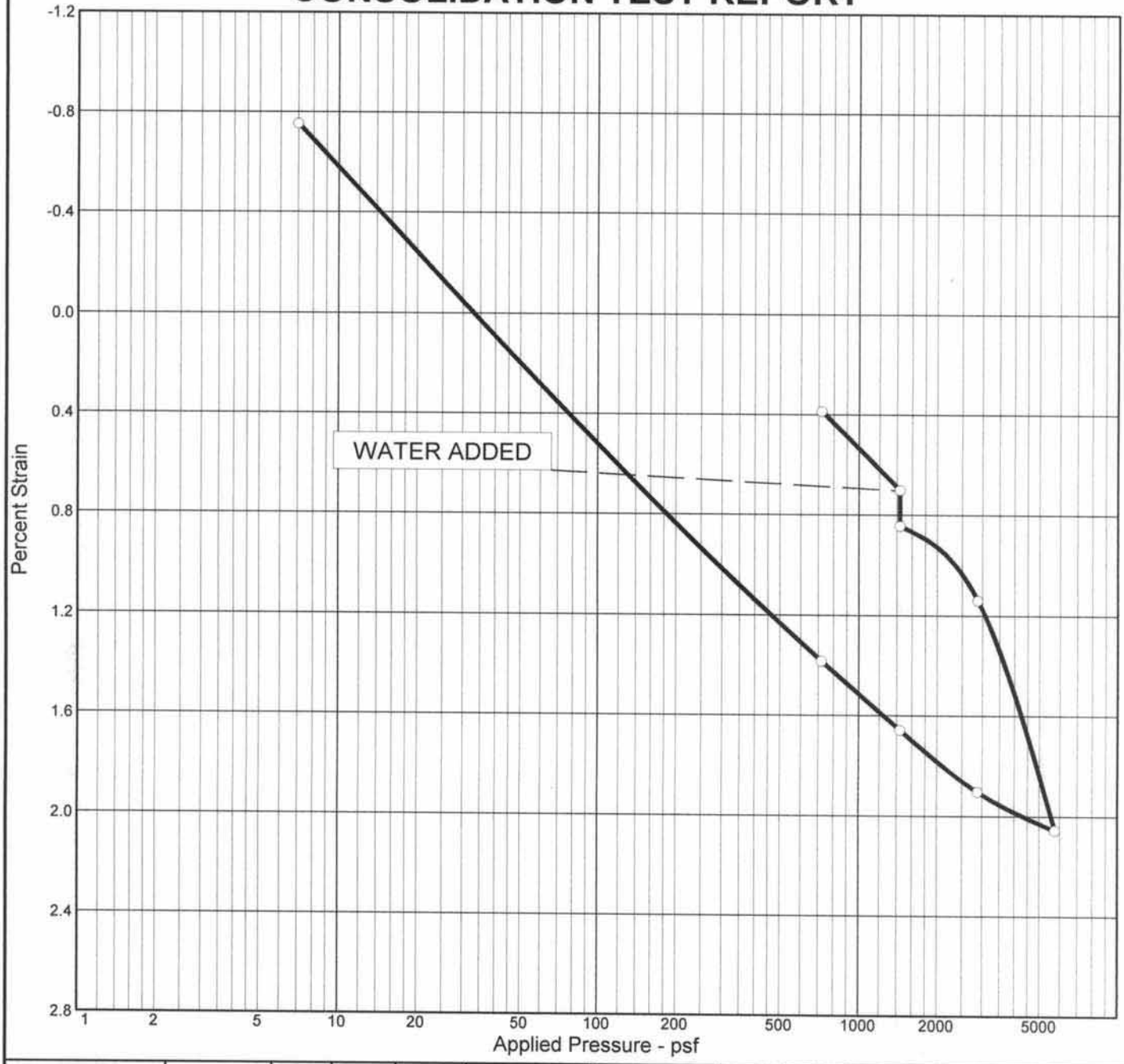

Natural		Dry Dens. (pcf)	LL	PI	Sp. Gr.	Overburden (psf)	P_c (psf)	C_c	C_s	Swell Press. (psf)	Swell %	e_o
Sat.	Moist.											
44.5 %	8.2 %	111.3	N/A	N/A	2.65	336	2856	0.05	0.01			0.487

MATERIAL DESCRIPTION	USCS	AASHTO
CLAYEY SAND light yellowish brown, medium Grade, Cohesive, non-plastic	SC	N/A

Project No. 10884 **Client:** Engineering Mechanics Corp. of Columbus

Project: Geotechnical Engineering & Testing Services
Axial Crack in Gas Pipeline Research Project

Location: Bottom or Clay Test Pit

Remarks:
Tested By: AL
Test Date: 08/26/04
Sample # 5613

CONSOLIDATION TEST REPORT

SOILS ENGINEERING, INC.

Figure B-2

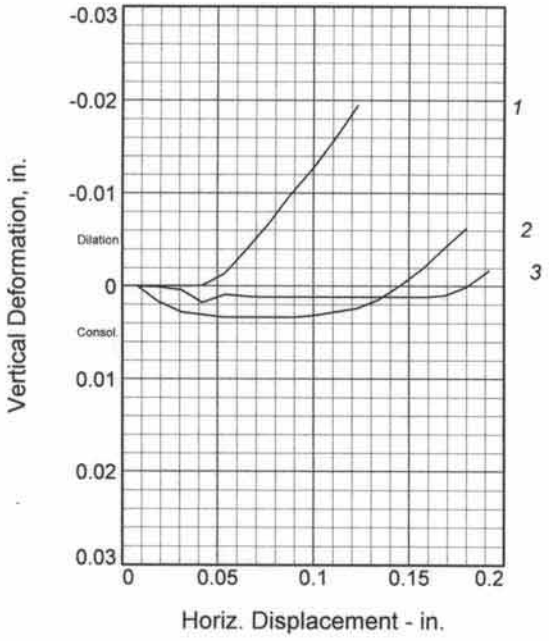

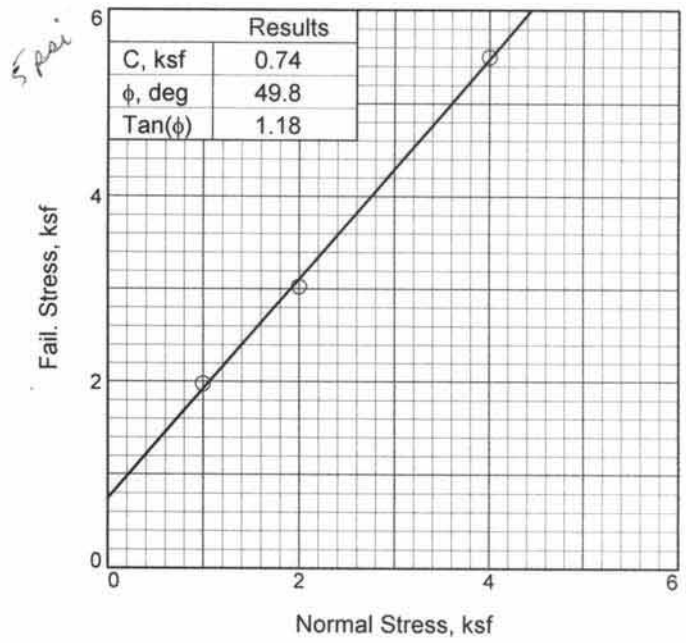

Results	
C, ksf	0.74
ϕ, deg	49.8
Tan(ϕ)	1.18

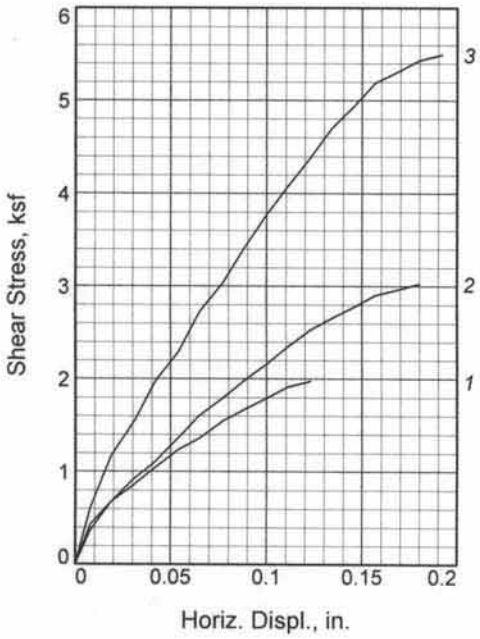

Sample No.		1	2	3
Initial	Water Content, %	14.9	14.7	13.3
	Dry Density, pcf	123.4	120.7	124.7
	Saturation, %	96.2	88.3	88.9
	Void Ratio	0.4418	0.4737	0.4269
	Diameter, in.	2.38	2.38	2.38
	Height, in.	1.00	1.00	1.00
At Test	Water Content, %	14.9	14.7	13.3
	Dry Density, pcf	123.4	120.7	124.7
	Saturation, %	96.2	88.7	88.9
	Void Ratio	0.4418	0.4737	0.4269
	Diameter, in.	2.38	2.38	2.38
	Height, in.	1.00	1.00	1.00
Normal Stress, ksf		1.00	2.00	4.00
Fail. Stress, ksf		1.98	3.03	5.50
Displacement, in.		0.12	0.18	0.19
Ult. Stress, ksf				
Displacement, in.				
Strain at peak, %		5.2	7.6	8.1

Sample Type: Bag Sample Remolded into a 2.5" X 6

Description: CLAYEY SAND

light yellowish brown, medium Grade, Cohesive,

LL= N/A **PL=** **PI=** N/A

Assumed Specific Gravity= 2.85

Remarks: Test Date: 08/30/04

Client: Engineering Mechanics Corp. of Columbus

Project: Geotechnical Engineering & Testing Services
Axial Crack in Gas Pipeline Research Project

Location: Bottom or Clay Test Pit

Sample Number: 5613 **Depth:** 3-4'

Proj. No.: 10884 **Date:** 08/23/04

DIRECT SHEAR TEST REPORT

SOILS ENGINEERING, INC.

Figure E-2

Tested By: BC **Checked By:** JW

DIRECT SHEAR TEST

9/27/2004

Date: 08/23/04
Client: Engineering Mechanics Corp. of Columbus
Project: Geotechnical Engineering & Testing Services
Axial Crack in Gas Pipeline Research Project
Location: Bottom or Clay Test Pit
Depth: 3-4' **Sample Number:** 5613
Description: CLAYEY SAND
light yellowish brown, medium Grade, Cohesive, non-plastic
Remarks: Test Date: 08/30/04
Type of Sample: Bag Sample Remolded into a 2.5" X 6" TUBE
Assumed Specific Gravity=2.85 **LL=**N/A **PL=** **PI=**N/A

Parameters for Specimen No. 1

Specimen Parameter	Initial	Consolidated	Final
Moisture content: Moist soil+tare, gms.			218.900
Moisture content: Dry soil+tare, gms.			197.500
Moisture content: Tare, gms.			54.000
Moisture, %	14.9	14.9	14.9
Moist specimen weight, gms.	164.9		
Diameter, in.	2.38	2.38	
Area, in.²	4.43	4.43	
Height, in.	1.00	1.00	
Net decrease in height, in.		0.00	
Wet Density, pcf	141.8	141.8	
Dry density, pcf	123.4	123.4	
Void ratio	0.4418	0.4418	
Saturation, %	96.2	96.2	

Test Readings for Specimen No. 1

Primary load ring constant = 1.9 lbs. per input unit
Secondary load ring constant = 1.9 lbs. per input unit
Crossover reading for secondary load ring = 1.9 input units
Normal stress = 1 ksf
Strain at peak, % = 5.2
Fail. Stress = 1.98 ksf **at reading no.** 11

No.	Horizontal Def. Dial in.	Load Dial	Load lbs.	Shear Stress ksf	Vertical Def. Dial in.
0	0.0000	0.00	0.0	0.00	0.0359
1	0.0080	7.00	13.3	0.43	0.0359
2	0.0190	11.00	20.9	0.68	0.0359
3	0.0310	14.00	26.6	0.86	0.0359
4	0.0420	17.00	32.3	1.05	0.0360
5	0.0540	20.00	38.0	1.24	0.0373
6	0.0650	22.00	41.8	1.36	0.0398
7	0.0770	25.00	47.5	1.54	0.0427
8	0.0880	27.00	51.3	1.67	0.0457
9	0.1000	29.00	55.1	1.79	0.0486
10	0.1110	31.00	58.9	1.91	0.0517

SOILS ENGINEERING, INC.

Test Readings for Specimen No. 1

No.	Horizontal Def. Dial in.	Load Dial	Load lbs.	Shear Stress ksf	Vertical Def. Dial in.
11	0.1230	32.00	60.8	1.98	0.0553

Parameters for Specimen No. 2

Specimen Parameter	Initial	Consolidated	Final
Moisture content: Moist soil+tare, gms.			193.600
Moisture content: Dry soil+tare, gms.			172.900
Moisture content: Tare, gms.			32.500
Moisture, %	14.7	14.7	14.7
Moist specimen weight, gms.	161.0		
Diameter, in.	2.38	2.38	
Area, in.²	4.43	4.43	
Height, in.	1.00	1.00	
Net decrease in height, in.		0.00	
Wet Density, pcf	138.4	138.5	
Dry density, pcf	120.7	120.7	
Void ratio	0.4737	0.4737	
Saturation, %	88.3	88.7	

Test Readings for Specimen No. 2

Primary load ring constant = 1.9 lbs. per input unit

Secondary load ring constant = 1.9 lbs. per input unit

Crossover reading for secondary load ring = 1.9 input units

Normal stress = 2 ksf

Strain at peak, % = 7.6

Fail. Stress = 3.03 ksf **at reading no.** 16

No.	Horizontal Def. Dial in.	Load Dial	Load lbs.	Shear Stress ksf	Vertical Def. Dial in.
0	0.0000	0.00	0.0	0.00	0.0338
1	0.0080	6.00	11.4	0.37	0.0338
2	0.0190	11.00	20.9	0.68	0.0321
3	0.0310	15.00	28.5	0.93	0.0310
4	0.0420	18.00	34.2	1.11	0.0307
5	0.0540	22.00	41.8	1.36	0.0304
6	0.0650	26.00	49.4	1.61	0.0304
7	0.0770	29.00	55.1	1.79	0.0304
8	0.0880	32.00	60.8	1.98	0.0304
9	0.1000	35.00	66.5	2.16	0.0306
10	0.1110	38.00	72.2	2.35	0.0310
11	0.1230	41.00	77.9	2.53	0.0314
12	0.1340	43.00	81.7	2.66	0.0323
13	0.1460	45.00	85.5	2.78	0.0340
14	0.1570	47.00	89.3	2.90	0.0357
15	0.1690	48.00	91.2	2.96	0.0380
16	0.1800	49.00	93.1	3.03	0.0400

Parameters for Specimen No. 3

Specimen Parameter	Initial	Consolidated	Final
Moisture content: Moist soil+tare, gms.			198.000
Moisture content: Dry soil+tare, gms.			178.700
Moisture content: Tare, gms.			33.700
Moisture, %	13.3	13.3	13.3
Moist specimen weight, gms.	164.3		
Diameter, in.	2.38	2.38	
Area, in.^{2}	4.43	4.43	
Height, in.	1.00	1.00	
Net decrease in height, in.		0.00	
Wet Density, pcf	141.3	141.3	
Dry density, pcf	124.7	124.7	
Void ratio	0.4269	0.4269	
Saturation, %	88.9	88.9	

Test Readings for Specimen No. 3

Primary load ring constant = 1.9 lbs. per input unit
Secondary load ring constant = 1.9 lbs. per input unit
Crossover reading for secondary load ring = 1.9 input units
Normal stress = 4 ksf
Strain at peak, % = 8.1
Fail. Stress = 5.50 ksf **at reading no.** 17

No.	Horizontal Def. Dial in.	Load Dial	Load lbs.	Shear Stress ksf	Vertical Def. Dial in.
0	0.0000	0.00	0.0	0.00	0.0364
1	0.0080	10.00	19.0	0.62	0.0364
2	0.0190	19.00	36.1	1.17	0.0363
3	0.0310	25.00	47.5	1.54	0.0360
4	0.0420	32.00	60.8	1.98	0.0346
5	0.0540	37.00	70.3	2.29	0.0355
6	0.0650	44.00	83.6	2.72	0.0353
7	0.0770	49.00	93.1	3.03	0.0352
8	0.0880	55.00	104.5	3.40	0.0352
9	0.1000	61.00	115.9	3.77	0.0352
10	0.1110	66.00	125.4	4.08	0.0352
11	0.1230	71.00	134.9	4.38	0.0352
12	0.1340	76.00	144.4	4.69	0.0352
13	0.1460	80.00	152.0	4.94	0.0352
14	0.1570	84.00	159.6	5.19	0.0352
15	0.1690	86.00	163.4	5.31	0.0354
16	0.1800	88.00	167.2	5.43	0.0363
17	0.1920	89.00	169.1	5.50	0.0381

SOILS ENGINEERING, INC.

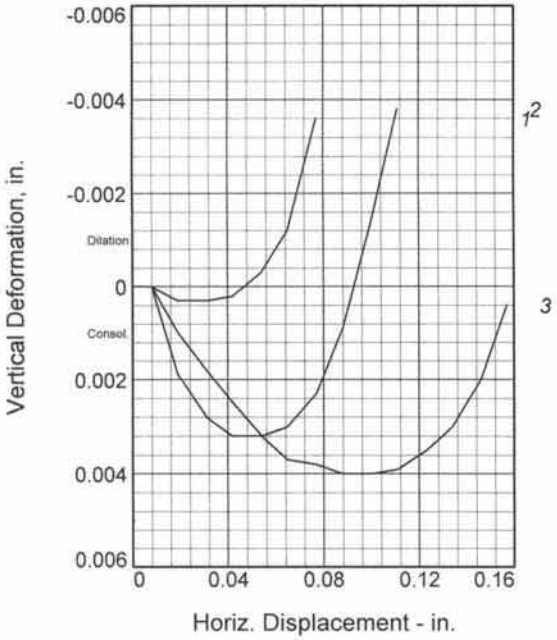

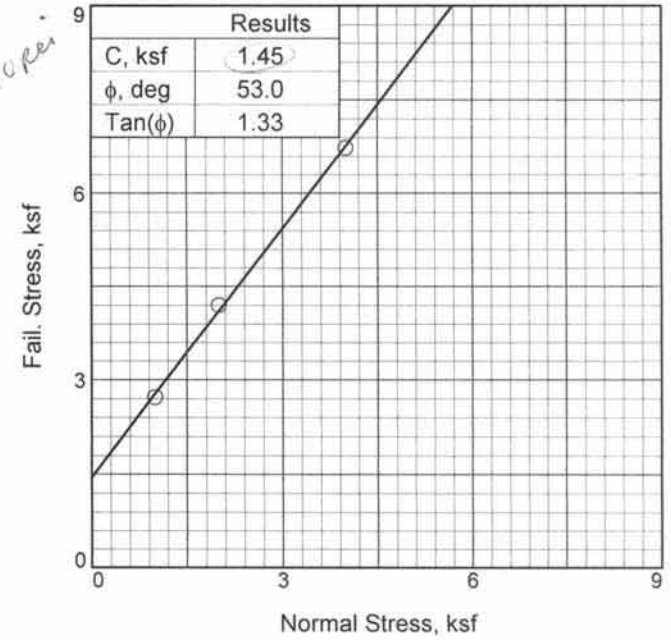

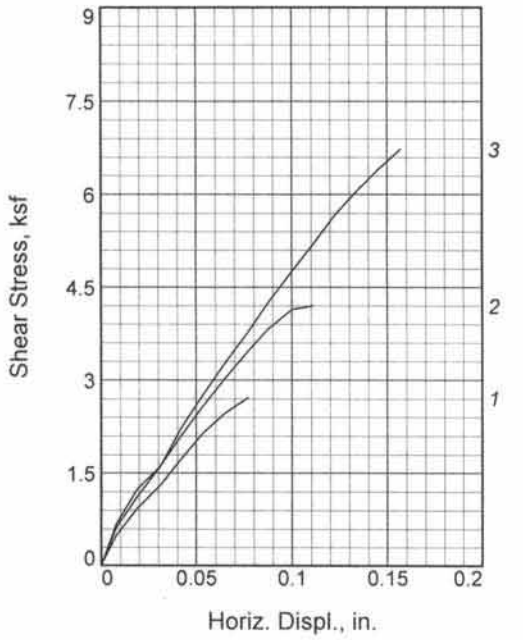

Sample No.		1	2	3
Initial	Water Content, %	8.0	8.0	8.0
	Dry Density, pcf	110.2	109.0	113.0
	Saturation, %	42.5	40.7	45.6
	Void Ratio	0.5018	0.5184	0.4641
	Diameter, in.	2.38	2.38	2.38
	Height, in.	1.00	1.00	1.00
At Test	Water Content, %	8.0	8.0	8.0
	Dry Density, pcf	110.2	109.0	113.0
	Saturation, %	42.5	40.7	45.6
	Void Ratio	0.5018	0.5184	0.4641
	Diameter, in.	2.38	2.38	2.38
	Height, in.	1.00	1.00	1.00
Normal Stress, ksf		1.00	2.00	4.00
Fail. Stress, ksf		2.72	4.20	6.73
Displacement, in.		0.08	0.11	0.16
Ult. Stress, ksf				
Displacement, in.				
Strain at peak, %		3.2	4.7	6.6

Sample Type: Remolded / Unsaturated
Description: SILTY SAND; dark olive brown, fine to med grade, med plasticity / Shear # 1 8% mc
LL= N/A **PL=** **PI=** N/A
Assumed Specific Gravity= 2.65
Remarks: Test Date: 11/08/05
Sample was remolded @ 8% moisture into a 2.5" x 6" tube. Then the sample was extracted into a 1" x 2.375" ring.
Figure C-3

Client: ENGINEERING MECHANICS CORP. OF COLUMBUS
Project: GAS PIPELINE CRACK ARREST RESEARCH
Location: Onsite Subsurface Deposit for Pit # 3
Sample Number: 11782 **Depth:** Random
Proj. No.: 11418 **Date:**

DIRECT SHEAR TEST REPORT

SOILS ENGINEERING, INC.

Tested By: PS **Checked By:** JW

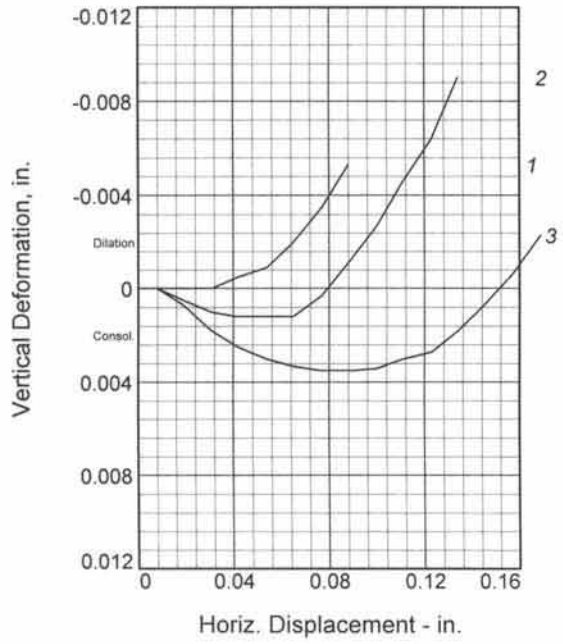

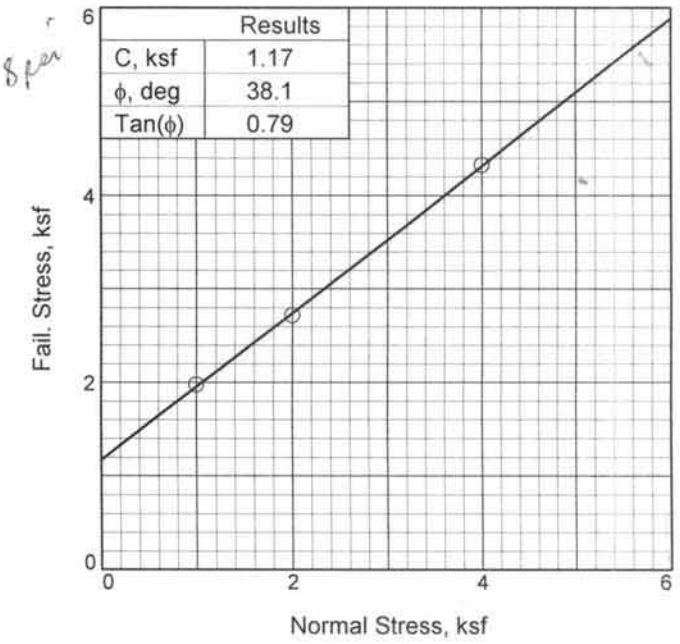

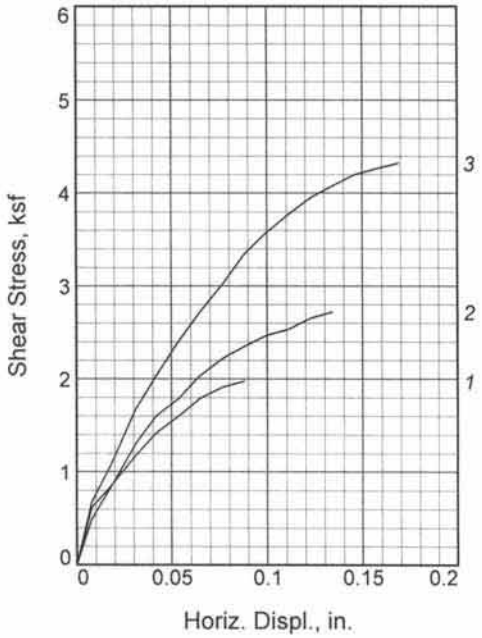

Sample No.		1	2	3
Initial	Water Content, %	13.3	13.3	13.3
	Dry Density, pcf	113.5	112.3	112.8
	Saturation, %	76.8	74.6	75.4
	Void Ratio	0.4574	0.4731	0.4663
	Diameter, in.	2.38	2.38	2.38
	Height, in.	1.00	1.00	1.00
At Test	Water Content, %	13.3	13.3	13.3
	Dry Density, pcf	113.5	112.3	112.8
	Saturation, %	76.8	74.6	75.4
	Void Ratio	0.4574	0.4731	0.4663
	Diameter, in.	2.38	2.38	2.38
	Height, in.	1.00	1.00	1.00
Normal Stress, ksf		1.00	2.00	4.00
Fail. Stress, ksf		1.98	2.72	4.32
Displacement, in.		0.09	0.13	0.17
Ult. Stress, ksf				
Displacement, in.				
Strain at peak, %		3.7	5.6	7.1

Sample Type: Remolded / Unsaturated
Description: SILTY SAND; dark olive brown, fine to med grade, med plasticity / Shear # 2 13.3% mc
LL= N/A **PL=** **PI=** N/A
Assumed Specific Gravity= 2.65
Remarks: Test Date: 11/08/05
Sample was remolded @ 13.3% moisture into a 2.5" x 6" tube. Then the sample was extracted into a 1" x 2.375" ring.
Figure C-4

Client: ENGINEERING MECHANICS CORP. OF COLUMBUS
Project: GAS PIPELINE CRACK ARREST RESEARCH
Location: Onsite Subsurface Deposit for Pit # 3
Sample Number: 11782 **Depth:** Random
Proj. No.: 11418 **Date:**

DIRECT SHEAR TEST REPORT

SOILS ENGINEERING, INC.

Tested By: PS **Checked By:** JW

Mojave Clay

Grain Size Distribution Report

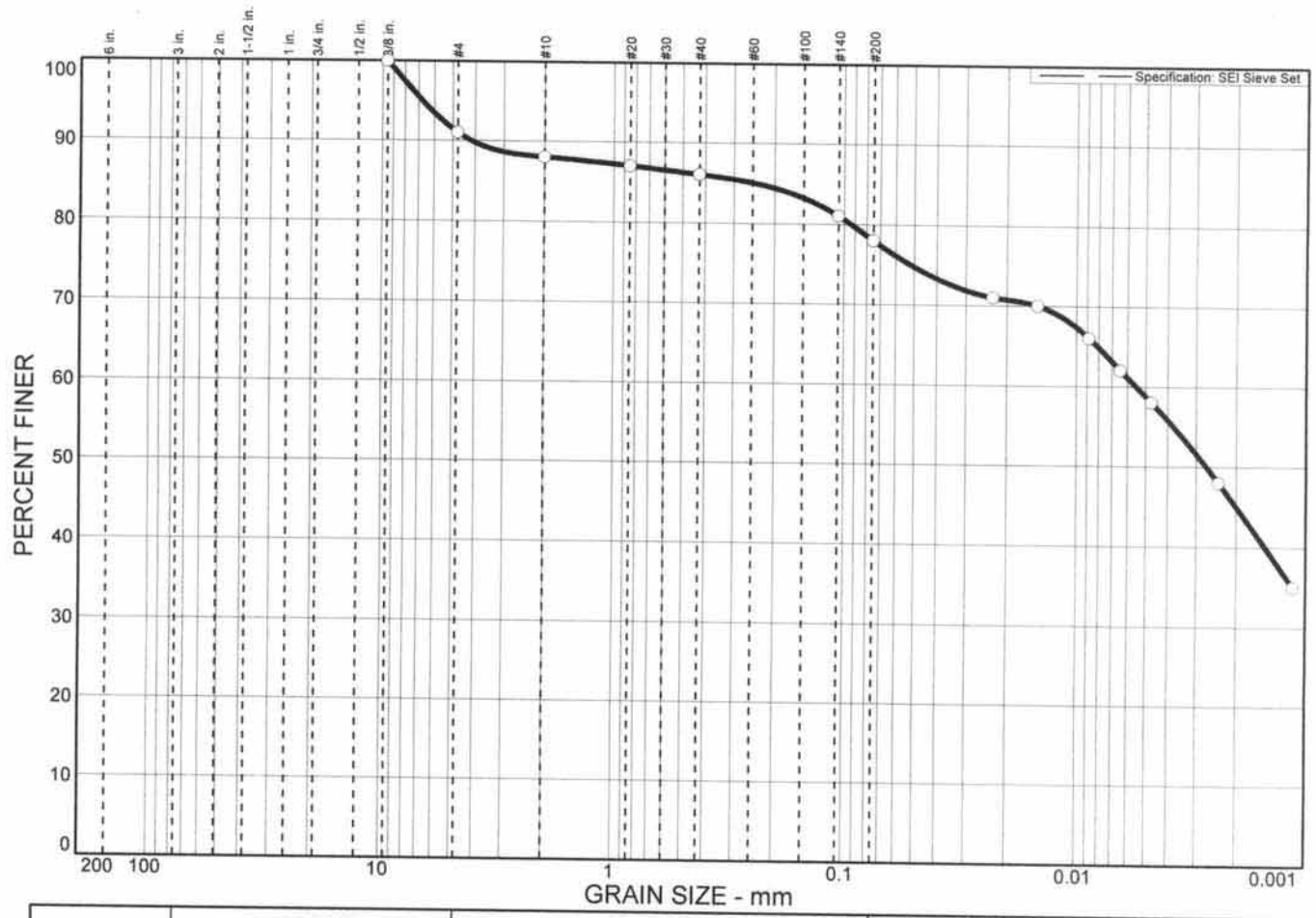

	% + 3"	% GRAVEL		% SAND			% FINES	
		CRS.	FINE	CRS.	MEDIUM	FINE	SILT	CLAY
○	0	0	9	3	2	8	19	59

SOIL DATA

SYMBOL	SOURCE	SAMPLE NO.	DEPTH (ft.)	DESCRIPTION	USCS
○		5593	Random	CLAY; greenish gray; fine grade, highly plastic	CH

Grain Size Distribution Report

SOILS ENGINEERING, INC.

Client: Engineering Mechanics Corp. of Columbus

Project: Geotechnical Engineering & Testing Services
Axial Crack in Gas Pipeline Research Project

Project No.: 10884

Figure A-1

GRAIN SIZE DISTRIBUTION TEST DATA

Client: Engineering Mechanics Corp. of Columbus
Project: Geotechnical Engineering & Testing Services
Axial Crack in Gas Pipeline Research Project
Project Number: 10884

Sample Data

Source:
Sample No.: 5593
Elev. or Depth: Random **Sample Length(in./cm.):**
Location: Ridgecrest - Boydston Construction
Description: CLAY; greenish gray; fine grade, highly plastic
USCS: CH

Mechanical Analysis Data

	Initial	After wash
Dry sample and tare=	850.30	288.90
Tare =	123.20	123.20
Dry sample weight =	727.10	165.70

Minus #200 from wash= 77 %
Tare for cumulative weight retained= 123.20

Sieve	Cumul. Wt. retained	Percent finer	Specification Limits, percent	Deviation, percent
.375 inch	123.20	100	0 to 0	+ 100
# 4	190.80	91	0 to 0	+ 91
# 10	211.10	88	0 to 0	+ 88
# 20	219.70	87	0 to 0	+ 87
# 40	222.70	86	0 to 0	+ 86
# 140	259.20	81	0 to 0	+ 81
# 200	284.10	78	0 to 0	+ 78

Hydrometer Analysis Data

Separation sieve is #10
Percent -#10 based upon complete sample= 88
Weight of hydrometer sample: 70.0
Calculated biased weight= 79.55
Table of composite correction values:

Temp, deg C:	23.0	27.0
Comp. corr:	-4.0	-3.0

Meniscus correction only=
Specific gravity of solids= 2.70
Specific gravity correction factor= 0.989
Hydrometer type: 152H
Effective depth L= 16.294964 - 0.164 x Rm

Elapsed time, min	Temp, deg C	Actual reading	Corrected reading	K	Rm	Eff. depth	Diameter mm	Percent finer
0.10	23.0	62.0	58.0	0.0130	62.0	6.1	0.1014	72
2.00	23.0	61.0	57.0	0.0130	61.0	6.3	0.0230	71
5.00	23.0	60.0	56.0	0.0130	60.0	6.5	0.0147	70
15.00	23.0	57.0	53.0	0.0130	57.0	6.9	0.0088	66
30.00	23.0	54.0	50.0	0.0130	54.0	7.4	0.0065	62
60.00	23.0	51.0	47.0	0.0130	51.0	7.9	0.0047	58

Elapsed time, min	Temp, deg C	Actual reading	Corrected reading	K	Rm	Eff. depth	Diameter mm	Percent finer
250.00	27.0	42.0	39.0	0.0124	42.0	9.4	0.0024	48
1440.00	23.0	32.0	28.0	0.0130	32.0	11.0	0.0011	35

Fractional Components

Gravel/Sand based on #4
Sand/Fines based on #200
% + 3" = **% GRAVEL =** 9 **(% coarse =** **% fine =** 9)
% SAND = 13 **(% coarse =** 3 **% medium =** 2 **% fine =** 8)
% SILT = 19 **% CLAY =** 59

D_{85}= 0.25 D_{60}= 0.01 D_{50}= 0.00

Maximum Density - Optimum Moisture Test Report

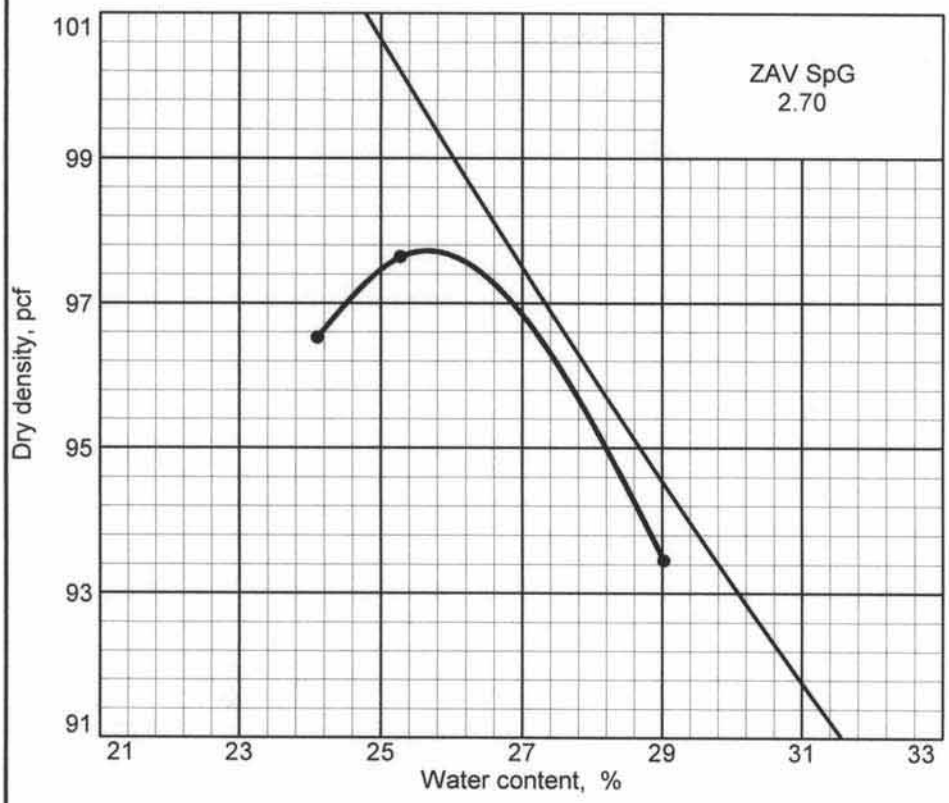

Curve No.
01

Test Specification:
ASTM D 1557-00 Method A Modified

Hammer Wt.: 10 lb.
Hammer Drop: 18 in.
Number of Layers: five
Blows per Layer: 25
Mold Size: .03333 cu.ft.

Test Performed on Material Passing No.4 **Sieve**

Soil Data

NM	N/A	**Sp.G.**	2.65
LL	72	**PI**	46
%>No.4	9	**%<#200**	78
USCS	CH	**AASHTO**	N/A

TESTING DATA

	1	2	3	4	5	6
WM + WS	3798.0	3821.2	4079.3			
WM	1987.0	1972.0	2256.4			
WW + T #1	420.30	415.10	474.70			
WD + T #1	377.90	372.00	413.20			
TARE #1	202.00	201.50	201.30			
WW + T #2						
WD + T #2						
TARE #2						
MOISTURE	24.1	25.3	29.0			
DRY DENSITY	96.5	97.6	93.5			

TEST RESULTS

Maximum dry density = 97.7 pcf

Optimum moisture = 25.6 %

Material Description

CLAY; greenish gray; fine grade, highly plastic

Project No. 10884 **Client:** Engineering Mechanics Corp. of Columbus
Project: Geotechnical Engineering & Testing Services
Axial Crack in Gas Pipeline Research Project
• **Location:** Ridgecrest - Boydston Construction

Maximum Density - Optimum Moisture Test Report

SOILS ENGINEERING, INC.

Remarks:
Tested By: BF
Test Date: 08/16/04
Sample # 5593

Figure C-1

MOISTURE DENSITY TEST DATA

Client: Engineering Mechanics Corp. of Columbus
Project: Geotechnical Engineering & Testing Services
Axial Crack in Gas Pipeline Research Project
Project Number: 10884

Specimen Data

Source:
Sample No.: 5593
Elev. or Depth: Random **Sample Length(in./cm.):**
Location: Ridgecrest - Boydston Construction
Description: CLAY; greenish gray; fine grade, highly plastic
USCS Classification: CH **AASHTO Classification:** N/A
Natural Moisture: N/A **Liquid Limit:** 72 **Plasticity Index:** 46
Testing Remarks: Tested By: BF
Test Date: 08/16/04
Sample # 5593
Percent retained on No.4 sieve: 9
Percent passing No. 200 sieve: 78 **Specific gravity:** 2.65

Test Data And Results For Curve 01

Type of test: ASTM D 1557-00 Method A Modified
Mold Dia.: 4.00 in. **Hammer Wt.:** 10 lb. **Drop:** 18 in.
Layers: five **Blows per Layer:** 25

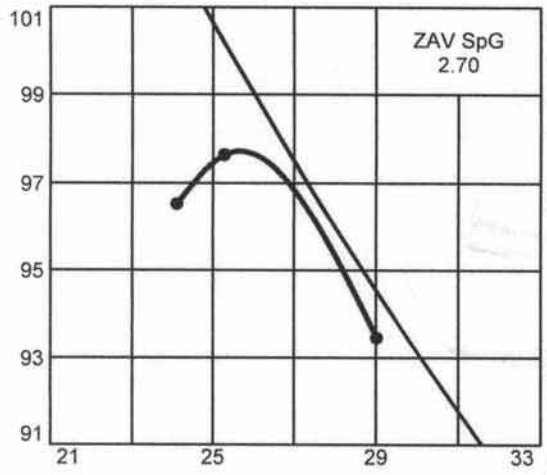

POINT NO.	1	2	3
WM + WS	3798.0	3821.2	4079.3
WM	1987.0	1972.0	2256.4
WW+T	420.30	415.10	474.70
WD+T	377.90	372.00	413.20
TARE	202.00	201.50	201.30
MOIST	24.1	25.3	29.0
MOISTURE	24.1	25.3	29.0
DRY DEN	96.5	97.6	93.5

Max dry den= 97.7 pcf **Opt moisture=** 25.6 %

Oversize Correction Not Applied

CONSOLIDATION TEST REPORT

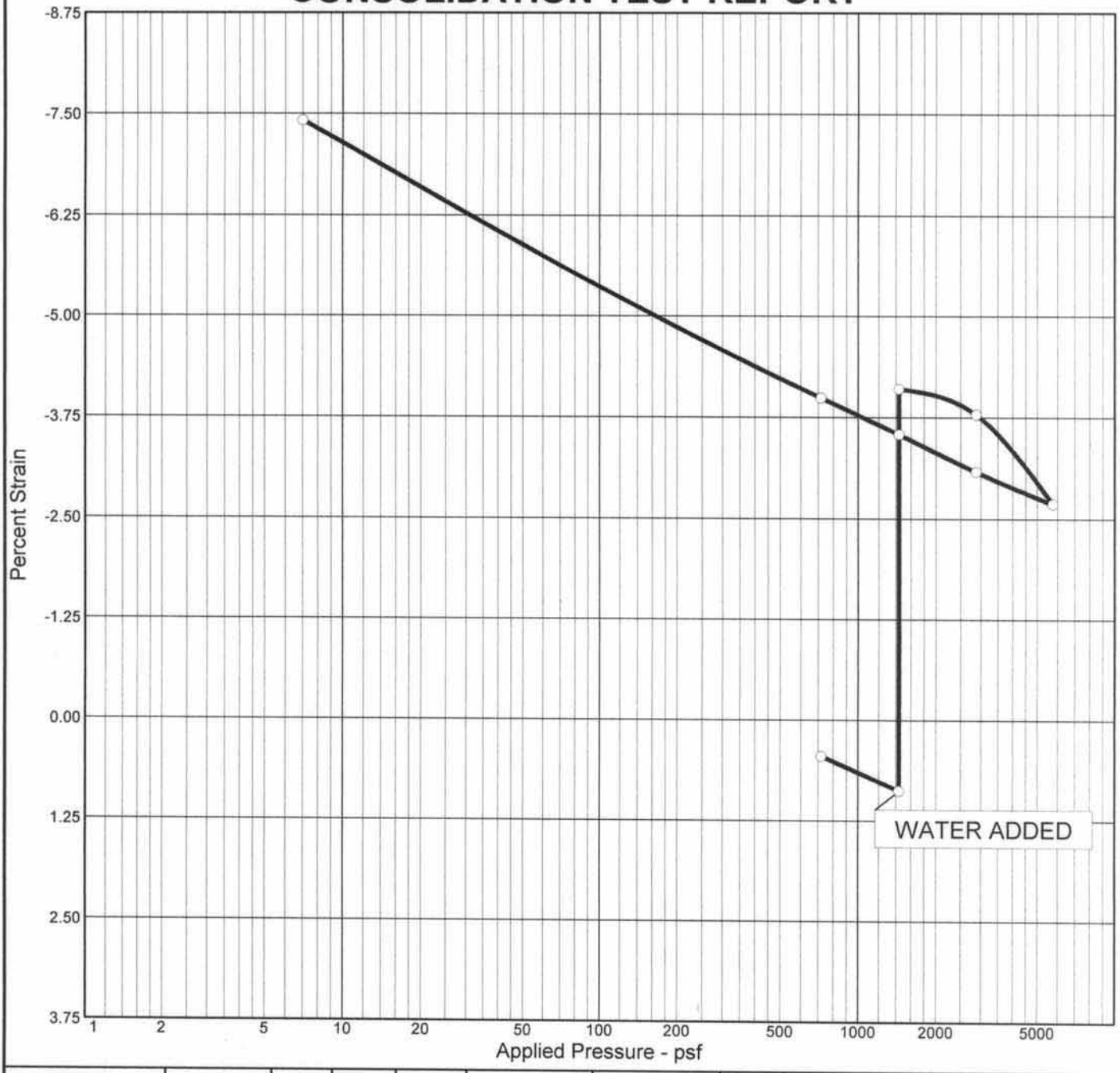

Natural		Dry Dens.	LL	PI	Sp.	Overburden	P_c	C_c	C_s	Swell Press.	Swell	e_o
Sat.	Moist.	(pcf)			Gr.	(psf)	(psf)			(psf)	%	
74.8 %	22.0 %	92.9	72	46	2.65	336	3060	0.07	0.03			0.781

MATERIAL DESCRIPTION	USCS	AASHTO
CLAY; greenish gray; fine grade, highly plastic	CH	N/A

Project No. 10884 **Client:** Engineering Mechanics Corp. of Columbus

Project: Geotechnical Engineering & Testing Services
Axial Crack in Gas Pipeline Research Project

Location: Ridgecrest - Boydston Construction

CONSOLIDATION TEST REPORT

SOILS ENGINEERING, INC.

Remarks:
Tested By: AL
Test Date: 08/16/04
Sample # 5593

Figure B-1

LIQUID AND PLASTIC LIMITS TEST REPORT

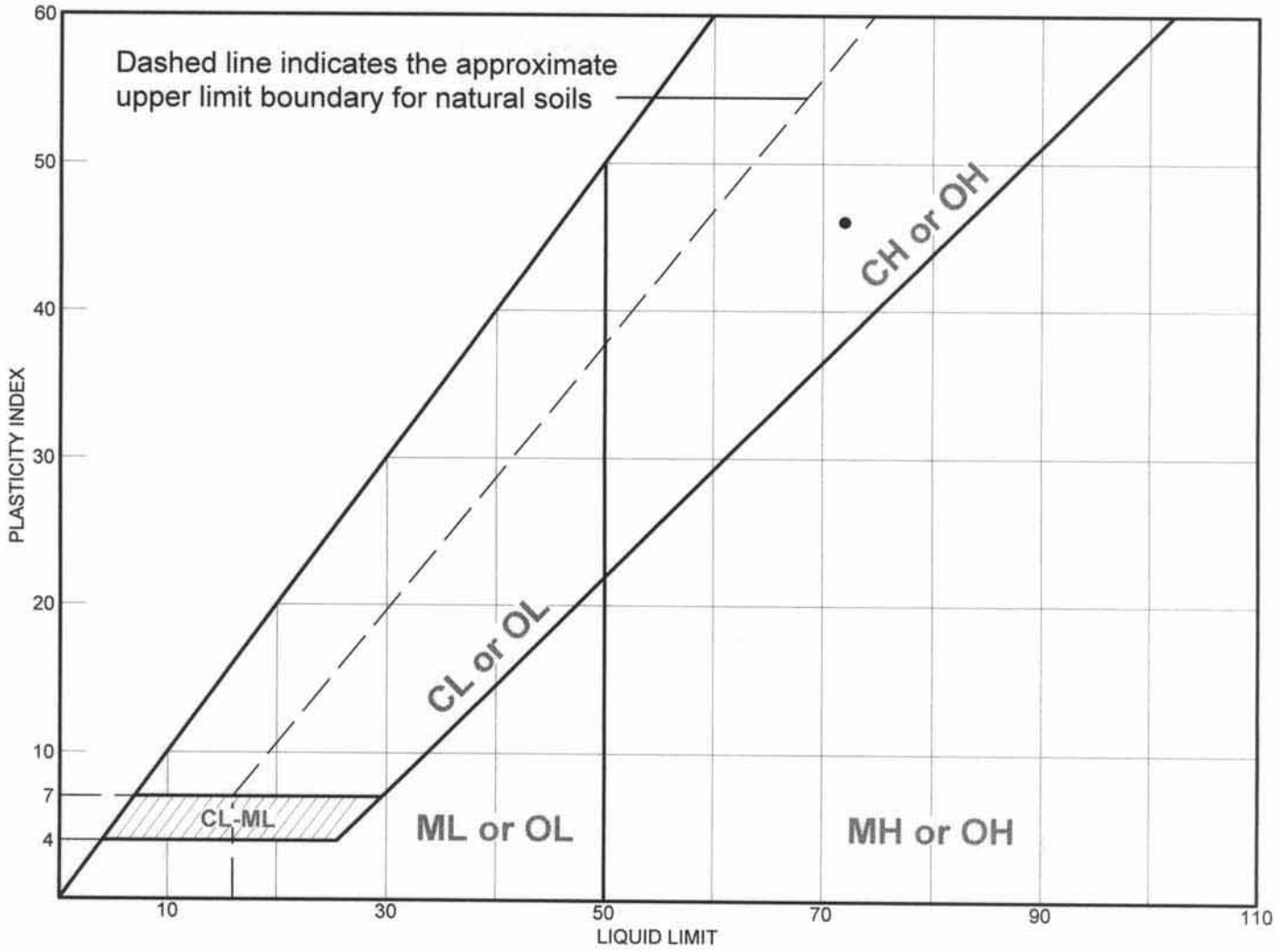

	MATERIAL DESCRIPTION	LL	PL	PI	%<#40	%<#200	USCS
●	CLAY; greenish gray; fine grade, highly plastic	72	26	46	86	78	CH

Project No. 10884 **Client:** Engineering Mechanics Corp. of Columbus

Project: Geotechnical Engineering & Testing Services

Axial Crack in Gas Pipeline Research Project

● **Location:** Ridgecrest - Boydston Construction

Remarks:

● Tested By: JW
Test Date: 08/17/04
Sample # 5593

LIQUID AND PLASTIC LIMITS TEST REPORT

SOILS ENGINEERING, INC.

Figure D-1

GEOTECHNICAL ENGINEERING & TESTING
Engineering Mechanics Corp. of Columbus
Axial Crack Arrest in Gas Pipeline Research
Mojave, CA

File No. 04-10884
September 27, 2004

TABLE 1

EXPANSION INDEX DATA

Sample No.	Sampling Location	Depth	% Expansion	Moisture Content % of dry wt.		Expansion Index
				Before Test	After Test	
5593	Boydston Construction	stockpile	16.0	21.0	45.3	160
5613	Bottom or Clay Test Pit	3 - 4'	3.5	8.5	17.8	35

TABLE 18A-I-B – CLASSIFICATION OF EXPANSIVE SOIL	
Expansion Index	Potential Expansion
0-20	Very Low
21-50	Low
51-90	Medium
91-130	High
Above 130	Very High

AXIAL CRACK ARREST IN GAS PIPELINE RESEARCH

ENGINEERING MECHANICS CORP OF COLUMBUS

File No. 04-10884
JANUARY 24, 2006

UNCONFINED COMPRESSION TEST

SEI

Test Location	Sample #	D_o (in inches)	L_o (in inches)	A_o	Delta/L (in inches)	Unit Strain	Load (in lbs)	Corr. Area	Stress	$Q_u/2$ (in psi)
Sample 1	5593	2.375	4	4.430	0.25	0.063	425	4.725	89.938	44.969
Sample 3 bottom or clay test pit	5613	2.375	3.5	4.430	0.25	0.071	350	4.771	73.361	36.681

$$\text{Unit Strain} = \frac{\text{Delta/L}}{L_o} \qquad \text{Corrected Area} = \frac{\text{Ao}}{1 - \text{Unit Strain}} \qquad \text{Stress} = \frac{\text{Load}}{\text{Corr. Area}}$$

D_O = Initial Diameter
L_o = Initial Height
Ao = Initial Area
Delta/L = Height Change
Q_u2 = Cohesion

.74 kip/ft² = ft²/144 in²

5.14 psi
10.07 psi
8.15 psi

1.4% Moisture
C = 0.74 ksf – Aug 23/2004
8% 1.45 ksf – 11/8/05
13% 1.17 ksf – 11/8/05

Figure D-1

Appendix C
JGA Soil Testing Details

Case 1 – November 2004

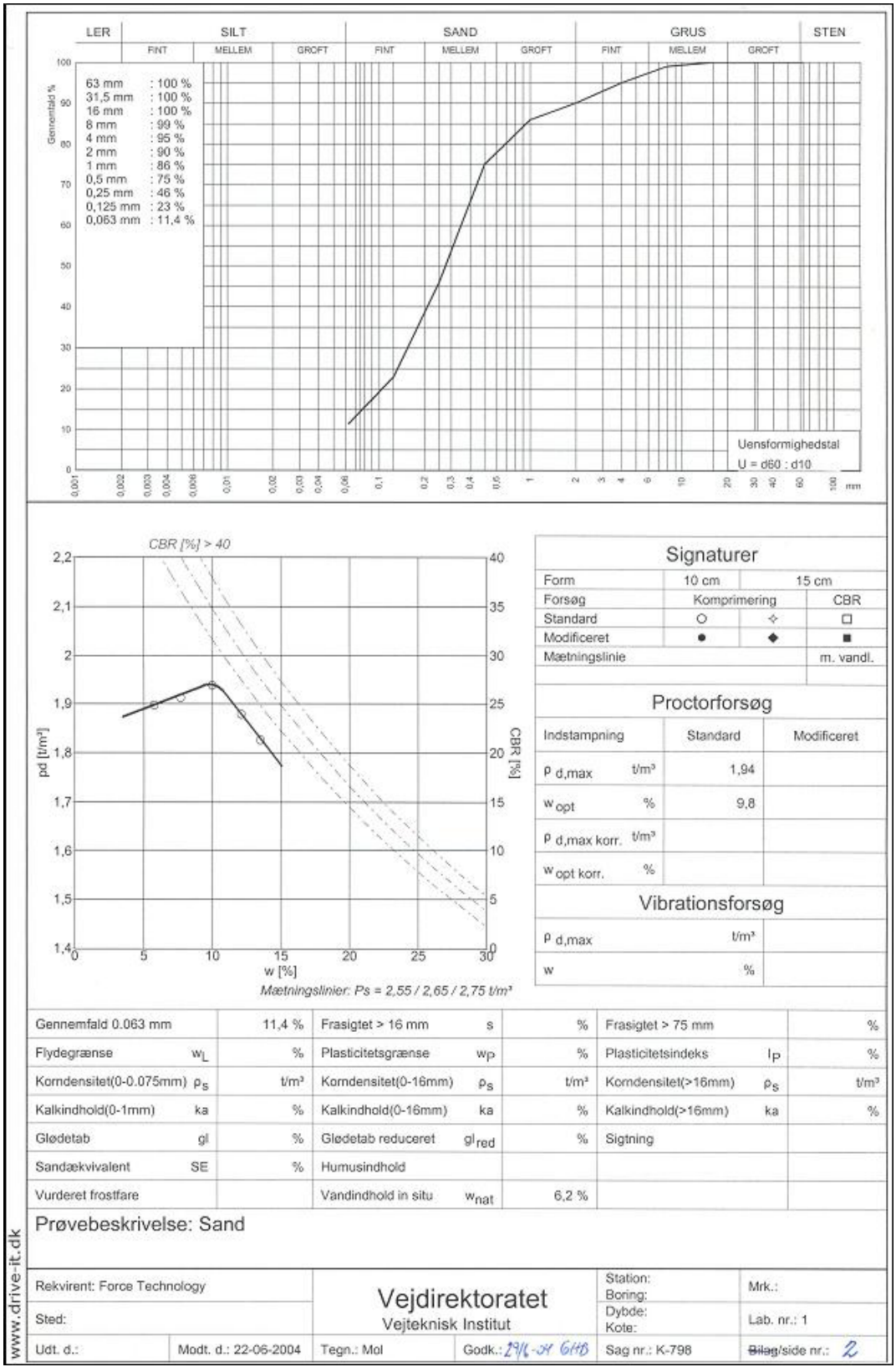

Figure 1 November 2004 soil characterization

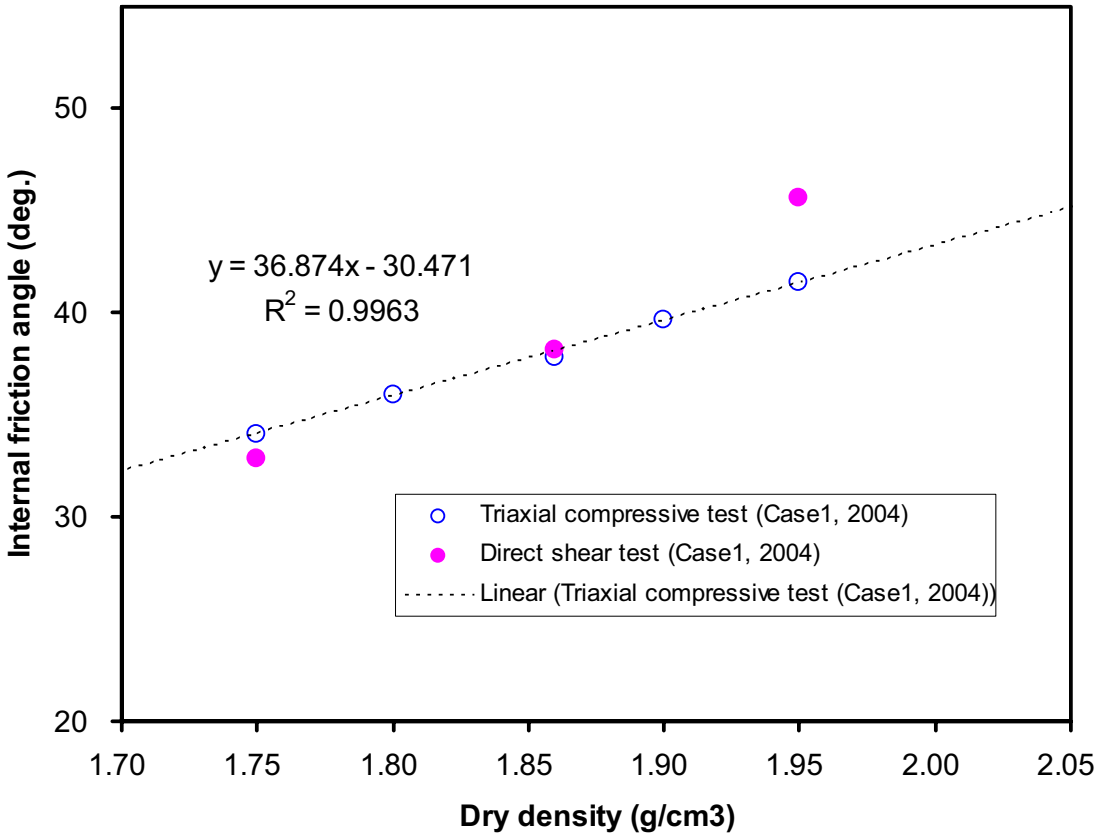

Figure 2 Direct shear and triaxial tests for JGA sands from November 2004

Case 3 – October 2005

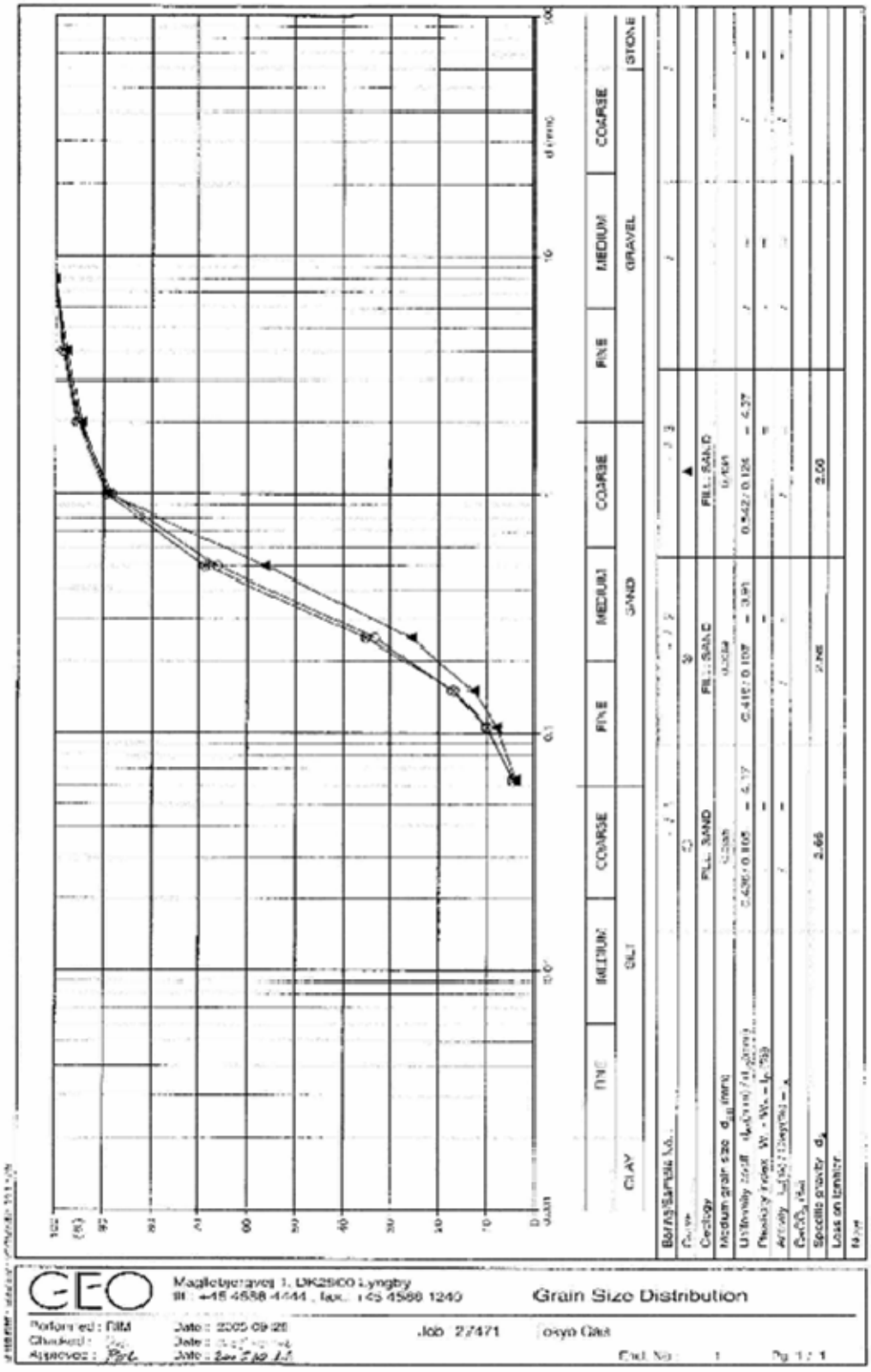

Figure 3 Grain size for October 2005 sand

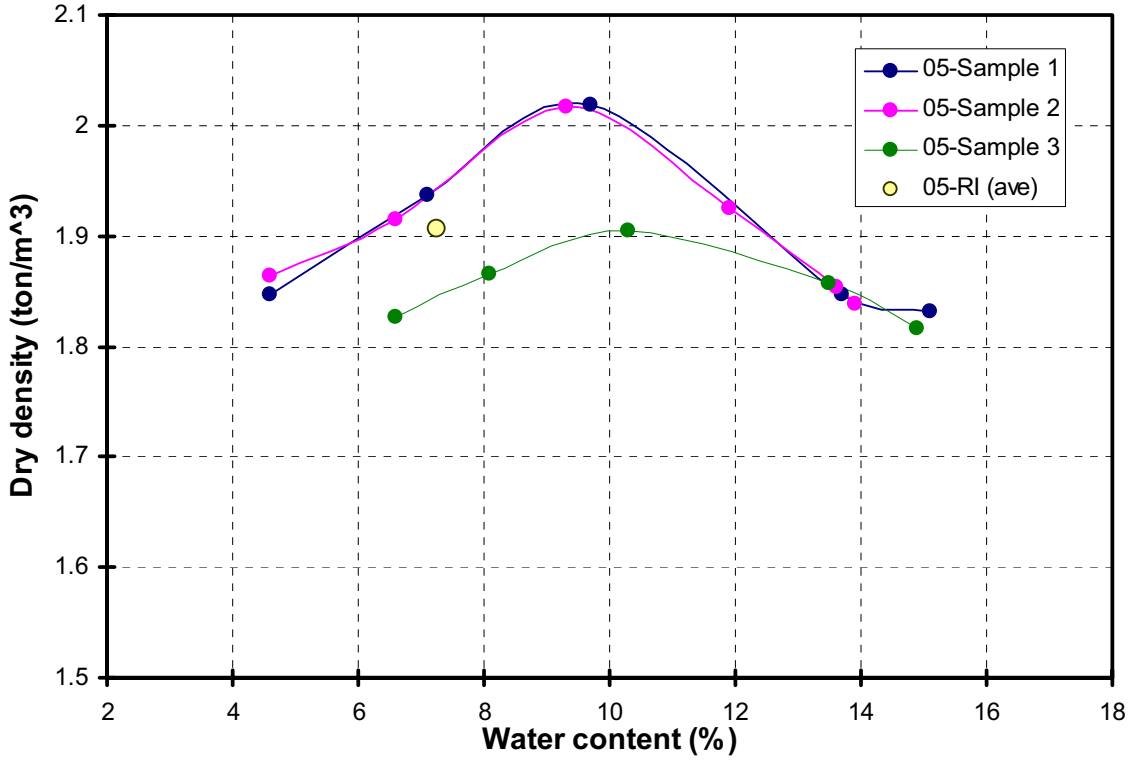

Figure 4 Optimum moisture for October 2005 sand

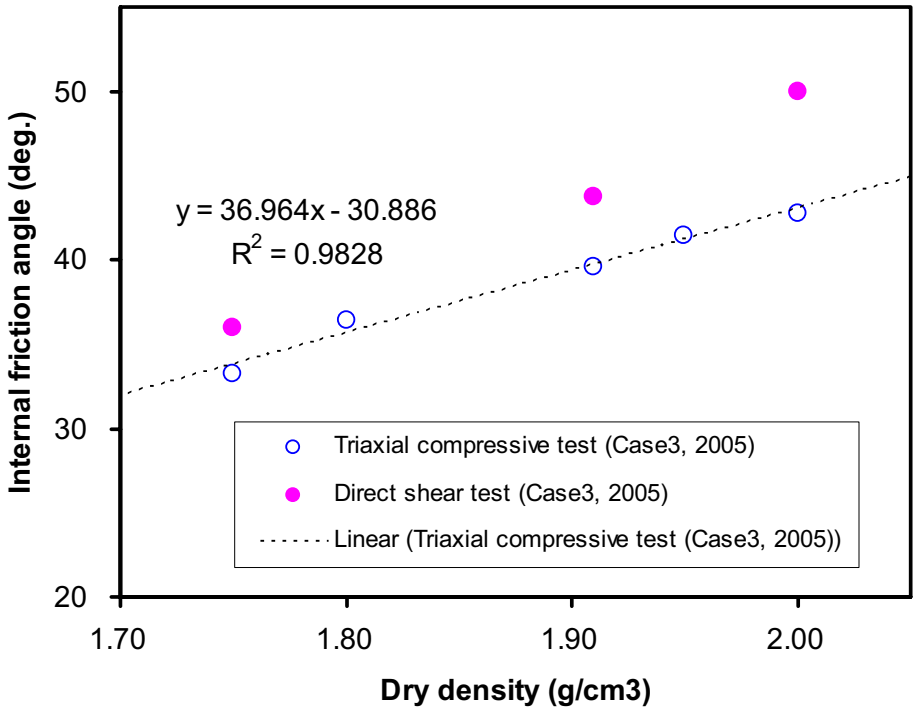

Figure 5 Direct shear and triaxial tests fro October 2005 sand

Case 4 – June 2006 Experiment

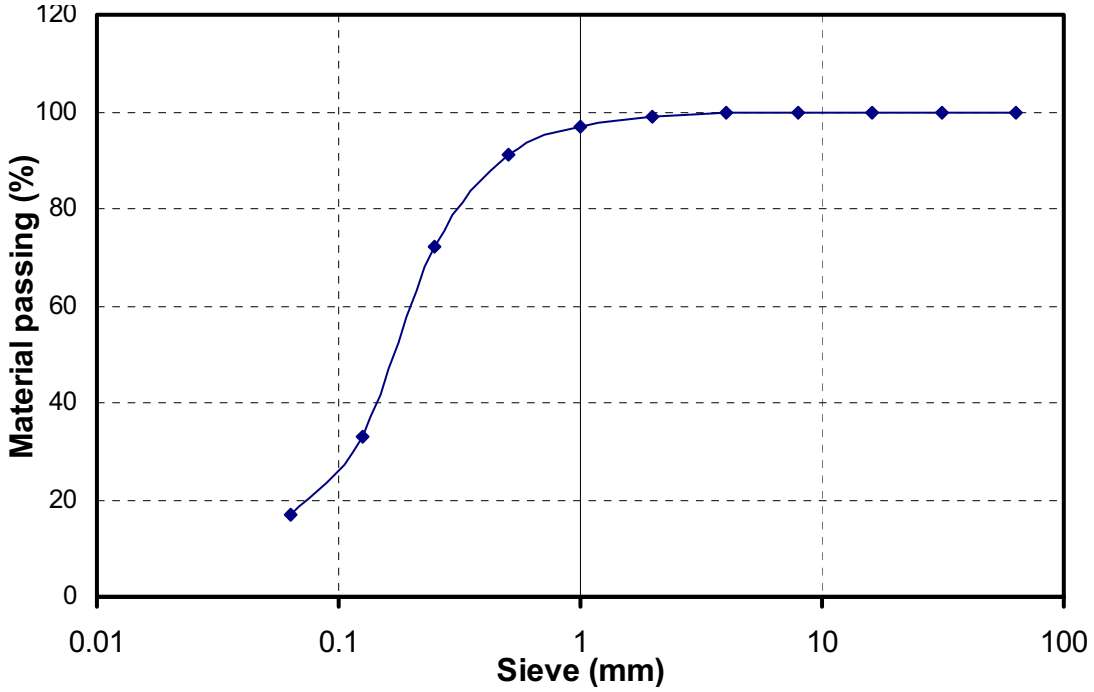

Figure 6 Sieve analysis for June 2006 sand

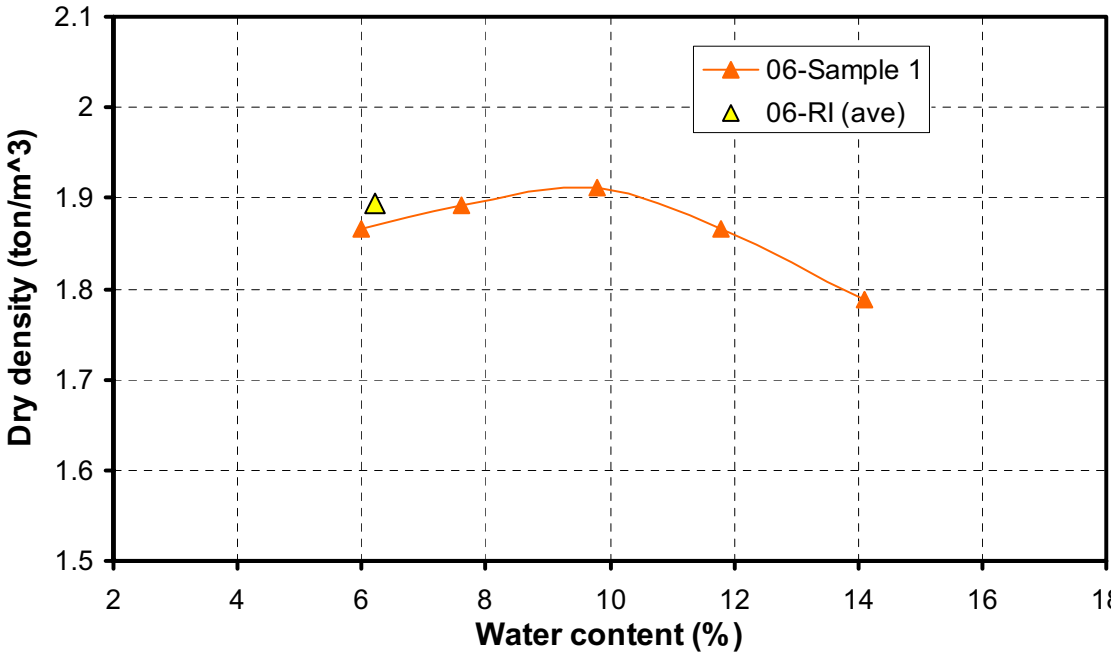

Figure 7 Optimum moisture for June 2006 sand

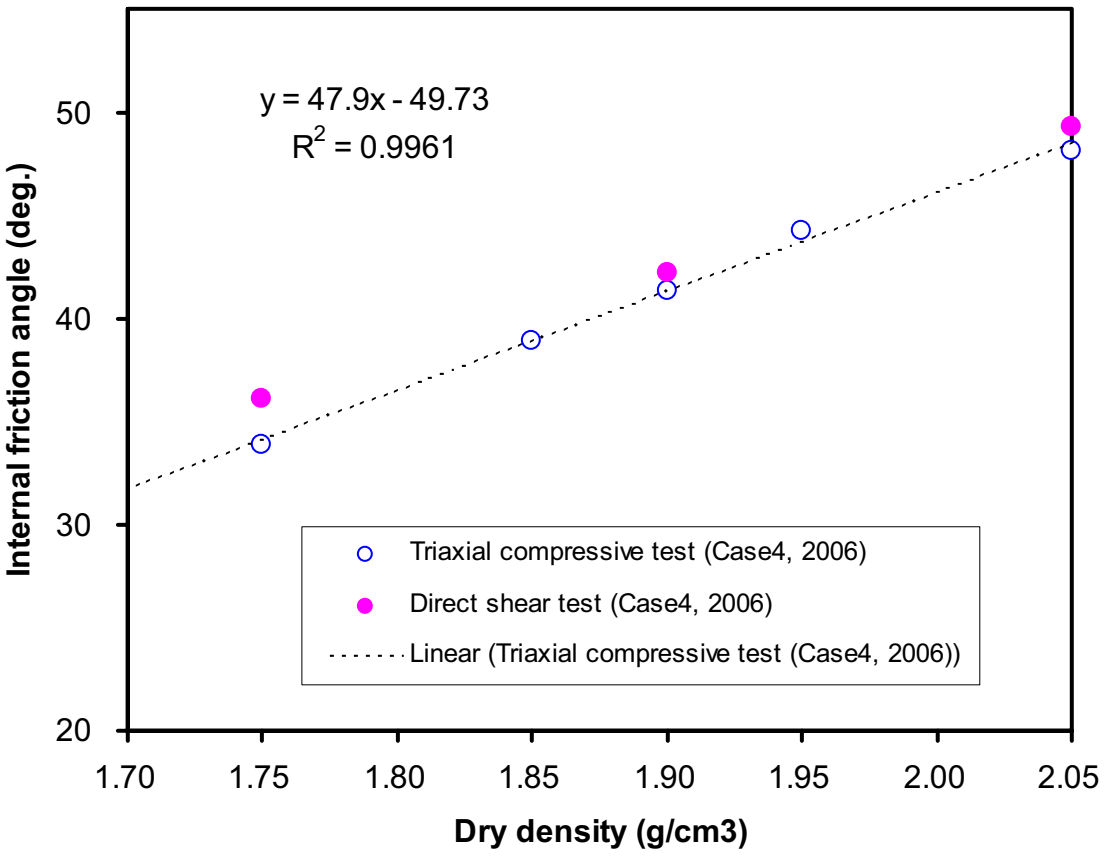

Figure 8 Direct shear and triaxial tests for June 2006 sand

Appendix D
Soil Data for CSM's Sardinian Test Site

V.D.A. N.	1472/1	**DEL**	14/02/07	**PIT**	/
CONTRACTOR	C.S.M. S.r.l.			**SAMPLE**	fill
PROJECT	Linea 36 - Perdasdefogu			**DEPTH**	1,50 m
				Date of sampling	14/02/07
REPORT N°		**DEL**		**Date of test**	19/02/2007

PARTICLE-SIZE ANALYSIS OF SOILS

ASTM D422-63 reapproved 1998

Sieve analysis (mm)	**PERCENTAGE PASSING %**
100,00	100,00
75,00	92,00
50,00	85,00
37,50	81,00
25,00	75,02
19,00	72,00
9,50	61,00
4,75	53,00
2,00	39,76
1,00	33,76
0,42	27,40
0,18	23,26
Hydrometer analysis	
0,075	20,51
0,0644	19,75
0,0457	19,59
0,0325	19,22
0,0234	17,92
0,0167	17,39
0,0123	16,87
0,0088	16,35
0,0063	14,78
0,0046	12,95
0,0033	11,64
0,0024	11,12
0,0014	9,28
0,0010	6,93

NOTES:

Specific gravity of soil particles	2,576 g/cmc

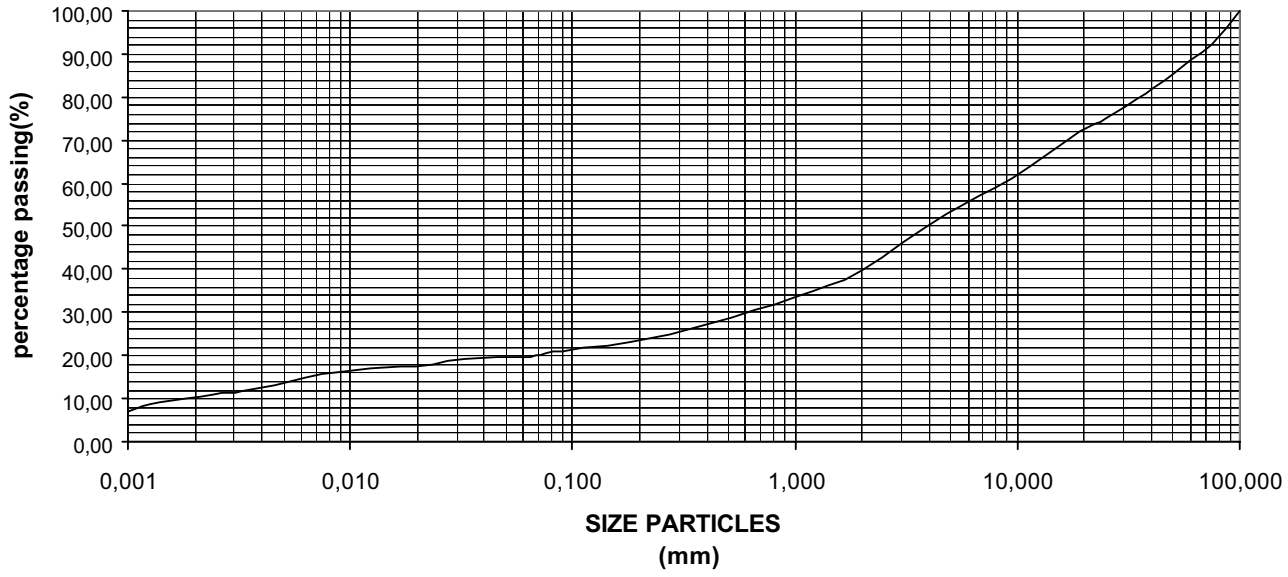

V.D.A. N.	1472/1	**DEL**	14/02/07	**PIT**	\
CONTRACTOR	C.S.M. S.p.A.			**SAMPLE**	fill
				LOCATION	\
PROJECT	Linea 36" - Perdasdefogu				
				DATE OF TEST	14/02/2007
REPORT N°		**DEL**		**DATE OF TEST**	16/02/2007

LABORATORY COMPACTION CHARACTERISTICS OF SOIL USING MODIFIED EFFORT

ASTM D 1557-Procedure C

Dry unit weight	WATER CONTENT
2,176 g/cmc	7,45 %

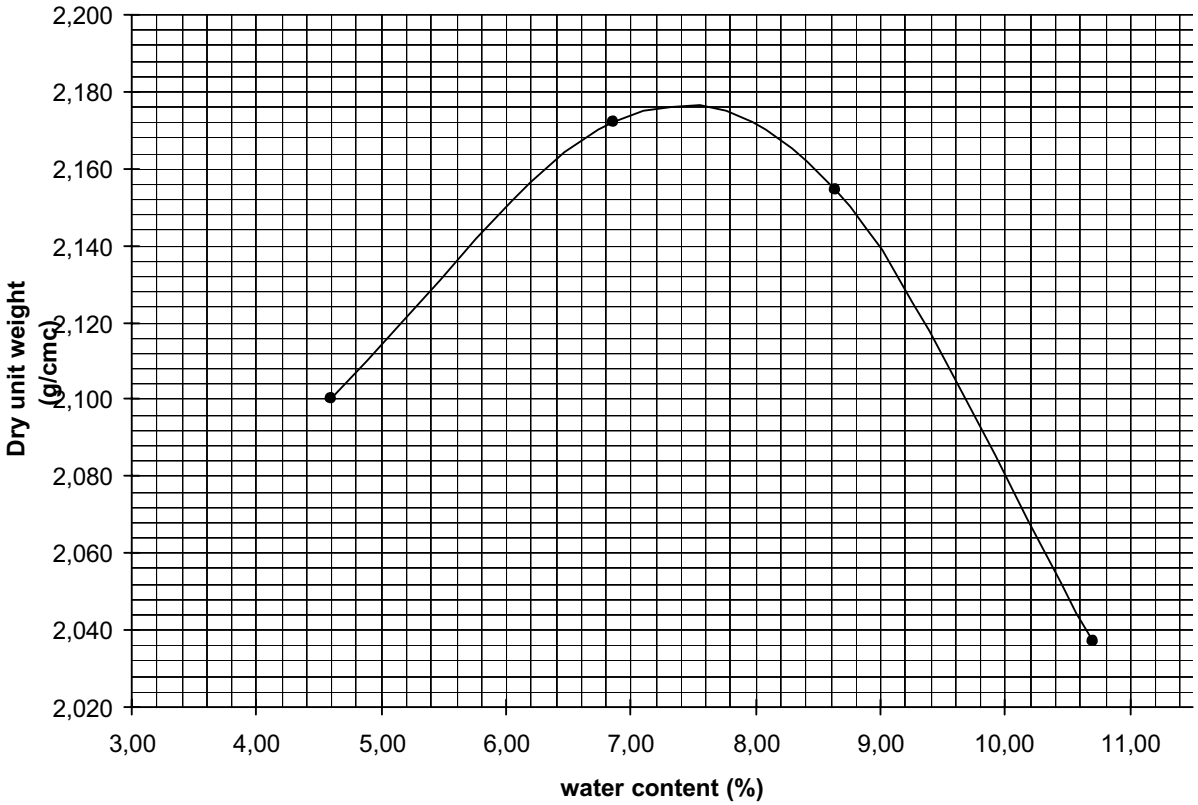

NOTES sampling made by laboratory Geosystem

V.D.A. N.	1472/1	**DEL**	14/02/07	**PIT**	\
CONTRACTOR	C.S.M. S.p.a.			**SAMPLE**	fill
PROJECT	Linea 36" Perdasdefogu			**Depth**	1,50 m
				Date of sampling	14/02/07
Report n°		**DEL**		**Date of test**	16/02/07

DIRECT SHEAR TEST

(SHEAR BOX OF CASAGRANDE) ASTM D3080-90

SAMPLE DESCRIPTION clay with pebbles

SAMPLE CONDITION compacted specimen passing sieve 2,00 mm

DISPLACEMENT RATE 0,02 mm/min

notes

INITIAL CONDITIONS		1	2	3
Specimen water content	W %	14,17	14,17	14,17
Initial unit weightt	g/cmc	2,012	2,023	2,011
Initial dry unit weight	g/cmc	1,762	1,772	1,762

CONSOLIDATION				
Normal stress	KPa	100,00	200,00	300,00
Vertical dispacement	mm	0,36	1,03	1,94
Final dry unit weight	g/cmc	1,794	1,868	1,951

ROTTURA				
Normal stress(σ)	KPa	100,00	200,00	300,00
Shear displacement	mm	3,54	3,95	5,78
Shear stress (maximum) t	KPa	71,05	141,18	198,02
Shear stress (residual) t	KPa	/	/	/

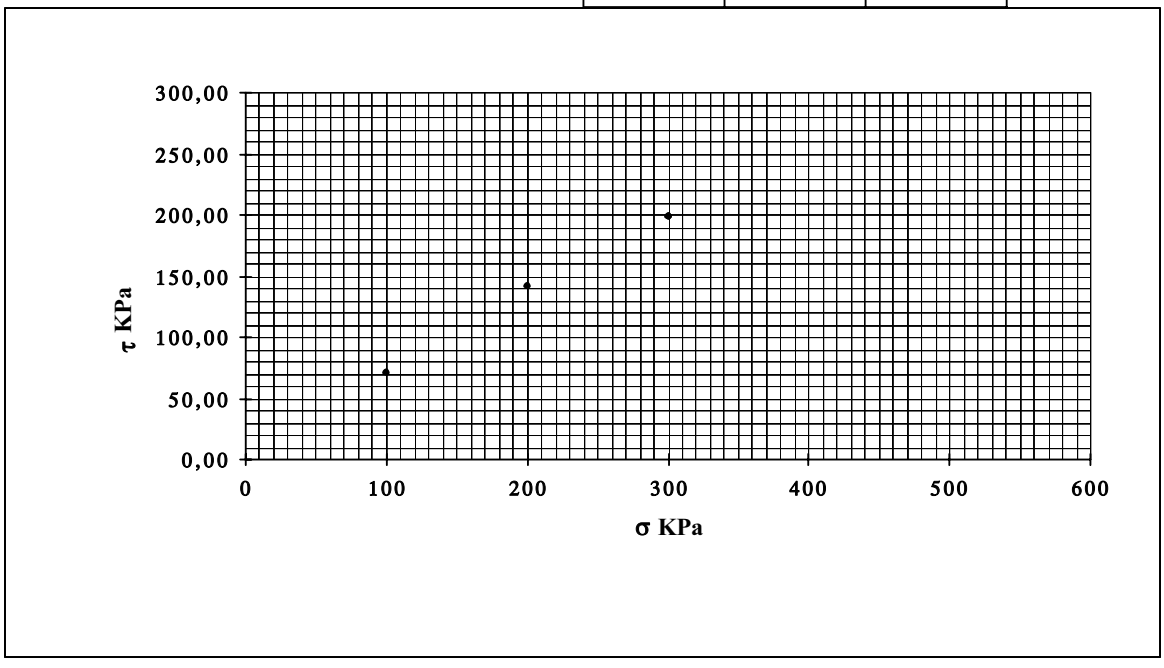

NOTES: sampling made by laboratory Geosystem

V.D.A. N.	1472/1	**DEL**	14/02/2007	**SAMPLE**	fill
CONTRACTOR	C.S.M. S.p.A.			**DEPTH**	1,50 m
PROJECT	Linea "36" - Perdasdefogu			**Date of sampling**	14/02/2007
REPORT N°		**DEL**		**Date of test**	19/02/2007

CONSOLIDATED UNDRAINED TRIAXIAL COMPRESSION TEST FOR COHESIVE SOILS

(ASTM D4767)

SAMPLE DESCRIPTION clay with pebbles
SAMPLE CONDITION compacted specimen passing sieve 2,00 mm
Pocket Penetrometer : N.D. Kpa
DISPLACEMENT RATE 0,02 mm/min
NOTES:

Initial condition of specimens

		Specimen 1	Specimen 2	Specimen 3
Height	(mm)	76,20	76,20	76,20
Diameter	(mm)	38,10	38,10	38,10
Volume	(cmc)	86,83	86,83	86,83
Specific gravity of soil particles	(g/cmc)	2,579	2,579	2,579
Unit weightt	(g/cmc)	2,088	2,075	2,071
Dry unit weight	(g/cmc)	1,829	1,817	1,814
Initial water content	(%)	14,17	14,17	14,17
Final water content	(%)	14,56	14,64	14,64
Void ratio		0,410	0,419	0,422
Initial degree of saturation	(%)	89,11	87,23	86,61

Final saturation

Chamber pressure applied(σ_3)	(Kpa)	400	400	400
Back Pressure applied	(Kpa)	280	280	280
Final pore pressure Uf	(Kpa)	392	385	384
Absorbed waterDS	(cmc)	2,00	2,35	3,50
Parameter B :		0,98	0,97	0,97

Consolidation

Chamber pressure $\sigma_3 = \sigma_1$	(Kpa)	400	500	600
Back Pressure applied	(Kpa)	300	300	300
Initial pore pressure Uf	(Kpa)	411,60	482,00	578,00
Final pore pressure Uf	(Kpa)	302,23	305,46	308,34
Expelled water	(cmc)	2,28	2,75	2,92

Failure

Deviator stress ($\sigma_1 - \sigma_3$)	(Kpa)	176,25	321,04	412,17
Axial strain	(%)	12,68	8,54	8,03
Final pore pressure Uf	(Kpa)	62,5	79,40	132,31
Stress path (s' f)	(Kpa)	126,13	281,52	374,090
Stress path (t' f)	(Kpa)	88,13	160,52	206,09
Parameter of pore pressure A		0,35	0,25	0,32

V.D.A. N.	1472/1	**DEL**	14/02/2007	**SAMPLE**	fill
CONTRACTOR	C.S.M. S.p.A.			**DEPTH**	1,50 m
PROJECT	Linea "36" - Perdasdefogu			**Date of sampling**	14/02/2007
REPORT N°		**DEL**		**Date of test**	

CONSOLIDATED UNDRAINED TRIAXIAL COMPRESSION TEST FOR COHESIVE SOILS

(ASTM D4767)

FAILURE

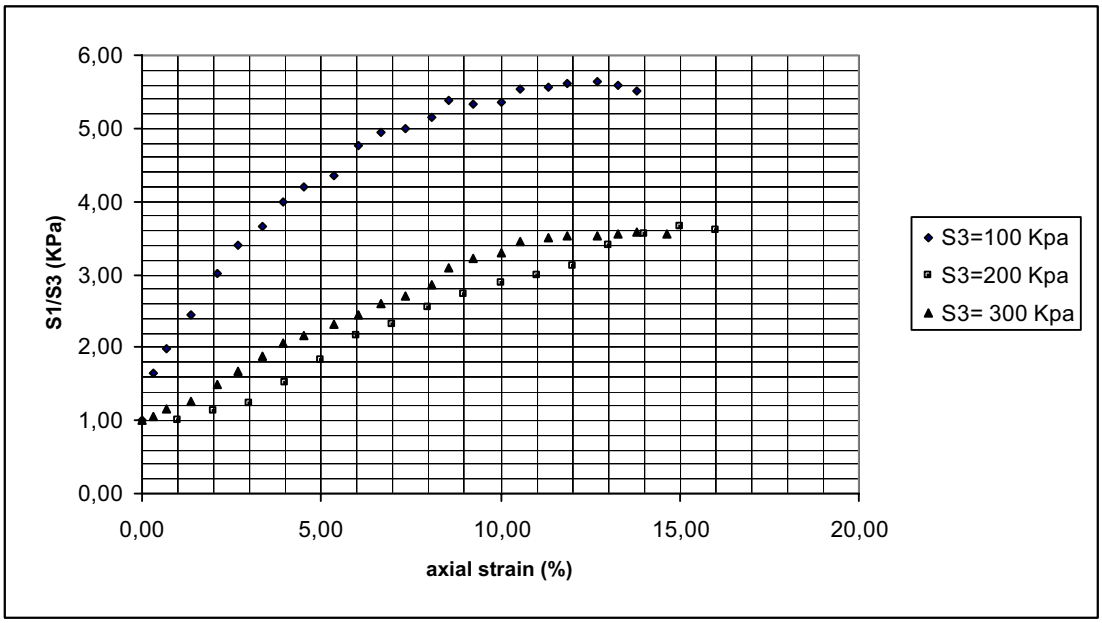

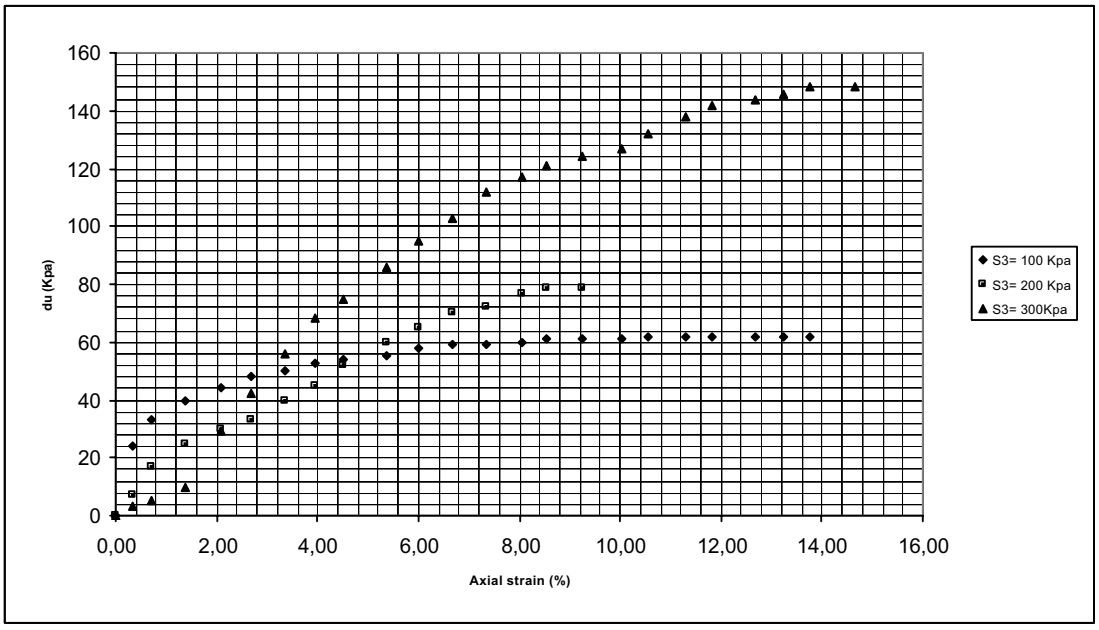

V.D.A. N.	1472/1	**DEL**	14/02/2007	**SAMPLE**	fill
CONTRACTOR	C.S.M. S.p.A.			**DEPTH**	1,50 m
PROJECT	Linea "36" - Perdasdefogu			**Date of sampling**	14/02/2007
REPORT N°		**DEL**		**Date of test**	19/02/2007

CONSOLIDATED UNDRAINED TRIAXIAL COMPRESSION TEST FOR COHESIVE SOILS

(ASTM D4767)

FAILURE

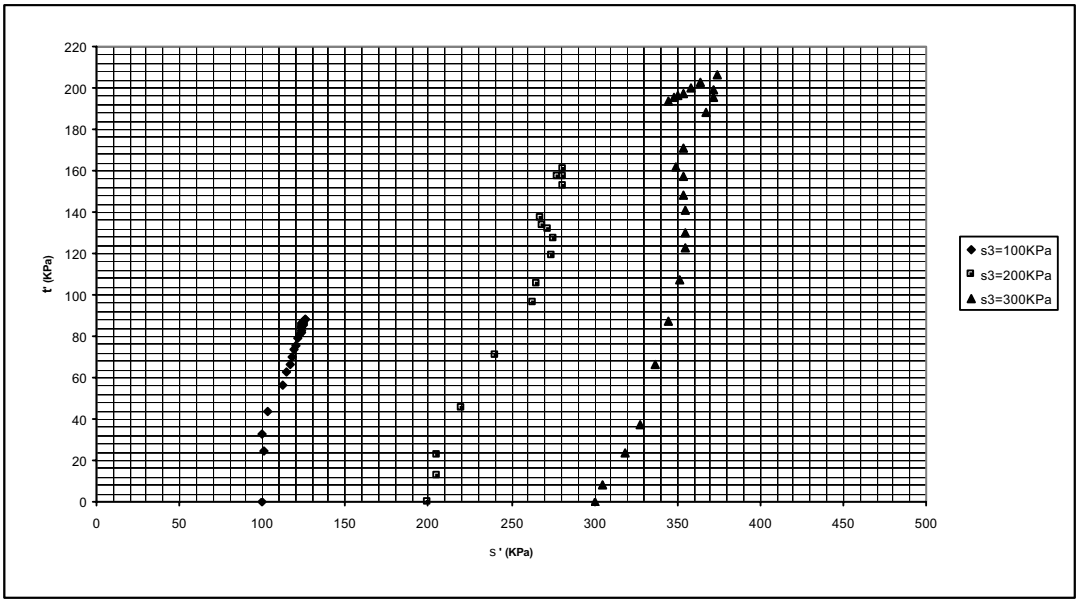

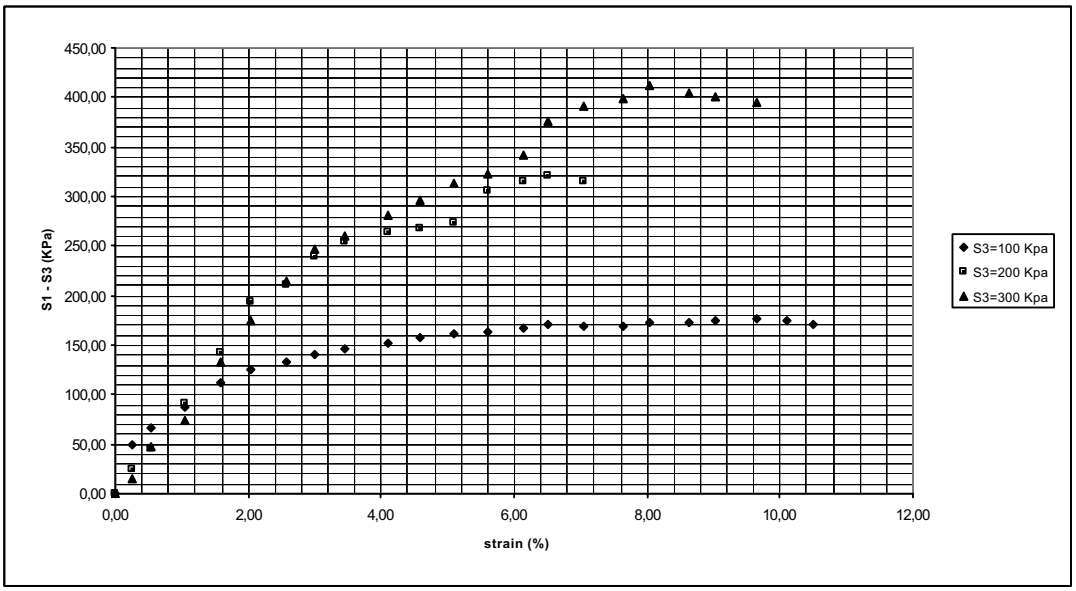

V.D.A.	N°1472/1	DEL 14 / 02 / 07	SAMPLE	Fill
CONTRACTOR	C.S.M. S.p.A.		DEPTH	1,50 m
PROJECT:	Linea "36" - Perdasdefogu		Date of sampling	14 / 02 / 07
			Date of test	19 / 02 /07

CONSOLIDATE UNDRAINED TRIAXIAL COMPRESSION TEST
FOR COHESIVE SOILS

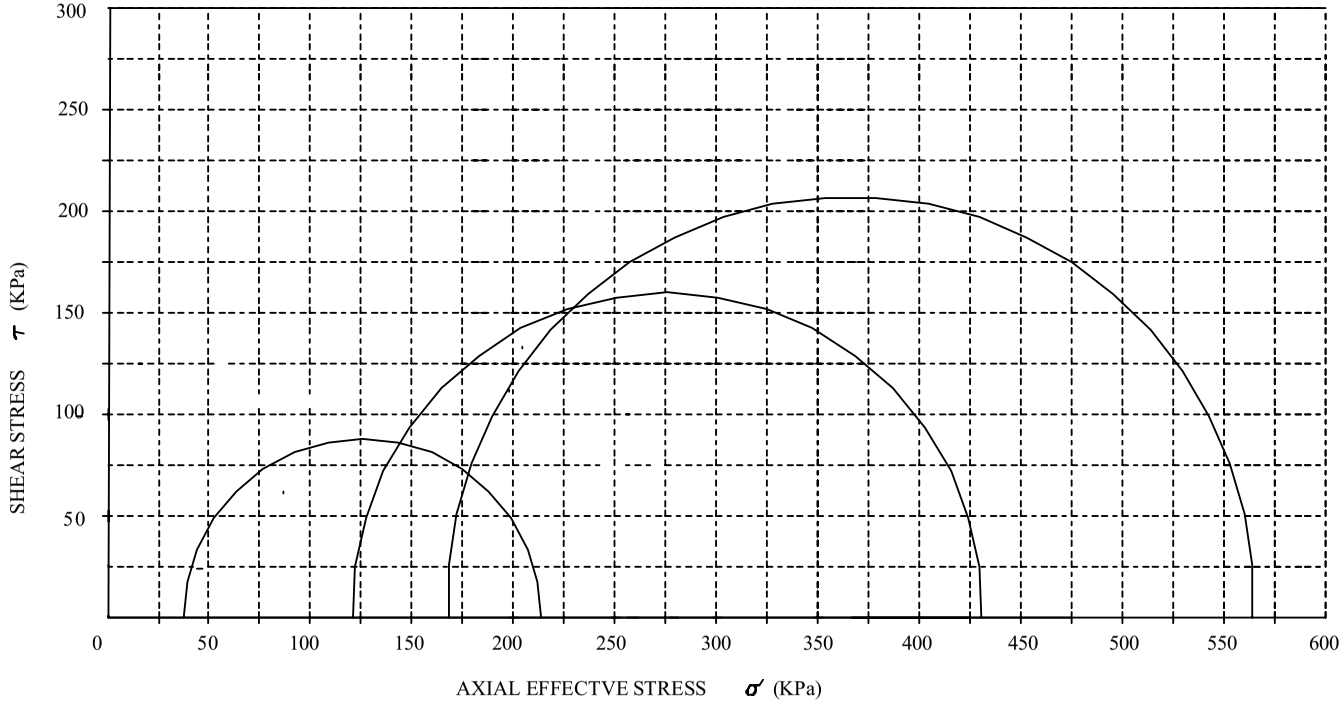

TECHNICIAN
P. M. Roberto Aste

DIRECTOR
Dott. Geol. Guido Demontis

Appendix E
Soil Results from Advantica's Spadeadam test site

PROJECT NAME SPADEADAM

PROJECT NO: GEO / 10934

Date	02/03/2007
Approved	J Sturges
Page	1 of 1

Sample details					Classification Tests					Density Tests		Undrained Triaxial Compression Tests			Chemical Tests			
Borehole No.	Depth (m)	No.	Type	Description	MC (%)	LL (%)	PL (%)	PI (%)	<425 mic (%)	Bulk (Mg/m³)	Dry (Mg/m³)	Cell Pressure (kPa)	Deviator Stress (kPa)	Shear Stress (kPa)	pH	2:1 W/S SO4 (g/l)	Ground Water SO4 (g/l)	Other tests and comments
-	-	1	B	Red brown CLAY / SILT and fine to coarse SAND, GRAVEL and SANDSTONE	16	32	16	16	70									Particle Size Distribution Test 2.5kg Compaction Test - OMC 12%
-	-	1	B	Red brown CLAY / SILT and fine to coarse SAND, GRAVEL and SANDSTONE	6.3					1.96	1.84	UCS =	319					UCS Test @ 50% OMC with 2.5kg compaction
-	-	1	B	Red brown CLAY / SILT and fine to coarse SAND, GRAVEL and SANDSTONE	10					1.91	1.73	UCS =	239					UCS Test @ 90% OMC with 2.5kg compaction
-	-	1	B	Red brown CLAY / SILT and fine to coarse SAND, GRAVEL and SANDSTONE	13					2.05	1.81	UCS =	222					UCS Test @ 110% OMC with 2.5kg compaction
-	-	1	B	Red brown CLAY / SILT and fine to coarse SAND, GRAVEL and SANDSTONE	6.2					1.95	1.84	25	409	205				QUTXL Test @ 50% OMC with 2.5kg compaction
-	-	1	B	Red brown CLAY / SILT and fine to coarse SAND, GRAVEL and SANDSTONE	10					1.96	1.77	25	314	157				QUTXL Test @ 90% OMC with 2.5kg compaction
-	-	1	B	Red brown CLAY / SILT and fine to coarse SAND, GRAVEL and SANDSTONE	13					2.09	1.84	25	284	142				QUTXL Test @ 110% OMC with 2.5kg compaction

SUMMARY OF GEOTECHNICAL TESTING

GEOLABS

BS1377 : Part 2 : Clause 9 : 1990

Determination of Particle Size Distribution

Sample Number: 1	Description: Red brown CLAY / SILT and fine to coarse SAND, GRAVEL and SANDSTONE

BS1377 : Part 2 : Clause 9.2 : 1990 Wet Sieving Method
BS1377 : Part 2 : Clause 9.4 : 1990 Sedimentation by the Pipette Method

SIEVE	
Sieve	% pass
200 mm	100
125 mm	100
90 mm	100
75 mm	100
63 mm	100
50 mm	100
37.5 mm	95
28 mm	93
20 mm	89
14 mm	87
10 mm	85
6.3 mm	81
5 mm	80
3.35 mm	79
2 mm	76
1.18 mm	74
600 µm	71
425 µm	70
300 µm	68
212 µm	65
150 µm	61
63 µm	50

PIPETTE	
Particle size	% pass
20.0 µm	44
6.0 µm	33
2.0 µm	23
Preparation: No Pre-treatment used	

Temp (°C)	25

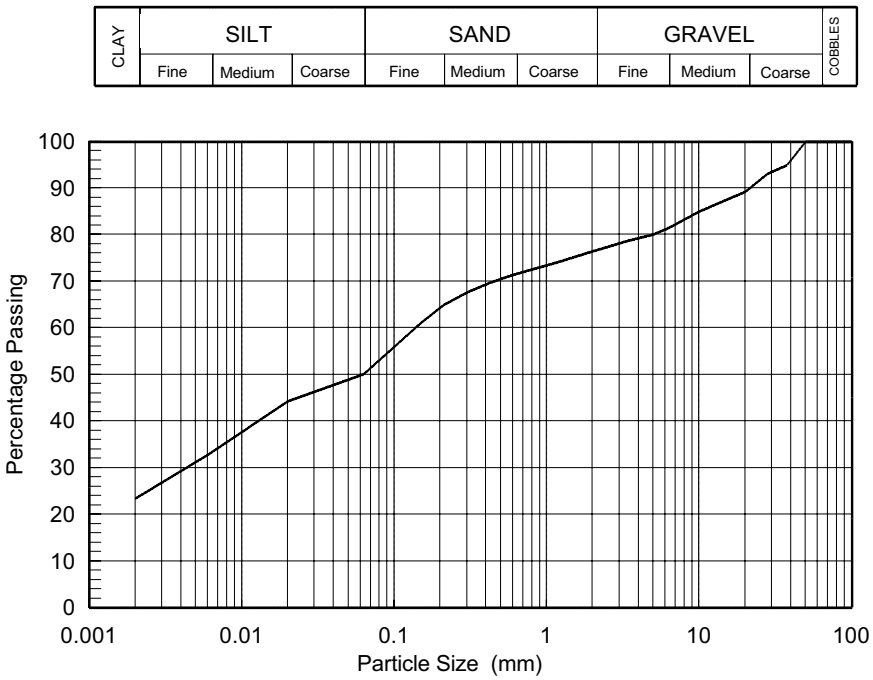

Particle Proportions		
Cobbles	0.0	%
Gravel	23.6	%
Sand	26.2	%
Silt	26.7	%
Clay	23.4	%

Checked and Approved	Project Number:	
Initials: JS		GEO / 10934
Date: 01/03/2007	Project Name:	SPADEADAM

GEOLABS

BS1377 : Part 4 : 1990

Moisture Content / Dry Density Relationship

Sample No: 1	Description: Red brown CLAY / SILT and fine to coarse SAND, GRAVEL and SANDSTONE

BS1377 : Part 4 : Clause 3.3.4.1 : 1990 2.5 kg Compaction Test

Sample Preparation: Material was air dried. Single sample
No particles were removed

Particle Density: 2.70 (assumed)

Material Retained
on 20 mm test sieve: 7 %
on 37.5 mm test sieve: 0 %

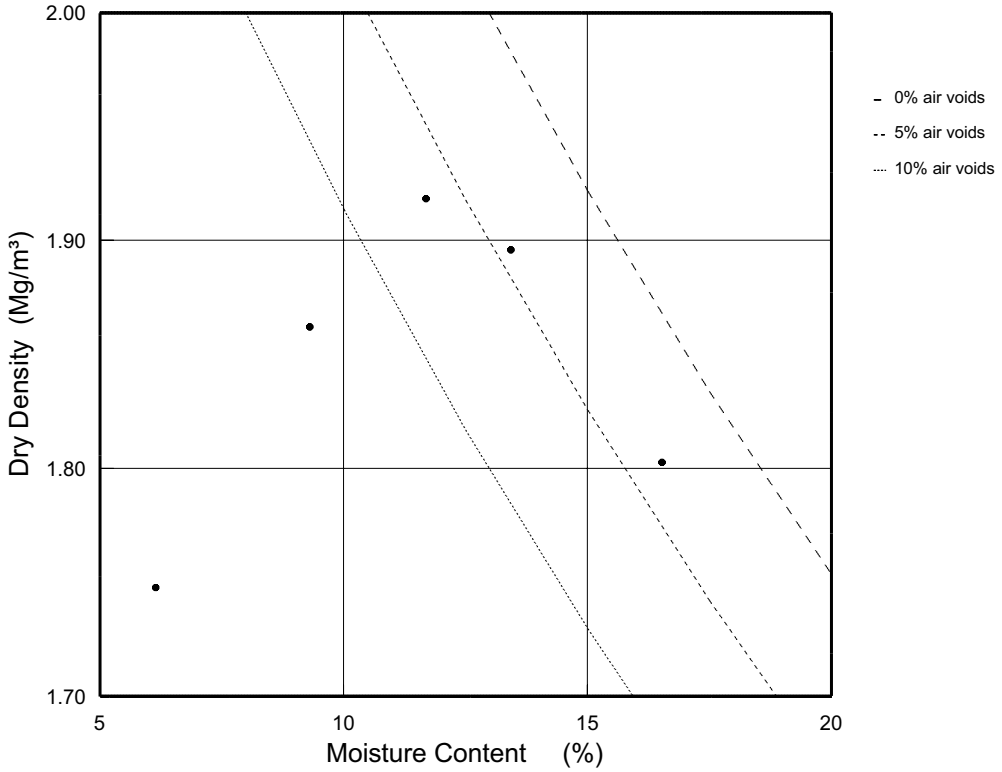

Maximum Dry Density **1.92 Mg/m³**

Optimum Moisture Content **12 %**

Natural Moisture Content **15 %**

Checked and Approved Initials: JS Date: 01/03/2007	Project Number: **GEO / 10934** Project Name: **SPADEADAM**	***GEOLABS***

BS1377 : Part 7 : Clause 7 : 1990

Unconfined Compressive Strength

Sample Number: 1 Depth (m): Tested @ 50% OMC	Description: Red brown CLAY / SILT and fine to coarse SAND, GRAVEL and SANDSTONE

Unconfined 102mm Nominal Diameter Specimen

Specimen details	Single Specimen
Specimen condition:	Undisturbed
Length (mm):	203.0
Diameter (mm):	101.9
Moisture Content (%):	6.3
Bulk Density (Mg/m³):	1.96
Dry Density (Mg/m³):	1.84
Test details	**Load Frame Method**
Latex membrane thickness (mm):	not applicable
Membrane correction (kPa):	not applicable
Axial displacement rate (%/min):	2.0
Cell pressure (kPa):	not applicable
Strain at failure (%):	1.2
Unconfined Compressive Strength (kPa):	319

Mode of failure:

Orientation and position of sample: n/a

Checked and Approved Initials: JS Date: 02/03/2007	Project Number: GEO / 10934 Project Name: SPADEADAM	GEOLABS

BS1377 : Part 7 : Clause 7 : 1990

Unconfined Compressive Strength

Sample Number: 1 Depth (m): Tested @ 90% OMC	Description: Red brown CLAY / SILT and fine to coarse SAND, GRAVEL and SANDSTONE

Unconfined 102mm Nominal Diameter Specimen

Specimen details	Single Specimen
Specimen condition:	Undisturbed
Length (mm):	203.0
Diameter (mm):	102.1
Moisture Content (%):	10
Bulk Density (Mg/m³):	1.91
Dry Density (Mg/m³):	1.73
Test details	**Load Frame Method**
Latex membrane thickness (mm):	not applicable
Membrane correction (kPa):	not applicable
Axial displacement rate (%/min):	2.0
Cell pressure (kPa):	not applicable
Strain at failure (%):	1.5
Unconfined Compressive Strength (kPa):	239

Mode of failure:

Orientation and position of sample: n/a

Checked and Approved Initials: JS Date: 02/03/2007	Project Number: GEO / 10934 Project Name: SPADEADAM	GEOLABS

BS1377 : Part 7 : Clause 7 : 1990

Unconfined Compressive Strength

Sample Number: 1 Depth (m): Tested @ 110% OMC	Description: Red brown CLAY / SILT and fine to coarse SAND, GRAVEL and SANDSTONE

Unconfined 102mm Nominal Diameter Specimen

Specimen details	Single Specimen
Specimen condition:	Undisturbed
Length (mm):	203.0
Diameter (mm):	102.0
Moisture Content (%):	13
Bulk Density (Mg/m³):	2.05
Dry Density (Mg/m³):	1.81
Test details	**Load Frame Method**
Latex membrane thickness (mm):	not applicable
Membrane correction (kPa):	not applicable
Axial displacement rate (%/min):	2.0
Cell pressure (kPa):	not applicable
Strain at failure (%):	3.2
Unconfined Compressive Strength (kPa):	222

Mode of failure:

Orientation and position of sample: n/a

Checked and Approved Initials: JS Date: 02/03/2007	Project Number: GEO / 10934 Project Name: SPADEADAM	GEOLABS

BS1377 : Part 7 : Clause 8 : 1990

Quick Undrained Triaxial Test

Sample Number: 1 Depth (m): Tested @ 50% OMC	Description: Red brown CLAY / SILT and fine to coarse SAND, GRAVEL and SANDSTONE

Single Stage Specimen

Specimen details	Single Specimen
Specimen condition:	Undisturbed
Length (mm):	203.0
Diameter (mm):	102.2
Moisture Content (%):	6.2
Bulk Density (Mg/m³):	1.95
Dry Density (Mg/m³):	1.84
Test details	
Latex membrane thickness (mm):	0.3
Membrane correction (kPa):	0.1
Axial displacement rate (%/min):	2.0
Cell pressure (kPa):	25
Strain at failure (%):	1.2
Maximum Deviator Stress (kPa):	409
Shear Stress Cu (kPa):	205

Orientation and position of sample: n/a

Mode of failure:

Checked and Approved Initials: JS Date: 02/03/2007	Project Number: **GEO / 10934** Project Name: **SPADEADAM**	***GEOLABS***

BS1377 : Part 7 : Clause 8 : 1990

Quick Undrained Triaxial Test

Sample Number: 1 Depth (m): Tested @ 90% OMC	Description: Red brown CLAY / SILT and fine to coarse SAND, GRAVEL and SANDSTONE

Single Stage Specimen

Specimen details	Single Specimen
Specimen condition:	Undisturbed
Length (mm):	204.0
Diameter (mm):	102.1
Moisture Content (%):	10
Bulk Density (Mg/m³):	1.96
Dry Density (Mg/m³):	1.77
Test details	
Latex membrane thickness (mm):	0.3
Membrane correction (kPa):	0.1
Axial displacement rate (%/min):	2.0
Cell pressure (kPa):	25
Strain at failure (%):	1.5
Maximum Deviator Stress (kPa):	314
Shear Stress Cu (kPa):	157

Orientation and position of sample: n/a

Mode of failure:

Checked and Approved Initials: JS Date: 02/03/2007	Project Number: GEO / 10934 Project Name: SPADEADAM	GEOLABS

BS1377 : Part 7 : Clause 8 : 1990

Quick Undrained Triaxial Test

Sample Number: 1 Depth (m): Tested @ 110% OMC	Description: Red brown CLAY / SILT and fine to coarse SAND, GRAVEL and SANDSTONE

Single Stage Specimen

Specimen details	Single Specimen
Specimen condition:	Undisturbed
Length (mm):	203.5
Diameter (mm):	102.2
Moisture Content (%):	13
Bulk Density (Mg/m³):	2.09
Dry Density (Mg/m³):	1.84
Test details	
Latex membrane thickness (mm):	0.3
Membrane correction (kPa):	0.4
Axial displacement rate (%/min):	2.0
Cell pressure (kPa):	25
Strain at failure (%):	5.4
Maximum Deviator Stress (kPa):	284
Shear Stress Cu (kPa):	142

Orientation and position of sample: n/a

Mode of failure:

Checked and Approved Initials: JS Date: 02/03/2007	Project Number: GEO / 10934 Project Name: SPADEADAM	GEOLABS

Appendix F – Hall Effect Sensor Data Sheet

Continuous-Time Ratiometric Linear Hall Effect Sensors

Features and Benefits

- Low-noise output
- Fast power-on time
- Ratiometric rail-to-rail output
- 4.5 to 6.0 V operation
- Solid-state reliability
- Factory-programmed at end-of-line for optimum performance
- Robust ESD performance

Packages: 3 pin SOT23W (suffix LH), and 3 pin SIP (suffix UA)

Not to scale

Description

The A1301 and A1302 are continuous-time, ratiometric, linear Hall-effect sensors. They are optimized to accurately provide a voltage output that is proportional to an applied magnetic field. These devices have a quiescent output voltage that is 50% of the supply voltage. Two output sensitivity options are provided: 2.5 mV/G typical for the A1301, and 1.3 mV/G typical for the A1302.

The Hall-effect integrated circuit included in each device includes a Hall sensing element, a linear amplifier, and a CMOS Class A output structure. Integrating the Hall sensing element and the amplifier on a single chip minimizes many of the problems normally associated with low voltage level analog signals.

High precision in output levels is obtained by internal gain and offset trim adjustments made at end-of-line during the manufacturing process.

These features make the A1301 and A1302 ideal for use in position sensing systems, for both linear target motion and rotational target motion. They are well-suited for industrial applications over extended temperature ranges, from –40°C to 125°C.

Two device package types are available: LH, a 3-pin SOT23W type for surface mount, and UA, a 3-pin ultramini SIP for through-hole mount. They are lead (Pb) free (suffix, $_{-T}$) with 100% matte tin plated leadframes.

Functional Block Diagram

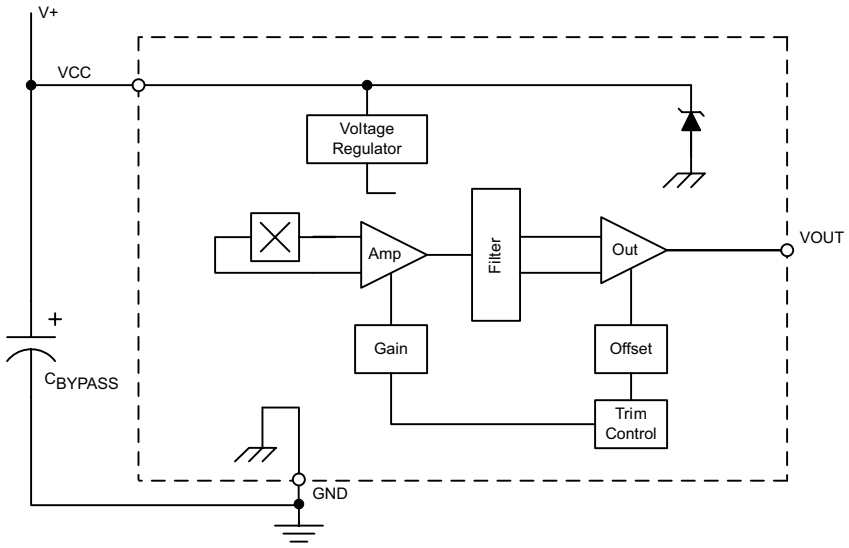

First Major Improvement to the Two-Curve Ductile Fracture Model

Selection Guide					
Part Number	Pb-free[1]	Packing[2]	Package	Ambient, T_A	Sensitivity (Typical)
A1301ELHLT-T	Yes	7-in. tape and reel, 3000 pieces/reel	Surface Mount	–40ºC to 85ºC	2.5 mV/G
A1301EUA-T	Yes	Bulk, 500 pieces/bag	SIP		
A1301KLHLT-T	Yes	7-in. tape and reel, 3000 pieces/reel	Surface Mount	–40ºC to 125ºC	
A1301KUA-T	Yes	Bulk, 500 pieces/bag	SIP		
A1302ELHLT-T	Yes	7-in. tape and reel, 3000 pieces/reel	Surface Mount	–40ºC to 85ºC	1.3 mV/G
A1302EUA-T	Yes	Bulk, 500 pieces/bag	SIP		
A1302KLHLT-T	Yes	7-in. tape and reel, 3000 pieces/reel	Surface Mount	–40ºC to 125ºC	
A1302KUA-T	Yes	Bulk, 500 pieces/bag	SIP		

[1]Pb-based variants are being phased out of the product line. Certain variants cited in this footnote are no longer in production The variants should not be purchased for new design applications. Samples are no longer available. Status change: May 1, 2006. These variants include: A1301ELHLT, A1301EUA, A1301KLHLT, A1301KUA, A1302ELHLT, A1302EUA, A1302KLHLT, and A1302KUA.

[2]Contact Allegro for additional packing options.

Absolute Maximum Ratings

Characteristic	Symbol	Notes	Rating	Units
Supply Voltage	V_{CC}		8	V
Output Voltage	V_{OUT}		8	V
Reverse Supply Voltage	V_{RCC}		–0.1	V
Reverse Supply Voltage	V_{RCC}		–0.1	V
Output Sink Current	I_{OUT}		10	mA
Operating Ambient Temperature	T_A	Range E	–40 to 85	ºC
		Range K	–40 to 125	ºC
Maximum Junction Temperature	T_J(max)		165	ºC
Storage Temperature	T_{stg}		–65 to 170	ºC

DEVICE CHARACTERISTICS over operating temperature range, T_A, and V_{CC} = 5 V, unless otherwise noted

Characteristic	Symbol	Test Conditions	Min.	Typ.	Max.	Units
Electrical Characteristics						
Supply Voltage	V_{CC}	Running, T_J < 165°C	4.5	–	6	V
Supply Current	I_{CC}	Output open	–	–	11	mA
Output Voltage	$V_{OUT(High)}$	I_{SOURCE} = –1 mA, Sens = nominal	4.65	4.7	–	V
	$V_{OUT(Low)}$	I_{SINK} = 1 mA, Sens = nominal	–	0.2	0.25	V
Output Bandwidth	BW		–	20	–	kHz
Power-On Time	t_{PO}	$V_{CC(min)}$ to 0.95 $V_{OUT;}$ B = ±1400 G; Slew rate = 4.5 V/µs to 4.5 V/100 ns	–	3	5	µs
Output Resistance	R_{OUT}	I_{SINK} ≤ 1 mA, I_{SOURCE} ≥ –1 mA	–	2	5	Ω
Wide Band Output Noise, rms	V_{OUTN}	External output low pass filter ≤ 10 kHz; Sens = nominal	–	150	–	µV
Ratiometry						
Quiescent Output Voltage Error with respect to ΔV_{CC}[1]	$\Delta V_{OUTQ(V)}$	T_A = 25°C	–	–	±3.0	%
Magnetic Sensitivity Error with respect to ΔV_{CC}[2]	$\Delta Sens_{(V)}$	T_A = 25°C	–	–	±3.0	%
Output						
Linearity	Lin	T_A = 25°C	–	–	±2.5	%
Symmetry	Sym	T_A = 25°C	–	–	±3.0	%
Magnetic Characteristics						
Quiescent Output Voltage	V_{OUTQ}	B = 0 G; T_A = 25°C	2.4	2.5	2.6	V
Quiescent Output Voltage over Operating Temperature Range	$V_{OUTQ(\Delta T_A)}$	B = 0 G	2.2	–	2.8	V
Magnetic Sensitivity	Sens	A1301; T_A = 25°C	2.0	2.5	3.0	mV/G
		A1302; T_A = 25°C	1.0	1.3	1.6	mV/G
Magnetic Sensitivity over Operating Temperature Range	$Sens_{(\Delta T_A)}$	A1301	1.8	–	3.2	mV/G
		A1302	0.85	–	1.75	mV/G

[1]Refer to equation (4) in Ratiometric section on page 4.
[2]Refer to equation (5) in Ratiometric section on page 4.

Characteristic Definitions

Quiescent Output Voltage. In the quiescent state (no significant magnetic field: B = 0), the output, V_{OUTQ}, equals one half of the supply voltage, V_{CC}, throughout the entire operating ranges of V_{CC} and ambient temperature, T_A. Due to internal component tolerances and thermal considerations, there is a tolerance on the quiescent output voltage, ΔV_{OUTQ}, which is a function of both ΔV_{CC} and ΔT_A. For purposes of specification, the quiescent output voltage as a function of temperature, $\Delta V_{OUTQ(\Delta T_A)}$, is defined as:

$$\Delta V_{OUTQ(\Delta T_A)} = \frac{V_{OUTQ(T_A)} - V_{OUTQ(25°C)}}{Sens_{(25°C)}} \quad (1)$$

where Sens is in mV/G, and the result is the device equivalent accuracy, in gauss (G), applicable over the entire operating temperature range.

Sensitivity. The presence of a south-polarity (+B) magnetic field, perpendicular to the branded face of the device package, increases the output voltage, V_{OUT}, in proportion to the magnetic field applied, from V_{OUTQ} toward the V_{CC} rail. Conversely, the application of a north polarity (–B) magnetic field, in the same orientation, proportionally decreases the output voltage from its quiescent value. This proportionality is specified as the magnetic sensitivity of the device and is defined as:

$$Sens = \frac{V_{OUT(-B)} - V_{OUT(+B)}}{2B} \quad (2)$$

The stability of the device magnetic sensitivity as a function of ambient temperature, $\Delta Sens_{(\Delta T_A)}$ (%) is defined as:

$$\Delta Sens_{(\Delta T_A)} = \frac{Sens_{(T_A)} - Sens_{(25°C)}}{Sens_{(25°C)}} \times 100\% \quad (3)$$

Ratiometric. The A1301 and A1302 feature a ratiometric output. This means that the quiescent voltage output, V_{OUTQ}, and the magnetic sensitivity, Sens, are proportional to the supply voltage, V_{CC}.

The ratiometric change (%) in the quiescent voltage output is defined as:

$$\Delta V_{OUTQ(\Delta V)} = \frac{V_{OUTQ(V_{CC})} \,/\, V_{OUTQ(5V)}}{V_{CC} \,/\, 5\ V} \times 100\% \quad (4)$$

and the ratiometric change (%) in sensitivity is defined as:

$$\Delta Sens_{(\Delta V)} = \frac{Sens_{(V_{CC})} \,/\, Sens_{(5V)}}{V_{CC} \,/\, 5\ V} \times 100\% \quad (5)$$

Linearity and Symmetry. The on-chip output stage is designed to provide linear output at a supply voltage of 5 V. Although the application of very high magnetic fields does not damage these devices, it does force their output into a nonlinear region. Linearity in percent is measured and defined as:

$$Lin+ = \frac{V_{OUT(+B)} - V_{OUTQ}}{2\,(V_{OUT(+B½)} - V_{VOUTQ})} \times 100\% \quad (6)$$

$$Lin- = \frac{V_{OUT(-B)} - V_{OUTQ}}{2(V_{OUT(-B½)} - V_{OUTQ})} \times 100\% \quad (7)$$

and output symmetry as:

$$Sym = \frac{V_{OUT(+B)} - V_{OUTQ}}{V_{OUTQ} - V_{OUT(-B)}} \times 100\% \quad (8)$$

Typical Characteristics
(30 pieces, 3 fabrication lots)

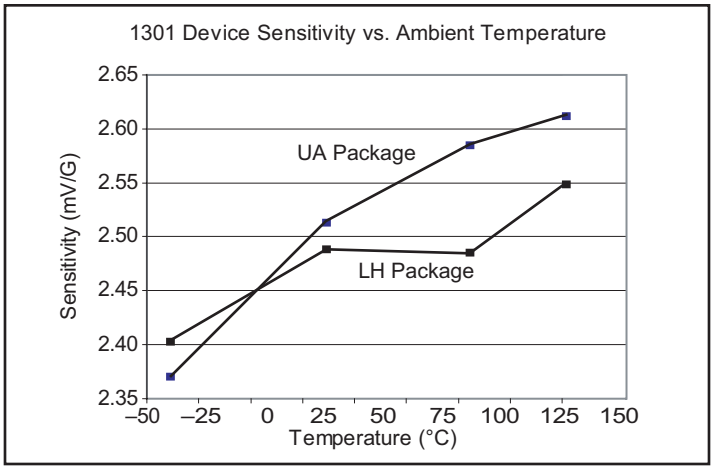

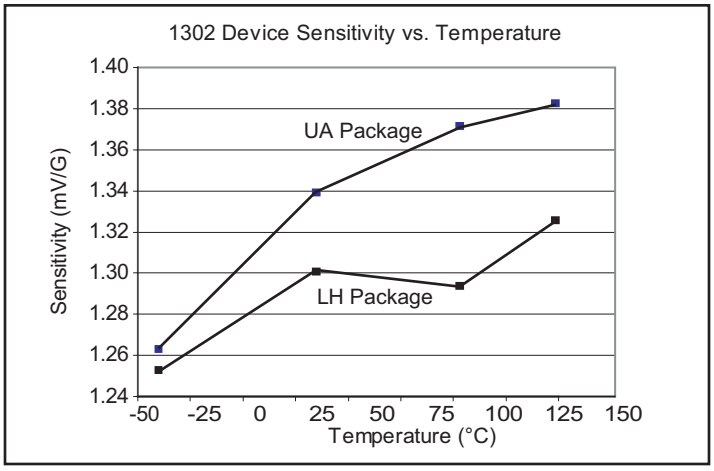

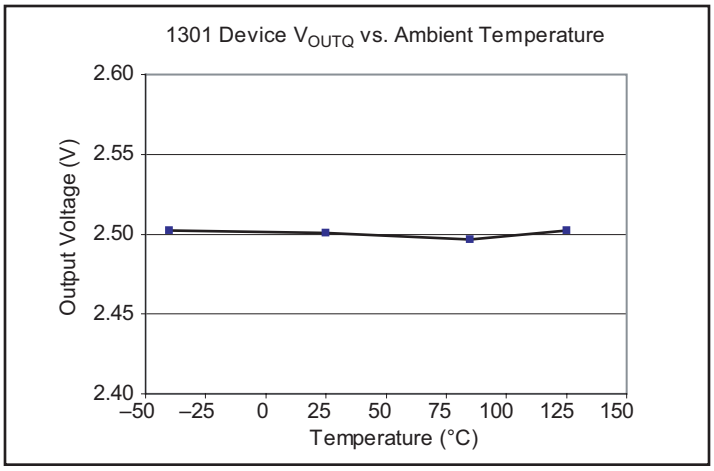

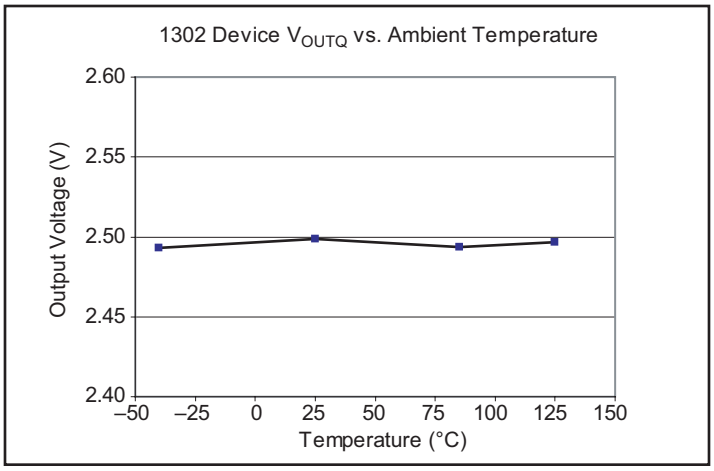

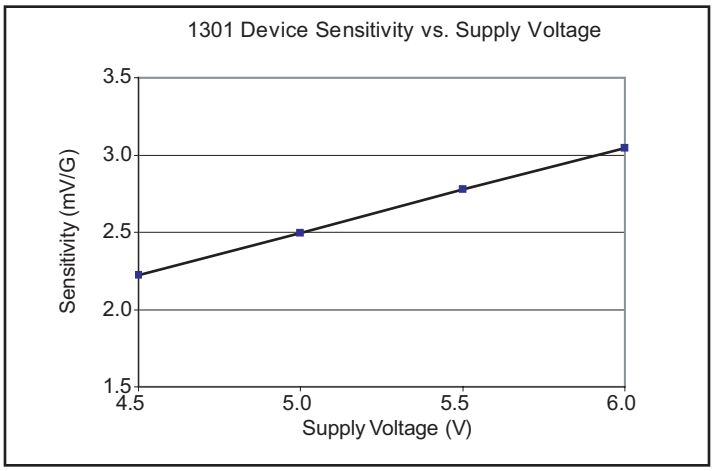

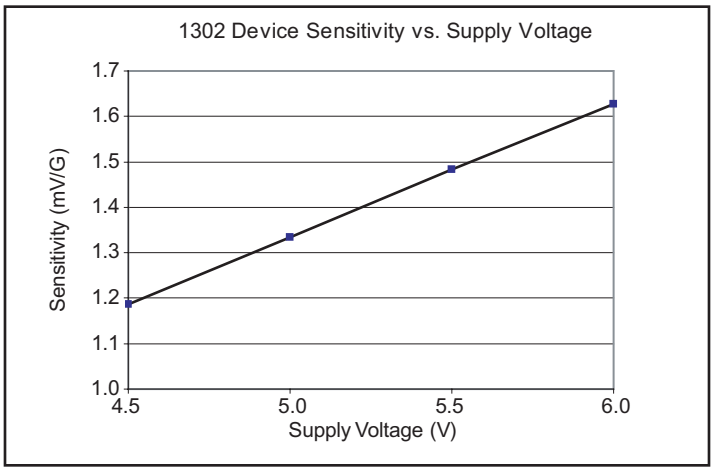

Continued on the next page...

Typical Characteristics, continued
(30 pieces, 3 fabrication lots)

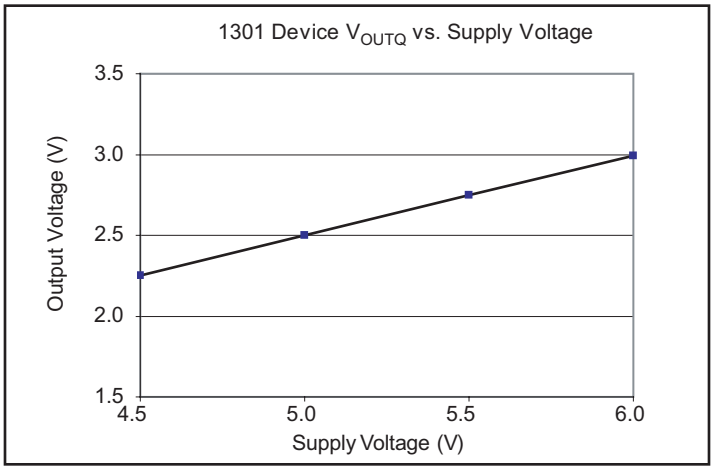

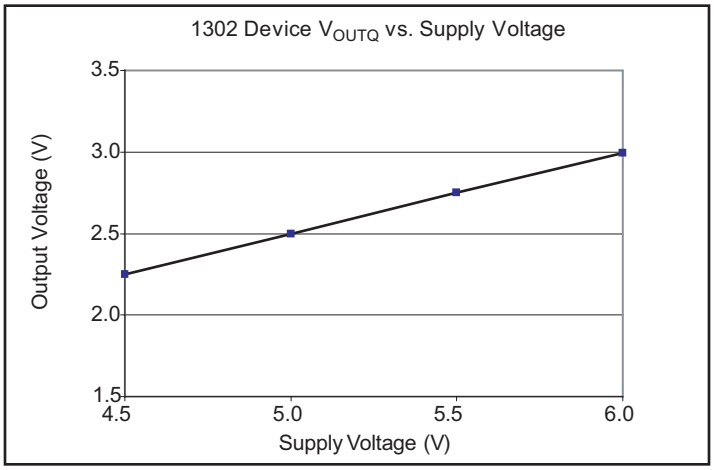

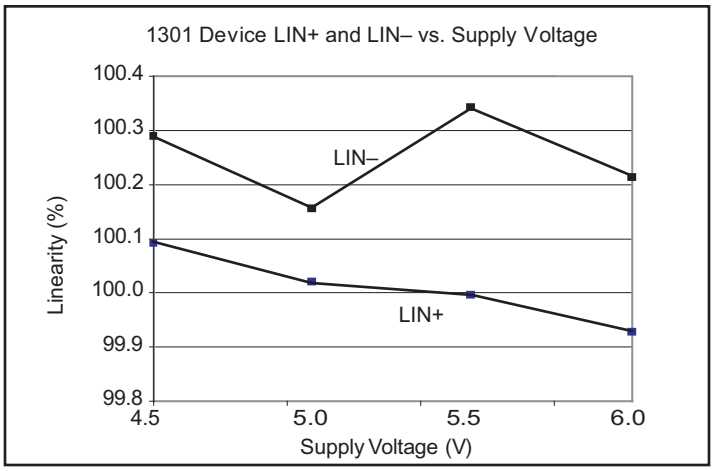

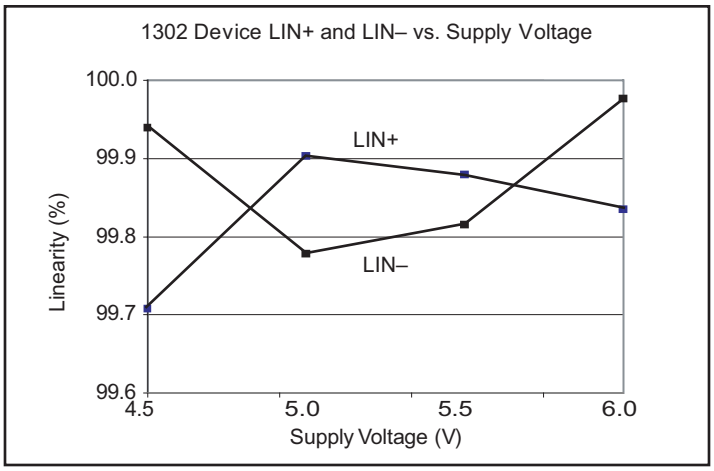

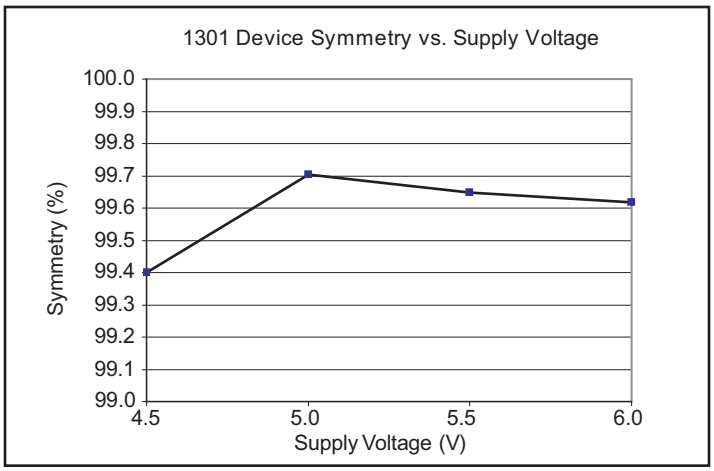

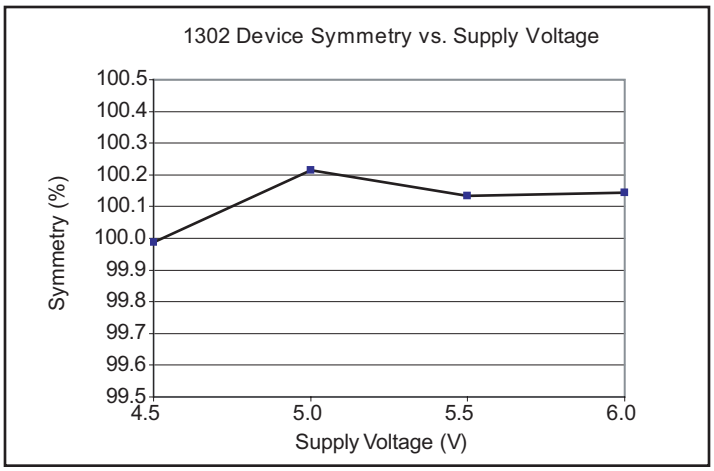

Package LH, 3-Pin; (SOT-23W)

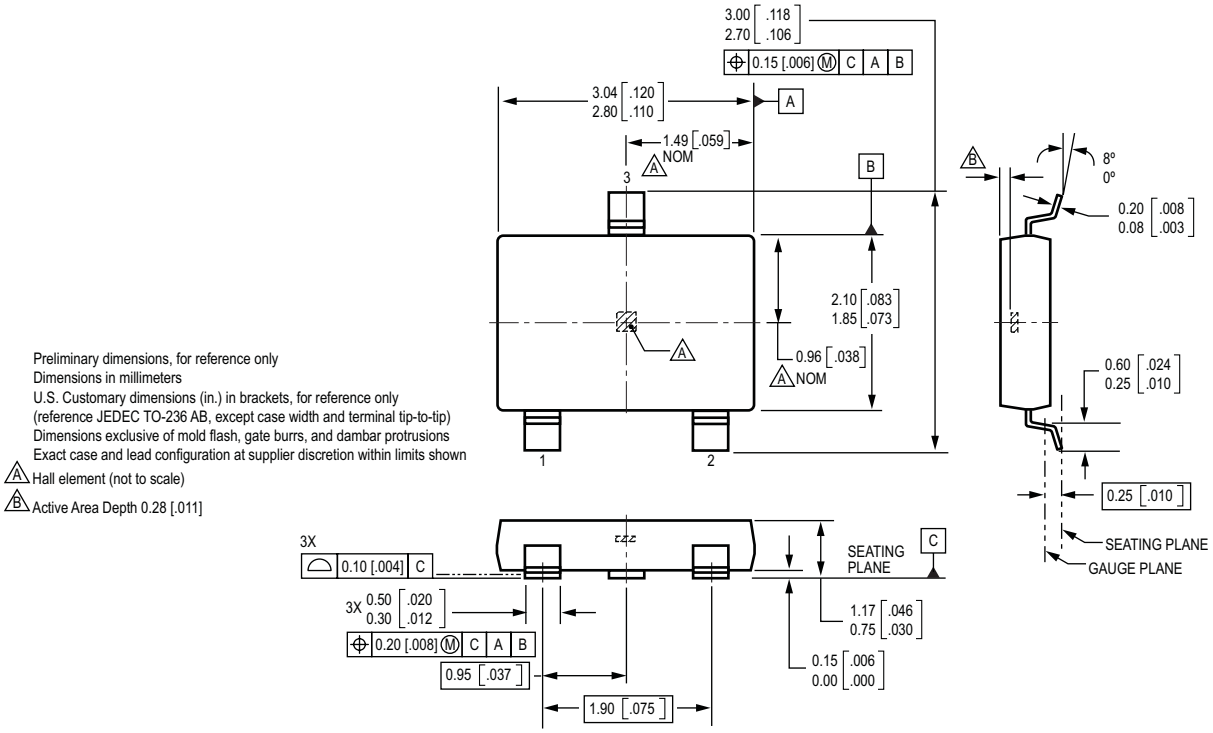

Preliminary dimensions, for reference only
Dimensions in millimeters
U.S. Customary dimensions (in.) in brackets, for reference only
(reference JEDEC TO-236 AB, except case width and terminal tip-to-tip)
Dimensions exclusive of mold flash, gate burrs, and dambar protrusions
Exact case and lead configuration at supplier discretion within limits shown

A Hall element (not to scale)

B Active Area Depth 0.28 [.011]

Pin-out Drawings

Package LH

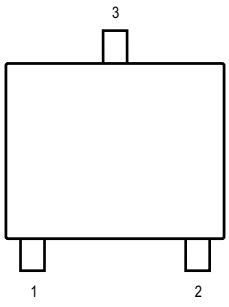

Package UA

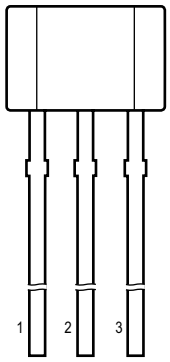

Terminal List

Symbol	Number		Description
	Package LH	Package UA	
VCC	1	1	Connects power supply to chip
VOUT	2	3	Output from circuit
GND	3	2	Ground

Package UA, 3-Pin SIP

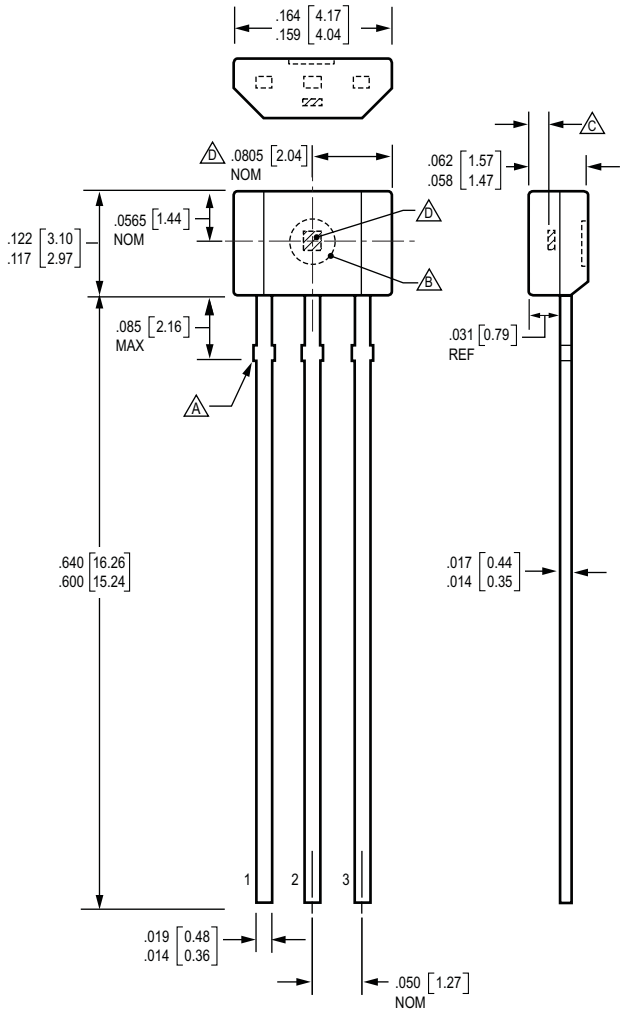

Dimensions in inches
Metric dimensions (mm) in brackets, for reference only

A Dambar removal protrusion (6X)
B Ejector mark on opposite side
C Active Area Depth .0195 [0.50] NOM
D Hall element (not to scale)

Appendix G – Hall Effect Wiring Details

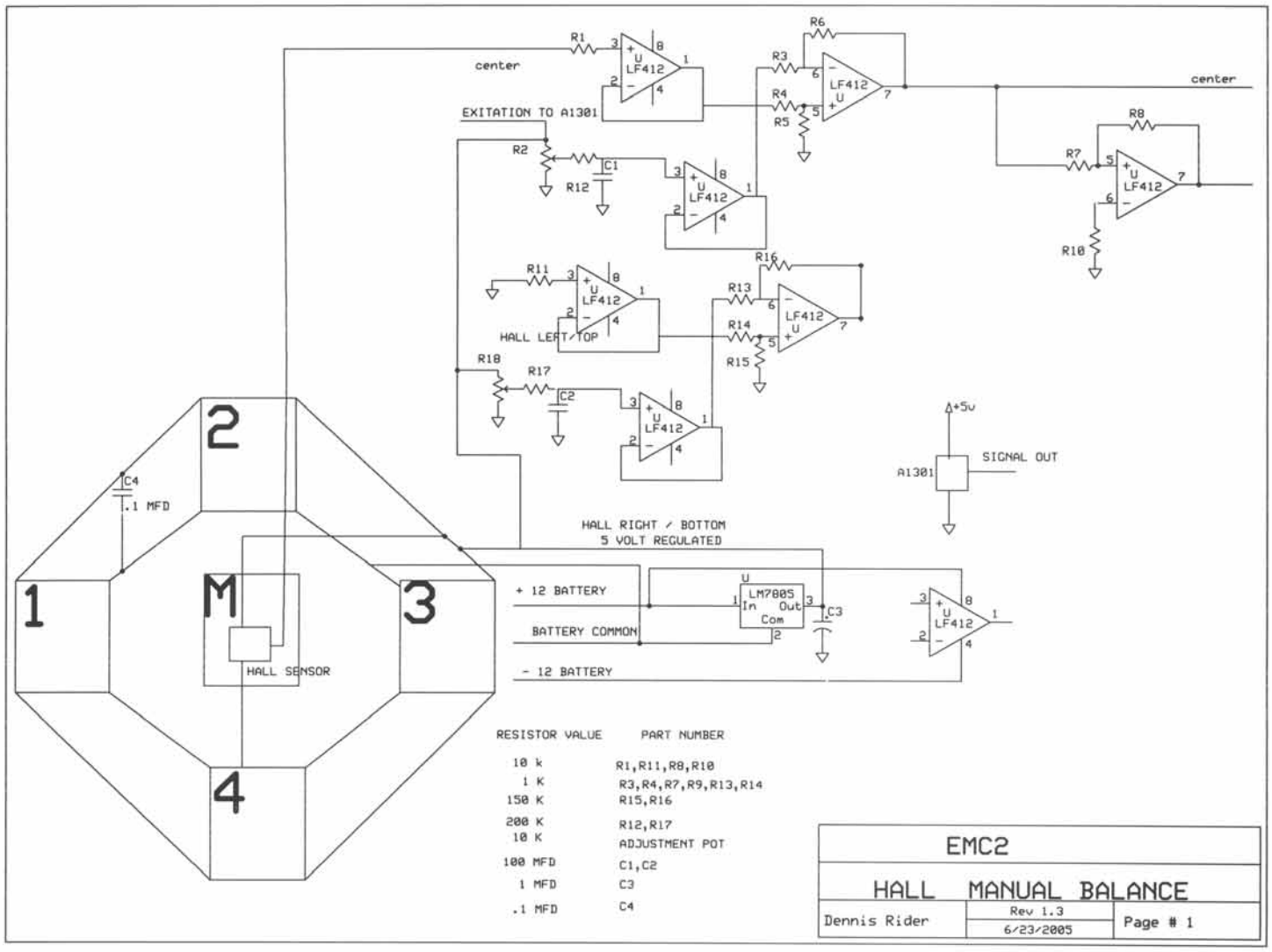
center
EXITATION TO A1301
HALL LEFT / TOP
HALL RIGHT / BOTTOM
5 VOLT REGULATED
+ 12 BATTERY
BATTERY COMMON
- 12 BATTERY
HALL SENSOR
SIGNAL OUT
A1301
+5v
LF412
LM7805
In Out Com
.1 MFD
RESISTOR VALUE PART NUMBER
10 k R1,R11,R8,R10
1 K R3,R4,R7,R9,R13,R14
150 K R15,R16
200 K R12,R17
10 K ADJUSTMENT POT
100 MFD C1,C2
1 MFD C3
.1 MFD C4
EMC2
HALL MANUAL BALANCE
Dennis Rider
Rev 1.3
6/23/2005
Page # 1

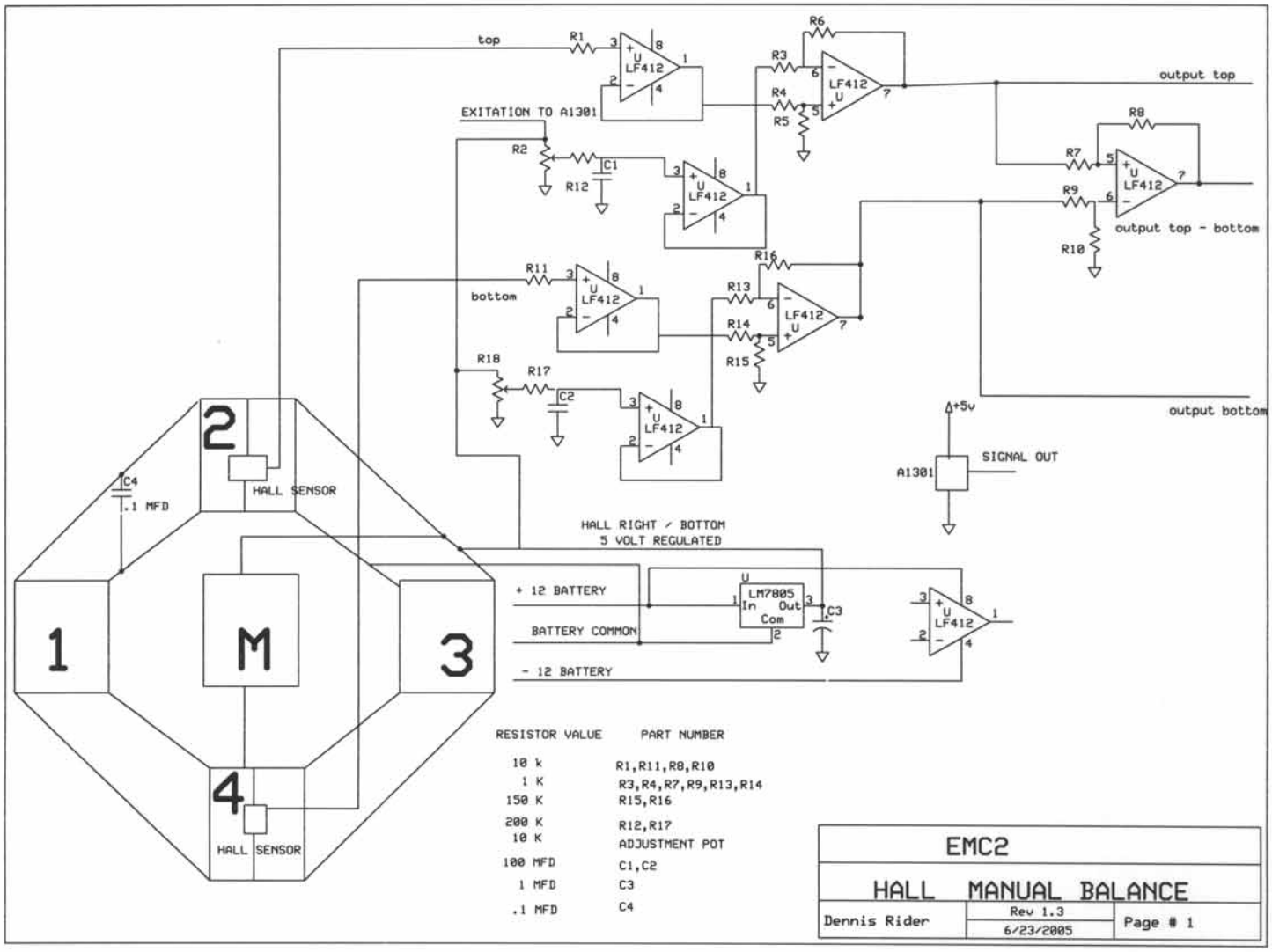
top
R1
R6
R3
R4
R5
output top
EXITATION TO A1301
R2
C1
R12
R8
R7
R9
output top - bottom
R10
R16
R11
bottom
R13
R14
R15
R18
R17
C2
output bottom
+5v
SIGNAL OUT
A1301
HALL RIGHT / BOTTOM
5 VOLT REGULATED
C4
.1 MFD
HALL SENSOR
+ 12 BATTERY
BATTERY COMMON
- 12 BATTERY
LM7805
In
Out
Com
C3
1
2
3
4
M
HALL SENSOR
LF412
RESISTOR VALUE
PART NUMBER
10 k
R1,R11,R8,R10
1 K
R3,R4,R7,R9,R13,R14
150 K
R15,R16
200 K
R12,R17
10 K
ADJUSTMENT POT
100 MFD
C1,C2
1 MFD
C3
.1 MFD
C4
EMC2
HALL MANUAL BALANCE
Dennis Rider
Rev 1.3
6/23/2005
Page # 1

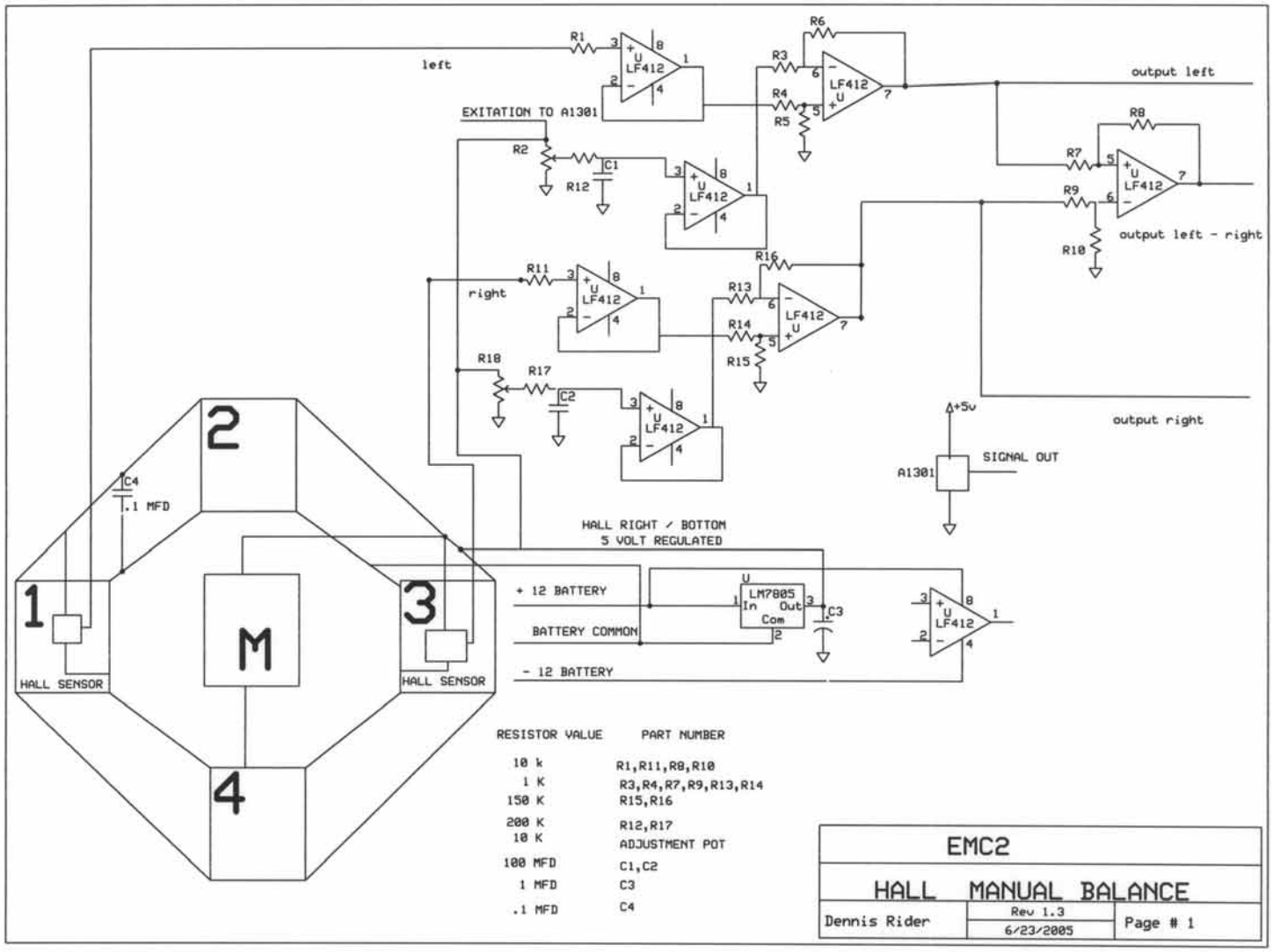
left
EXITATION TO A1301
right
output left
output left - right
output right
+5v
SIGNAL OUT
A1301
HALL RIGHT / BOTTOM
5 VOLT REGULATED
+ 12 BATTERY
BATTERY COMMON
- 12 BATTERY
LM7805
In
Out
Com
LF412
HALL SENSOR
HALL SENSOR
M
1
2
3
4
RESISTOR VALUE PART NUMBER
10 k R1,R11,R8,R10
1 K R3,R4,R7,R9,R13,R14
150 K R15,R16
200 K R12,R17
10 K ADJUSTMENT POT
100 MFD C1,C2
1 MFD C3
.1 MFD C4
EMC2
HALL MANUAL BALANCE
Dennis Rider
Rev 1.3
6/23/2005
Page # 1

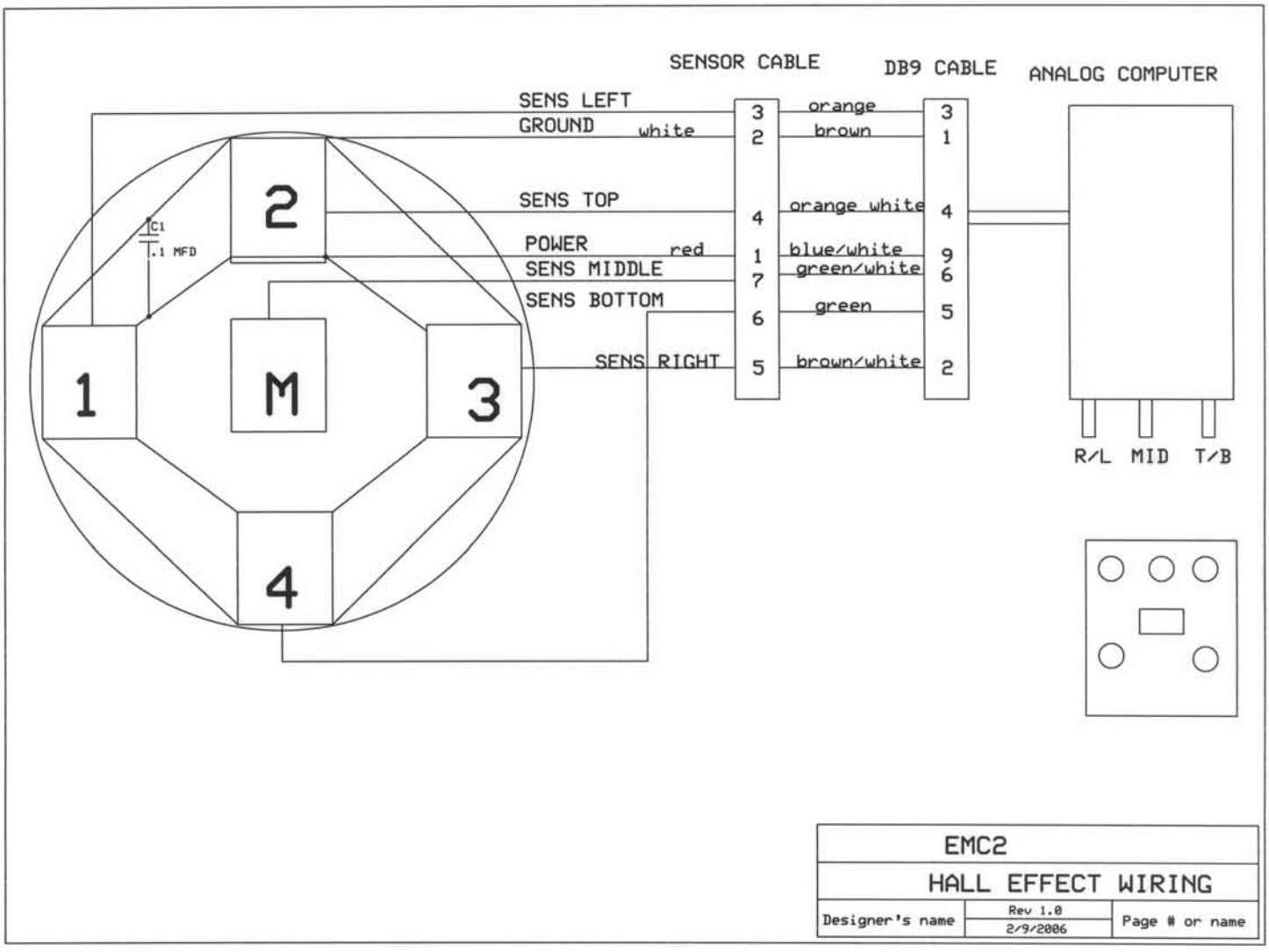
SENSOR CABLE
DB9 CABLE
ANALOG COMPUTER
SENS LEFT
GROUND
white
SENS TOP
POWER
red
SENS MIDDLE
SENS BOTTOM
SENS RIGHT
orange
brown
orange white
blue/white
green/white
green
brown/white
C1
.1 MFD
1
2
3
4
M
R/L
MID
T/B
EMC2
HALL EFFECT WIRING
Designer's name
Rev 1.0
2/9/2006
Page # or name

Appendix H
Dynamic Ductile Crack Growth Simulation Details

TABLE OF CONTENTS

LIST OF FIGURES

H.1 DYNAMIC DUCTILE CRACK GROWTH SIMULATION

In this effort, a dynamic ductile crack growth model was developed to simulate an axially running crack in a pipe with no (air) backfill. The model was developed using the finite element (FE) program ABAQUS/Explicit [1]. Two different types of models were considered for the ductile fracture model, i.e. cohesive element based model and contact surface based model. Also, a 2-D pressure decay model was used to simulate the gas decompression behind the moving crack tip. The initial model was used to simulate one of the Mojave 6-inch pipe test (Test 1-5) with no backfill (air backfilled).

H.1.1 Summary of Mojave Test 1-5

Test 1-5 was a full-scale pipe test conducted for a 6-inch 1020 DOM tubing (t = 0.127 inch) with half of the pipe backfilled with soil and the other half with no backfill (air backfilled). For the numerical simulation only the unbackfilled side is considered.

The average test temperature was 144F and the pipe was initially pressurized to 20.3 MPa (2,950 psi) using N_2. A 152.4 mm (6 inch) explosive cutter was ignited to initiate the crack growth. The crack on the air backfilled side ran the entire length of that side of the pipe and was arrested by the crack arrestor approximately 1.07 m (3.5 feet) from the endcap. The crack distance-time plot for this experiment is shown in Figure 1. From this figure, the steady state fracture speed on the air backfilled side was approximately 197 m/s (647 ft/sec). More detailed information on this test is reported in Section 5.1.10 in Part II of this report.

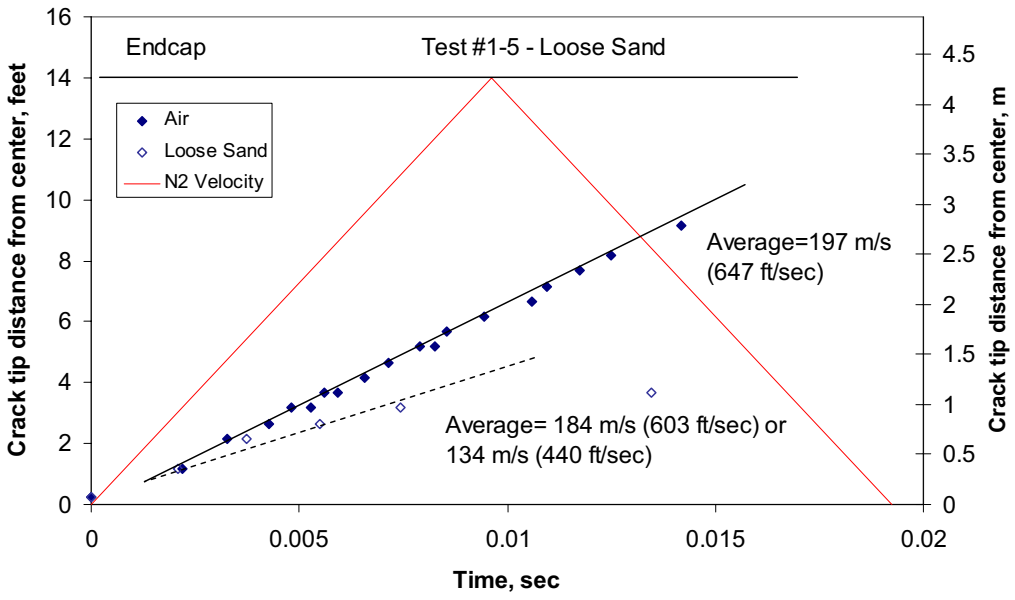

Figure 1 Crack distance-time plot for Test 1-5

H.1.2 Dynamic ductile fracture model based on cohesive elements

Three-dimensional, dynamic, elastic-plastic FE analyses were performed using the general purpose program ABAQUS/Explicit [1] to simulate the ductile crack growth. The cohesive zone model was employed for the crack growth. The interaction between the gas decompression and the structural deformation was model via 2-D pressure decay model developed from experimental results.

H.1.2.1 Finite element model

Figure 2 shows the FE mesh employed in the present effort. Since the current effort was aimed to simulate the air backfilled side of Test 1-5, the FE model was generated for a pipe with no backfill on both sides. For this model, due to symmetry conditions, a quarter model was employed as shown in Figure 2. The cutter crack was modeled as an initial crack. Also, only a portion of the pipe (five times the diameter in length) was modeled in the axial direction since the crack reached steady-state fracture speeds after it grew approximately two times the diameter of the pipe in the actual pipe test. This length restriction was also done to reduce the computational time required for explicit analysis.

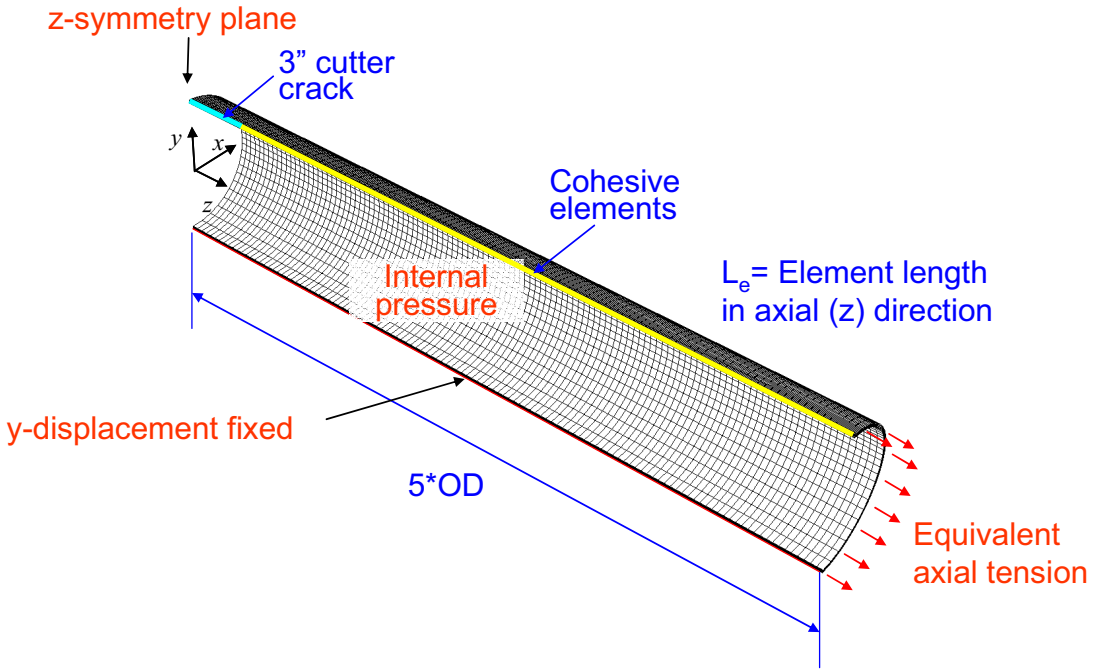

Figure 2 Finite element model used for the present work

8-noded solid elements were used to model the pipe and 8-noded cohesive elements (initially zero thickness) were used to model the cohesive zone which is actually the predefined crack path. In order to capture the through-wall bending effects, five layers of elements were used through the thickness of the pipe. Two different size elements (L_e = 6.35 mm and L_e = 3.175 mm) were used in the axial direction to investigate the mesh size effect. The number of nodes and elements used in these meshes are 37,740 nodes/30,588 element and 75,168 nodes/61,176 elements, respectively.

To hold the pipe in place and provide support, the bottom of the pipe was fixed in the y-direction. Internal pressure was applied to the inner surface of the pipe based on the 2-D pressure decay model described in the following subsection. Furthermore, the corresponding equivalent tension was also applied to the end of the pipe to simulate the end cap effect.

Since only the actual yield (513.7 MPa) and tensile (603.3 MPa) strengths (no full stress-strain curve) for the pipe material were available, the true stress-strain curve was predicted using the actual yield and tensile strengths [2]. Figure 3 shows the predicted true stress-strain curve used for the FE model. The elastic modulus and Poisson's ratio used for the analysis were 206GPa and 0.3, respectively.

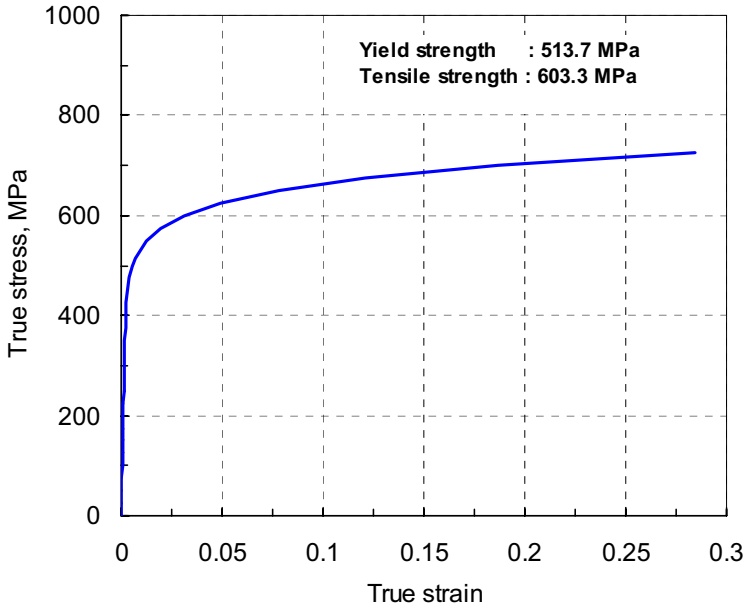

Figure 3 True stress-strain curve of pipe material

The moving crack tip location was calculated from the FE model to calculate the fracture speed. Also, the CTOA values were calculated from the cohesive element at the crack tip.

H.1.2.2 2-D Pressure decay model

In the present effort, a fluid-structure coupled analysis is not considered between the gas decompression and the structural deformation. However, a simplified 2-D pressure decay model based on experimental data was employed. In this model, the internal pressure is divided into two regions, i.e., region ahead of the moving crack tip and the region behind the crack tip. For the region ahead of the crack tip, the pressure is assumed to be equal to the crack tip pressure, i.e., the decay from full-pressure to the steady-state crack tip pressure ahead of the crack was ignored. For the region behind the crack tip, where the flap opening occurs, the pressure decay is expressed as an exponential function that varies around the circumference as shown in Figure 4.

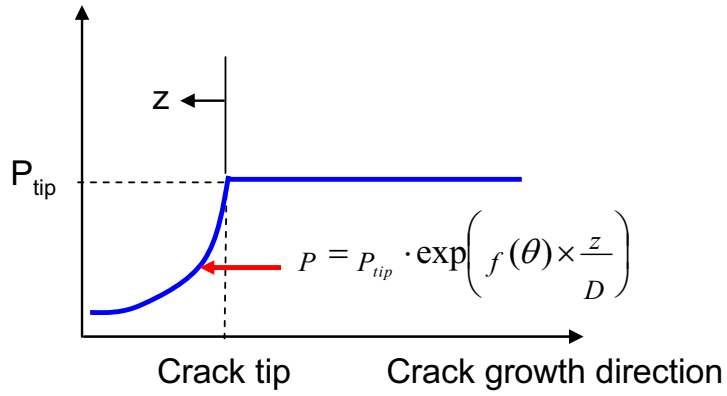

Figure 4 Internal pressure distribution based on 2-D decay model

First, in order to calculate the steady state crack tip pressure for Test 1-5, PIPE-DFRAC was employed. Figure 5 shows the decompression curve predicted for Test 1-5. The pressure at the experimentally measured fracture velocity, 197.2 m/s (647 ft/sec), is defined as the steady state crack tip pressure, which is 9.93 MPa (1.44 ksi).

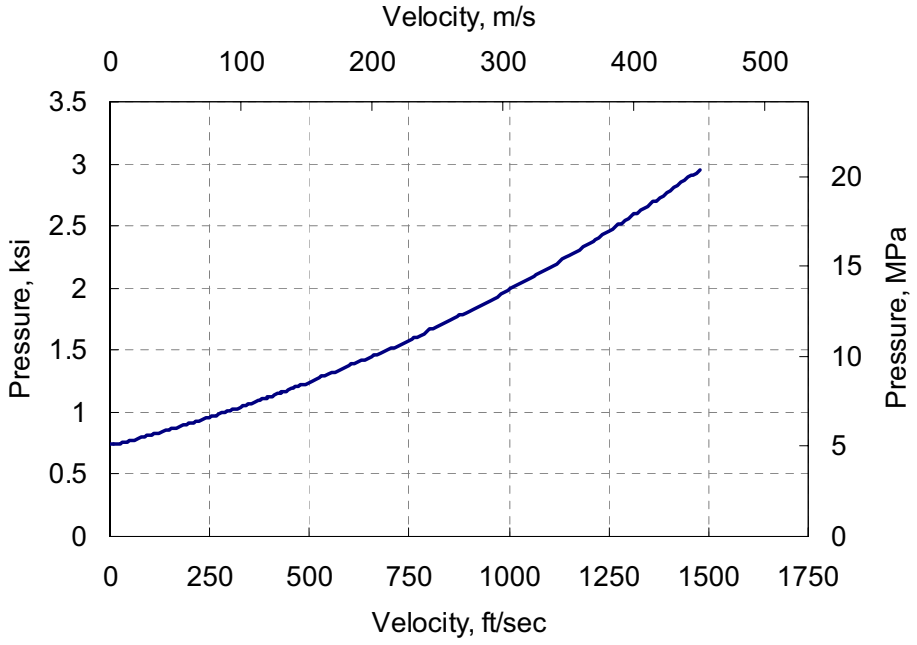

Figure 5 Decompression curve of Test 1-5 calculated from PIPE-DFRAC

In the present FE model, the initial crack tip pressure was set equal to the initial internal pressure, i.e. 20.3 MPa. Moreover, the crack tip pressure was linearly reduced to the steady state crack tip pressure (9.93 MPa) in 0.2 ms. From this linear pressure drop, the crack tip reached steady state in 1.5 ms which is close to the time measured from the actual pipe test, 2.0 ms.

The exponential function for the pressure decay behind the crack tip was developed by curve fitting the pressure values obtained during a full-scale test conducted for a 56-inch diameter pipe [3]. The insert and the dashed lines in Figure 6 show the actual test data from Ref. [3]. In this figure, the normalized pressure (P/P_{tip}) is plotted against the normalized distance behind the crack tip (z/D), where z is the distance from the crack tip. As shown in this figure, the pressure was measured at four different locations around the circumference. The solid lines in Figure 6 show the exponential pressure decay used in the present model. Linear interpolation of these four curves is used to determine the pressure around the circumference.

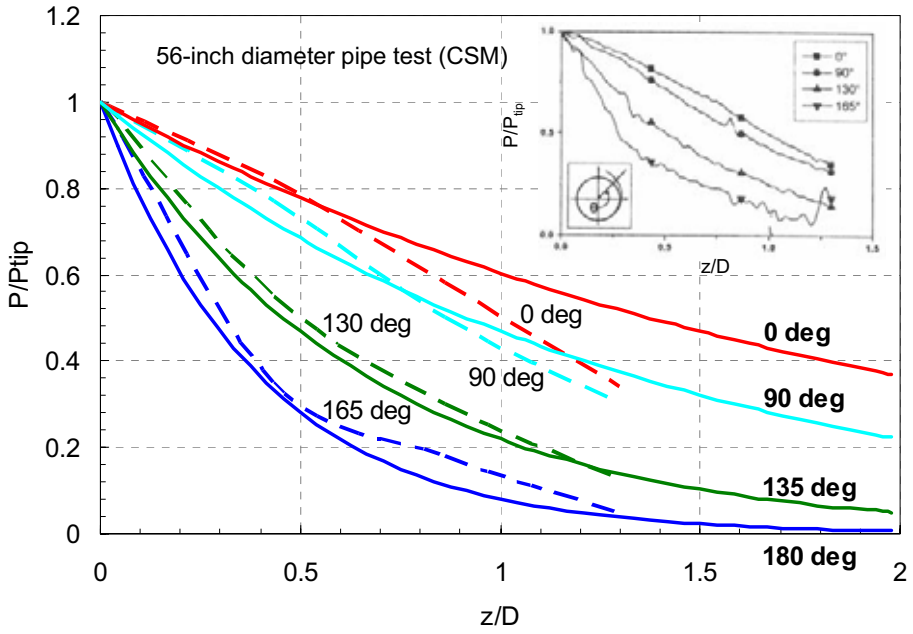

Figure 6 2-D pressure decay behind the crack tip based on pipe test results

Since the test data from Ref. [3] was from a 56-inch pipe, another set of test data was examined to investigate the effect of pipe diameter on the pressure decay behavior. Figure 7 shows a pressure decay curve obtained from a 12.75-inch diameter pipe test [4]. The pressure was measured at 140 degrees from the bottom of the pipe. This curve is compared with the present 2-D decay model in Figure 7 and shows reasonable agreement near the crack tip. However, as the distance from the crack tip increases, the test data is higher than the present model. Since data was provided for only one location around the circumference, it was not clear if this difference was a diameter effect. Based on the results shown in Figure 6 and Figure 7, the present 2-D decay model was applied to account for the pressure decay behind the crack tip.

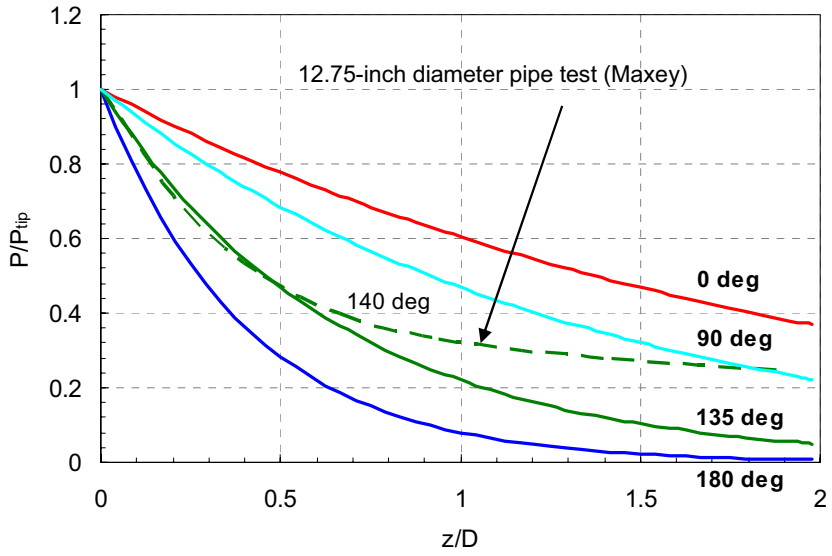

Figure 7 Pipe diameter effect on 2-D pressure decay behind the crack tip

H.1.2.3 Determination of cohesive model parameters

The cohesive model idealizes the fracture process in solids as occurring within thin layers confined by two adjacent virtual surfaces. The loss of cohesion and thus crack formation/extension within a solid may be viewed as the progressive decay of otherwise intact tension and shear stresses across the adjacent surfaces. The introduction of interface constitutive laws specified between the tractions and displacement jumps across the surfaces provides a phenomenological description for the progressive fracture in ductile metals caused by micro-void nucleation, growth and coalescence. Such cohesive models introduce an intrinsic length-scale in the local fracture process which enables fracture process zones on the specimen/component scale to evolve as a natural outcome of the computations.

In the present model, the cohesive element embedded in ABAQUS is employed. A bilinear type of traction-separation curve is used to define the constitutive behavior of the cohesive elements as shown in Figure 8. To define the bilinear curve in Figure 8, two of the three parameters, i.e. Γ, σ_{max}, and $\delta_{critical}$, are required. Here, Γ is the area under the curve which is actually the effective cohesive energy density, or the work of separation per unit area of cohesive surface, σ_{max} is the maximum traction which corresponds to damage initiation point, and $\delta_{critical}$ is the critical separation between the two surfaces when the cohesive element are deleted from the FE model.

The cohesive parameters must be determined by parameter fitting. Typically, $_{J}$IC is used to define the effective cohesive energy density, Γ [5,6]. Since $_{J}$IC value was not available for the pipe material used in Test 1-5, an estimation was made from a Charpy V-notch plateau energy, CPV, using the relationship reported in Ref. [7]. Figure 9 shows the relationship between CVP and $_{J}$IC for several ferritic piping steels. As shown in this figure, there is a wide range of scatter for such relationship. Since the dynamic fracture

toughness is typically higher than the quasi-static fracture toughness [8], the upper bound value of the $_{J}$IC at CVP = 46 J (33.9 ft-lb) was defined as Γ(= 120 kJ/m^2). The maximum traction, σ_{max}, is usually defined as a value between 2.5σ_y-3.0σ_y [6]. In the present model, the σ_{max} was varied within this range until the calculated fracture speed matched that of the experiment. The final value used for the model was σ_{max} = 1450 MPa.

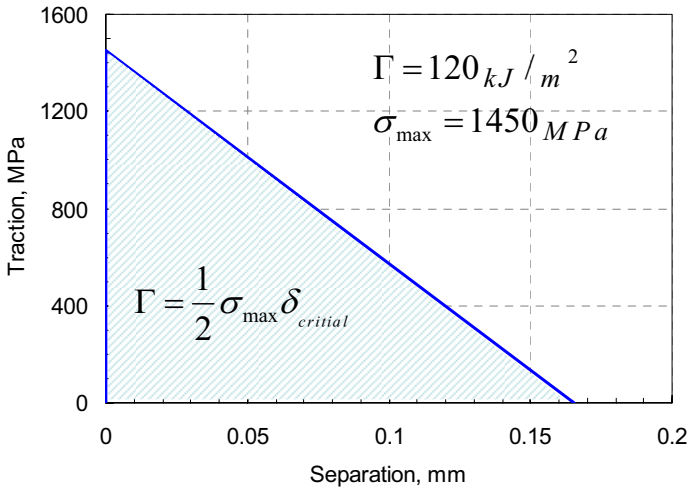

Figure 8 Traction-separation curve for cohesive elements used in the present model

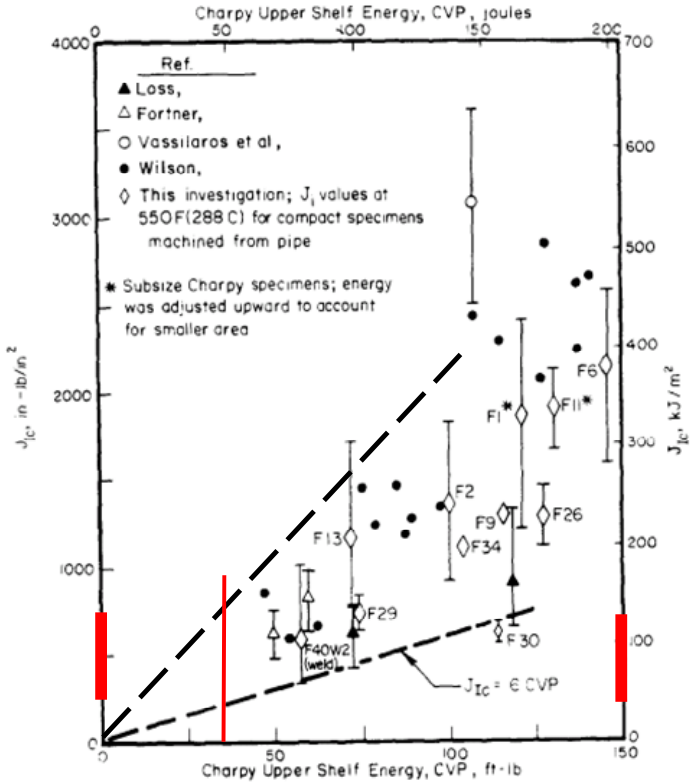

Figure 9 J_{IC} versus Charpy V-notch plateau energy for several ferritic piping steels

H.1.2.4 Results

Figure 10 shows the crack tip location obtained from the FE analyses as a function of time. The results are plotted for the two different FE meshes (Le = 6.35, 3.175 mm) employed in the present effort. As shown in this figure, the two meshes showed a slight difference in crack length as a function of time. However, the slope of the curve, i.e. the fracture speed, showed good agreement in the steady state region (time>1.5ms). The fracture speed obtained from the present models showed good agreement with the experimentally measured fracture speed (197.2 m/s). This good agreement is due to the fact that the cohesive parameters were calibrated to match the test fracture speed. In the later part of this subsection, the cohesive parameters are validated by comparing the calculated and measured CTOA values.

In Figure 11, the present FE results in the steady-state region are linearly extrapolated for comparison with the actual test result. As shown in this figure, the FE results match well with the test result under steady state conditions. It is also shown that the difference of the two FE models fall within the scatter of the test data.

It has been demonstrated in past research [5,6] that cohesive zone models can be used to estimate the experimentally measured CTOA values. Figure 10 shows the CTOA values calculated from the present model as a function of time. As shown on the right-hand side of the figure, the CTOA was calculated at element extinction of the cohesive element at the crack tip. The CTOA values at the beginning of the crack growth are relatively high, however as the crack growth increases, the CTOA values decrease and become independent of crack growth. This is consistent with the experimental results reported for quasi-static crack growth experiments [5,6]. As shown in Figure 10, although the two meshes yielded the same fracture speed, the meshes produced different CTOA values (8.5 degree versus 15.2 degree), which demonstrates that the fracture model developed in this effort is mesh dependent for calculating CTOA.

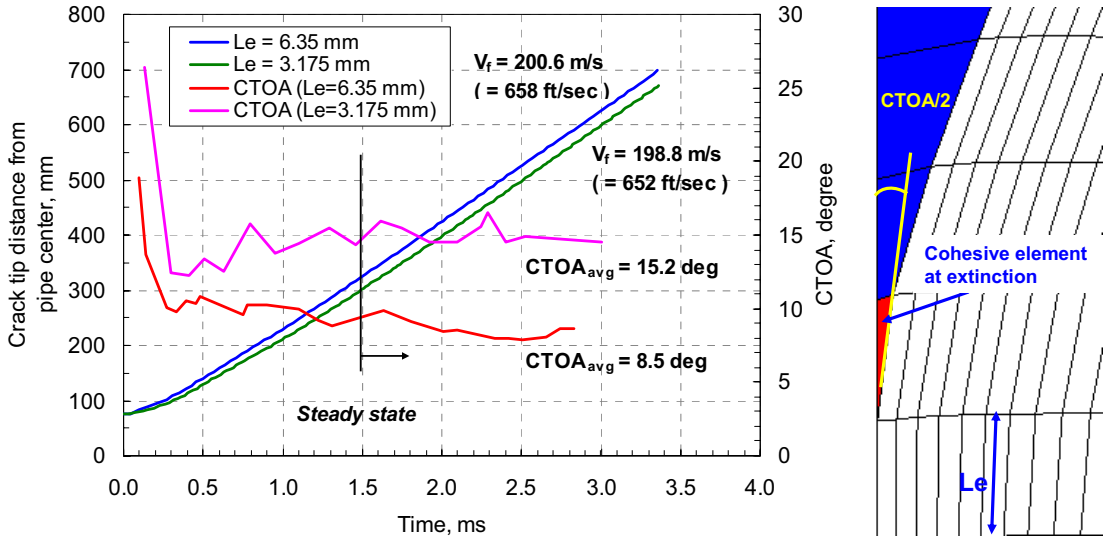

Figure 10 Fracture speed and CTOA calculated from FE analyses

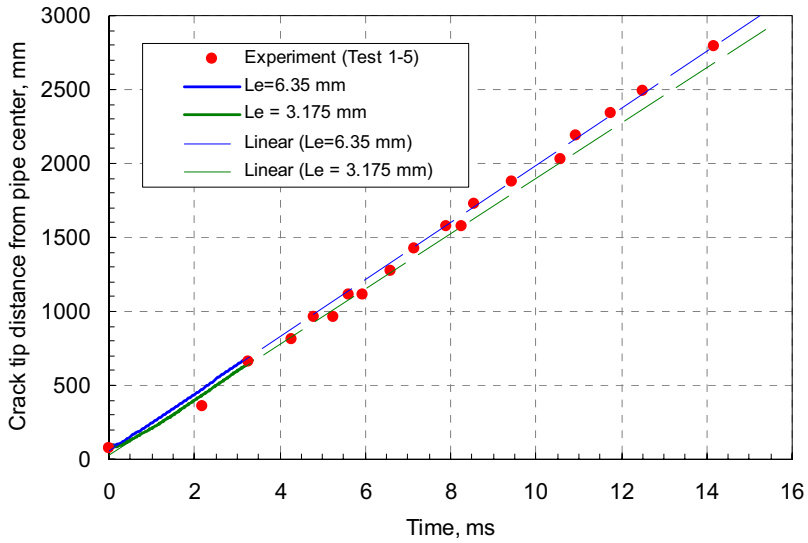

Figure 11 Comparison between test result and linearly extrapolated FE results

To validate the CTOA value calculated from the FE model, Drop Weight Tear Test (DWTT) was performed for the pipe material. Since the pipe thickness was too thin, it was not possible to make a one pipe thickness DWTT specimen (which would buckle during the DWTT). To overcome this limitation, a laminated DWTT specimen was designed. Figure 12 briefly shows how the laminated DWTT specimen was manufactured. Six pipe segments were cut out from three pipes (Pipe 1-2, 1-4, 1-5; two segments from each pipe) from which had similar CVP values as the pipe used for Test 1-5. These segments were flattened, welded together and press-notched for DWTT.

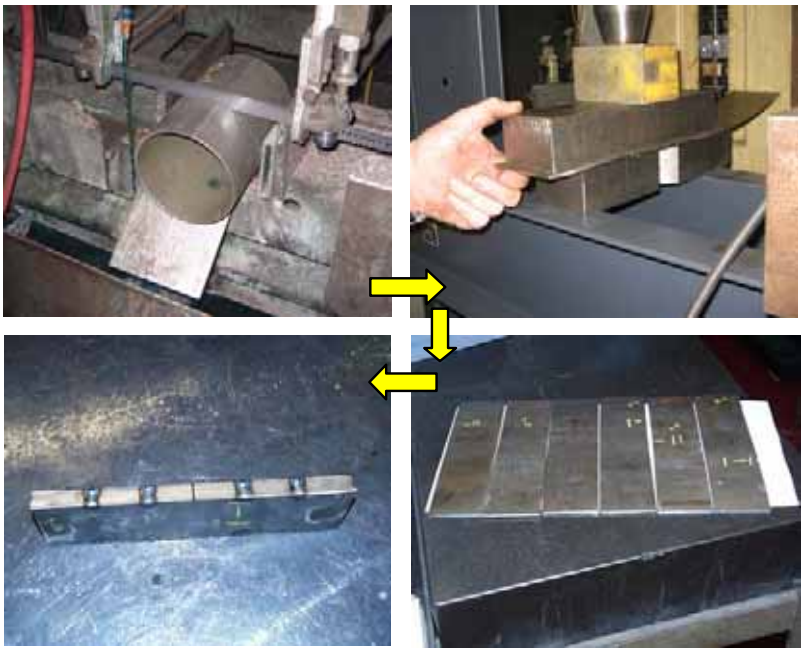

Figure 12 Manufacturing process of a laminated DWTT specimen

An instrumented DWTT was conducted using the laminated specimen, where the crack length and CTOA were measured using a high-speed camera. This method was used successfully in many past programs [9]. The plot on the left side of Figure 13 shows the measured crack length and CTOA as a function of time. As shown in this plot, there is a region where the crack speed and the CTOA remain constant, i.e. steady state crack growth. The average CTOA value during the steady state crack growth was 7.81 degree. The image on the right side of Figure 13 shows a close-up view of the crack tip in the DWTT specimen, illustrating how the COTA was measured from the high-speed video data.

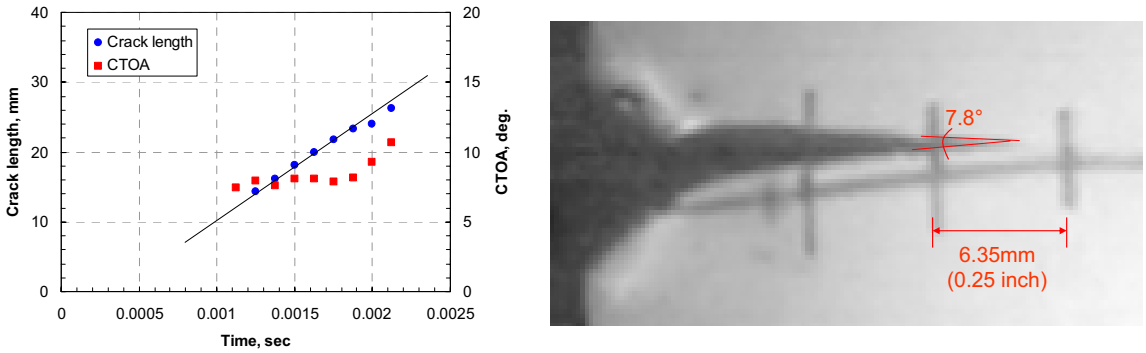

Figure 13 Experimental data illustrating constant crack speed and CTOA region (left) and close-up view of crack tip in DWTT specimen (right)

Results obtained from the instrumented DWTT demonstrate that the CTOA value calculated from the FE model with Le=6.35 mm shows reasonable agreement with the CTOA measured from the laminated DWTT specimen (8.5 degree versus 7.81 degree).

Figure 14 shows the deformed pipe shape during crack growth, which is similar to the actual pipe test, where the flaps show a wavy deformation behind the moving crack tip.

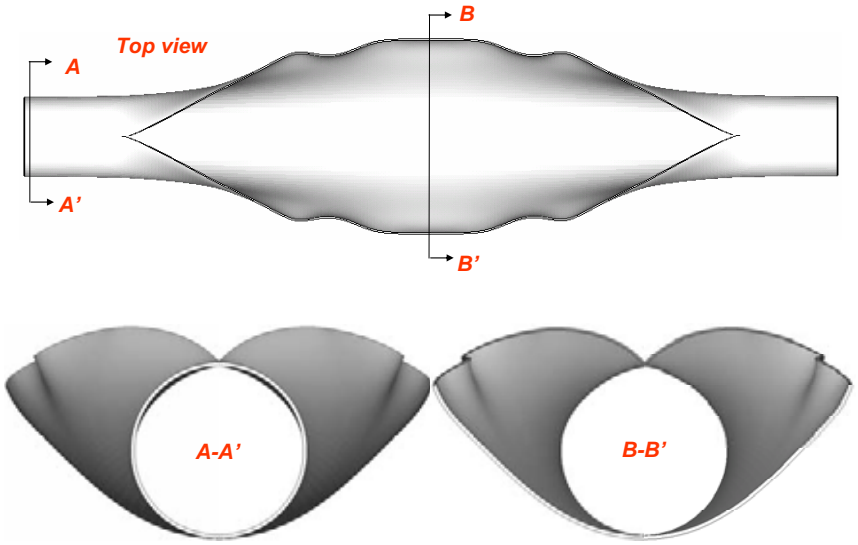

Figure 14 Pipe deformation due to crack growth (Le=6.35mm, time=2.76ms)

H.1.3 Dynamic ductile fracture model based on contact surfaces

In this effort, the feasibility of simulating crack propagation using contact surfaces in ABAQUS/Explicit has been investigated. The basic idea is to model the cracking plane as a surface-to-surface contact. An initial crack is simulated by setting the stress on the crack face to zero. The other portion of the surface on the cracking plane is kept closed by proper surface stress, which is implemented in a user subroutine VUINTER in ABAQUS. This surface stress is a particular value that is greater than the hoop stress in the pipe. This method includes the following steps:

1) Calculate the CTOA from coordinates and displacements of the nodes on slave surface.
2) If the CTOA is greater than a given critical CTOA, the crack propagates a given length, typically the size of one element in axial direction.
3) Release the stress on the new crack face.
4) For each node on the contact surface but not on the crack face, calculate contact stress that can cancel the hoop stress to keep the surfaces in contact closed.
5) In another user subroutine, i.e., VDLOAD, the applied pressure is redistributed according to the gas decompression curve and current crack tip position.

Two methods were examined in this preliminary study. In the first method, the model consisted of shell elements and 3-D solid elements as shown in Figure 15(a). The 3-D solid elements were used to capture the through-wall bending effects and provide surface-to-surface contact. Shell elements were used to reduce the computation time.

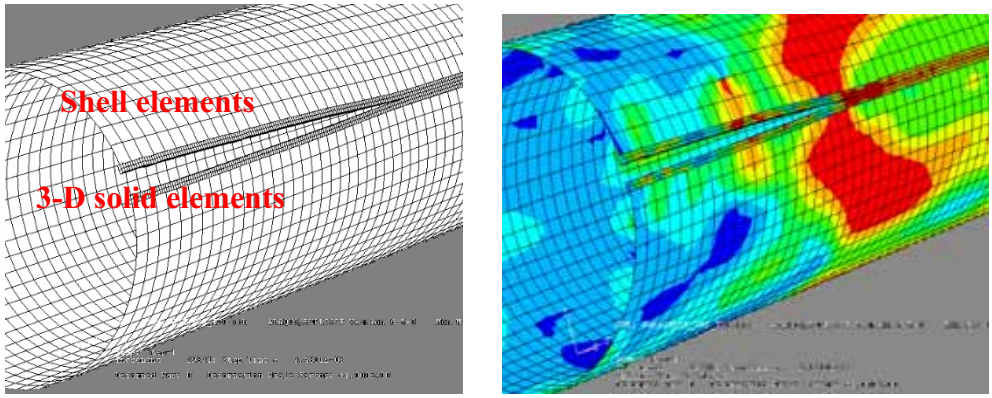

(a) (b)

Figure 15 Crack growth simulation using shell elements and 3-D solid elements

Although this method reduced the computational effort, it was found that the stress field is discontinuous between solid elements and shell elements as shown in Figure 15(b). Therefore, the second method was proposed to use 3-D solid elements for the pipe, while a rigid shell was put on the symmetric cracking plane to serve as a master surface for the contact. Only a quarter pipe model was used due to symmetry, as shown in Figure 16(a). The boundary conditions and loadings were the same as the model using cohesive elements. To reduce the computation time, different mesh densities were applied. The mesh is finer close to cracking plane and coarser away from cracking plane. The equivalent plastic strain plot in Figure 16(b) shows a smooth contour plot.

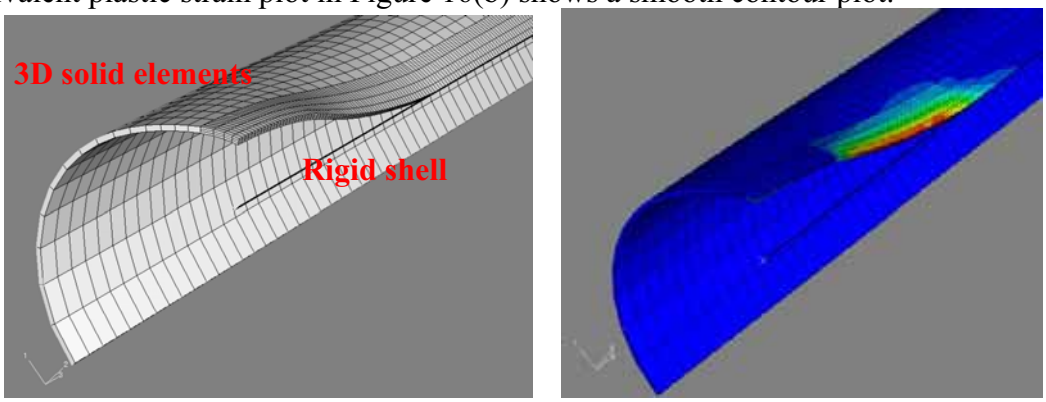

(a) (b)

Figure 16 Crack propagation simulation using 3-D solid elements

A great effort was used for adjusting the contact properties since the distance between the surfaces in contact should be kept as small as possible for CTOA calculations, which means a high stiffness for the contact elements. However, a high stiffness in ABAQUS/Explicit produces a small time increment and unacceptable computer time.

From the results generated, the fracture velocity was not constant using this contact definition. Instead, it seems to have a constant acceleration, as shown in Figure 17. Figure 18 compares the crack growth profile obtained from the cohesive element model and contact surface model. In the early stage of crack growth, the fracture speed of the contact surface model is lower than that of the cohesive element model. However, as the

crack propagates, the fracture speed of the contact surface model increases and becomes higher than that of the cohesive model. The contact surface model is either not working or requires additional time to find the right contact properties or some compromise between acceptable contact tolerance and computer time.

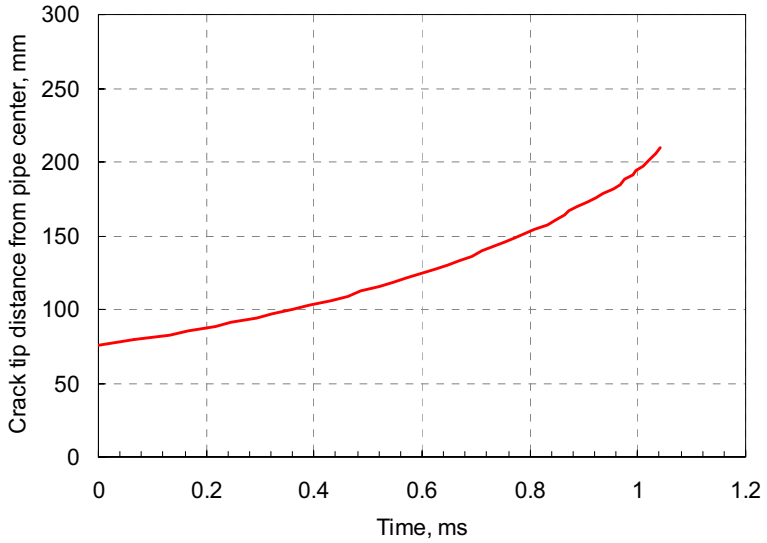

Figure 17 Crack tip location calculated from the contact surface model as a function of time

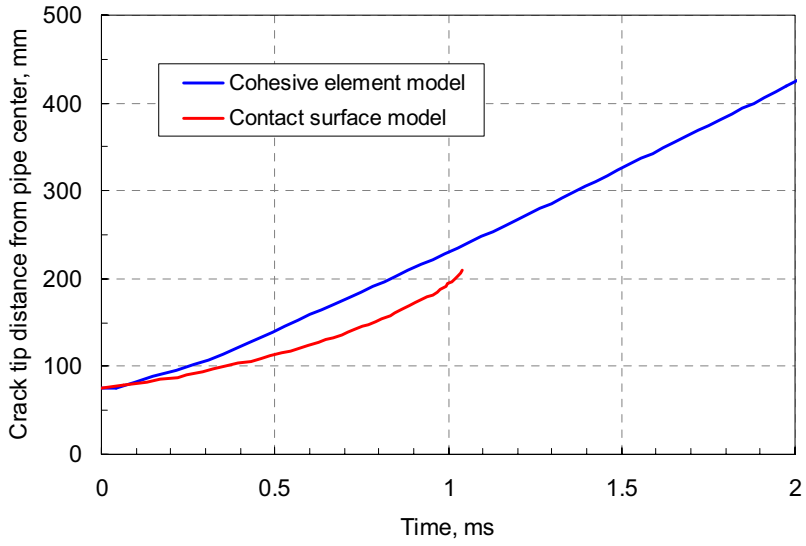

Figure 18 Comparison between cohesive element model and contact surface model

H.2 VERIFICATION OF FRACTURE SPEED FOR SMALL DIAMETER PIPES

In Section 5.5.3, Part II of this report, the original Battelle Two-Curve(BTC) analysis was modified (i.e., the exponent in the fracture velocity equation was modified from 1/6 to 1/2.65) for small-diameter pipes based on limited full-scale pipe test results (for detailed information see Section 5.5.3 in Part II). In the present effort, an attempt is made to verify the modified fracture velocity equation for small-diameter pipes using the dynamic ductile crack growth model (cohesive element model) developed in the previous section.

Figure 19 shows the fracture velocity predictions made for Test 1-5 using the original and the modified BTC method. As shown in this figure, the fracture speed predicted from the original BTC is 281 m/s, which is approximately 43% higher than the measured fracture speed (197 m/s). On the other hand, the fracture speed predicted from the modified BTC is 198 m/s, which shows excellent agreement with the test results. Note that the fracture speed calculated from the FE based model was 200.6 m/s (the cohesive parameters were calibrated for the FE model to match the test fracture speed).

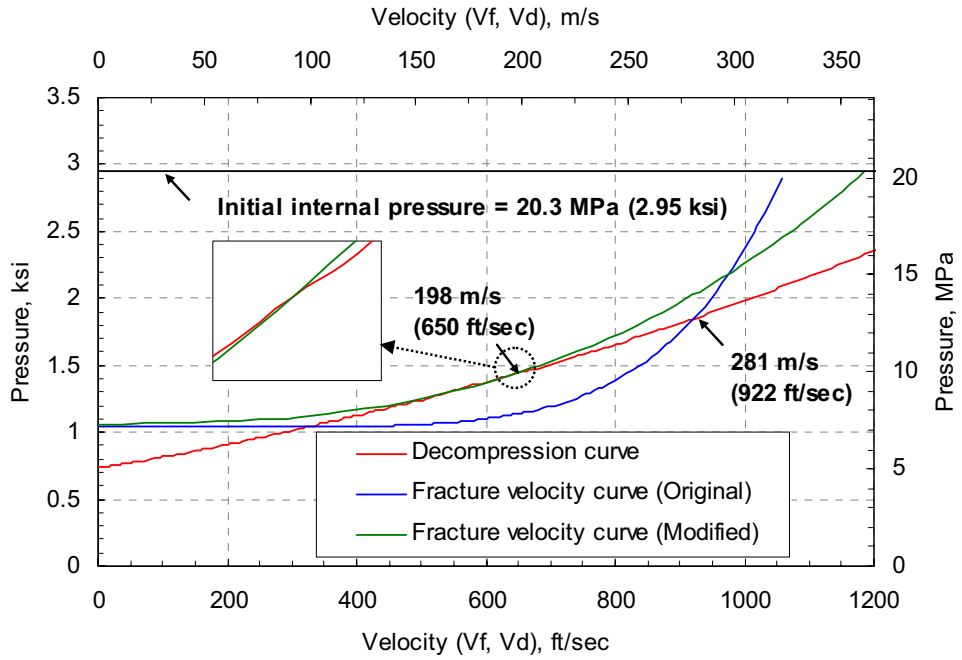

Figure 19 Fracture speed predictions for Test 1-5 using the original and the modified Battelle-Two-Curve method

To further verify the applicability of the modified BTC, an additional FE analysis was performed for a case with a different initial pressure (21.4 MPa), whereas the other parameters (including the cohesive parameters) were kept same as the FE model used for Test 1-5. Note that the FE mesh with Le=6.35 mm was used for this analysis. Figure 20 shows the fracture speed and CTOA calculated from the FE analysis. Due to the increase of the initial pressure (from 20.3 MPa to 21.4 MPa), the fracture speed increased from

200.6 m/s to 214 m/s. As expected, the CTOA value for this case showed good agreement with the CTOA value calculated for Test 1-5. This demonstrates that the CTOA calculated from the present dynamic ductile crack growth model can be used as a steady state fracture resistance criterion.

The original and the modified BTC were used to predict the fracture speed. As shown in Figure 21, the fracture speed predicted from the original BTC was 287 m/s, where as the modified BTC predicted 244 m/s. The fracture speed predicted from the modified BTC was much closer to that of the FE result compared to the original BTC (14% versus 34% higher than FE result). The results shown in Figure 19 and Figure 21 demonstrate that the original BTC overpredicts the fracture speed for small-diameter pipes. Although the modified BTC seems to work well for the cases considered in the present effort, further investigation is needed since the modified BTC proposed in this effort is based on limited test results.

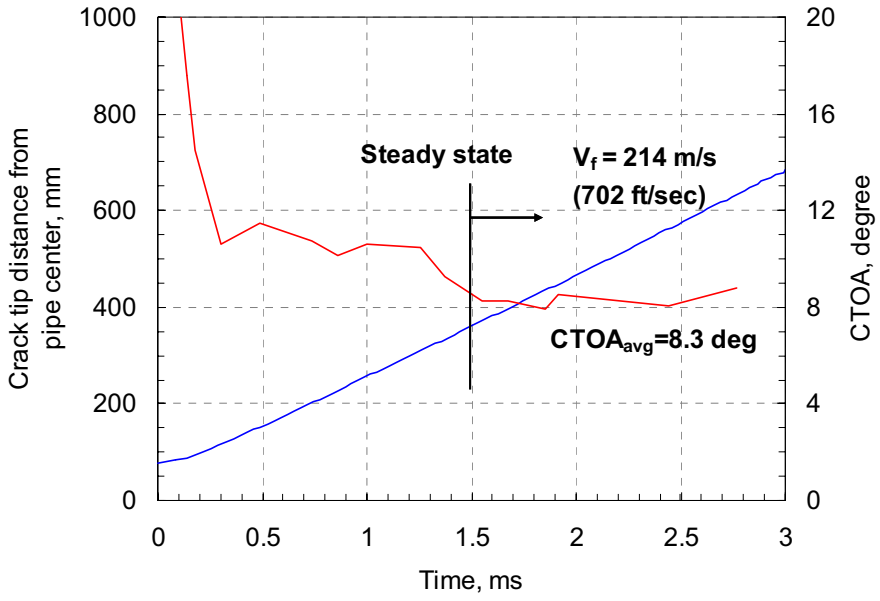

Figure 20 Fracture speed and CTOA calculated for the case with initial pressure of 21.4 MPa

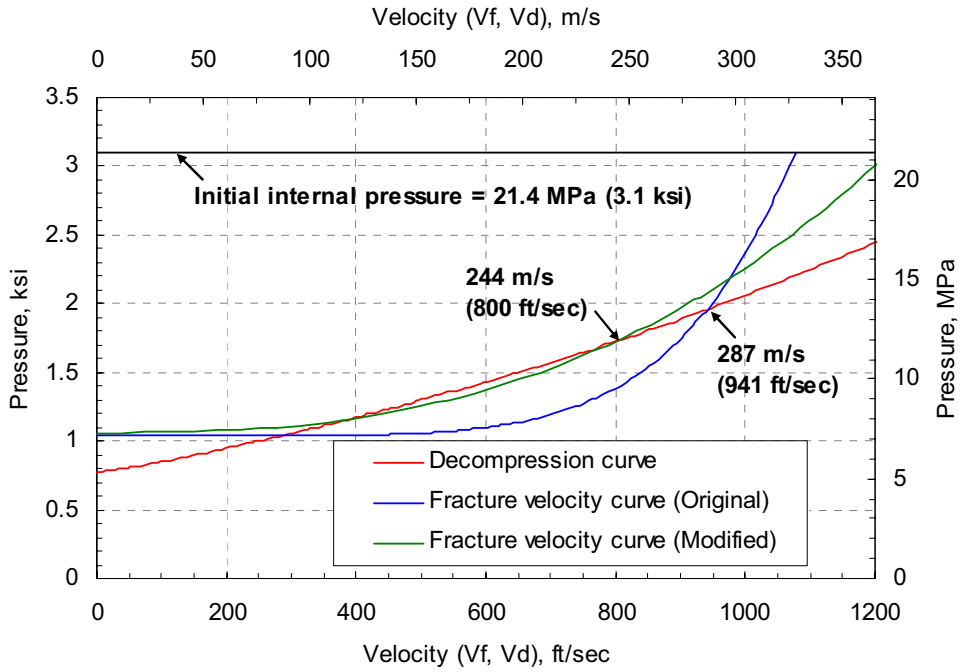

Figure 21 Fracture speed predictions using the original and the modified Battelle-Two-Curve method for case with initial pressure of 21.4 MPa

H.3 REFERENCES

1 *ABAQUS Version* 6.5, ABAQUS Inc., Providence, USA (2005).

2 Bloom, J. and Malik, S., "Procedures for the Assessment of the Integrity of Nuclear Pressure Vessels and Piping Containing Defects," EPRI NP-2431 (1982).

3 Berardo, G., Salvini, P., Mannucci, G., and Demofonti, G., "On Longitudinal Propagation of a Ductile Fracture in a Buried Gas Pipeline: Numerical and Experimental Analysis," Proceedings of the International Pipeline Conference 2000, Calgary, Canada, Vol. 1 (2000), pp. 287-294.

4 Maxey, W.A., "Gas Expansion Studied," NG-18 Report, No. 133 (1983).

5 Scheider, I., Schödel, M., Brocks, W., and Schönfeld, W., "Crack Propagation Analyses with CTOA and Cohesive Model: Comparison and Experimental Validation," *Engineering Fracture Mechanics,* 73 (2006), pp. 252-263.

6 Roy, Y.A. and Dodds, R.H., "Simulation of Ductile Crack Growth in Thin Aluminum Panels Using 3-D Surface Cohesive elements," *International Journal of Fracture,* 110 (2001), pp.21–45.

7 Wilkowski, G.M. and Scott, P.M., "A Statistical Based Circumferentially Cracked Pipe Fracture Mechanics Analysis for Design or Code Implementation," Nuclear Engineering and Design, 111 (1989), pp.173-187.

8 Anderson, T.L., "Fracture Mechanics-Fundamentals and Application," CRC Press (1995)

9 D.L. Rudland, G.M. Wilkowski, Z. Feng, Y.-Y. Wang, D. Horsley, A. Glover, "Experimental Investigation of CTOA in Linepipe Steels," *Engineering Fracture Mechanics*, 70 (3-4) (2003) pp. 567-577.

Program Final Report

on

FIRST MAJOR IMPROVEMENTS TO THE TWO-CURVE DUCTILE FRACTURE MODEL – PART II MOJAVE TESTING DETAILS

Emc^2 project number 03-G78-01

to

U.S. Department of Transportation
Research and Special Programs Administration
Washington DC 20590
Agreement No. DTRS56-03-T-0007

and

Pipeline Research Council International, Inc.
Arlington, VA 22209
PR-276-04505

by

D. Rudland, D.-J. Shim, H. Xu, D. Rider,
P. Mincer, D Shoemaker and G. Wilkowski

Engineering Mechanics Corporation of Columbus
3518 Riverside Drive
Suite 202
Columbus, OH 43221

May 2007

TABLE OF CONTENTS

LIST OF FIGURES

LIST OF TABLES

1 INTRODUCTION

Part II of this report gives the details of the Mojave testing program. In this effort, small diameter burst tests were conducted with different well-controlled backfill conditions to determine the effect of the soil properties on the steady-state crack propagation speed. The experiments were conducted in two series, one each year of the program.

2 DEVELOPMENT OF TEST PLAN

The original plan for the Mojave experiments was to perform six small diameter crack propagation experiments each year of the program (12 total). Each of these crack propagation experiments was to be conducted with different soil types under different moisture/compaction conditions. Each experiment would use one soil type on one half of the pipe and no soil on the other side of the pipe. This way a relative change in the crack fracture speeds could be determined. The original plan for the first year Mojave experiments was to perform four experiments on a clay soil (cohesive) and two experiments with the native Mojave sand soil (non-cohesive). The second year of experiments was to include four experiments on the third soil type (some combination of cohesive and non-cohesive) and the remaining two experiments on the native sand. However, as is typical with large experimental programs, budget issues, experimental difficulties, and unexpected results caused the test plan to be modified as the program progressed. Details of the experimental test matrix per year are given in the discussion below.

3 PIPE MATERIALS

One of the most difficult parts of this program was the ability to find pipe material suitable for this type of testing. Smaller diameter pipe was desired in order to keep costs reasonable, and the smaller the pipe size, the lower the Charpy energy needed to guarantee a ductile propagating crack. In order to meet the objectives, it was essential to conduct the tests so that a steady-state ductile fracture propagates through the test soil, as well as the reference backfill (air).

Current day steel-making practice is much better than it was in the 1980's. API pipe purchased in the past (high sulfur content) for similar tests is currently not available in North America, Japan, or Europe. Importing pipe from 3rd world countries and getting the suitable mechanical properties was not possible. Consequently, alternative pipe/tubular products were investigated Down-hole tubular goods, such as N80 casing, were a possibility, but discussions with Lone Star Steel Company were not encouraging.

The material chosen for use in this program was 1020 DOM (drawn over mandrel) mechanical tubing. This material was chosen over linepipe steel since current pipe mills can not produce line pipe steels with the sufficiently low toughness that is required for crack propagation in these experiments. This DOM tubing material was successfully used in a number of past small-scale ductile fracture pipe tests [1]. This tubing is heavily cold-worked so the yield strength is high and the Charpy energy is low. One-foot rings from each of the 23 pipes were sent for material property characterization. Tensile properties were extracted from one pipe length in both the longitudinal and transverse direction to verify the mill test report.

In addition to longitudinal and transverse tensile specimens, Charpy specimens were machined from the pipe joints. These specimens were used to measure the upper-shelf Charpy toughness and the transition temperature of each pipe. It should be noted that since this pipe material is very thin (3.1 mm [0.125 inch] thickness), double-thick Charpy specimens were tested. These specimens are a composite of two full thickness specimens welded together on the ends of the specimens giving a specimen with a thickness of 6.2 mm (0.25 inch). This type of specimen is needed to eliminate the possibility of specimen buckling for the thin specimens, and has been used in the past with success.

The measured tensile properties are shown in Table 1, while the Charpy results for all 23 pipes are shown in Figure 1. The tensile tests results shown in Table 1 provide a slightly higher yield strength than was published by the mill specification, allowing sufficient strength for use in these pipe tests. The Charpy results suggest that most of the pipe lengths have a transition temperature between 100 F and 130 F. The pipes chosen for the experiments, i.e., Pipe numbers 3, 4, 5, 7, 8, 10, 11, 15 had a transition temperature between 110 F and 120 F, as shown in Figure 2.

Table 1 Longitudinal and transverse tensile properties for DOM tubing

Specimen	Yield Strength, MPa (ksi)	Tensile strength, MPa (ksi)	Elongation, %
TT-1	513.7 (74.5)	603.3 (87.5)	11
TT-2	506.8 (73.5)	603.3 (87.5)	11
LT-1	510.2 (74.0)	579.2 (84.0)	15
LT-2	513.7 (74.5)	579.2 (84.0)	16

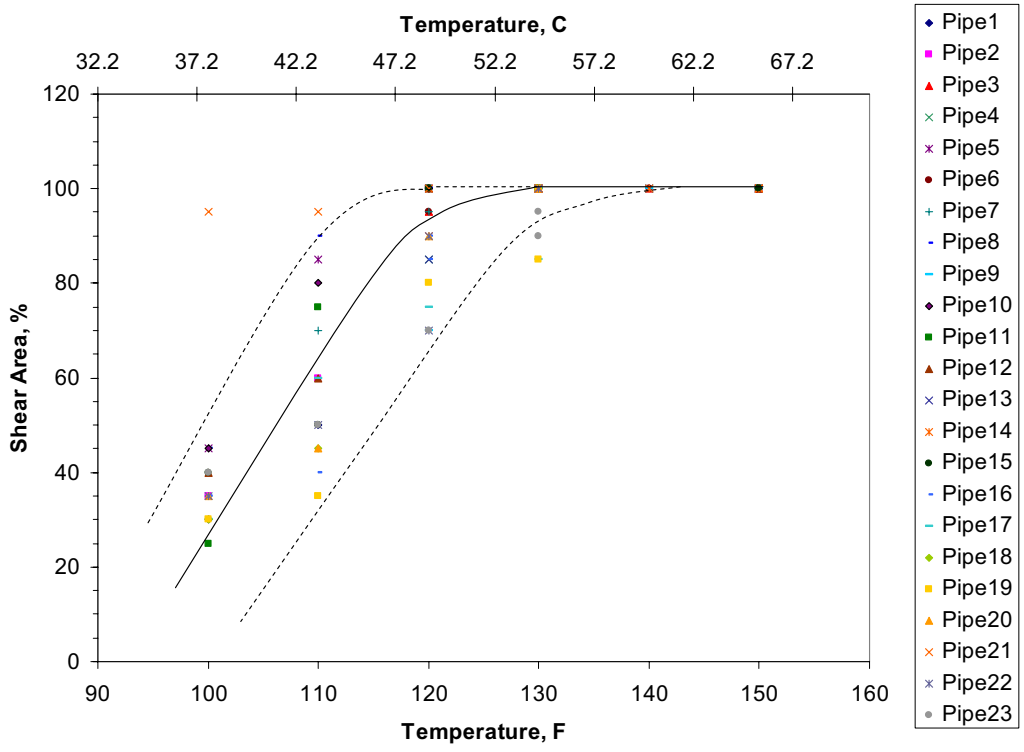

Figure 1 Shear area percent as a function of temperature for DOM tubing

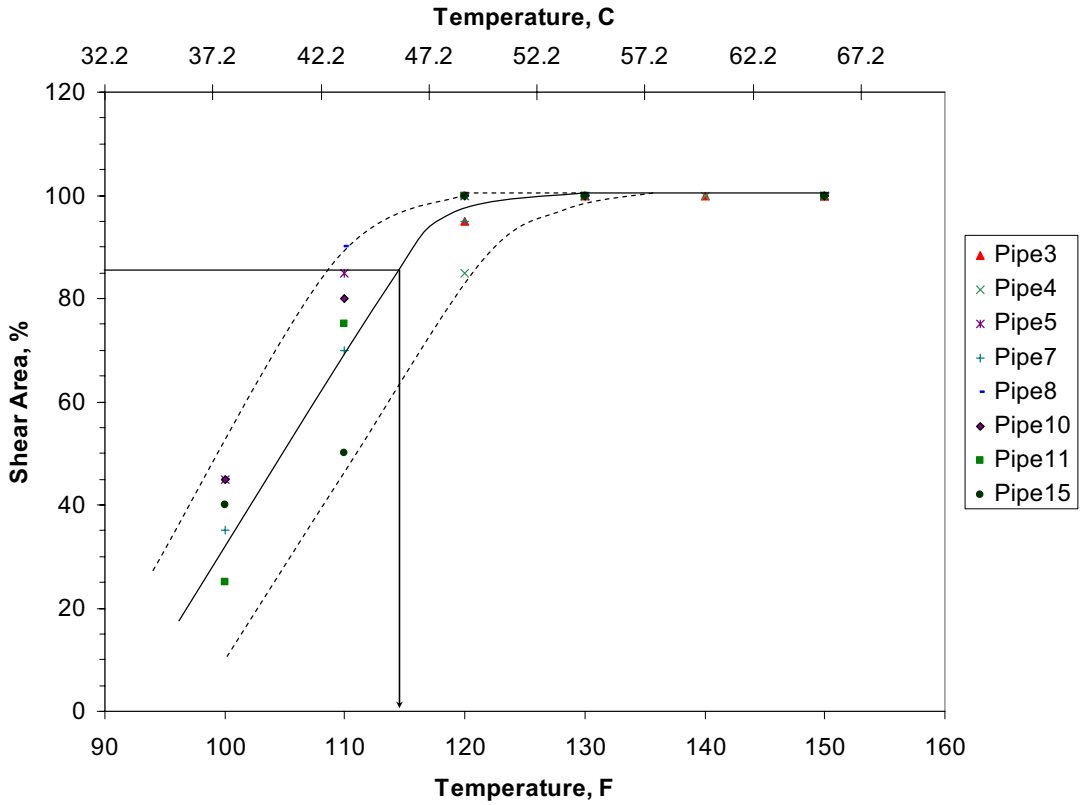

Figure 2 Shear area percent as a function of temperature for DOM tubing used in Mojave testing

4 SOIL SELECTION

The selection of the soil for these experiments is very important to the outcome of the project. It is known that the different soil types at the full-scale test sites around the world vary greatly and could lead to scatter in the minimum arrest toughness values from those experiments. Therefore, in developing a backfill coefficient that is a function of soil properties, a wide range of soils need to be used.

It is known that the soil at the Advantica test site in the UK and the original Battelle Athens test site contained very wet clay, while the test site at CSM in Italy and the Emc^2 test site contain dry sand. Therefore, it was desired to use these types of soils in the experiments.

4.1 Soil Classification

The Unified Soil Classification System from the American Society for Testing and Materials D 2487 standard classifies soils into three major categories, coarse grain, fine grain, and organic. The classification levels for the grain soils are based on their sieve number and are shown in Table 2. This classification system was used in this program to label the soils chosen.

Table 2 Unified Soil Classification System (ASTM D2487)

Major Divisions			Group Symbol	Typical Names
Coarse-Grained Soils More than 50% retained on the 0.075 mm (No. 200) sieve	**Gravels** 50% or more of coarse fraction retained on the 4.75 mm (No. 4) sieve	Clean Gravels	GW	Well-graded gravels and gravel-sand mixtures, little or no fines
			GP	Poorly graded gravels and gravel-sand mixtures, little or no fines
		Gravels with Fines	GM	Silty gravels, gravel-sand-silt mixtures
			GC	Clayey gravels, gravel-sand-clay mixtures
	Sands 50% or more of coarse fraction passes the 4.75 (No. 4) sieve	Clean Sands	SW	Well-graded sands and gravelly sands, little or no fines
			SP	Poorly graded sands and gravelly sands, little or no fines
		Sands with Fines	SM	Silty sands, sand-silt mixtures
			SC	Clayey sands, sand-clay mixtures
Fine-Grained Soils More than 50% passes the 0.075 mm (No. 200) sieve	**Silts and Clays** Liquid Limit 50% or less		ML	Inorganic silts, very fine sands, rock four, silty or clayey fine sands
			CL	Inorganic clays of low to medium plasticity, gravelly/sandy/silty/lean clays
			OL	Organic silts and organic silty clays of low plasticity
	Silts and Clays Liquid Limit greater than 50%		MH	Inorganic silts, micaceous or diatomaceous fine sands or silts, elastic silts
			CH	Inorganic clays or high plasticity, fat clays
			OH	Organic clays of medium to high plasticity
Highly Organic Soils			PT	Peat, muck, and other highly organic soils

Prefix: G = Gravel, S = Sand, M = Silt, C = Clay, O = Organic
Suffix: W = Well Graded, P = Poorly Graded, M = Silty, L = Clay, LL < 50%, H = Clay, LL > 50%

4.2 Selected Soils

It was known from the start of the program, that both a sand and clay were required to bound the behavior experienced by the full-scale test facilities throughout the world. Since the Emc^2 Mojave test site has sand as its native soil, this was the first soil that was selected. Sieve analysis

of this soil suggests that more than 50% of the grains passed a No.4 sieve, giving it a rating as a fine-grain sand. Further inspection found no fines and characterized the sand as yellowish-brown in color with a non-cohesive behavior.

For the second soil, clay was desired. Extensive searching in the area of the Mojave, California Emc^2 test site revealed few suppliers of clay. Boydston Construction in Ridgecrest California found a supply of calcium bentonite clay from Matcon Corporation. Matcon characterizes the soil as medium swelling California bentonite clay containing a mixture of clay materials. Though it has many uses, the main application of this material is an additive to natural soils to reduce permeability and provide an effective water barrier. Sieve analysis of this soil suggested that 78% passed a No. 200 sieve, giving it a rating of a fine grain soil. Further inspection characterized the soil has a highly plastic, greenish-gray clay.

The third soil was taken about 3-to-4 feet below the sandy surface in Mojave. This soil contained a large amount of calcium, which significantly increased the cohesiveness and bonding of the soil. Sieve analysis suggested that 64% of the soil passed a No. 200 sieve, while 99% passed the No. 4 sieve, giving it a rating of sand. Further inspection found 36% silt present giving it a characterization of Sandy Silt that is medium grade, cohesive, and non-plastic. Details of the strength characteristics of these soils are given in the main body (Part I) of this report.

5 DETAILED BURST TEST RESULTS

5.1 Year 1

5.1.1 Experimental set-up

All test pits for the first year experiments were prepared in a similar manner. A schematic of the size and shape of the test is shown in Figure 3. The tests pits were about 3 m (10 feet) wide, by about 12 m (40 feet) long and 1 m (3 feet) deep. These dimensions allow 10 diameters on either side of the pipe and 2 diameters below the pipe to be filled with the test soil. This size was necessary in order to ensure that the test soil fully resists the pipe movement during the fracture event.

From Figure 3, the backfilled side covers about 3 m (10 feet) of pipe, which is sufficient for this size pipe to obtain steady-state fracture speeds. The overburden is set at 3 pipe diameters above the pipe. Plywood is used to restrain the soil within the ten-foot length.

In all cases, the test soil was used under the entire length of the test pipe and was prepared to the moisture content and compaction level that was used above the pipe in the buried section.

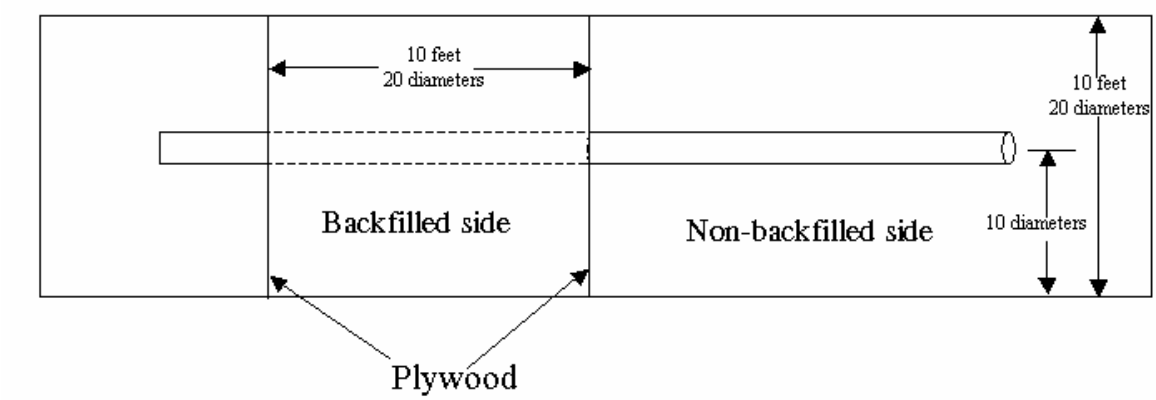

a.) Top view

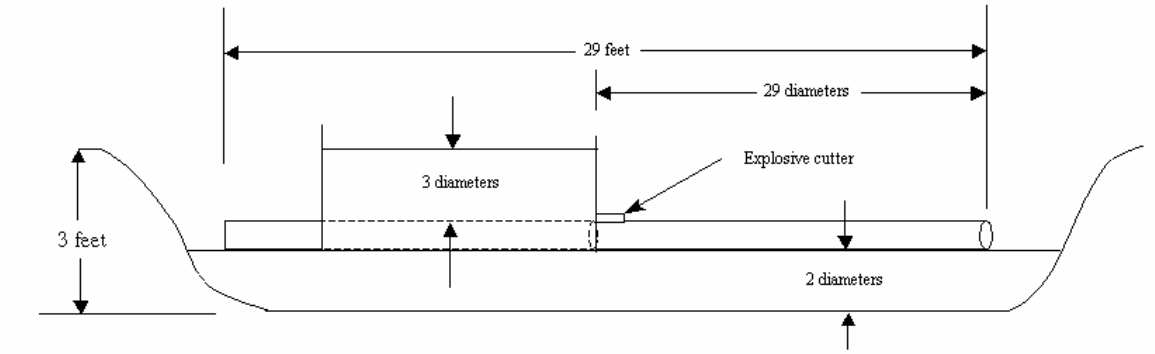

b.) Side view

Figure 3 Schematic of test pit

For the tests that contained moisture, the bottom of the test pit was prepared first. Plastic was placed at the bottom of the test pit along the whole length in order to retain the moisture. The soil was then added on top of the plastic in about 0.15 m (6-inch) lifts. After each lift, water was added, and the soil was mixed using a rototiller. After the soil is mixed, the moisture is checked with a Troxler 3430 nuclear moisture-density meter. If the soil is at the desired moisture content, another lift with water is added, otherwise more moisture is added and the soil is mixed again. When the soil is at the appropriate moisture level, the soil is compacted to a minimum level of 90% using either a remote controlled sheepfoot, or hand compaction tools, see Figure 4. Again, the moisture and compaction is checked with the Troxler meter. Once the bottom of the pit is prepared, the pipe is placed into position, and plywood supports are put into place to contain the overburden soil.

Figure 4 Compaction of test soil

5.1.2 End plugs

In order to reduce the cost of welding endcaps to each of the pipe lengths, reusable high-pressure end-plugs were planned to be used. A photograph of one of these plugs is shown in Figure 5. These plugs are slipped into the test pipe and as the pipe is pressurized, they grip the ID of the pipe. The use of the end-plugs also eliminates the concern from past experience that these heavily cold-worked carbon steels would lose considerable strength in the HAZ if welded. End-plugs from a different manufacturer were used routinely in the past work in the 1980's, but that manufacturer could not be located.

Six end-plugs were ordered from Expansion Seals Technology and shipped to the Mojave test site. The manufacturer suggested that a support ring be placed over the OD of the pipe in order to limit the overexpansion of the end-plugs. Since the end-plug only extended six inches into the pipe, a six-inch support ring was employed.

Figure 5 Photograph of high pressure end plug

5.1.3 Explosive cutter

In starting these types of burst tests, a shaped linear explosive charge (also referred to as a cutter) that cuts a tight axial slit in the pipe has been used in the past for initiating the running axial crack. The cutters used in past experiments and purchased through licensed explosive technicians in Mojave California are too large for this small pipe, i.e., they would cut through the top and bottom of the pipe and could start cracks at both locations. A smaller cutter was located through Pacific Scientific Company in California.

Even though this cutter was considerably smaller than what was in stock for thicker pipe tests, it was too large for the pipe tested in this program. Therefore, a small rectangular section of pipe was placed over the cutter location to allow for a thicker section under the cutter. The addition of this plate allowed the cutter to make excellent slits through the wall thickness without affecting the bottom of the pipe. Photographs of the cutter on the pipe and the slit in this pipe material are shown in Figure 6.

(a) Cutter on pipe

(b) Axial slit made with cutter

Figure 6 Explosive cutter

5.1.4 Instrumentation

The instrumentation in the first series of experiments included timing wires, pressure transducers, thermocouples, soil pressure gages and a first generation Hall Effect device.

5.1.4.1 Timing wires

Since the objective of these experiments was to measure the steady-state fracture velocity of both the backfilled and unbackfilled side of the test, the most important instrumentation was the timing wires. Therefore, each pipe was instrumented with 41 timing wires. The layout of these wires is shown in Figure 7. Timing Wire 41 is not shown in this figure and was placed under the cutter to mark the start of the experiment.

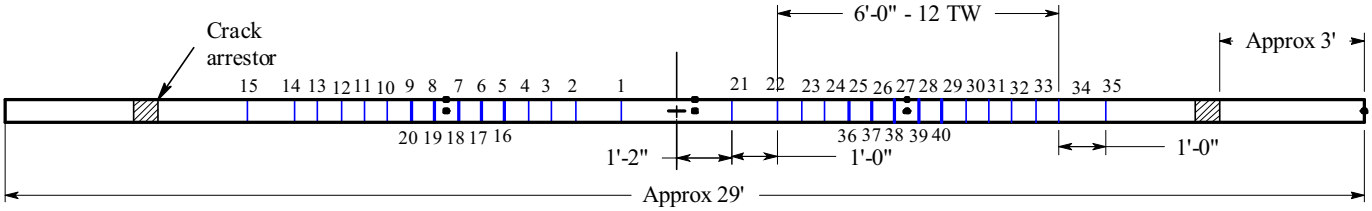

Figure 7 Pipe instrumentation layout

The timing wires labeled 1-15 and 21-35 were single strand copper wire timing wires spaced as shown in Figure 7 to capture the steady-state fracture speed. In addition, five, three-conductor braided timing wires (labeled 16-20 and 36-40) were placed at select locations on each side of the pipe. These braided timing wires were used as a redundancy for the copper wires in critical locations. Each set of five timing wires (eight sets total), were fed into specially made timing wire boxes. These boxes were designed and produced specifically for Emc^2 Mojave testing and provide a unique voltage change for each wire broken. These boxes allow each timing wire to be identified by both location and individual voltage, making data reduction much easier.

5.1.4.2 Pressure transducers and thermocouples

A limited amount of pressure transducer data was recorded during these experiments. For each experiment, one pressure transducer was added to the end of the pipe length at the filling location. This transducer was recorded dynamically during the experiment. In addition, a static pressure transducer was taken off the fill line and was used to monitor the pressure as the pipe is being filled and not during the dynamic event.

Several thermocouple readings were taken both on the pipe, and in the gas during the pressurization process. The location of the thermocouples on the pipe surface included at the top and side of the pipe at three locations: center, between Timing Wires 7 and 8, and between Timing Wires 27 and 28. An additional sheath thermocouple was placed in the gas. These readings were taken statically and not during the rupture event.

5.1.4.3 Soil pressure

In some of the first year pipe tests, soil pressure transducers were used to measure the pressure the soil exerted on the pipe during the fracture event. These small, round (0.375 inch diameter), flat transducers were attached to the pipe between Timing Wires 5 and 6 on select pipe experiments, see Figure 8. These gages were calibrated for a range of 1,000 lbs. Four gages were used on each selected pipe experiment spaced at 22.5-degree increments starting at the top of the pipe. On the pipes that were instrumented with the soil pressure transducers, pressure sensitive film was also used to attempt to capture the maximum soil-to-pipe pressure during the rupture event. This film was calibrated to four different levels, medium (9.6 MPa – 49MPa [1,400 -7,100 psi]), low (2.4 MPa – 9.6 MPa [350-1400 psi]), superlow (0.5MPa – 2.4 MPa [70-350 psi]) and ultra low (0.2MPa – 0.5 MPa [28-85 psi]).70 to 350 psi and 350 to 1,400 psi.

Figure 8 Soil pressure transducers mounted on pipe

5.1.4.4 First generation Hall Effect sensor

On select first year tests, first generation Hall-Effect devices were installed on the test pipe. These devices can be used to measure the dynamic displacement of the crack opening during the rupture event. The device consists of a small magnet and sensor that are attached directly to the pipe. The development of the device is described in the main body (Part I) of this report. For the first generation device, each magnet and sensor was embedded into a small wood block that was epoxied to the OD of the pipe. The device was calibrated to have an initial spacing of 0.375 inch, and has the capability of measuring displacements up to 2.5 inches. The magnet and sensor were placed equidistance from the centerline of the pipe, which is the expected fracture path. As the crack passes through the devices, they will measure the opening as a function of time. By using two devices that are coordinated with the crack tip location from the timing wires, an estimate of the CTOA can be made.

Figure 9 Hall Effect device installed on pipe

5.1.5 Test 1-1

Test 1-1 was conducted on August 23, 2004. The pipe that was tested was Pipe 11. The test pit was prepared with loose sand, with no additional moisture added. The test pressure was to be increased to 18.96 MPa (2,750 psi, 88%SMYS). At 12:43 pm, the pressure in the pipe was 14.13 MPa (2,050 psi) and the average pipe temperature was 130 F (117 F in the buried section). As the pressure was increased further, a failure at the end-plug occurred, see Figure 10. The teeth from the end-plug caused an axial crack that ran down the length of the pipe and hit the arrestor, three feet from the end of the pipe. No data was recovered from this experiment, but the pipe is reusable for future testing.

Figure 10 Photograph of end plug failure from Test 1-1

5.1.6 Test 1-2

Test 1-2 was conducted on August 25, 2004. The pipe number tested was 8. The test pit was prepared with saturated clay, with approximately 38% moisture with a compaction of 72%. A pair of first generation Hall Effect sensors was placed between TW 36 and 38. Pressurization began at 8:38 am, and by 9:58 am the pipe was at 19.65 MPa (2,850 psig, 100 psig above the test pressure of 2,750 psi) with an average temperature of 130F. The additional pressure was to allow for the cooling time from when the nitrogen truck has to disconnect and move a safe distance away from the test site. Nitrogen flow was stopped and the pipe system was capped off. Immediately, the pipe pressure began to slowly drop (due to a leak at the endplug), and just before testing the rate of pressure loss increased. At the instant that the test was executed, the pipe pressure dropped to 14.82 MPa (2,150 psi), which was much more of a drop than expected. Due to the low-test pressure, the crack only propagated 1.02 m (40 inches) from the cutter tip on the unbackfilled side and 0.66 m (26 inches) on the backfilled side. Due to the short fracture lengths, only limited data was taken. In fact, no data was available on the backfilled side, but some timing wire data was taken on the air backfilled side as shown in Figure 11. This data shows that the crack quickly arrested within about 1.2 m (4 feet), see Figure 12. No steady-state fracture speed data was produced in this experiment. In addition, the crack did not reach the position of the Hall Effect sensors.

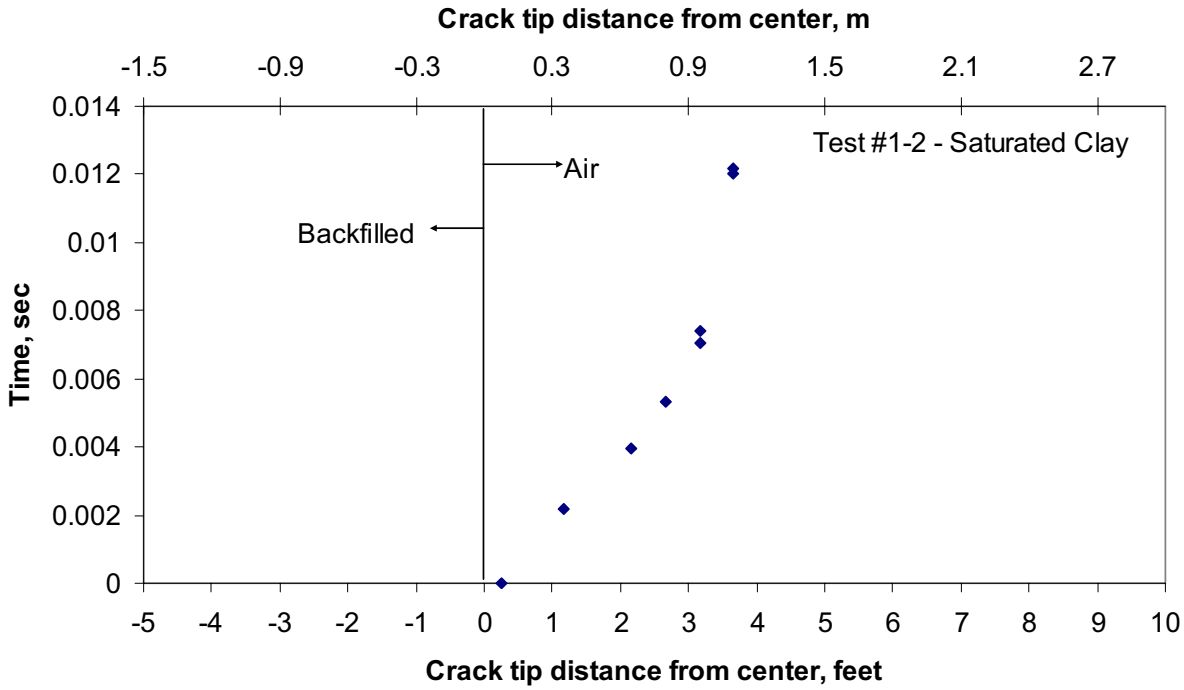

Figure 11 Crack distance-time plot for Test 1-2

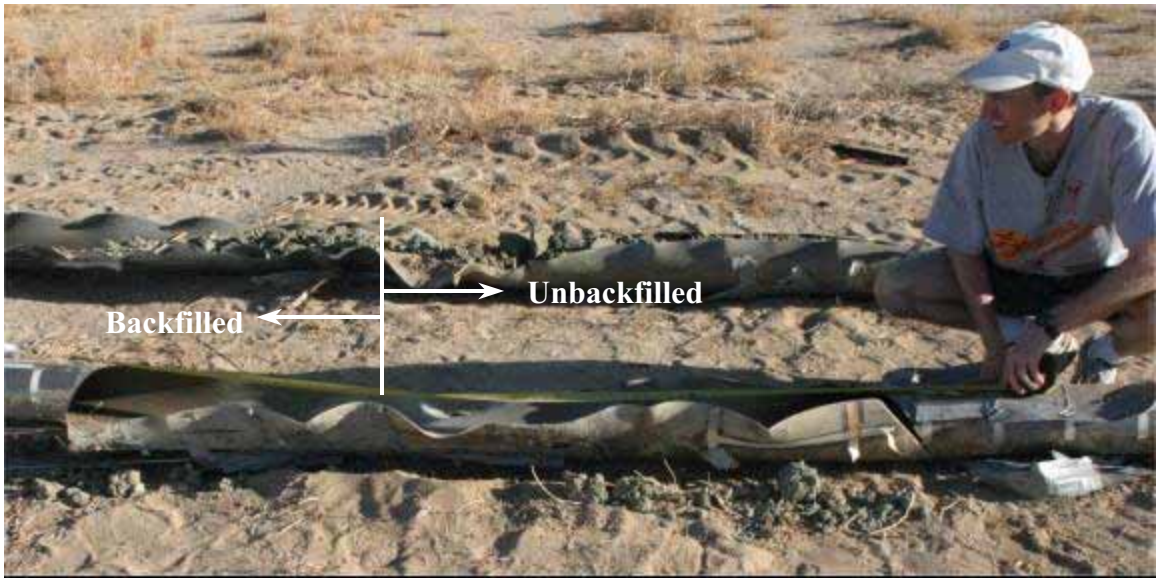

Figure 12 Photograph of the fracture from Test 1-2

5.1.7 Test 1-3

Test 1-3 was conducted on August 26, 2004. The pipe number tested was 10. The test pit was prepared with clay containing 15% moisture. Compaction equipment was used until the soil was 90% compacted. The same end plugs that were used in Test 1-2 were used in this experiment. Pressurization began at 4:49 pm. At 5:40 pm, the pipe reached 12.4 MPa (1,800 psi). At this pressure level, the north end plug was ejected from the pipe, causing the pipe to slide out of the pit, destroying the instrumentation on the pipe.

5.1.8 Elimination of endplugs

Due the failures in the first three experiments, it was decided that the endplug purchased were incapable of handling the pressures used in these experiments. Upon inspection of the ID surface of the pipe from Experiment 1-3, it was clear that the end plugs were not sufficiently gripping to the pipe surface, making it impossible for consistent results. It was decided that with three different types of end-plug failures that these end-plugs were undependable and unsafe. Consequently, endcaps were welded on the remaining test pipes. Standard end caps were purchased and welded to the pipes for Tests 1-4, 1-5, and 1-6 as shown in Figure 13. A support ring was used to help aid in the welding and to reinforce the pipe in the hoop direction in case softening occurred during the welding process.

Figure 13 Pipe with welded end cap

5.1.9 Test 1-4

Test 1-4 was conducted on August 27, 2004. The pipe number tested was 15. The test pit was prepared with clay containing 25% moisture. Compaction equipment was used until the soil was 90% compacted. End caps were welded to the end of the pipe to retain the pressure boundary. A pair of Hall Effect sensors was placed between TW 36 and 38. Soil pressure gages were placed between TW 5 and 6. High speed video was also taken during this experiment. Pressurization began at 3:38 pm. By 4:31 pm, the pipe was at 20.3 MPa (2,950 psi) at an average temperature of 124 F (118 F in the buried clay). The crack on the air backfilled side ran approximately 2.9 m (115.5 inches), while on the soil side, it ran about 1.08m (42.5 inches). The distance-time plot from the timing wire data is shown in Figure 14. From this figure, the steady-state crack speed on the air backfilled side was 178 m/s (585 ft/sec). The fracture speeds in the backfill are slower and average about 130m/s (425 ft/sec) before arresting. The fracture from this experiment is shown in Figure 15.

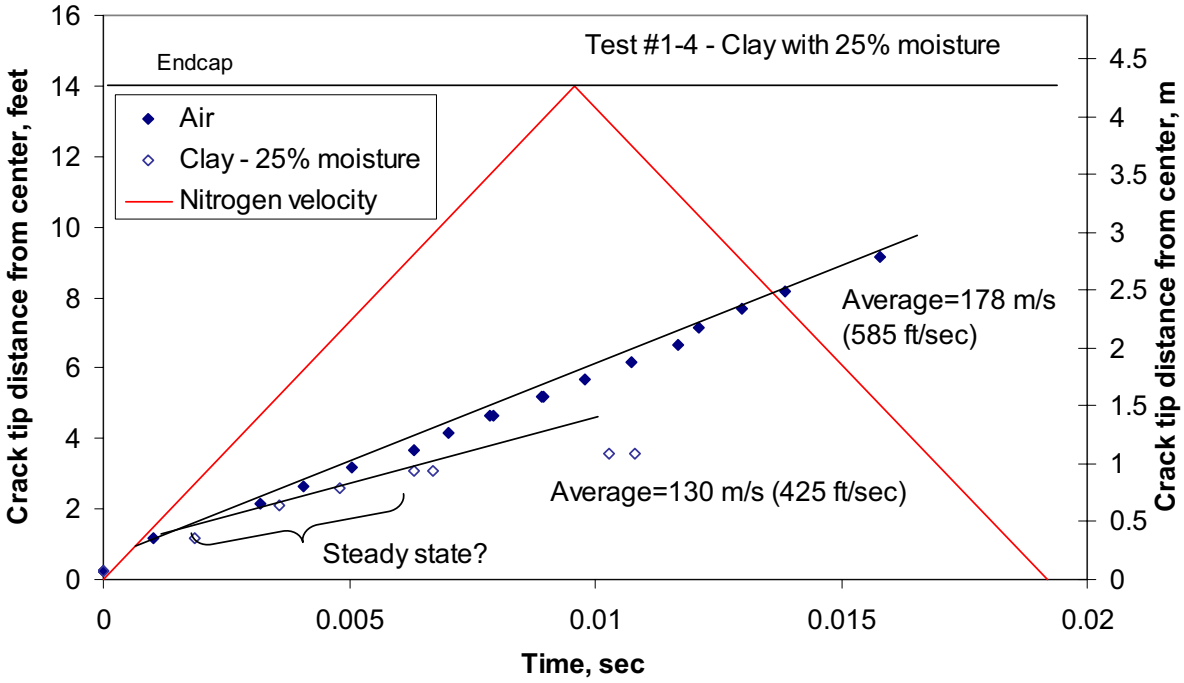

Figure 14 Crack distance-time plot for Test 1-4

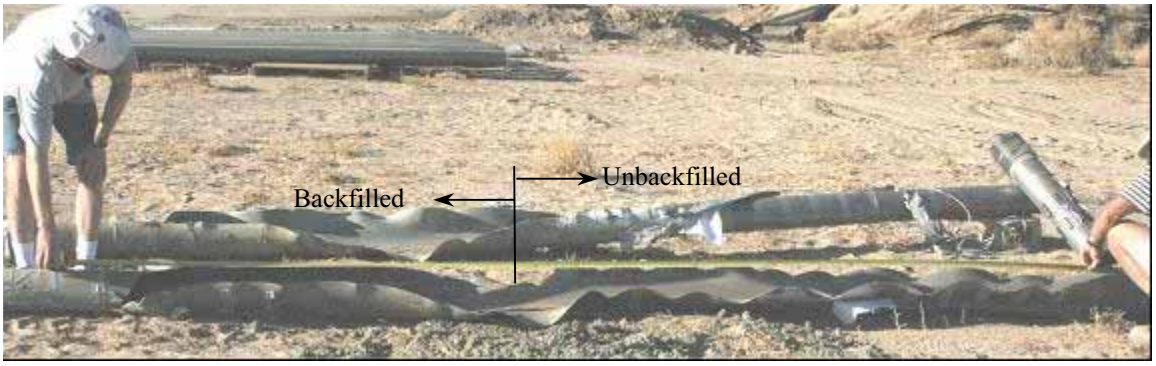

Figure 15 Fracture surfaces from Test 1-4

The data from the first generation Hall Effect sensors are shown in Figure 16. From this data, the results suggest that the Hall Effect sensor labeled HE1 showed an output as soon as the crack passed its location, however, the sensor labeled HE2 showed no response until after the crack was past its location. The high speed video suggests that the bond between the wood block supports and the pipe failed due to the plasticity from the running crack. Even though a revision to the design is needed to ensure that the device remains bonded to the pipe, this test demonstrates that the Hall Effect can capture the dynamic displacement.

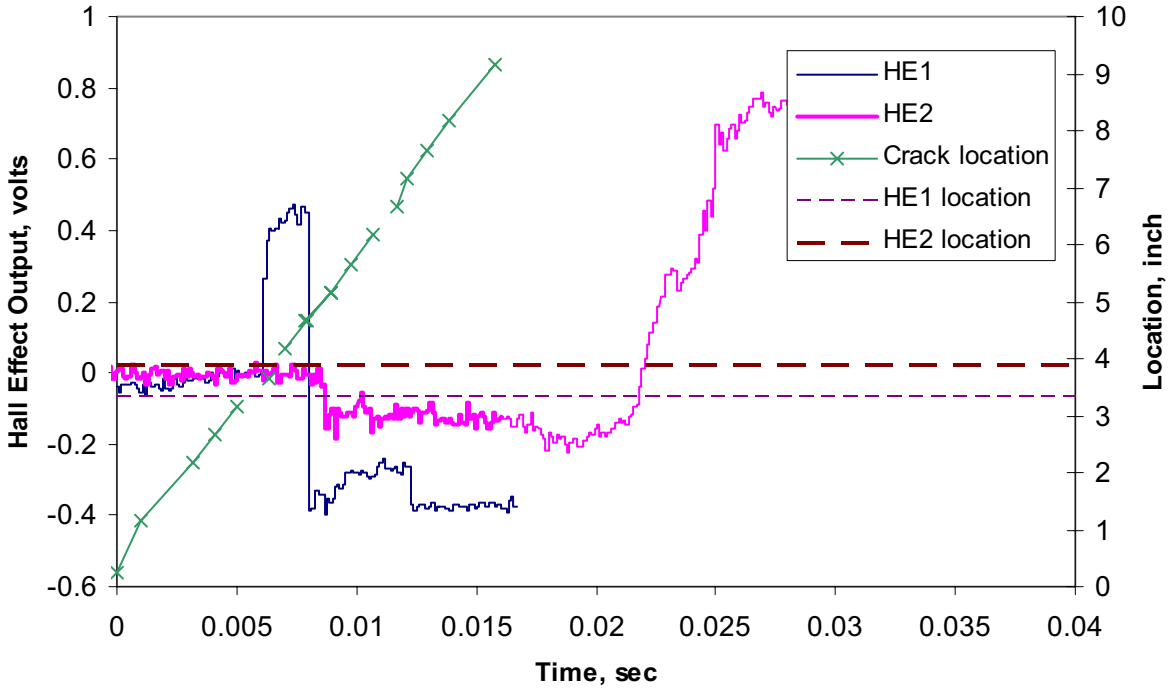

Figure 16 Data from the first generation Hall Effect Sensors

5.1.10 Test 1-5

Test 1-5 was conducted on August 28, 2004. The pipe number for this experiment was 1. The test soil in this case was loose dry sand. This test was a repeat of Test 1-1, and no additional instrumentation was used on this experiment. After fixing a few leaks from the endcap welds and bushings, pressurization began at 9:34 am. By 11:22 am, the pipe was at 20.3 MPa (2,950 psi) and an average temperature of 144 F (143 F in buried section). The explosive cutter was ignited at approximately 11:40 am. The crack on the air backfilled side ran the entire length of that side of the pipe and was arrested by the crack arrestor approximately 1.07 m (3.5 feet) from the endcap. The crack on the soil backfilled side ran about 0.99 m (39 inches) and was arrested. In this experiment, the explosive cutter caused a circumferential tear to occur at the initiation location. This tear ran circumferentially, causing the pipe to be ejected from the pit, destroying the instrumentation lead wires. Upon reducing the timing wire data, it was clear that the circumferential tear occurred after the arrest of the axial cracks.

The crack distance-time plot for this experiment is shown in Figure 17. From this figure, the steady-state fracture speed on the air backfilled side was approximately 197 m/s (647 ft/sec). The limited data on the sand side of the experiment suggests that the crack speed is probably

about 184 m/s (603 ft/sec), but could be as low as 134m/s (440ft/sec). A photograph of the fracture from this experiment is shown in Figure 18.

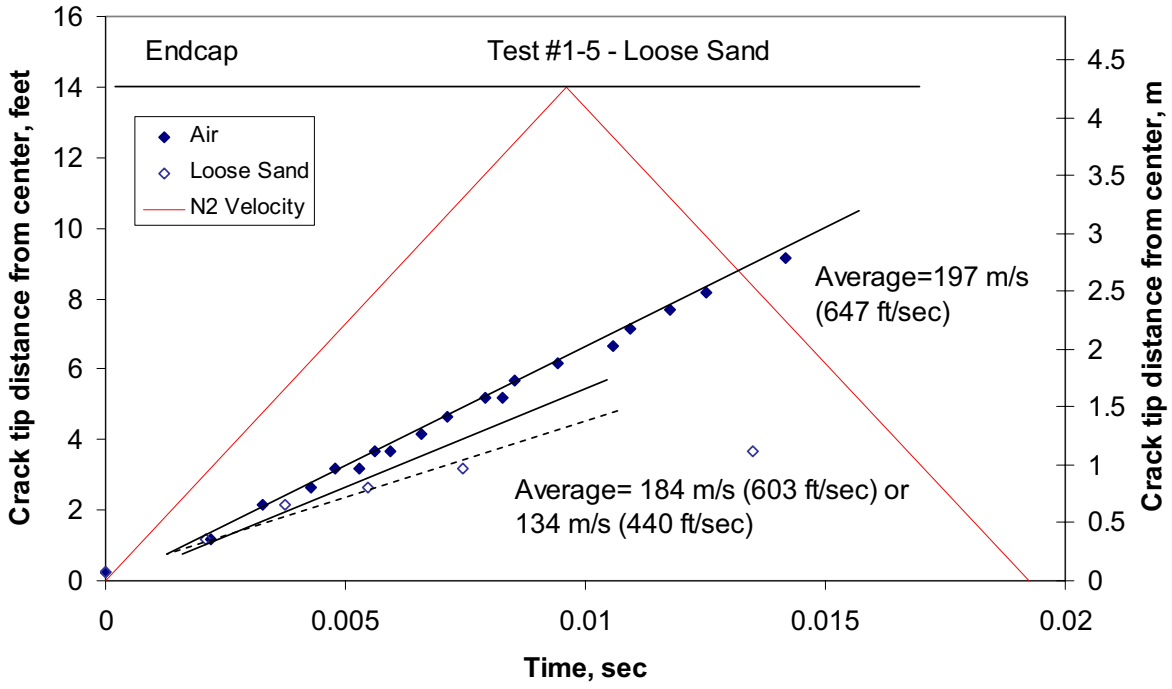

Figure 17 Crack distance-time plot for Test 1-5

Figure 18 Ejected portion of fracture surface from Test 1-5

5.1.11 Test 1-6

The test pipe number for this experiment was 5. The pipe was fully prepared with instrumentation and endcaps, and was placed in the test pit. The soil backfill was prepared with saturated clay, with 34% moisture added. The natural compaction level was measured at 60%. Soil pressure gages were placed on the pipe between Timing Wires 5 and 6 at 22.5, 45, 62.5, and 90 degrees from the top of the pipe.

This pipe was not tested because of two reasons. First, the available time at the test site for this series of experiment was limited. The company that Emc^2 rents the land from needed to use it the week of August 30 though September 3, and we had to evacuate the site during this testing. Secondly, the pipe movement that occurred during Test 1-5 severely damaged the

instrumentation lead wire, and there was not enough available time to make the necessary repairs.

Therefore, this pipe was fully buried in the prepared condition in hopes that it would be tested during the second year series of experiments. The wet clay soil was wrapped in plastic and covered with dry sand for protection. Since the pipe is not coated and would be buried for a considerable amount of time, a test section of pipe was buried along with the test pipe to track the amount of corrosion damage that may occur before this pipe can be tested.

5.2 Year 2

After the first series of experiments in August 2004, the remaining pipe material was buried in the dry sand to protect it from the environment. During the preparation of the second set of experiments, these pipes were unburied and inspected. Due to unusually excessive rain in Mojave during the Jan-Feb 2005 timeframe, moisture on the pipe caused some pitting corrosion, see Figure 19. To better inspect the pipe, each test pipe was sand blasted to remove the scale and the damage inspected. The pits that had formed were small, shallow and localized. Molds were taken on several of the more severe pit areas. The maximum pit depth was approximately 0.76 mm (0.03 inch) and the average size was about 2.5 mm (0.1 inch) in diameter. In order to verify that these pits were not going to influence the burst pressure of the pipes, a hydrotest to failure was conducted on one of the test pipes. This pipe failed at 27.6 MPa (4,000 psi), which is very close to an ultimate strength failure of the unflawed pipe, i.e., calculations gave the failure pressure ranging from 26.2 MPa to 31 MPa (3,800 to 4,500 psi) depending on the failure equations assumed. In addition, the pipes that were to be tested were hydrotested to 25.8 MPa (3,750 psi), which is 1MPa higher than the 24.8 MPa (3,600 psi) test pressure.

Figure 19 Pipe photograph showing some corrosion

Due to the condition of the pipes buried in the dry sand, it was decided to not test the specimen (Experiment 1-6) buried in the saturated clay due to the excessive corrosion on this specimen.

5.2.1 Modification to tests

Due to the costs of conducting the first year experiments, the test plan for the second year set of experiments was revised. The first year experiments were conducted with one half of the pipe unbackfilled and the other half of the pipe with a certain soil backfill. In order to reduce the number

of experiments and still develop the same amount of data, the pipe were prepared with each side of the pipe partially backfilled and partially unbackfilled as shown in Figure 20.

With this configuration, the crack is initiated in the unbackfill region, and enters the backfilled region at steady-state speeds. By investigating the change in fracture velocity as the crack enters the soil, the effects of backfill can be determined.

Each pipe was instrumented with the following:

- 51 timing wires for measuring crack speed,
- Three soil pressure gages in each backfilled section. The gages were located at 22, 45 and 90 degrees from the top of the pipe,
- Soil pressure film located near the soil pressure gages to get an average measure of the soil forces,
- WireCTOA device (Figure 21) both in the unbackfilled and backfilled section of one side of the pipe, and
- Second generation Hall Effect device (Figure 22) both in the unbackfilled and backfilled section of one side of the pipe.

The details of the development of the WireCTOA and Hall Effect sensors can be found in the main body of this report (Part I).

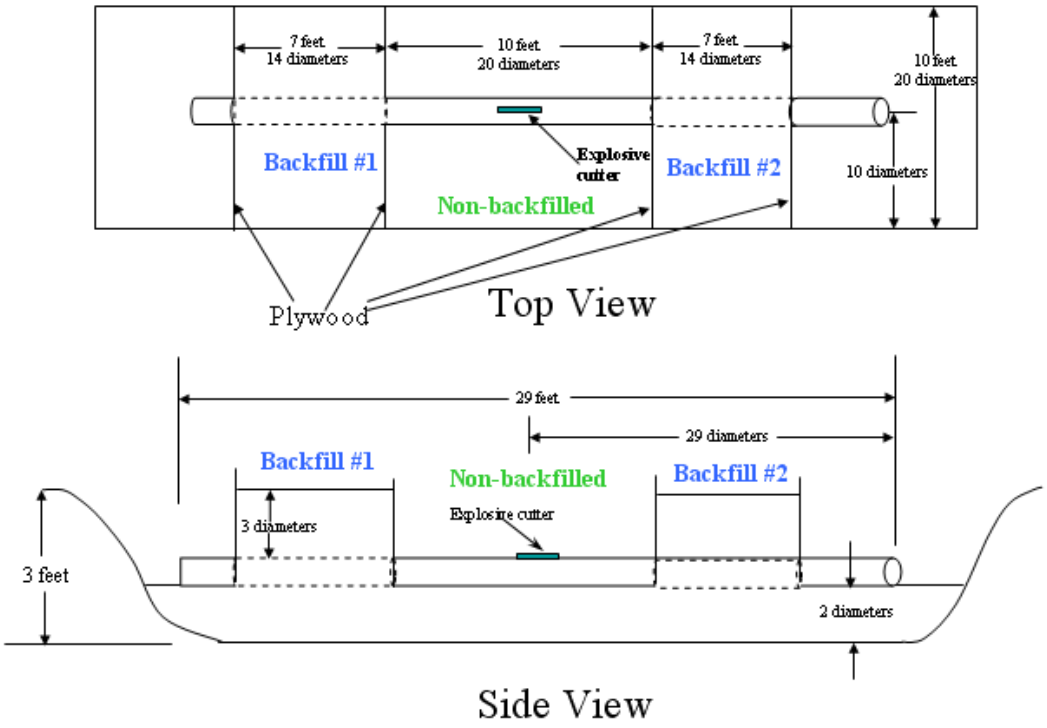

Figure 20 Schematic of test layout for Year 2 tests

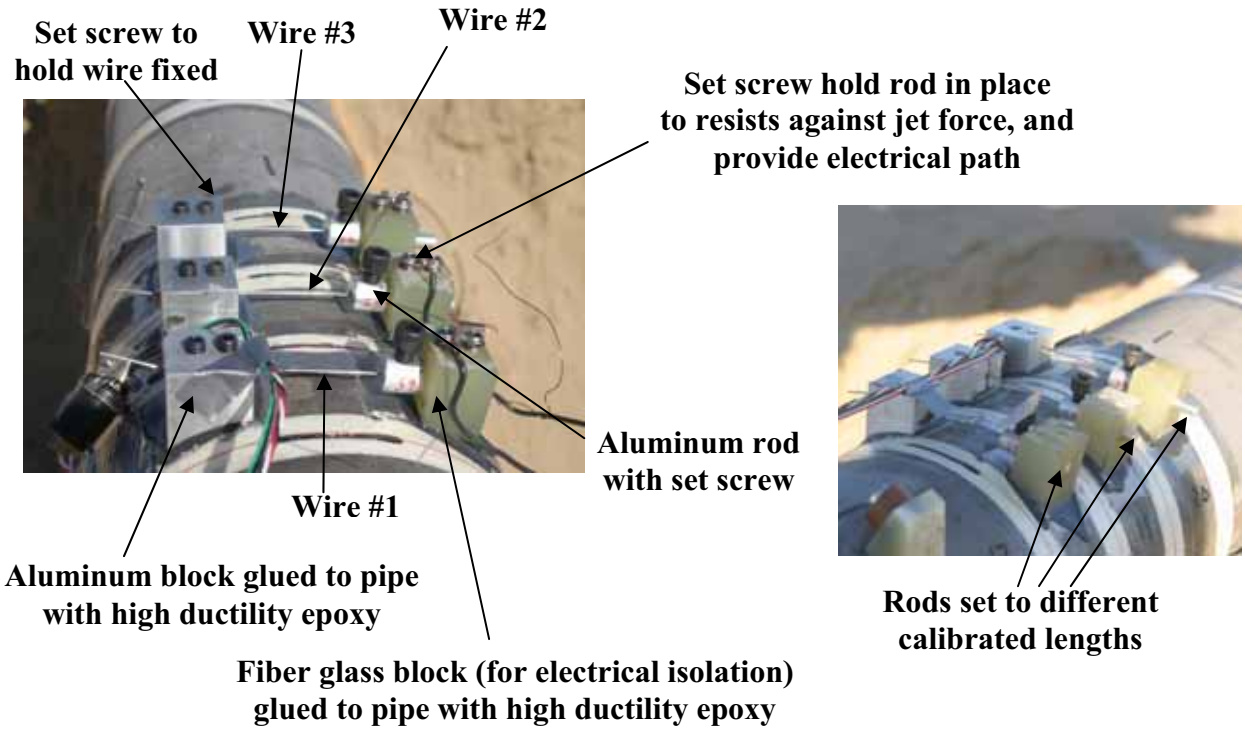

Figure 21 Photo of three WireCTOA device and timing wires on Mojave test pipe

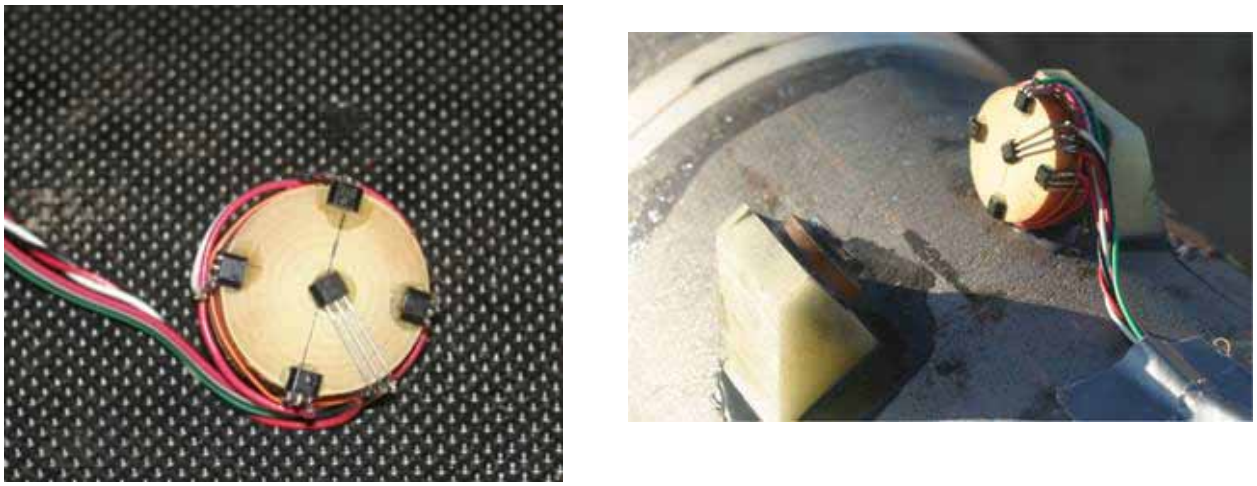

Figure 22 Hall Effect device mounted on pipe

5.2.2 Test 2-1

Experiment 2-1 was conducted on August 31, 2005. The pipe identification number was 4. For this experiment, the pit was prepared with the clay used in the first year experiments. The north end of the pipe was prepared with 27% moisture and was 90% compacted, while the south side was prepared with 19.3% moisture with a compaction of 92%. For this soil, the optimum moisture is 25.5%.

Pressurization of this pipe began at 6:30 pm. A liquid nitrogen pumper truck was used to add nitrogen to pressurize the system. Because of the poor control on the pumper truck valve, a ball valve at the end of the piping system was used to manually vent the pipe in order to control the test pressure. The target pressure for this experiment was 24.8 MPa (3,600 psi). As the pressure passed 20.7 MPa (3,000psi), the relief ball value failed in the closed position. Before word could get to the nitrogen pumper truck operator, the pressure in the pipe rose above 27.6 MPa (4,000psi) and the pipe failed. On the south side of the pipe, a ring-off occurred, while on the north side of the pipe, an axial crack propagated into the soil and was arrested approximately 2.7 m (8.8 feet) from the center of the pipe. Since this was an unexpected failure, no data was collected for this experiment. The fracture features for this experiment are shown in Figure 23. The arrest location at the north end of the pipe is shown in Figure 8.

Figure 23 Fracture features for Test 2-1

Figure 24 Arrest location at North end of Test 2-1

On the north side of the pipe, the crack arrested due to the reflected wave, which suggests it was propagating through the very moist soil.

5.2.3 Test 2-2

Experiment 2-2 was conducted on September 1, 2005. The pipe identification number was 3. For this experiment, the pit was prepared with the native sand used in the first year experiments. The north end of the pipe was prepared with 2% moisture and was 86% compacted, while the south side was prepared with 10.5% moisture with a compaction of 98%. For this soil, the optimum moisture is 11.8%.

Pressurization of this pipe began at 4:01pm. The test pressure was set at 24.8 MPa (3,600 psi). At 4:55pm, the 0.15m (6 inch) long, linear explosive cutter was ignited. An axial fracture ran for about

0.6m in both directions and then rang off at both ends. The fractured ends of the pipe are shown in Figure 25.

Figure 25 Ring off at ends of Experiment 2-2

Because of the short axial fracture before the ring-off, only one timing wire on each side of the pipe was broken, therefore insufficient data exists to extract the fracture speeds.

This test results raises an important point about conducting these types of experiments. In this particular test, the soil underneath the pipe in the unbackfilled regions was very loosely compacted. It is suspected that due to the minimal support under the pipe, a large bending moment was placed on the pipe from the downward jet force that occurs as the crack propagates. This large bending moment, coupled with the tearing action from the large flap movements behind the crack, can cause the maximum principal stress to shift from circumferential to some combination of circumferential and axial causing the pipe to tear around the circumference.

Ring-offs in small diameter pipe tests are not uncommon and have occurred near the origin in some past 2-inch and 4-inch pipe tests by British Gas [2], and University of Washington [3]. All of these tests had the pipes fully supported on the bottom. Also in some 6-inch diameter nuclear pipe test with axial cracks, the pipe was supported by jacks close to the origin, and the cracks rang off before reaching the support [4].

Because of this difficulty, more care was taken to support the pipe in the next experiment.

5.2.4 Test 2-3

Experiment 2-3 was conducted on September 2, 2005. The pipe identification number was 7. For this experiment, the pit was prepared with the native sandy silt that is found about 1-1.5m (3-5 feet) under the sand in the Mojave desert The north end of the pipe was prepared with 9% moisture and was 90% compacted, while the south side was prepared with 12.5% moisture with a compaction of 94%. For this soil, the optimum moisture is 10%.

To prevent the ring-off that occurred in the previous test, special care was taken to compact the soil underneath the pipe and in the haunch region. Pressurization of the pipe began at 10:08am, with the target pressure at 24.8 MPa (3,600 psi). At 11:34am, the 0.15m (6inch) explosive cutter was ignited.

An axial fracture ran for about 2.6m (8.5 feet) in both directions before it arrested. The fractured ends of the pipe are shown in Figure 26.

The fracture speed data was reduced from the timing wires and the results are shown in Figure 27. Also included in this figure is the speed of the decompression wave as it travels to the endcap, and reflects back to the running crack. Note that this plot assumes that the decompression wave does not change speed as it reflects off the endcap. In reality, the reflected decompression wave will slow as it travels back through already decompressed gas. From this figure, it is clear that the fracture speed begins to slow rapidly as the reflected wave reaches the fracture path, indicating that the arrest was caused by the reflected wave and not the material toughness.

The results also indicate that the fracture speeds slowed down as the crack entered the soil backfill. On the 12.5% moisture side, the average fracture speed in air was 174 m/s, and slowed to 159 m/s in the soil, which is about an 8.5% drop in speed. On the drier side, the crack speed dropped 10% from 188 m/s to 169 m/s. Within the uncertainty of the experiments, it appears that this difference is negligible.

North South

Figure 26 Arrest ends for Experiment 2-3

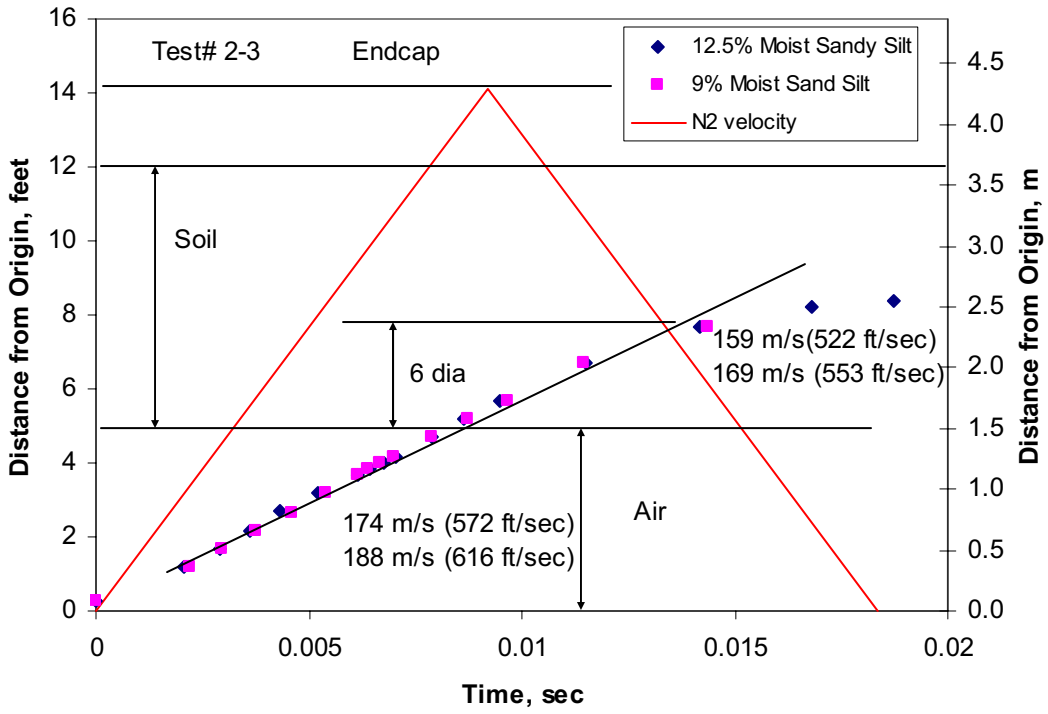

Figure 27 Fracture speed data from Experiment 2-3

Of the extra instrumentation, data was only available from the soil pressure film and the Hall Effect device. In all cases, the WireCTOA failed incorrectly as the crack passed the device. The torque on the set screws holding the aluminum rod in place was too large in all cases; the wire failed or was pulled out of the aluminum block before the aluminum rod slipped out of the fiberglass base. It is suspected that the angle that is created as the crack opens may have caused side loading on the aluminum rod, which would increase the force required for pull-out. In addition, this angle may have bent the high strength wire, which may have cause premature failure of the wire. Further refinement of this device is needed before incorporating this device on future tests. In addition, no data was available for the soil pressure transducers since the crack never reached these devices in the experiments.

Data from the second generation Hall Effect device is shown in Figure 28. The output of the Hall Effect device gives relative displacements in the circumferential, longitudinal, and radial directions. The results indicate that most of the movement is in the circumferential (opening) direction, with some minimal movement in the other directions. The output is also linear with fracture speed, as indicated by the constant velocity curve (169 m/s) that is cross plotted with the Hall Effect data. Therefore, this data suggests that if the output of this device is linear with displacement, then the opening of the crack (CTOA) is constant with crack location. However, a direct calibration for the Hall Effect sensor output was not generated for this generation Hall Effect Device. Further refinement of the device and calibrations occurred for the application to the JGA experiment discussed in the main body (Part I) of this report.

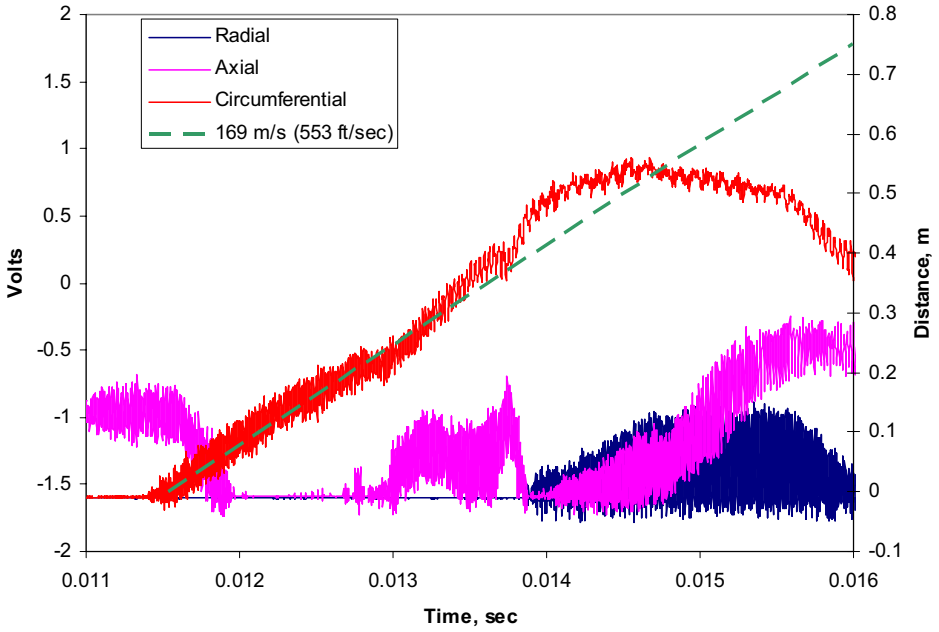

Figure 28 Hall Effect data for Experiment 2-3

The final set of data from this experiment was from the soil pressure film. On this experiment there were four types of film placed on the pipe: medium (9.6 MPa – 49MPa [1,400 -7,100 psi]), low (2.4 MPa – 9.6 MPa [350-1400 psi]), superlow (0.5MPa – 2.4 MPa [70-350 psi]) and ultra low (0.2MPa – 0.5 MPa [28-85 psi]). For this experiment, a photograph of the film after the experiment is shown in Figure 29. The data from this figure indicates that the superlow and ultra low films were saturated. In addition, the medium film shows almost no change in color. Therefore, the results indicate that the soil pressure falls between 2.4 MPa (350 psi) and 9.6 MPa (1,400 psi).

Figure 29 Soil pressure film data from Experiment 2-3

5.3 Analysis of Results

5.3.1 Mojave fracture speed data

The reduced fracture speed data for the experiments conducted in this effort are shown in Table 3. This table also indicates the test pressure used in each experiment as well as the extent of the crack extension in each case. Finally, notes as to the problems that occurred during the experiment are included to help explain why some tests do not have the relevant data. Note that a "P" in this table indicates that the crack propagated completely through that section of pipe.

Table 3 Reduced fracture speed data for first series of experiments

Test Number	Description	Test Pressure	Unbackfill		Backfill			Note
			Vf	Crack length	Vf	Crack length	Length/ Diameter	
		MPa(ksi)	mps (fps)	m(in)	mps (fps)	m(in)		
1-1	Loose Sand	19 (2.75)	N/A	N/A	N/A	N/A		Failure at endplug
1-2	Clay, 39% moisture, 72% compacted	14.8 (2.15)	N/A	1.02 (40)	N/A	0.7 (28.5)	4.75	
1-3	Clay, 15% moisture, 90% compacted	8.6 (1.25)	N/A	N/A	N/A	N/A		Endplug failure
1-4	Clay, 25% moisture, 90% compacted	20.3 (2.95)	178 (585)	2.9 (115.5)	130 (425)	1.1 (45)	7.50	
1-5	Loose Sand	20.3 (2.95)	197 (647)	3.2 (124.5)	184 (603)	1.05 (41.5)	6.92	
2-1a	Clay (26% moisture, 90% compact)	27.6 (4.0)	N/A	P	N/A	2.7 (108)		Valve failure
2-1b	Clay(19% moisture, 92% compact)	27.6 (4.0)	N/A	~0.6 (24)	NA	NA		Valve failure
2-2a	Dry sand (2% moisture, 86% compact)	24.8 (3.60)	NA	~0.6 (24)	NA	NA	4.00	Base metal ring off
2-2b	Wet sand (10.5% moisture, 98% compact)	24.8 (3.60)	NA	~0.6 (24)	NA	NA	4.00	Base metal ring off
2-3a	Sandy Silt (9% moisture, 90% compact)	24.8 (3.60)	188 (616)	P	169 (553)	2.6 (101.5)	16.92	Reflected wave arrest
2-3a	Sandy Silt (12.5% moisture, 94% compact)	24.8 (3.60)	174 (572)	P	159 (522)	2.6 (101.5)	16.92	Reflected wave arrest

5.3.2 Comparison with past experiments

To assess the validity of the experiments and the design analyses, an analysis of the available past small-diameter pipe tests was conducted. Data was available from three different programs conducted previously at Battelle [1, 5, 6]. These reports were proprietary reports to private gas

companies or PRCI. The proprietary part of the work was on crack arrestor design or effects of frozen backfill, so only the non-proprietary unfrozen backfill crack propagation data are presented.

The tests were conducted on 6-inch diameter by 0.125-inch thick 1020 DOM steel tubing (identical to tubes used in this program), 6-inch diameter by 0.123-inch thick X65 API pipe, and 12-inch diameter by 0.218-inch thick X70 API line pipe. The API pipes were special heats made for those projects. The steel to make similar API pipe with low toughness is no longer available in North America.

The pressurizing medium was nitrogen (same as used in this program), air, a combination of air and propane to simulate rich gas decompression behavior, or liquid CO_2 which has a severe subcooled liquid decompression behavior, i.e., it depressurizes very slightly and then the pressure level remains constant.

The backfill surrounding the pipes was either an uncompacted masonry sand (large grain), or air (no backfill). In some cases the moisture content of the sand was measured.

The test data are given in Table 4 [1], Table 5 [5], and Table 6 [6].

The analysis conducted involved using the original Battelle Two-Curve Ductile Fracture analysis for each of the 34 cases, where the actual properties and gas decompression behavior were used to calculate the steady-state fracture speed for comparison to the experimental steady-state fracture speeds. The results of the analysis of the data are presented in Figure 30. Note that Sets 1, 2, and 3 correspond to the data in References 1, 5 and 6, respectively. In examining the data in this figure, it can be seen that the soil (sand) backfilled tests are reasonably predicted, however, the no backfill (air) tests are predicted to have the same fracture speed as the previously presented results, i.e., about 305 m/s (1,000 fps).

Table 4 Experimental data and calculated values for tests from Reference 1

Test #	A	B	C	D	E
Pipe number	1020-3	MP-3	MP-1	MP-5	MP-4
Pipe OD, inch	6	6	6	6	6
Pipe thickness, inch	0.125	0.125	0.125	0.125	0.125
Yield strength, ksi	73.4	71.7	69	68.2	70.1
Backfill	Air	Air	Air	Air	Air
Charpy energy, ft-lb	16.5	12.5	16.5	14	15
Total thickness of Charpy specimen, inch	0.25	0.25	0.25	0.25	0.25
% of full size	64%	64%	64%	64%	64%
Equivilent full-size Charpy energy, ft-lb	25.98	19.69	25.98	22.05	23.62
Test pressure, psig	2,330	2,330	2,330	2,330	2,330
Hoop stress at start of test, ksi	55.92	55.92	55.92	55.92	55.92
Initial hoop stress/yield strength	76.2%	78.0%	81.0%	82.0%	79.8%
Gas temperature, F	~75	~75	~75	~75	~75
Gas Composition	N_2	N_2	N_2	N_2	N_2
Actual steady-state fracture speed in air, fps	709	870	660	635	515
Calculated steady-state fracture speed in air, fps	1,001	1,257	1,001	1,152	1,077
Calculated 2-curve no backfill arrest toughness, FSE CVP, ft-lb	42.6	43.3	44.8	45.3	44.1
Actual Charpy/arrest CVP	61%	45%	58%	49%	54%

Table 5 Experimental data and calculated values for tests from Reference 5

Test #	1	2	3	4	5
Pipe number	229	225	214	252	253
Pipe OD, inch	6.625	6.625	6.625	12.75	12.75
Pipe thickness, inch	0.123	0.123	0.124	0.226	0.227
Yield strength, ksi	62.4	63.4	62.8	75.3	72.8
Backfill type	Masonry sand	Masonry sand	Masonry sand	Masonry sand	Masonry sand
Backfill moisture content, % by weight	6.43	7.05	16.27	7.9	5.16
Compaction	loose	loose	loose	loose	loose
Charpy V-notch energy, ft-lb	11.25	10.9	11.7	12.5	11
% of full size	31%	31%	31%	57%	58%
Equivalent full-size Charpy energy, ft-lb	36.0	34.9	37.1	21.8	19.1
Test pressure, psig	2300	2000	2300	1805	1600
Hoop stress at start of test, ksi	61.9	53.9	61.4	50.9	44.9
Initial hoop stress/yield strength	99.3%	85.0%	97.8%	67.6%	61.7%
Gas temperature, F	55	54	25	27.5	26.5
Gas Composition (% propane, % nitrogen)	16, 84	16, 84	12, 88	12, 88	10, 90
Actual steady-state fracture speed in **loose sand**, fps	635	460	740	906	782
Calculated steady-state fracture speed in **soil**, fps	587	575	590	853	890
Calculated 2-curve **soil** arrest toughness, FSE CVP, ft-lb	263.9	75.85	180.6	49.7	36.866
Actual Charpy/arrest CVP	14%	46%	21%	44%	52%

Table 6 Experimental data and calculated values for tests from Reference 6

(a) 6” DOM Tubing data

Datapoint #	1	2	3	4	5	6	7	8
Test #	79-1-1	79-1-2	79-1-2	79-1-3	80-10	80-11	80-11	80-12
Pipe number	MP-6	MP-8	MP-8	1020-2	MP-7	MP-9	MP-9	MP-21
Pipe OD, inch	6	6	6	6	6	6	6	6
Pipe thickness, inch	0.125	0.125	0.125	0.125	0.125	0.125	0.125	0.125
Yield strength, ksi	69.3	68.6	68.6	71	69.3	69.2	69.2	64.2
Backfill	Air	Air	Air	Air	Air	Air	Air	Air
Equivilent 2/3-size Charpy V-notch energy, ft-lb	14	14	14	17	15.2	15.2	15.2	16.4
% of full size	67%	67%	67%	67%	67%	67%	67%	67%
Equivalent full-size Charpy energy, ft-lb	21.0	21.0	21.0	25.5	22.8	22.8	22.8	24.6
Test pressure, psig	2330	2330	2330	2330	2330	2400	2400	2400
Hoop stress at start of test, ksi	55.9	55.9	55.9	55.9	55.9	57.6	57.6	57.6
Initial hoop stress/yield strength	80.7%	81.5%	81.5%	78.8%	80.7%	83.2%	83.2%	89.7%
Gas temperature, F	~75	~75	~75	~75	~75	~75	~75	~75
Gas Composition (% propane, % nitrogen)	N_2	N_2	N_2	N_2	N_2	N_2	N_2	N_2
Actual steady-state fracture speed in **air**, fps	635	385	410	618	508	525	560	800
Calculated steady-state fracture speed in **air**, fps	1,187	1,187	1,187	1001	1115	1122	1122	1045
Calculated 2-curve **air** arrest toughness, FSE CVP, ft-lb	44.6	44.6	44.6	43.6	44.6	48.3	48.3	53.6
Actual Charpy/arrest CVP	47%	47%	47%	58%	51%	47%	47%	46%

(b) 6” API pipe data

Datapoint #	10	11	12	13
Test #	81-1	81-1	81-2	81-2
Pipe number	MP-216	MP-216	MP-212	MP-212
Pipe OD, inch	6.625	6.625	6.625	6.625
Pipe thickness, inch	0.123	0.123	0.123	0.123
Yield strength, ksi	67.4	67.4	64.9	64.9
Backfill	Masonry sand	Masonry sand	Masonry sand	Masonry sand
Compaction	loose	loose	loose	loose
Equivilent 2/3-size Charpy V-notch energy, ft-lb	21.4	21.4	19.8	19.8
% of full size	67%	67%	67%	67%
Equivalent full-size Charpy energy, ft-lb	32.1	32.1	29.7	29.7
Test pressure, psig	2000	2000	2000	2000
Hoop stress at start of test, ksi	53.9	53.9	53.9	53.9
Initial hoop stress/yield strength	79.9%	79.9%	83.0%	83.0%
Gas temperature, F	~55	~55	~55	~55
Gas Composition (% propane, % nitrogen)	16, 84	16, 84	16, 84	16, 84
Actual steady-state fracture speed in **sand**, fps	571	574	613	630
Calculated steady-state fracture speed in **soil**, fps	608.5	608.5	640	640
Calculated 2-curve **soil** arrest toughness, FSE CVP, ft-lb	75.85	75.85	75.85	75.85
Actual Charpy/arrest CVP	42%	42%	39%	39%

(c) 12” API pipe data – pressurized with air

Datapoint #	14	15	16	17	18	19	20	21
Test #	80-19	80-19	81-5	81-5	82-1	82-1	82-2	82-2
Pipe number	MP-260	MP-260	MP-268	MP-268	MP-259	MP-259	MP-261	MP-261
Pipe OD, inch	12.75	12.75	12.75	12.75	12.75	12.75	12.75	12.75
Pipe thickness, inch	0.219	0.219	0.224	0.224	0.224	0.224	0.218	0.218
Yield strength, ksi	62.7	62.7	66	66	68.8	68.8	63.6	63.6
Backfill	Masonry sand	Masonry sand	Masonry sand	Masonry sand	Masonry sand	Masonry sand	Masonry sand	Masonry sand
Compaction	loose	loose	loose	loose	loose	loose	loose	loose
Equivilent 2/3-size Charpy V-notch energy, ft-lb	13.9	13.9	15.8	15.8	18	18	17.5	17.5
% of full size	67%	67%	67%	67%	67%	67%	67%	67%
Equivalent full-size Charpy energy, ft-lb	20.9	20.9	23.7	23.7	27.0	27.0	26.3	26.3
Test pressure, psig	2000	2000	2000	2000	2000	2000	2000	2000
Hoop stress at start of test, ksi	58.2	58.2	56.9	56.9	56.9	56.9	58.5	58.5
Initial hoop stress/yield strength	92.9%	92.9%	86.2%	86.2%	82.7%	82.7%	92.0%	92.0%
Gas temperature, F	~75	~75	~75	~75	~75	~75	~75	~75
Gas Composition (% propane, % nitrogen)	Air	Air	Air	Air	Air	Air	Air	Air
Actual steady-state fracture speed in sand, fps	706	851	793	852	645	690	769	742
Calculated steady-state fracture speed in soil, fps	823	823	743	743	657	657	700	700
Calculated 2-curve soil arrest toughness, FSE CVP, ft-lb	42.7	42.7	38.9	38.9	38.2	38.2	42.8	42.8
Actual Charpy/arrest CVP	49%	49%	61%	61%	71%	71%	61%	61%

(d) 12” API pipe data – pressurized with nitrogen/propane or CO_2

Datapoint #	22	23	24	25
Test #	80-18	80-18	80-20	80-20
Pipe number	MP-251	MP-251	MP-266	MP-266
Pipe OD, inch	12.75	12.75	12.75	12.75
Pipe thickness, inch	0.223	0.223	0.222	0.222
Yield strength, ksi	72	72	62.6	62.6
Backfill	Masonry sand	Masonry sand	Masonry sand	Masonry sand
Compaction	loose	loose	loose	loose
Equivilent 2/3-size Charpy V-notch energy, ft-lb	21.2	21.2	14.6	14.6
% of full size	67%	67%	67%	67%
Equivalent full-size Charpy energy, ft-lb	31.8	31.8	21.9	21.9
Test pressure, psig	2000	2000	1200	1200
Hoop stress at start of test, ksi	57.2	57.2	34.5	34.5
Initial hoop stress/yield strength	79.4%	79.4%	55.0%	55.0%
Gas temperature, F	~55	~55	80	80
Gas Composition (% propane, % nitrogen)	16, 84	16, 84	Liquid CO2	Liquid CO2
Actual steady-state fracture speed in sand, fps	708	833	647	655
Calculated steady-state fracture speed in soil, fps	871	871	770	770
Calculated 2-curve soil arrest toughness, FSE CVP, ft-lb	74	74	Impossible	Impossible
Actual Charpy/arrest CVP	43%	43%	~0	~0

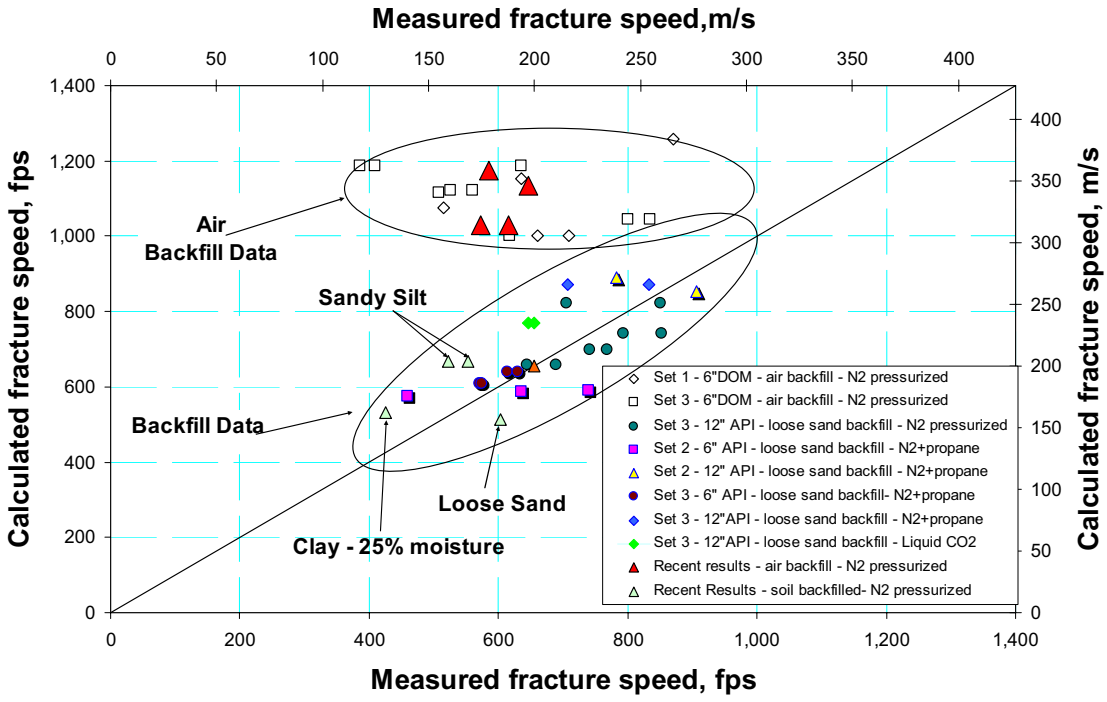

Figure 30 Comparison of experimental and calculated fracture speeds from current and past small-diameter pipe fracture experiments

5.3.3 Modified fracture speed for small-diameter pipes

To further investigate the applicability of the Battelle Two-Curve Ductile Fracture analysis for small-diameter pipes, current and past data were replotted as shown in Figure 31 and Figure 32. Figure 31 shows the results for the no backfill (air) tests and Figure 32 shows the results for the soil (sand) backfilled tests. In these figures, the x-axis represents the fracture velocity normalized by flow strength and Charpy energy of the pipe. The y-axis represents the ratio of the decompressed pressure at the crack tip and the arrest stress. Also shown in these figures are the fracture velocity curves with the original soil coefficient and the original air coefficient developed by Maxey. Note that in the original Maxey equation the fracture speed is proportional to the 1/6 power of the normalized decompressed pressure [see Equation (8) in the main body (Part I) of this report].

As shown in Figure 31, the results for the small-diameter pipe tests with no backfill (air) deviate from the original curve as the normalized fracture velocity increases. This explains the overprediction of the fracture speeds in Figure 30. Also note that the range of the normalized fracture velocity is relatively lower than that of the large-diameter pipe test results [see Figure 4 in the main body (Part I) of this report]. The results from the present study fall within the trend of the past test results.

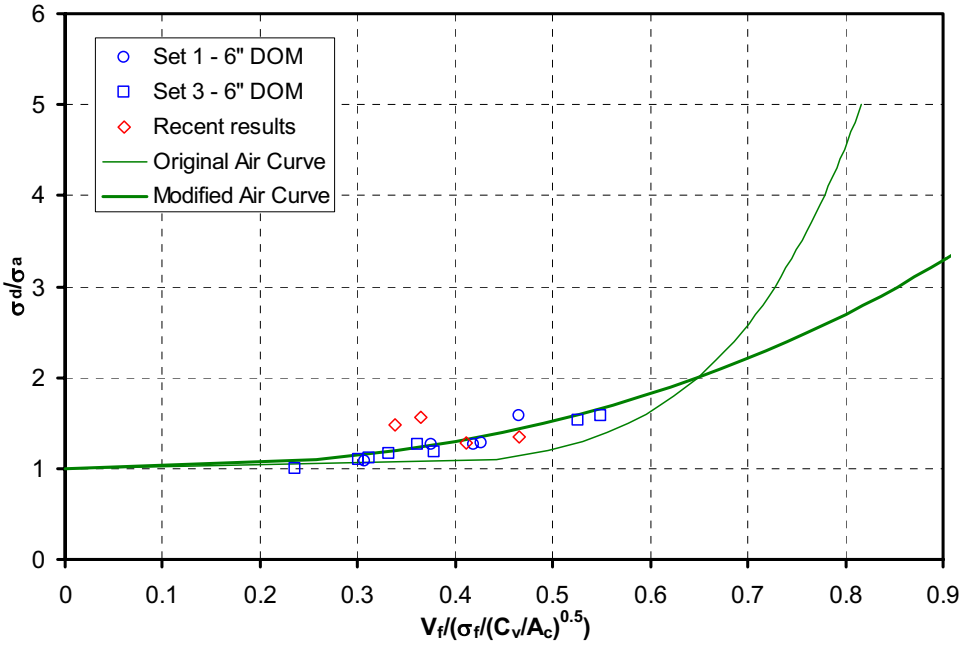

Figure 31 Fracture velocity as a function of decompressed stress for small-diameter pipes with no backfill (air)

In Figure 30, it seems that the original Battelle Two-Curve Ductile Fracture analysis does a reasonable job of predicting the fracture speed for the soil backfilled case. However, Figure 32 demonstrates that some of the small-diameter test results fall near the original curve, whereas others are mostly spread wide to the right side of the original curve and do not follow the trend of the original curve. All the data shown in Figure 32 were reanalyzed to make sure there were

no outliers. The normalized fracture speeds from the current study were relatively lower than the past results. However, the results seem to follow the trend of the past test results.

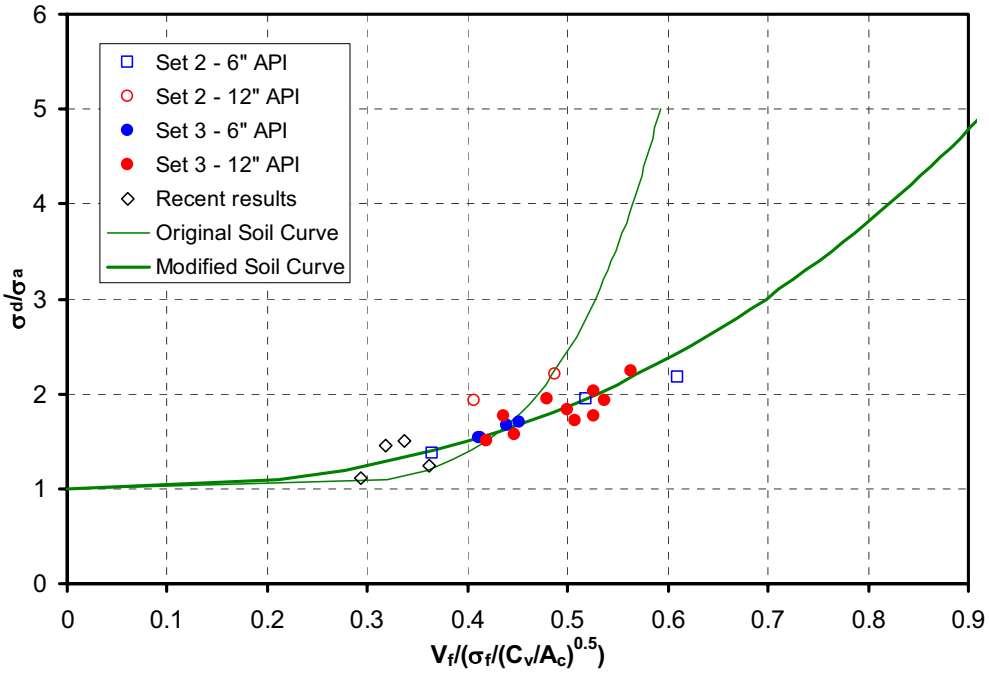

Figure 32 Fracture velocity as a function of decompressed stress for small-diameter pipes with soil (sand) backfill

Based on the results shown in Figure 31 and Figure 32, the original Battelle Two-Curve Ductile Fracture analysis method was modified for small-diameter pipes. All the data, including the data from the current study, were curve fitted by minimizing the distance from the modified curve. The final equation of the modified curve for small-diameter pipes is given as

$$V_f = \left[\frac{C_B{}' \sigma_f}{\sqrt{CVP}}\right]\left[\frac{\sigma_d}{\sigma_a} - 1\right]^{1/2.65} \qquad (1)$$

V_f = Fracture speed, fps
C_B = Small diameter backfill constant (53.7 for no backfill and 43.9 for soil backfilled pipe when using U.S. customary units and with 2/3-thickness Charpy energy in ft-lb)
σ_f = Flow stress (average of yield and ultimate strength), ksi
CVP = Charpy V-notch energy for a 2/3-thickness specimen, ft-lb
σ_d = Decompressed hoop stress ($P_d R_m/t$), ksi
σ_a = Arrest stress, ksi
P_d = Decompressed pressure, ksi
R_m = Mean pipe radius, inch
t = Pipe or tube thickness, inch
σ_a = Arrest stress as given in Equation 9 in Part I of this report

Interestingly, the modified curves for both no backfill (air) and soil (sand) backfilled cases yielded the same exponent, i.e. 1/2.65. Moreover, the backfill coefficient for no backfill (air) case is same as the original curve, i.e. 53.7. The modified curves for both no backfill and soil backfilled cases are shown in Figure 31 and Figure 32, respectively. Figure 33 shows the comparison between the original curves and the modified curves.

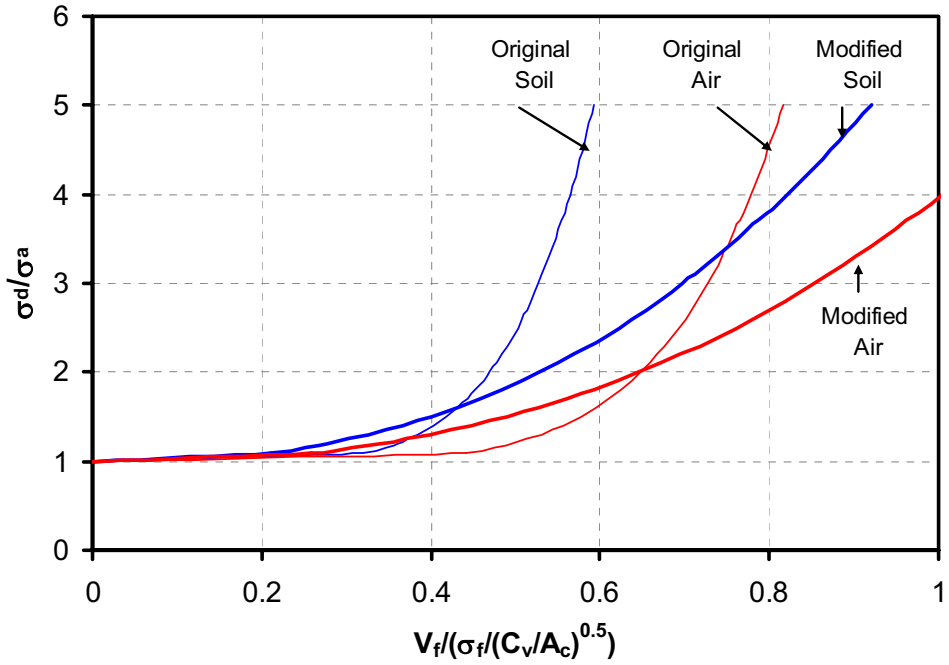

Figure 33 Comparison of the original Battelle Two-Curve and the modified curve for small-diameter pipes

6 EFFECTS OF BACKFILL USING MOJAVE TEST RESULTS

Comparing the measured fracture speeds from the Mojave experiments with the soil properties can give valuable insight into the true effect of the soil on the fracture behavior. If the moisture content alone is considered, the comparison plot is shown in Figure 34. In this figure, the diamond data points represent the average moisture content in the soil at the measured fracture speed while the horizontal error bars give the range of in-situ moisture content measured. The triangle symbols represent the predicted fracture speeds (using the original backfill coefficient) at the same average moisture content. For this set of tests, it appears that the fracture speeds are directly related to the moisture content. In addition, it appears that the behavior in the cohesive soils is overpredicted and the results in the non-cohesive soils are accurately predicted.

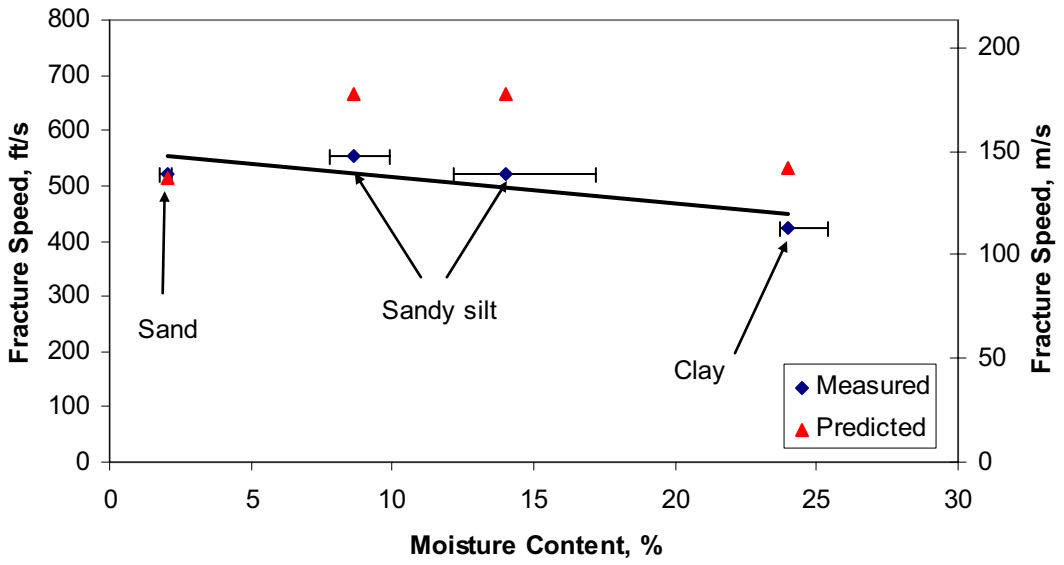

Figure 34 Comparison of fracture speed and moisture content

Since there were variations in the Charpy energy of the pipe joints used in the experiments, the same plot can be presented in terms of a normalized fracture velocity as shown in Figure 35. In this figure, the fracture velocities are normalized by both the materials flow stress as well as the Charpy energy. This term[a] is the same as Battelle used in developing the original backfill coefficients. As shown in Figure 35 the trend follows a power relationship with moisture, but only slightly varies with large changes in moisture.

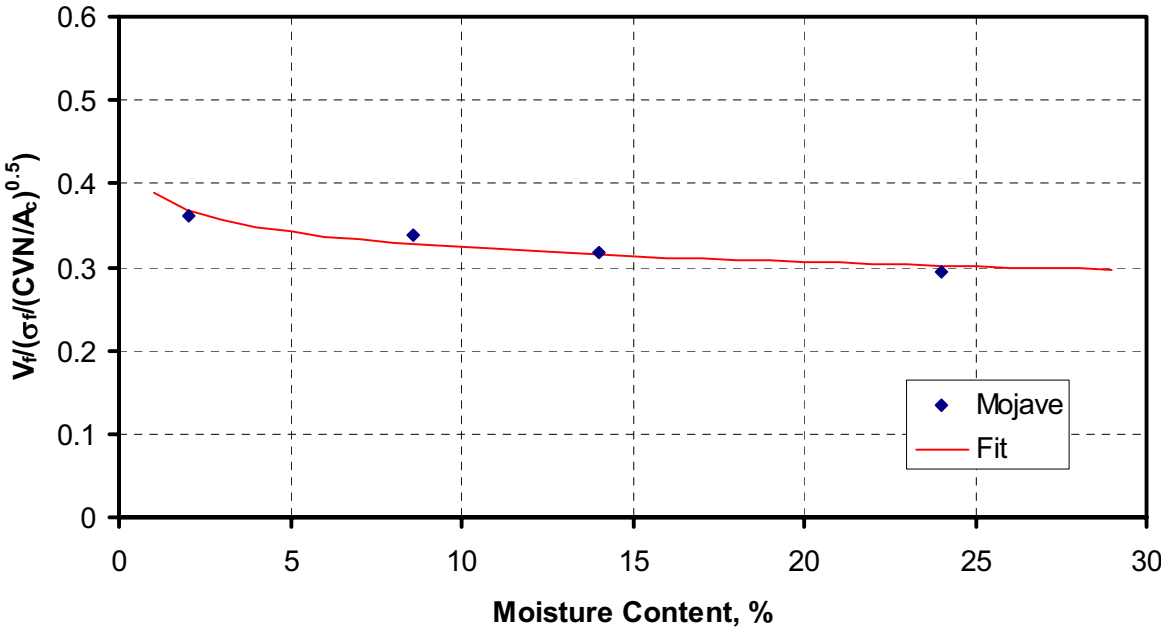

Figure 35 Comparison of normalized fracture speed and moisture content

[a] See the Y-axis from Figure 4 of the main body (Part I) of this report.

If the total density is considered, no clear trend is apparent, see Figure 36. Interestingly, the sand and the wet clay had about the same total density, but a large difference in fracture speed.

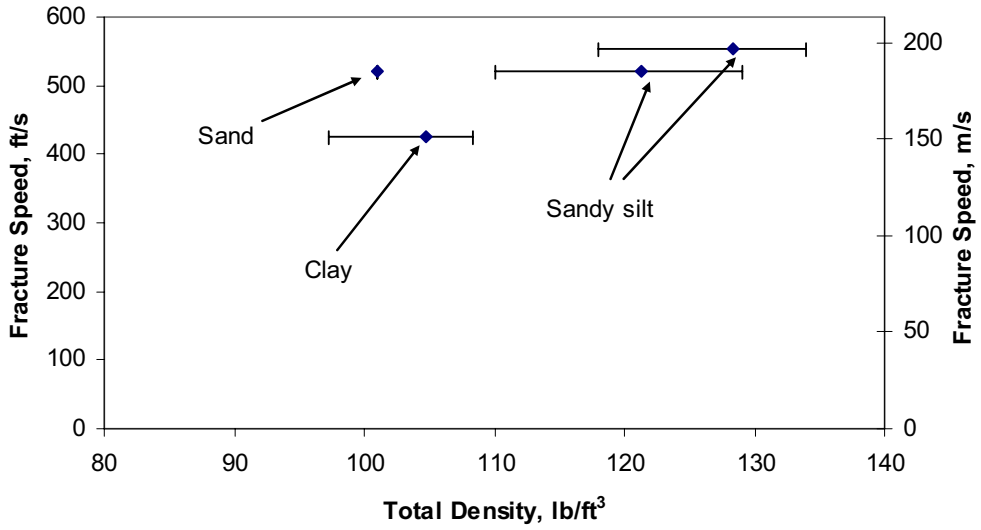

Figure 36 Comparison of fracture speed with total soil density

If it is assumed that the weight of the soil adds a normal stress, the shear strength of the sand and sandy silt can be estimated from the direct shear[b] tests. As shown in Figure 37, there appears to be a relationship between the shear strength of the soil and the fracture speeds. Also shown in Figure 37 are the trends of fracture speeds with ultimate shear stress calculated from a confined compression test. Even though it is unlikely that a compressive failure occurs during the pipe experiments, the trend of the strength data developed is similar to those from the direct shear tests.

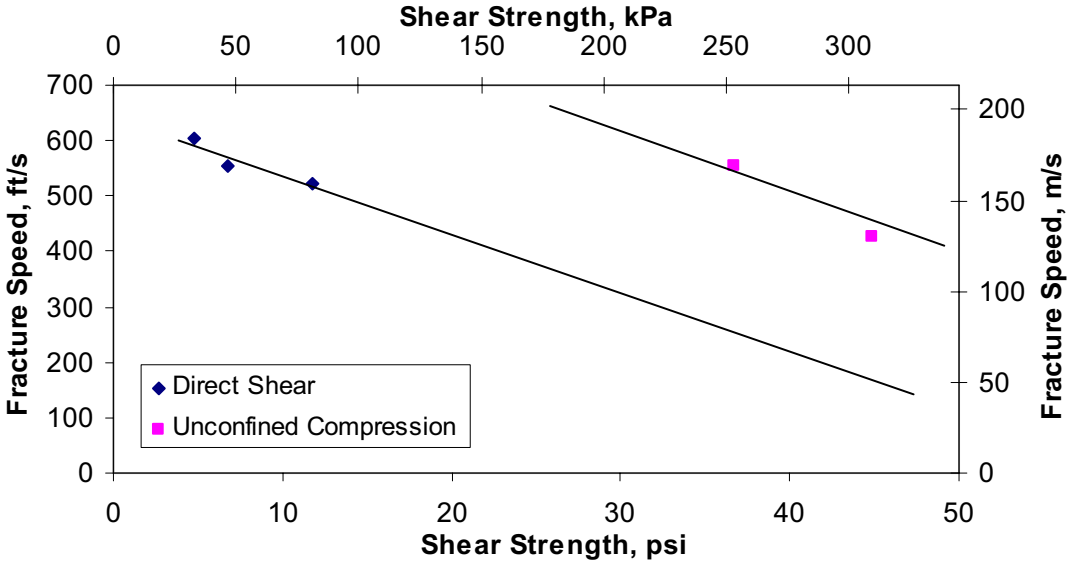

Figure 37 Comparison of soil shear strength with fracture speed

[b] See Part I for soils strength details

7 SUMMARY

In this volume (Part II) of the report, the details from the Mojave small-diameter pipe burst tests were presented. These experiments were conducted with different well-controlled backfill conditions to determine the effect of the soil properties on the steady-state crack propagation speed. The experiments were conducted in two series, one each year of the program. Even with the experimental difficulties in this series of experiment, the results indicate that there is a relationship between fracture speed and soil properties. These results are combined with the results from the JGA effort to form a solid conclusion in the main body of the report (Part I).

8 REFERENCES

1 Wilkowski, G. M., and Eiber, R. J., "CAGSL Model Crack Arrestor Program," Report to Northern Engineering Services Company, Ltd., July 1977

2 Poynton, W.A., and Christian, J.R., "An Experimental Study of Shear Fracture Propagation using Small Scale Models," Symposium of Crack Propagation in Pipelines, Paper 5, British Gas Corporation, Newcastle upon tyne, England, March 26&27, 1974.

3 Kobayashi, A.S., Emery, A,F., Love, W.J., and Chao, Y. –H., "Subsize Experiments and Numerical Modeling of Axial Rupture of Gas Transmission Lines," Journal of Pressure Vessel Technology, Vol. 110, May 1988, pp. 155-160.

4 Tang, H.T., Duffey, R.B, Singh, A., abd Bausch, P., "Experimental Investigation of High Energy Pipe Leak and Rupture Phenomena," Proceedings of the 1985 Pressure Vessel and Piping Conference, ASME, PVP-Vol 98-8, June 23-26 1985, pp. 125-134.

5 Wilkowski, G. M. and Eiber, R. J., "The Evaluation of Ductile Fracture Propagation Behavior in Frozen Soil," proprietary report to Northwest Alaskan Pipeline Company, September 4, 1980.

6 Wilkowski, G., Scott, P., and Maxey, W., "Design and Optimization of Mechanical Crack Arrestors for Pipelines," NG-18 Report 134, July 1983.

Program Final Report

on

FIRST MAJOR IMPROVEMENTS TO THE TWO-CURVE DUCTILE FRACTURE MODEL – PART III JGA TESTING DETAILS

Emc^2 project number 03-G78-01

to

U.S. Department of Transportation
Research and Special Programs Administration
Washington DC 20590
Agreement No. DTRS56-03-T-0007

and

Pipeline Research Council International, Inc.
Arlington, VA 22209
PR-276-04505

by

D. Rudland, D.-J. Shim, H. Xu, D. Rider,
P. Mincer, D. Shoemaker and G. Wilkowski

Emc^2

Engineering Mechanics Corporation of Columbus
3518 Riverside Drive
Suite 202
Columbus, OH 43221

May 2007

TABLE OF CONTENTS

LIST OF FIGURES

LIST OF TABLES

1 INTRODUCTION

This section of the report described the details relevant to the full-scale experiments conducted by the Japanese Gas Association. These data were made available to this project through an information exchange agreement between JGA and PRCI/DOT. The details of this agreement can be found in Appendix A of the main body of this report (Part I). As part of that agreement, this section of the report was generated to document for the PRCI and DOT the details of the full-scale experimental results that were used to generate the trends given in Part I. As the main deliverable of this agreement, the total document (Part I, II and III) will be delivered to all parties.

The full-scale test program conducted by the JGA consisted of four large diameter (30 and 24-inch diameter) burst experiments conducted on Japanese X80 linepipe material. Full material characterization including tensile, Charpy, and DWTT experiments were conducted and documented in the applicable test reports referenced in this section and are therefore not presented here. The experiments were conducted by FORCE technology at their high-energy pipe test facility near Copenhagen, Denmark. The experiments were designed and analyzed by JGA with assistance by Emc^2 through a separate consulting agreement.

After a brief description of the test site in Denmark, the details of each individual test will be given. These details include the experimental results relating to fracture speeds and decompression behavior as well as fracture behavior and any additional data collected in the experiments. Following this section, analysis results for the four experiments are discussed. These results illustrate the effects of backfill and moisture content on the minimum arrest toughness and fracture speeds. This section of the report concludes with a suggested modification to the backfill coefficient using the JGA test results.

2 DESCRIPTION OF FORCE TEST SITE

The full-scale pipe experiments were performed in Denmark, at the military Jaegerspris Camp, which is a military shooting area owned and operated by Defense Command of Denmark. The facility is situated 50 km from Copenhagen City Centre and the driving time by car is approximately 60 minutes.

The test facility location is shown on the maps in Figure 1 and Figure 2. A photo of the test facility is seen in Figure 3. The test facility is approved for full-scale burst tests by Danish Police and Danish Emergency Management Agency.

A strict safety control system for the test facility has been set up in corporation with Defense Command Denmark. The security distance is 1,000 m (prescribed and regulated by the Defense Command Denmark). Before and during an experiment, fourteen military guards control the secured area.

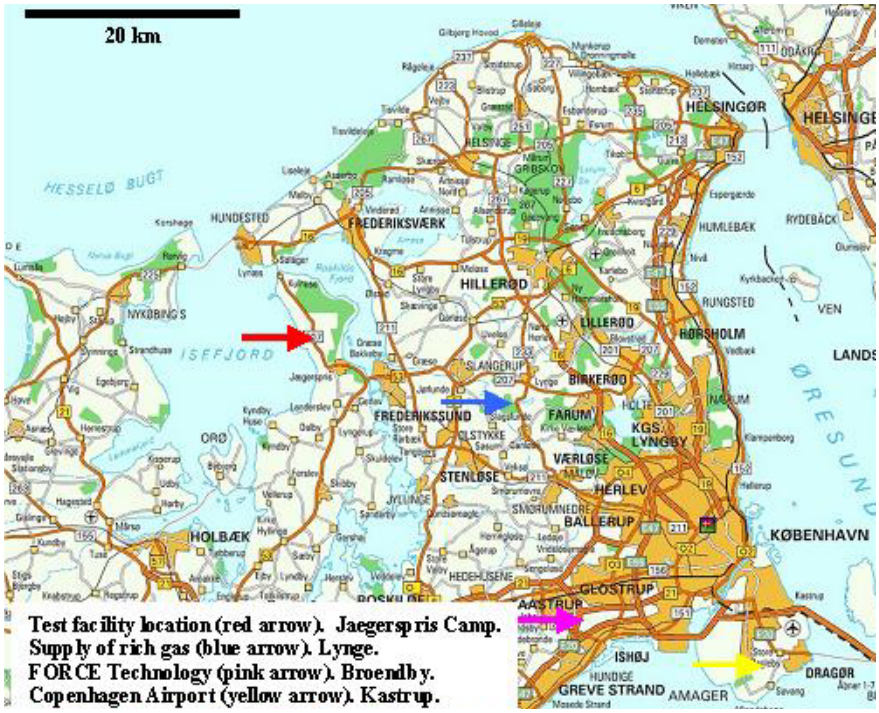

Figure 1 Map showing key location in Denmark

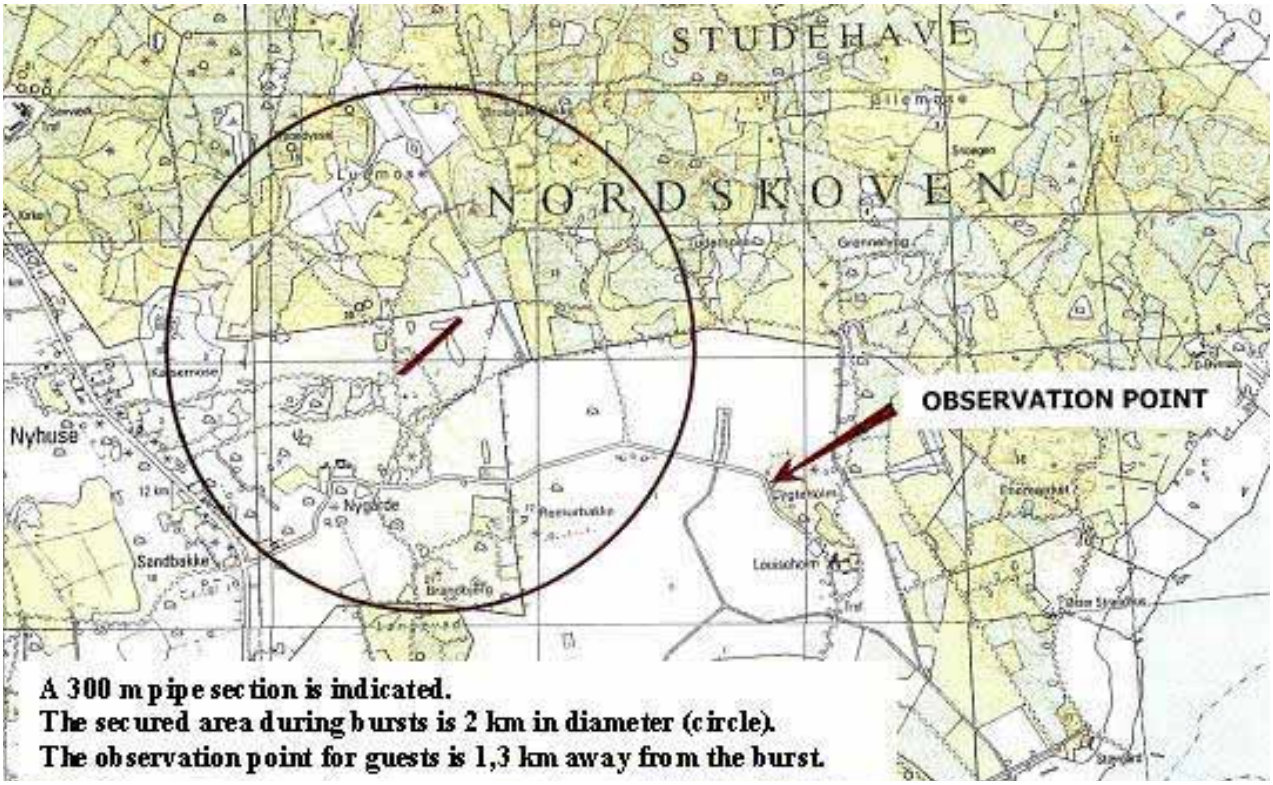

Figure 2 Map of test facility location in Denmark

Figure 3 Photograph of test facility

3 DETAILED BURST TEST RESULTS

3.1 November 2004

The first JGA full-scale crack-arrest experiment was conducted on November 2004 at FORCE Technology. The details of the test specification and results are given in Reference 1. The pipe test was conducted at an average temperature of 6.2 C at a pressure of 18.42 MPa. The west side of the pipe was not backfilled, while the east side of the pipe was backfilled with wet compacted sand. The moisture content of the sand was not controlled, but was measured in three locations along the buried side at two depths. On average, the water content was about 13% (8.6% is optimum) and the compaction level was approximately 93%. Details of the sand measurements can be found in Reference 1. The layout for this experiment is shown in Figure 4.

The test section consisted of ten, 762-mm diameter, 17.5-mm wall thickness, 10-m joints of X80 material. The toughness arrangement for the test joints can be found in Figure 5 A weld overlay procedure was used at each of the test girth welds, and crack arrestors were installed at the start of the reservoir section. Strain gages were used to measure the axial movement of the pipe during pressurization, but not measured during the actual crack arrest experiment. Data from 32 pressure transducers, 138 timing wires, and four accelerometers were recorded dynamically throughout the experiment. Thermocouple readings were taken on both the pipe surface and in the gas prior to the start of the experiment. The location of the instrumentation on this experiment is shown in Figure 6.

The burst test was conducted successfully, with crack propagation in the backfilled side traveling through the first two test sections and arresting within about 4 meters in the third test section.

On the unbackfilled side, the crack traveled though all of the pipe joints and arrested 5.5 meters into the last pipe joint. A schematic of the crack profile is shown in Figure 7.

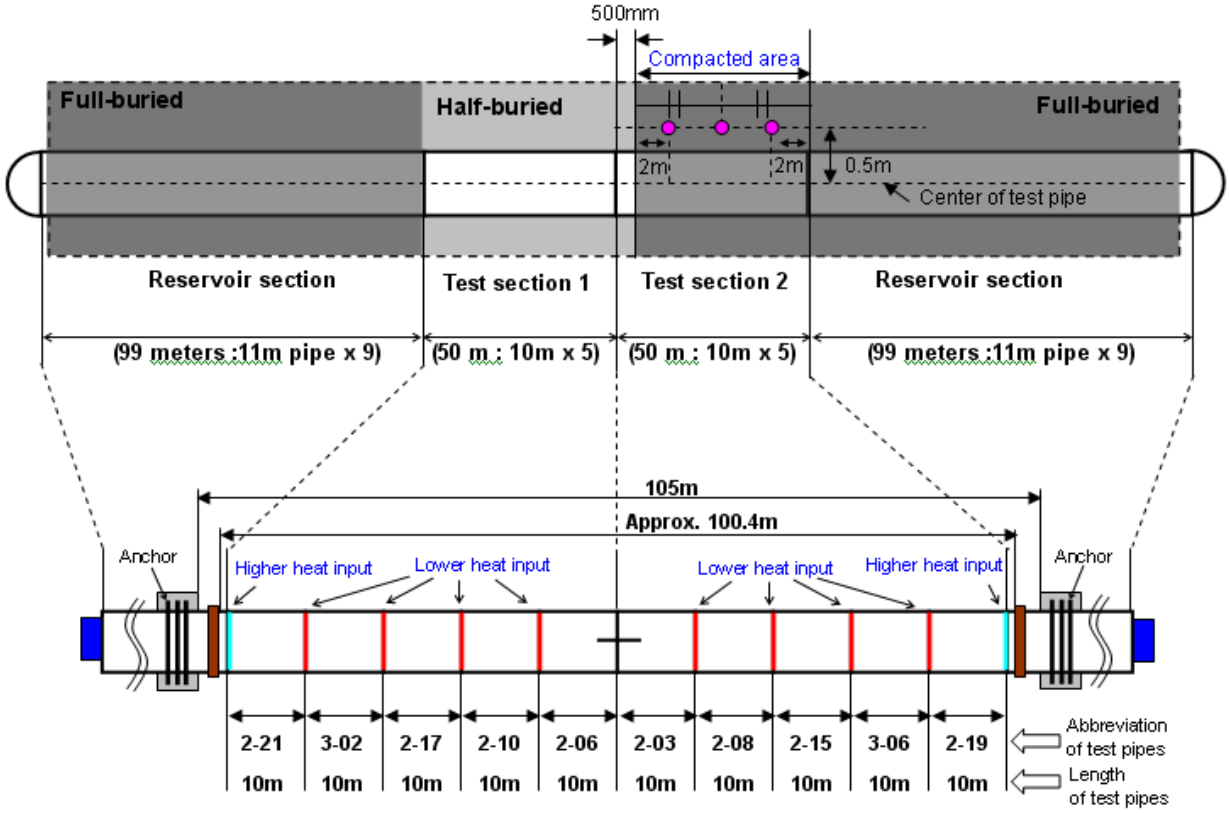

Figure 4 Layout for the November 2004 experiment

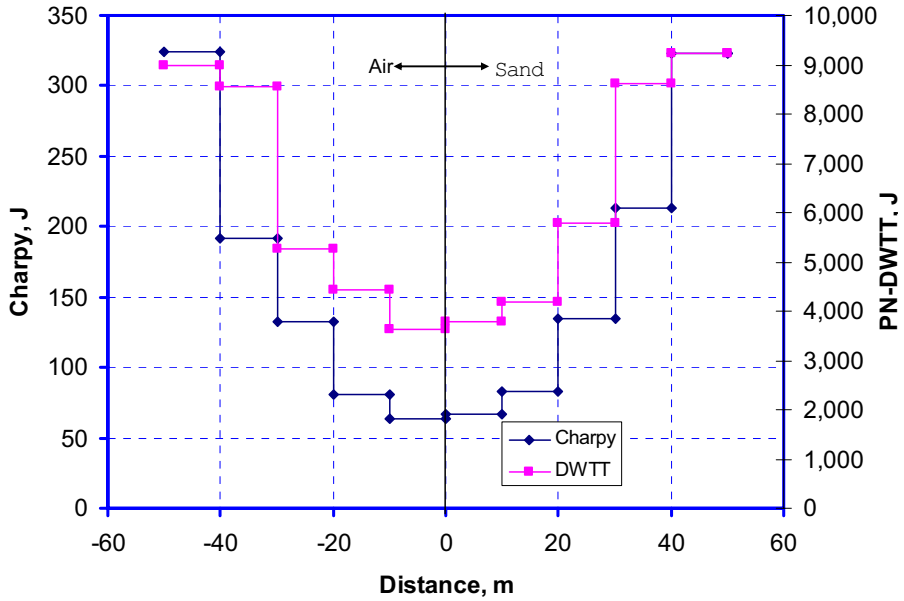

Figure 5 Toughness arrangement for November 2004 experiment

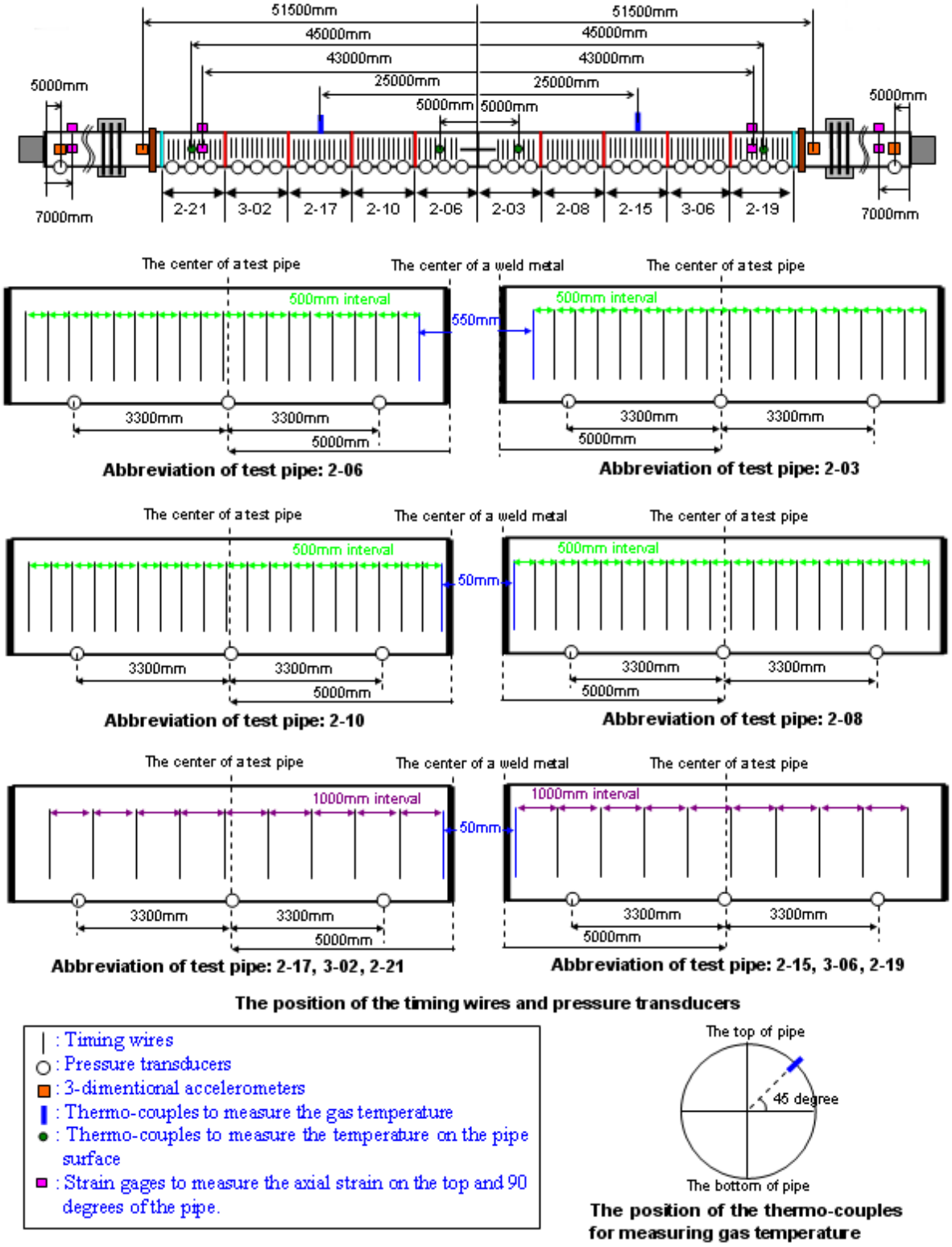

Figure 6 Instrumentation layout for November 2004 experiment

The high-speed video of the experiment showed that the pipe lifted vertically a considerable amount during the running fracture event. From some strain-gauged tests conducted by AISI [2] in the past, it was shown that the axial strains from pipe movement during the burst process decay to zero about 4 diameters ahead of the crack tip. From the video taken during the experiment, it appears that the thrust forces from the crack opening have both a vertical and axial component (the escaping vapors are at an angle relative to the pipe). The axial component of the force is what causes the pipe to lift ahead of the running crack tip. As the crack approaches the inboard anchor, the pipe is not allowed to move naturally, and the upward motion is amplified as the pipe movements are forced to zero at the anchor. It is very difficult to know the magnitude of the axial strains ahead of the running crack and the effect on the crack-driving force without conducting a numerical analysis. Logically, the increased vertical movement equates to increased axial strains, but how these axial strains affect the crack driving force is unknown without detailed finite element analyses.

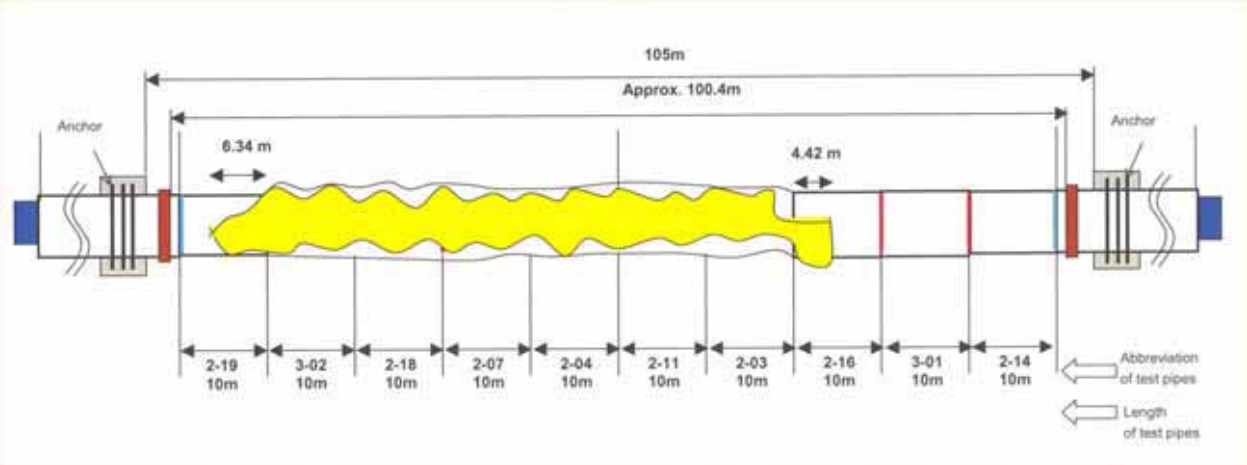

Figure 7 Schematic of fracture pattern in November 2004 experiment

3.1.1 Timing-wire data and fracture speeds

The timing wire and fracture-speed data for the November 2004 test was fully reduced for both the backfilled and unbackfilled side of the experiment. The quality of the timing-wire data on the unbackfilled side was acceptable. A sample of the raw timing wire data on the unbackfilled side for this experiment is shown in Figure 8. However, the data on the soil side was not well behaved. As shown in Figure 9, there may be instances where it appears that timing wires were breaking sooner than expected, suggesting that deformation, or connector failure may be the cause of the timing wire failures. There were at least seven cases where this behavior occurred. The reduced crack distance versus time data are shown in Figure 10. This data shows clearly, that in the second pipe joint, timing wire failures made it impossible to determine crack velocity history.

When incremental velocities are plotted, as shown in Figure 11, it can be seen that on the unbackfilled side of the pipe, the crack decelerated for the first two meters of each pipe joint before reaching a steady-state speed. Looking at the last joint on the unbackfilled side, it appears that the crack was decelerating after entering the last joint, but the rate of deceleration is not as great as between the second and third joints. The final incremental fracture speed was about 100 meters per second on the unbackfilled side, which is close to the slowest steady-state fracture

speed that could occur with a material having slightly lower than the minimum toughness for arrest.

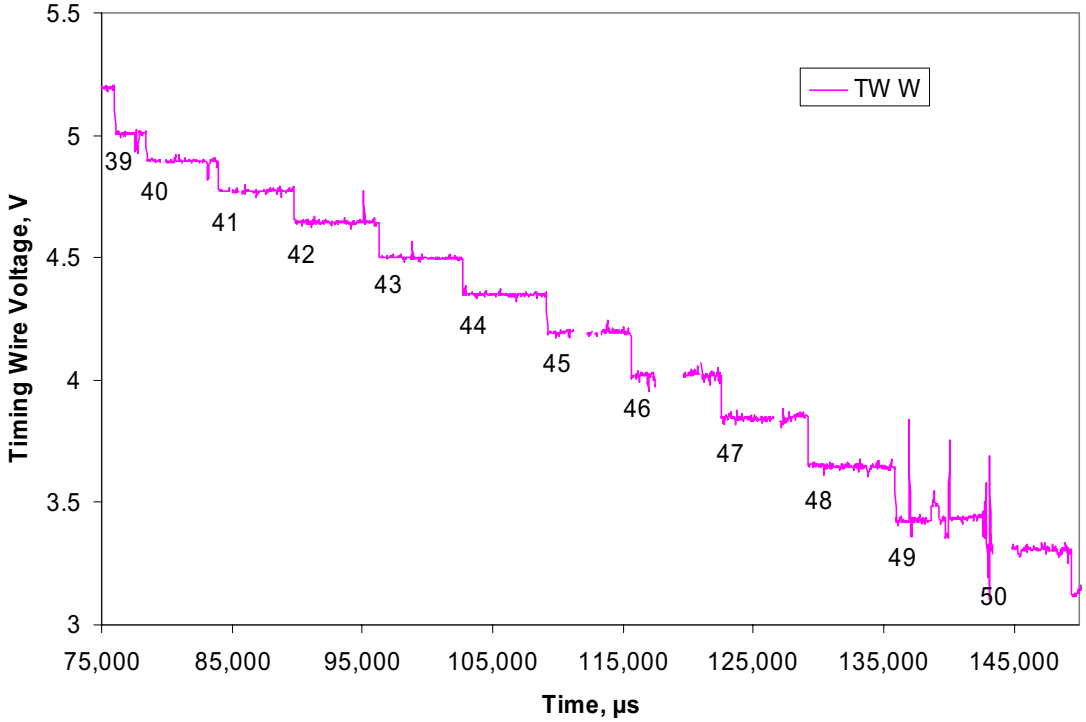

Figure 8 Unbackfilled side (West) timing wire data for Timing Wires 39-50

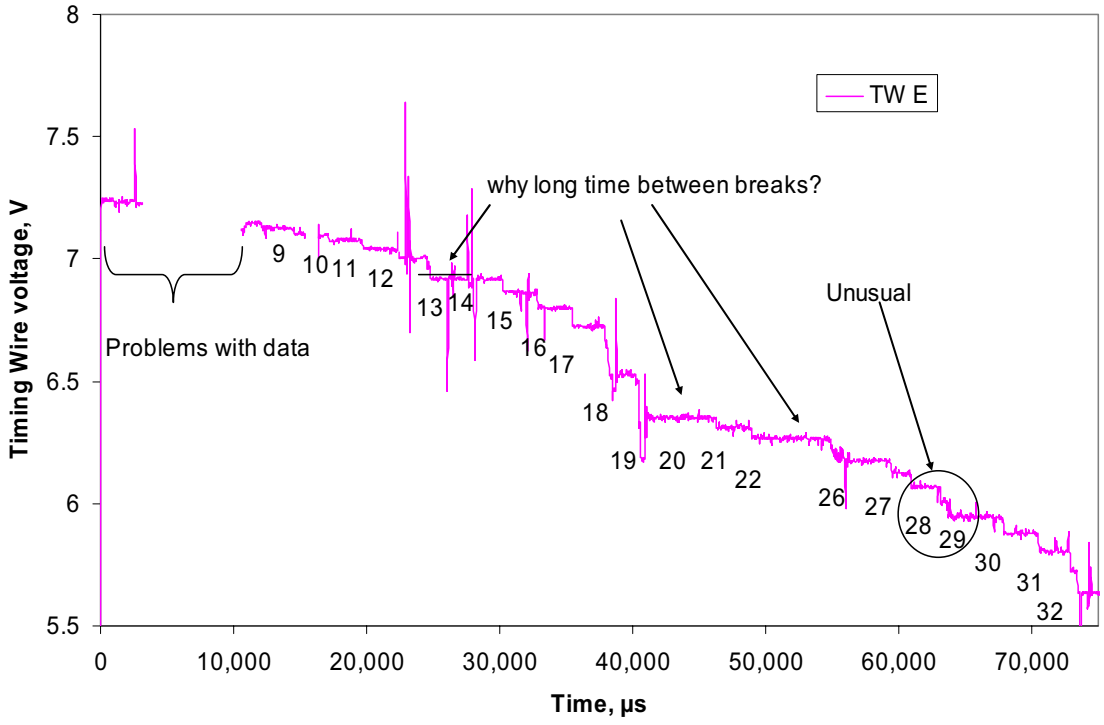

Figure 9 Sand backfilled side (East) timing wire data for Timing Wires 1-32

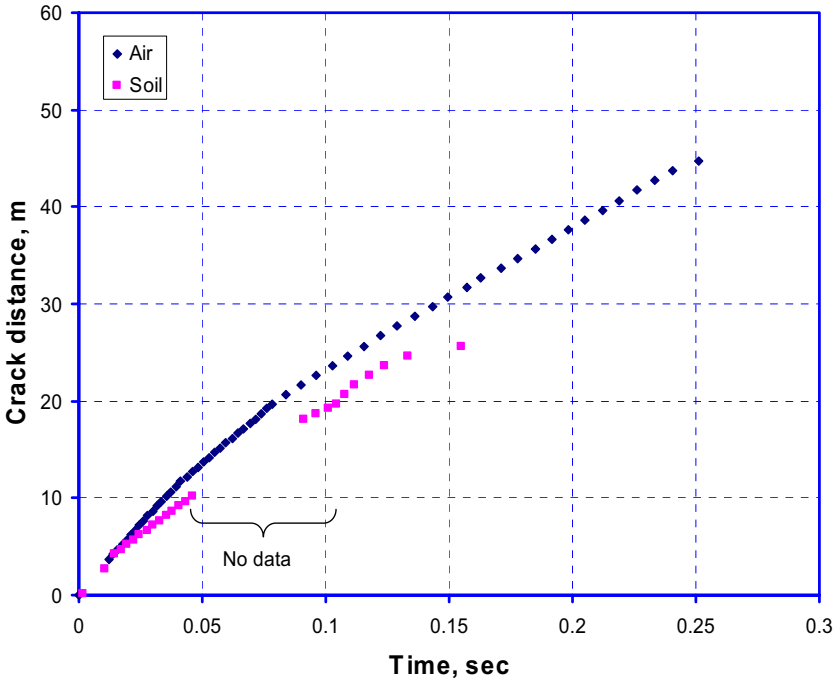

Figure 10 Crack distance versus time for November 2004 JGA crack arrest experiment

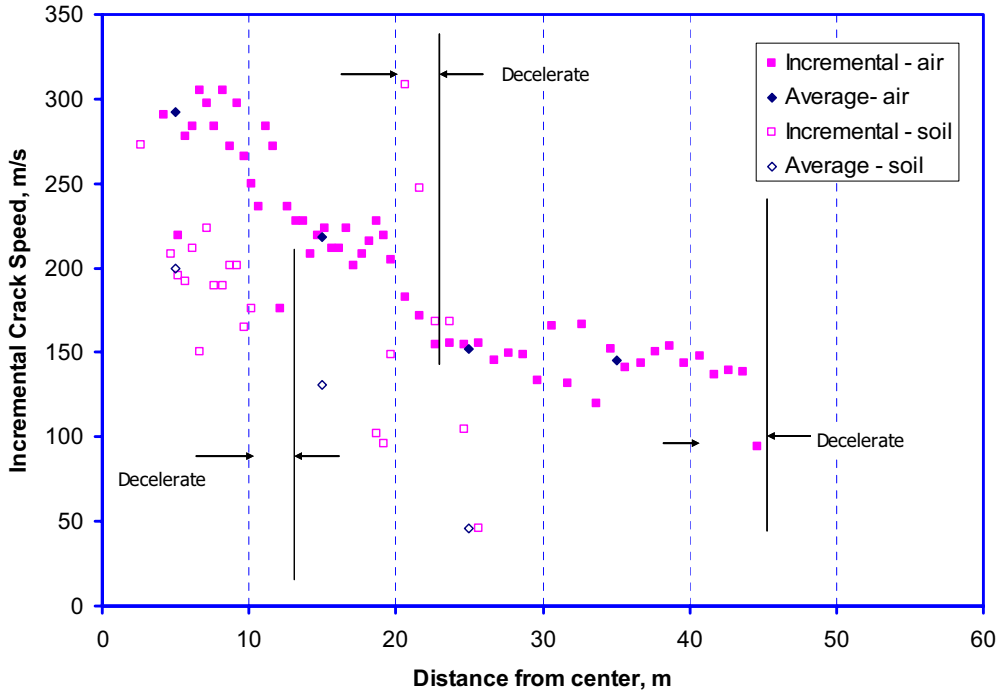

Figure 11 Incremental fracture speeds from November 2004 experiment

From the available timing-wire data, average fracture speeds can be calculated. For each joint where sufficient timing wire data was available, areas of deceleration and steady-state propagation were observed. The steady-state fracture speeds were extracted for each applicable pipe joint and the results are shown in Table 1 and Figure 11. Note that in both the backfill and

unbackfilled (air) side, the last pipe joint that the cracks propagated in did not have sufficient crack propagation length to determine steady-state fracture speed due to the arrest; therefore, the data in Table 1 represents the best engineering approximation of the fracture speed just before arrest.

Table 1 Average steady-state fracture speeds from November 2004 JGA crack arrest experiment

	Fracture speed, m/s				
Backfill/Joint #	**1**	**2**	**3**	**4**	**5**
Air	292	218	152	145	~100
Sand	200	130	~46		

3.1.2 Pressure transducer data

The pressure transducer data can be used to make an estimate of the decompression behavior of the gas, as well as a rough estimate of the fracture speed. A typical pressure decay plot is shown in Figure 12. In this plot, the experiment was started at a time of zero. At time 0.04 seconds, decompression occurs as the decompression wave passes the transducer. At approximately 0.11 seconds, the crack passes the transducer location as is illustrated by a distinct change in the pressure decay. By plotting the transducer location against the time at which the crack passes the transducer, an estimate of the fracture velocity can be made. In addition, if time versus location is plotted for curves of constant pressure, an estimate of the decompression behavior can be calculated. These results are discussed next.

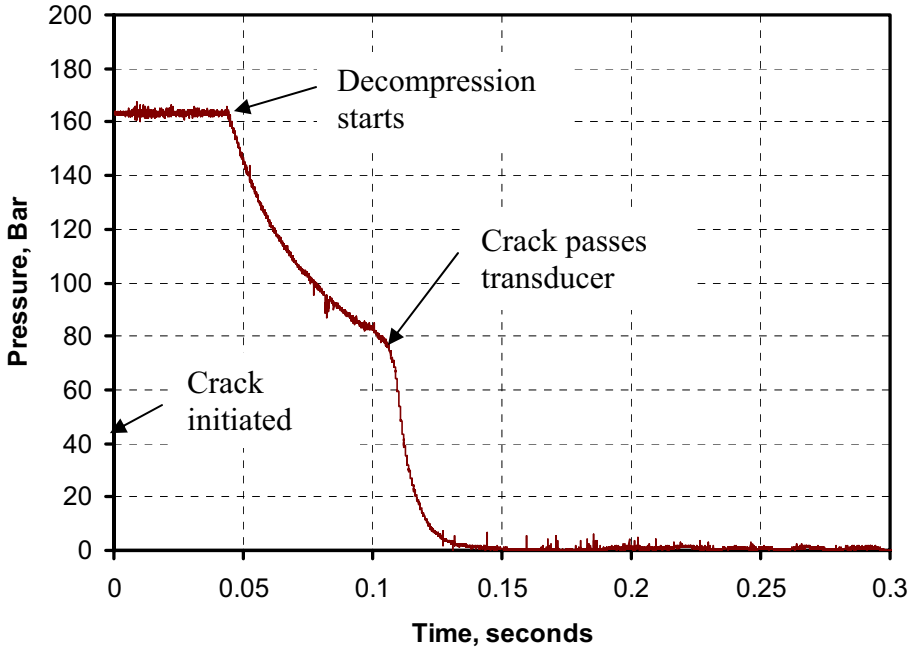

Figure 12 Typical pressure decay for a crack propagation experiment

In the November 2004 crack-arrest experiment, thirty-two pressure transducers were monitored dynamically throughout the course of the experiment. For the most part, the transducers on the

unbackfilled side were well behaved, while many of the transducers on the soil side acted poorly. In fact, it was theorized that water from the hydrotest was trapped in the pressure transducer cavity between the opening and the diaphragm. An overnight freeze occurred, probably causing ice expansion in the pressure transducer cavity and damaging the diaphragm.

From the available pressure transducer data, an estimate of the decompression behavior can be made as shown in Figure 13. Also shown in this figure are the predictions using GASDECOM for the actual gas composition that existed during the experiment. Due to the crack arrest, and the timing of the data collection, experimental data below the two-phase plateau do not exist.

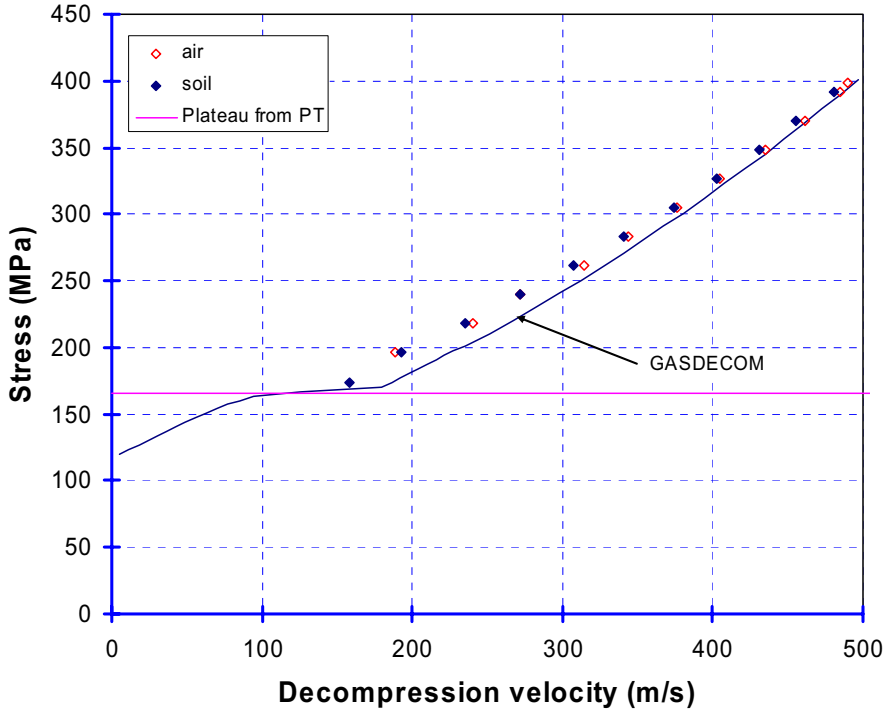

Figure 13 Decompression behavior for November 2004 JGA crack arrest experiment

The results in Figure 13 suggest that GASDECOM overpredicted the decompression velocity above the plateau, although the plateau stress appeared to be captured correctly. For both the soil and air cases, the predictions of arrest occur below the plateau, so conclusions about the effects of the decompression behavior on the arrest toughness cannot be made from this data. However, the minimum arrest toughness predictions fall close to the knee of the decompression curve, which adds a great amount of uncertainty to the predictions, i.e., a small change in decompression behavior at the plateau can make large changes in the required minimum arrest toughness.

The pressure transducer data on the unbackfilled side can also be used to make an approximation of the fracture speeds. The data on the soil side was not sufficient for making this prediction. If the pressure transducer data on the unbackfilled side are plotted with the crack distance-time plot from the timing wires, a comparison can be made, see Figure 14. As shown in this figure, the pressure transducer data and the timing wire data are very similar and confirm the accuracy of the fracture speeds on the unbackfilled side of the experiment.

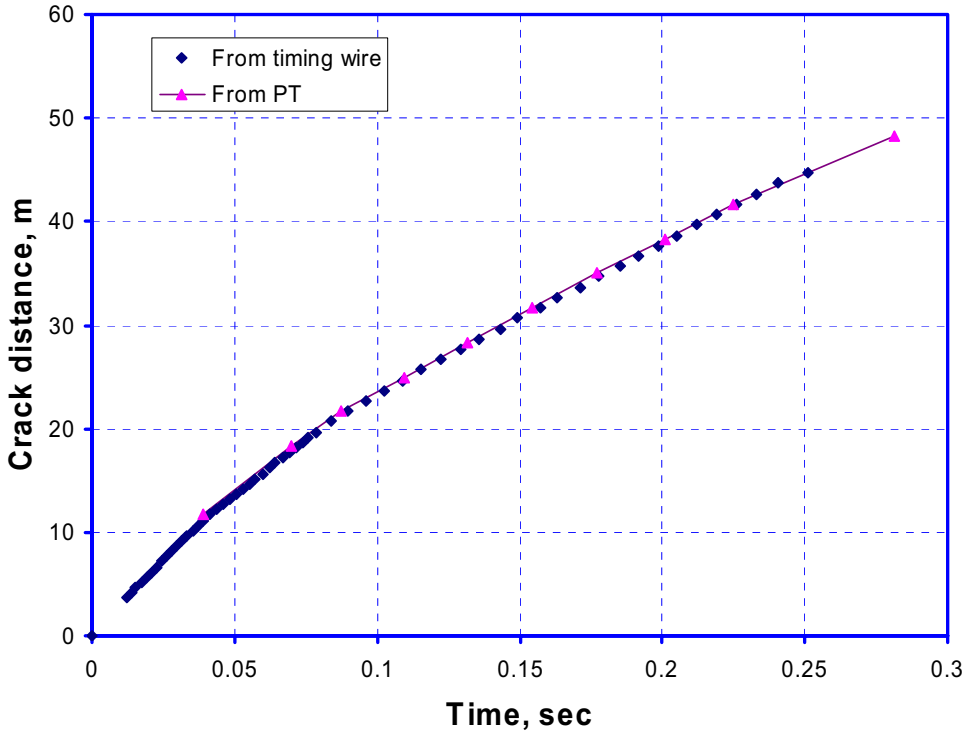

Figure 14 Comparison of crack distance versus time from timing wires and pressure transducer data

3.2 June 2005

This test was conducted on June 21, 2005 at FORCE Technology. The details of the test specification and results are given in Reference 3. The pipe test was conducted at an average temperature of 19C and at a pressure of 16.16 MPa. Both the east and west sides of the pipe were unbackfilled. The layout for this test is shown in Figure 15.

The test section consisted of nine 10 m sections and two 5 m sections. Each pipe joint had an outer diameter of 762 mm and a wall thickness of 17.5 mm. The toughness arrangement for the test is given in Figure 16. A weld overlay procedure was used at each girth weld on both the pipe ID and OD to prevent ring-off at the girth welds. In addition crack arrestors were used at the end of the test section to protect the reservoir pipe. Strain gages were used to measure axial movement of the pipe during pressurization but were not recorded dynamically during the experiment. Data from 100 timing wires and 30 pressure transducers (both type A205a and FP2000[a] pressure transducers were investigated) were recorded dynamically throughout the experiment. Thermocouple readings were taken on both the pipe surface and in the gas prior to the start of the experiment.

[a] In the November 2004 experiment there were some problems with the reliability of the FP2000 transducers. These transducers are recessed diaphragm transducers that were placed about 100 degrees from the pipe top dead center. Water from the hydrotest became trapped in the transducer cavity, and froze causing the transducer to fail. A205a are flush diaphragm transducers that were thought to solve this problem.

There were two main objectives to this experiment

1. Evaluate the correction needed to the Battelle Two-Curve Method minimum arrest toughness predictions for unbackfilled pipe. In the November 2004 experiment, the crack traveled much farther than expected on the unbackfilled side of the pipe. In fact, the correction factor on the Battelle Two-Curve Method minimum arrest toughness prediction was approximately 2, which is much larger than the 1.3 to 1.4 experienced with other X80 pipes[b].
2. The test pressure on this experiment was reduced to 16 MPa (63% SMYS) to investigate the effect of the lower pressure on the results and predictions.

The instrumentation layout for this experiment is given in Figure 17. The burst test was completed successfully, with the crack traveling through the starter and first test joints in an axial manner. As the crack entered the second test joint on the west side, the crack turned circumferentially and severed about 2.2 m after entering the second test joint. As indicated in the video of the event, the double-ended break caused the pipe on the west end of the test section to jump out of the pit and plastically deform the reservoir pipe outboard of the crack arrestor. After the circumferential break in the pipe, the axial strains in the pipe may be lower and the crack running in the east side of the pipe may be affected. However, it is unknown to what extent this effect will have on the fracture speeds and arrest toughness. The large movements in the pipe can increase the driving force causing the crack to travel farther than would be expected. The fracture pattern for the June 2006 experiment is shown in Figure 18.

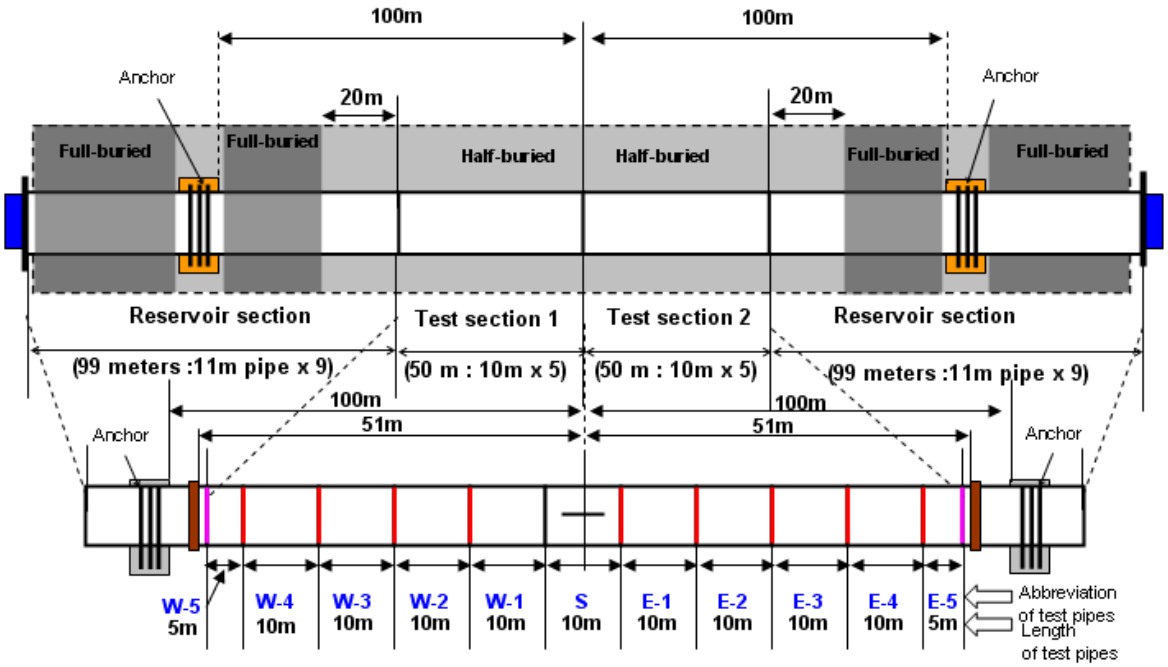

Figure 15 Layout for June 2005 experiment

[b] It is not typical to run a full-scale experiment unbackfilled; therefore, the correction factor of 1.3 to 1.4 times the minimum arrest toughness is based on soil backfill experiments and may not be applicable for unbackfilled tests.

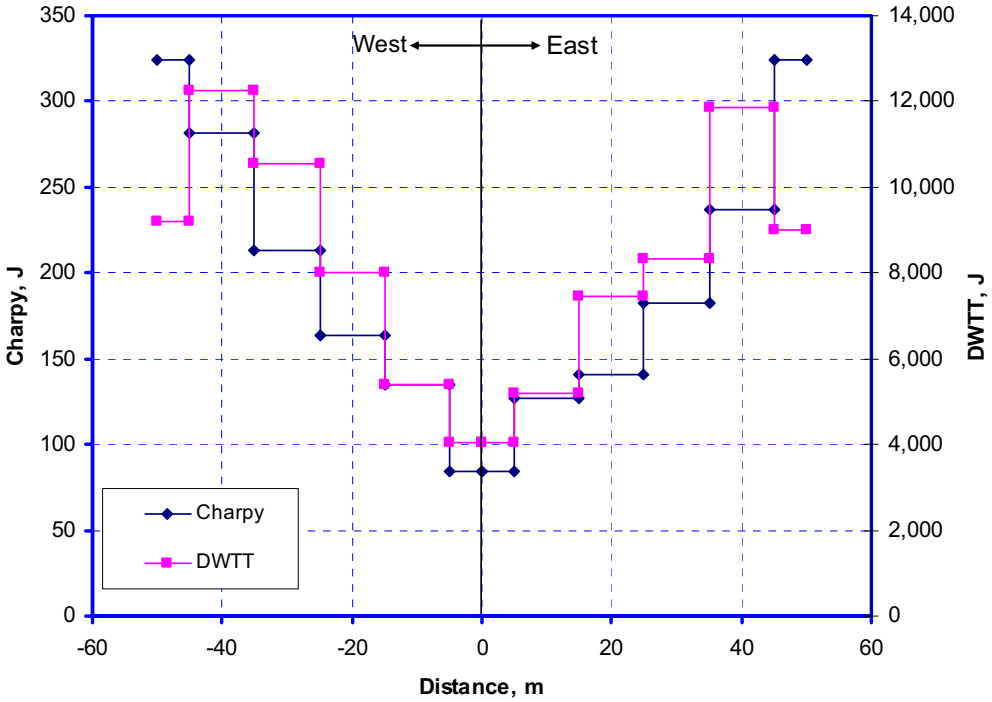

Figure 16 Toughness arrangement for June 2005 experiment

In addition, upon viewing the video for this experiment, it seemed that the pipe was not straight before the burst test. This may have been an optical illusion, but if the pipe was not welded straight, the eccentricity imparted on the pipe may cause the principal stress direction to change during the experiment causing a ring-off in the pipe.

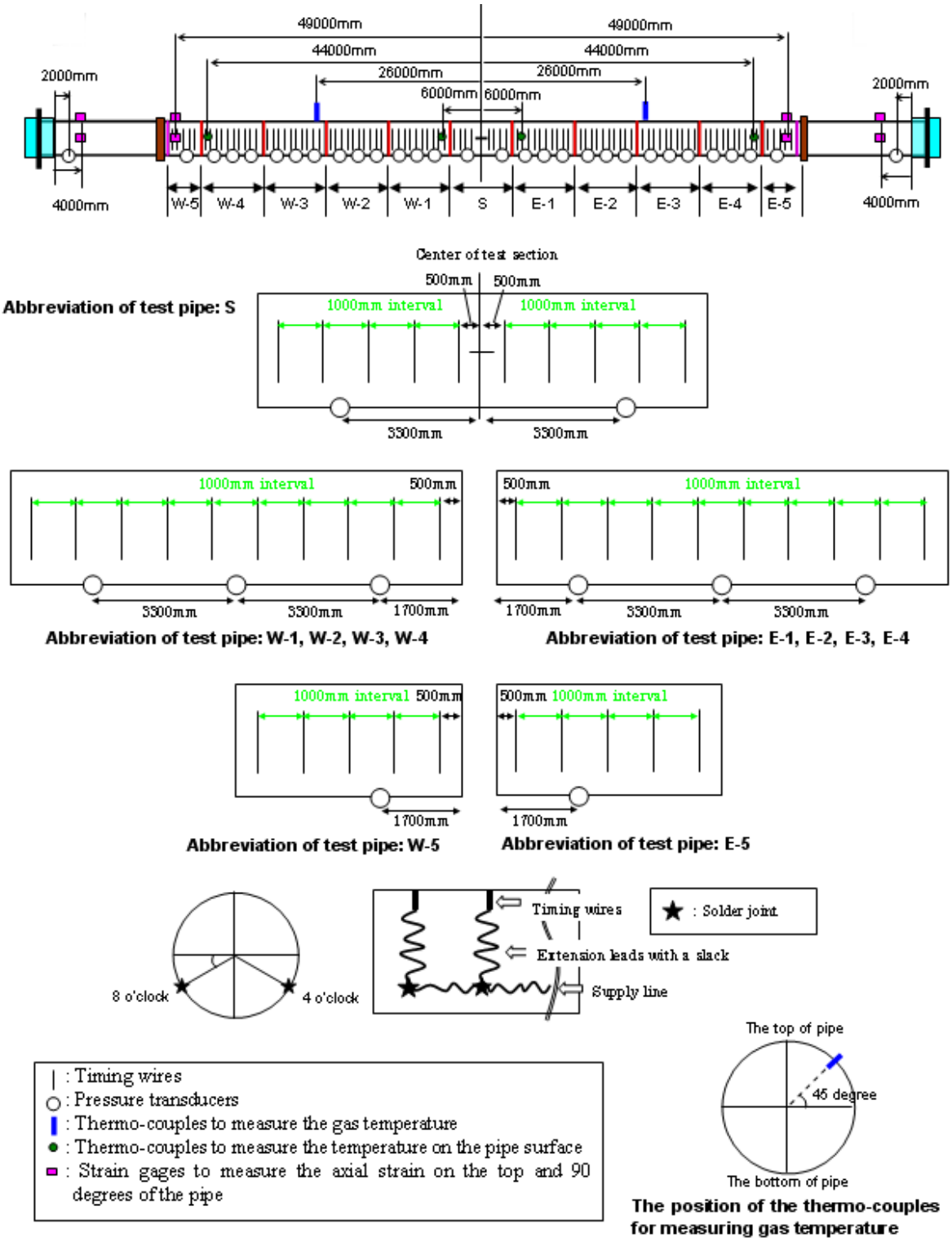

Figure 17 Instrumentation layout for June 2005 experiment

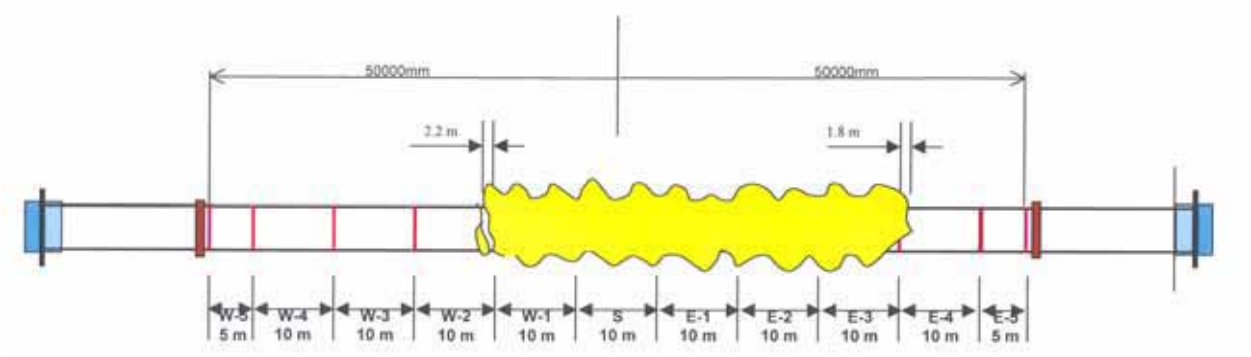

Figure 18 Fracture pattern for the June 2005 experiment

3.2.1 Timing wire data and fracture speeds

The timing wire break times and incremental fracture velocities can be found in Figure 19 and Figure 20, respectively. Note again, that in this experiment, the crack ran into the second test joint and then rung off on the west side of the pipe. The behavior is clearly seen in the incremental fracture speeds as the crack decelerates rapidly[c] as it enters the second test joint. After the pipe severed, the timing-wire instrumentation was destroyed before the crack on the east side of the pipe left the second test joint.

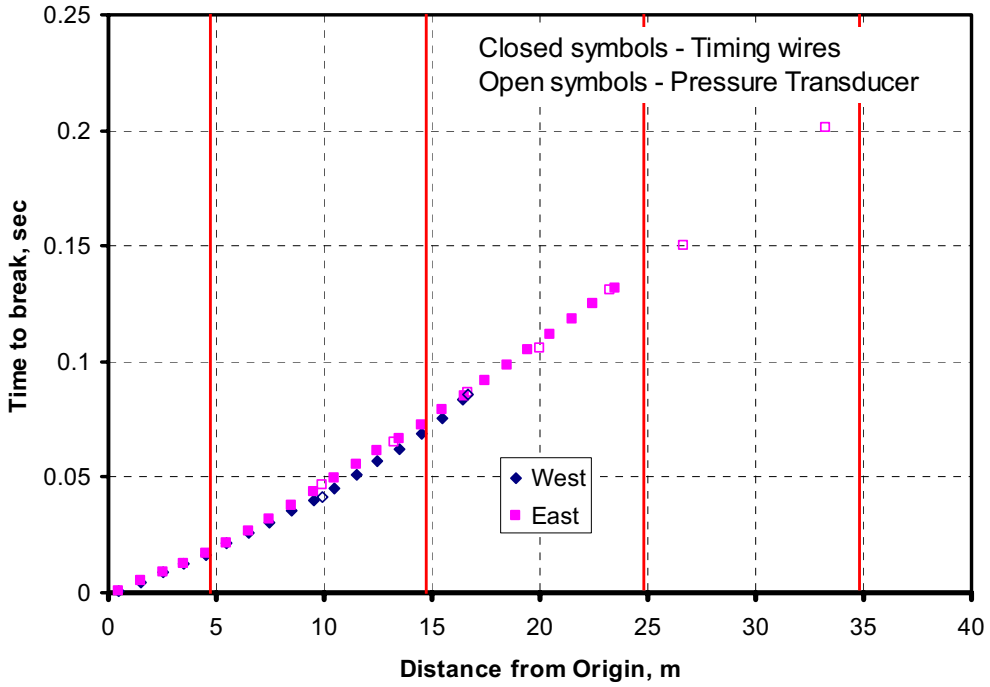

Figure 19 Timing-wire data for June 2005 experiment

[c] Incremental velocity values are very sensitive to small errors in the precise spacing between the wires, or precise time being picked off the data acquisition, and the precise relationship between when the wire breaks relative to the crack tip location. Hence these data are susceptible to much more scatter than averaging speeds over larger distances.

In addition to the timing wire data, the pressure transducer data can also be used to make an estimate of the fracture speeds. As shown in the next section of the report, the pressure transducer data shows a change in behavior as the crack passes the transducers, which can be plotted as a function of time to estimate the fracture speed. As shown in the preceding figures, the pressure transducer data agrees very well with the timing wire data, and illustrates that the crack does not slow down significantly on the east side of the pipe after the crack rings off on the west side of the pipe. However, this is not definite proof that the ring-off on the west side of the pipe did not affect the crack propagation behavior on the east side of the pipe.

In addition, the video from the experiment indicates that the pipeline may not have been straight at the start of the test. If this was the case, then the ring-off may have been caused by something other than a toughness arrest. For future tests, steps were taken to make a measurement of the straightness of the pipe before backfilling or testing.

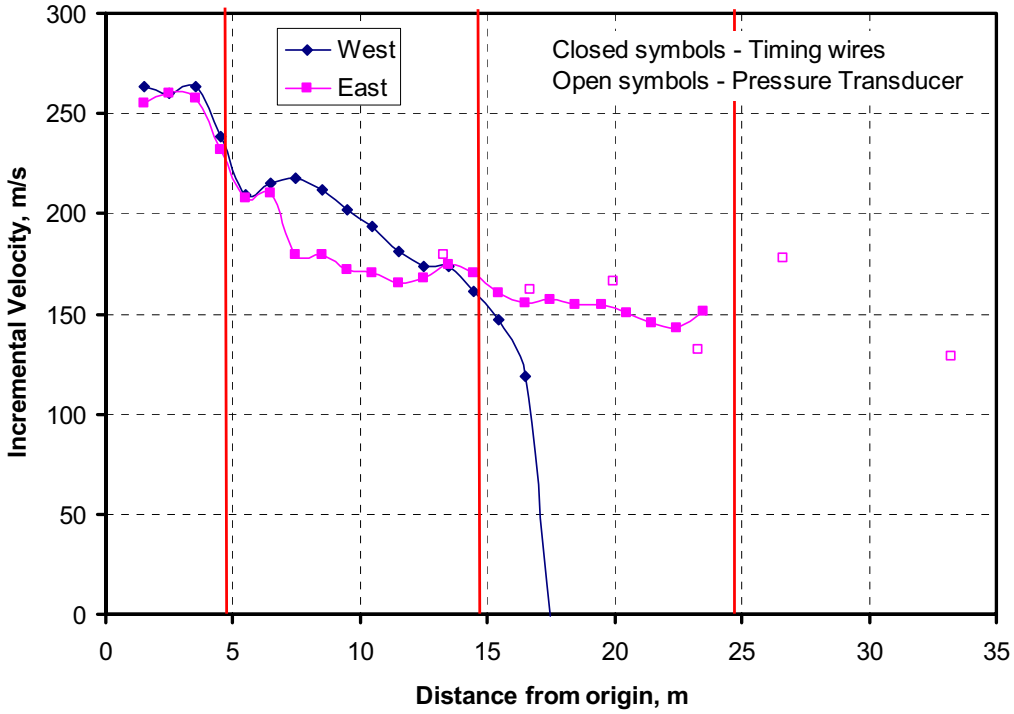

Figure 20 Incremental velocities for June 2005 experiment

3.2.2 Pressure transducer data

For the June 2005 experiment, two different pressure transducers were considered. Both were Sensotec transducers, but the A205a is a miniature, flush diaphragm type, pressure transducer while the FP2000 is a recessed diaphragm, larger pressure transducer. In the November 2004 experiment, only the FP2000 transducers were used, and some of the transducers possibly failed due to freezing water that may have been trapped in the transducer cavity after the hydrotest. It was then thought that the flush diaphragm transducers would eliminate this possible failure scenario.

However, using the A205a transducers on the June 2005 experiment illustrated one of the main shortcomings of this transducer. When the A205a pressure transducers were calibrated in the laboratory, each of the transducers acted very stably and the calibrations matched very closely. However, after the transducers were installed on the pipe, the calibrations seemed inconsistent. For instance, at full pressure, the FP2000 gage output was within 1% of the highly calibrated transducer on the pipe and the scatter between the FP2000 gages had a coefficient of variance of 0.1%. On the contrary, the A205a transducer output was 3% lower than the highly calibrated transducer and the scatter between the A205a transducer had a coefficient of variance of 5%. This large difference only seemed to be apparent in the initial calibration. If the A205a transducers were post calibrated, the behavior of these transducers was very similar to the FP2000 transducers. These trends are observed from the prediction of the decompression behavior shown for the east and west side of the pipe in Figure 21 and Figure 22, respectively.

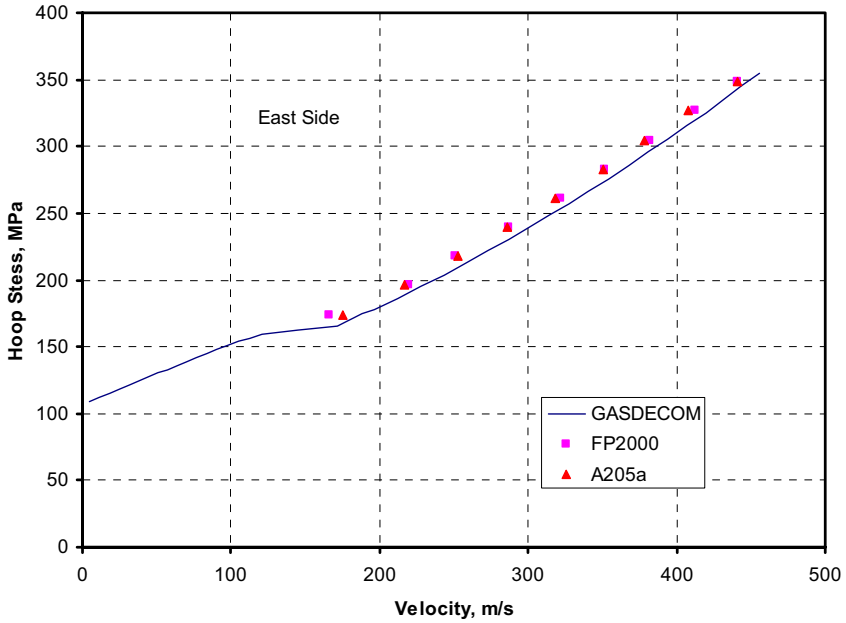

Figure 21 Measured versus predicted decompression behavior for the east side of the pipe in the June 2005 experiment

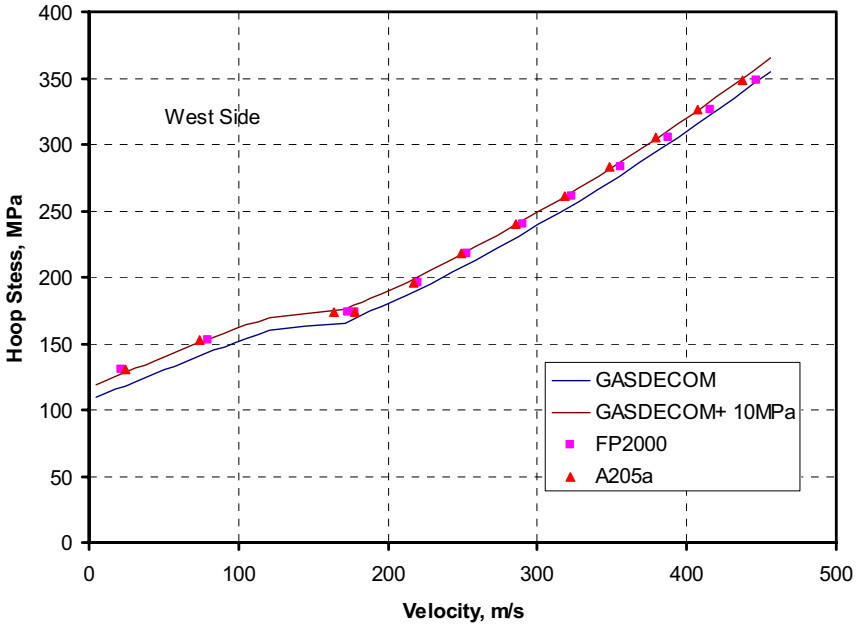

Figure 22 Measured versus predicted decompression behavior for the west side of the pipe in the June 2005 experiment

As shown in these figure, the measurements of pressure for both the FP2000 and A205a transducers are very similar. In comparison to the predictions using GASDECOM, the measured velocity is lower for the same hoop stress than the predictions. In fact for this experiment, the offset seems to be constant over the entire decompression curve. For the west side of the pipe, the data was sufficient to measure the pressures below the knee of the decompression curve. With this data, it was shown in Figure 22 that the measured decompression pressure could be predicted if 10 MPa is added to the stresses predicted from GASDECOM. This result is a bit inconsistent with the results from the November 2004 experiment, see Figure 13. In this experiment, the measured pressure was very close to the predicted pressures for high wave velocities, but as decompression occurred, the difference between the measured and predicted pressures became greater.

3.3 October 2005

This experiment was conducted on October 11, 2005 at the FORCE Technology site. The details of the test specification and results are given in Reference 4. The pipe test was conducted at an average temperature of 13.7 C and at a pressure of 18.59 MPa. In this test, the west side of the pipe was backfilled with sand to a depth of 0.5 m, while the east side of the pipe was backfilled with sand to a depth of 1.0 m. The moisture content of the sand was not controlled, but was measured in six locations along the pipe at two depths. The average results of the density and moisture measurements are shown in Table 2. The sand in this test was considerable more dry than the 13% moist sand in the November 2004 experiment. The layout for this test is shown in Figure 23.

Table 2 Density and moisture measurements for the sand in the October 2005 experiment

Pipe Side	Position	Backfill depth	Total Density	Dry Density	Moisture
		m	kg/m^3	kg/m^3	%
West	Outboard	0.5	1,993	1,879	6.1
West	Center	0.5	2,096	1,936	8.3
West	Inboard	0.5	2,101	1,961	7.1
East	Inboard	1	1,994	1,860	7.2
East	Center	1	2,019	1,916	5.4
East	Outboard	1	2,122	1,958	8.3

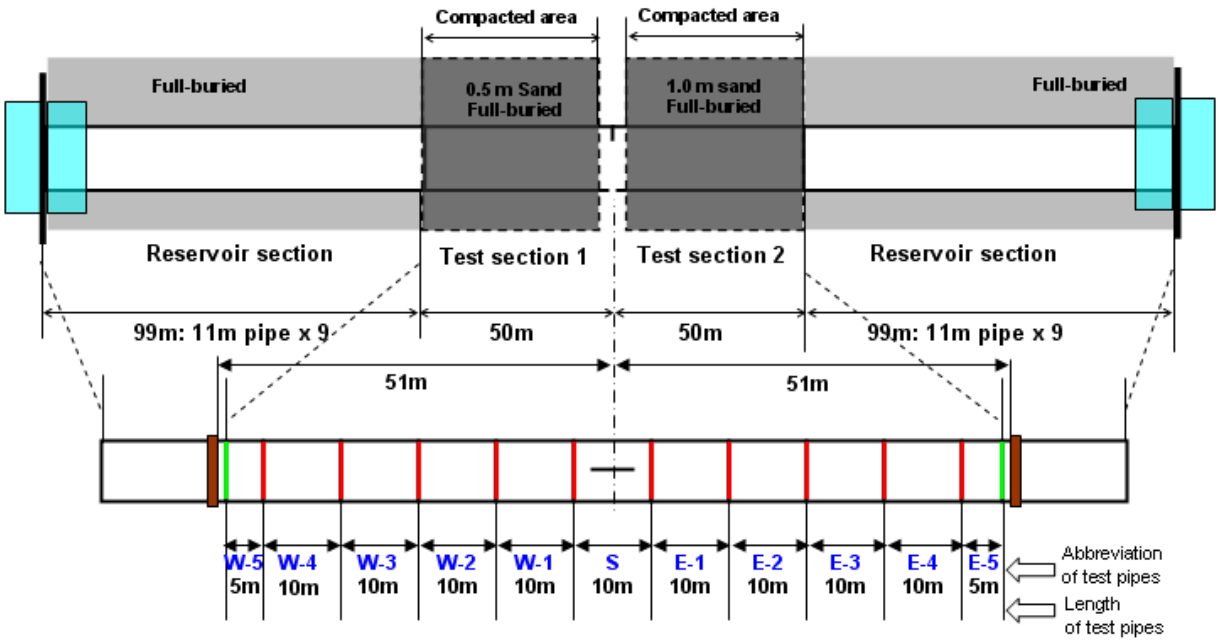

Figure 23 Layout for the October 2005 experiment

The test section consisted of nine 10 m sections and two 5 m sections. Each pipe joint had an outer diameter of 762 mm and a wall thickness of 17.5 mm. The toughness arrangement for the test is given in Figure 24. A weld overlay procedure was used at each girth weld on both the pipe ID and OD to prevent ring-off at the girth welds. In addition crack arrestors were used at the end of the test section to protect the reservoir pipe. Strain gages were used to measure axial movement of the pipe during pressurization but were not recorded dynamically during the experiment. Data from 100 timing wires[d] and 30 pressure transducers (only FP2000 pressure transducers were investigated in this experiment) were recorded dynamically throughout the

[d] In this experiment, two different types of timing wires were used. In the first, a Japanese wire embedded in paper (TML) was used. This is the same wire that was used in the November 2004 and June 2005 experiments. In addition, heavier gage, single strand, coated wire was used to see if this type of wire would be more reliable than the TML wire.

experiment. Thermocouple readings were taken on both the pipe surface and in the gas prior to the start of the experiment. The instrumentation layout for this experiment is shown in Figure 25.

There were two main objectives to this experiment:

1. Evaluate the effect of backfill moisture content and depth in detail. In the November 2004 experiment, the moist, very compact sand appeared to reduce the driving force and lower the expected arrest toughness. This experiment will address the effect of less moisture and smaller backfill depths on this result.
2. Evaluate the correction needed to the Battelle Two-Curve Method predictions for different backfilled pipe.

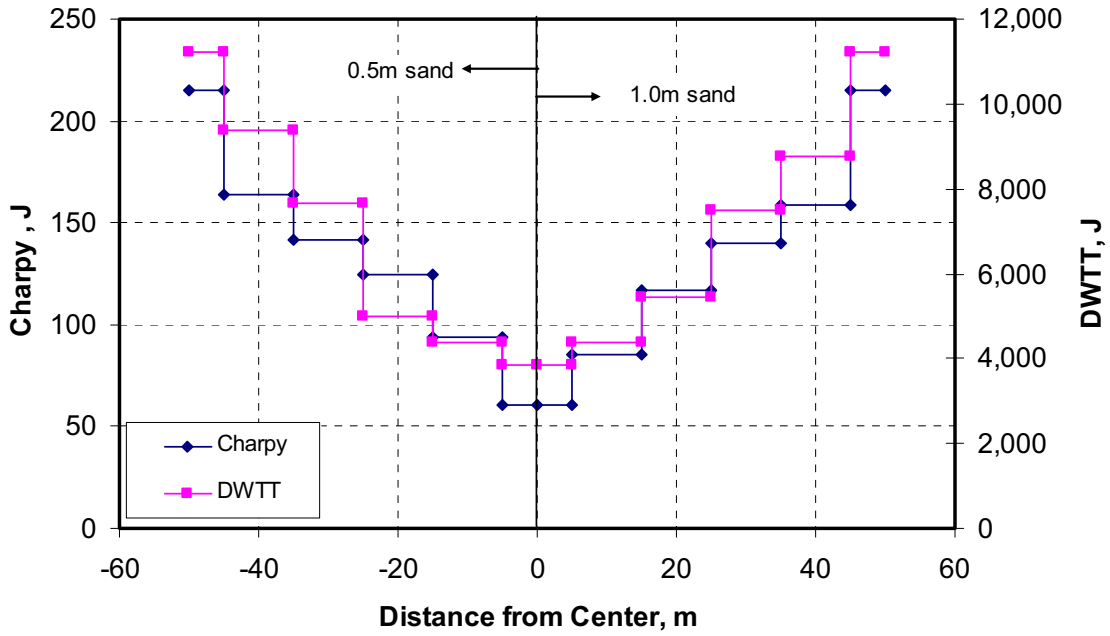

Figure 24 Toughness arrangement for the October 2005 experiment

Since the effects of the soil were investigated in detail in this experiment, more extensive soil characterization was completed. The soil experiments done were divided into laboratory and in-situ experiments. The laboratory experiments conducted included;

1. ASTM D854 – Specific gravity of soil solids,
2. ASTM D422 – Particle size analysis of soils,
3. ASTM D698 – Laboratory compaction characteristics of soils using standard effort – Proctor curve, and
4. ASTM D1883 – CBR of laboratory compacted soils. CBR gives a ratio of the load capacity of the soil relative to that of standard crushed limestone.

The in-situ soil experiments conducted included;

1. ASTM D2922 – Density of soils using radioisotope,
2. ASTM D1556 and D4914 – Density of soils using sand-cone procedure,
3. ASTM D3441 – Cone penetration tests of soil,
4. ASTM D1586 – Standard penetration tests, and

5. JGS 1433 – Portable dynamic cone penetration test.

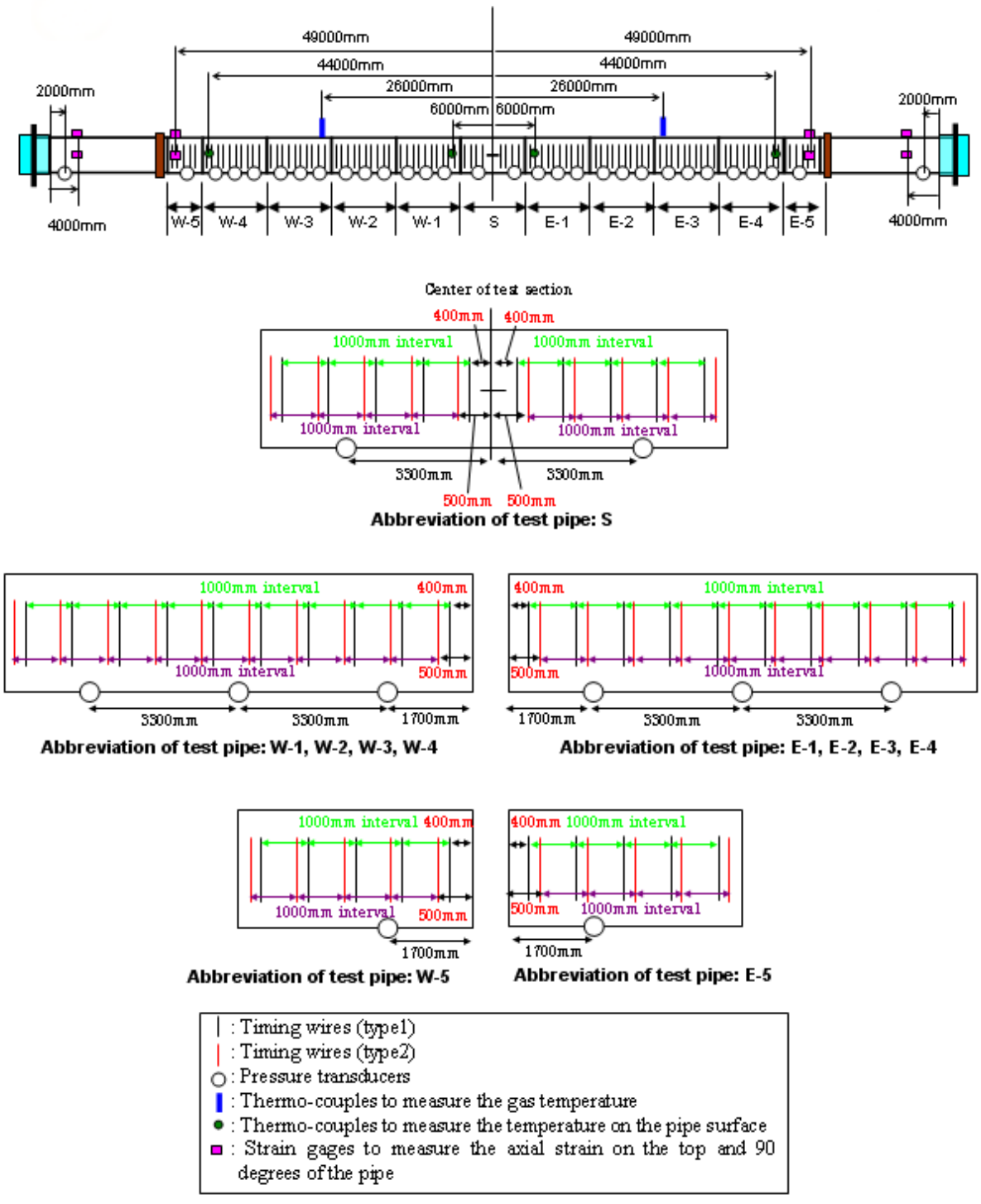

Figure 25 Instrumentation layout for the October 2005 experiment

In addition some additional data was taken during this experiment:

1. Soil pressure gages. Small soil pressure transducers were supplied by Emc^2 and placed on the pipe section W1 and E1 to measure the force between the soil and the pipe as the crack propagates. These gages were placed at 0, 22.5, 45, and 90 degrees from the crack plane and 7 m from the center of the test section.
2. Pressure sensitive film. These films had ranges including 28-85 psi, 70-350 psi, 250-1,400 psi, and 1,400 to 7,100 psi. Emc^2 supplied FORCE with the film and a procedure for installing the film on the pipe.
3. Heat flux sensors were placed at a distance of 100, 200, 300, and 400 m from the pipe during the burst. Each sensor was aimed so that the sensor would be pointing about 100 m above the pipe.
4. Pipe straightness measurement. A laser was used to check the straightness of the pipe and showed that the pipe did not deviate more than ± 20mm along its length.

The burst test was conducted successfully with the crack extending until the third pipe joint on the east side of the pipe, and to the end of the fourth pipe joint on the west side of the pipe. On the west side of the pipe, the crack ran until about 0.2 m from the girth weld into the last test pipe joint. The axial crack turned in a circumferential manner and severed as it arrested. On the east side, the crack ran about 1.9 m into third test joint, turned in a circumferential manner and arrested before it severed. A schematic of the fracture pattern in shown in Figure 26

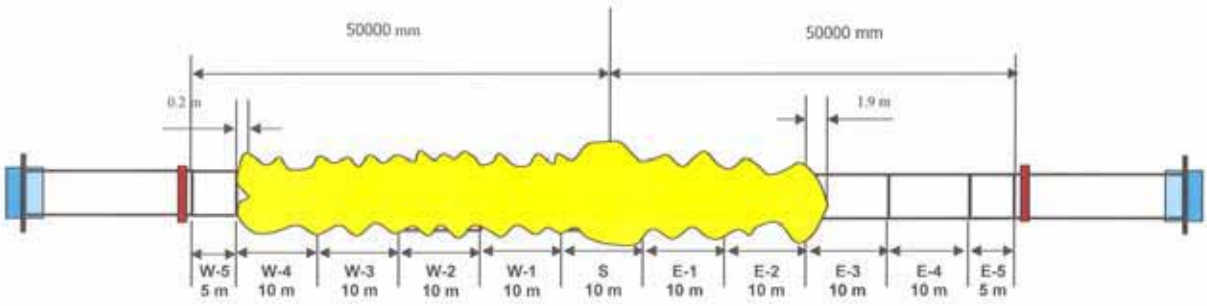

Figure 26 Fracture pattern for the October 2005 experiment

3.3.1 Timing wire and fracture speed data

A sample of the raw timing wire data from the October 2005 experiment is shown in Figure 27. As shown in this figure, there were two locations where the noise in the signal made it very difficult to locate the break time[e] for several of the timing wires. In these cases, either a best estimate of the break time was made, or the data was eliminated from the analysis.

[e] Further review of the data suggests that the wire under the cutter may have caused this noise. FORCE uses a positive voltage to locate the wire break and if this broken wire contacts the pipe surface, it may short causing noise in the other data channels. The noise seen in Figure 27 corresponds to noise seen in the trigger channel.

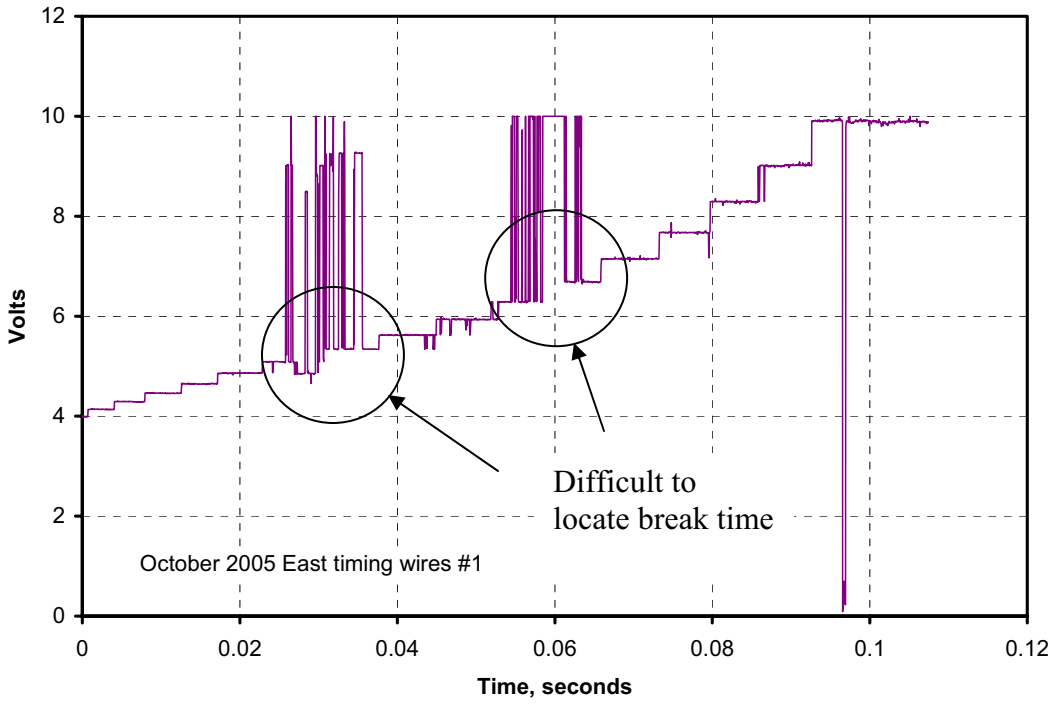

Figure 27 Sample timing-wire data from October 2005 experiment

For each of the experiments, the timing-wire break times were extracted from the raw timing wire data and plotted against location along the pipeline. From this data, the average and incremental fracture velocities can be calculated.

The timing wire break times and the incremental velocities for the October 2005 experiment can be found in Figure 28 and Figure 29, respectively. Note that in this case, both TML and heavier coated copper wire were used in the timing wire circuits. There were so many inconsistencies with the TML wire data that it was not considered in these analyses. As discussed previously, for this experiment, the crack traveled on the east side of the pipe (1.0 m of sand backfill) until the third test joint where it arrested. On the west side of the pipe (0.5 m of sand backfill), the crack traveled until the fourth pipe joint and arrested approximately 0.2 m from the fifth test joint. Both the timing wires and pressure transducer data verify these trends.

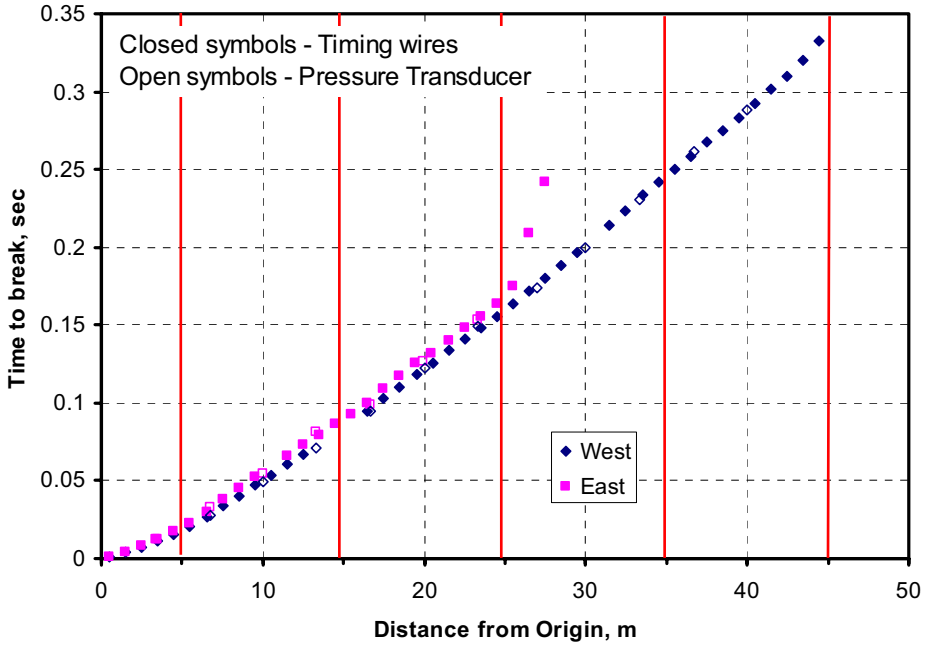

Figure 28 Timing wire data for October 2005 experiment

The incremental velocities show a steep decrease in the fracture speeds as the crack travels out of the starter joint and continue deceleration into the first joint until steady-state fracture is observed. As the crack passes into a higher toughness joint, it decelerated slightly before reaching steady-state speeds. After the crack arrests on the east side of the pipe, the crack on the west side does not appear to decelerate significantly until it arrests in the fourth pipe joint.

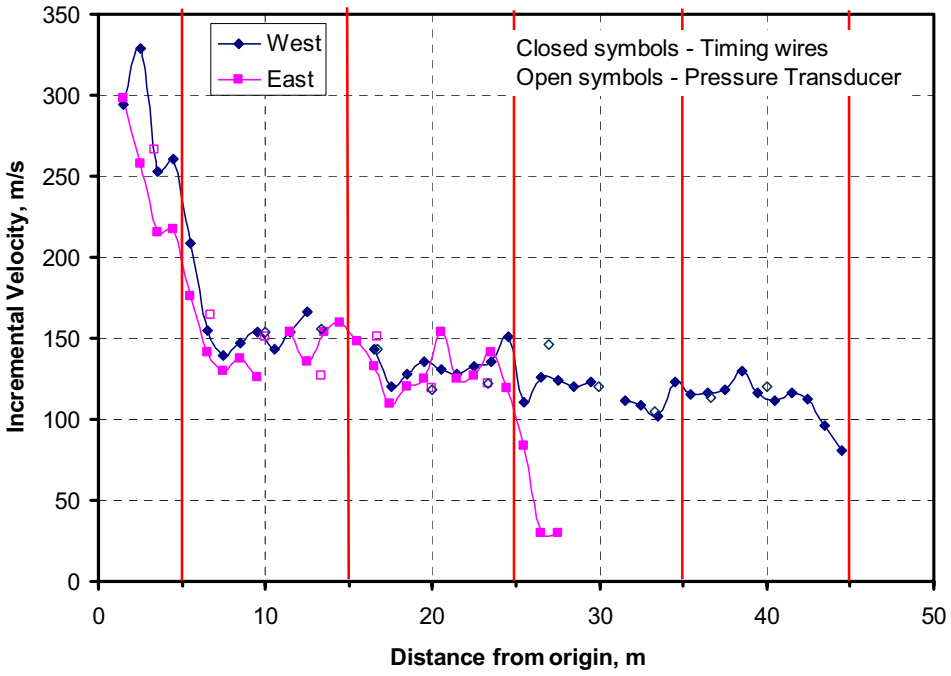

Figure 29 Incremental velocities for October 2005 experiment

3.3.2 Pressure transducer data

Because of the issues with the calibration of the A205a transducers, they were eliminated from the October 2005 experiment. In this case, only the FP2000 transducers were used. These transducers were placed at a location around the pipe circumference that would allow hydrotest water to drain from the chamber between the pipe wall and the recessed diaphragm.

The predicted versus measured decompression behavior for the October 2005 experiment is shown in Figure 30. Due to instrumentation issues, data was not available for predictions of pressure below the knee in the decompression behavior. The data suggests that the decompression behavior was very similar between the east and west sides of the pipe during the experiment. As compared to the GASDECOM predictions, the measured decompression speeds are lower for a particular pressure than the predictions. This trend is very similar to that measured in the November 2004 experiment, see Figure 13. This behavior is not completely unexpected. The GASDECOM code works reasonably well for typical gas compositions that are 85-percent pure methane or leaner and pressures below 15.2 MPa (2,200 psig). As an example, the Alliance pipeline full-scale experiments [5] showed similar results. In this case, the decompression speeds were overpredicted by GASDECOM above the two-phase plateau, but were predicted accurately below the plateau.

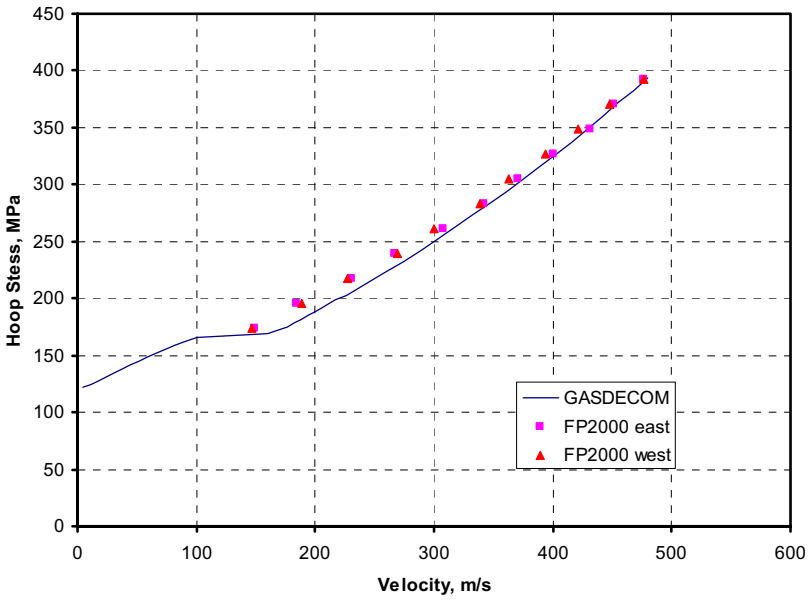

Figure 30 Measured versus predicted decompression behavior for the October 2005 experiment

3.3.3 Soil pressure data

At the request of Emc^2, FORCE technology installed eight FlexiForce A201 force transducers to the surface of the pipe in the October 2005 experiment to measure the force between the sand and the pipe during the burst. These gages have an active cell that is 9.5 mm (0.375 inch) in diameter and were glued directly to the pipe. The gages were located in the first test joint on both sides of the pipe. Circumferentially, they were placed on the south side of the pipe and at locations:

1. 50 mm from top dead center,

2. 22.5 degrees from top dead center,
3. 45 degrees from top dead center, and
4. 90 degrees from top dead center.

The amplifiers for these gages were built by Emc^2 and calibrated statically in the laboratory. A sample of the calibration curves is shown in Figure 31. During calibration it was noticed that the output of the gage was sensitive to the actual gage used and the exactness of the loading. For instance, the output changed slope if the load was applied to the gage with an offset of 1.5 mm. However, since the goal of these gages was to output an order of magnitude load between the soil and pipe, it was decided that an average calibration would suffice. It should be noted that in no cases did the gage output a positive voltage for any loading arrangement. In addition, in all cases, the gages returned to their initial output voltage after the load was removed from the sensor.

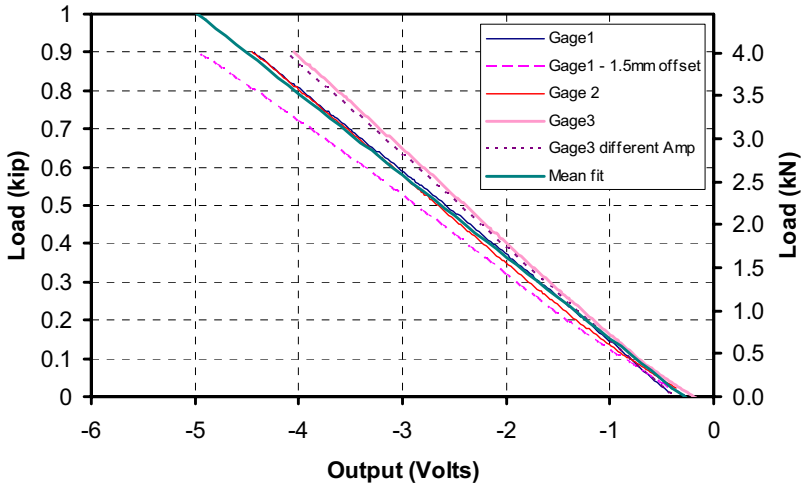

Figure 31 Calibration for the soil pressure gages

The output of the gages from the October 2005 experiment is shown in Figure 32. The trends for the data on the east side of the pipe were similar and are not shown here. The trends shown in Figure 32 were highly unexpected. In this figure, the y-axis is the output of the gage, while the x-axis is the crack tip distance from the gage location. As the crack approached the gages, the signal from the gages was relatively quiet. About 0.5 m before the crack reached the sensor location, the output began to change. In fact, the initial movement is negative, but then the response from the gages is both positive and negative, which was never observed in the laboratory.

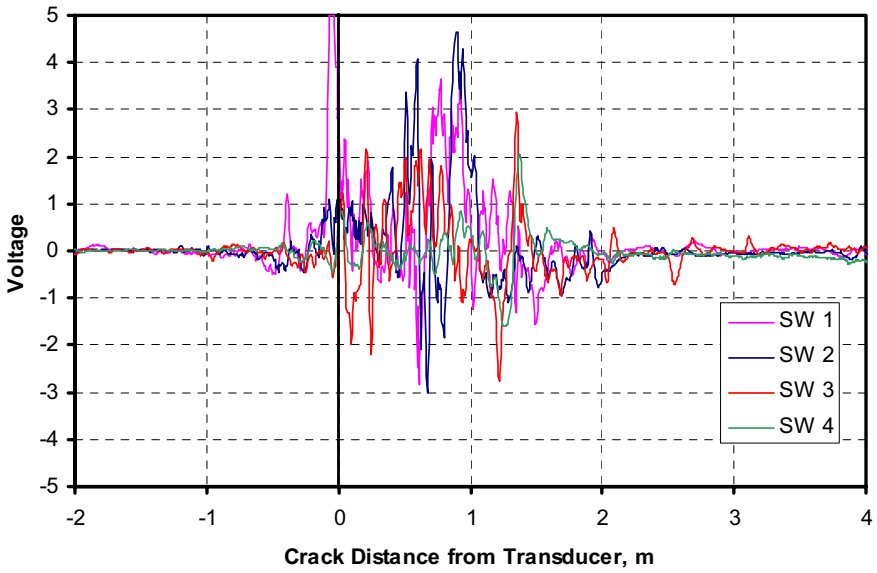

Figure 32 Soil pressure transducer output from the west side of the October 2005 experiment

After checking and rechecking the amplifier and gages, impact experiments on these gages were conducted. In this case, the gage was placed between two flat platens and struck with a hammer. An oscilloscope was attached to the gage and without the excitation or amplification of the signal, the gage output a sinusoidal type signal, see Figure 33. This result implies that the gage is producing an EMF signal as a dynamic load is applied. Emc^2 has had several conversations with the manufacturer of the gages and they were unaware of any EMF signal issues from their gages. According to the manufacturer brochures, the gages have a response time of 5 microseconds and can respond to large impact loads. However, they have admitted that the gages are piezoelectric elements, which by nature generate EMF signals. Further investigation of these gages is required before they can be used in this type of application.

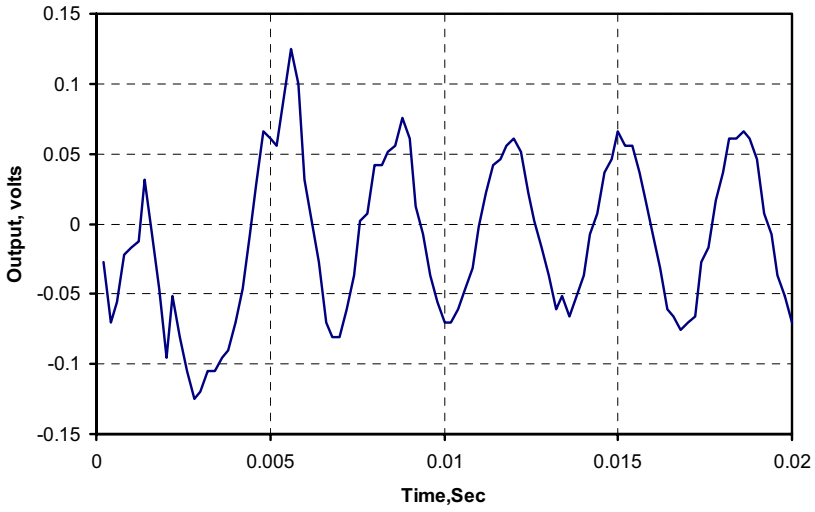

Figure 33 Output of soil gage with no amplification or excitation when impacted with hammer

In addition to the soil pressure gages, pressure sensitive film was placed on the July 2005 preliminary and the October 2005 full-scale experiment. For the July 2005 experiment, the procedure for attaching the film to the pipe was not sufficient and much of it was destroyed in the experiment. For what did survive the experiment, the film looked saturated.

For the October 2005 experiment, the film was secured to the pipe in different ways. First, most of the films consisted of two sheets of material, i.e., a donor and a receiver. The only exception to this was the higher capacity film (1,400-7,100 psi), which was only one sheet of film. For the 350-1,400 psi sheet, the film was secured to the pipe two different ways, i.e., with the donor side to the pipe in one case and the receiver side to the pipe in another case. In all other cases, the receiver side was placed to the pipe. Emc^2 supplied FORCE technology with the procedure for gluing the film to the pipe surface. The results from the October 2005 experiment are shown in Figure 34. From this figure, the film with only one sheet and the film where the donor was placed to the pipe did not withstand the force of the burst and were destroyed as the pipe pushed through the sand. For the cases, where the receiver was placed on the pipe, some useful data was obtained. As shown in Figure 34, the ultra low film (28-85 psi) seems fully saturated, while the low film (350-1,400 psi) appears to have no color at all on top of the pipe, but appears saturated at 90 degrees. Therefore, the forces at the top of the pipe appear to fall between 70-350 psi. Since the color seems more white than red for this film, it can be suggested that the stress on the pipe falls closer to the 70 psi than the 350 psi. Looking at the saturated ultra low film, we know that the stress must be greater than 85 psi. Using engineering judgment, it can be assumed that the stress on the pipe falls in the range of 100-150 psi. These results are very similar to the results generated in the small-diameter Mojave tests discussed in Part II of this report.

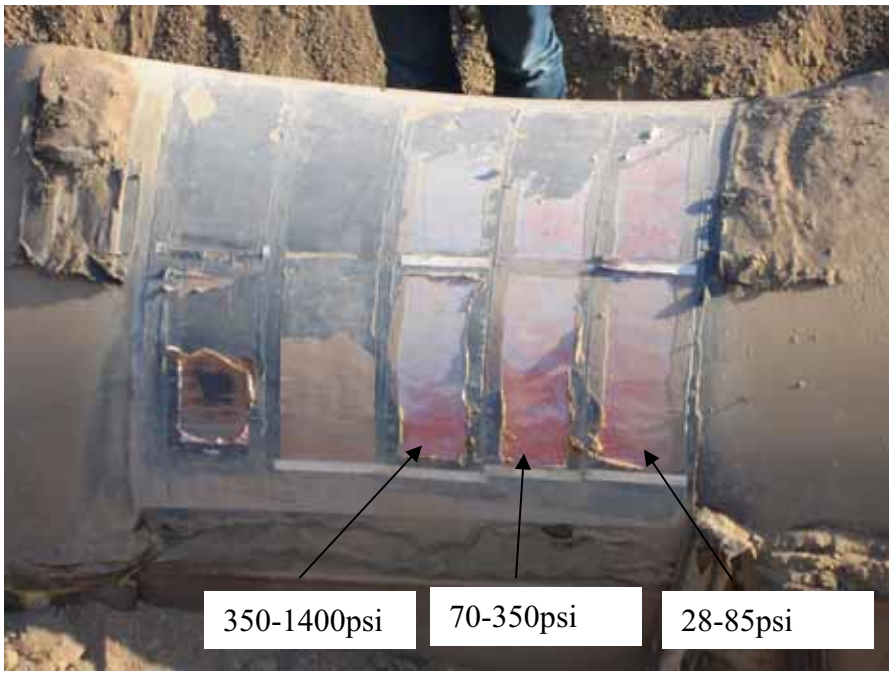

Figure 34 Photograph of soil sensitive film on west side of pipe used in October 2005 experiment

3.4 June 2006

This test was conducted on June 20, 2006 at FORCE Technology. The details of the test specification and results are given in Reference 6. The pipe test was conducted with an average temperature of 20C and at a pressure of 18.31 MPa. The east side of the pipe was backfilled with 1.5m of sand, while the west side was unbackfilled. The layout for this test is shown in Figure 35.

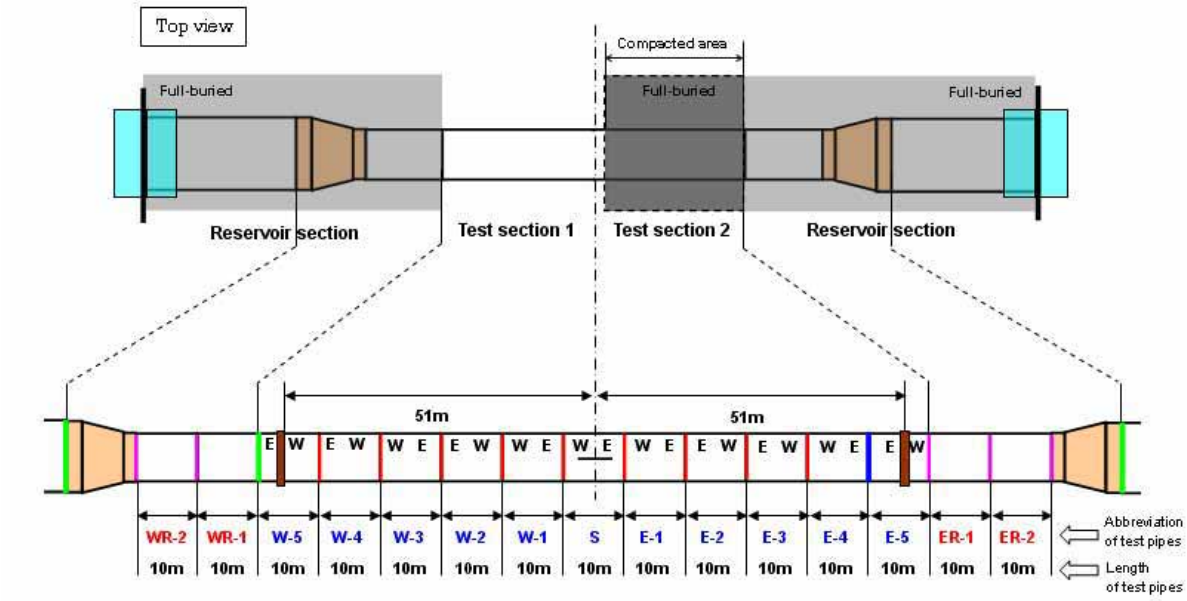

Figure 35 Layout for June 2006 experiment

(Note; the E and W notations on the pipes correspond to the pipe end locations when the rings were cut off at the mill. This notation is not the same orientation that the pipes were located in the test section.)

The test section consisted of eleven 10 m long sections. Each pipe joint had an outer diameter of 610 mm and a nominal wall thickness of 14 mm. The Charpy energy arrangement for the test is given in Figure 36. A weld overlay procedure was used at each girth weld on both the pipe ID and OD to prevent ring-off at the girth welds. In addition crack arrestors were used at the end of the test section to protect the reservoir pipe. Data from 100 timing wires and 40 pressure transducers (both type FP2000 and Endevco model 8511A pressure transducers were investigated[f]) were recorded dynamically throughout the experiment. Thermocouple readings were taken on both the pipe surface and in the gas prior to the start of the experiment. In addition, high-speed video and extra instrumentation to dynamically measure the crack-tip-opening angle (CTOA) were added to this experiment. The instrumentation layout for this experiment is shown in Figure 37.

[f] The Senostec FP2000 transducers are recessed diaphragm transducers that were screwed into weld-o-lets attached to the pipe. The Endevco transducers are miniature flush diaphragm transducers that are screwed into the pipe wall. These transducers were placed with the diaphragm slightly recessed from the pipe ID and had the face of the transducer coated with layer of silicone to guard against temperature influences on the transducer calibration.

There were two main objectives to this experiment;

1. Evaluate the correction needed to the Battelle Two-Curve Method minimum arrest Charpy energy predictions for unbackfilled pipe. In the November 2004 experiment, the crack traveled much farther than expected on the unbackfilled side of the pipe. In fact, the correction factor on the Battelle Two-Curve Method minimum arrest Charpy energy prediction was approximately 2, which is much larger than the 1.3 to 1.4 experiences with other backfilled X80 pipe tests[g].
2. The pipe diameter was reduced for this experiment to 610 mm (24 inch) from the prior 762 mm (30 inch) diameter in order to investigate the effect of pipe diameter on the arrest Charpy energy.

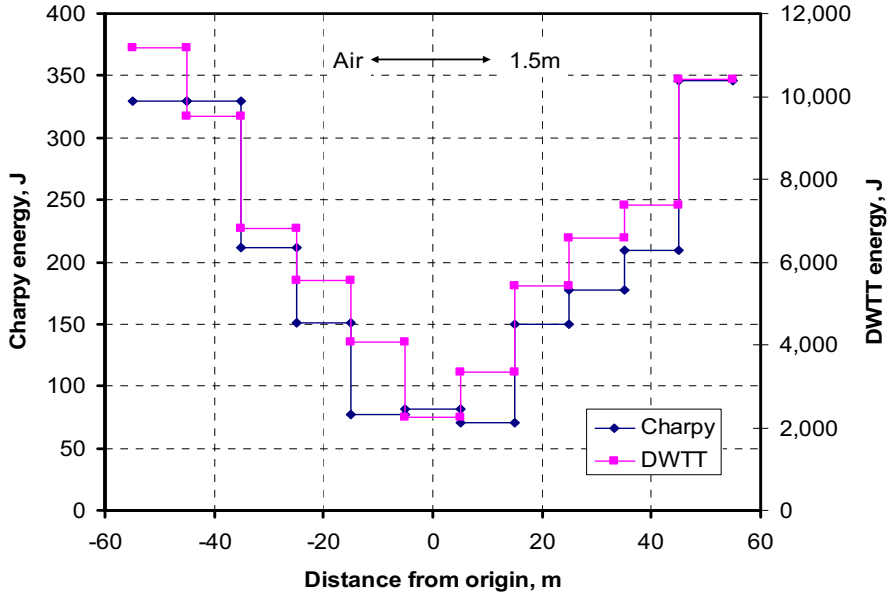

Figure 36 Toughness arrangement for the June 2006 experiment

[g] It is not typical to run a full-scale experiment unbackfilled; therefore, the correction factor of 1.3 to 1.4 times the minimum arrest toughness is based on soil backfill experiments and may not be applicable for unbackfilled tests.

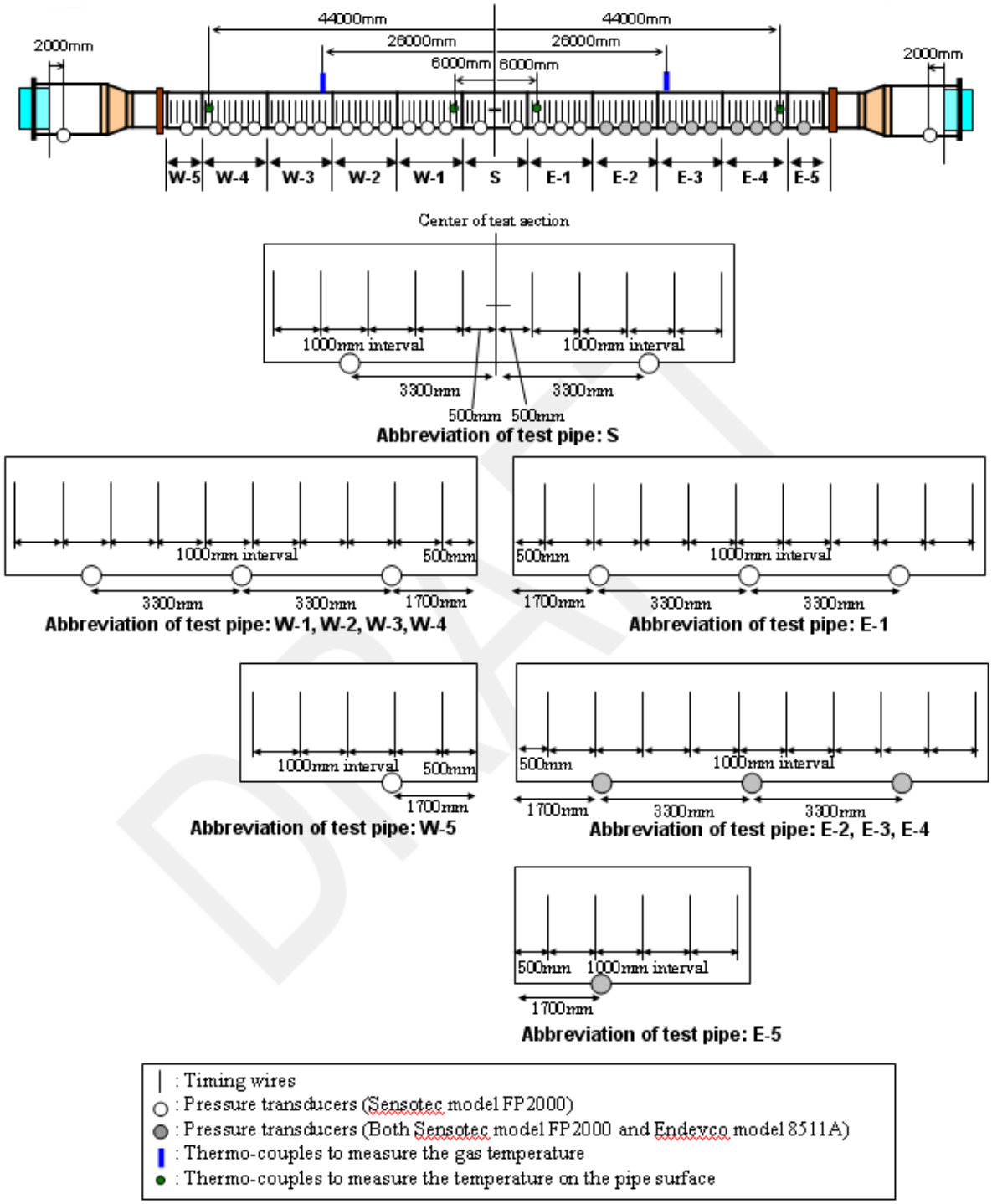

Figure 37 Instrumentation layout for the June 2006 experiment

The burst test was completed successfully, with the crack traveling through the starter and first test joints in an axial manner. As the crack entered the second test joint on the east (backfilled) side, the crack turned circumferentially (after about 0.8m of growth) and severed about 2.2 m after entering the second test joint. As indicated in the video of the event, the double-ended

break resulted in having the pipe on the west end of the test section come out of the pit and buckle about 8m from the crack arrestor very close to west girth weld #6. The movement of the pipe caused two complete circumferential breaks on the west side of the pipe, causing four sections of the pipe to be ejected from the test pit. One of these sections contained the crack propagation region that included the cutter location, two sections were complete pipe sections, and the final section contained a short section of cracked pipe, see Figure 38.

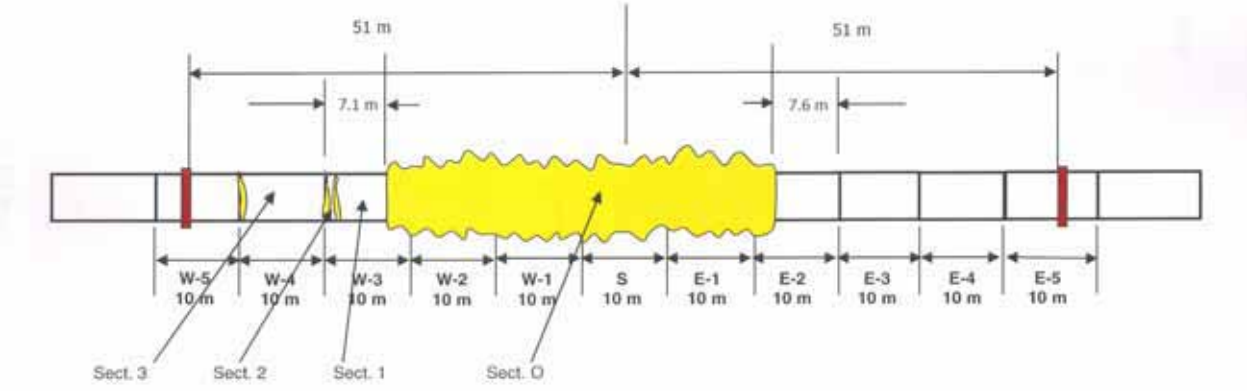

Figure 38 Schematic of fracture pattern in June 2006 experiment

After the circumferential break on the east side of the pipe, the axial stresses in the pipe may have been lower and the crack running in the west side of the pipe may have been affected. However, it is unknown to what extent this effect will have on the fracture speeds and arrest toughness. The large movements in the pipe may increase the driving force causing the crack to travel farther than would be expected. There will be some change in the crack driving force, but it is difficult to quantify and determine if the difference is significant.

3.4.1 Timing wire and fracture speed

For the measurement of fracture speed, FORCE technology placed 100 timing wires on the pipe for the June 2006 experiment. These timing wires were similar to those used successfully in the October 2005 backfilled experiment. The timing wires consisted of single strand, coated wires that were epoxied to the pipe at a spacing of 1m. The timing wire circuit was designed by FORCE and consisted of three individual circuits for each side of the pipe. By taking the voltage change versus time for each wire, the crack location as a function of time can be developed as shown in Figure 39. As noted in this figure, the solid symbols represent the individual timing wire data for both the west (diamond) and east (square) side of the pipe. In addition, the pressure transducer data can be used to locate the crack and these data are illustrated as open symbols in Figure 39. As shown in this figure, the data suggests that on the backfilled side of the pipe, the crack ran into the second test pipe, and arrested (after 0.8m of crack growth it turned circumferentially and arrested after 2.2m), while on the unbackfilled side of the pipe, the crack ran into the third pipe joint before arrest. Both the timing wire and pressure transducer estimate of the crack location appear to be similar. Note that the crack lengths at arrest are discussed later in Table 7.

If the data from Figure 39 is plotted in terms of incremental velocities (crack speed between timing wires), the results[h] can be seen in Figure 40. For the unbackfilled case, the data shows typical behavior where the crack slightly decelerates as it enters a joint and reaches steady-state speeds after 2m of growth into each joint. In addition, the fracture speeds calculated from the pressure transducer data is very similar to that of the timing wires. However, the data on the soil backfilled side does not look as well behaved. In fact, it is difficult to determine the steady-state speeds from the timing wire data. The crack appears to speed up and slow down as it travels along the pipe, which is highly unlikely. In contrast, the fracture speeds from the pressure transducers appear better behaved than the timing wire data. The steady-state, average fracture speeds are shown in Table 3.

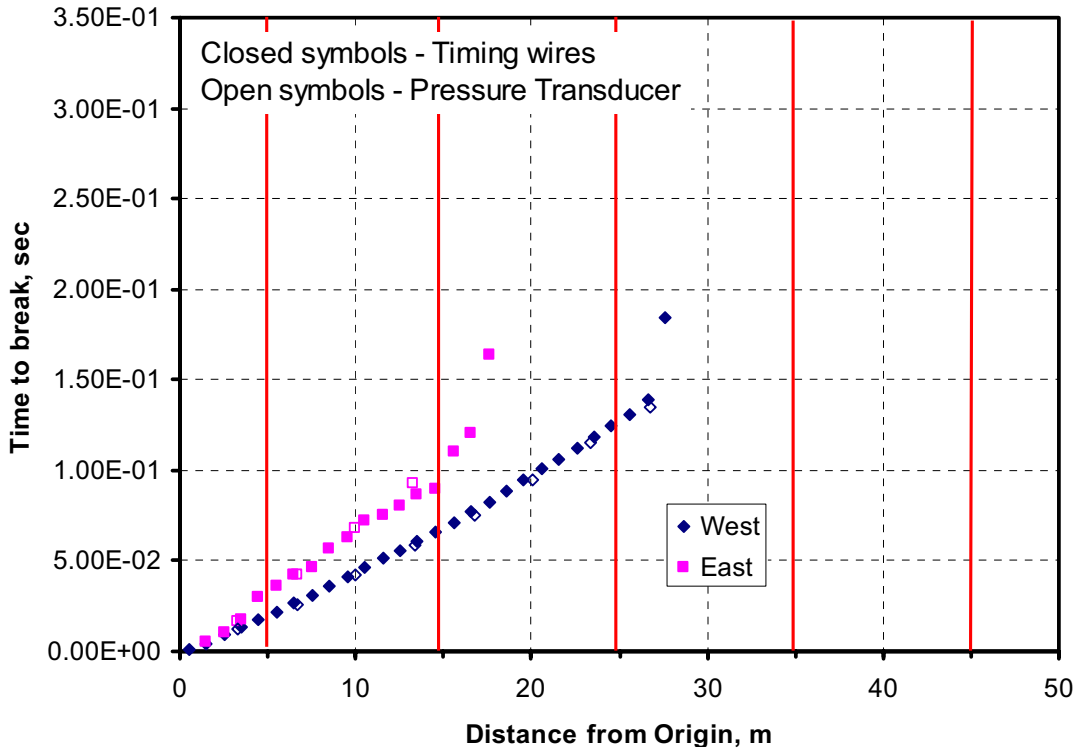

Figure 39 Timing wire data from the June 2006 experiment

Table 3 Steady-state fracture speed for the June 2006 experiment

Device	Fracture Speed, m/s				
	W2	W1	Starter Pipe (West)	Starter Pipe (East)	E1
Timing Wire	167.3	202.9	223.7	110.6	186.7
Pressure Transducer	166.2	201.4	244.6	176.0	132.4

[h] Incremental velocity values are typically subject to significantly more scatter than determining average velocities from a time distance plot over a larger number of timing wires.

3.4.2 Decompression behavior

The decompression behavior during the June 2006 experiment was measured using 40 pressure transducers placed along the pipe length. Of these transducers thirty were Sensotec (FP2000) transducers and ten were Endevco (8511A) transducers. The Endevco transducers were placed at the same axial position along the pipe length as the Sensotec transducers but different circumferential positions, i.e., the Sensotecs were placed at 3 o'clock and the Endevcos were placed at 2 o'clock.

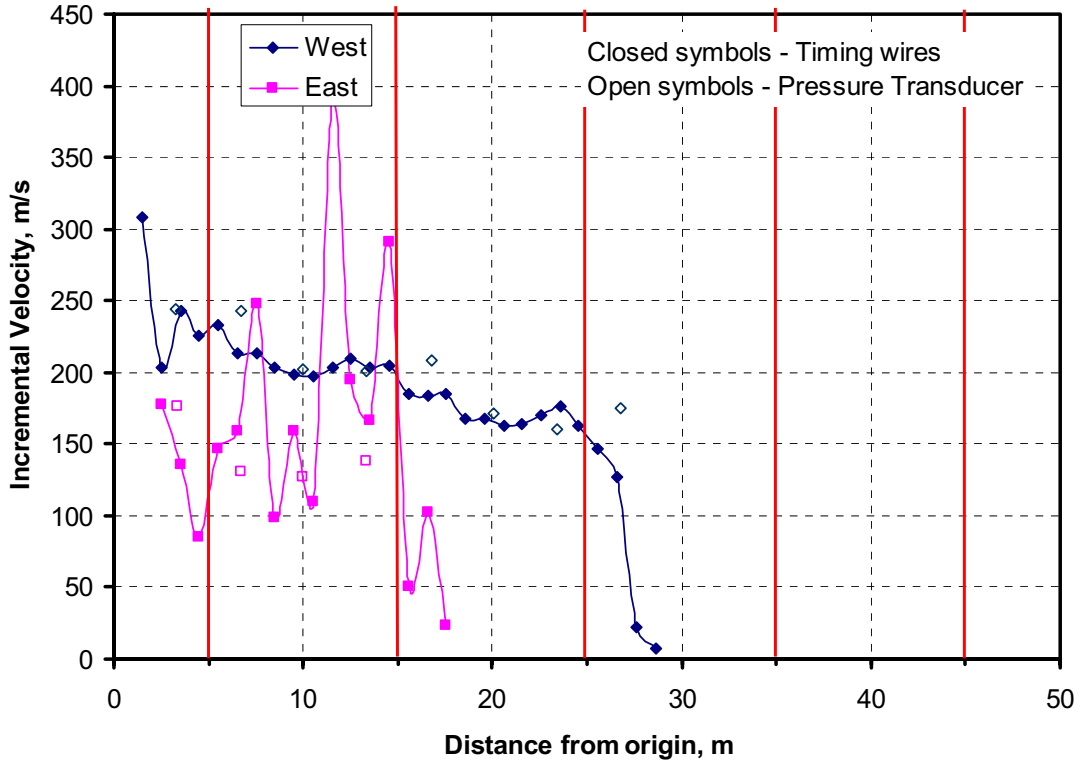

Figure 40 Incremental fracture speeds from the June 2006 experiment

In the axial locations where both transducers were located, the Endevco transducers showed a response that was slightly higher in pressure than the Sensotec transducers in almost all cases, see Figure 41. For example, pressure transducers 5 (Sensotec) and 20 (Endevco) are both located at 16.68m from the origin, and as shown in this figure, the pressure drop is larger in the Sensotec than in the Endevco at the same time period[i]. However, the extent of the data to compare is limited since the Endevco transducers were placed on the soil backfilled side, which experienced a ring-off in the second test joint that severed the pressure transducer wires.

[i] If the decompression wave was not one dimensional as assumed in the decompression analysis, i.e., the crack opening might cause the decompression to occur sooner at the top of the pipe as compared to the bottom of the pipe, then the pressure would be higher at the 3 o'clock position than the 2 o'clock position. This is not the same trend as the shown by the experimental data, so there may be some other electronic response aspect or thermal straining aspect from the cooler gas at the lower decompressed pressures.

The gas decompression behavior as a function of the wave speed can be calculated from the pressure transducer data, as shown in Figure 42. For this plot, the data from all available transducers were used. Also included in this plot are the predictions from the GASDECOM software using the actual gas composition and temperature at the time of the test. Note that the temperature on the pipe surface on the backfilled side at the time of the test was 20C, while the temperature on the unbackfilled side of the pipe was 27C. The temperature of the gas was 20C.

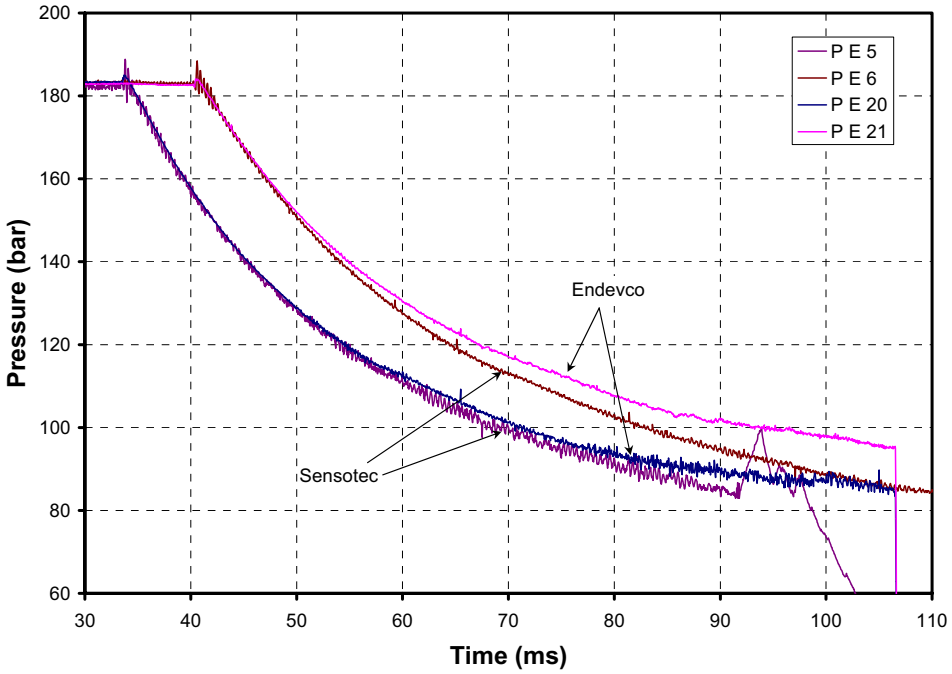

Figure 41 Comparison of Sensotec and Endevco pressure transducers from the June 2006 experiment

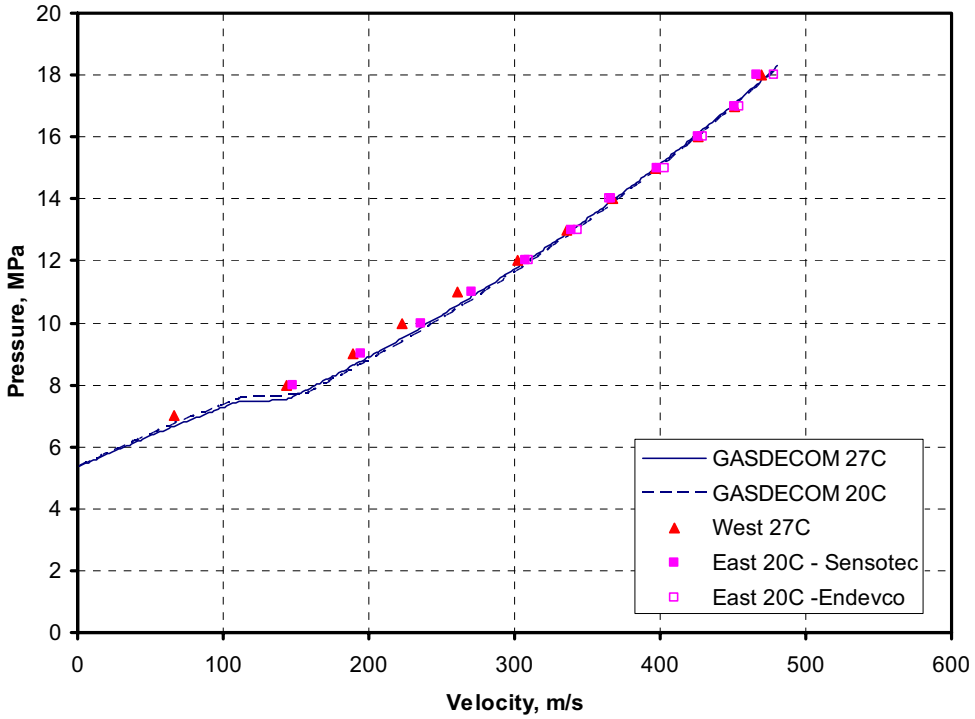

Figure 42 Comparison of gas decompression behavior measured in the June 2006 experiment with that calculated from GASDECOM

The comparison between the measured and predicted gas decompression is good. In fact, the predictions are excellent at the higher pressure, but the wave speeds are slightly overpredicted at the lower pressures and the pressures are underpredicted in the two-phase region. This is consistent with the past JGA experiments.

3.4.3 Extra instrumentation

Details from the extra instrumentation to measure CTOA are given in the main body (Part I) of this report.

Through an effort funded solely by the JGA, an attempt to take high speed video of the crack propagation was made. Originally, the plan was to use the Emc^2 Olympus 600L 3X Digital High-Speed Camera to capture the digital video during this experiment. This camera is capable of obtaining digital video at a frame rate of 8,000 frames per second. This camera is the one that has been used in numerous other burst tests to capture similar images at the Emc^2 Mojave burst test site.

About two weeks before the planned trip to install the camera in Denmark, the Emc^2 camera began experiencing difficulties, and had to be sent to the manufacturer for service. Unfortunately, while in service, other problems arose, and it was clear that this camera would not be repaired before the June 20, 2006 test date. As a secondary plan, Emc^2 rented a high-speed camera from Del Imaging, Inc. The camera rented was a Redlake[j], MotionPro HS-4. This camera is an updated version of the Emc^2 600L camera with higher resolution, larger onboard

[j] Redlake is the OEM manufacturer of the Olympus 600L.

memory, and a self-contained unit. Using a similar resolution[k] as the 600L camera, this camera is capable of taking digital video at 140,000 frames per second. The rented camera was shipped to Emc^2 in time to test and verify its applicability for this experiment.

Since the camera needed to be placed remotely from the pipe in order to protect it from the burst, a large camera stand was constructed. Using a 6-inch I-beam, FORCE Technology constructed an 18m tall camera stand and welded the beam to the instrumentation booth, see Figure 43. The camera was attached to the camera stand using a high strength, 3/8-inch bolt screwed though the camera stand and into the camera swivel. The camera was protected by a steel protective box made from 1/16-inch steel sheet metal, with a ¼-inch thick piece of Plexiglas protecting the lens. The camera power and USB lines were secured to the camera stand I-beam with duct tape and covered in heat-shielding metallic tape.

Figure 43 Photograph of camera stand for the high-speed camera

For the ease of visually measuring the CTOA, targets were placed on the pipe. The targets had two purposes: 1.) provides a location where the camera could focus, and 2.) gives a known angle so that the CTOA could be measured from the camera (accounts for parallax errors). In addition, contrast lines of black and white stripes were placed on the pipe in order to add contrast to the view for ease in locating the crack tip. The layout of the focal location for the high speed video on the June 2006 experiment is shown in Figure 44.

[k] At the highest resolution, it can take up to 5,100 frames per second.

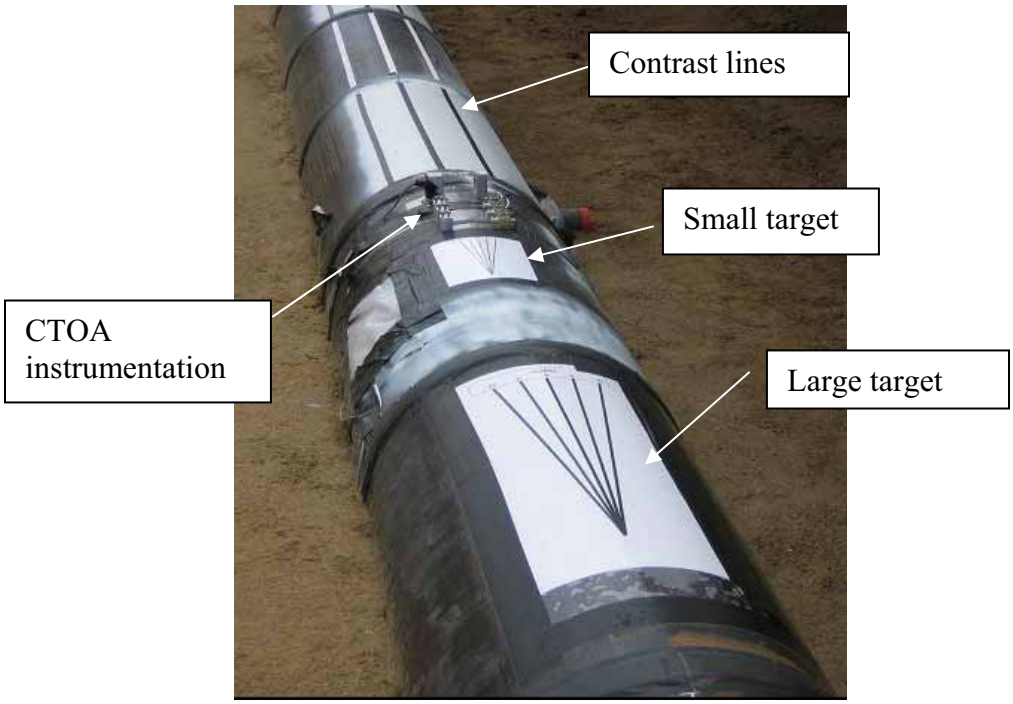

Figure 44 Focal point on pipe for high-speed camera

The camera was set up to take data for one second, with a tenth of a second pre-trigger. After the burst test, it was noticed that the camera was no longer attached to the camera stand. It was lying on the top of the instrumentation bunker. The power was still on and the camera appeared to be working. The data from the camera was downloaded to the laptop. Upon viewing the video, it was clear that the camera was damaged. The video shows the pipe at the start of the event and the explosive cutter igniting. Approximately 0.0094 seconds after the cutter was ignited, the video signal was lost. Several attempts were made to download good video, but all were unsuccessful.

After taking the camera back to the US, it was shipped to the manufacturer for diagnostics. The manufacturer found two main defects with the camera. Their report stated "Found cracks on left memory board and left memory board disconnected from motherboard. Sensor had noisy column and overexposure defect."

It is the conclusion of Emc^2 that the noisy column and overexposure defect were caused by what seemed to be an electromagnetic pulse that was generated from the explosion that interfered not only with the camera but also some of the additional instrumentation (for measurement of CTOA, see Part I of this report) on the pipe. This is unusual and was not experienced in other tests where similar cameras were used. However back in the 1960's this type of pulse was thought to be the reason why burst tests containing gas ignited without the use of flares. Interestingly, the interference with the additional instrumentation (see the next section of this report) and the problems with the camera happened at the same time, so it is expected that an electromagnetic pulse like this was present. Figure 45 shows an example of a frame from the camera before the burst test, and one that was captured from the camera after the electric magnetic pulse. As shown in this figure, the resolution in the second picture appears much lower quality than the first, and many vertical white lines are present. These white lines are the noisy

column and overexposure defect indicated by the manufacturer. The overexposure may have also come from the very large explosive cutter device used in the FORCE tests. Emc^2 uses a much more efficient linear cutting tape that can cut through 25-mm thick pipe without producing much light, i.e., no light from the cutting device is visible about 2 meters from the origin.

Secondly, during the burst test, there were two complete circumferential breaks in the pipe close to the camera, which caused an extra jet of gas and flames to be aimed directly at the camera. This is very clear from the video taken by FORCE technology. This unexpected extra explosion was aimed directly at the camera stand and was strong enough to knock the camera off the camera stand by shearing the bolts that held the camera to the stand. Since there we no significant dents in the camera box, it is suspected that the camera did not hit the top of the instrumentation booth with much force. The duct tape circumferentially wrapped around the I-beams may have sequentially torn and cushioned the camera box landing on the top of the instrumentation building. Therefore, the blast from the secondary explosion must have shaken the camera enough to dislodge the memory chip. The small crack in the memory card could have happened either from the fall or from the impact of the blast.

Therefore there were two issues that caused the high-speed video to be lost, the electromagnetic pulse generated by the burst, and the unexpected secondary explosion aimed at the camera stand from two double-ended breaks that occurred near the instrumentation building. The camera was damaged, and the significant portion of the video was lost.

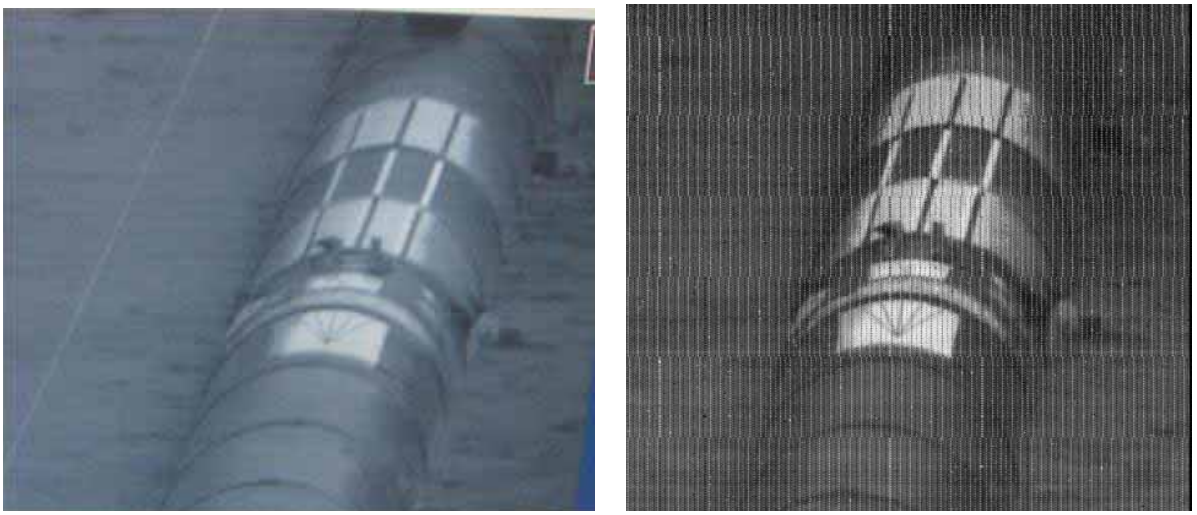

(a) before burst test **(b) during burst test**

Figure 45 Photograph before and during the burst test illustrating camera damage

4 DATA REDUCTION EFFORT

This section of the report presents a summary of the data analysis effort for the four JGA pipe experiments. Included in this section are discussions on the ability of the Battelle Two-Curve approach to predict the minimum arrest toughness for these materials, the influence of pipe diameter, backfill depth and moisture content. This was done for arrest Charpy energy and

fracture speeds predictions, as well as a comparison of the JGA data with the historical X80 data from the full-scale database at Emc[2].

It is important to keep in mind that when looking at just one set of full-scale test data from any program, there is a tendency to draw certain conclusions. There may be certain variables that can affect that data set so that the trends from that data set are not universally applicable. Some of these factors could be; compaction or condition of soil, relationship of Charpy energy to actual toughness, actual thickness variation in pipe from the nominal thickness, differences between predicted gas decompression curves and actual decompression curves, etc. Therefore, it is not the purpose of these analyses to draw general conclusions about crack arrest, but to point out obvious trends that are specific to these results that may affect the general methodology for predicting axial crack arrest in line pipe materials.

4.1 Summary of Four JGA Experiments

The JGA experimental burst test program consisted of four[l] major full-scale experiments on X80 line pipe materials. The details of these experiments are not reported here and can be found in appropriate reports by FORCE technology [1, 3, 4, 6]. For the tests conducted, the test conditions can be found in Table 4, while the average gas composition[m] can be found in Table 5.

Table 4 Test conditions for four JGA experiments

Experiment Date	Diameter, mm	Nominal Wall thickness, mm	Pressure, MPa	Hoop Stress, %SMYS	Temp, C	Backfill	
						Type	Depth, m
Nov 2004	762	17.5	18.5	73	6.1	Sand/Air	1.5
June 2005	762	17.5	16.2	64	19.2	Air/Air	N/A
Oct 2005	762	17.5	18.5	73	13.7	Sand/Sand	1.0/0.5
June 2006	610	14	18.2	72	20	Sand/air	1.5

Table 5 Average gas composition for four JGA experiments

Gas	Composition, mole%
methane	89.24
ethane	5.93
propane	2.39
i-butane	0.39
n-butane	0.54
i-pentane	0.12
n-pentane	0.08
hexane	0.07
nitrogen	0.35
carbon dioxide	0.90
Total	100.00

[l] Other smaller scale verification experiments were conducted but not reported here.
[m] The actual gas compositions were used in analyzing each experiment.

4.2 Material Toughness

Tensile (both round bar and strip – 2 specimens each), Charpy (3 specimens) and DWTT (3 specimens) tests were conducted from the top and bottom locations of each pipe joint used in the test section of each JGA experiment. This data is documented in the FORCE final reports [1, 3, 4, 6] for the experiments.

The relationship between the Charpy and DWTT energies for the materials tested in this program are shown in Figure 46 for the backfilled cases, and in Figure 47 for the unbackfilled cases. In both of these figures, all of the test pipe joints are shown and the values represent the average Charpy or DWTT energies measured in that joint. In addition, the solid line represents the original 1977 Wilkowski trends [7] from the older linepipe data (X70 and lower strength pipes)

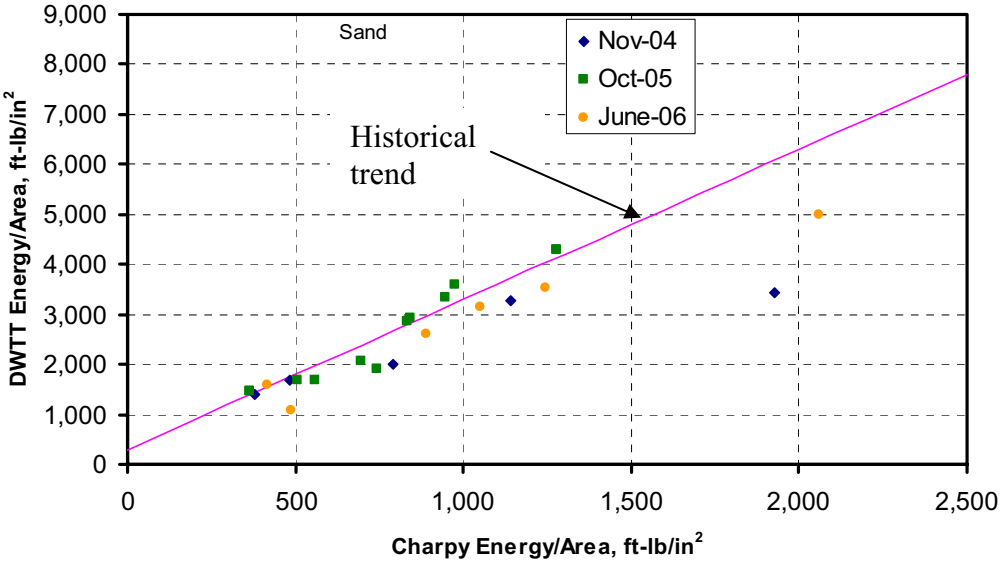

Figure 46 DWTT versus Charpy energy for the backfilled pipes

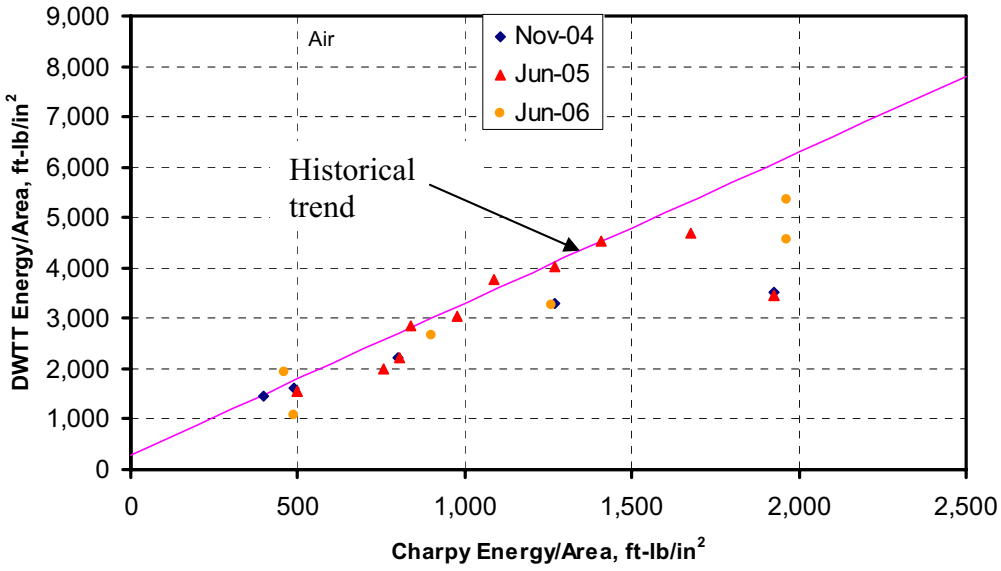

Figure 47 DWTT versus Charpy energy for the unbackfilled pipes

The trends from these data are very close to the trend developed from the older line pipe steel in the 1970's. This trend suggests that most of the analyses developed using this relationship would be applicable to the pipe joints used in these experiments. There are several pipe joints that fell below the line, indicating a much larger Charpy energy for the same DWTT energy. This trend usually indicates a material where the Charpy energy is not a good representation of the steady-state fracture resistance. In fact, an observation from the results in the previous figures is that there are some materials from the same experiment, i.e., November 2004, where there is a 90 percent difference in the Charpy energy for approximately the same DWTT energy. It is suggested that these specimen be looked at more closely (i.e., conduct instrumented DWTT tests) to see what may be causing this extreme difference.

The data from Figure 46 and Figure 47 are replotted in Figure 48 without the uncracked pipe joints shown, i.e., only the arrest and propagate joints are shown. The data follows the original Wilkowski trend very closely, with most of the data falling within the scatter band created from the original 1977 data. However, one data point falls much farther to the right of the curve than the other data. This difference is beyond the typical scatter for this type of data. It is suggested that this pipe joint be invested further. However in most cases, the original Charpy-DWTT analysis is appropriate to use for predicting the results of these experiments.

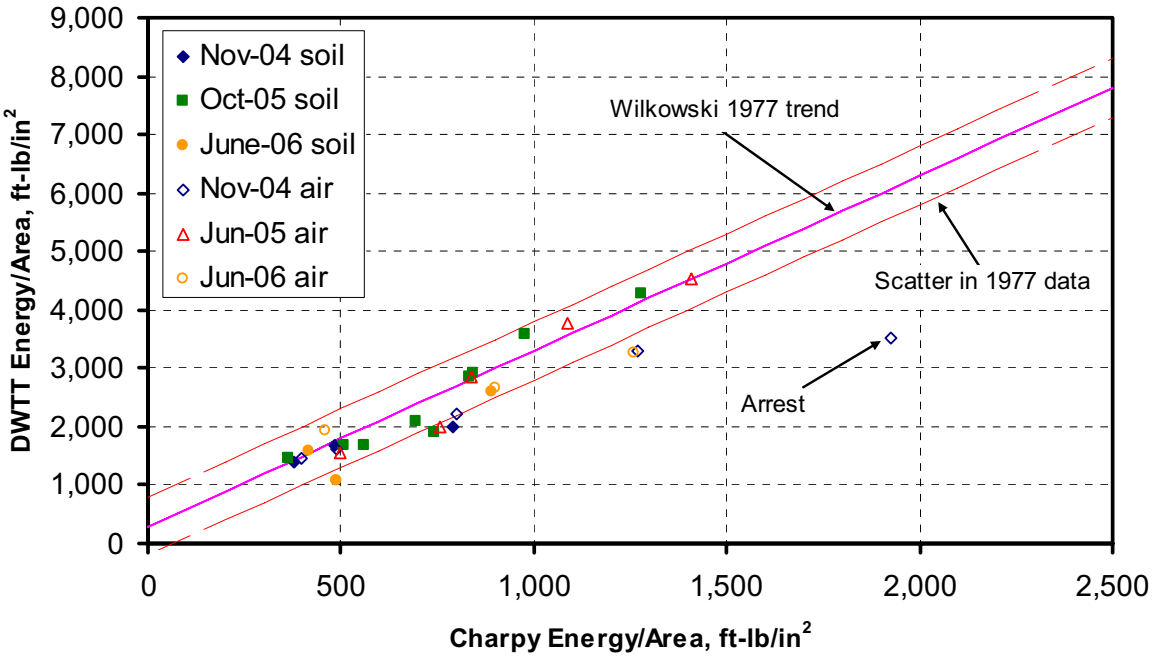

Figure 48 DWTT versus Charpy for the pipe joint with either propagation or arrest

4.3 Minimum Arrest Toughness Predictions

In this section of the report, a discussion of the predictions of minimum arrest toughness is presented. Included in this discussion are the effects of nonlinear behavior of the Charpy energy, the effects of backfill and pipe diameter on the minimum arrest Charpy energy, and a comparison of the JGA data with the X80 full-scale database experiments. A discussion of the effects of these parameters on fracture speed will be presented in the next section.

4.3.1 BTC predictions

Using the actual gas composition and test conditions measured directly before the experiment, predictions of minimum arrest Charpy energy were made using the Battelle Two-Curve approach. In these analyses, it was assumed that the GASDECOM program correctly predicts the decompression behavior and the original backfill coefficient correctly captures the effect of the backfill. The results of these analyses are shown in Table 6.

During the experiments, pressure transducers were used to measure the decompression behavior that occurred. As shown previously, these results can be compared to the GASDECOM predictions to verify the predictions. In all cases, the predictions from GASDECOM overpredicted the wave velocity as measured during the experiment, i.e., under predicted the decompressed pressure where the required toughness would be higher with this higher pressure level. For higher pressures, the GASDECOM predictions were very close to the measured wave speeds; however, as the decompression approached the plateau, the predictions became farther away from the measurements. Unfortunately, the arrest in all cases occurred at the knee of the decompression curve, which is a highly variable location. In many of the cases, the pressure transducer data was insufficient to obtain the decompression behavior at and below the plateau. In one case, June 2005, some data was available, and the results suggested that the GASDECOM

prediction could be offset by 10MPa to match the experimental behavior, see Figure 49. Using this offset value, the minimum arrest Charpy energy would be increased from 111J to 134J. However, in the other cases, the data was insufficient to make this calculation. As an example, the data in Figure 50, which is for the November 2004 experiment, shows no data points at or below the plateau. However, one pressure transducer suggested that the plateau stress was very close to that estimated by GASDECOM. This trend is very similar to that from the Alliance experiments [5], as shown in Figure 51. Because of the lack of data, the trends from the Alliance experiments, and the fact the arrest happens at the knee of the decompression behavior, the minimum arrest Charpy energy predictions using the Battelle Two-Curve approach were not modified for the difference between the actual and measured decompression.

Table 6 Minimum arrest Charpy energy predictions using the Battelle Two-Curve approach

Exp. Date	East				West			
	Backfill	CVN, J		BTC, J	Backfill	CVN, J		BTC, J
		Last Prop	Arrest			Last Prop	Arrest	
Nov 2004	1.5m sand	81	133	119	Air	214	324	141
June 2005	Air	135	164	111	Air	183	237	111
Oct 2005	1.0m sand	117	140	118	0.5m sand	142	164	118
June 2006	1.5m sand	70	150	92	Air	151	212	110

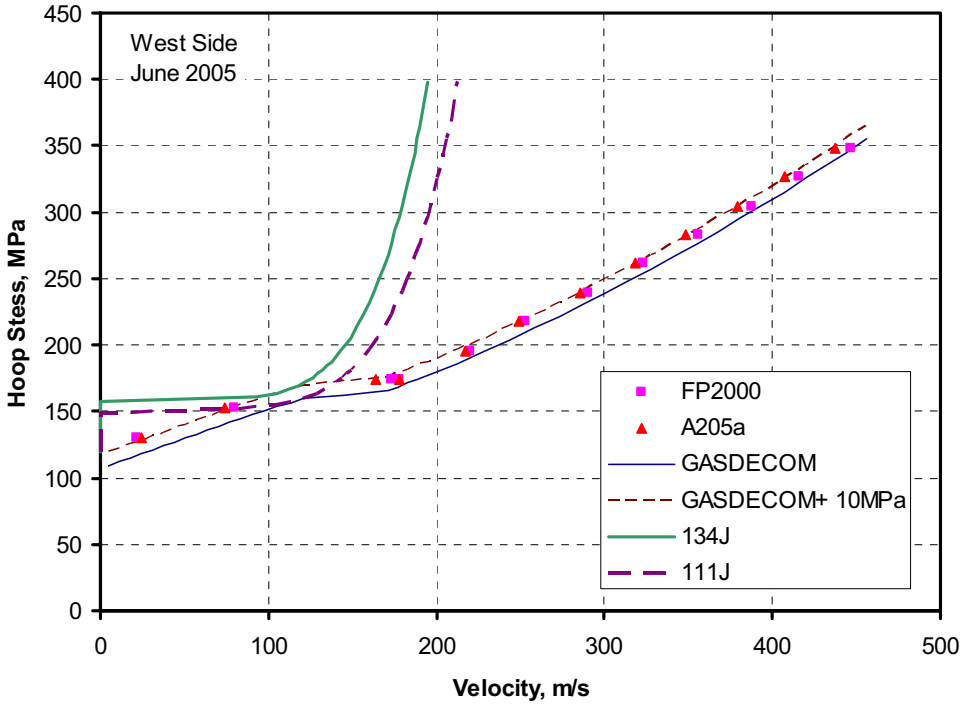

Figure 49 Effects of actual decompression behavior on minimum arrest Charpy energy predictions for June 2005 experiment

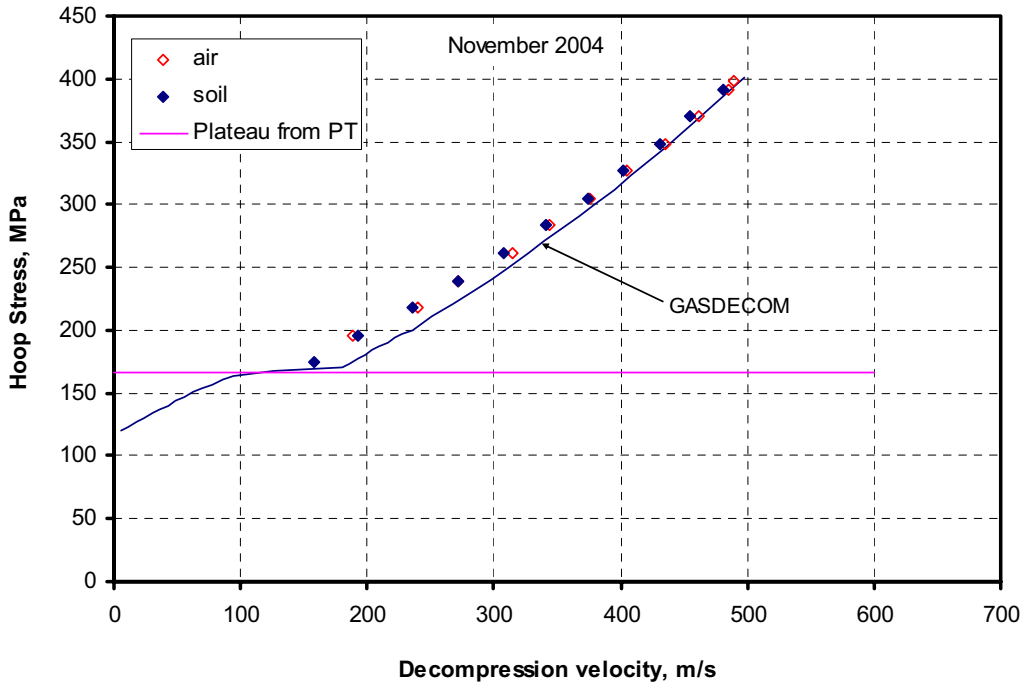

Figure 50 Measured versus predicted gas decompression for November 2004 experiment

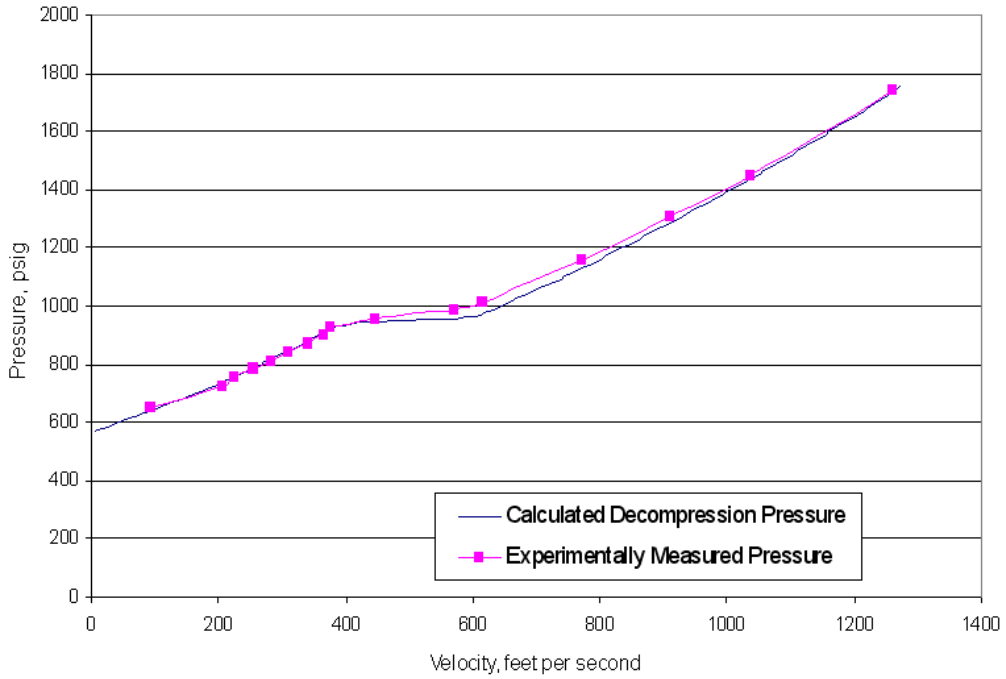

Figure 51 Actual versus measured decompression behavior from Alliance experiment [5]

4.3.2 Influence of backfill depth and pipe diameter on arrest Charpy energy

In order to determine if pipe diameter and backfill have an influence on the minimum arrest Charpy energy, a few more comments about the test results need to be made. First of all, the arrest pipe joints shown in Table 6 do not necessarily represent the minimum arrest Charpy energy. In fact, the minimum arrest Charpy energy may fall someplace between the Charpy energy of the last propagate joint and the arrest joint.

Table 7 Arrest length in arrest pipe joint

Exp Date	Arrest Length[n] in arrest joint, m	
	East	West
Nov 2004	4.4	6.3
June 2005	1.0	2.2
Oct 2005	0.95	9.8
June 2006	0.8	2.0

In order to make this estimation, data developed by Maxey was used. In Reference 8, Maxey investigated the arrest length as a function of increase in Charpy energy over the minimum arrest Charpy energy for cracks traveling at steady-state speeds, see Figure 52. This data was explained in detail and used in the Tokyo Gas program described in Reference 9.

[n] These arrest lengths were measured from the beginning of circumferential turning during arrest and not after complete arrest.

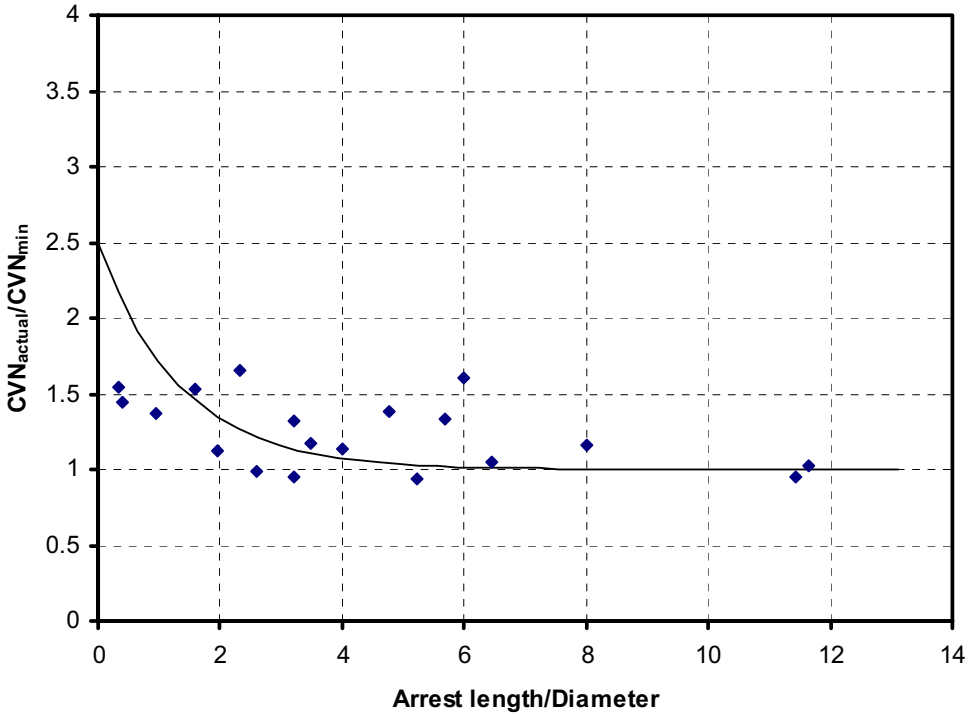

Figure 52 Increase in required Charpy energy as a function of arrest length away from the origin, data from Reference 8 (for 30-inch diameter, backfilled pipe)

Using these data and the arrest crack lengths from Table 7, the average or best predicted Charpy energy at arrest was calculated and is shown in Figure 53 and Figure 54. If the crack traveled almost the whole length of pipe, the arrest joint Charpy energy was used. The following is an example of the calculation using Figure 52:

- For the June 2006 experiment, on the sand backfilled side of the experiment, the crack arrested in a joint with a Charpy energy of 150J. However, it traveled 0.8m into that joint before turning circumferentially and arresting.
- Using the fact that the length at arrest over the diameter is equal to 1.31, and the trend shown in Figure 52, the increase in Charpy energy over the Battelle Two-curve prediction is 1.57.
- Reducing the Charpy energy in the arrest joint by the factor from Figure 52, gives an arrest Charpy energy of 96J.
- Since the predicted arrest Charpy energy was 92J, the factor for Figure 54 is 1.04.

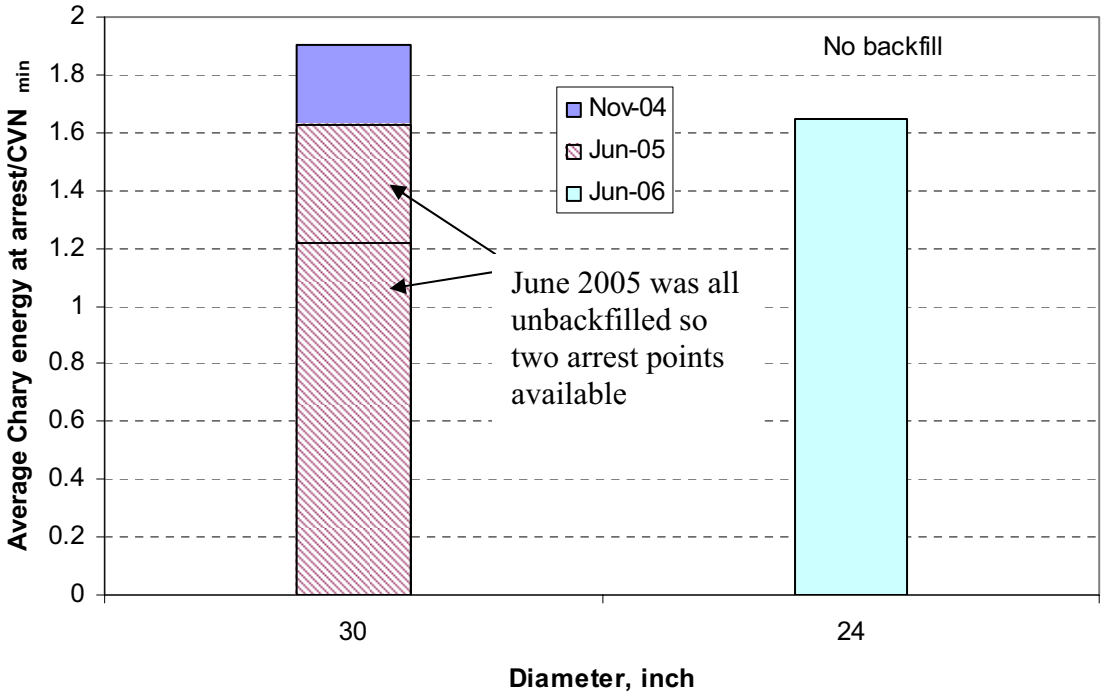

Figure 53 Effect of pipe diameter on arrest for unbackfilled pipe

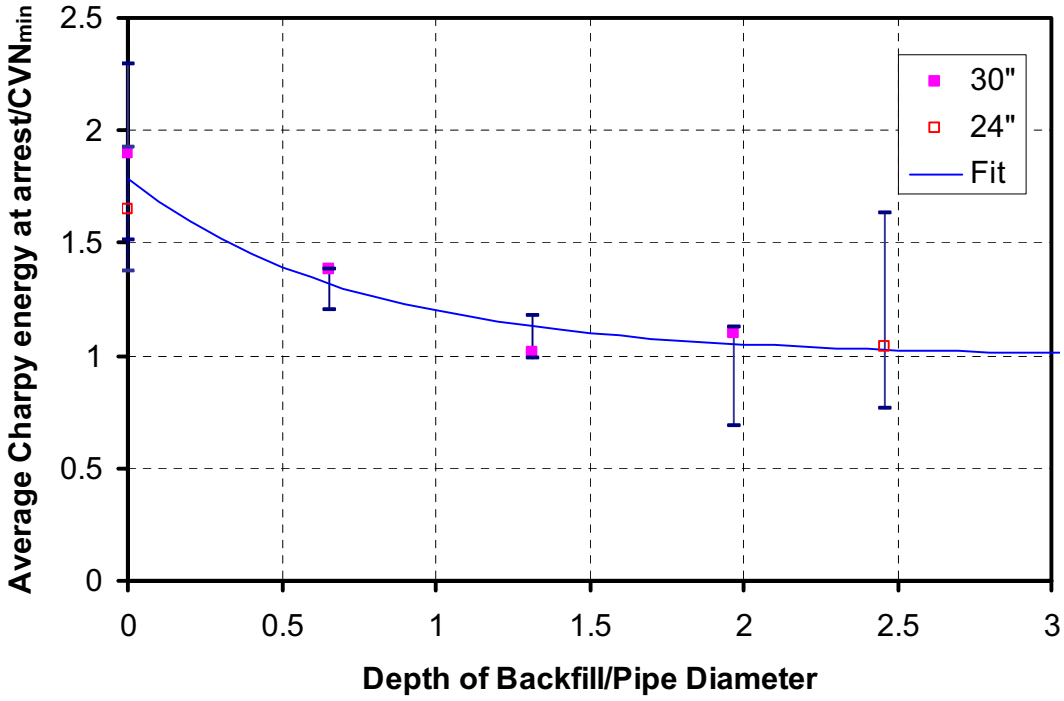

Figure 54 Effects of backfill depth and pipe diameter on minimum arrest Charpy energy

In Figure 53, only the unbackfilled experiments are shown. Note for the June 2005 experiment, two datapoints are shown (line at $CVN/CVN_{min}=1.2$) since both sides of this experiment were unbackfilled. For the 30-inch diameter pipe, the average Charpy energy at arrest ranged from 1.2

to 1.9 times (1.58 average) the calculated minimum arrest Charpy energy from the Battelle Two-Curve approach, while for the 24-inch diameter pipe, the average Charpy energy at arrest was 1.6 times the calculated minimum arrest Charpy energy from the Battelle Two-Curve approach. Even though there may be some non-linear effects on Charpy energy that may slightly lower these results, the trends indicate that there is not a significant effect of pipe diameter on the minimum arrest Charpy energy (once it is accounted for in the Battelle Two-Curve analysis).

The effect of backfill depth can be illustrated by plotting the same data for the backfilled side of the experiments, as shown in Figure 54. In this figure, the depth of the backfill was normalized by the pipe diameter. In addition, the data points represent the average or best predicted as described above, while the error bands represent the range of Charpy energy between the last propagate and arrest joints. A trend has formed which illustrates that there is significant relationship between the backfill depth and the minimum arrest Charpy energy. These data also suggest that for this soil, with its moisture, compaction and strength properties, a depth of 1.5*Diameter is needed for accurate predictions of the minimum Charpy energy at arrest.

4.3.3 Comparison with X80 database

The results from the JGA experiments can be compared directly to the X80 pipe results in the full-scale pipe experimental database at Emc[2]. A comparison of the JGA backfilled data with the X80 database materials is shown in Figure 55. In this figure, the X-axis is the actual Charpy energy, while the Y-axial is the predicted Charpy energy using the Battelle Two-Curve approach with no corrections. The solid symbols represent the arrest points, while the open symbols represent the propagate points. Using a best-fit analyses, while minimizing the error in the mispredictions [10], a statistical correction factor can be generated[o]. As shown in Figure 55, that factor is 1.167 for the JGA data and 1.457 for the X80 database experiment.

There are two factors that may explain the differences seen on this figure:

- The JGA experiments showed an effect of backfill depth, and there was at least one experiment where the backfill depth was small (0.5m), i.e., the Charpy energy at arrest predictions were affected by the backfill depth.
- Three of the propagate data points from the database experiments appear to be “outliers”. This point appears to be supported when the Charpy-DWTT data is examined as will be discussed next.

If these data points are removed from the regression fits, the best-fit correlations become close to the 1:1 fit as shown in Figure 56. Even with these points removed, the Battelle Two-Curve analysis predicts the JGA minimum arrest Charpy energy about 16% better than it does the full-scale database.

[o] As explained in Reference 10, a short computer code was written to minimize the error in the mispredicted arrest and propagate datapoints. The best-fit lines shown in the following figures does not evenly split the arrest/propagate data, but reduces the distance between the best-fit line and those data that are mispredicted by the best-fit line.

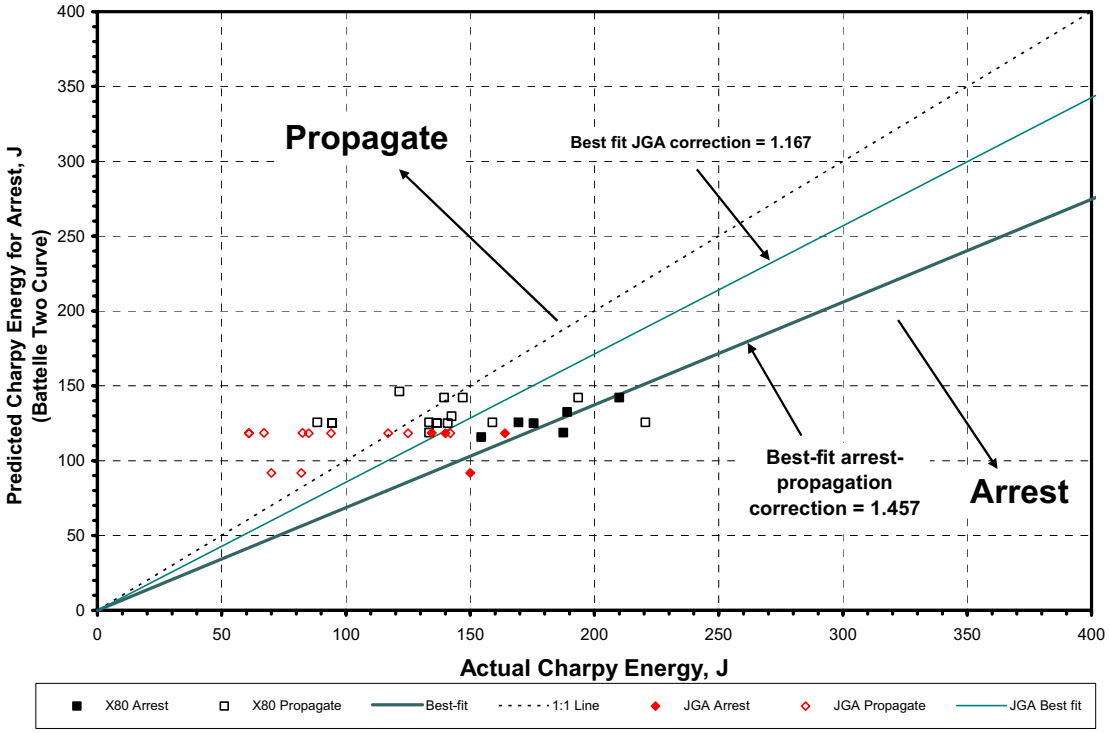

Figure 55 Comparison of X80 database experiment with backfilled JGA experiments

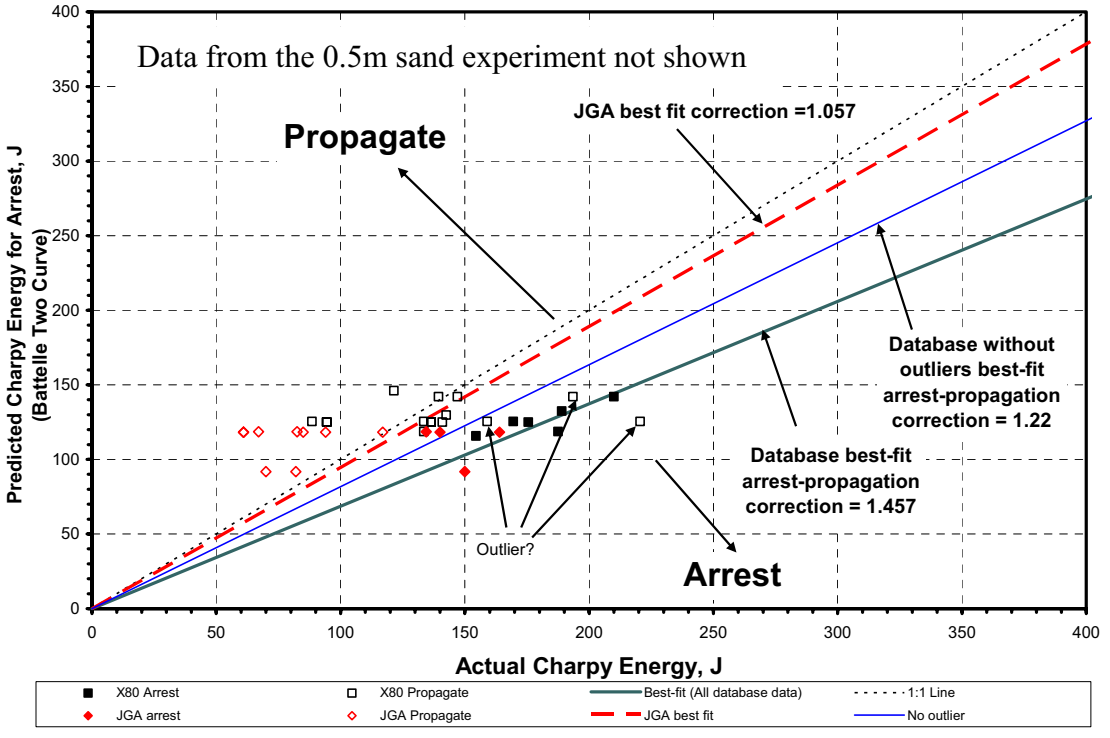

Figure 56 Comparison of JGA data with X80 database experimental results using Battelle Two-Curve predictions.

The difference in the behavior for the outlier datapoints in the Emc^2 database is explained by the relationship between the Charpy and PN-DWTT as shown in Figure 57. As shown in this figure, there are several datapoints that fall well below the Wilkowski 1977 relationship. In fact, the three solid square points that fall well below the 1977 trend line are the same datapoints labeled as "outliers" in Figure 56. This suggests that applicability of the Battelle Two-Curve approach is directly related to the materials conformance to the 1977 trend established by Wilkowski.

The best-fit line for the JGA data represents an equal division between the arrest and propagate data points. As shown in Figure 56, the 1:1 line also splits the arrest and propagate data, but some of the propagate data falls closer to this line than the arrest data. Therefore, even though the best-fit line is calculated to have a slope of 1.057, the 1:1 line also adequately represents the arrest/propagate boundary. The same trend is not true for the X80 database results, because of the Charpy to DWTT energy relationships for the materials used in those tests.

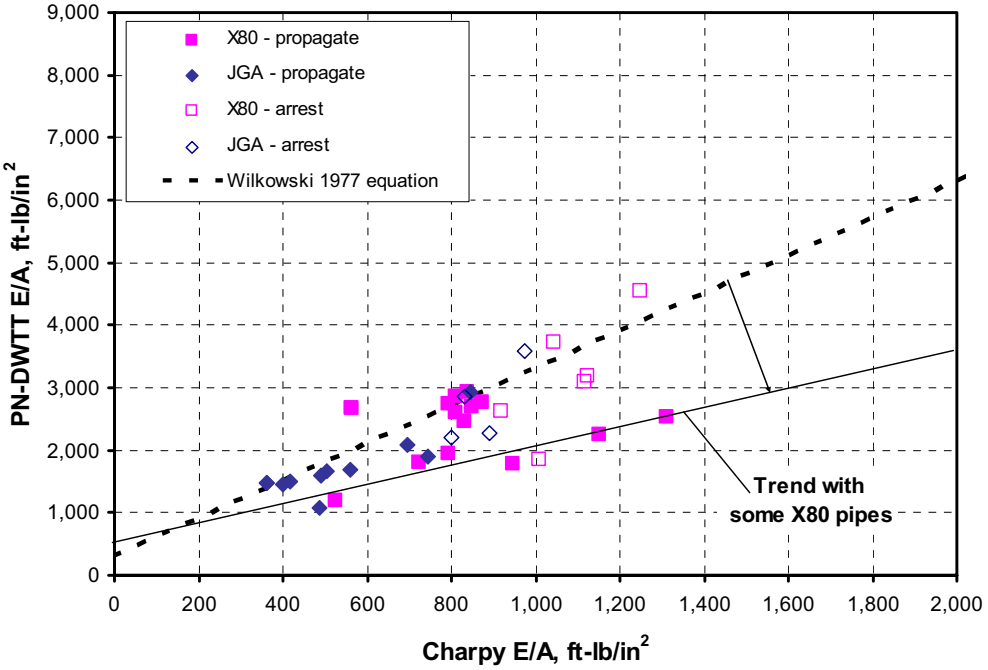

Figure 57 Comparison of PN-DWTT versus Charpy energies for the JGA and X80 database experiments

Another interesting point that may contribute to the difference between the JGA experiment and the X80 database experiment is the treatment of the backfill. In the old X80 experiments, there was no documentation about the moisture or compaction level of the soil. In fact, most of experiments were conducted without any organized compaction, i.e., no compaction equipment was used and frequently the soil itself naturally compacted under its own weight or some backhoe equipment may have been carefully driven over the soil (they were more concerned about damaging wires on the pipes). In addition, the level of backfill in the older experiments was not strictly maintained; however, typically, the backfill depth was approximately 30-36 inches in the U.S. It is suspected that the moisture content and compaction level affects the strength of the soil, and this strength is affecting the flap formation behind the crack. Therefore the strength of the soil is directly affecting the crack-driving force. In the JGA experiments, the

highly compacted sand (>90%) may lower the crack-driving force, and thus require less toughness for arrest. When compared to similar experiments with less compacted soil, it may show a higher minimum arrest Charpy energy. For higher grade piping, the pipelines are typically operating at higher pressures. The pressure pushing the flaps outward against the soil is greater for these pipelines than older pipelines with lower grade steels. Hence, the flap pressure relative to the soil strength is generally going up as the grade levels increases. Following this logic, it may be possible that the higher grade steels require more strength in the soil for the same arrest Charpy energy as the lower grade steels.

This effect can also be seen when the non-linear Charpy energy correction factors are investigated. The corrections investigated here are the Leis 2000 and Wilkowski 2002 analyses. Details of these analyses can be found in Reference 10. The comparison of the JGA data and the X80 database data using the Leis 2000 predictions is shown in Figure 58. As with the previous comparison, a fit with and without the X80 database "outliers" is shown. In all cases, the Leis 2000 approach underpredicts the X80 database experimental results by about 10%, while the approach overpredicts the JGA results by about 4%.

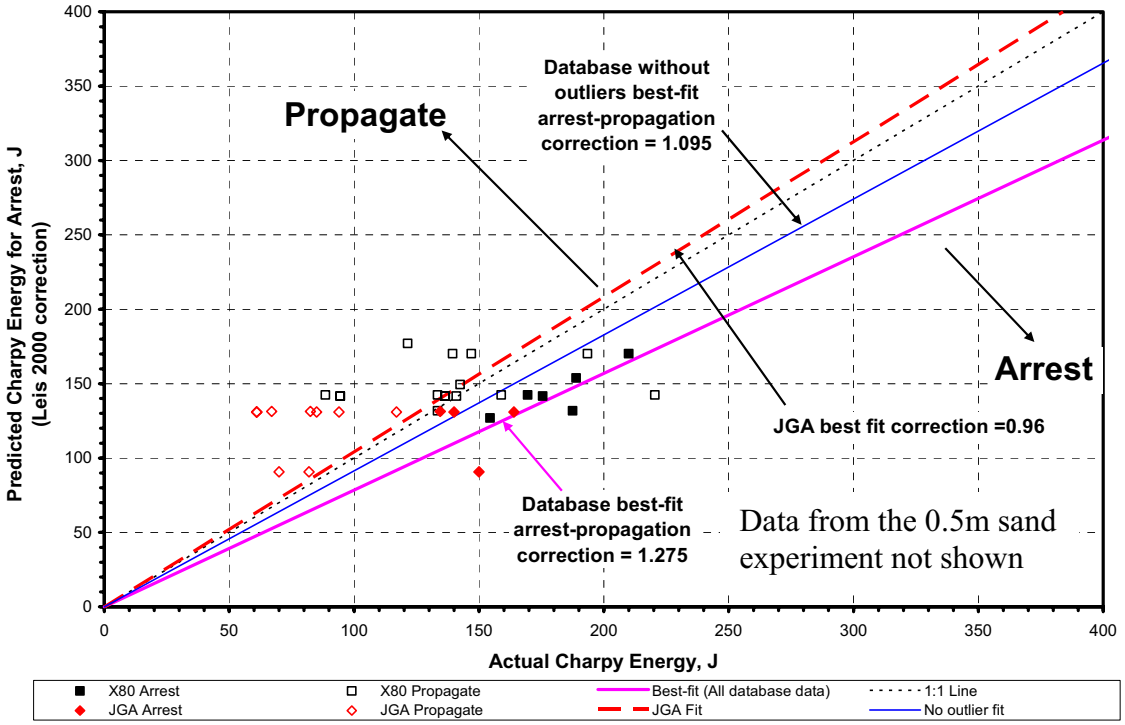

Figure 58 Comparison of JGA data with X80 database experimental results using the Leis 2000 predictions.

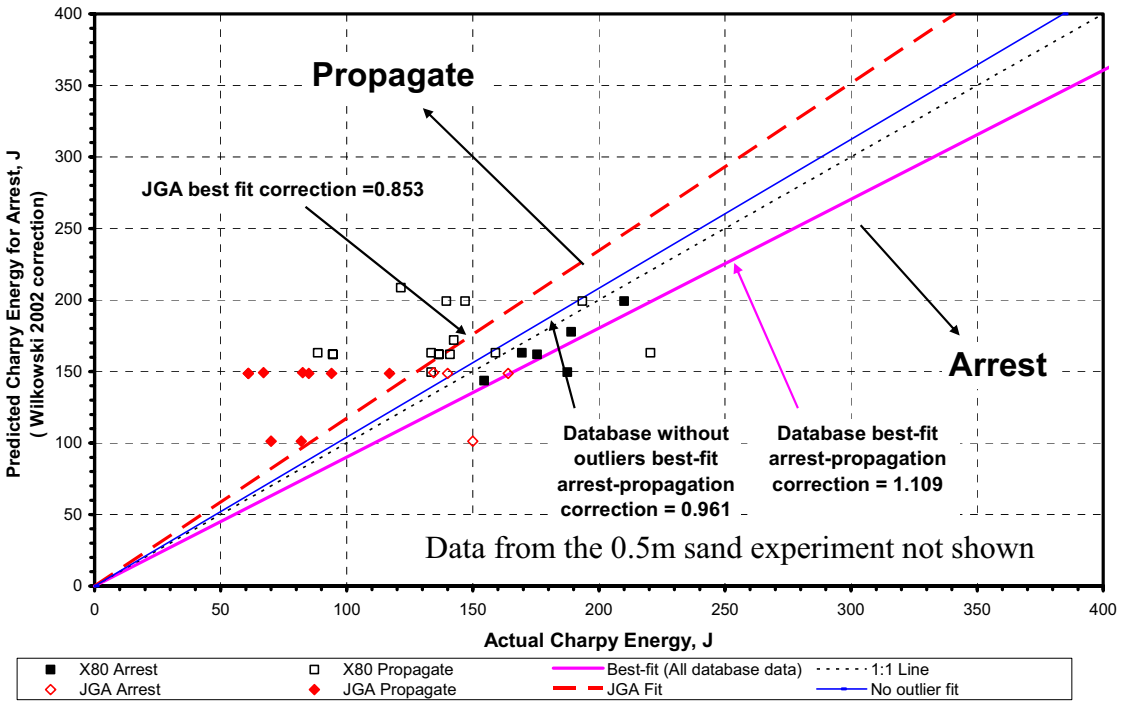

Figure 59 Comparison of JGA data with X80 database experimental results using the Wilkowski 2002 predictions.

In contrast, for the X80 database tests, the Wilkowski 2002 approach, see Figure 59, slightly overpredicts the Charpy energy for arrest when the outliers are removed. This method also severely overpredicts the JGA results (~15%). These results suggest that the non-linearity of the Charpy energy to actual toughness is not as prevalent in the JGA materials as it was in the X80 database materials.

This fact is further supported by the DWTT results shown in Figure 60. As discussed in Reference 10, the Wilkowski 2000 DWTT analysis showed no significant grade affect and was able to predict the actual DWTT arrest energy without any additional[p] correction factor, see Figure 61. When the JGA data is analyzed using this procedure, the results are overpredicted, see Figure 60. This difference may be due to the non-linear effects between the Charpy and DWTT energies, but is most likely an indication of the effects of the soil. As stated earlier, the highly compacted soil would reduce the crack driving force, and require less DWTT energy for arrest.

[p] The Wilkowski 2000 analysis with the small correction shown in Figure 61 is called the Wilkowski 2002 correction

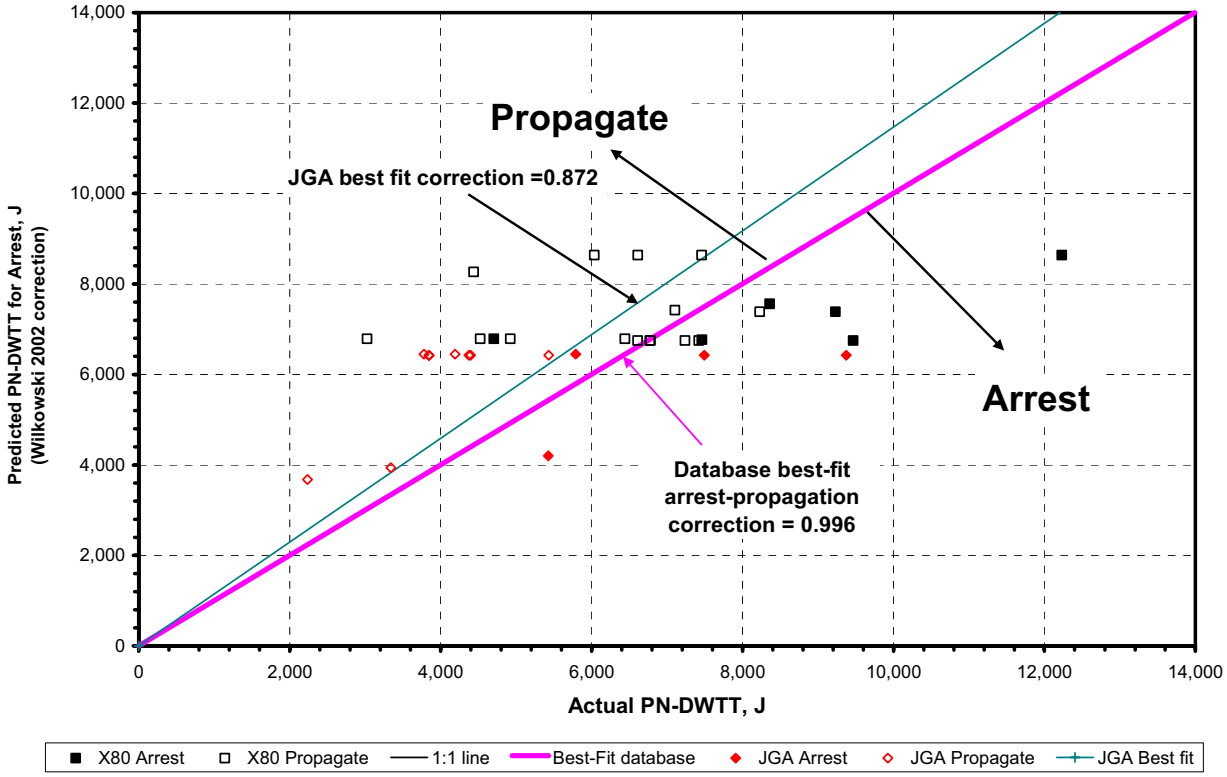

Figure 60 Comparison of JGA DWTT data with X80 database DWTT experimental results using the Wilkowski 2002 predictions

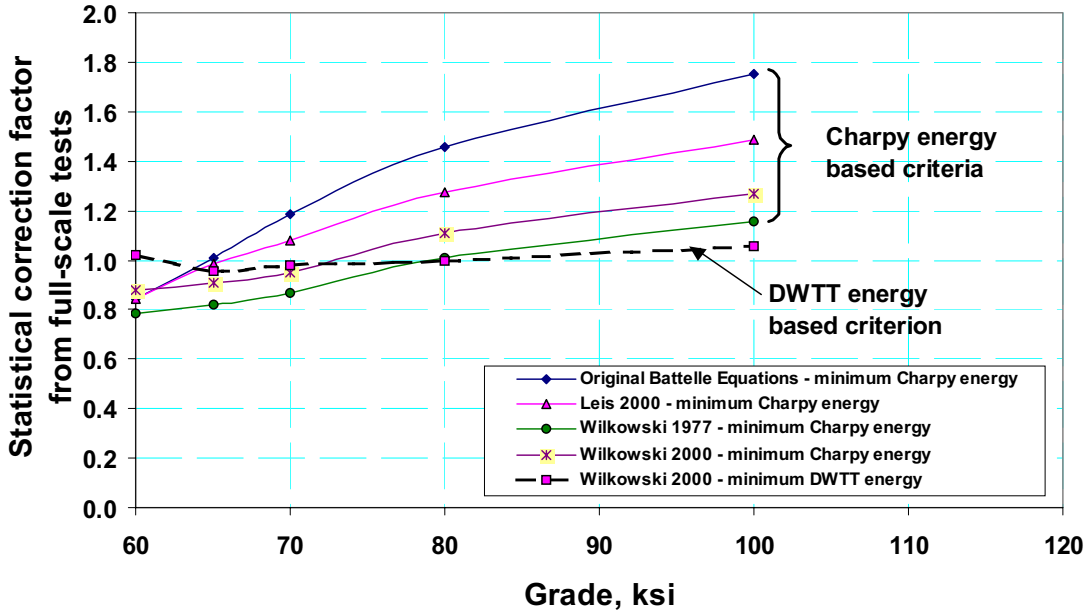

Figure 61 Summary of statistical comparisons of arrest-propagate boundary predictions with full-scale pipe burst test data [10]

These predictions may be suggesting that the X80 materials used in the JGA experiments do not have the non-linear Charpy behavior that is prevalent in other X80 experiments. As mentioned earlier, this behavior may be due to the effect of the soil on the fracture event, or may be due to the unique behavior of this material. In order to isolate the material response, it is suggested that additional material characterization experiments be conducted that will illustrate this non-linearity. Tokyo Gas is currently investigating this effect in a separate effort.

4.4 Fracture Speed Predictions

Since there appears to be an effect of the soil depth on the minimum arrest Charpy energy, the effect of the soil depth on the fracture speeds was invested as shown in Figure 62. In this figure, the x-axis is the steady-state fracture speed as measured in the experiment, and the y-axis is the fracture speed predicted using the Battelle Two-Curve approach *with no correction* and the original backfill coefficient. Along with the JGA data, the original Battelle data used by Maxey in the development of the original soil backfill coefficient is shown. The black solid line in this figure represents a perfect fit between the measured and predicted fracture speeds. Note that in the case of the 0.5m sand experiment; only one datapoint was available for this study. This limitation adds uncertainty to the results of this comparison.

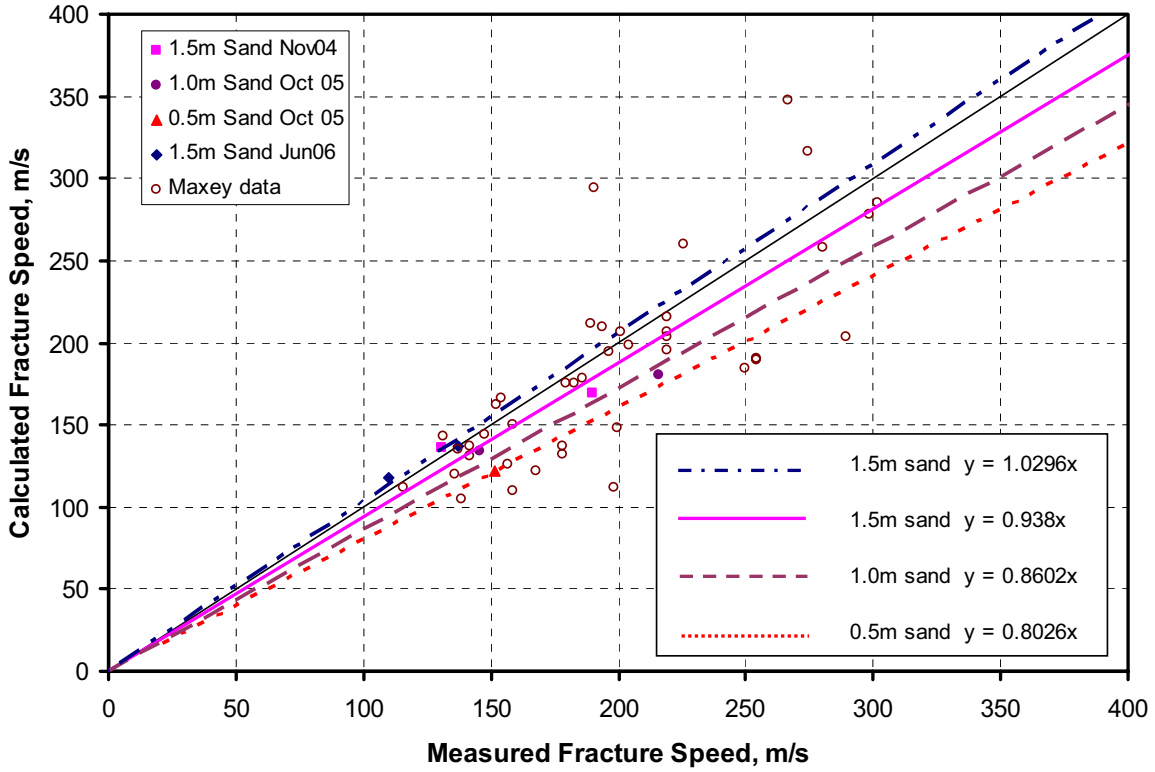

Figure 62 Fracture speed predictions for the JGA experiments

As shown in this figure, the Maxey data is highly scattered, but is centered on the 1:1 line. The JGA data either fall on the 1:1 line or slightly below it, suggesting that the measured fracture speed is higher than that predicted with the original backfill coefficient. However, the JGA data

falls within the scatter of the Maxey data. This data suggests that the slope of the calculated versus measured fracture speed may be driven by the backfill depth. This point will be investigated in the next section of the report.

4.4.1 Effects of backfill depth and pipe diameter

If the slopes of the curves shown in Figure 62 are plotted against the ratio of the depth of the backfill and the pipe diameter, a clear trend is formed as shown in Figure 63. In this figure, the unbackfilled cases were reanalyzed with the original backfill coefficient so that a common analysis was used for all data points.

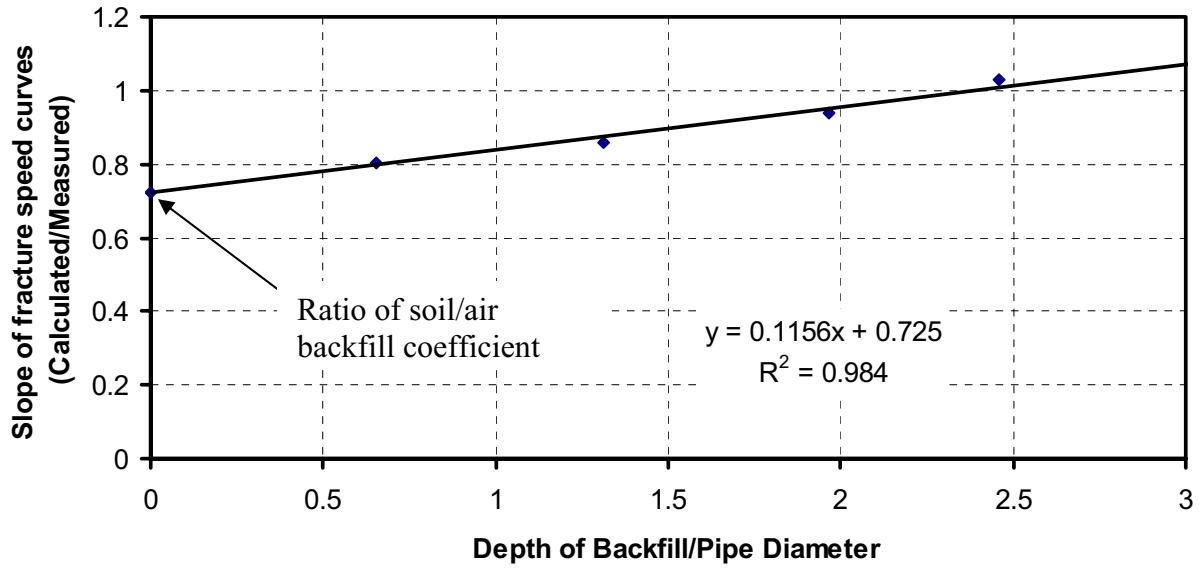

Figure 63 Relationship between the fracture speed and the depth of backfill from the JGA experiments

This figure illustrates an increase in fracture speed slope as the depth of backfill increases. This figure also suggests that when using the original soil backfill coefficient, the calculated fracture speeds (with the original backfill coefficient) will under predict the actual fracture speeds until the backfill depth is between 2 and 2.5 times the diameter of the pipe.

4.4.2 Effects of moisture content

Using the trends in Figure 63, the effects of the backfill depth on the fracture speed can be accounted for in the analysis. If the adjusted data is plotted against moisture content, the fracture speeds show a slight dependence on moisture content as shown in Figure 64. In this figure, the y-axis is the normalized fracture velocity predicted by the Battelle Two-Curve approach with the original backfill coefficient and the correction to the fracture speeds from Figure 63. The dashed line represents the trends from the Mojave experiments (see Part II) which used different types of soil, with different moisture contents, but the same level of backfill depth, i.e., backfill depth/pipe diameter = 3. The trends suggest a slightly decreasing fracture velocity with increasing moisture content, but a regression through the available JGA experiment shows a minimal effect on the fracture speed for the moisture contents used in the JGA experiments. This may be due to the fact that the strength of the sand is not highly sensitive to the moisture

content, while the silts and clays used in the Mojave experiments [11, and Part II] showed an increasing strength with increased moisture content.

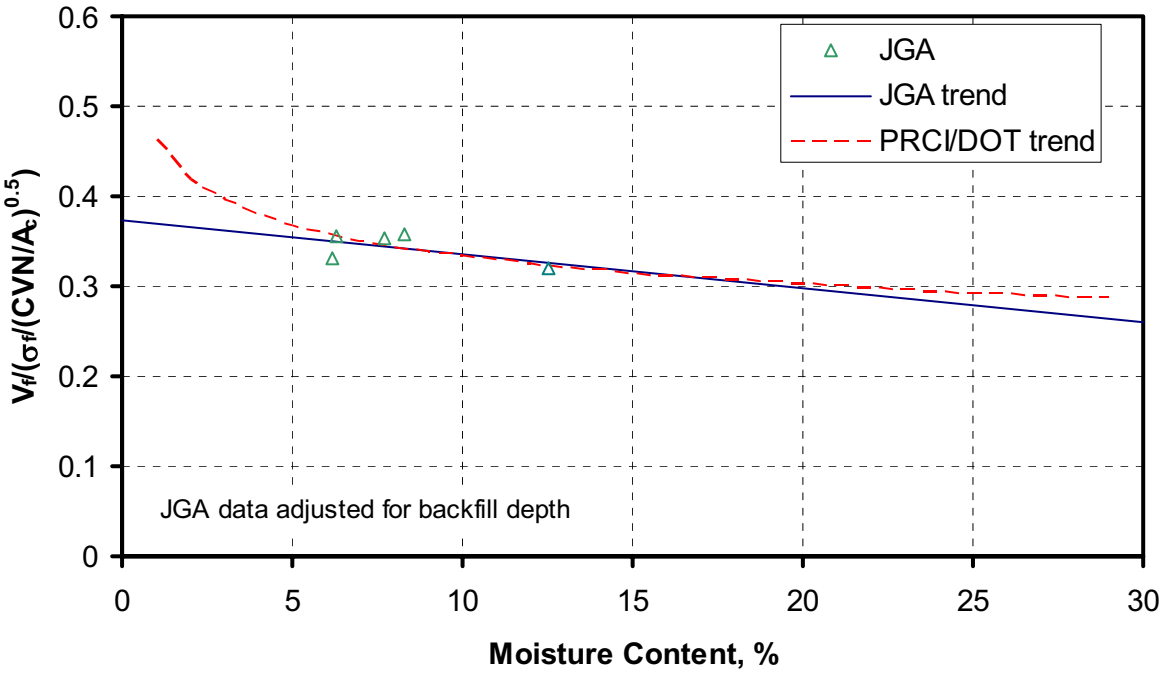

Figure 64 Effect of moisture content on fracture speeds

5 MODIFICATIONS TO THE BACKFILL COEFFICIENT

The results from these experiments suggest that a modification to the backfill coefficient may be in order to account for the depth and strength of the backfill. Some of the trends from the JGA experiments that provide evidence for this modification include:

- Depth of backfill. There appears to be a correlation between the depth of the backfill and the minimum arrest toughness and the fracture speeds from these experiments. When the backfill approaches two times the diameter of the pipe, both the minimum arrest Charpy energy and the fracture velocity are accurately predicted with the original Battelle Two-curve approach and the original backfill coefficient. Although not illustrated in these experiments, intuitively it stands to reason that if the backfill depth is greater than 2.5 times the diameter, the fracture velocities would be overpredicted using the original backfill coefficient.
- Soil properties. Typically, X80 pipe materials need a correction to the Battelle Two-Curve analysis to account for the grade effects and a non-linear relationship that occurs between the propagation resistance and the Charpy energy for this toughness level (>100J). For the X80 database, when the outliers that do not follow the Wilkowski 1977 relationship were eliminated, that correction factor was 1.22. The JGA results suggest a correction factor of 1.06. Note that the 1.06 was developed from a best fit of the available data. Visual inspection of the data from Figure 56 shows that the 1:1 line separates the arrest and propagate data points for these experiments. In addition, when the Leis 2000 and Wilkowski 2002 non-linear corrections are applied to the JGA data, the

predictions all overestimate the Charpy energy at arrest. This data suggests that either the material response is different than the database materials, or the soil conditions are affecting the minimum arrest Charpy energy predictions. If the possibility of material differences is eliminated by additional material testing, then the soil compaction level, i.e., strength, or the backfill depth may be causing the reduction in the multiplier. As stated earlier, the compaction level of the sand in the JGA experiments was highly controlled, i.e., compaction was always greater than 90% on every lift of soil added. In past tests, the compaction was not controlled and frequently was only compacted under the natural weight of the soil. In some cases, backhoes were driven over the buried pipe, therefore there was some unknown level of compaction.

In addition, the results from the Mojave [11 and Part II] study on backfill suggest:

- For a set of 6-inch diameter Mojave experiments with very controlled backfill conditions using soils ranging from fine grain sand to cohesive clays, the fracture speeds measured appear to be a function of both the moisture content of the soil and the strength of the soil. The strength of the soil was measured using direct shear and unconfined compression experiments at standard ASTM testing rates for applicable soils.
- The effect of backfill depth was not investigated, but held constant at a depth-to-diameter ratio of three.

As explained in Part I of this report, the strength of sand is not highly variable and small in magnitude, therefore only the effect of backfill depth can be considered.

5.1 Possible Modification to Backfill Coefficient

Using the original Battelle Two-Curve approach, the experimental data from the JGA experiments, and that used by Maxey in developing the original backfill coefficient can be plotted as shown in Figure 65. In this figure, the x-axis represents the fracture velocity normalized by the flow strength and Charpy energy of the pipe. The y-axis represents the ratio of the decompressed stress at the crack tip and the arrest stress. Also shown in this figure are the fracture velocity curves with the original soil backfill coefficient and the air coefficient developed by Maxey. The square and triangular data points represent the original data used by Maxey in developing these backfill coefficients. The circle and diamond data points represent the JGA data from this investigation. Any data whose Charpy energy fell above 100J were eliminated from this plot in order to rule out any influence of the non-linear behavior that may exist between the propagation energy and the Charpy energy.

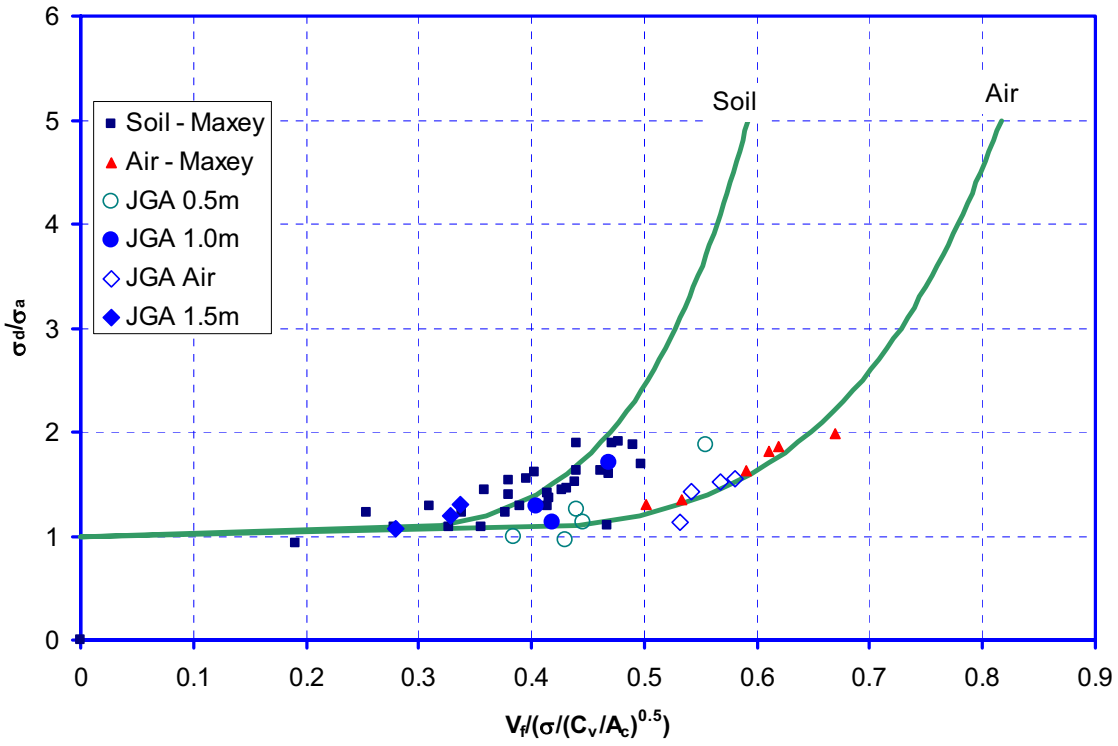

Figure 65 Fracture velocity as a function of decompressed stress for JGA and original Battelle pipe experiments

The data from this figure shows that when the backfill depth of the JGA experiments was 1.0 or 1.5 m, the original soil backfill coefficient was adequate at predicting the behavior. For the unbackfilled cases, the air backfill coefficient was also sufficient to describe the behavior. However, for the 0.5m backfill case, the trends fall between that described by the soil backfill coefficient and the air backfill coefficient.

Using the trend in Figure 63, the fracture velocities were modified, and replotted in Figure 66. In this figure, it was assumed that the backfill depth for the original soil experiments used by Maxey was two pipe diameters[q]. As illustrated in this figure, all of the data, including the no backfilled cases, collapse onto one curve.

[q] This fact is under question. The data record books for these older experiments do not explicitly state the backfill depth for most of the experiments. From conversations with Bob Eiber, it is suspected that this number may be more like 1-1.5*diameter. This data is further investigated in the main body of this report.

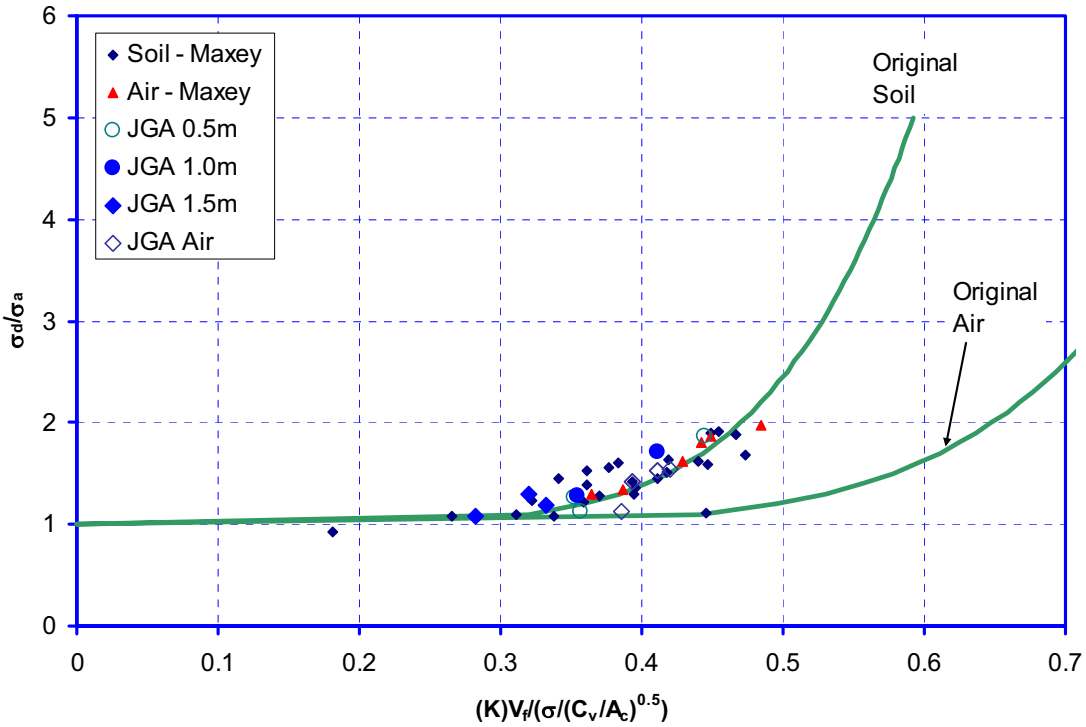

Figure 66 Modified fracture velocity[r] as a function of decompressed stress for JGA and original Battelle pipe experiments

However, making the assumption that the data used by Maxey had one pipe diameter of backfill, shifts its behavior to the left in Figure 66, which indicates that the original backfill coefficient would have over predicted the fracture velocity in those cases. As shown in Figure 62, using the original soil backfill correlation, on average, the predictions of fracture speed for those older experiments is very close to the measured speeds. However, the data is highly scattered, and may be due to both backfill strength and depth. This point is further investigated in the main body of this report.

6 SUMMARY OF TEST RESULTS

In this part of the report, the details of the four full-scale pipe experiments conducted by the JGA at the FORCE technology test site were presented. This series of experiments investigated the effects of sand backfill with different depths and moisture contents on the minimum arrest toughness and fracture velocities. In addition, 30-inch and 24-inch diameter pipes were tested to investigate the effects of pipe diameter on these critical parameters. The results suggested that both the minimum arrest toughness and the fracture velocities are influenced by the depth of the backfill, and for fracture speeds that trend appears linear. However, no significant influence of pipe diameter was noticed for the pipe sizes tested in this series of experiments. Finally, soil experiments conducted illustrated that non-cohesive sands do not have significant strength and thus the moisture content does not change the fracture speeds appreciably in these experiments.

When the results from these experiments were compared with the experimental full-scale database for X80 materials, the results suggested that the correction factor to the Battelle Two-

[r] The K in the x-axis equation represents the fit from Figure 63.

curve analysis suggested by the database is too severe for the experiments in this program., i.e., these experiments had a lower correction factor. These differences may be due to either a different material response or the influence of the highly controlled/compacted sand in the experiments. The currently available material data for the JGA pipe suggests that the material is similar to the historical data, but Tokyo Gas plans to conduct fully-instrumented DWTT experiments on the materials used in these experiments to address this concern.

Using the trends of backfill depth and fracture speed, a correction to the backfill coefficient was made to predict the JGA experiments. With this correction, all of the JGA data fall on a similar trend, which compares closely to the Maxey data assuming a certain backfill depth. Continued analysis of the Maxey data and development of backfill coefficient modification is given in Part I of this report.

7 REFERENCES

1 Jacobsen, D., Christensen, C., Nielsen, H.P., Jacobsen, D., and Ludwigsen, P.B., "Full-scale Ultra-high Pressure Gas Burst test of 30-inch X80 Pipe – Test Report," Final report to JGA from FORCE Technology, 12-22-2004.

2 AISI Technical Report, "Running Shear Fracture in Line Pipe," Subcommittee of Large Diameter Pipe Producers, September 1, 1974.

3 Ludwigsen, P.B and Nielsen, H.P., "Full-Scale Ultra-High Pressure Gas Burst Test of 30-inch X80 Pipe – Test Report," Final report to JGA from FORCE Technology, 06-30-2005.

4 Schmidt, M., Nielsen, H.P., and Ludwigsen, P.B., "Full-Scale Ultra-High Pressure Gas Burst Test of 30-inch X80 Pipe – Test Report," Final report to JGA from FORCE Technology, 11-3-2005.

5 Eiber, R.J., Carlson, L., and Leis, B., "Fracture Control for the Alliance Pipeline," Proceedings of the 2000 International Pipeline Conference, Calgary, Alberta, Canada, October 1-5, 2000, pp. 267-277.

6 Ludwigsen, P.B and Nielsen, H.P., "Full-Scale Ultra-High Pressure Gas Burst Test of 24-inch X80 Pipe – Test Report," Final report to JGA from FORCE Technology, 07/07/2006.

7 Wilkowski, G. M., Maxey, W. A., and Eiber, R.J., "Use of a Brittle Notch DWTT Specimen to Predict Fracture Characteristics of Line Pipe Steels," presented at the ASME 1977 Energy Technology Conference, Houston, Texas, Paper 77-Pet-21, September 18-22, 1977.

8 W. A. Maxey, "Fracture Propagation" Paper J, *5th Symposium on Line Pipe Research*, American Gas Association Catalogue No. L30174, Nov. 1974.

9 Rudland, D.L., and Wilkowski, G., "Determination Of Conditional Probability Of Propagation Greater Than 12m For The Tokyo Gas Chiba X60 Pipeline," Final report to Tokyo Gas, December 2002.

10 Wilkowski, G.M., Rudland, D.L., Xu, H., and Sanderson, N., "Effect of Grade on Ductile Fracture Arrest Criteria for Gas Pipelines," PC2006-10350, Proceedings of IPC 2006, 2006 International Pipeline Conference, September 25-29, 2006, Calgary, Alberta, Canada

11 D. Rudland, G. Wilkowski, and B. Rothwell, "The Effects of Soil Properties on the Fracture Speeds of Propagating Axial Cracks in Line Pipe Steels," IPC2006-10086, Proceedings of IPC 2006, 2006 International Pipeline Conference, September 25-29, 2006, Calgary, Alberta, Canada